

Proceedings of the 2004 NASA/ONR Circulation Control Workshop

Edited by
Gregory S. Jones
Langley Research Center, Hampton, Virginia

Ronald D. Joslin
Office of Naval Research, Arlington, Virginia



The NASA STI Program Office . . . in Profile

Since its founding, NASA has been dedicated to the advancement of aeronautics and space science. The NASA Scientific and Technical Information (STI) Program Office plays a key part in helping NASA maintain this important role.

The NASA STI Program Office is operated by Langley Research Center, the lead center for NASA's scientific and technical information. The NASA STI Program Office provides access to the NASA STI Database, the largest collection of aeronautical and space science STI in the world. The Program Office is also NASA's institutional mechanism for disseminating the results of its research and development activities. These results are published by NASA in the NASA STI Report Series, which includes the following report types:

- **TECHNICAL PUBLICATION.** Reports of completed research or a major significant phase of research that present the results of NASA programs and include extensive data or theoretical analysis. Includes compilations of significant scientific and technical data and information deemed to be of continuing reference value. NASA counterpart of peer-reviewed formal professional papers, but having less stringent limitations on manuscript length and extent of graphic presentations.
- **TECHNICAL MEMORANDUM.** Scientific and technical findings that are preliminary or of specialized interest, e.g., quick release reports, working papers, and bibliographies that contain minimal annotation. Does not contain extensive analysis.
- **CONTRACTOR REPORT.** Scientific and technical findings by NASA-sponsored contractors and grantees.

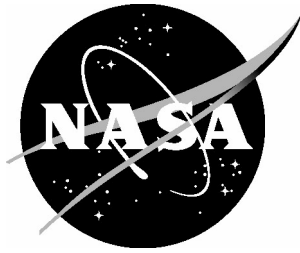
- **CONFERENCE PUBLICATION.** Collected papers from scientific and technical conferences, symposia, seminars, or other meetings sponsored or co-sponsored by NASA.
- **SPECIAL PUBLICATION.** Scientific, technical, or historical information from NASA programs, projects, and missions, often concerned with subjects having substantial public interest.
- **TECHNICAL TRANSLATION.** English-language translations of foreign scientific and technical material pertinent to NASA's mission.

Specialized services that complement the STI Program Office's diverse offerings include creating custom thesauri, building customized databases, organizing and publishing research results ... even providing videos.

For more information about the NASA STI Program Office, see the following:

- Access the NASA STI Program Home Page at [*http://www.sti.nasa.gov*](http://www.sti.nasa.gov)
- E-mail your question via the Internet to [*help@sti.nasa.gov*](mailto:help@sti.nasa.gov)
- Fax your question to the NASA STI Help Desk at (301) 621-0134
- Phone the NASA STI Help Desk at (301) 621-0390
- Write to:
NASA STI Help Desk
NASA Center for AeroSpace Information
7121 Standard Drive
Hanover, MD 21076-1320

NASA/CP-2005-213509/PT1



Proceedings of the 2004 NASA/ONR Circulation Control Workshop

Edited by
Gregory S. Jones
Langley Research Center, Hampton, Virginia

Ronald D. Joslin
Office of Naval Research, Arlington, Virginia

Proceedings of a workshop sponsored by the National Aeronautics and
Space Administration and Office of Naval Research, Arlington, Virginia
and held at Radisson-Hampton, Hampton, Virginia
March 16 – 17, 2004

National Aeronautics and
Space Administration

Langley Research Center
Hampton, Virginia 23681-2199

June 2005

Available from:

NASA Center for AeroSpace Information (CASI)
7121 Standard Drive
Hanover, MD 21076-1320
(301) 621-0390

National Technical Information Service (NTIS)
5285 Port Royal Road
Springfield, VA 22161-2171
(703) 605-6000

TABLE OF CONTENTS

Part 1

Introduction	vii
--------------------	-----

SESSION 1: CC APPLICATIONS

1 – Circulation Control in NASA’s Vehicle Systems Program.....	1
Paul Rich, Bob McKinley, and Gregory S. Jones – NASA Langley Research Center	
2 – Overview of Circulation Control Pneumatic Aerodynamics: Blown Force and Moment Augmentation and Modification as Applied Primarily to Fixed Wing Aircraft	37
Robert J. Englar – Georgia Tech Research Institute	
3 – Experimental Development and Evaluation of Pneumatic Powered-Lift Super-STOL	101
Robert J. Englar – Georgia Tech Research Institute Bryan A. Campbell – NASA Langley Research Center	

SESSION 2: NCCR AIRFOIL CFD TEST CASE

4 – Full Reynolds Stress Modeling of Circulation Control Airfoils.....	141
Peter A. Chang, Joseph F. Slomski, Thomas A. Marino, Michael P. Ebert and Jane Abramson– Naval Surface Warfare Center; Carderock Division	
5 – RANS and Detached-Eddy Simulation of the NCCR Airfoil.....	167
Eric G. Paterson and Warren J. Baker – Pennsylvania State University	
6 – Numerical Analysis of Circulation Control on a NCCR 1510-7607N Airfoil using RANS Models	197
Aroon K. Viswanathan and Danesh K. Tafti – Virginia Polytechnic Institute and State University	

SESSION 3: CFD MODELING

7 – Aspects of Numerical Simulation of Circulation Control Airfoils.....	227
Charlie C. Swanson, Chris L. Rumsey and Scott G. Anders – NASA Langley Research Center	

8 – Role of Turbulence Modeling in Flow Prediction of Circulation Control Airfoils ...275

Greg McGowan, Ashok Gopalarathnam, X. Xiao and Hassan A. Hassan – North Carolina State University

9 – Computational Evaluation of the Steady and Pulsed Jet Effects on the Performance of a Circulation Control Wing Section295

Yi Liu, Lakshmi N. Sankar, Robert J. Englar, Krishan K. Ahuja and R. Gaeta – Georgia Institute of Technology

10 – Investigation of Turbulent Coanda Wall Jets Using DNS and RANS.....337

PeteH. Fasel, A. Gross and S. Wernz– University of Arizona

SESSION 4: EXPERIMENTS

11 – Some Circulation Control Experiments369

D. Cerchie, L. Cullen, J. Goldstein, G. Han, L. Taubert and I. Wygnanski – University of Arizona

E. Halfon – Tel Aviv University

L. Troune – L'Ecole Nationale Supérieure de Mécanique et d'Aérotechnique

12 – A Wind Tunnel Experiment for Trailing Edge Circulation Control on a 6% 2-D Airfoil up to Transonic Mach Numbers407

Mike G. Alexander, Scott G. Anders and Stuart K. Johnson – NASA Langley Research Center

13 – Experimental Investigation of a Morphing Nacelle Ducted Fan435

Shayne Kondor – Georgia Tech Research Institute

Mark Moore – NASA Langley Research Center

14 – A Novel Airfoil Circulation Augment Flow Control Method Using Co-Flow Jet...469

Ge-Cheng Zha and Craig Paxton – University of Miami

15 – Noise Reduction Through Circulation Control.....497

Scott E. Munro – Naval Air Warfare Center; Weapons Division

Krish K. Ahuja and Robert J. Englar – Georgia Tech Research Institute

Part 2

Introduction	vii
--------------------	-----

SESSION 5: APPLICATIONS AND SYSTEMS

16 – Circulation Control – Issues for NAVAL Applications	553
---	------------

Ron Joslin – Office of Naval Research

17 – Exploratory Investigations of Circulation Control Technology: Overview for Period 1987–2003 at NSWCCD.....	577
--	------------

Robin Imber – Naval Surface Warfare Center; Carderock Division

18 – Why Have Only Two Circulation-Controlled STOL Aircraft Been Built and Flown in Years 1974–2004	603
--	------------

John Loth – West Virginia University

19 – Wake Vortex Wingtip-Turbine Powered Circulation Control High-Lift System... 641	
---	--

Mark D. Moore – NASA Langley Research Center

20 – The Use of Circulation Control for Flight Control	657
---	------------

Steven P. Frith and Norman J. Wood – University of Manchester, United Kingdom

21 – Time-Accurate Simulations of Synthetic Jet-Based Flow Control for a Spinning Axisymmetric Body	689
--	------------

Jubaraj Sahu – U.S. Army Research Laboratory

22 – Design and Fabrication of Circulation Control Test Articles.....	723
--	------------

Kenneth P. Burdges – Novatek, Inc.

23 – Selected Topics Related to Operational Applications of Circulation Control	743
--	------------

Ernest O. Rogers and Jane Abramson – Naval Surface Warfare Center; Carderock Division

24 – From Concept to Production of the of the Coanda Driven Exhaust Deflector for the V-22	771
---	------------

Thomas Wood – Bell Helicopter

25 – Simulation of Steady Circulation Control for the General Aviation Circulation Control (GACC) Wing	791
---	------------

Warren J. Baker and Eric G. Paterson – Pennsylvania State University

26 – CFD Analysis of Circulation Control Airfoils Using Fluent	813
Gregory McGowan and Ashok Gopalarathnam – North Carolina State University	
27 – Pneumatic Flap for a 2D Circulation Control Airfoil, Steady and Pulsed	845
Gregory S. Jones – NASA Langley Research Center	
28 – Experimental and Computational Investigation into the use of the Coanda Effect on the Bell A821201 Airfoil.....	889
Gerald M. Angle, Wade W. Huebsch and James E. Smith – West Virginia University	
29 – Low-Cost, High-Quality Wind Tunnel Testing of a 30% Elliptical Circulation Control Airfoil at Low Blowing Levels for Application to Wind Turbines	911
Frederick J. Kelso, Kenneth L. Laubsch and Rikard K. Haraldsson – AdvanTek International	
30 – Commercial Applications of Circulation Control (Wind Turbines, Pumps, Aerosol Sprays, Vacuum Cleaners, etc.)	921
Terence R. Day – Vortex Dynamics Pty Ltd	
31 – Measurement and Analysis of Circulation Control Airfoils	947
F. Kevin Owen – Complere, Inc. Andrew K. Owen – Oxford University	
32 – Application of Pneumatic Aerodynamic Technology to Improve Drag Reduction, Performance, Safety, and Control of Advanced Automotive Vehicles.....	957
Robert J. Englar – Georgia Tech Research Institute	
33 – Aerodynamic Heat Exchanger: A Novel Approach to Radiator Design using Circulation Control.....	997
Richard J. Gaeta, Robert J. Englar and G. Blaylock – Georgia Tech Research Institute	
Summary	1023
Ron Joslin – Office of Naval Research Gregory S. Jones – NASA Langley Research Center	
Editorial Remarks.....	1051
Gregory S. Jones – NASA Langley Research Center Ron Joslin – Office of Naval Research	
List of Attendees.....	1055

Introduction: 2004 NASA/ONR Circulation Control Workshop

Gregory S. Jones¹ and Ronald D. Joslin^{2,a}

¹NASA Langley Research Center, Hampton, Virginia

²Office of Naval Research, Arlington, Virginia

This conference proceeding is comprised of papers that were presented at the NASA/ONR Circulation Control Workshop held 16-17 March 2004 at the Radisson-Hampton in Hampton, VA. Over two full days, 30 papers and 4 posters were presented with 110 scientists and engineers in attendance, representing 3 countries.

As technological advances influence the efficiency and effectiveness of aerodynamic and hydrodynamic applications, designs, and operations, this workshop was intended to address the technologies, systems, challenges and successes specific to Coanda driven circulation control in aerodynamics and hydrodynamics. A major goal of this workshop was to determine the state-of-the-art in circulation control and to assess the future directions and applications for circulation control.

The 2004 workshop addressed applications, experiments, computations, and theories related to circulation control, emphasizing fundamental physics, systems analysis, and applied research. The workshop consisted of single session oral presentations, posters, and written papers that are documented in this unclassified conference proceeding. The format of this written proceeding follows the agenda of the workshop. Each paper is followed with the presentation given at the workshop. The editors compiled brief summaries for each effort that is at the end of this proceeding. These summaries include the paper, oral presentation, and questions or comments that occurred during the workshop.

The 2004 Circulation Control Workshop focused on applications including Naval vehicles (Surface and Underwater vehicles), Fixed Wing Aviation (general aviation, commercial, cargo, and business aircraft); V/STOL platforms (helicopters, military aircraft, tilt rotors); propulsion systems (propellers, jet engines, gas turbines), and ground vehicles (automotive, trucks, and other); wind turbines, and other non-traditional applications (e.g., vacuum cleaner, ceiling fan).

As part of the CFD focus area of the 2004 CC Workshop, CFD practitioners were invited to compute a two-dimensional benchmark problem for which geometry, flow conditions, grids, and experimental data were available before the workshop. The purpose was to accumulate a database of simulations for a single problem using a range of CFD codes, turbulence models, and grid strategies so as to expand knowledge of model performance/requirements and guide simulation of practical CC configurations.

The comparison benchmark was the NCCR 1510-7067N circulation control airfoil that was tested at David Taylor Naval Surface Research and Development Center (currently, Naval Surface Warfare Center-Carderock Division). The airfoil is an eight-inch cambered elliptic section foil with thickness-to-chord ratio of 15% and a spiral Coanda trailing edge. It had a blowing slot located on the suction side at $x/c = 0.967$ and which has a height-to-chord ratio of $h/c = 0.003$.

^a The views expressed in this article are those of the authors and do not reflect the official policy or position of the US Office of Naval Research, the US Department of Defense, or the US Government. Distribution Statement A: Approved for public release; distribution is unlimited.

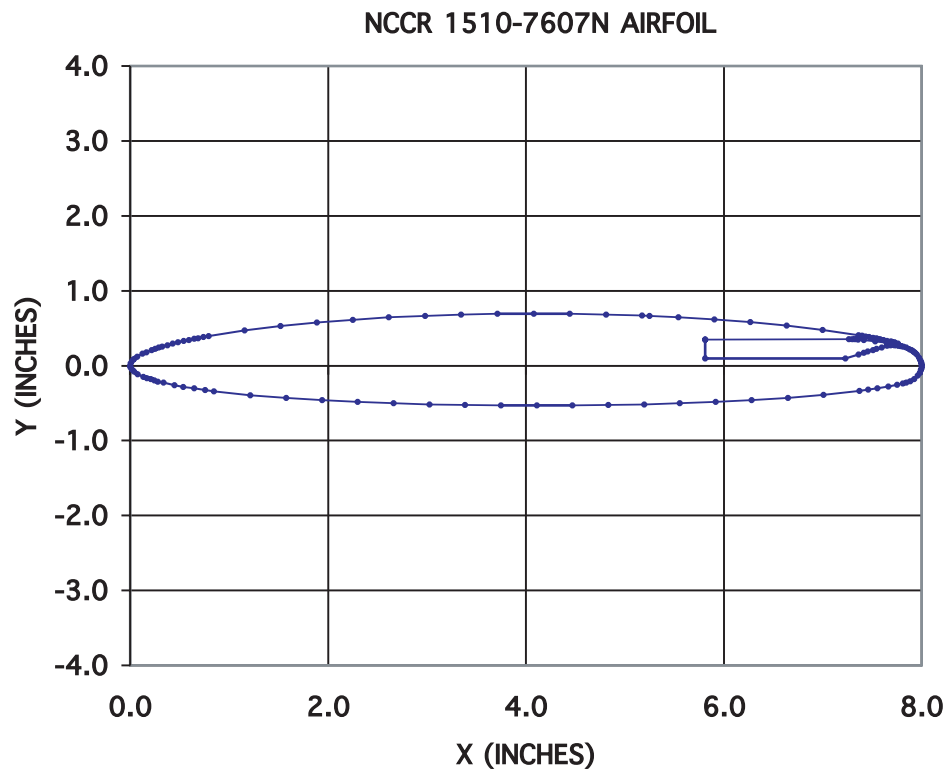


Figure 1. Sketch of the NCCR airfoil used for CFD test case.

Table 1. Coordinates for NCCR airfoil used in CFD test case.

1510-7067N Circulation Control Airfoil		h/c=0.0030	
UPPER		LOWER	
X(inches)	Y(Inches)	X(inches)	Y(Inches)
5.810000	0.351000	0.000000	0.000000
7.263000	0.356468	0.005000	-0.029000
7.298000	0.356600	0.021000	-0.057000
7.326875	0.352687	0.040000	-0.080000
7.355750	0.348775	0.077000	-0.112000
7.413500	0.340950	0.133000	-0.147000
7.529000	0.325530	0.170000	-0.165000
7.644500	0.309650	0.207000	-0.181000
7.760000	0.294000	0.244000	-0.196000
7.724000	0.310950	0.281000	-0.211000
7.688000	0.322210	0.336000	-0.228000
7.652000	0.333060	0.446000	-0.259000
7.616000	0.343910	0.538000	-0.281000
7.579000	0.353760	0.648000	-0.304000
7.543000	0.363610	0.757000	-0.326000
7.507000	0.372460	0.848000	-0.342000
7.470000	0.381710	1.212000	-0.393000
7.435000	0.390170	1.576000	-0.432000
7.398000	0.399020	1.938000	-0.462000
7.362000	0.406870	2.301000	-0.485000
6.999000	0.479380	2.663000	-0.503000
6.635000	0.535890	3.024000	-0.516000
6.270000	0.581400	3.386000	-0.525000
5.905000	0.616900	3.748000	-0.530000
5.540000	0.646000	4.109000	-0.532000
5.250000	0.664000	4.471000	-0.530000
5.175000	0.668000	4.832000	-0.524000
4.809000	0.684000	5.194000	-0.515000
4.443000	0.693000	5.555000	-0.501000
4.078000	0.695000	5.918000	-0.483000
3.712000	0.692000	6.280000	-0.459000
3.346000	0.683000	6.649000	-0.428000
2.980000	0.667000	7.006000	-0.388000
2.615000	0.644000	7.370000	-0.335000
2.250000	0.614000	7.461000	-0.319000
1.885000	0.576000	7.553000	-0.301000
1.520000	0.529000	7.662000	-0.277000
1.156000	0.469000	7.754000	-0.254000
0.793000	0.394000	7.809000	-0.239000
0.739000	0.381000	7.843000	-0.227000
0.688000	0.368000	7.887000	-0.205000
0.648000	0.358000	7.924000	-0.177000
0.594000	0.343000	7.961000	-0.134000
0.540000	0.328000	7.981000	-0.099000
0.485000	0.312500	7.993000	-0.061000
0.431000	0.294000	7.998000	-0.034000
0.377000	0.275000	8.000000	0.000000
0.323000	0.255000	7.998000	0.019000
0.287000	0.240000	7.994000	0.046000
0.251000	0.225000	7.987000	0.072000
0.215000	0.208000	7.972000	0.110000
0.162000	0.181000	7.952000	0.147000
0.126000	0.160000	7.934000	0.170603
0.073000	0.122000	7.915000	0.190000
0.038000	0.088000	7.897000	0.206049
0.020000	0.066000	7.878000	0.220487
0.004000	0.030000	7.845000	0.240735
0.000000	0.000000	7.816000	0.254000
		7.793000	0.261565
		7.770000	0.267000
		7.748000	0.270347
		7.724000	0.272000
		7.687000	0.270000
		7.652000	0.264000
		7.598000	0.245000
		7.543000	0.224000
		7.507000	0.210000
		7.453000	0.188000
		7.417000	0.174000
		7.363000	0.152000
		7.228000	0.096000
		5.810000	0.096000
		5.810000	0.351000

Circulation Control in NASA's Vehicle Systems

Paul Rich, Bob McKinley, and Greg Jones

Langley Research Center

Specific to the application of any technology to a vehicle, such as circulation control, it is important to understand the process that NASA is using to set its direction in research and development. To see how circulation control fits into any given NASA program requires the reader to understand NASA's Vehicle Systems (VS) Program. The VS Program recently celebrated its first year of existence with an annual review—an opportunity to look back on accomplishments, solicit feedback, expand national advocacy and support for the program, and recognize key contributions. Since its formation last year, Vehicle Systems has coordinated seven existing entities in a streamlined aeronautics research effort. It invests in vehicle technologies to protect the environment, make air travel more accessible and affordable for Americans, enable exploration through new aerospace missions, and augment national security. This past year has seen a series of valuable partnerships with industry, academia, and government agencies to make crucial aeronautics advances and assure America's future in flight.

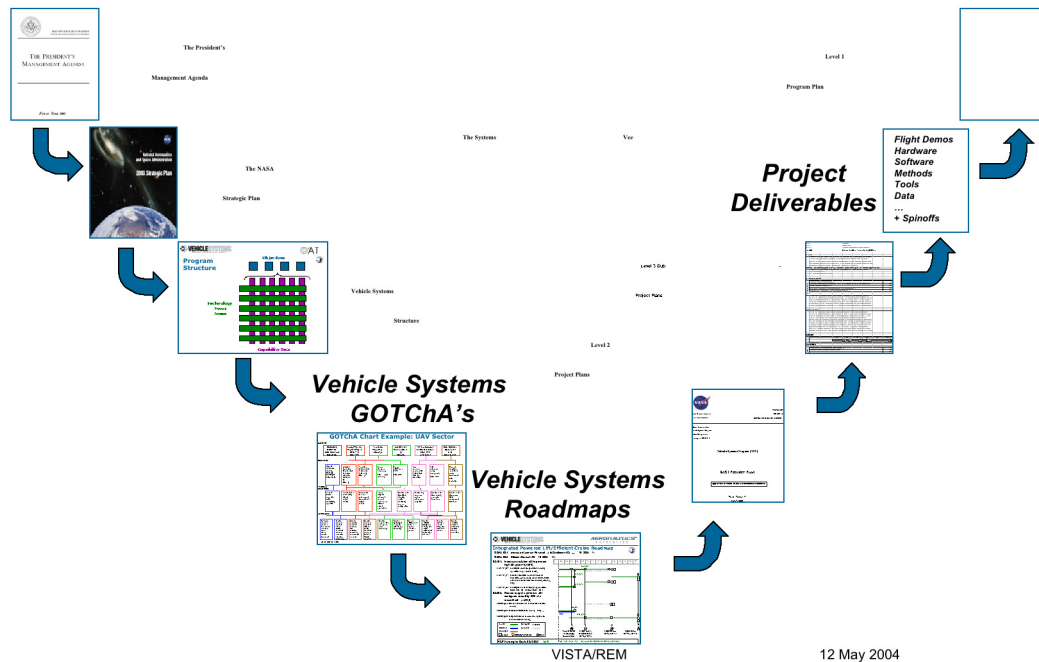
The Vehicle Systems Program is made up of seven core projects, including Efficient Aerodynamic Shapes and Integration (EASI) and Flight and Systems Demonstrations (FSD). In addition, an internal reorganization last year produced six vehicle sectors, managed by a group of NASA strategists—the Vehicle Integration, Strategy, and Technology Assessment (VISTA) Team. Vehicle sector managers provide near- and long-term planning for the projects in order to align aeronautics research with national and Agency priorities. Through technology integration and “roadmaps,” which track VSP investments to minimize redundancy, VISTA synthesizes project activities to meet a set of common goals. The Project teams execute work for the program, and using Program resources, they are responsible for delivering technologies that meet the goals defined through the VISTA activities.

VS Projects cover a wide scope. From the Quiet Aircraft Technology (QAT) Project, which works to mitigate aircraft noise impacts on travelers and airport neighbors, to the Low Emissions Alternative Power (LEAP) Project, which develops energy-efficient alternative propulsion and power systems, the VSP promises a variety of applications for industry, the military, and civilians. Advances have already been made in the Autonomous Robust Avionics (AuRA) Project, among others. AuRA team leaders are creating on-board flight systems to reduce human interaction, with eventual plans for unmanned aerial vehicles and aircraft technology for unskilled operators. The Ultra Efficient Engine Technology (UEET) Project has also introduced innovative technologies. To combat global warming, UEET is developing combustors for gas turbine propulsion systems capable of reducing nitrogen oxide emissions by 70% at takeoff and landing.

The annual review recognized the hard work of a number of employees and outlined plans for even greater future successes. The Extreme Short Takeoff and Landing (ESTOL) and the Rotorcraft (RC) sectors will continue to direct project activities toward vertical or near-vertical takeoff and landing research and development. The Personal Air Vehicle (PAV) and Uninhabited Air Vehicle (UAV) sectors will encourage aeronautics innovations that eliminate the need for a professional pilot, including affordable aircraft for ordinary Americans. Finally, the Supersonic Aircraft (SSA) and Subsonic Transport (ST) sectors will work to maximize efficiency and strive for global reach.

With sector oversight now providing strategic direction, the VSP projects will move forward with their near-term focuses. Continual self-correction and program evolution will help yield valuable aeronautics advances. Much of the program's success this year was due to the advent of VISTA and the incorporation of sectors to coordinate project activities. By linking strategy and implementation, the VSP has established clear organizational goals for its active projects—guidelines that will operate throughout the year to ensure that next year's annual review is equally outstanding.

VS Linkage: the Whole Enchilada



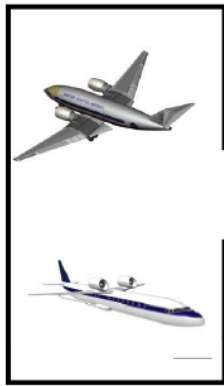
The Vehicle systems program has a number of revolutionary projects leading the Aerospace industry into an exciting future. Circulation control concepts may play a role in several of these projects. The projects discussed below are likely candidates where circulation control may have the largest impact in the near term.

ITAS (Integrated Tailored Aero Structures) Project

The primary focus of the ITAS project is to develop ultra-light smart materials and structures, aerodynamic concepts, and light weight subsystems to increase vehicle efficiency, leading to high-altitude long-endurance vehicles, planetary aircraft, advanced vertical and short takeoff and landing vehicles and beyond.

This project is divided into five areas: Actively Tailored High-Lift Systems, Highly-Loaded Lightweight Structures, Adaptive Ultra-Lightweight Airframe Systems, Planetary Flight Vehicles, and Multifunctional Structures Foundation Technologies.

An example of a sub-project in the Actively Tailored High-Lift Systems area is the Integrated Wing Concepts for ESTOL. The challenge in this area is to increase the circulation of the low speed powered high lift system by 50% to generate more lift on takeoff while decreasing the drag to maintain efficient cruise. Figure 1 illustrates the set of capabilities for a notional ESTOL vehicle. Nominally one can achieve many of these capabilities, but the challenge for ESTOL is to meet all of the capabilities at the same time. Figures 2 and 3 are examples of GOTChA and roadmaps related to ESTOL.



Required Capability	SOA	5-Years	15-Years
Balanced Field Length	4,000 ft	2,000 ft	2,000 ft
T/O & Landing Speed	120 kts	65 kts	50 kts
Turn Radius in Terminal Area	1 1/4 nm	1/2 nm	1/4 nm
Cruise Mach	0.60	0.70	0.80
Range	1,000 nm	1,400 nm	1,400 nm
Payload	90 PAX	90 PAX	90 PAX
Noise Footprint W/I Airport	No	Yes	Yes
Terminal Ops	CTOL IFR	* CAT IIIA	* CAT IIIC

Figure 1. Targeted ESTOL Notional Vehicle Capabilities.

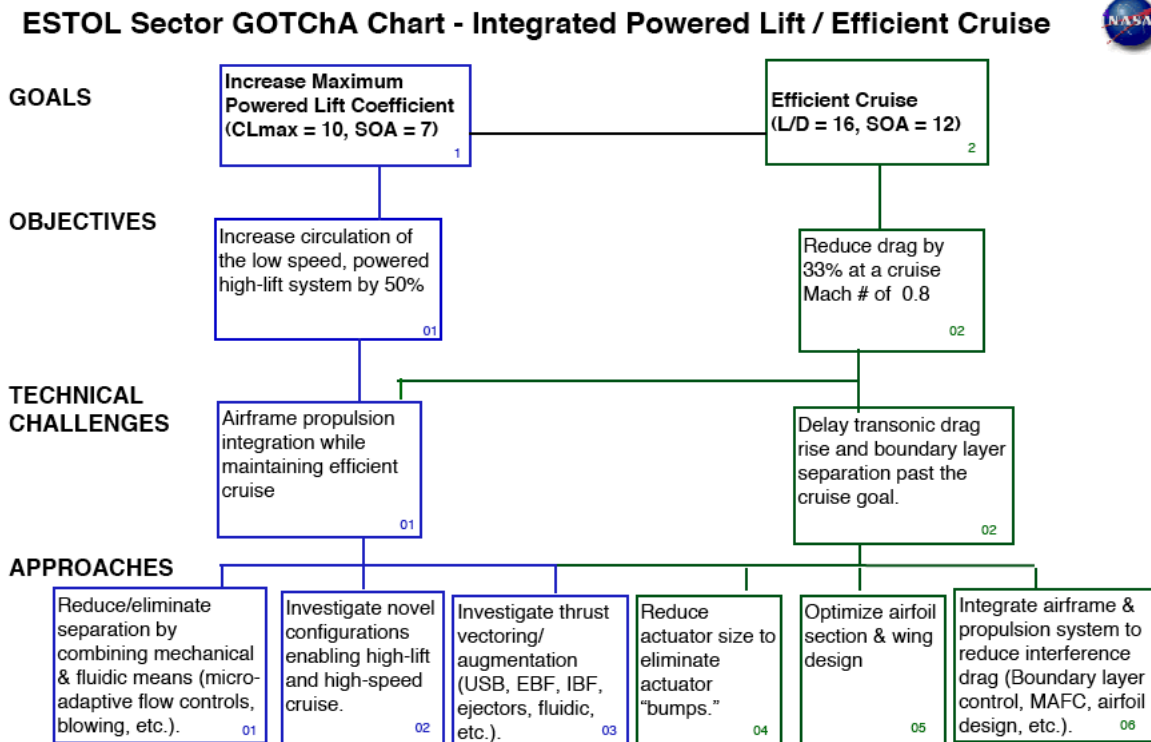


Figure 2. Example of GOTChA chart for ESTOL (living document that updates regularly).

Integrated Powered Lift/Efficient Cruise Roadmap



GOAL ES1: Increase Maximum Powered-Lift Coefficient ($CL_{max} = 10$, SOA = 7)

GOAL ES2: Efficient Cruise ($L/D = 16$, SOA = 12)

ES101: Increase circulation of the powered high-lift system by 50%.

ES10101.02: Investigate novel configurations enabling high-lift and high-speed cruise.

ES10101.01: Increase circulation & reduce/eliminate separation by combining mechanical & fluidic means (micro-adaptive flow controls, blowing, etc.).

ES10101.03: Investigate thrust vectoring/ augmentation (USB, EBF, IBF, ejectors, fluidic, etc.).

ES202: Reduce drag of a powered-lift configured aircraft by 33% at a cruise Mach # of 0.8.

ES20203.04: Reduce actuator size to eliminate actuator "bumps."

ES20203.05: Optimize airfoil section & wing design.

ES20203.06: Integrate airframe & propulsion system to reduce interference drag.

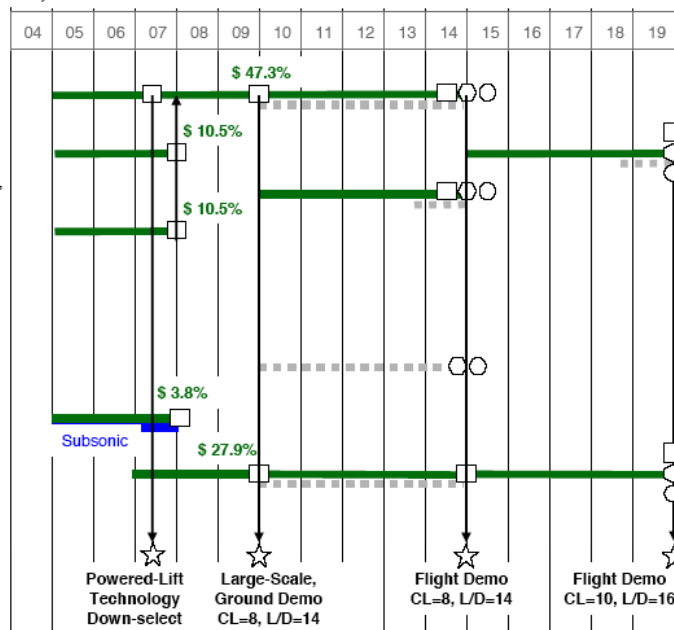
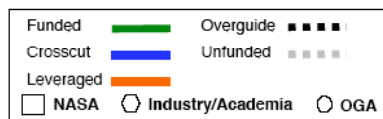


Figure 3. Example of a portion of the roadmap for ESTOL (living document).

Other sub-projects within the Actively Tailored High-Lift Systems area include morphing leading edges for the subsonic transport and investigations into the Aero-Propulsion-Servo-Elastic technology. In the Highly-Loaded Lightweight Structures area, sub-projects are enabling technology to reduce the fuselage structural weight of the Blended Wing Body aircraft to a range competitive with conventional air transports.

A subproject in the Adaptive Ultra-Lightweight Airframe Systems area is investigating weight reduction for High Altitude Long Endurance (HALE) vehicles to improve endurance payload, launch and recovery, performance under adverse flight conditions and durability.

In the Planetary Flight Vehicle area a number of sub-projects are focused on establishing a mature baseline vehicle for Mars exploration for a potential 2011 mission. These sub-projects will establish aerodynamic performance, demonstrate flight controls, evaluate propeller and other new vehicle concepts, including VTOL and mother ship concepts.

Examples of sub-projects in the Multifunctional Structures Foundation Technologies area are Bio-inspired Nano-structured Materials Development and Adaptive Aero Structures. Both of these sub-projects, using adaptive structures and micro-flow concepts, will significantly reduce vehicle weight to improve community access and enable new missions.

EASI (Efficient Aerodynamic shapes and Integration) Project

The primary focus of the EASI project is to improve aerodynamic efficiency, structures, materials technologies, and design tools and methodologies to reduce fuel burn and minimize environmental impact and enable new vehicle concepts and capabilities for public mobility and new science missions.

This project is divided into 4 areas: Configuration and Component Aerodynamic Technology, Aerodynamics for Heavy Lift Rotorcraft, Variable Fidelity Conceptual Design Tool, and Computational Methods for Flight Performance Prediction.

One of the sub-projects under Configuration and Component Aerodynamic Technology is the Blended Wing Body Flight Dynamics and Control effort. One of the near-term tests uses a 5% dynamically scaled free-flight model to characterize 1-g departures. A free-flight test in a NASA Full Scale Wind Tunnel will be conducted to assess envelope protection schemes, assess asymmetric thrust control limits, assess center engine thrust vectoring control and assess 1g-departure onset control. Other contemplated tests include high Reynolds number transonic stability and control characterization. Another subproject on Advanced Wing Technology will be developing and testing a closed loop adaptive bump to minimize transonic wave drag.

A sub-project under Variable Fidelity Conceptual Design Tool is a “Conceptual Design Shop” which advances concept design state-of-the-art. This will enable NASA to design and assess unconventional atmospheric vehicle concepts and advanced technologies to meet NASA’s aeronautics goals. The “Conceptual Design Shop” will incorporate variable fidelity analysis tools and methods, quantify uncertainty, and create a knowledge database for NASA.

One of the sub-projects under Computational Methods for Flight Performance Prediction is COMSAC (computational methods for stability and control). This effort will benchmark, validate and develop computational tools for the prediction and analysis of stability, controllability and flight dynamics of advanced aircraft. This will potentially lead to large reductions in test requirements in Stability and Control. Other sub-projects in this area are investigating 3-D Physics-based mesh adaptation technology and physics-based transition prediction for subsonic vehicles. Both of these latter efforts will support improved design techniques for the future.

A sub-project under Aerodynamics for Heavy Lift Rotorcraft is Large Lightweight Rotor Concepts. This effort will focus on identifying large, fast, long-range VTOL transports to revolutionize air transport.



AERONAUTICS
enterprise



Future Vehicle Capabilities & the Potential Contribution of Circulation Control

*NASA Circulation Control Workshop
Hampton, VA
16 March 2004*



AERONAUTICS
enterprise

Synopsis



- **Vehicle Systems (VS) Program Overview**
 - Drivers for the “new” Program
 - Semantics and Planning Constructs
 - Program Structure
 - So What?
- **Future Vehicle Capabilities**
 - History and Development
 - Status and Description
- **Circulation Control as a Potential Solution**
 - Relation to Sectors and Capabilities
- **Summary**
 - Next Steps
 - Points of Contact



National Policy Shift

- Federal R&D investment policies are no longer viewed as predominantly for national security but rather for **stimulation of national innovation, economic competitiveness, and basic health and science research**
- **Continual budget pressure** and a call for efficient and effective use of tax payer dollars, including those targeted for federal R&D
- Increased oversight of programs with **proof of return on the investment**
- Greater emphasis on science and engineering education and training
- Government investment in **R&D will continue to take a backseat** to that of industry



New policies set by Congress, the Clinton and the Bush Administrations demand maximizing ROI through greater efficiency, accountability, and success of the U.S. science & technology portfolio and Agency programs



Congressional Guidance

Recent Report Language Directed at OAT/NASA*

- "...continue to pursue actions and reforms directed at **reducing institutional costs**, including management restructuring, facility consolidation, procurement reform, and convergence with defense and commercial sector systems.."
- ".... should invest in the types of research and innovative technology in which United States commercial providers do not invest, while avoiding competition with the activities in which United States commercial providers do invest."
- "NASA and the Department of Defense should **cooperate more effectively** in leveraging the mutual capabilities of these agencies...."
- "To achieve the public goal of price reduction and **innovation through competition**.."
- "...must articulate a comprehensive agenda and strategy through an agency performance plan for each of NASA's primary centers that identifies a **linkage between resources and activities in a way that guarantees an advanced technology strategy** that will ensure the preeminence of NASA in the area of space transportation, .., and aerospace technology, including aeronautical research and technology."

* Compiled from Authorization and Appropriations bills, fiscal years 1999 through 2003



Desirable Vehicle Systems Characteristics

- Defensible (to funders)
- Integrated (across program)
- Simplified (understandable)
- Focused (on goals)
- Innovative (technologically)
- Linked (to product users)

VISTA / RBM

12 March 2004

5



VS: Vocabulary



- **Theme Objective**
 - Objectives set by Aeronautics Theme that directly relate to public good Agency goals as defined in the NASA Strategic Plan.
- **Program (a.k.a., Level 1 or L1)**
 - An element of the Theme. Led by a Program Manager (L1) that defines a group of projects and processes aligned to accomplish goals that enable the Theme Objectives, e.g., Vehicle Systems Program.
- **VISTA**
 - Vehicle Integration, Strategy and Technology Assessment. VS Program component that defines technical strategy.
- **Vehicle Sector**
 - An element of VISTA. Led by a Vehicle Sector Manager (VSM) that defines the capabilities and priorities for a class of aircraft, then relates impact of associated work to the Theme Objectives. VSM's define the what and when of VS research.
- **Capability Set**
 - Definition of the capabilities desired for future aircraft and how it relates to public good.

VISTA / RBM

12 March 2004

6

VS: Vocabulary, continued

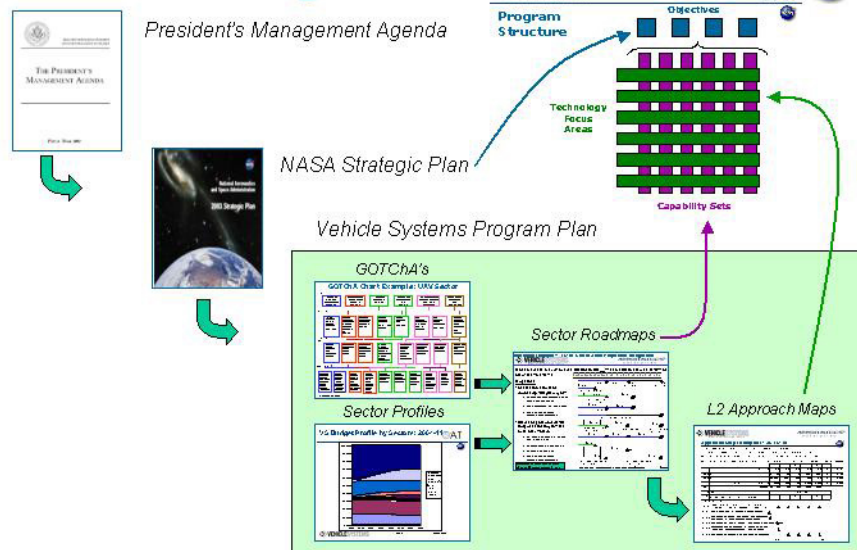
- **GOTChA Chart**
 - Chart that relates Program **G**oals, **O**bjectives, **T**echnical **C**hallenges and **A**pproaches in a top-down decomposition
- **Roadmap**
 - A depiction of the work required to achieve the Goals from the GOTChA chart. Includes related resources and projects that will execute the work.
- **Technology Focus Area (a.k.a., Technology Foci)**
 - Theme construct that describes enduring areas of research related to aeronautics. Functionally represented over a period of time by a project with start/end dates and deliverables.
- **Project (a.k.a., Level 2 or L2)**
 - An element of a Program. Led by a Project Manager (L2) that defines a group of activities (approaches to work) that deliver technologies that achieve the Objectives required to achieve the Goals required by a Vehicle Sector to reach a capability set. L2's define the who and how of VS research.
- **Approach Map**
 - A depiction of the work required to complete the Objectives that achieve the Objectives and Goals from the GOTChA chart. Includes related resources and specific activities required to complete the work.

VISTA/RBM

12 March 2004

7

VS Process Linkage

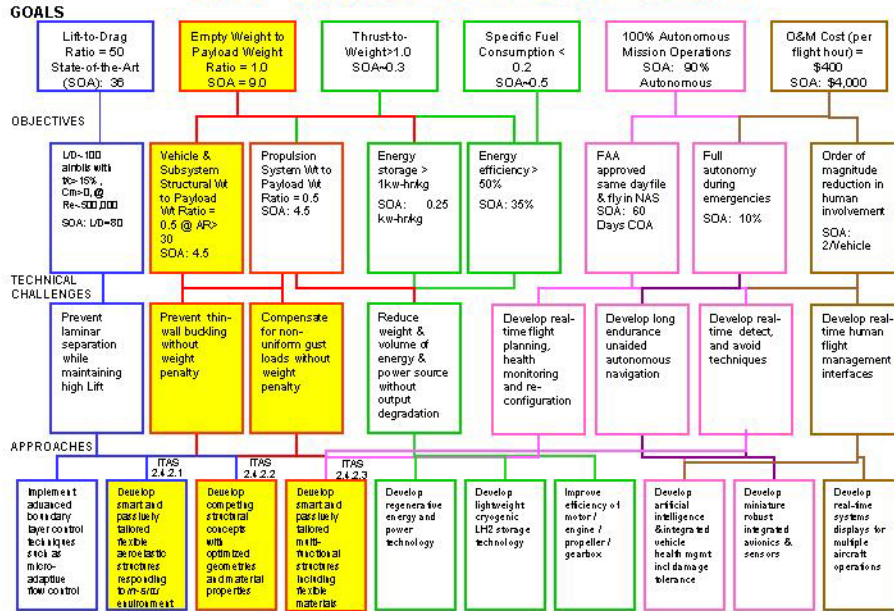


VISTA/RBM

12 March 2004

8

UAV Sector GOTChA Chart



As of Mar 01, 2004



Weight Management Roadmap (UAV)

GOAL: Empty Weight to Payload Weight Fraction = 1.0

As of Mar 9, 2004

SOA = 9

OBJECTIVES

Subsystem & vehicle structural wt to payload wt ratio = 0.5 @ AR>30
SOA: 4.5

- Develop smart and passively tailored flexible aeroelastic structures responding to in-situ environment

- L2 PM: F&SD
- L2 PM: ITAS

- Develop competing structural concepts with optimized geometries and material properties

- L2 PM: ITAS

- Develop smart and passively tailored multifunctional structures including flexible materials

- L2 PM: ITAS

Propulsion system wt to payload wt ratio = 0.5

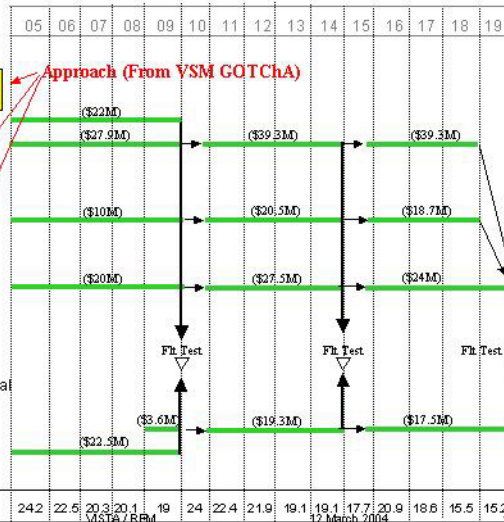
SOA: 4.5

- Develop smart and passively tailored multifunctional structures including flexible materials

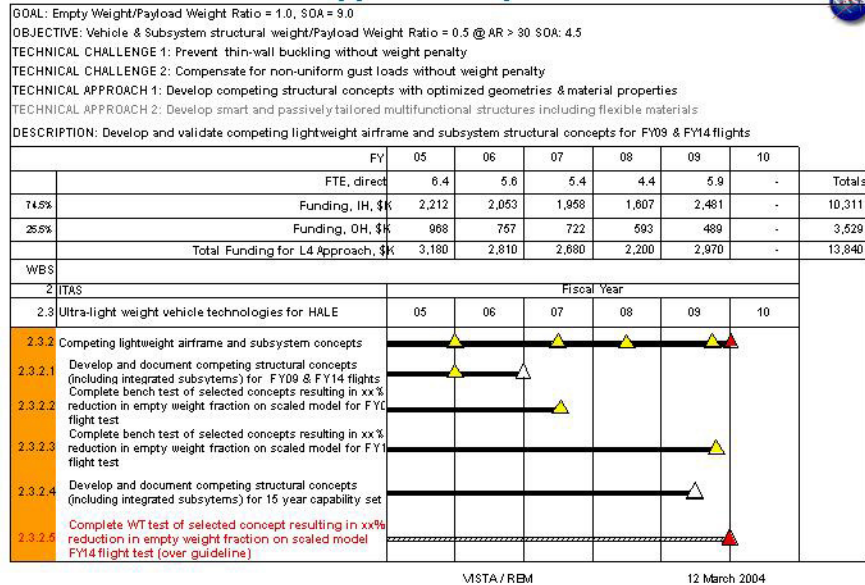
- L2 PM: LEAP
- L2 PM: F&SD

VSP Funding (\$M)

\$290M



ITAS Approach Map - 2.4.3.2



Program Structure

Objectives

Technology Focus Areas

Capability Sets

VISTA / RBM 12 March 2004 12



Aeronautics Theme Objectives for the Public Good



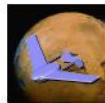
Protect the Environment

Protect local and global environmental quality by reducing aircraft noise and emissions.



Increase Mobility

Enable more people and goods to travel faster and farther with fewer delays



Explore New Aerospace Missions

Pioneer novel aerospace concepts and technologies to support science missions and terrestrial and space applications



Partnerships for National Security

Enhance the Nation's security through aeronautical partnerships with DOD, DHS, and other U.S. or international government agencies

VISTA / RBM

12 March 2004

13



6 Vehicle Sectors



Subsonic Transports

Fay Collier & Bob Plencner

**Associate Program Manager
for VISTA**
Bob McKinley
Teresa Kline



Supersonic Aircraft

Peter Coen & Mary Jo Long-Davis



Rotorcraft

Gloria Yamauchi



Uninhabited Air Vehicles

Larry Camacho



Personal Air Vehicles

Mark Moore



Extreme STOL

John Zuk

VISTA / RBM

12 March 2004

14

7 Projects

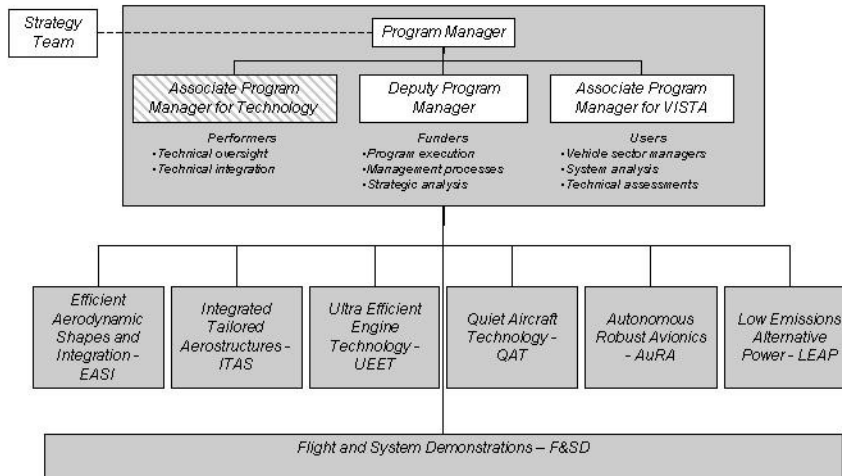


VISTA / RBM

12 March 2004

15

Vehicle Systems Organizational Chart



VISTA / RBM

12 March 2004

16

So What?

- **The Vehicle Systems Program is replanned and restructured**
 - New goals, new focus, new structure, new processes
- **Industry, academia and other government agencies have been a key part of the new Program vector**
 - Via workshops, sharing of expert opinion and existing analyses
 - Peer review
- **Vehicle Systems is now executing fewer activities with more specific, capability-driven deliverables**
 - Direct linkage between work activities, Program goals, Agency Objectives, and National Needs

VISTA/RBM

12 March 2004

17

Future Vehicle Capability Sets



VISTA/RBM

12 March 2004

18

QuEST Quiet, Efficient Subsonic Transport



(DRAFT Metrics: 65 dB contour <55 sqmi, -25% CO₂, -70% NO_x, 300 passenger or equivalent)

Low-noise, low-emission, highly efficient transport aircraft

VISTA / RBM

12 March 2004

19

Subsonic Transport Sector



Sector Technology Area

- Lift to Drag Ratio
- Empty Weight / Payload Weight Ratio
- TSFC (installed @ cruise)
- Engine T/W (installed)
- Community Noise (EPNdB)
(-20dB at each of 3 certification points)
- Noise Footprint (sqmi, 65 dBA single event)
- Emissions (kg NO_x /LTO)

Goal

25
3.8
0.51
5.75
SOA – 20
55
27

VISTA / RBM

12 March 2004

20



HeVSTOL

Heavy-Lift Vertical/Short Takeoff and Landing



120-passenger, 1200nm, V/STOL

VISTA/RBM

12 March 2004

21



HALE ROA

High Altitude Long Endurance Remotely Operated Aircraft



14-day endurance, 60-70K ft ops, 400 lb payload

VISTA/RBM

12 March 2004

22

S⁴T

Silent Small SuperSonic Transport



(DRAFT Metrics: <0.5 psf boom overpressure, $M_{cr} > 1.6$, 6500' TOFL, 8-10 passengers or equivalent)

Overland supercruise with acceptable sonic boom

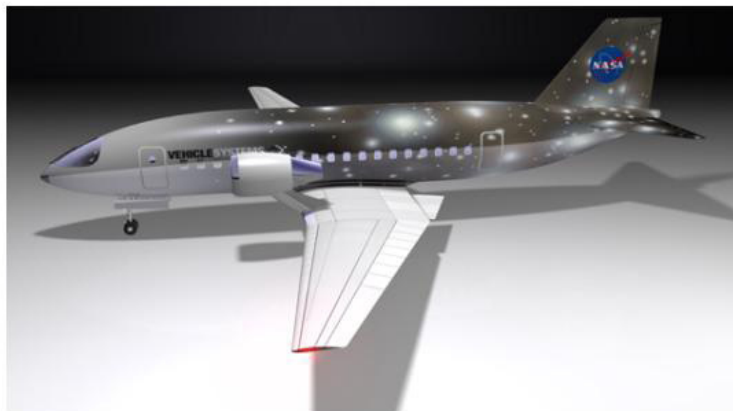
VISTA/RBM

12 March 2004

23

ExSTOL

Extreme Short TakeOff and Landing Transport



$<2000'$ TOFL, $M=0.8$ cruise, quiet, $V_{mceo} \sim 50$ kts

VISTA/RBM

12 March 2004

24

EQuiPT

Easy-to-use, Quiet Personal Transportation



-30 dB vs. SOA, auto-like ease of use, \$75K

VISTA/RBM

12 March 2004

25

Circulation Control as a Potential Solution for the Capability Sets

- **Circulation control (CC) may be applicable to all of the Vehicle Sectors**
 - ESTOL: Obvious connection (see following chart)
 - PAV: Strong connection (see 2nd chart following)
 - SSA: Not so obvious, but also strong (see 3rd chart following)
 - ST: May need CC to achieve noise goals
 - Rotorcraft: Use CC on rotors?
 - UAV: Possible use of CC in the far-term, depending on the mission requirements
- **VISTA team will be working with technologists to define the potential contribution of CC and related technologies towards meeting the Program goals.**

VISTA/RBM

12 March 2004

26

ESTOL and Circulation Control



- **ESTOL: Investment in short-field capability is a top priority**
- **Key is simultaneous achievement of all elements of the capability set**
 - $\leq 2000'$ LTO (landing/takeoff) field length (related goal of $C_{Lmax} = 10$)
 - Cruise at $M=0.8$
 - Quieter than other small transports
 - Engine out control at ~ 50 knots
- **Current state of the art (SOA) enables 2 or perhaps 3 of the elements at one time**
- **CC is a strong candidate for enabling the whole set**



VISTA/RBM

12 March 2004

27

PAV and Circulation Control



- **PAV: Investment in high-lift technology is a 2nd priority**
 - First priorities are for ease of use and noise
- **Cruise-sized wing**
 - LTO wing size drives current general aviation aircraft
 - Compromise between V_{stall} and V_{cruise}
 - Optimum is cruise-sized wing with proper C_L (~ 3) for $V_{stall} < 61$ knots
- **V/STOL**
 - CC may be enabling to this class of vehicle
 - CC Nacelle
- **CC is a strong candidate for enabling PAV capabilities**



VISTA/RBM

12 March 2004

28

SSA and Circulation Control



- **SSA: Investment in high-lift technology is a 2nd priority**
 - First priority is establishing low-boom boundary conditions
- **Low-Boom vs. All Other Performance Issues**
 - Existing low-boom designs need loooong runways
 - i.e., Edwards AFB long
 - Desired LTO field length is ≤ 6500 ft.
 - LTO-sized wing is not suitable for low-boom (wrong lift distribution)
 - LTO noise is a show-stopper
 - Remember HSR?
- **CC may enable a boom-sized wing that also meets the LTO noise and field length requirements**

VISTA/RBM

12 March 2004

29

Next Steps



- Finish detailed connection of plans to GOTChA's and Roadmaps
 - Finish FY05 Project Plans
- Begin Baseline Vehicle Assessments and Scenario-Based Analysis
 - Define L1 Milestones based on Sector capabilities and relation to Theme Objectives
 - Solicit technology plans from every sub-project in every project
 - Execute Vehicle Sector Analysis Plan
- VS Annual Meeting on 11-13 May, Atlanta, GA
- VS Program Non-Advocates Review on 21-24 June, Alexandria, VA
- Begin VS Program execution on 1 October 2004
- Refine the plan annually
 - Solicit industry/academia/government input
 - Tweak the plan
 - Execute

VISTA/RBM

12 March 2004

30



Points of Contact

- **Vehicle Sectors Managers**

- ESTOL: John Zuk
(jzuk@mail.arc.nasa.gov)
- PAV: Mark Moore
(mark.d.moore@nasa.gov)
- Rotorcraft: Gloria Yamauchi
(gloria.k.yamauchi@nasa.gov)
- SSA: Peter Coen
(peter.g.coen@nasa.gov)
& Mary Jo Long-Davis
(mary.j.long-davis@nasa.gov)
- ST: Fay Collier
(fayette.s.collier@nasa.gov)
& Bob Plencner
(robert.m.plencner@nasa.gov)
- UAV: Larry Camacho
(lawrence.camacho@mail.dfrc.nasa.gov)

- **Project Managers**









- AuRA: Jim Burley
(james.r.burley@nasa.gov)
- EAS: Jim Pittman
(james.l.pittman@nasa.gov)
- F&SD: David McBride
(david.d.mcbride@nasa.gov)
- ITAS: Long Yip
(long.p.yip@nasa.gov)
- LEAP: Anita Liang (acting)
(anita.d.liang@nasa.gov)
- QAT: Mike Marcolini
(michael.a.marcolini@nasa.gov)
- UEET: Gary Seng (acting)
(gary.t.seng@nasa.gov)

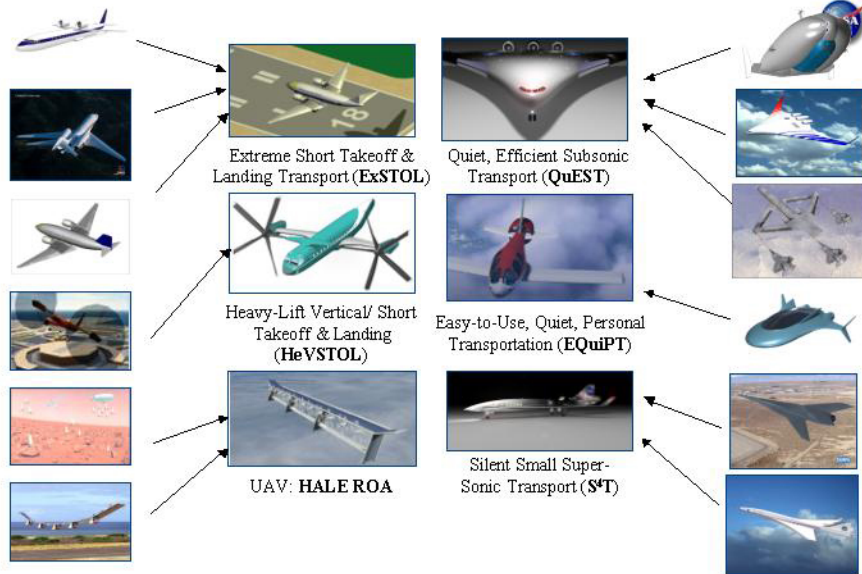


Sectors & Capabilities: History

- **Vehicle capability sets and notional concepts**
 - Reno workshop, January 2003
 - Industry/Academia/Government teams brainstormed to come up with 31 vehicles and associated capability sets (1st chart following) and 178 technology challenges
 - NASA VSM's distilled to 12 capability sets, 15 common tech challenges (2nd chart following)
- **Roadmaps to capability sets**
 - Phoenix workshop, April/May 2003
 - Industry/Academia/Government teams developed roadmaps from rough GOTChA charts for the 12 capability sets and 15 common tech challenges
- **Today**
 - 6 sectors and capability sets distilled from the Phoenix work and subsequent prioritization efforts (3rd chart following)

ST	SSA	RIA	PAV	UAV
				
				
				
				
				

 <p>Minimum environmental impact, maximum efficiency</p> <p><i>Clean Transport</i></p>	 <p>Strengthen national security through rapid deployment and global reach</p> <p><i>Global Strike</i></p>	 <p>Conduct extended science and exploration missions</p> <p><i>Planetary Flight Vehicles</i></p>
 <p>All hour access to any location without noise disturbance</p> <p><i>Santa Monica at Midnight</i></p>	 <p>Global reach and on-demand delivery</p> <p><i>Global Reach Transport</i></p>	 <p>Easy-to-use personal transportation</p> <p><i>Personal Air Vehicle</i></p>
 <p>Rural and regional economic growth, time critical transport</p> <p><i>Heartland Express</i></p>	 <p>Automated refueling capability, ultra-long endurance, wide speed range</p> <p><i>Tanker</i></p>	 <p>Enables city center access in all weather</p> <p><i>V/STOL Commuter</i></p>
 <p>Expands the use of existing airport infrastructure</p> <p><i>Extreme STOL Transport</i></p>	 <p>Reduce passenger flight time by at least a factor of 2</p> <p><i>Supersonic Overland</i></p>	 <p>High altitude observations for science and defense</p> <p><i>High Altitude Long Endurance</i></p>



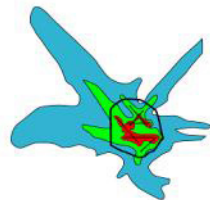
Theme Objectives

VISTA / RBM

12 March 2004

37

Environmentally Friendly Aircraft



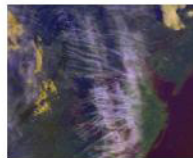
Noise within airport boundaries

Constrain objectionable noise to within airport boundaries



Smog-free

Minimize the contribution of air vehicles to the production of smog



No impact on global climate

Minimize the impact of air vehicles on global climate

VISTA / RBM

12 March 2004

38

Aircraft for Public Mobility

More Convenient

Expand access to aviation to more locations and make it available on-demand

More Affordable

Make air travel available to the entire population



...without compromising safety

Faster

Increase the speed of air travel

VISTA / RBM

12 March 2004

39

Air Vehicles for New Missions



Science platforms

Develop innovative air vehicles for science missions in the earth's atmosphere and beyond



Hazardous environments

Enable uninhabited air vehicles to fly in hazardous environments

VISTA / RBM

12 March 2004

40

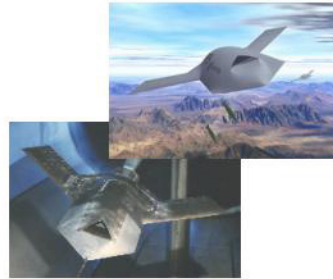


Superior Air Power



Technological superiority

Cooperatively develop technologies
that enable air superiority



Partners in freedom

Support the development of
advanced military aircraft

VISTA / RBM

12 March 2004

41

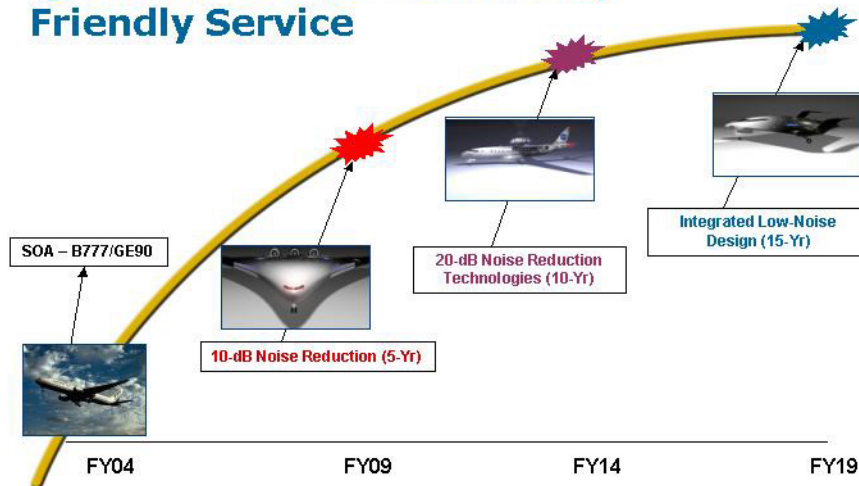
Projects

VISTA/RBM

12 March 2004

42

Quiet Aircraft for Community Friendly Service



VISTA/RBM

12 March 2004

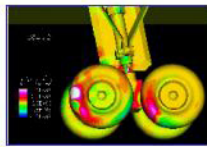
43



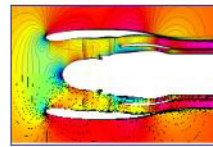
QAT Quiet Aircraft Technology



*Aircraft
Operations*



*Airframe Noise
Reduction*



*Source Noise
Reduction*

VISTA / RBM

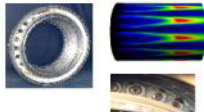
12 March 2004

44

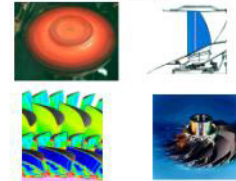


UEET Ultra Efficient Engine Technology

*70% LTO NO_x
Combustor*



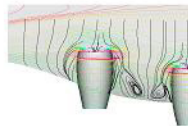
*Highly Loaded. Low
Weight Compressor &
Turbine*



*UEET Integration
and Demonstration*



Highly Integrated Inlet



*Intelligent Propulsion
System Foundation
Technologies*



VISTA / RBM

12 March 2004

45



AuRA

Autonomous Robust Avionics

*Integrated Vehicle
Systems Management*



*Autonomous Vehicle
Operations*



*Adaptive Optimal
Flight Controls*



*Intelligent Mission
Management*



VISTA / RBM

12 March 2004

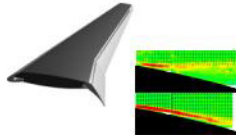
46



ITAS

Integrated Tailored Aerostructures

*Actively Tailored High-Lift
Systems*



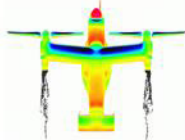
*Adaptive, Ultra-Lightweight
Airframe Systems*



*Highly-loaded,
Lightweight Structures*



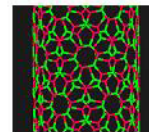
*Integrated Tailored VTOL
Concepts*



Planetary Vehicles



*Weight Reduction &
Community Access
Foundation Technologies*



VISTA / RBM

12 March 2004

47



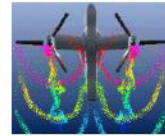
EASI

Efficient Aerodynamic Shapes and Integration

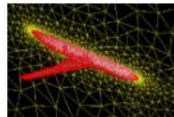
*Reduced Fuel Burn
Transport Wing*



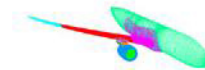
*Sub-Scale Efficient Heavy
Lift VTOL Aeromechanics
Demonstration*



*Variable Fidelity Conceptual
Design Tool Development &
Validation*



*Computational Methods
for Flight Performance
Prediction*



VISTA / RBM

12 March 2004

48



LEAP

Low Emissions Alternative Power



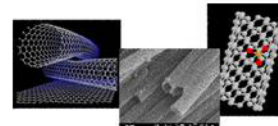
*Aircraft Fuel
Cell Power
Systems*



*Constant
Volume
Combustion
Cycle Engine*



*University Research,
Engineering &
Technology Institute
(URETI)*



*Alternate Fuel
Foundation
Technologies*

VISTA / RBM

12 March 2004

49



F&SD

Flight and Systems Demonstrations

Intelligent Flight Control Systems



Advanced Aeroelastic Wing



Flight Research Productivity Tools



HALE ROA Capabilities

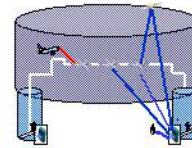


Earth Science Capability Demos



VISTA/RBM

HALE ROA in the NAS

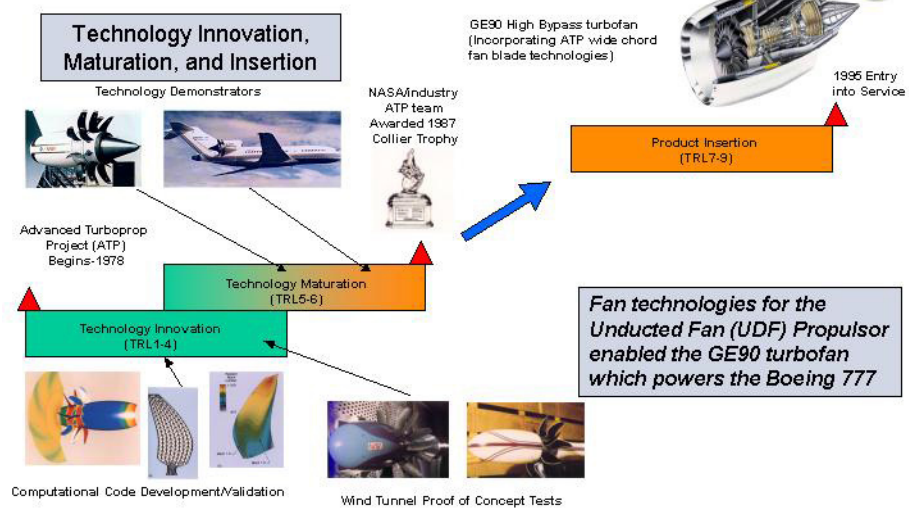


12 March 2004

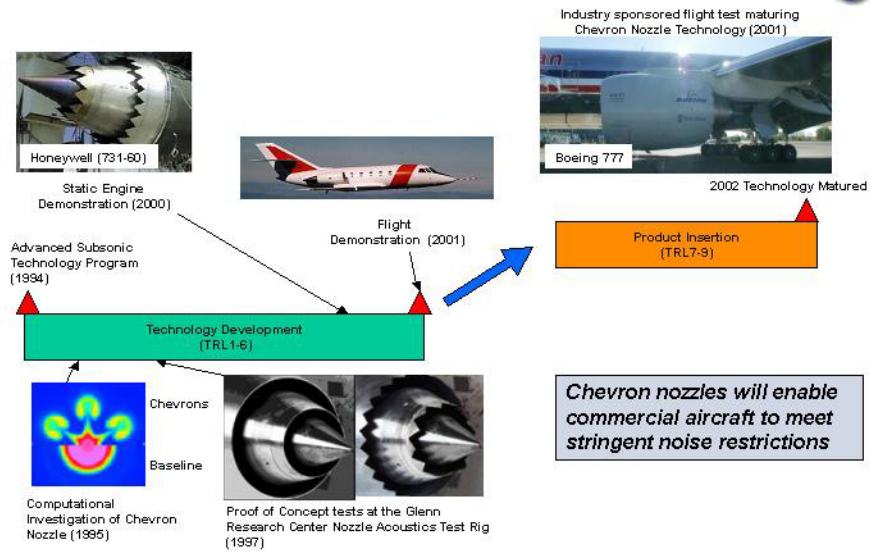
50



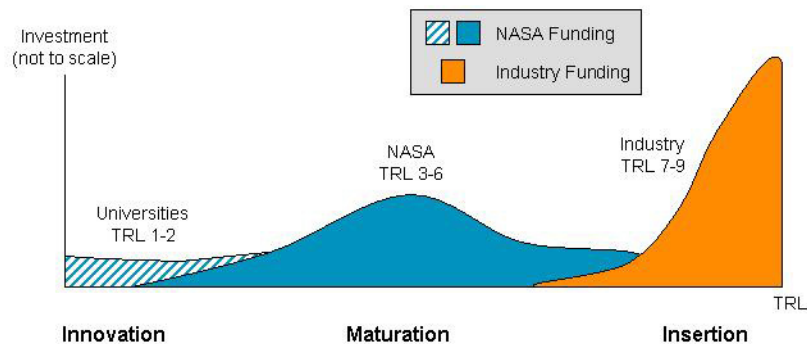
Wide Chord Fan Blade Technologies

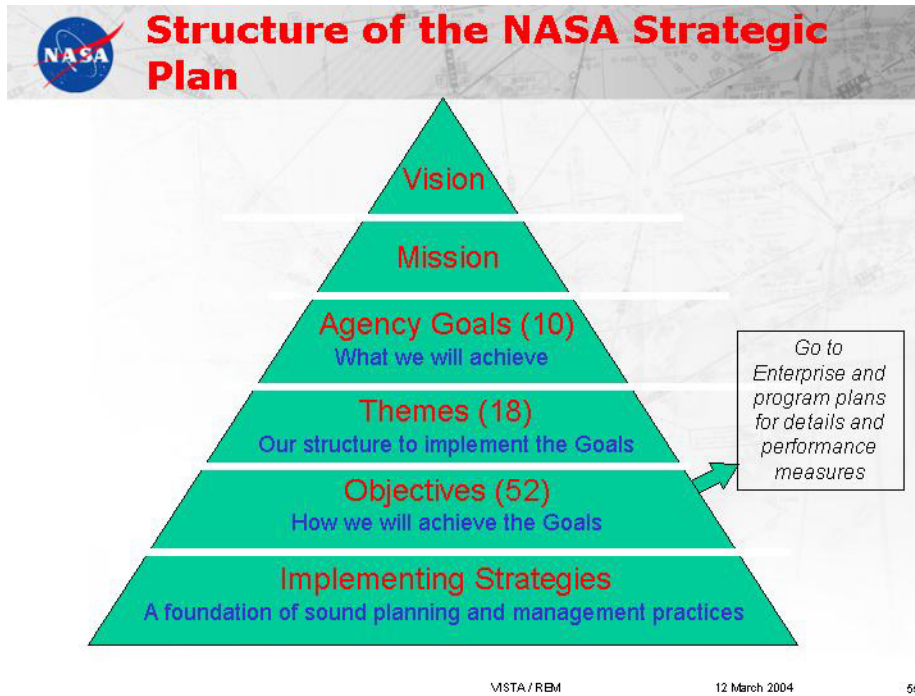


Chevron Nozzle Noise Reduction Technology



NASA Role in Technology Innovation and Maturation





Overview of Circulation Control Pneumatic Aerodynamics: Blown Force and Moment Augmentation and Modification as Applied Primarily to Fixed-Wing Aircraft

Robert J. Englar*

Georgia Tech Research Institute
Aerospace, Transportation and Advanced Systems Laboratory
Atlanta, Georgia

Abstract

The use of tangential jet blowing over highly curved aerodynamic surfaces has been shown to yield very strong flow entrainment and resulting aerodynamic/hydrodynamic force and moment augmentation or modification with few or even no moving surfaces. Known as Circulation Control (CC) aerodynamics, this concept has been shown to augment airfoil lift coefficient by as much as 8000% of the input blowing jet momentum. This paper presents and discusses a wide range of proven CC applications including: lift or down-force augmentation; drag reduction or increase; roll, pitch, and yaw amplification/control; thrust deflection; stability augmentation; boundary layer control; hydrodynamic devices; automotive applications; pneumatic propulsors; and micro aircraft surfaces; but primarily emphasizes the application to fixed-wing aircraft.

Introduction

The use of pneumatic devices in the form of blown jet airfoils has been employed or under consideration in the field of aerodynamics as far back as the 1930s, perhaps even earlier^{1,2}. In most of these devices, which generally fall into the categories of jet flaps or blown flaps, a jet sheet exits from the trailing edge of the airfoil at a fixed angle or tangent to a flap with a sharp trailing edge. This augments aerodynamic forces by entraining and deflecting the airfoil flowfield pneumatically, rather than solely by deflecting a mechanical surface. These are in fact “pneumatic flap” lift augmentors, and have been shown to be successful if a sufficient on-board source of compressed air is available. The aerodynamic concept now known as Circulation Control (Figure 1) is a logical follow-on to these devices, with one very important difference which has made a significant performance improvement. The tangential jet sheet exits over the curved trailing edge of the surface replacing the flap, and this curvature can turn through a full 180° or more. The jet remains attached to that curved surface because of a balance between the sub-ambient pressure in the jet sheet and the centrifugal force in the jet going around the curvature. Initially, at very low blowing values, the jet entrains the boundary layer to prevent aft flow separation, and is thus a very effective boundary layer control (BLC, see Fig. 1 lift plot). Eventually, as the jet continues to turn, a rise in the static pressure plus viscous shear stress and centrifugal force combine to separate the jet sheet, and a new stagnation point and stagnation streamline are formed on the lower surface. The large flow entrainment rate of this jet and the large deflection of the stagnation streamline produce a pneumatic camber, and thus pneumatic control of the airfoil’s circulation and lift. Although it is a very effective BLC device, the interest in this concept comes from its ability to further augment the circulation and lift, and thus the name of

*Principal Research Engineer

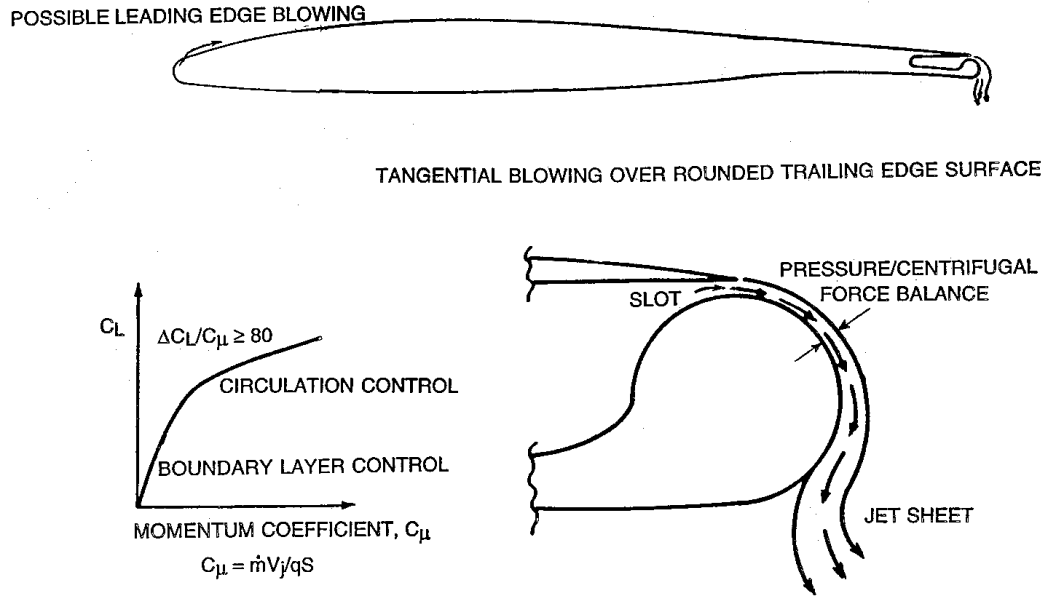


Fig. 1 - Basics of Circulation Control Aerodynamics

Circulation Control (CC). Several additional benefits became obvious from early experimental investigations of the concept as a means of lift augmentation:

- Only very small flap size or even non-moving control surfaces were required
- Lift augmentation could be achieved independent of airfoil angle of attack
- Jet turning angle was no longer limited by physical jet exit angle or blown flap deflection angle
- Very high force augmentation was generated per unit of input blowing momentum

Roughly 70 years have evolved since the very earliest revelation of this type of curved pneumatic device, and a very large variety of pneumatic configurations have been proposed and evaluated. The author has been actively involved with many of these since around 1967. To further expose this wide range of actual and potential applications, this paper will discuss a large number of these pneumatic devices with which the author is familiar from both past and current research, as well as provide an indication of where the use of CC aerodynamics may be heading. It is by no means a complete and exhaustive study of all efforts known, but rather contains representative cases from a wide variety of pneumatic force/moment augmenting and modifying devices. This paper concentrates primarily on fixed wing aircraft, but CC is certainly not limited to that application alone. The following examples will confirm the multiple uses of CC devices as:

- Aerodynamic force and moment augmentors (Fig. 1 shows $\Delta C_l/C_{\mu} = 80$, or 8000% return on the invested momentum)
- Aerodynamic force and moment reduction if/when needed (drag in climb out and cruise)
- Aerodynamic moment control and stability augmentation
- Aerodynamic device simplifier (moving parts elimination, complexity and weight reduction)

The Coanda Effect

The Circulation Control concept is actually based on the now well-known Coanda Effect, named after the Romanian inventor Henri Coanda^{3,4,5} who claimed to have discovered it in Paris prior to 1935. There is a Romanian postage stamp (and associated story) showing that Coanda had originally used the Coanda device for a totally different purpose: as a means to deflect the exhaust of a radial piston engine away from a wooden aircraft fuselage. During its first flight, these shielding plates actually entrained the hot exhaust flow inward, igniting and destroying the aircraft. Figure 2 shows the basic Coanda device as later formulated by him (after the fiery exhaust incident) and its application to a fixed wing aircraft (which in this case appears to be a form of BLC). Note that in these (and in all other Coanda cases found), Coanda aligns acute-angle "steps" downstream of one side of a jet nozzle to deflect the jet to that side and entrain large masses of fluid from the opposite side. The distinctive steps and angles were intended to generate a separated vortex flow at each corner, and thus enhance mixing there. The concept was applied by Coanda to many other

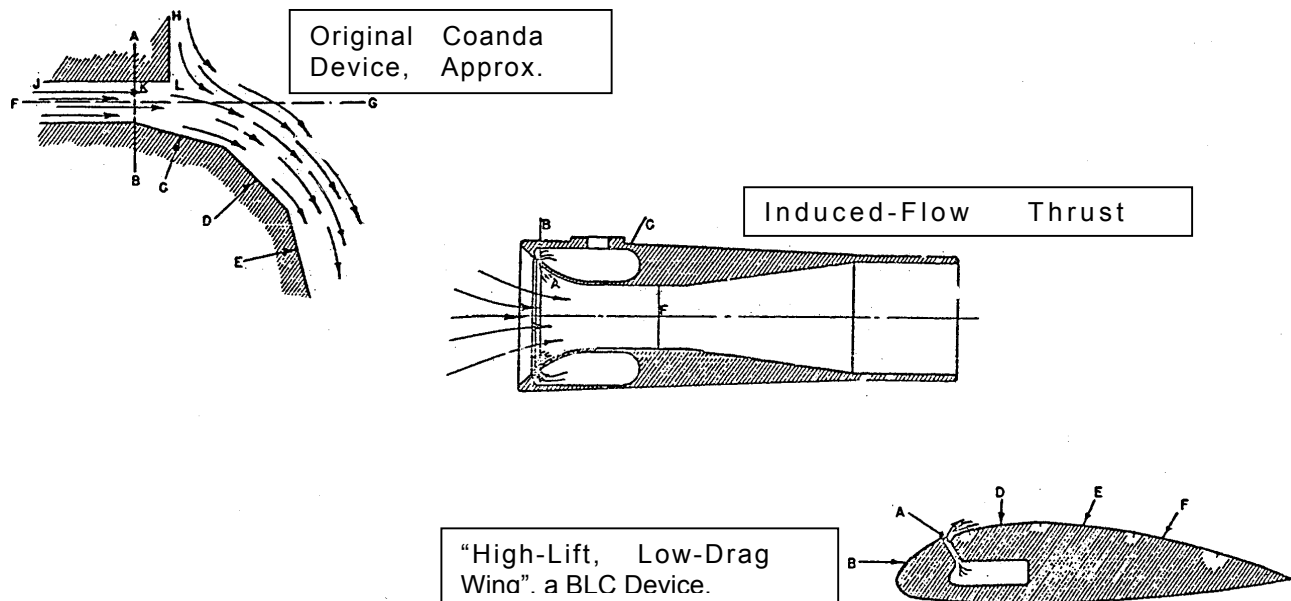


Fig. 2– Coanda Devices and High-Lift Low-drag Wing, from Reference 5

devices, including car engine exhaust scavengers, wind-tunnel turning vanes, thrust augmentors, water propulsion units, injection wind tunnels, deflection surfaces, and rotary pumps. However, efficiency questions arose because of added friction along all the steps and separated flow at each corner. Nevertheless, the concept forms the basis for the present CC aerodynamics: an infinite number of small-angled steps simply becomes a continuous curved surface with even greater entrainment capability and less energy loss due to lack of discrete corners.

The following discussion will present a number of favorable applications of CC aerodynamics, where the governing difference between Circulation Control and the jet flap/blown flap will be the continuously curving surface downstream of the tangentially blown jet, with force augmentation/modification being mainly a factor of jet blowing parameters, not the angles of the sharp flap trailing edge or the jet angle relative to the chord line. The main emphasis here will be on fixed-wing devices and applications. Application of CC to rotary-

wing aircraft offers many additional benefits, as discussed in Refs. 6, 7, 8, and 9. These are based on high-lift generating capability independent of angle of attack, as Fig. 3 shows, and thus can eliminate previously required cyclic and collective pitch blade mechanisms.

Blowing Parameters: Before proceeding, it is important to define the blowing momentum coefficient C_{μ} as:

$$C_{\mu} = m V_j / (qS) = 2 \rho_j A_j V_j^2 / (\rho_{\infty} V_{\infty}^2 S) \\ = 2 h_j V_j^2 / (c V_{\infty}^2) = 2 h_j / c (V_j / V_{\infty})^2$$

where the lower definition only holds for two-dimensional incompressible flow ($\rho_j = \rho_{\infty}$). Typically, the jet velocity in feet/sec is calculated from isentropic relationships as:

$$V_j^2 = 2 \gamma R T_d / (\gamma - 1) \times [1 - (P_{\infty} / P_d)^{(\gamma - 1)/\gamma}]$$

where subscript d implies total conditions in the blowing plenum duct, sub ∞ is freestream, $R = 1716 \text{ ft}^2 / (\text{sec}^2 \text{ } ^\circ\text{R})$, and $\gamma = 1.4$ for air. A jet expansion to the actual static pressure just outside the jet slot would yield higher calculated values of V_j and thus C_{μ} , but would vary as the external flow conditions or shape changed, so would be hard to duplicate as a universal design parameter. Mass flow m is almost always measured under test conditions using appropriate flow meters, but can be calculated isentropically as well using compressible flow relationships¹⁰. Before we go any further, let's note that there is nothing that prohibits the jet velocity from being supersonic unless the geometry is such that a shockdown back to subsonic flow causes the jet to detach from the curved surface. We will soon see that many times it is advantageous to have a higher-speed jet than a lesser-speed one. The momentum term mV_j can, of course, also be thought of as a jet thrust.

Applications of Circulation Control, Past & Present

Circular Cylinder Stopped-Rotor Aircraft: An early application of CC was developed by the British National Gas Turbine Establishment (NGTE) in the mid 1960s, when it was desired to produce a stoppable-rotor VTOL aircraft. In this concept, a blown two-bladed rotor could produce very high lift per blade just to get the aircraft to hover, then be stopped and stowed within the helicopter fuselage for forward fixed-wing flight^{6,7}. A circular-cylinder cross section slotted-pipe rotor appeared to be an ideal solution, since as Figure 3 shows, its thickness/chord ratio of 1.0 presents the possibility of $C_l = 4\pi$ if flow can be made to stay attached. As the figure shows, values even greater than 4π were generated by blown CC cylinder rotor blades when excess thrust in the vertical direction (the jet flap effect) was included at higher t/c values. However, the high drag of a 100% thick circular-cylinder airfoil proved to be a difficult problem and reduced the aerodynamic efficiency of these airfoils to unacceptable values.

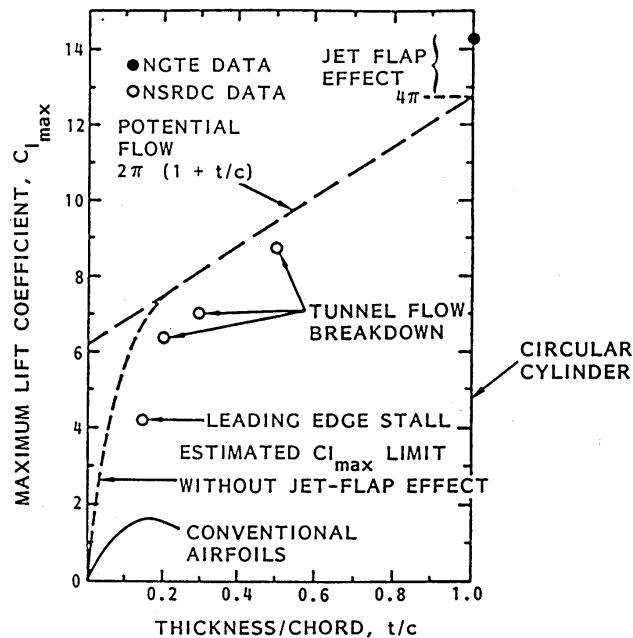


Fig. 3- Maximum Lift of Blown Circulation Control Airfoils

A similar circular lifting surface⁸ was also pursued by NASA Langley in the 1960s to provide lift on takeoff and landing by blowing on the circular fuselage cross section of a hypersonic aircraft, as well as for return after launch of missile or rocket boosters having circular cross sections. Whereas lift coefficient values over 20 were measured at very low Reynolds number for an end-plated-cylinder tunnel model with multiple slots, a single-slotted cylinder produced $C_l=18$ at $C_{\mu}=6$. This lift augmentation of only 3 times the input C_{μ} implied the need for a large air supply. The associated drag coefficient of over 9 gave a lift/drag ratio of only 2, or even less if the blowing coefficient were added to the drag to yield an equivalent drag coefficient. Clearly, high lift was available, but the lift-associated drag and required blowing coefficient posed serious problems.

Elliptic-Airfoil CC Rotor: As interest in circular cylinder CC blades for helicopters was lessening in England, it was rising dramatically in the US in the late 1960s as a possible means to increase rotorcraft performance while greatly simplifying the entire rotor system mechanical hardware. The US effort was centered at the Navy's David Taylor Naval Ship R&D Center (DTNSRDC), where the approach taken was to develop lower-drag, high-lift rotor blade sections by converting the circular cylinder profile into a much thinner blown elliptic airfoil. These efforts also became the basis for fixed-wing efforts as well, and are presented here to clarify understanding of these CC pneumatic devices. Figure 4 shows several such single-slotted CC Rotor elliptic airfoils where the obtainable C_l is lower than for the cylindrical airfoil, but the required C_{μ} is a factor of 10-20 less. Note that this performance is all at angle of attack $\alpha = 0^\circ$, providing a non-pitching alternative to both the mechanical cyclic and collective angle of attack variation required of conventional rotor blades. Note the very high force augmentation, $\Delta C_l / C_{\mu}$ of 80, representing an 8000% return on the momentum invested. Also shown for comparison is a typical 30° jet flap applied to a 15%

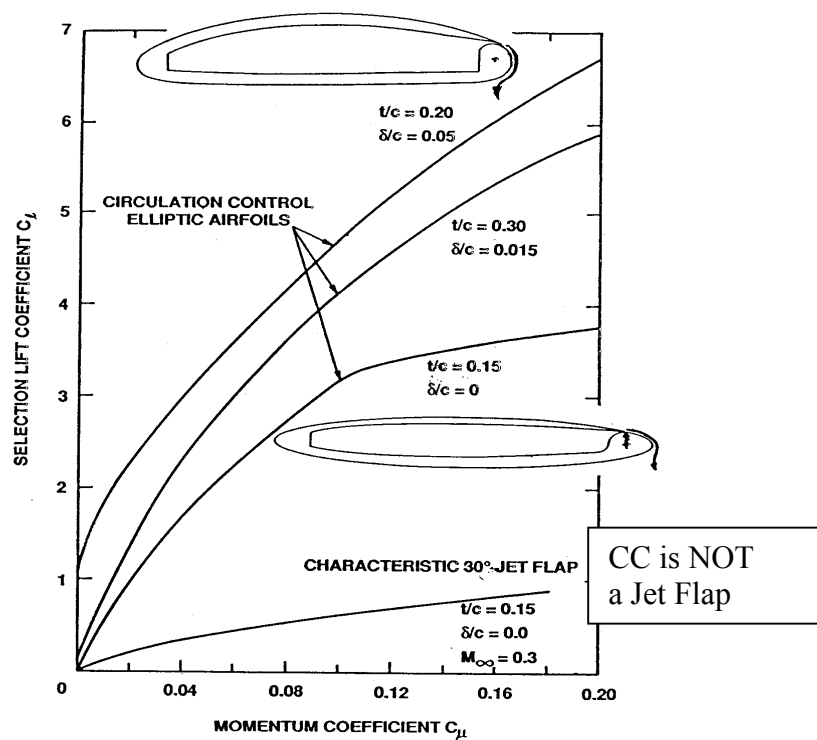


Fig. 4– Typical Blown-Lift Capabilities of 2-D CC Elliptic Airfoils at $\alpha = 0^\circ$

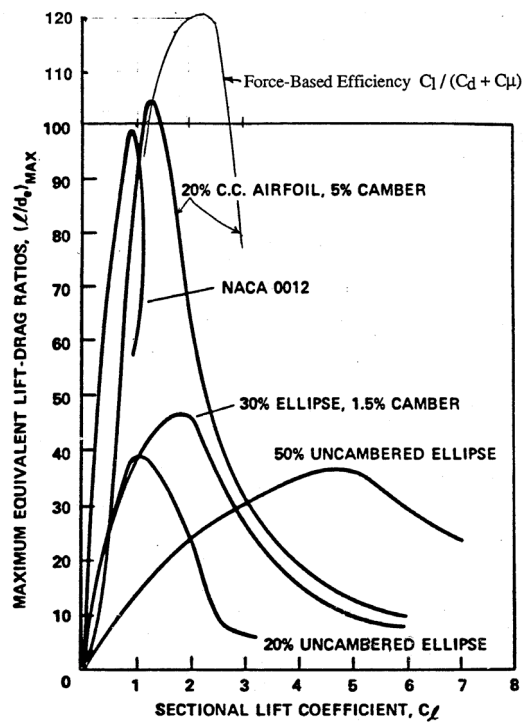


Fig. 5– Equivalent Efficiencies for CC and Conventional 2-D Airfoils

thick ellipse airfoil – the greatly reduced force augmentation of the jet flap is evident because the jet exits from the lower surface of the airfoil at a fixed angle. It should be clear that CC is **not** a jet flap, but achieves its high lift capability because the stagnation stream line movement and resulting circulation can be controlled and increased well beyond that of a sharp trailing edge. Figure 5 shows the equivalent lift-to-drag ratio of sample elliptic CC airfoils, where the equivalent drag in the denominator now includes a severe penalty for compressor power required as well as for intake ram pressure^{10,11}. Maximum equivalent L/D values roughly 6-7% greater than the conventional unblown rotor blade NACA 0012 airfoils (varying only α) are seen for the 20% CC ellipse (at $\alpha=0^\circ$), but at a lift coefficient 30% higher at about 1.3. Furthermore, the C_l can be increased up to 6 or 7 if desired, but at a lesser L/D_{eq} . For additional comparison, if the equivalent drag is defined as merely adding C_{μ} to the measured drag, (i.e., $C_{de} = C_d + C_{\mu}$) then L/D_e values of over 120 at $C_l = 2.5$ are possible, all at $\alpha = 0^\circ$ (almost 3 times the C_l of the 0012 airfoil at stall). The efficiency and simplicity of CC was obvious from these 2-D airfoil results, and a serious effort to develop these CC airfoils was undertaken. Reference 12 summarizes much of this Navy effort at DTNSRDC for the years 1969 through 1983, as well as providing a summary of CC-related research conducted by other agencies (US and abroad) outside the Navy from 1956 – 1983.

In 1979, a CC Rotor flight demonstrator based on a Kaman H-2 helicopter was flown with pneumatic aerodynamic and control systems replacing conventional mechanical cyclic and collective blade pitch^{13,14,15}. Whereas this flight vehicle was hindered by control system response phasing problems which limited its flight test envelope, it did demonstrate the ability to substitute pneumatics for mechanical blade lift and control devices for hover and forward flight. It also led to the possibility of higher harmonic control of helicopters, where cyclic lift variations at frequencies higher than one per revolution were possible to eliminate rotor-induced vibrations. The absence of blade collective and cyclic pitch links is possible; they can be replaced by internal control cams or valves to vary blowing pressures.

CC Airfoil Development: Considerable CC airfoil development was ongoing at this time, both experimental and analytical. A number of CFD techniques using various Navier-Stokes codes have been developed and used to understand the relevant viscous flow fields. These will not be discussed here but can be found in much detail in summarizing References 12 and 16. A typical example of CFD-calculated streamlines and velocity vectors¹⁷ is seen in Figures 6 and 7 for a generic flat-sided semi-elliptic CC airfoil. Of particular interest here are the computed velocity vectors and streamlines downstream of the slot on the blown trailing edge, Figure 7, where the stagnation point of the jet sheet appears to be turned nearly $130\text{--}140^\circ$ from the jet exit. A considerable number of additional CFD analyses, both subsonic and transonic, were conducted by various investigators^{12,16,17}.

A number of experimental programs were also conducted to understand the CC phenomenon and the details within the blown curved surface region. Two-dimensional laser-velocimeter measurements at Lockheed¹⁸ for the same CC airfoil as in Figures 6 and 7 showed mean velocities which confirmed the CFD results above. Again, jet flow turning to a separation point/stagnation streamline approximately $130\text{--}145^\circ$ from the slot was seen, Figure 8. Experimental investigations by this author¹⁹ of a very similar generic airfoil, Figure 9, used surface static pressure, static pressure across the jet and a rotatable hot-film shear stress probe to measure the actual separation point location (where shear stress = 0) as a

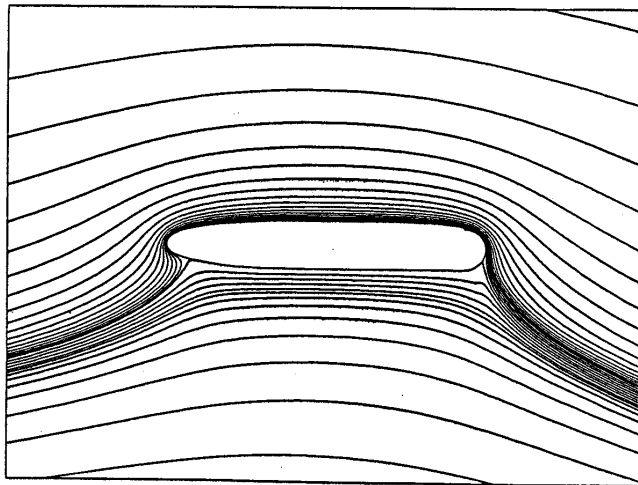


Fig. 6- Computed Streamlines for simplified CC Airfoil,
 $\alpha = -2^\circ$, $C_l = 4.6$, Reference 17

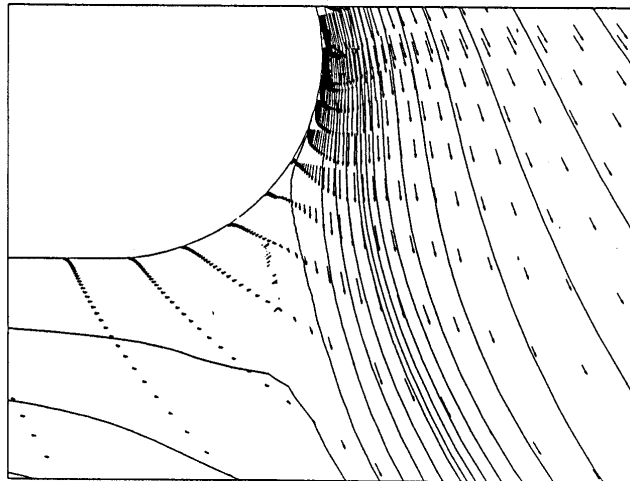


Fig. 7- Computed Velocity Vectors and Streamlines, Reference 17 CC Airfoil

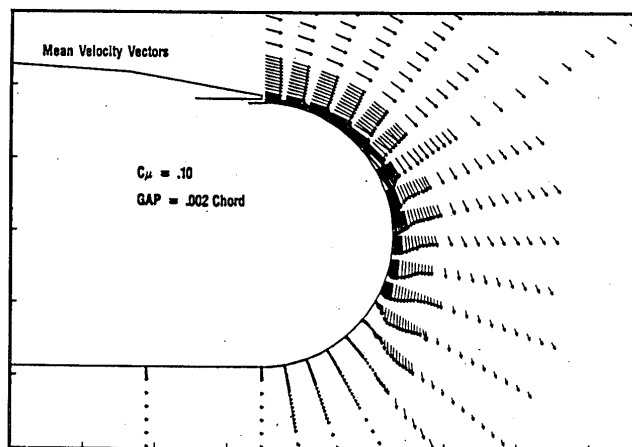


Fig. 8- CC Velocity Vectors Recorded by Lockheed Laser Doppler Velocimeter, Reference 18

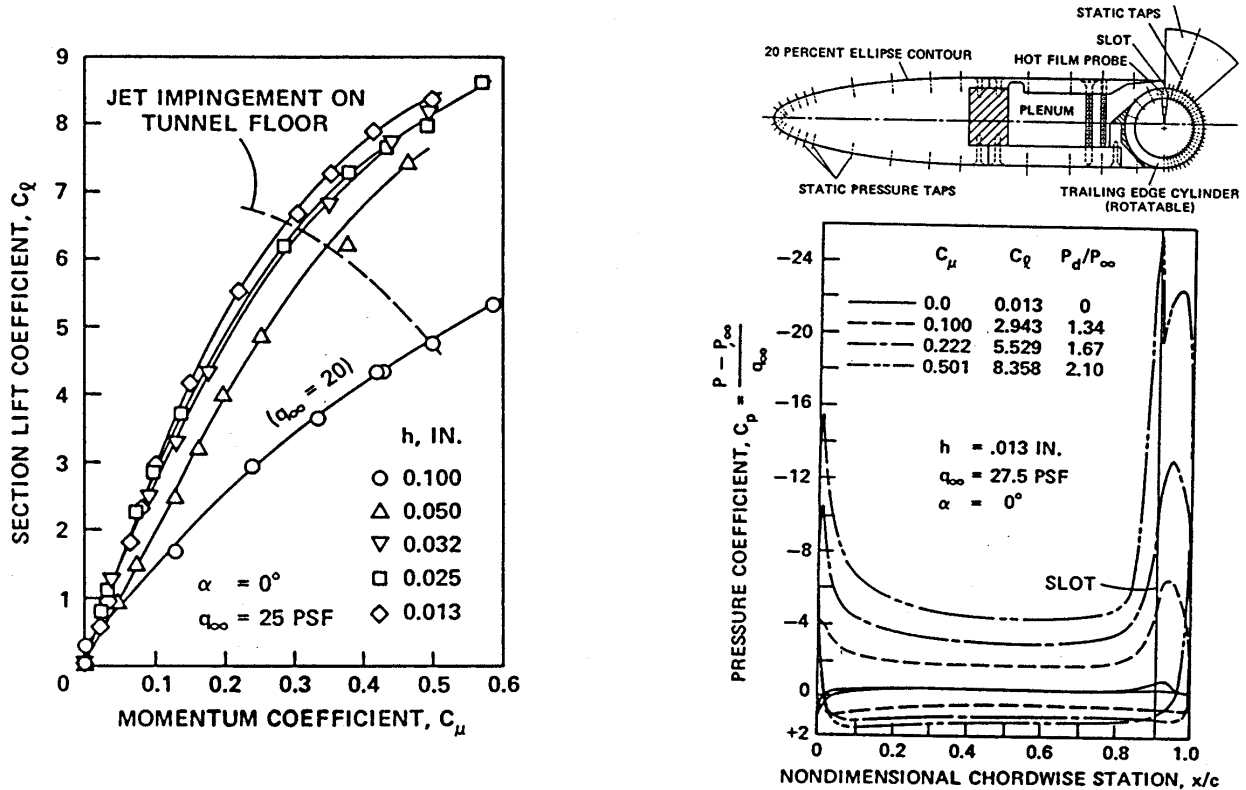


Fig. 9- 2-D Semi-ellipse CC Model Geometry, plus Measured Lift and Static Pressures as Functions of C_μ and Slot Height

function of blowing and slot height. The resulting C_l and C_p distributions are seen in Figure 9. As Figure 10 shows, jet turning as high as 170 - 175° was measured for this airfoil. At a constant C_μ , greater turning occurred with a smaller slot height because the resultant jet velocity and entrainment are higher as jet area reduces. Figure 9 (left plot) shows that this greater velocity and jet turning clearly results in generation of higher C_l , where values nearing 9 are possible at $\alpha = 0^\circ$ (although tunnel flow impingement occurs here). Figure 9 (right plot) presents associated static pressure distributions on the airfoil. These analytical and experimental data confirm the effectiveness of blowing to greatly deflect the entire flow field and then strongly increase the circulation and lift on these very generic airfoils, to the point that very high lift is produced without wing flaps and slats and at 0° angle of attack. Some additional information on generic CC airfoil performance is provided in Reference 20.

One last note on CC airfoil performance: as mentioned above, smaller slot height yields a larger return in C_l at constant C_μ than does a larger slot height, primarily because of greater V_j / V_∞ and extra flow field entrainment. Figures 9 and 10 show this trend. However, if the static pressure coefficient just outside the slot exit (C_{ps}) is known or can be determined, a new parameter defined in Figure 11 can be used (when V_j is expanded to this local condition to yield C_{BLC}) to collapse the different slot height results (left) into a single curve (right).

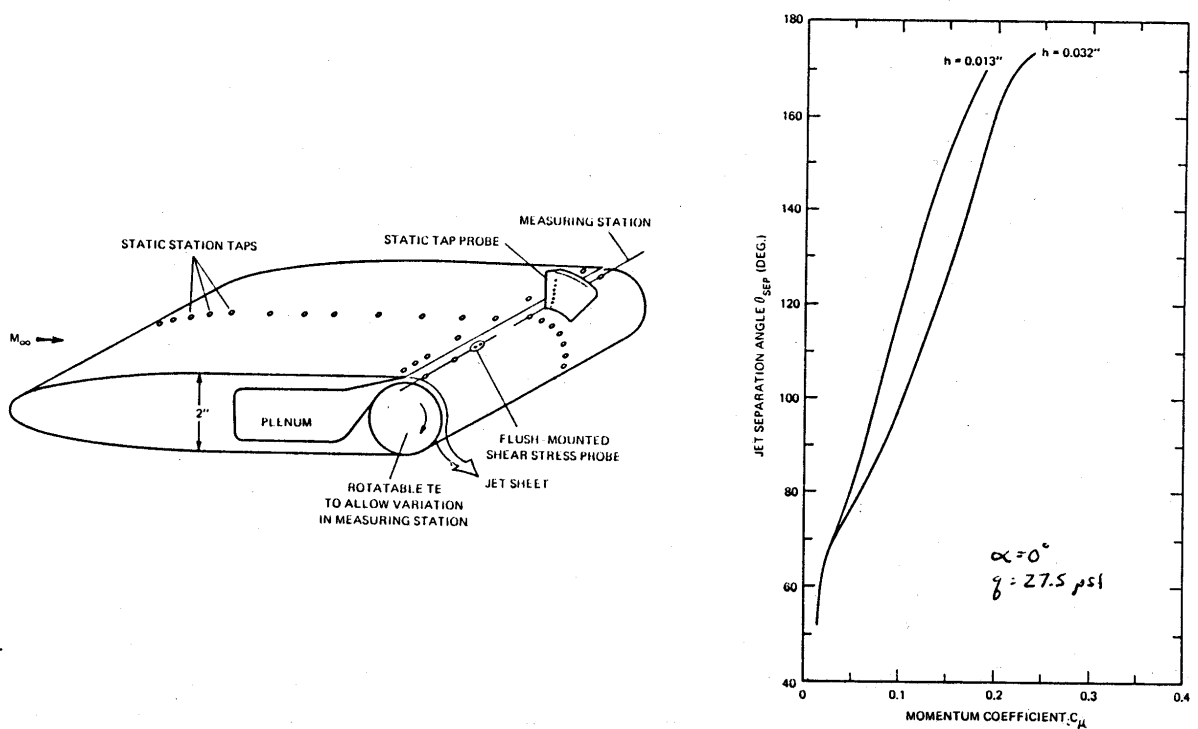


Fig. 10- Blowing Jet Separation Point Location Measured by Hot Film Shear Stress Probe

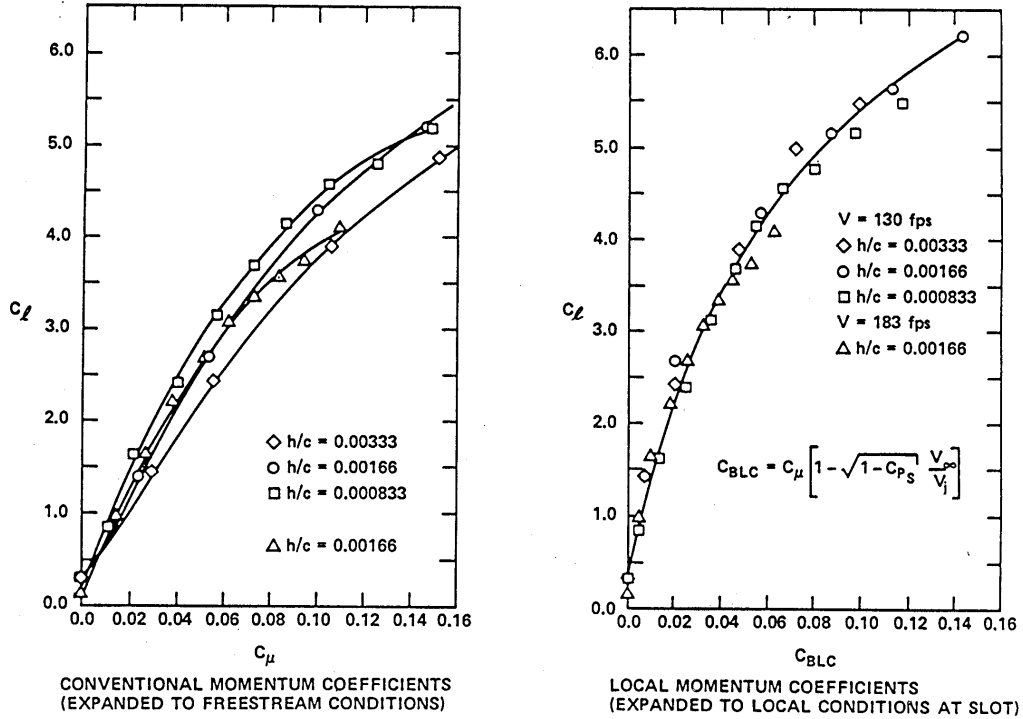


Fig. 11- Comparison to Momentum Coefficients based on Local Jet Exit Static Pressure (right) and Variation with Slot Height

X-Wing: An extraordinary use of unusual CC airfoils is the X-Wing VTOL vehicle ^{21,22,23}, a combined rotary/fixed-wing aircraft. Equipped with a 4-bladed rotor, the vehicle was designed to take off and hover with the same non-mechanical cyclic and collective benefits as above. However, forward flight at speeds roughly twice the limit on conventional rotors could be achieved using a “reverse velocity” blown rotor/wing concept, Figure 12. Typically, as vehicle speed increases, the retreating blade of a rotor sees a resulting velocity that is the difference between the vehicle forward speed and the blade rotational velocity; this can rapidly become a reverse flow at the blade trailing edge, an unacceptable region which moves further inboard as speed increases. Lift on that “stalled” blade segment can actually be negative; the rotor might not be trimable in roll, and drag increases dramatically. The X-wing avoids this problem at high speeds by employing CC on each end of the blade, Figure 12, and a “clever” control system can blow whichever slot is currently on the airfoil’s trailing

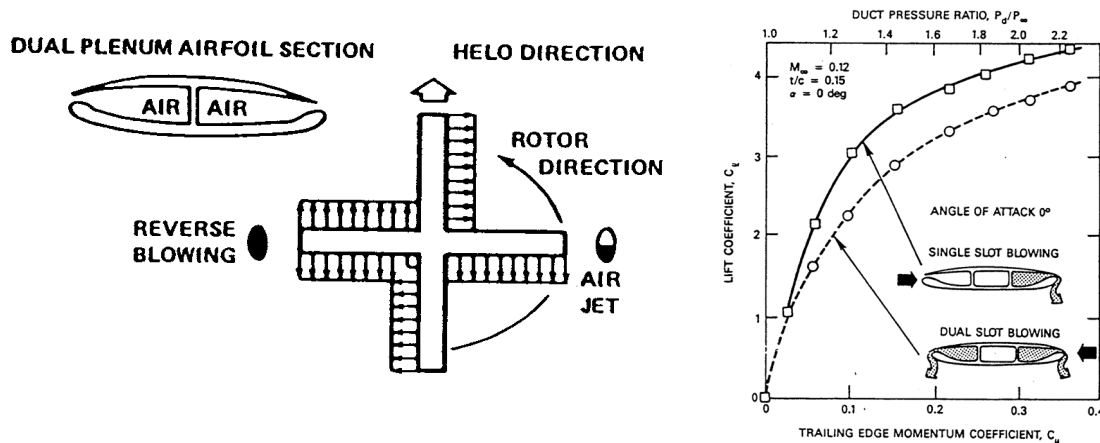


Fig. 12- Dual Blowing on a Reverse Velocity Rotor (Reference 21) and Blown Lift of Dual-Slotted CC Airfoils

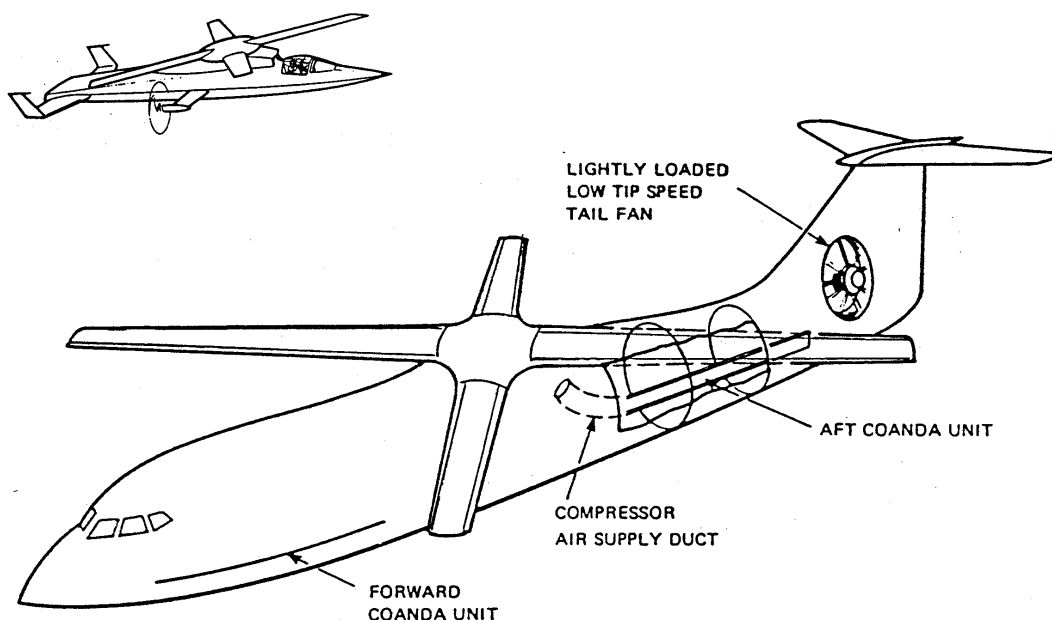


Fig. 13- X-Wing Rotor Configuration with Rotor Stopped, and Control Systems

edge. Thus, the airfoil never experiences flow from the “wrong” direction. The entire system can be simplified even further by use of simultaneous blowing from both leading and trailing edges of the double-ended airfoils²⁴, Figure 12 (right). Note that even if the flow is coming from the wrong direction (dashed curve), the dual-slotted airfoil still yields 80-90% of the single-slotted airfoil’s lift, even when the leading edge is counter the conventional direction (that compares to little, zero or negative lift from a conventional airfoil). This allows rotor-borne flight at much higher speed until eventual conversion to a fixed wing in an X-configuration is achieved, with the representative TE slots on each blade of the now fixed wing being used for roll and pitch control without moving surfaces. This concept was actually “flown” full-scale in the NASA Ames 40’ x 80’ tunnel and successfully completed the transition from hover to stopped-wing using pneumatics. Two representative configurations are shown in Figure 13 from Refs. 16 and 25.

Circulation Control Wing (CCW): The high-lift capability independent of angle of attack which was demonstrated by the CC Rotor airfoils above led to the application of CC as a simplified very-high-lift device for STOL aircraft. The airfoil in Figure 1 is representative of this simplified pneumatic concept, where both the mechanical trailing edge flap and the leading edge flap or slat have been replaced with non-moving pneumatic systems. Primary development of the concept took place in conjunction with CC Rotor development efforts at the Navy’s DTNSRDC^{12,16,26,27,28,29,30} in the time frame of late 1960s to early 1980s. Initially, the concept was modeled as a small add-on device²⁸ that would convert the wing flap’s sharp training edge into the round CC Wing (Figure 14, right), which was tested at DTNSRDC in specialized 2-D high-lift test facilities¹⁰. Compared to results from a family of more-conservative blown flaps, (Figure 15 from Ref. 30), the CCW profiles showed two significant advantages. They could generate greater C_l than the blown flap because of much greater streamline displacement and no sharp TE to limit streamline turning, or for the same chord-length device, could generate the same incremental C_l at much less C_{μ} required. An

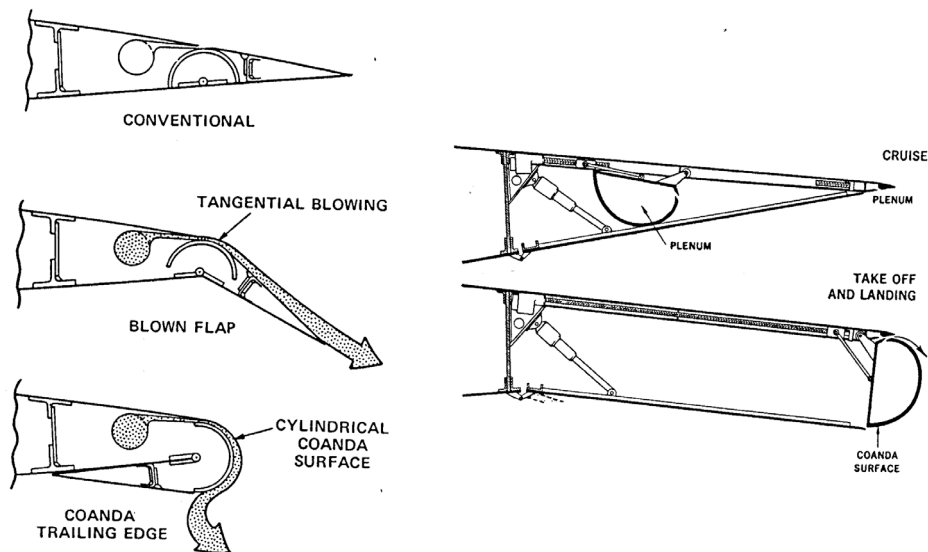


Fig. 14- Retractable/Storable CCW Trailing Edges

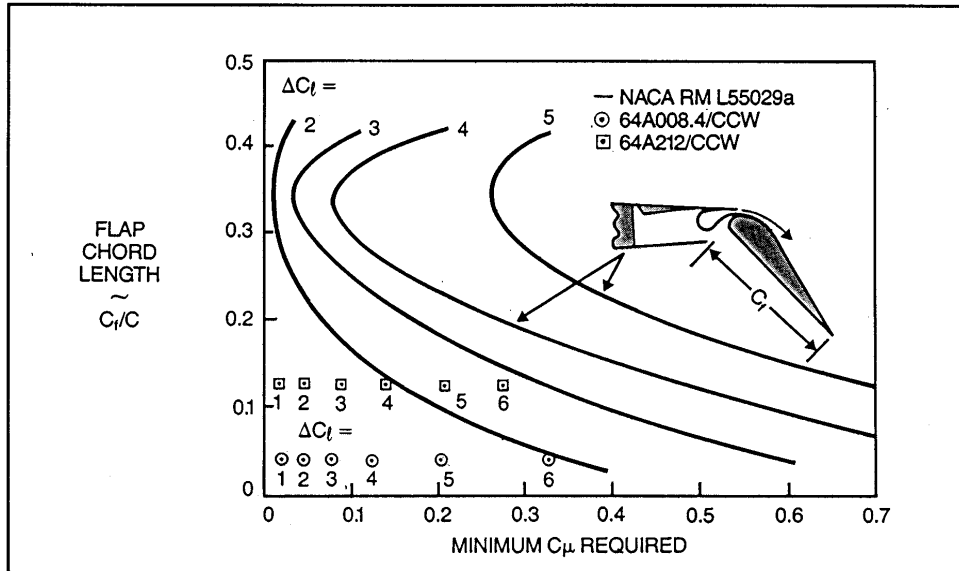


Fig. 15- Comparisons between CCW and Blown Flap Airfoils at $\alpha = 0^\circ$

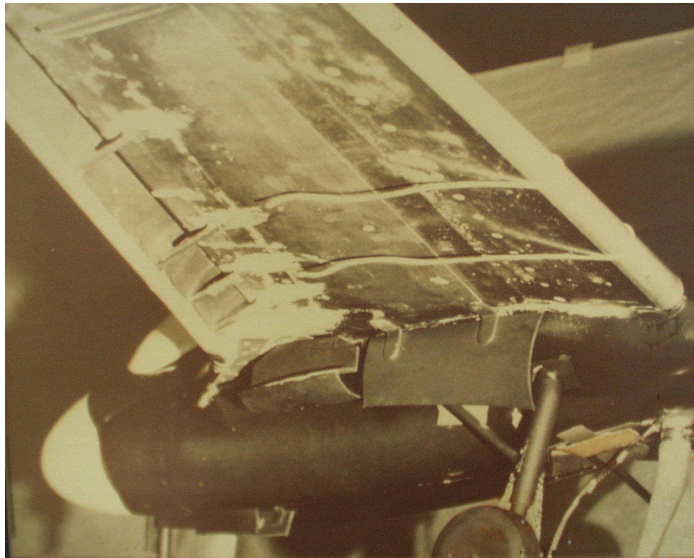


Fig. 16- CCW Jet Turning on the A-6/CCW Wind Tunnel Model at DTNSRDC

alternative 180° rotatable CCW TE is also shown in Fig 14 (left), which although it may be mechanically simpler, pays the penalty of losing wing area in the blown high-lift mode.

Numerous 2-D and 3-D wind-tunnel evaluations and feasibility studies led up to flight test of a fixed CCW device on an A-6/CCW STOL demonstrator aircraft³¹⁻³⁴ in 1979. Flow visualizations in Figure 16 show a full 180° of jet turning on a static 1/8-scale model of the test aircraft in the DTNSRDC tunnel, and Figure 17 shows the CCW installation on the fixed flap of the A-6 flight-test aircraft. Since this was a proof-of-concept flight test, the CCW device was not retractable and the air supply lines were mounted externally and cross-ducted in the fuselage, wherein they connected to the high-pressure bleed ports of the

standard J-52-P8A turbojet engine. Results using only available bleed air from the engines confirmed maxi-



Fig 17- A-6/CCW STOL Flight Demonstrator Aircraft

imum C_L values 120% greater than the conventional Fowler flap, or even more applicable, 140% increase in the usable lift coefficient at takeoff/approach angles of attack. Also confirmed were 30-35% reductions in the takeoff and approach speeds resulting in 60-65% reductions in takeoff and landing ground roll distances, and yielding values as short as 600-700 ft. This full-scale confirmation of CCW also implied that there was sufficient extra C_L generated to increase the liftable payload by 75% if the conventional takeoff ground roll distance were used. Also shown was that the additional lift-induced drag resulted in much steeper glide slopes on approach, where higher engine power settings (which could also be used for quicker response during waveoff) were offset by this excess drag.

A smaller CCW demonstrator based on a prop-driven BD-4 general aviation aircraft had been flown earlier by West Virginia University^{16,35,36}. In the flight-tested configuration, the CC blown cylinder was mounted at the trailing edge of a hinged flap that rotated 180° aft to increase the effective high-lift area by 20%, and included a BLC suction slot at the flap hinge upper surface (Figures 18, 19). The blowing air was supplied by an onboard 200 HP

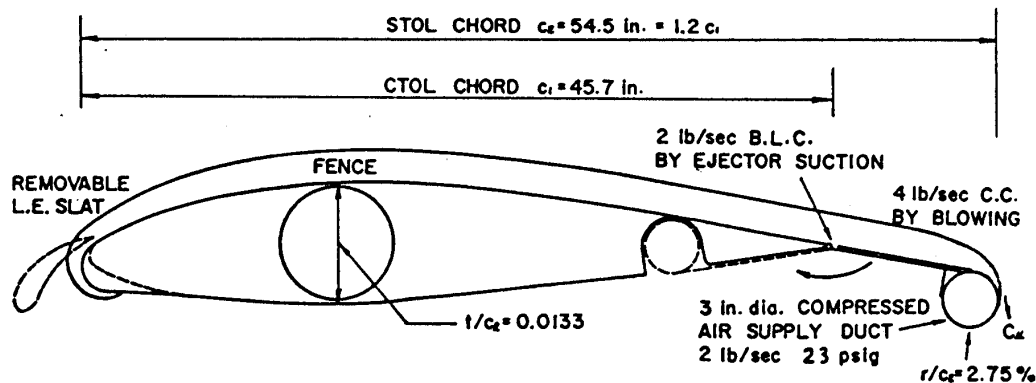


Fig. 18- WVU STOL Demonstrator CC Airfoil, Ref. 35

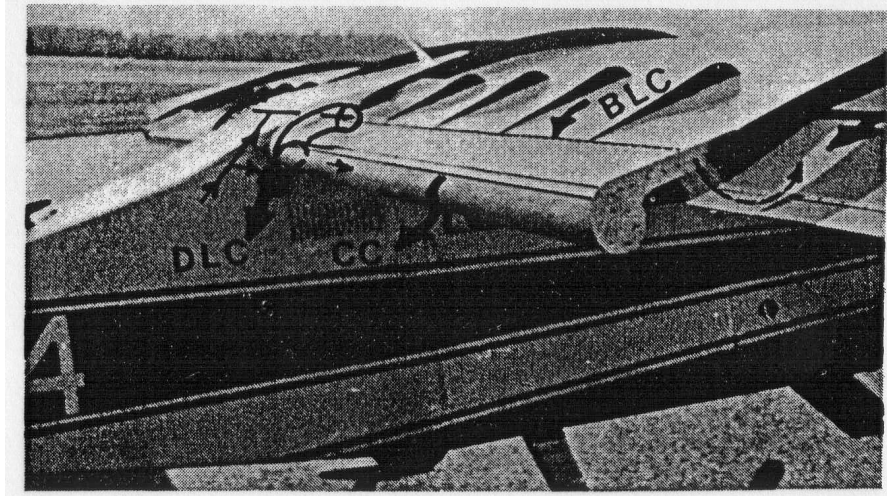


Fig. 19- WVU BD-4 Based STOL Demonstrator Aircraft, Ref. 35

compressor (APU), which provided enough air for blown ailerons in addition to the CCW. Section lift coefficient on the blown CCW wing section was increased by a factor of nearly 2.5 with blowing. Wing downwash on the tail reduced trimmed C_{Lmax} increase to a factor of 1.92, but provided 3-D lift augmentations of $\Delta C_L/C_{L0} = 15.2$, a significant increase should the required airflow be available from a general-aviation aircraft engine, say if using a supercharger or turbocharger.

Both of these fixed-wing flight programs demonstrated the feasibility of CCW as an operational STOL system in terms of high lift, short takeoff and landing, and simplicity, but also identified issues still to be resolved. Among these were the drag of the device in cruise flight (WVU solved this but at the cost of a mechanical 180° rotating flap that stowed in the aft wing cavity, and GTRI solved it with the dual-radius airfoil discussed below), and of course, the need for an onboard air source. Figure 20, turbojet engine ground test data³¹ taken during the A-6/CCW program, shows that the airflow acquired from high-pressure compressor bleed ports could be increased up to 3 to 4 times that of the standard engine

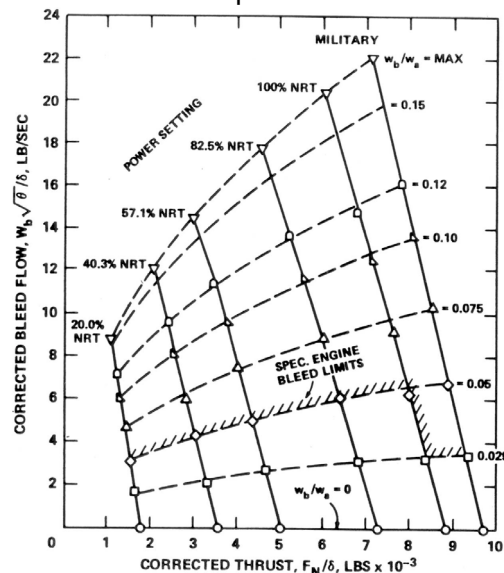


Fig. 20- Thrust Performance of J-52-P8A Turbojet Engine with Bleed

spec bleed limit without overheating, but obviously at the cost of takeoff thrust lost. Similar data for turbofan engines shows that engine core bleed is much more costly in thrust loss (although lower-pressure fan bleed is possible), and thus the idea of an ejector to trade excess pressure for extra mass flow appears feasible. However, the need to reduce CCW drag in cruise is a necessity for operational aircraft.

Advanced CCW Airfoils

DTNSRDC and Grumman took two approaches to the drag problem^{16,37,38,39}, one a fixed simple radius reduction and the second, a very-small-chord deflectable CCW flap. From the non-deflectable standpoint³⁷, a supercritical-type airfoil was employed as the baseline because it already had a bluff base thickness between $0.005c$ and $0.010c$. CCW rounded and semi-round (96° arc instead of 180°) designs were tested including a series of smaller radii, looking for reduced drag without loss of lift augmentation. The CCW/Supercritical airfoil was developed primarily from a low-speed standpoint, where a trailing-edge radius of $0.009c$ was found to produce very little drag penalty yet have superb lifting capability. Figure 21 shows its lift curves at constant C_{μ} compared to a family of mechanical multi-element flaps. Not only do the no-moving-parts CCW airfoils generate the same or greater lift as the maximum C_l of a triple-slotted-flap airfoil with mechanical slat, they also do so at $\alpha=0^\circ$. Note that the large leading edge of the supercritical airfoil provides a natural non-moving leading-edge device, which generated similar stall angles to the mechanical slat. One further benefit is the cruise drag polar (Figure 22), which is slightly higher unblown than the baseline supercritical airfoil, but with very slight blowing can reduce C_d to less than the baseline while increasing lift as well, both at constant α . Additional benefits of blown CC airfoils at speeds up to transonic were shown in the compressible flow tests of Reference 40, where blowing was seen to produce a very favorable boundary layer/shock interaction, drag reduction and increased C_l (Figure 23).

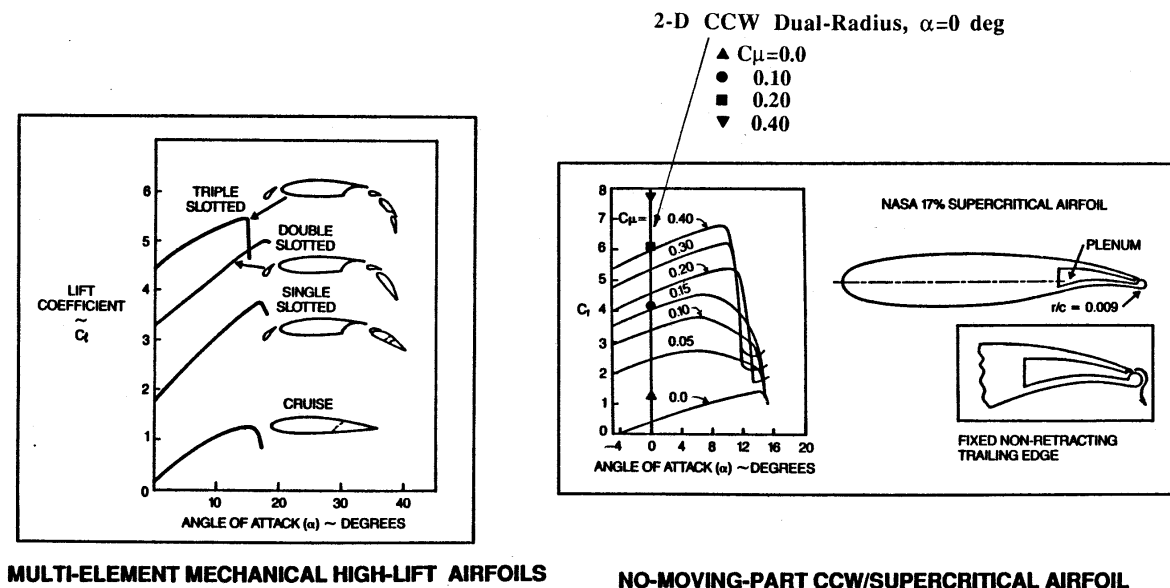


Fig 21- CCW/Supercritical, Dual-Radius CCW, and Conventional Mechanical Flap Airfoil Comparisons

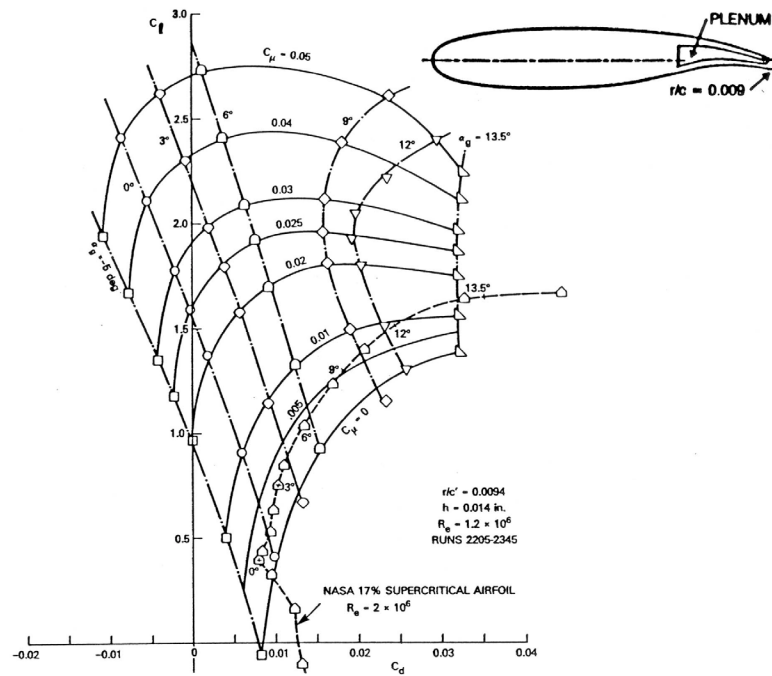


Fig. 22- Low-speed Drag Polars for CCW/Supercritical Airfoil

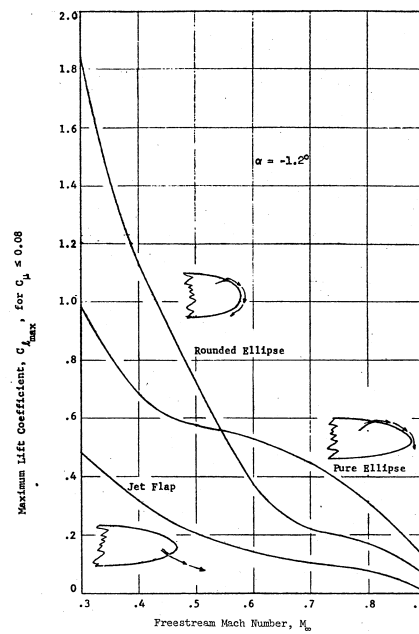


Fig. 23- Transonic Lift due to Blowing for 3 Pneumatic Ellipse Airfoils, Ref. 40

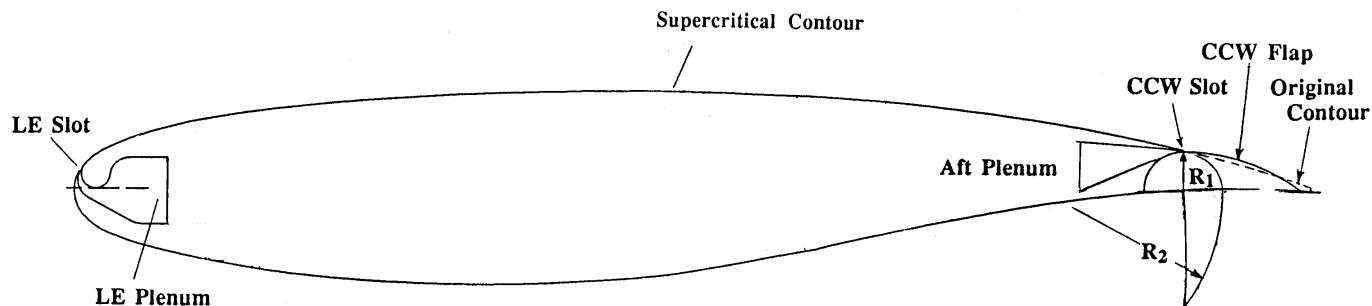


Fig. 24- Dual Radius CCW Airfoil with LE Blowing

The second approach to the drag problem was a simple CCW flap with a curved upper surface and a sharp trailing edge, Figure 24 from Refs. 38 and 41. Here, a short-chord flap (less than $0.10c$) pivots about a hinge on the lower surface and exposes a smaller-radius CCW surface downstream of the tangential slot. This radius is approximately the airfoil thickness at the slot location, less the slot height. The upper surface of this flap is a second much-larger-radius arc, the radius being chosen to keep the arc close to the airfoil aft contour. As the small flap is deflected on this Dual-Radius CCW airfoil, the large radius produces an arced CC aft surface with a turning arc much larger than the flap deflection angle. For the 90° flap shown here, the jet turning angle is about 135° (compare to Figures 8 and 10), limited by the trailing-edge corner. With flap retracted to 0° , the airfoil is in a sharp-trailing-edge cruise configuration. The slight mechanical addition provides unblown camber as well. The leading edge employs an inverted tangential slot to replace any mechanical flap there. Lift data for the 90° flap configuration is also shown in Figure 21, where C_l increases of 35% over the CCW/Supercritical airfoil occur, with considerably greater increases over the conventional flaps.

Figures 25 and 26 also show additional advantages of this configuration: the ability to dramatically interchange lift and drag as the small-chord CCW flap is deployed (Fig 25) and the increased lift and stall α as leading-edge blowing is activated (Fig 26). The thrust/drag interchange in Figure 25 implies the potential for high lift and drag for STOL approach (remember, induced drag due to high lift is not included in this data for 2-D airfoils) or high lift and reduced drag for takeoff. Figure 26 shows the capability of this non-moving LE device to re-attach flow, prevent stall and dramatically increase C_{lmax} . Figure 27 combines the above data in terms of C_l versus L/D_e , where the equivalent drag coefficient is defined as $C_{de} = C_d + C_{\mu}$ to account for the blowing required to yield these drag changes. This data includes 4 CCW flap angles and various LE and TE blowing values. Figure 27 includes a locus of achievable C_l versus the associated efficiencies in comparison to the clean cruise airfoil (Flap= 0° , $C_{\mu LE}=0$, $C_{\mu TE}=0$). This plot confirms the ability of CCW airfoils to generate very high lift and associated drag (reduced L/D_e) for approach, plus much higher L/D_e at somewhat lower C_l for takeoff and climb out. Because of the latter, the 30° CCW flap at reduced C_{μ} appears to be an excellent configuration for takeoff.

2-D CCW SUPERCRITICAL AIRFOIL, DUAL - RADIUS FLAPS, DRAG POLARS, THE PENALTY FOR LIFT ??

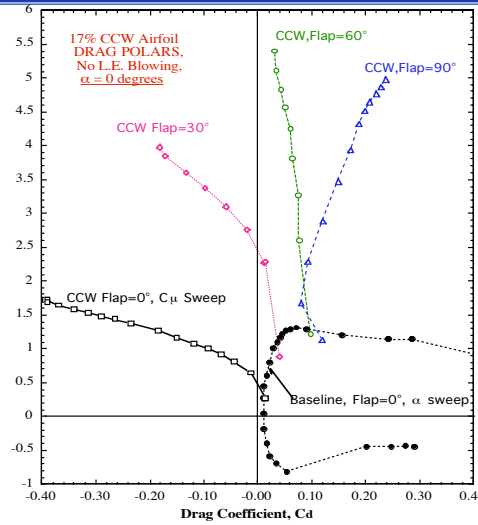
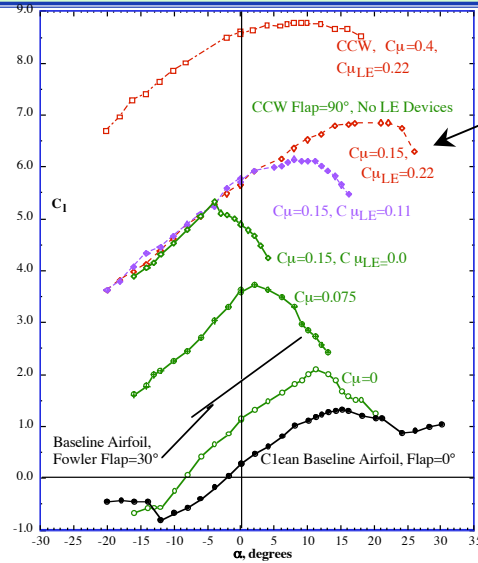


Fig. 25- Drag Polars of CCW Dual Radius Airfoil at Various Flap angles

2-D CCW/SUPERCritical AIRFOIL, DUAL-RADIUS CCW, R1=0.25", FLAP=90°, BLOWN L.E. DEVICE



Leading Edge Protection is Essential during High lift, whether from α or from Blowing

Fig. 26- Dual Radius 90° Flap CCW Airfoil Lift as Functions of α and C_{μ} , with LE Blowing

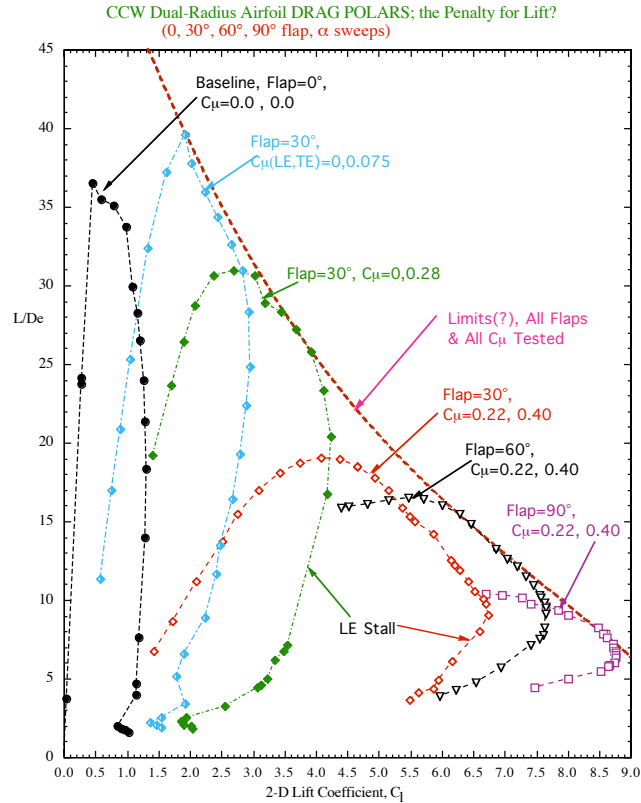


Fig. 27- Lift and Equivalent Efficiencies of Dual Radius CCW Airfoil

One additional benefit results for the 0° flap CCW case. While in cruise, drag is low due to the sharp trailing edge, but should blowing be initiated without flap deflection, Figure 28, significant lift is generated by the flap curvature, while drag reduction occurs due to thrust recovery. Note the comparison to the NASA Energy Efficient Transport slotted, flapped airfoil. Not only is lift greater for the CCW cruise airfoil, the drag polars move into the thrust recovery region. From these results, one can also immediately realize the potential of this high-lift system as a non-moving roll/yaw device. Blowing only the undeflected right wing's flap will produce a lift (roll with right wing up) and favorable yaw (nose left), thus yielding favorable roll/yaw coupling from a non-moving surface, instead of the usual adverse roll/yaw coupling from a conventional aileron.

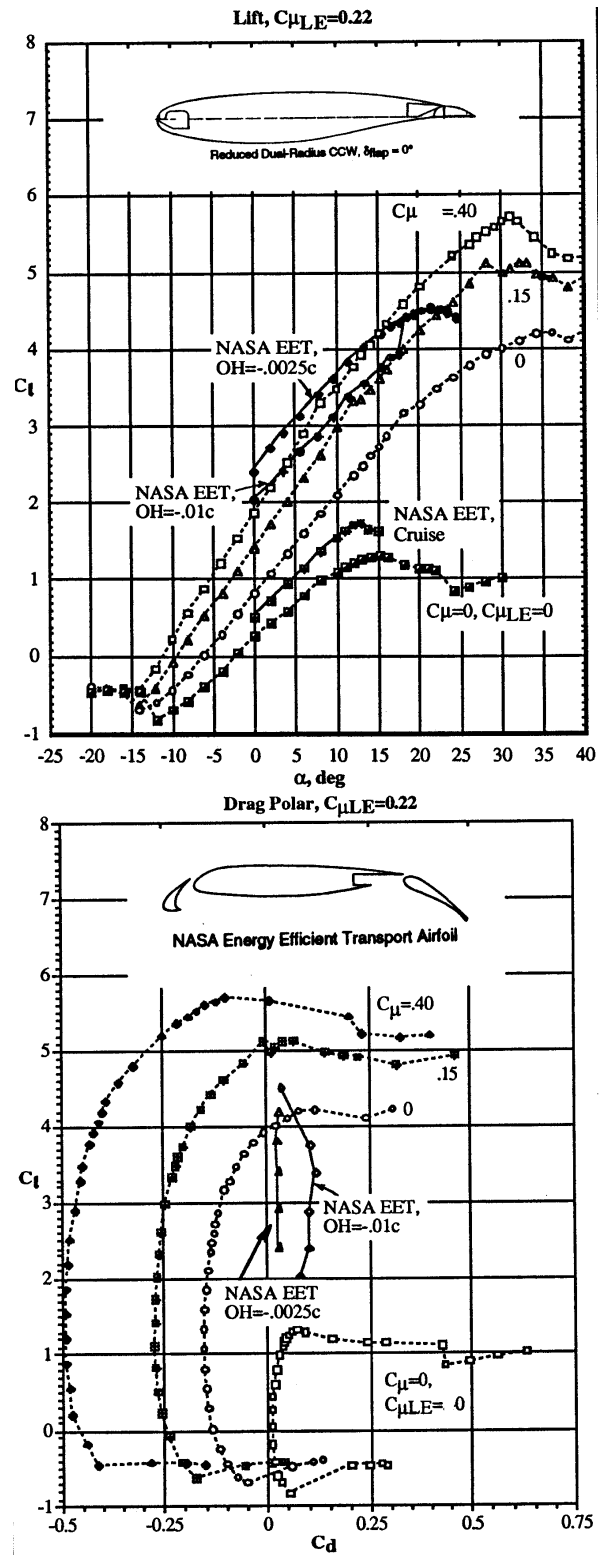


Fig. 28- Comparison of Cruise Dual-Radius CCW (0° flap) with Mechanical Flap Airfoil

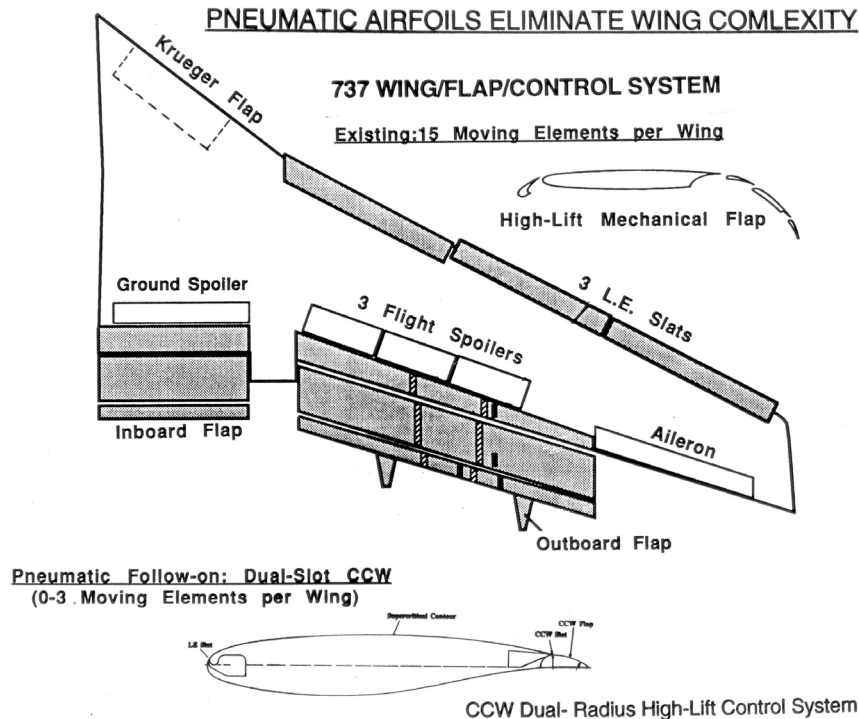


Fig. 29- Pneumatic Airfoils Simplify Wing Complexity

WOD=0.0 kt.

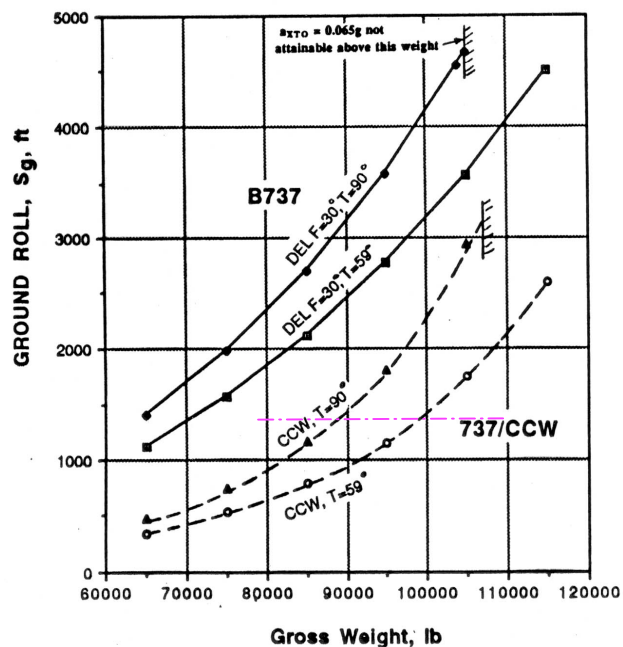


Fig. 30- 737/CCW Takeoff Ground Rolls, Sea Level, 0 kt Headwind

A study⁴¹ was conducted for NASA Langley Research Center to evaluate the effectiveness of applying this concept to an Advanced Subsonic Transport. Here, the Dual-Radius CCW of Figure 24 was applied to a 737 wing characterized in Figure 29. The typical 15 moving elements per wing were replaced with the CCW single element flaps and leading-edge blowing, yielding perhaps a maximum of 3 components per wing (the outboard CCW

flap became the aileron, and blowing differentially on the CCW flap replaced the spoilers for roll). Using only fan bleed air (and the associated lower thrust lost), replacing the conventional flaps with CCW was able to triple the usable lift at takeoff and produce the ground roll reductions shown in Figure 30. For lighter aircraft weights, blown takeoff rolls of 400-500 feet are possible with 0 Kt headwind, about 1/3 that of the conventional aircraft; with a 20 knot headwind (WOD), 200-300 feet rolls were predicted for the 737/CCW configuration. The tradeoff in increased liftable weight at constant ground roll is possible here as well. For the conventional 737's ground roll of 1350 ft at $W=70,000$ lb., the 737/CCW can increase the liftable weight to near 100,000 lb. with the same runway length, a 43% increase in gross weight (fuel, payload, etc.). Climb angle over the 50-foot obstacle is slightly less for the CCW aircraft⁴¹ than for the conventional one.

These pneumatic benefits are not limited to subsonic transports. Reference 42 reports on the application of CCW to a generic High Speed Civil Transport (HSCT) configuration developed by GTRI for NASA LaRC. Here the intention was to reduce takeoff wing area required (and thus increase cruise performance) by employing simplified CCW flaps and trading increased lift coefficient for reduced wing area. The extra lift would also allow a reduction in takeoff/approach angle, and eliminate the need for fuselage nose droop, aft fuselage upsweep, extended nose gear and/or synthetic vision. Reference 42 reports 90° jet turning on the CCW flap, over 100% increase in C_{Lmax} and 45% increase in stall angle. High lift generation from various blown devices and blown canards is seen in Figure 31. Note the effect of the blown canard on stall α . In-house feasibility studies⁴³ have been conducted and confirm this potential for pneumatic wings/canards on high-speed aircraft.

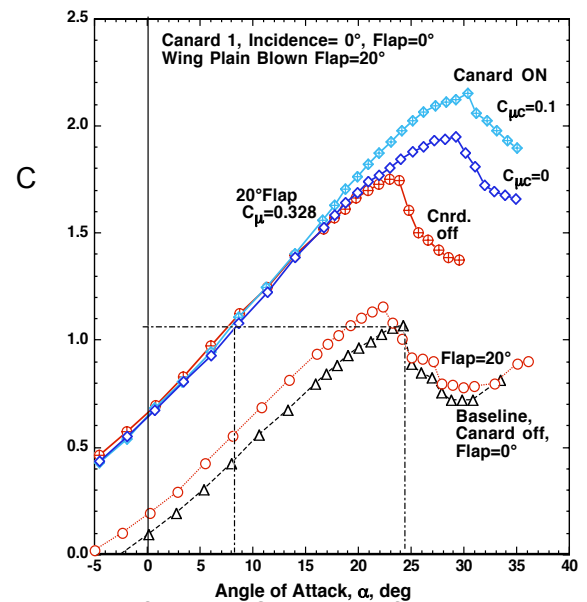


Fig. 31- Lift Augmentation on the GTRI HSCT/CCW Semi-span Model & Blown Canard (Ref 42)

Powered Lift and Engine Thrust Deflection

CCW/USB: Whereas mechanical flaps have been employed to entrain and deflect thrust from engines mounted on the wing upper surface (Upper Surface Blowing, USB), it was envisioned that the entrainment capabilities of CCW could do the same without the mechanical complexity, and thus CCW/USB^{30,44,45,46,47,48} was born, Figure 32. Subsonic

wind tunnel investigations⁴⁴ at DTNSRDC showed no-moving-part pneumatic capability to entrain and turn USB engine thrust well past the 60 or so degrees of a mechanical USB system, but also continue through 90°, and then rotate the thrust forward as a thrust reverser through 165°, Figure 33. The possibility then exists for high lift and thrust reversing all in one system just by varying the CCW blowing rate, with a possibility of VTOL in between (depending on installed thrust levels). Wind-on data (Figure 34) shows very interesting lift- drag polars at $\alpha=0^\circ$, with the ability to vary lift and drag by blowing alone, independent of angle of attack. The enhanced lift capability is far more than mere thrust deflection (i.e., $\Delta C_L = C_T [\sin \delta_{jet} + \alpha]$). It results from the increased velocity from the engine exhaust being entrained onto the blown lift surfaces, and the greatly increased circulation lift beyond the powered wing only.

A full-scale ground test was performed by the author at NASA Ames with the CCW/USB mounted behind one engine of the NASA Quiet Short haul Research Aircraft, with the aircraft mounted on a force balance ^{47,49,50,51}. Figure 35 shows the installation behind the left inboard engine of the QSRA. Thrust deflections as high as over 100° were recorded behind

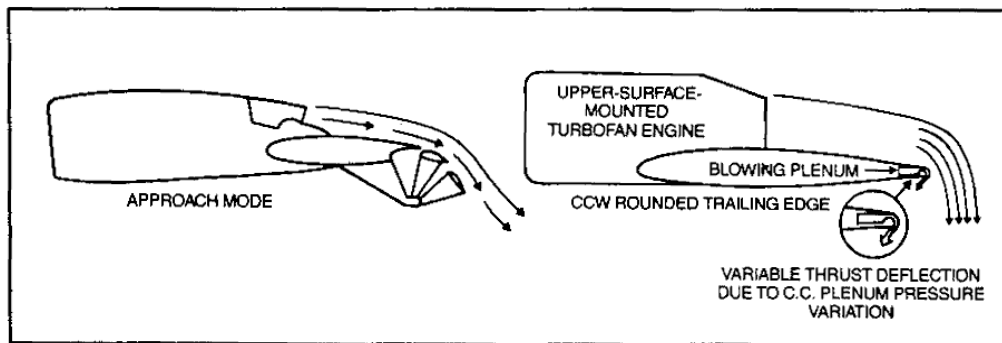


Fig. 32- USB and CCW/USB Powered-Lift Concepts

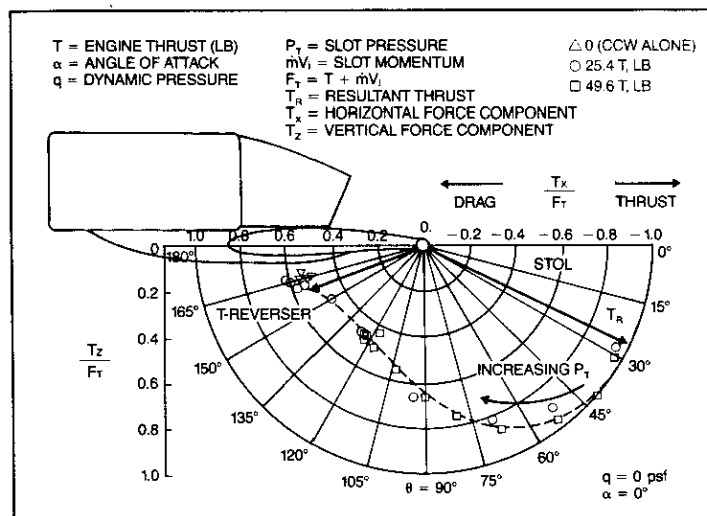


Fig. 33- CCW/USB Model Static Thrust Deflection by Blowing only

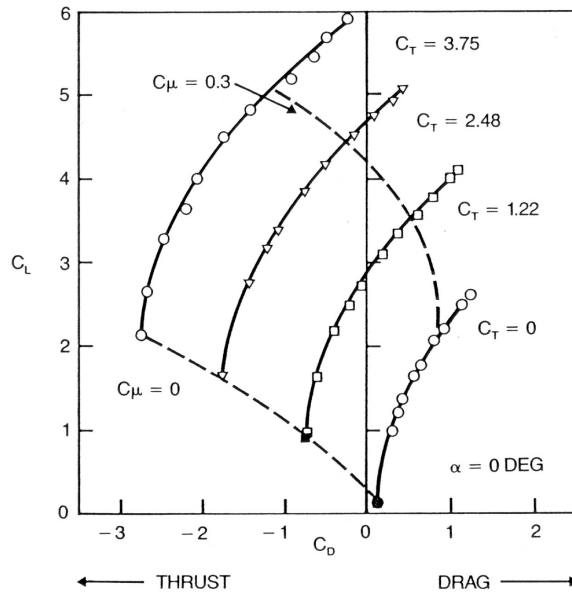


Fig. 34- CCW/USB Model Lift-Drag Polars, $\alpha=0^\circ$



Fig. 35- CCW/USB Test Assembly on the QSRA Aircraft

this single operating engine. These data are expected to improve if the two engines per wing are operated together and the two exhaust sheets converge for even better turning. As a result of this test, Navy feasibility studies⁴⁶ were conducted for a sea-based turbofan-powered STOL aircraft using both CCW and CCW/USB, Figure 36. These studies, based on the above powered model wind-tunnel tests, showed takeoff ground rolls of 100-200 feet (Figure 37), varying with weight, blowing and thrust levels, and resulting from powered C_L values of 8-9.



Fig. 36- Proposed CCW/USB Navy STOL Aircraft

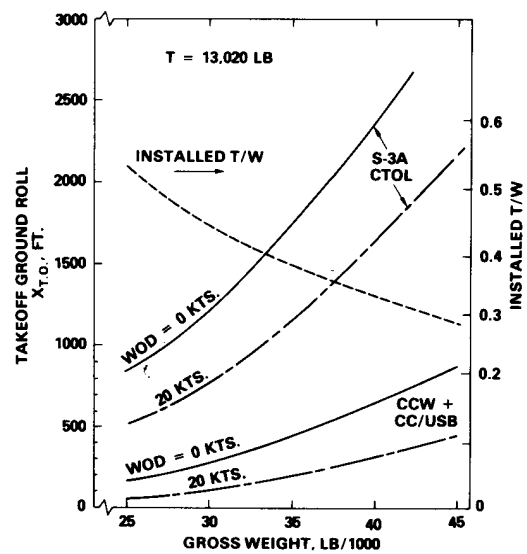


Fig. 37- Takeoff Ground Rolls for Proposed CCW/USB Navy STOL Aircraft

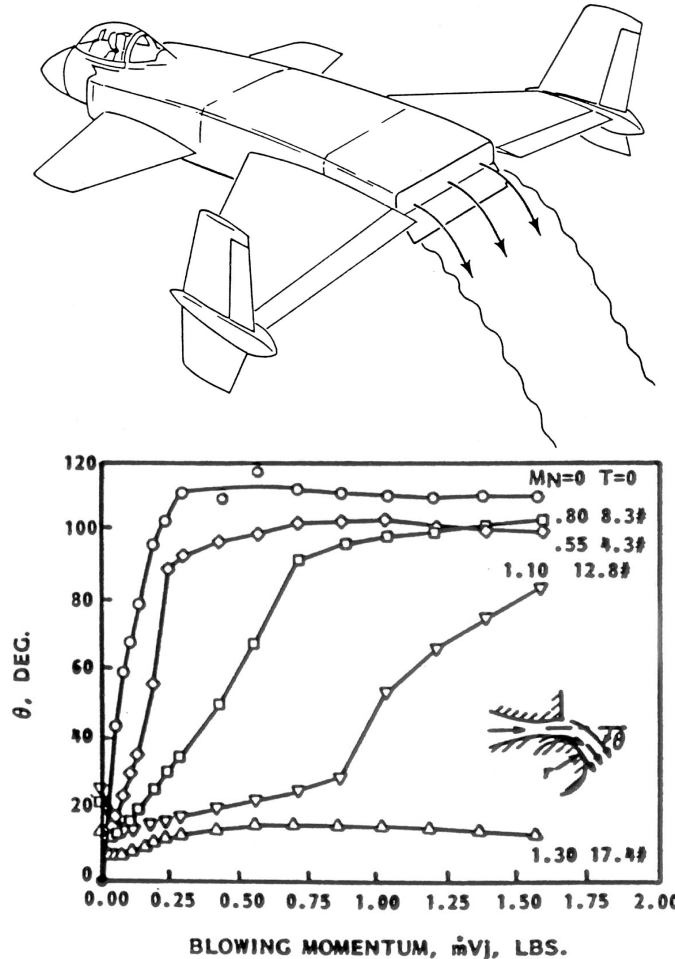


Fig. 38- Pneumatic Thrust Deflection of Rectangular Jet Exhaust (left, from Reference 52) and Unpublished Static Test Results of a Similar Configuration (right)

CC/Jet Deflection: In a related effort⁵², CC entrainment was also applied to high performance aircraft to yield thrust deflection for much higher engine exhaust velocities, where lesser jet turning could still provide excellent STOL potential due to higher thrust/weight ratio. An example is shown in Figure 38. In-house unpublished experimental work by the present author provided similar studies, where we were able to deflect supersonic jets from rectangular nozzles by more than 80°, using blowing jet momentum values around 10% of the engine thrust.

Pneumatic Channel Wing: A configuration using similar thrust deflection capability of a CC trailing edge has recently been under development by GTRI for NASA Langley Research Center. Called the Pneumatic Channel Wing, Figure 39, it employs blowing at the trailing edge of a 180° channel (similar to the much earlier but unblown Custer Channel Wing) to entrain the propeller's thrust, augment the velocity in the channel and thus generate high powered lift. Figure 40 (from Refs. 53 and 54) shows typical GTRI wind tunnel lift data as a function of both blowing and thrust compared to the baseline unblown channel wing configuration, where untrimmed C_{Lmax} is increased by a factor of over 7 to a value of 10.5 - 11. Reference 54 shows predicted takeoff ground rolls of less than 100 feet on a hot day at 3000' altitude using wing angle of attack of only 10°.

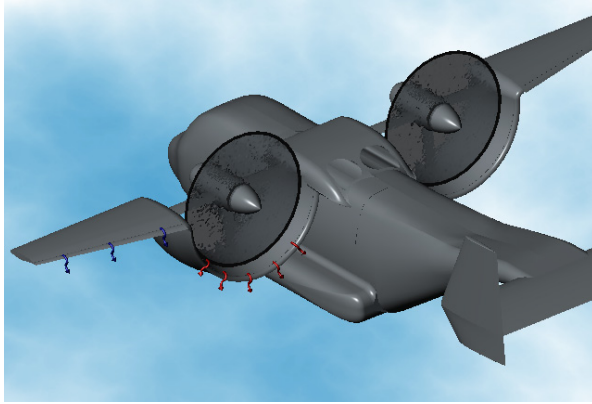


Fig. 39- Conceptual Pneumatic Channel Wing and Semi-span Model in GTRI MTF tunnel

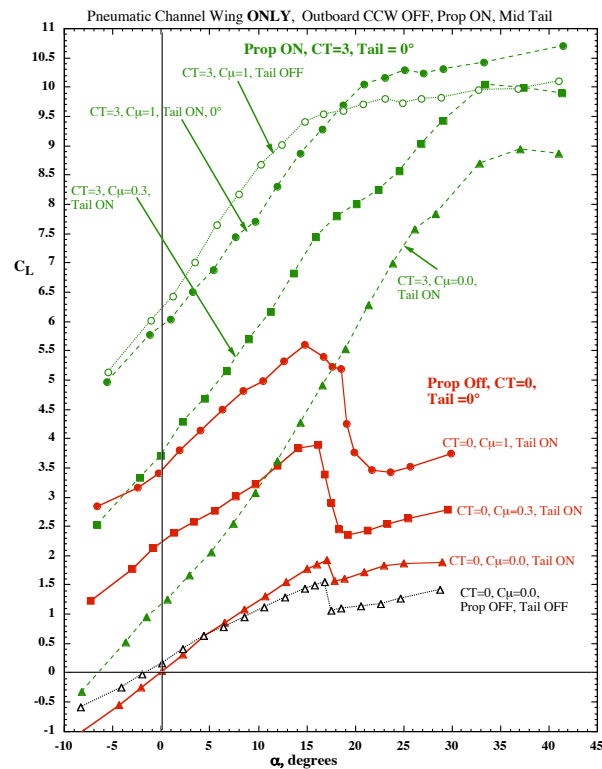


Fig. 40- Pneumatic Channel Wing Lift from Thrust and Blowing (from Ref. 54)

Other Aircraft Applications

CC Propeller: In a manner somewhat similar to the CC Rotor above, CC airfoils have also been incorporated into general aviation propeller designs to replace complex and expensive mechanical variable-pitch blades with fixed-pitch pneumatic blades that change aerodynamic and thrust characteristics through mass flow variation to each blade. Figure 41 shows a proposed application, where the propeller blade airfoil is the CCW/Supercritical type of Figure 21. Refs. 55, 56, and 57 discuss feasibility studies which concluded that such

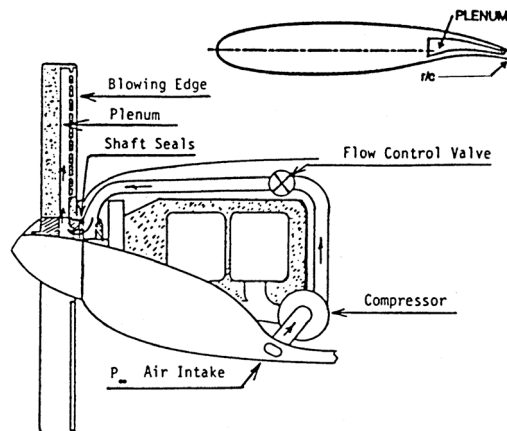


Fig. 41- Circulation Control Propeller System

a pneumatic variable-pitch propeller was possible and held interesting promise depending on the details and costs of an air compressor (such as an aircraft supercharger or turbo-charger) to supply the blowing. The study also envisioned supersonic jet blowing to be a possible problem, but much of the CCW data already presented above have blowing pressures well above choked (sonic).

Moment Control, Stability Augmentation, Induced Drag Reduction

The above data and applications show the ability to pneumatically augment or modify lift and drag without use of moving parts (except possibly very short chord dual-radius CCW devices) and with a high rate of return on input jet momentum. The application to a pneumatic rudder or even winglets can provide side force generation as well⁵⁸. It should be obvious that augmenting the aerodynamic force capability of any control surface by blowing can also either increase the control power or reduce the required area of the device, with associated benefits including maintaining stability levels but reducing cruise drag. Now mentioned will be only a few further and less obvious examples of pneumatic control devices; many others can be found in Refs. 12, 16, and 58.

The aft suction peak downstream of the CCW slot (usually at 95% chord or greater) produces very large nose-down pitching moment, which besides having to be trimmed, also produces greatly enhanced longitudinal pitch stability. In fact, the A-6/CCW flight demonstrator had such large negative values of dC_M/dC_L that the center of gravity of the flight-test aircraft was moved aft by an additional 10 - 15% chord to aid in trim, and the aircraft still had greater longitudinal stability than the conventional A-6, flaps down^{32,34}. A clever application of CCW is shown in Figure 42 on a forward swept wing⁵⁹. Previously, increasing blowing on an aft-swept trailing edge pulled the center of pressure (cp) outboard and aft, but during this tunnel evaluation⁵⁹, the cp was made to move outboard and thus forward with blowing. The amount of x_{cp} movement was controlled by which segments of the trailing-edge slots were blown, and by how much.

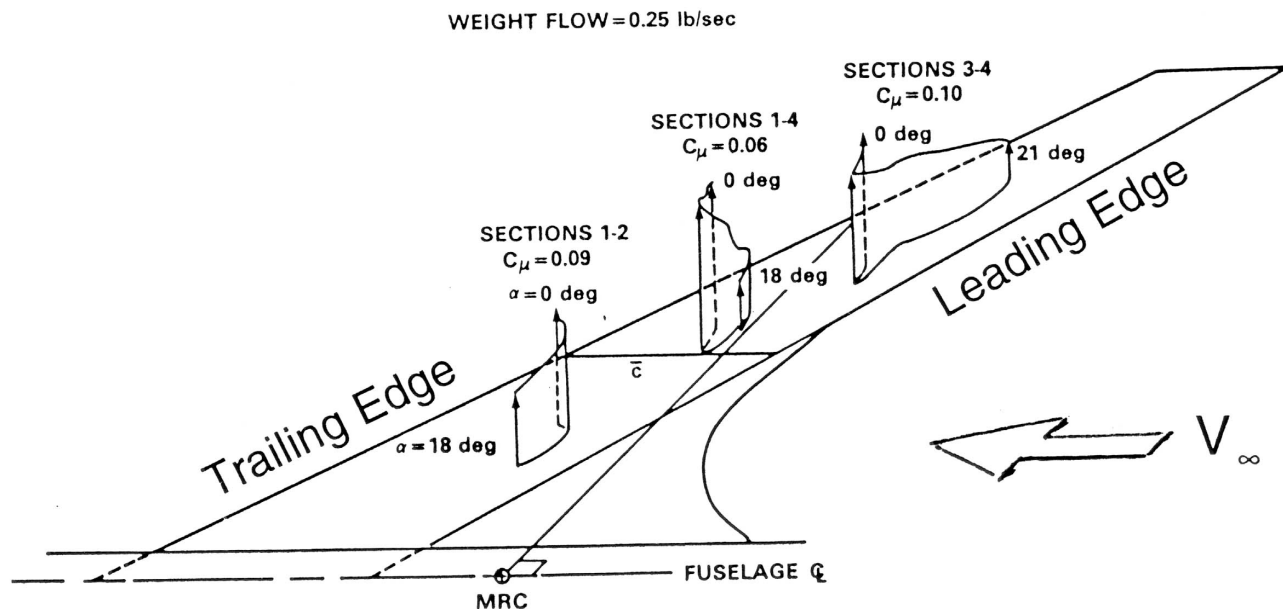


Fig. 42- CCW Applied to Forward Swept Wing for Pitching Moment Reduction

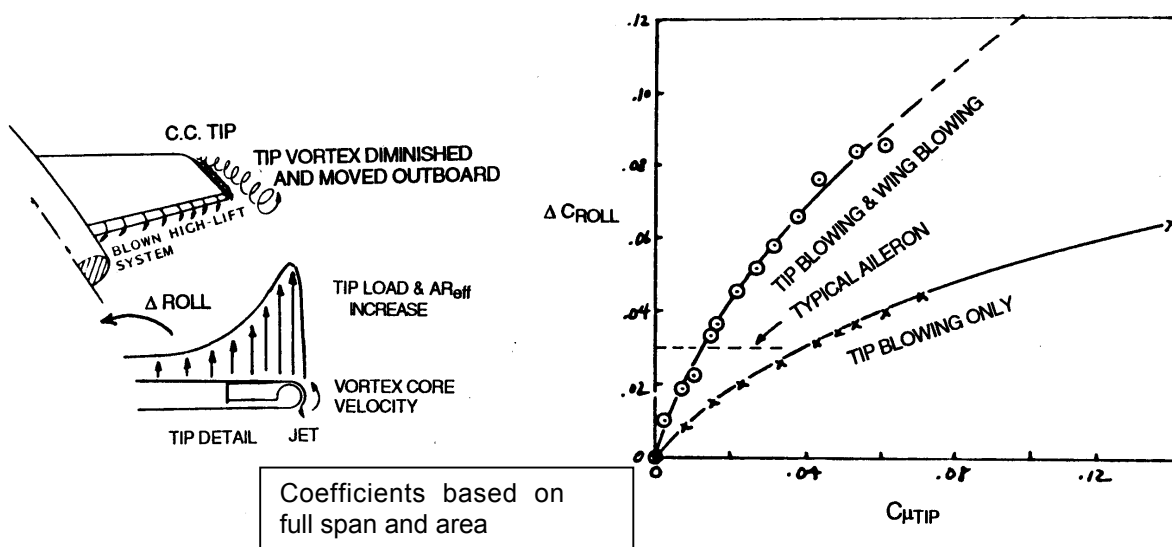


Fig. 43- Roll Due to CC Wingtip Blowing, $\alpha = 0^\circ$

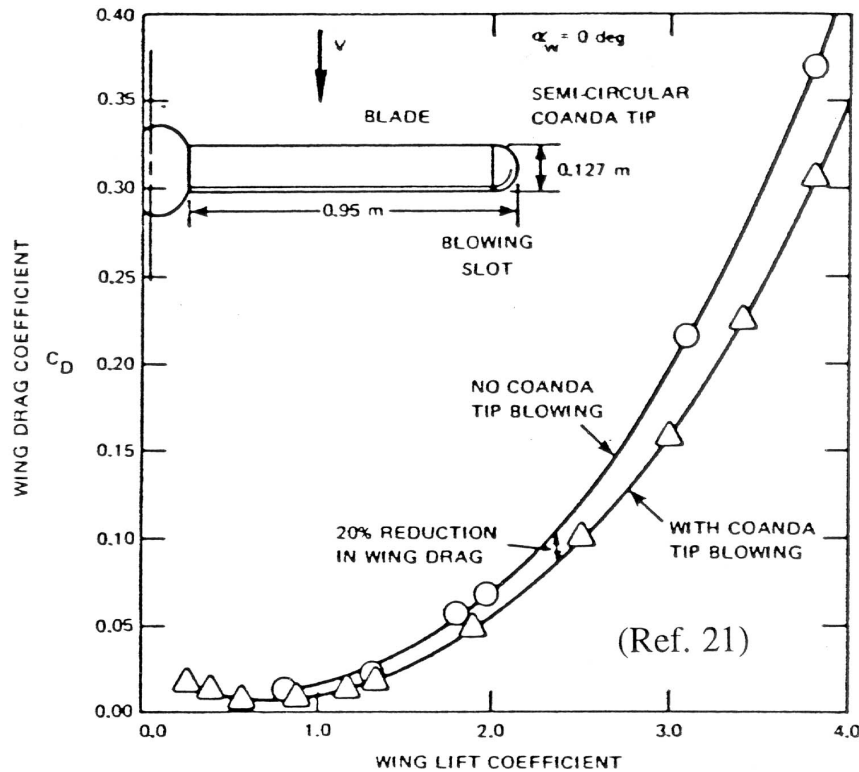


Fig 44- Tip Blowing for Induced-Drag Reduction

Pneumatic roll control by differential wing blowing can produce phenomenal rolling moment increments, Figure 43, where only one wing of a CCW configuration is blown. A second innovation is also shown here: letting the slot continue around the wing tip. Now, high suction peaks at the wing tip, having a maximum moment arm, can yield even greater rolling moment. For reference, a conventional 0.20-chord aileron deflected down 30° on the outboard 50% span of this wing produced an incremental $\Delta C_{roll} = -0.03$. Figure 44 leads to one further advantage of the CC wing tip, where blowing down around the tip directly counteracts the tip vortex rollup and relocates it further outboard, creating an effective aspect ratio increase. Figure 44 shows the effective drag reductions due to tip blowing²¹ on an already high-aspect-ratio CC Rotor blade. At the higher C_L values where induced drag usually dominates, C_D reductions of 17 to 19% are seen, with greater percentage reductions at lower C_L . Lower aspect ratio aircraft wings using this technique should yield even greater C_D reduction. One can also alter the spanwise lift distribution with spanwise tapered blowing to approximate an elliptic distribution, and thus minimize induced drag both in cruise and during climb out.

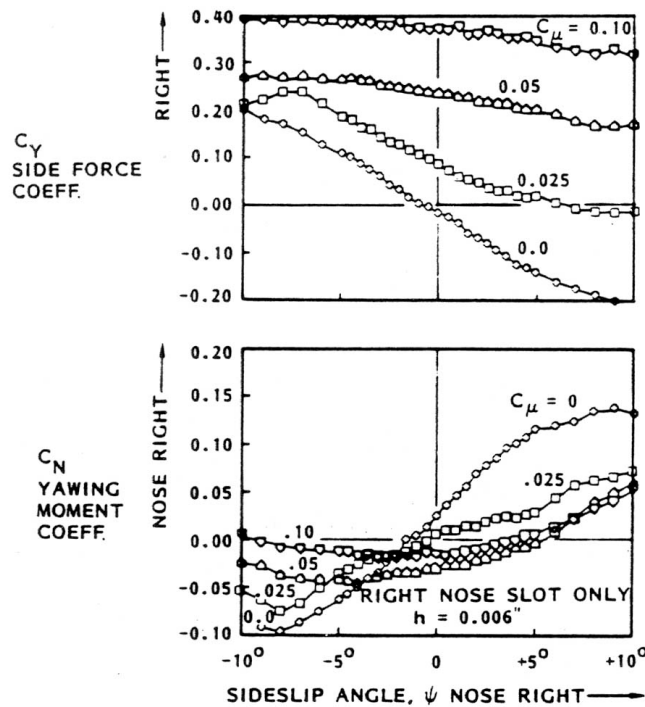


Fig. 45- Tangential Forebody Blowing for Yaw and Side Force Control, $\alpha=35^\circ$

In 1986, this author experimentally applied blowing from a tangential slot along the nose of a generic high- α vortex-lift configuration, thus turning the fuselage into a side-force and yawing-moment generator. Other investigators have more recently tried similar schemes, but the results shown in Figure 45 summarize these effects. At $\alpha=35^\circ$, the conventional rudder was useless because of fuselage blockage and separated flow (see $C_{\mu}=0$ curve), but blowing on the right side of the nose restored directional stability when the vehicle was yawed to the left, and vice versa. Large side force was also generated by blowing.

Microflyer and Pulsed Blowing

A combination of all of the above force and moment control applications has been pursued recently at GTRI relative to a very small Unmanned Aerial Vehicle, the Pneumatic Microflyer⁶⁰. Jet turning on a small-scale, low-Reynolds-number wing is seen in Figure 46. Pneumatic lift and control surfaces will be driven by gas generated by a GTRI proprietary engine powering the flapping wings of a 6-inch-span flying-insect-like UAV. The opportunity also exists here to take advantage of pulsed blowing, investigated in Refs. 61 and 62 for application to blown flaps and in Ref. 63 relative to CCW. Here, for properly shaped blowing wave forms, mass flow required was greatly reduced experimentally by up to 40 to 50% (Figure 47), or conversely, greater lift could be generated by the same mean mass flow levels. Also, as a simplifying means, all pneumatic Microflyer control moments would be generated by differential blowing, rather than by very small moving mechanical parts.



Fig. 46- Low-Reynolds-number Microflyer Wing with CCW Turning

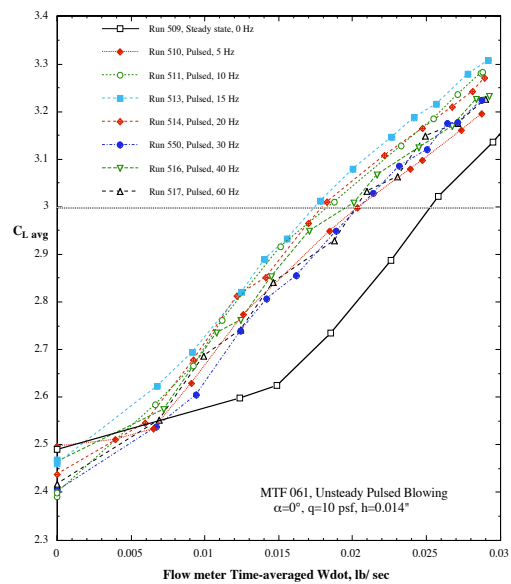
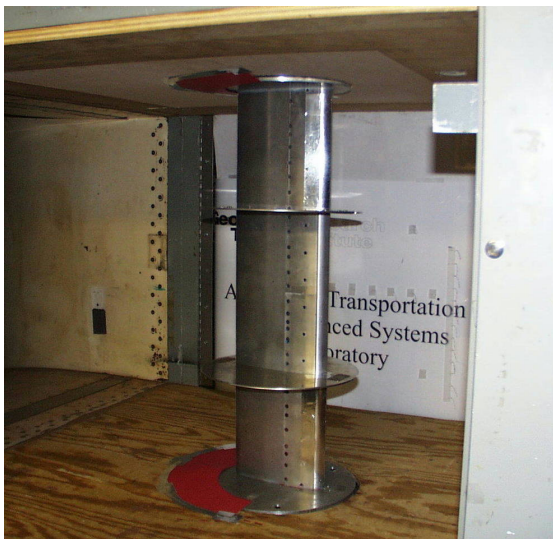


Fig. 47- GTRI/NASA Pulsed Blowing Investigations to Reduce Required Mass Flows (Ref. 63)

Non-Flying Applications of Circulation Control

A number of non-flying applications have been investigated, where the Circulation Control phenomenon was used to augment or modify flowfields for unique purposes.

In order to provide pitch and/or yaw control for submarines without using mechanical stern planes, a dual-slotted “pneumatic” stern plane⁶⁴ was designed for submerged applications, Figure 48. Here, up or down pitch of the submarine (or right or left yawing moment) could all be provided by blowing the appropriate slot. Towing basin tests of this

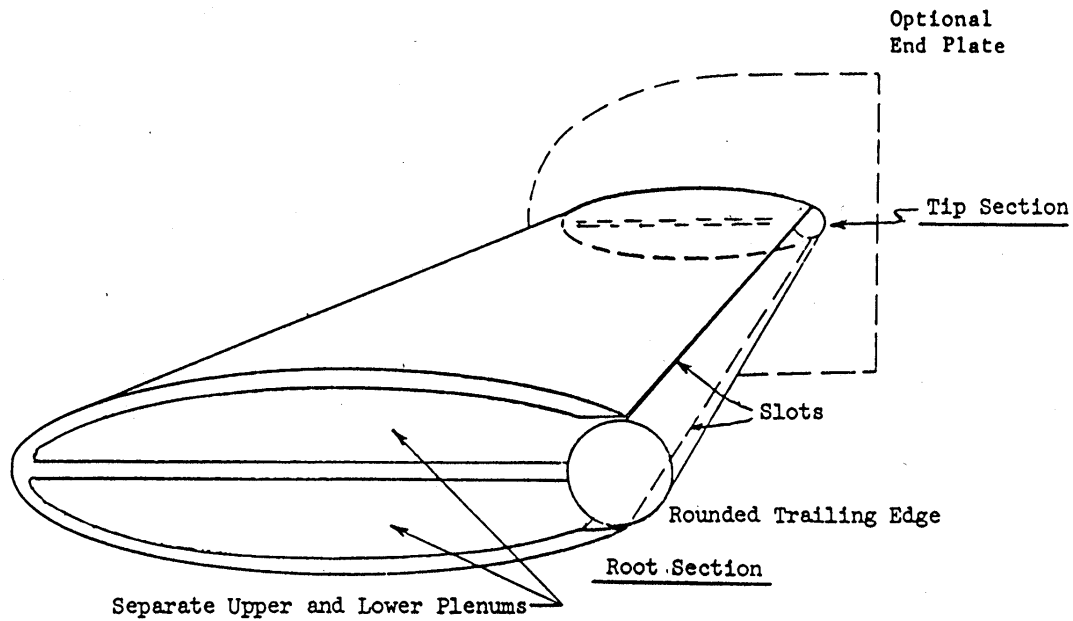


Fig. 48- Blown Model Stern Plane Design, 2 slotted

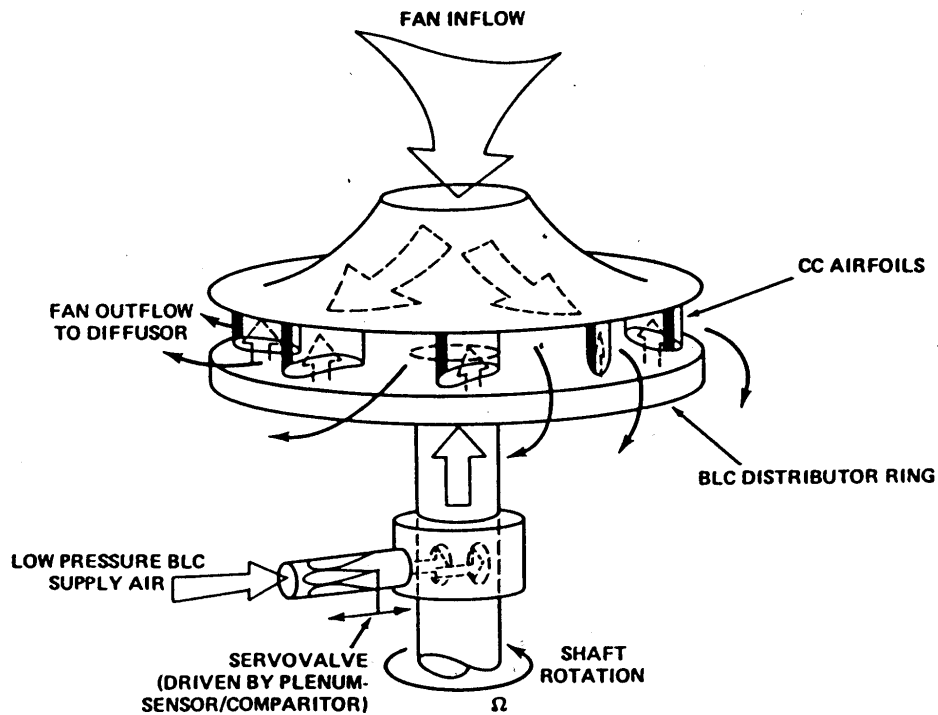


Fig. 49- Circulation Control Fan Concept

concept verified that blowing water from the slots when underwater was equally as effective as pneumatic devices (even if the power required might be higher), and provided the opportunity for smaller stern-, bow- or sail planes, or avoided the possible control plane jam problem of moving hydrodynamic surfaces.

Applications of pneumatics similar to the CC rotor were both the CC Fan (Figure 49 from Ref. 65) and the CC windmill. Here, variation in blowing parameters through the individual blade slots could vary the output of the fan, or conversely, for a pneumatic windmill, vary the sensitivity of each individual blade to the incoming wind angle and strength, as well as the radial load distribution on the blades. For the windmill, blade pitch would not be required to change mechanically for maximum performance or avoidance of rotor overspeed.



Fig. 50- Pneumatic Formula 1 Car Model in GTRI Tunnel

More recently, application of pneumatic concepts to improve the aerodynamic performance of automotive vehicles has been heavily pursued at GTRI. Tests on European Formula 1 cars (Figure 50) have verified that proper application of blowing can dramatically increase the downforce frequently required for higher-speed cornering of these cars, or reduce the required wing area and its associated drag (note the absence of the conventional inverted fore and aft multi-element wings). The high suction (negative static pressure) difference across a blown lifting wing inverted on a race car can also entrain sufficient flow to provide cooling through a radiator located therein. Figure 51 shows a Formula SAE car with an aft blown wing including a pneumatic radiator (unit developed and tested at GTRI⁶⁶ with assistance from the GT Motorsports team). It is now possible to have a multi-point aerodynamic race car design which had previously been prohibited by the “non-moving-aerodynamic-components” rule.



**Fig. 51- GTRI-Patented Pneumatic Aerodynamic Heat Exchanger installed on Formula SAE Race Car
by GT Motorsports Team**

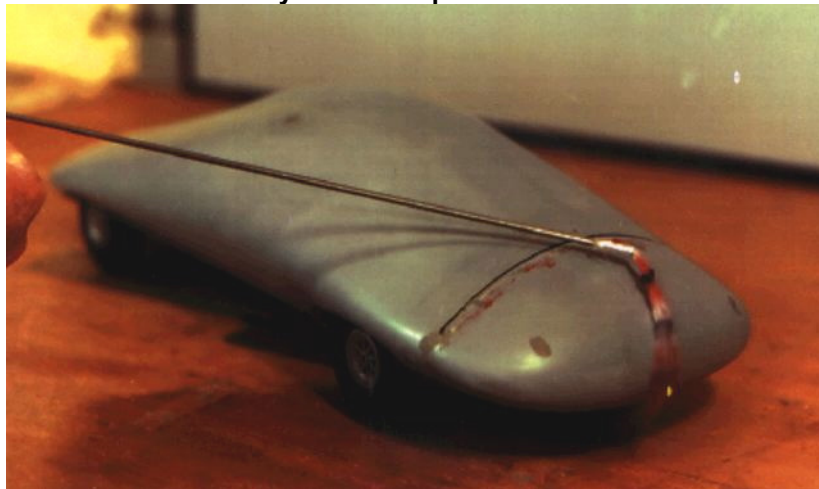


Fig. 52- GTRI Pneumatic FutureCar Model for Drag Reduction, Showing Jet Turning

A GTRI program originally intended only to reduce aerodynamic drag on production cars for increased fuel economy has recently led to additional benefits. Blowing on the curved aft panels⁶⁷ of a generic streamlined car, Figure 52, showed drag reductions of up to 35%, but also drag increases of over 100% by blowing different elements, which could be used as a form of aero braking. Lift could also be increased by up to 170% over the unblown car, or conversely, a lower surface slot could also yield downforce if so desired. GTRI tests also showed that yawing and pitching moments could be dramatically changed by blowing, and lateral and directional stability could be restored by blowing only one side of the slot. Interestingly, the blowing required for all of this could be provided by turbochargers or superchargers now being installed on high performance cars.

This experimental data for automobiles has now been extended to and adapted in a GTRI program for the Department of Energy^{68,69} to improve the aerodynamics, performance and economics of Heavy Vehicles (i.e., large tractor/trailer trucks). Figure 53 shows blowing on all four aft corners of the trailer; this combination is able to reduce drag, turbulent separated flow, spray, and aft suction on the back doors. Blowing the lower slot only can increase download and aid in braking or provide traction in wet/icy weather, while blowing the top slot only can generate lift and thus reduce effective weight on the tires and rolling resistance. Blowing either side slot can offset yaw due to gusts or sidewinds (which can yield a large component of increased highway drag), or can help to restore lateral/directional stability. Since the response of the blowing system can be virtually instantaneous (pressure of only 13-14 psig can produce sonic jet velocity), safety of operation is very promising,

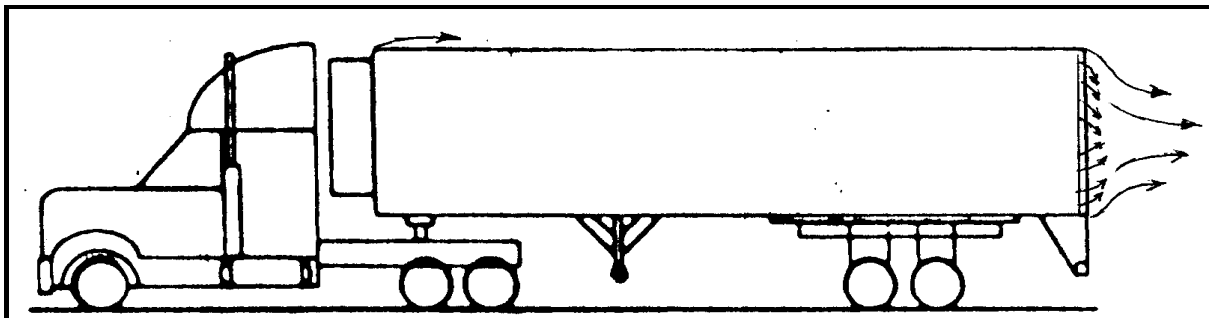


Fig. 53- Pneumatic Heavy Vehicle Configuration with Potential for 5 Blowing Slots

including the ability to prevent jack-knifing by generating opposite yawing moment for the trailer. Blowing on the trailer top leading edge also appears promising as it can provide not only a boundary layer control device, but also can entrain flow up through the cab/trailer gap and eliminate strong separation and vorticity there, plus enhance cooling. Wind tunnel investigations of this concept on a smaller-scale model of a blown Pneumatic Heavy Vehicle^{68,69} have shown drag reductions of up to 80% relative to a baseline generic HV model, plus the ability to increase drag if needed for braking, as well as provide side forces and lateral/directional control in side winds. They have also confirmed that blowing only one vertical side slot at the rear of the trailer can eliminate the de-stabilizing yawing moments due to sidewinds and generate counter-yaw in the opposite direction if needed. These tunnel tests have led to development of a full-scale test vehicle and on-road test program of a PHV test rig, Figure 54, now ongoing for DOE.



Fig. 54- Pneumatic Heavy Vehicle Test Rig Undergoing Road Tests

Conclusions

The high flow-entrainment capability of tangential blowing over curved aerodynamic surfaces has been shown in the above discussions to yield augmentation and control of virtually all aerodynamic/hydrodynamic forces and moments by simplified means which frequently require no moving external components. Among the capabilities of the Circulation Control devices demonstrated are:

- 2-D lift coefficients as high as 20 without moving parts; similar high C_l for download as desired in automotive applications. This extra high lift can also provide aircraft Super-STOL capability or the downsizing of wing area for more efficient cruise.
- Lift augmentations $\Delta C_l/C_{l0}$ of 80 and very effective boundary layer control
- Drag reduction due to flow re-attachment and thrust recovery, or drag increase due to flow turning and lift-induced drag, and the ability to pneumatically activate these as needed by the pilot or driver—this is particularly applicable in automotive usage
- Aerodynamic moment increases from blowing or differential blowing to provide large control increases over those of mechanical devices, or to allow control surface downsizing
- Pneumatic engine thrust deflection to 165° or more without moving surfaces
- Pneumatic propellers or rotor blades to achieve variable thrust and control moment without mechanical cyclic pitch

- Automotive applications to vary all forces and moments, including racing vehicle download and drag, without moving parts using only onboard air sources such as turbochargers. Also a low-drag aerodynamic heat exchanger using pneumatic-generated pressure difference can cool the vehicle while controlling aerodynamic forces and moments.

The Future of Circulation Control:

The above capabilities offer the potential for aerodynamic/hydrodynamic vehicles simplified by pneumatic multi-purpose surfaces synergistically augmenting lift, drag, moments, control, stability and propulsive functions without any moving mechanical parts. The force augmentation capability also offers the potential for reduction in wing and control surface areas for improved cruise performance, or multi-point designs with lift/control surfaces sized for optimal points of operation. Future investigations could include improved pulsed blowing to even further reduce the required input mass flows, or to simplify the operation of complex devices such as higher harmonic rotors. Application of CC pneumatics to automotive and hydrodynamic vehicles offers the use of aerodynamic surfaces for functions not currently employed, such as aerodynamic drag reduction or increase; download; heat exchange; thrust augmentation; and stability and control. The opportunity to incorporate all of these devices into a synergistic blown vehicle from the initiation of the design, rather than as an add-on, offers the potential for a very effective and efficient multi-purpose vehicle, wherein the pneumatic effectiveness, including the propulsion system air supply source and the control systems, is incorporated from the very beginning. A perfect example of how Circulation Control could be applied to a new and unique Super-STOL vehicle would be its application to the new NASA Extreme-STOL concept aircraft, where desired goals include C_L of 10, balanced field lengths of 2000' or less and, of course, the necessity to trim and control this vehicle at its very low speeds, plus the ability to interchange drag increase and drag elimination between approach and takeoff operations, respectively.

References

1. "The Use of Slots for Increasing the Lift of Airplane Wings," NACA Translation, PW 635, August 1931. Proceedings *L'Aeronautique* June 1931.
2. "Wings with Nozzle Shaped Slots," NACA Translation, TM 521, July 1929, from *Berichte Der Aerodynamischen Versuchsanstalt in Wien* Vol. 1, #1, 1928.
3. Metral, A. R., "On the Phenomenon of Fluid Veins and their Application, the Coanda Effect," AF Translation, F-TS-786-RE, 1939.
4. Sproule, R. S. and S.T. Robinson, "Combined Intelligence Objective Sub-Committee report," WF Document Library Item 5, File No. IX-1, X-2, XII-1, D52.420/27, 1944.
5. Voedisch, Alfred, Jr., "Analytical Investigation of the Coanda Effect (Project No. FP-188)," Air Material Command, Wright Field, Dayton, Ohio, Report No. F TR-2155-ND, April 3, 1947
6. Cheeseman, I. C. and A. R. Reed, "The Application of Circulation Control by Blowing to Helicopter Rotors," *Journal of Royal Aeronautical Society*, Vol. 71, No. 848, July 1966.
7. Cheeseman, I. C., "Circulation Control and Its Application to Stopped Rotor Aircraft," AIAA Paper 67-747, October, 1967.
8. Lockwood, Vernard E., "Lift Generation on a Circular Cylinder by Tangential Blowing from Surface Slots," Technical Note D-244, NASA Langley Research Center, May, 1960.
9. Englar, R. J., "Circulation Control Pneumatic Aerodynamics: Blown Force and Moment Augmentation and Modification; Past, Present and Future," AIAA Paper 2000-2541, presented at AIAA Fluids 2000 Meeting, Denver, CO, June 19-22, 2000.
10. Englar, Robert J. and R.M. Williams, "Test Techniques for High Lift Two-Dimensional Airfoils with Boundary Layer and Circulation Control for Application to Rotary Wing Aircraft," *Canadian Aeronautics and Space Journal*, Vol. 19, No. 3, pp. 93-108 (Mar 1973).
11. Englar, Robert J., "Two-Dimensional Subsonic Wind Tunnel Tests on a Cambered 30-Percent -Thick Circulation Control Airfoil," NSRDC Technical Note AL-201, AD 913-411L, May, 1972.
12. Englar, R. J. and C. A. Applegate, "Circulation Control - A Bibliography of DTNSRDC Research and Selected Outside References (January 1969 through December 1983)," DTNSRDC-84/052, September, 1984.
13. Wilkerson, J.B., D. R. Barnes, and R. A. Bill, "The Circulation Control Rotor Flight Demonstrator Test Program," *American Helicopter Society Paper AHS 79-51*, May, 1979.
14. Mayfield, Jerry, "Aeronautical Engineering-Navy Sponsors Coanda Rotor Program," *Aviation Week and Space Technology*, March 31, 1980, pp. 69-74.
15. Wilkerson, J. B., K. R. Reader, and D. W. Linck, "The Application of Circulation Control Aerodynamics to a Helicopter Rotor Model," *American Helicopter Society Paper AHS-704*, May, 1973.
16. Nielson, J. N., Editor, "Proceedings of the Circulation Control Workshop, 1986", NASA Ames Research Center, NASA CP-2432, February 19-21, 1986.
17. Shrewsbury, G., "Numerical Evaluation of Circulation Control Airfoil Performance Using Navier-Stokes Methods," AIAA Paper 86-0286, January, 1986.
18. Novak, C. J. and K. C. Cornelius, "An LDV Investigation of a Circulation Control Airfoil Flowfield," AIAA Paper 86-0503, January, 1986.
19. Englar, Robert J., "Experimental Investigation of the High Velocity Coanda Wall Jet Applied to Bluff Trailing Edge Circulation Control Airfoils," DTNSRDC Report 4708, Aero

- Report 1213, AD-A-019-417, September, 1975. Also M.S. Thesis, University of Maryland, Department of Aerospace Engineering, June 1973.
20. Wood, N., and J. Nielson, "Circulation Control Airfoils Past, Present, and Future," AIAA Paper 85-0204, January, 1985.
 21. Williams, R. N., R. T. Leitner and E. O. Rogers, "X-Wing: A New Concept In Rotary VTOL," Presented at AHA Symposium on Rotor Technology, Philadelphia, Pa., August, 1976.
 22. Reader, K. R. and J. B. Wilkerson, "Circulation Control Applied to a High Speed Helicopter Rotor," DTNSRDC Report 77-0024, February, 1977.
 23. Rogers, E. O., A. W. Schwartz and J. S. Abramson, "Applied Aerodynamics of Circulation Control Airfoils and Rotors," presented at 41st Annual AHS Forum, Fort Worth, Texas, May 15, 1985.
 24. Ottensosser, J., "Two-Dimensional Subsonic Evaluations of a 15-Percent Thick Circulation Control Airfoil with Slots at Both Leading and Trailing Edges," NSRDC Report 4456, July, 1974.
 25. Williams, R. M. and I. C. Cheeseman, "Potential Acoustic Benefits of Circulation Control Rotors," presented at AHS Meeting on Rotor Acoustics, NASA Langley Research Center, May, 1978.
 26. Englar, Robert J., "Investigation into and Application of the High Velocity Circulation Control Wall Jet for High Lift and Drag Generation on STOL Aircraft," AIAA Paper No. 74-502, June 17-19, 1974.
 27. Englar, Robert J., "Subsonic Two-Dimensional Wind Tunnel Investigations of the High Lift Capability of Circulation Control Wing Sections," DTNSRDC Report ASER-274, April, 1975.
 28. Englar, Robert J., "Circulation Control for High Lift and Drag Generation on STOL Aircraft," *AIAA Journal of Aircraft*, Vol. 12, No. 5, pp. 457-463, May 1975.
 29. Englar, R.J., L. A. Trobaugh and R. A. Hemmerly, "Development of the Circulation Control Wing to Provide STOL Potential for High Performance Aircraft," AIAA Paper No. 77-578, June 6-8, 1977.
 30. Englar, R. J. "Circulation Control Technology for Powered-Lift STOL Aircraft," *Lockheed Horizons*, Issue 24, September, 1987.
 31. Englar, R. J., R. A. Hemmerly, H. Moore, V. Seredinsky, W. G. Valckenaere, J. A. Jackson, "Design of the Circulation Control Wing STOL Demonstrator Aircraft," AIAA Paper No. 79-1842, August, 1979. Also published in *AIAA Journal of Aircraft*, January, 1981.
 32. Englar, R. J., "Development of the A-6/Circulation Control Wing Flight Demonstrator Configuration," DTNSRDC Report ASER-79/01, January, 1979.
 33. Mayfield, Jerry, "Circulation Control Wing Demonstrates Greater Lift," *Aviation Week and Space Technology*, March 19, 1979.
 34. Pugliese, A. J and R. J. Englar, "Flight Testing the Circulation Control Wing," AIAA Paper No. 79-1791, August, 1979.
 35. Loth, J. L., J. D. Fanucci and S. C. Roberts, "Flight Performance of a Circulation Control STOL Aircraft," AIAA Paper 74-994, April, 1974; *AIAA Journal of Aircraft*, Vol. 13, No. 3, pp. 169-173, March, 1976.
 36. Roberts, S. C., "West Virginia University Circulation Control STOL Aircraft Flight Test," WVU Aerospace Technical Report No. 42, July, 1974.
 37. Englar, R. J., "Low-Speed Aerodynamic Characteristics of a Small Fixed-Trailing-Edge Circulation Control Wing Configuration Fitted to a Supercritical Airfoil," DTNSRDC Report ASER-81/08, March, 1981.

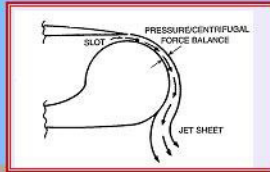
38. Englar, R. J. and G. G. Huson, "Development of Advanced Circulation Control Using High-Lift Airfoils," AIAA Paper No. 83-1847, July 13-15, 1983. Also published in *AIAA Journal of Aircraft*, pp. 476-483, July, 1984.
39. Carr, John E., "An Aerodynamic Comparison of Blown and Mechanical High Lift Airfoils," AIAA Paper 84-2199, August, 1984.
40. Englar, R. J., "Two-Dimensional Transonic Wind Tunnel Tests of Three 15-Percent-Thick Circulation Control Airfoils," NSRDC Technical Note AL-182, AD 882-075, December, 1970.
41. Englar, Robert J., Marilyn J. Smith, Sean M. Kelley and Richard C. Rover III, "Development of Circulation Control Technology for Application to Advanced Subsonic Transport Aircraft," AIAA Paper No. 93-0644, January 11-14, 1993. Also published as *AIAA Journal of Aircraft*, Vol. 31, No. 5, p. 1160-1177, September-October 1994.
42. Englar, Robert J., Niebur, Curt S., and Gregory, Scott D., "Pneumatic Lift and Control Surface Technology Applied to High Speed Civil Transport Configurations," AIAA Paper 97-0036, January, 1997.
43. Mavris, D. N., et. al., "Systems Analyses of Pneumatic Technology for High Speed civil Transport Aircraft," GTRI Final Technical Report, A-5676, October 3, 1999.
44. Nichols, J. H. Jr., R. J. Englar, M. J. Harris, and G. G. Huson, "Experimental Development of an Advanced Circulation Control Wing System for Navy STOL Aircraft," AIAA Paper No. 81-0151, January 12, 1981.
45. Harris, M. H., J. H. Nichols Jr., R. J. Englar, and G. G. Huson, "Development of the Circulation Control Wing/Upper Surface Blowing Powered-Lift System for STOL Aircraft," Paper No. ICAS-82-6.5.1, in Proceedings of the ICAS/AIAA Aircraft Systems and Technology Conference, Seattle, August 22-27, 1982.
46. Yang, H. T. and J. H. Nichols, Jr., "Design Integration of CCW/USB for a Sea-Based Aircraft," Paper No. ICAS-82-1.6.1, August, 1982.
47. Englar, R. J., J. H. Nichols, Jr., M. J. Harris, J. C. Eppel and M. D. Shovlin, "Circulation Control Technology Applied to Propulsive High Lift Systems," SAE Paper No. 841497, October, 1984.
48. Lowndes, J. C., "Aeronautical Engineering: Studies Show Lift Coefficient Tripling," *Aviation Week and Space Technology*, December 1, 1980.
49. Englar, R. J., J. H. Nichols, Jr., M. J. Harris, J. C. Eppel, and M. D. Shovlin, "Development of Pneumatic Thrust-Deflecting Powered-Lift Systems," AIAA Paper No. 86-0476, January, 1986.
50. Eppel, J.C., M. D. Shovlin, D.N. Jaynes, R. J. Englar, and J. H. Nichols, Jr., "Static Investigation of the CCW/USB Concept Applied to the Quiet Short-Haul Research Aircraft," NASA TM 84232, July, 1982.
51. Shovlin, M.D., R. J. Englar, J. C. Eppel and J. H. Nichols, Jr., "Large-Scale-Static Investigation of Circulation-Control-Wing Concepts Applied to Upper-Surface-Blowing Aircraft," NASA Technical Paper 2684, January, 1987.
52. Bevilaqua, P. M. and J. D. Lee, "Design of Supersonic Coanda Jet Nozzles," In Proceedings of the Circulation Control Workshops 1986, NASA CP 2432, pp. 289-312, February, 1986.
53. Englar R. J. and B. A. Campbell, "Development of Pneumatic Channel Wing Powered-Lift Advanced Super-STOL Aircraft," AIAA Paper 2002-2929, presented at AIAA 20th Applied Aerodynamics Conference, St. Louis, MO, June 25, 2002.
54. Englar, R. J. and B. A. Campbell, "Experimental Development and Evaluation of Pneumatic Powered-Lift Super-STOL Aircraft," Paper at NASA/ONR Circulation Control Workshop, Hampton, VA, Mar., 2004
55. Braslow, A. L., "Aerodynamic Evaluation of Circulation Control Propellers," Bionetics Corp., NASA Contractor Report 165748, June, 1981.

56. Taback, I., A. L. Braslow, and A. J. Butterfield, "Circulation Control Propellers for General Aviation, Including a BASIC Computer Program," NASA Contractor Report 165968, April, 1983.
57. Garner, D., "No Moving Parts, The Circulation Control Airfoil and Fluidic Propeller, *EAA Sport Aviation*, Vol. 37, No. 3, pp. 27-30, March, 1988.
58. Wilson, M. B. and C. von Kerczek, "An Inventory off Some Force Producers for Use in Marine Vehicle Control," DTNSRDC-79/097, November, 1979.
59. Wellman, L.K., and C. Jacobsen, "Wind Tunnel Investigation of the Application of Circulation Control to a Forward Swept Wing," DTNSRDC/ASED-82/05, June, 1982.
60. Englar, R. J., "Pneumatic High-Lift and Control Surfaces Applied to Micro-Aerial Vehicles," published in Conference Proceedings of GTRI International Conference on Emerging Technologies for Micro Air Vehicles, Atlanta, GA, February 19-20, 1997.
61. Oyler, T.E. and W.E. Palmer, "Exploratory Investigation of Pulsed Blowing for Boundary Layer Control," North American Rockwell Report NR72H-12, January, 1972.
62. Walters, R.E., et al., "Circulation Control by Steady and Pulsed Blowing for a Cambered Elliptic Airfoil," West VA University, Dept of Aerospace Engr., Report TR-32, July, 1972.
63. Jones, G. S., and R. J. Englar, "Advances in Pneumatic-Controlled High-Lift Systems Through Pulsed Blowing", AIAA 2003-3411, presented at AIAA 21st Applied Aerodynamics Conference, Orlando, June 23-26, 2003.
64. Englar, R. J. and R. M. Williams, "Design of a Circulation Control Stern Plane For Submarine Applications," NSRDC Technical Note AL-200, March, 1971.
65. Fury, R. J. and R. E. Whitehead "Static Evaluation of a Circulation Control Centrifugal Fan," DTNSRDC Report 77-0051, AD A041-463, June, 1977.
66. Gaeta, R. J. and R. J. Englar, "Pneumatically Augmented Aerodynamic Heat Exchanger," Paper at NASA/ONR Circulation Control Workshop, Hampton, VA, Mar., 2004.
67. Englar, Robert J., M. J. Smith, C. S. Niebur and S. D. Gregory, "Development of Pneumatic Aerodynamic Concepts for Control of Lift, Drag, Moments and Lateral/Directional Stability of Automotive Vehicles," SAE Paper 960673, February 26-29, 1996; also published in SAE SP-1145, "Vehicle Aerodynamics", February, 1996
68. Englar Robert J., "Drag Reduction, Safety Enhancement and Performance Improvement for Heavy Vehicles and SUVs Using Advanced Pneumatic Aerodynamic Technology", SAE Paper 2003-01-3378, presented at 2003 SAE International Truck and Bus Meeting and Exhibition, Ft Worth TX, November 10-12, 2003.
69. Englar, Robert J. "The Application of Pneumatic Aerodynamic Technology to Improve Performance and Control of Advanced Automotive Vehicles," Paper at NASA/ONR Circulation Control Workshop, Hampton, VA, Mar., 2004

***Circulation Control Pneumatic Aerodynamics Overview:
Blown Force & Moment Augmentation and Modification,
as Applied Primarily to Fixed Wing Aircraft***

by
Robert J. Englar, Principal Research Engineer
Georgia Tech Research Institute
Aerospace, Transportation & Advanced Systems Laboratory
Atlanta GA, 30332-0844

2004 Circulation Control
Workshop; March 16,17



Circulation Control
Aerodynamics



Circulation Control Wing



CCW/Upper Surface Blowing



Pneumatic Channel Wing

RE-01

AGENDA
Outline of Background & Applications:

- Introduction: the Coanda Effect & the Circulation Control (CC) Concept
- CC Airfoil Lift & Drag Characteristics
- Rotary Wing: Lift & Drag Independent of α - Defer for Now
- High-Lift Fixed-Wing Application: Lift Augmentation; Drag increase or decrease
- Powered Lift: Pneumatic Lift/Thrust Integration: USB & Pneumatic Channel Wing
- Pneumatic Thrust Deflection
- Blown Non-deflecting Augmented Control Surfaces
- Transonic Applications: Lift, Drag & Control
- Hydrodynamic Applications: Blowing water in water
- Automotive: Drag reduction or increase, Down force or not, Augmented Control
- Pulsed Blowing, Unsteady Pneumatic Aerodynamics
- Aerodynamic Heat Exchanger

...Where do we go from here??.....

Numerous Application Opportunities for Non-Moving Pneumatic Aero & Propulsive
Force/Moment Augmentors & Reducers at NASA, ONR, and.....

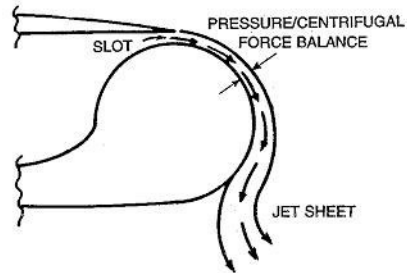
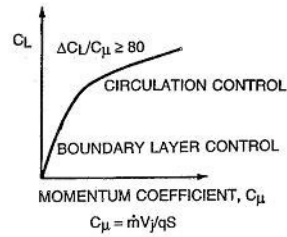
RE-3

The Basics of Pneumatic Circulation Control Aerodynamics

POSSIBLE LEADING EDGE BLOWING

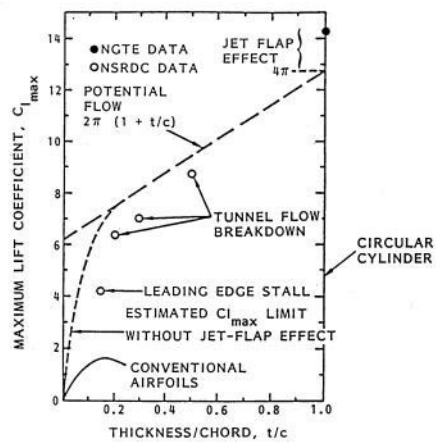


TANGENTIAL BLOWING OVER ROUNDED TRAILING EDGE SURFACE



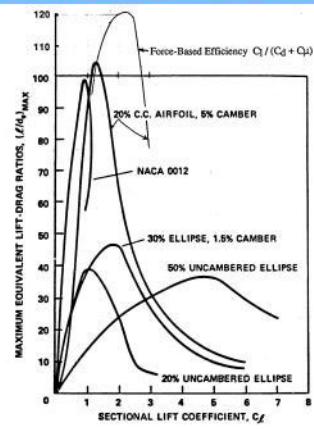
RE-2

Maximum Lift of Blown Airfoil Sections



RE-17

Equivalent Efficiencies ($1/d_{eq}$) for 2-D CC and Conventional Airfoils, Including Penalties for Blowing



COMPARATIVE EQUIVALENT EFFICIENCIES (K.E + RAM INTAKE) FOR C.C. AND CONVENTIONAL AIRFOILS

RE-17

CCW Jet Turning on A-6/CCW Wind Tunnel Model



RE-67

A-6 / CIRCULATION CONTROL WING STOL DEMONSTRATOR AIRCRAFT & FLIGHT TEST RESULTS

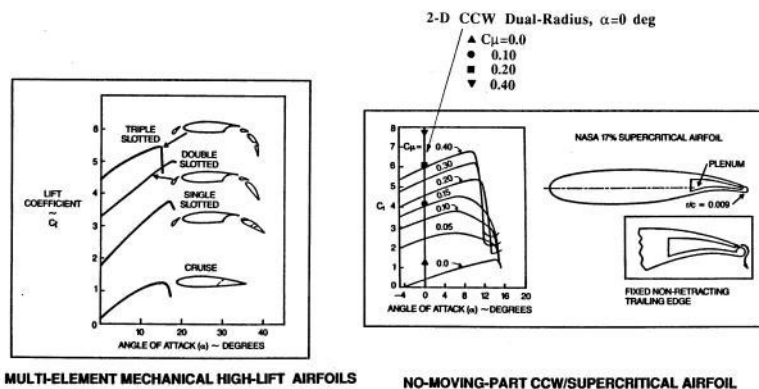


FLIGHT TEST RESULTS : 140% Increase in Usable C_L
 30-35% Reduction in Takeoff & Approach Speeds
 60-65% Reduction in Takeoff & Landing Ground Roll
 75% Increase in Lifiable Takeoff Payload

CONFIRMATION OF
FULL-SCALE CCW

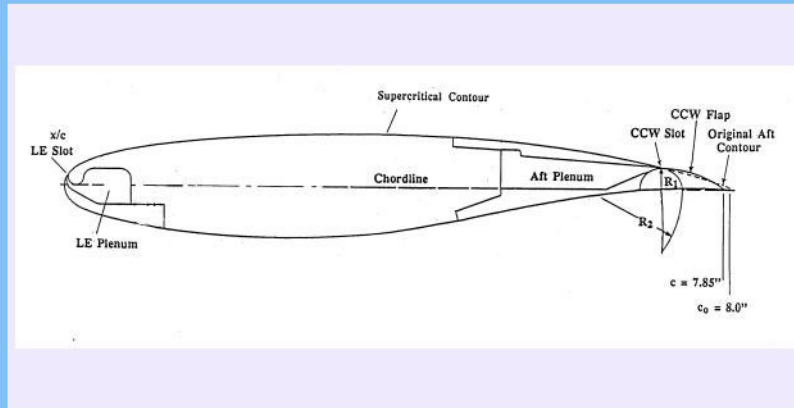
RE-22

Comparison between Conventional, CCW (No Moving Parts) and Advanced CCW High-Lift Airfoils



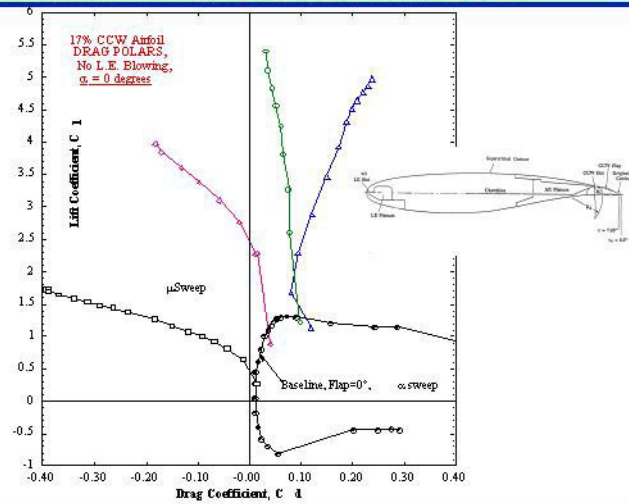
RE-16

Dual-Radius Simple CCW Flap, Dual Slot, Advanced CCW High-Lift, Variable-Drag Airfoil

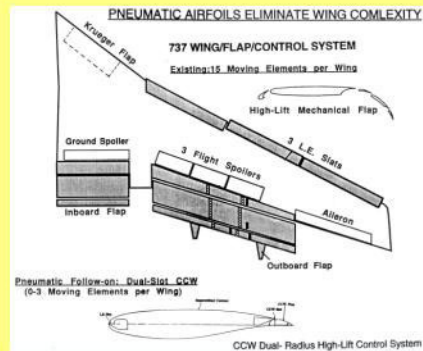


RE-43

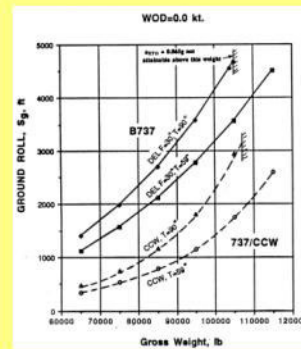
2-D CCW SUPERCRITICAL AIRFOIL, DUAL - RADIUS FLAPS, DRAG POLARS, THE PENALTY FOR LIFT ??



CCW Commercial Airliner & STOL Takeoff

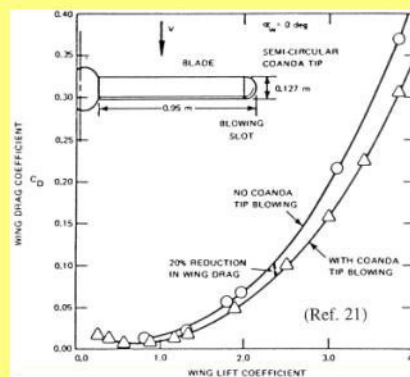


CCW Wing Simplification

737/CCW STOL Takeoff
Roll Reduction

RE-67

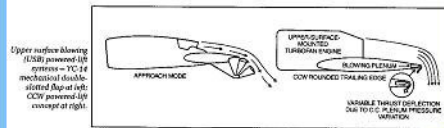
Induced Drag Reduction



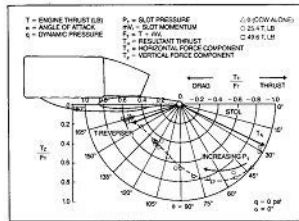
Tip Blowing to Counteract Tip Vortex and Reduce/Eliminate Induced Drag, plus provide roll control

RE-67

Demonstrated Static Thrust-Turning Capability of CCW/Upper Surface Blowing Wind Tunnel Model



Upper surface blowing (USB) powered lift systems = VC-14 mechanical double-slotted flap at left CCW powered lift concept at right



Static thrust deflection of CCW/USB wind tunnel model

Proposed NAVY CCW/USB Super STOL Aircraft

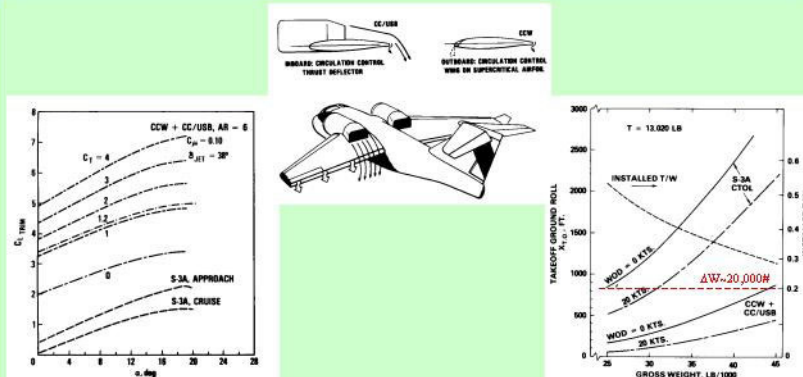


Pneumatic STOL, V/STOL, and Thrust-Reversing Capability with NO Moving Parts

Basis for Pneumatic Channel Wing Concept Developed in NASA LaRC Program : Augment Channel-Flow Lift and Produce Greater Thrust Turning + Variable Drag

RE142

SuperSTOL Takeoff & Overload Capability of CCW/USB on Navy S-3A Aircraft; Applicable to Typical Transports, Sea- and Land-Based



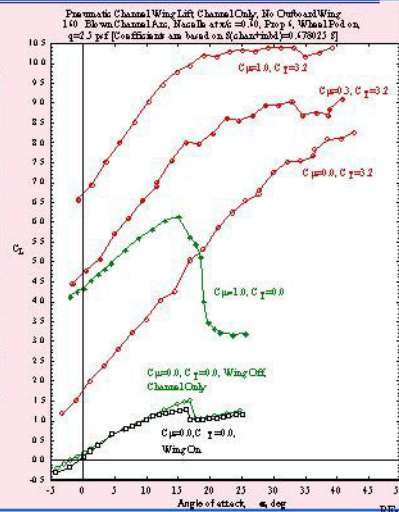
- Pneumatic Deflection of Engine Thrust, Adds to Wing Lift: C_L approaching 7-8
- Allows Thrust/Drag Interchange for Short Takeoffs & Landings
- Pneumatic Thrust Reversal with No Moving Parts
- Pneumatic Augmentation of all Forces and Moments for Low-speed Flight

RE-76

Pneumatic Channel Wing Lift due to Blowing and Thrust with Outboard CCW Panel Removed



[.....Also See Paper 3 today]



Pneumatic Circulation Control Aerodynamic and Propulsive Capabilities Already Demonstrated Full-Scale



Navy A-6 CCW STOL Flight Demonstrator

- A-6 Approach C_L Increased by 140%
 $C_{L_{max}}$ Doubled
- Reduced Takeoff and Approach Speeds by 30-35%
- Reduced Takeoff and Approach Ground Roll Distances by 60-65%
- Increased Lifiable Takeoff Payload by 75%
- Blowing Air Limited by Existing Engine Bleed
- Full Round CCW Turning Surfaces

ALSO: WVU BD-4 CCW; X-Wing; NOTAR & H-2 CCR Helos; V-22 T-Deflector

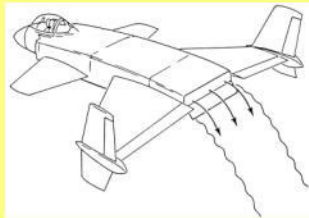


CCW/Upper Surface Blowing Ground Test for NASA/Naval

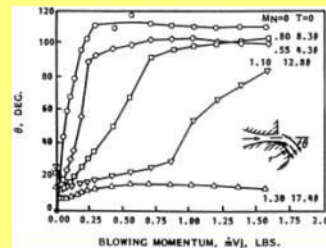
- Full-scale Ground Test on NASA Quiet Short-Haul Research Aircraft
- Limited Blowing Air, Ground Starter Cart
- Pneumatic Thrust Deflection Confirmed Statically
- Thrust Deflected up to 103 deg (forward)
- One Engine Only Tested

RE-67

Pneumatic Engine Thrust Deflection



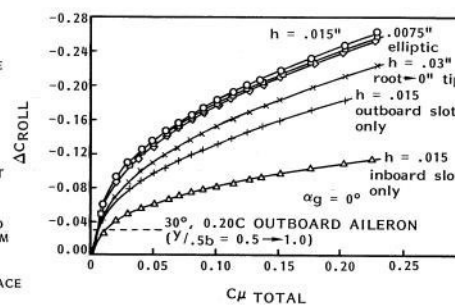
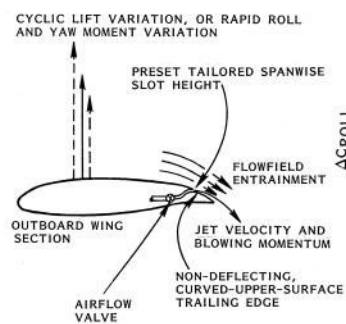
Rectangular Jet Exhaust Nozzle



Pneumatic Deflection of Jet Exhaust

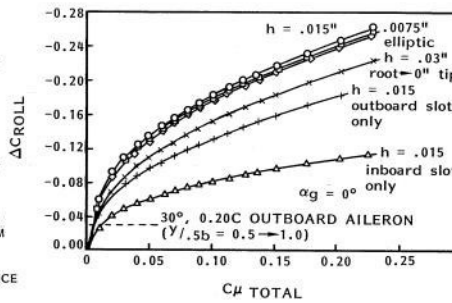
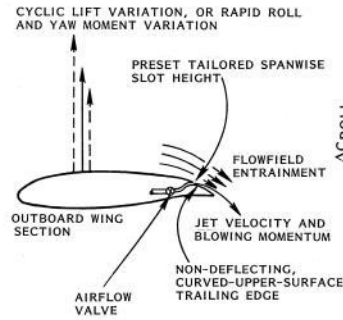
RE-67

No-Moving-Part Pneumatic Control Surfaces (Rolling Moment Shown)



RE-56

No-Moving-Part Pneumatic Control Surfaces (Rolling Moment Shown)

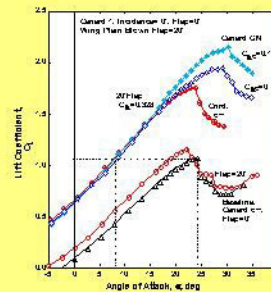


RE-56

Additional Pitching Moment Control and Lift Augmentation On Pneumatic High Speed Civil Transport



Blown CC Canard on Semi-span HSCT With CC Wing



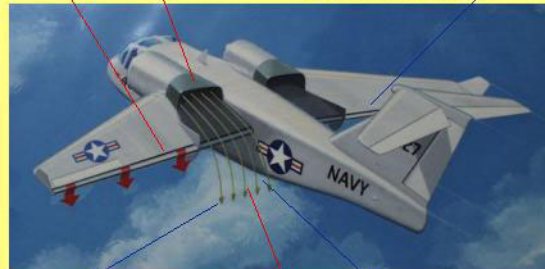
CC Canard provides Nose-up Pitch, $+\Delta C_L$
To trim and α_{stall} increase (vortex burst delay)
Due to upwash elimination

RE-67

The Integrated Pneumatic Powered High-Lift AND Low-Speed Controllable SuperSTOL Aircraft

High Lift from CCW/USB Inboard
and CCW Outboard

Differential Channel & Wing Blowing
Yields Roll, Yaw, and Pitch Control,
No Moving Surfaces



Interchangeable Thrust and Drag for
SuperSTOL Takeoffs and Landings

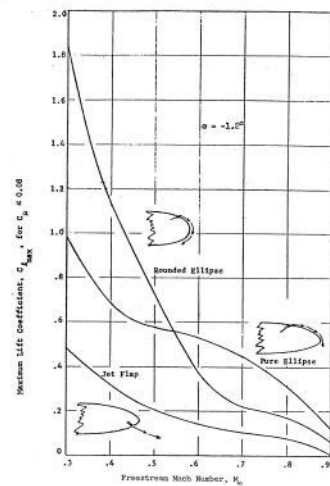
In Cruise, Blowing OFF Reduces
Thrust Deflection and Cruise Drag

Engines, Wing and Blowing may Differ
Considerably from those Depicted Here
& Still Obtain these Benefits

Pneumatic STOL, V/STOL, and
Thrust-Reversing Capability
with NO Moving Parts

RE142

Transonic Circulation Control Airfoil Performance and Effect of Trailing Edge Geometry

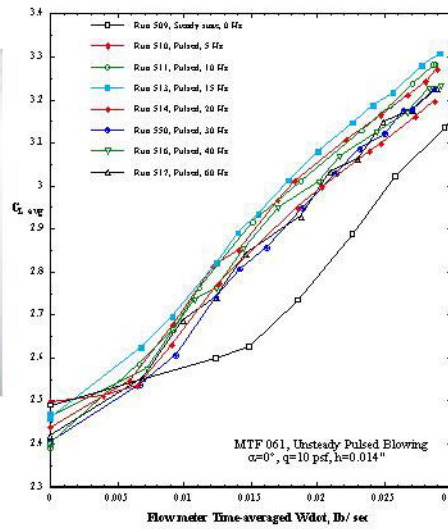


Blowing Offers the Ability to:
Control Shock/BL Interactions,
Reduce cruise drag,
Augment Lift & Maneuverability,
Provide high-speed 3-axis control...

BUT, Blown Geometry may be
quite different from Low-speed

RE43

GTRI Pulsed Blowing Investigation Conducted with NASA LaRC



RE-39

Pneumatic Aerodynamic Heat Exchanger Wing/Radiator Applied to Formula SAE Demonstrator Race car



GTRI
Patented
Technology



SUMMARY: Circulation Control Pneumatic Aerodynamic Devices' Potential and Applications

- C C flow entrainment can **simplify and augment** all aero/hydro force and moment devices
 - 2-D Lift coefficients up to 20 with no moving parts at $\alpha=0^\circ$, $\Delta C_l/C_{l0}=80$
 - Equivalent lift/drag of 120 at lift of 2-3 times conventional airfoils
 - Drag reduction (separation prevent & T recovery) or drag increase (induced, jet turning)
 - Non-moving moment control and augmentor; stability augmentation
 - Non-moving pneumatic thrust deflection (165° static, less wind-on), powered lift
 - Simplified blown rotors and propellers eliminate mechanical cyclic/collective/pitch
 - Microflyer and UAV wing/control surface simplification and downsizing
 - Automotive applications: aero performance, control and safety
- Where from here? Integrated pneumatic vehicle design with multi-purpose surfaces
Pulsed blowing, unsteady devices: much emphasis on low-speed control



RE-67

BACKGROUND OF CIRCULATION CONTROL AERODYNAMICS EXPERTISE, NOW RESIDING AT GTRI

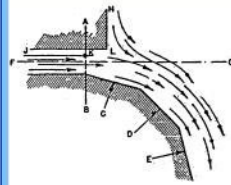
1967-1968: "Imported" from England, (C.C. Stowed Rotor at NGTE) by U.S. Navy, David Taylor Naval Ship R&D Center	Aerodynamics Lab., DTNSRDC
1968-1972: Development of C.C. Airfoils for Rotary Wing (CCR, X-Wing)*	DTNSRDC
1973-1975: C.C. Wing High-Lift Airfoil Development*	DTNSRDC
1975-1979: A-6/CCWing STOL Demonstrator Flight Test	DTNSRDC
1979-1984: Advanced CCW and CCW/Powered Lift Programs*	DTNSRDC
1984-1989: Advanced CCW, Powered Lift & Pneumatic Concepts*	Advanced Flight Sciences Dept. Lockheed-Georgia Co.
1989-1999: Advanced Aerodynamic Concept Development*	Aerospace Sciences Lab Georgia Tech Research Institute
1990-1999: In-Ground-Effect Unlimited Hydroplane & Race Car Development *	Aerospace Sciences Lab, GTRI
1993-2002: CCW for Advanced Transports (NASA) & High Speed Aircraft (AF) *	Aero & Transportation Lab, GTRI
1994-2001: Pneumatic Automobile Research & DOE Heavy Vehicles Programs*	Aero & Transportation Lab, GTRI
1998-2004: Pneumatic Channel Wing, Pulsed CCW (NASA) *, Advanced CCW*	Aero, Trans & Adv. Sys Lab, GTRI

* Miscellaneous advanced pneumatic concepts and applications in other categories were developed in this time period. A large number of invention disclosures produced more than 15 patents.

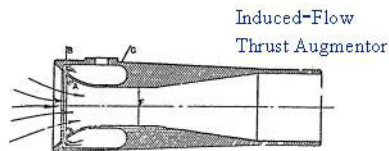
* GTRI's Robert J. Englar led or was heavily involved in every one of these developments.

RE-7

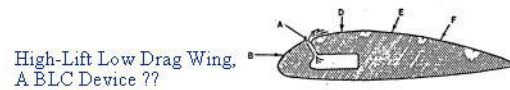
The COANDA Device & Related Pneumatic Concepts



Initial Coanda Device,
Approximately 1935



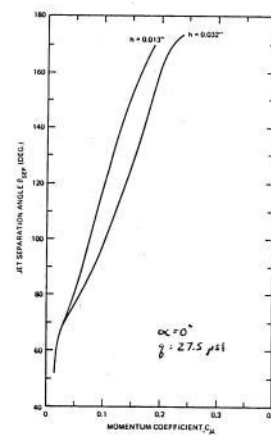
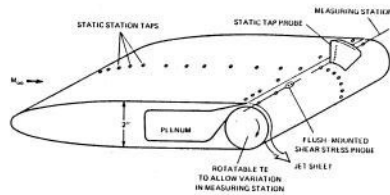
Induced-Flow
Thrust Augmentor



High-Lift Low Drag Wing,
A BLC Device ??

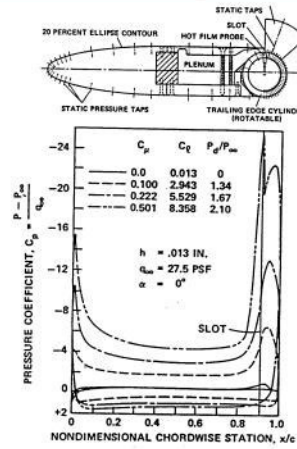
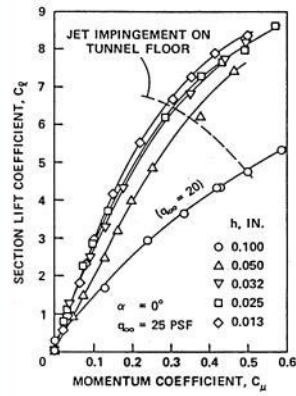
RE-2

Jet Separation Point Location (~ Jet Turning and C_p) Measured by Hot Film Probe, 2 Slot Heights, $\alpha=0^\circ$



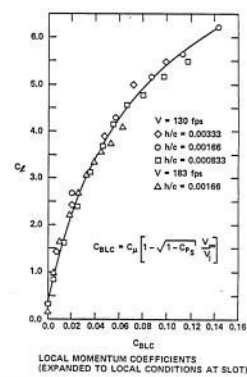
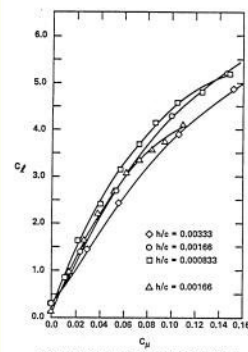
RE-16

Measured Lift Coefficient and Pressure Distributions for Generic CC Airfoil, $\alpha=0^\circ$, $q=25$ psf



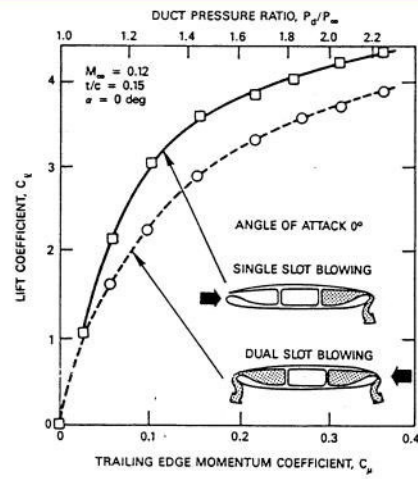
RE-13

Comparison of Momentum Coefficients and Slot Height Effects



RE-67

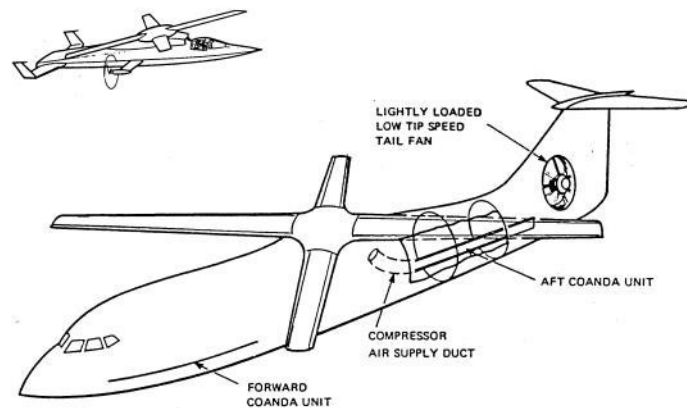
Lift Measured on 2-D Dual-Slotted Reverse-Velocity Rotor Blade Section for Use on X-Wing Concept



Note: Only Small Lift Loss Even When Freestream Flow is from the Trailing Edge

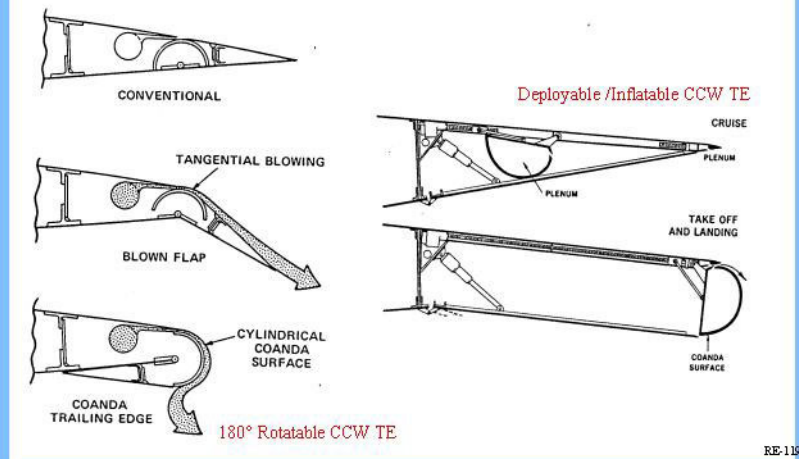
RE-20

X-Wing Configurations and Control Systems

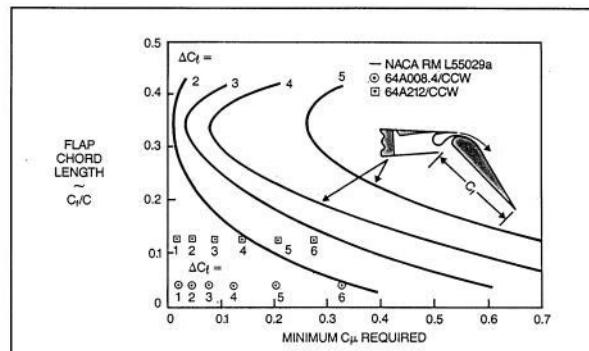


RE-21

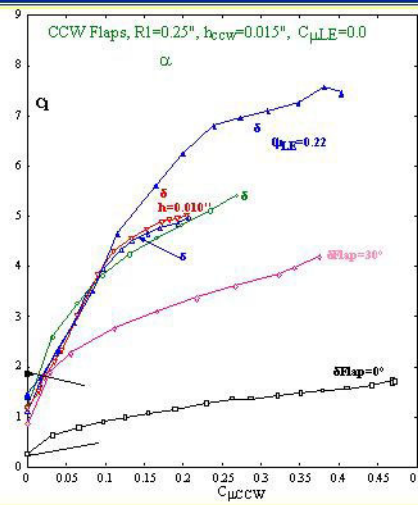
Retractable, Deflectable, or Stowable Early Circulation Control Wing Trailing Edge Configurations



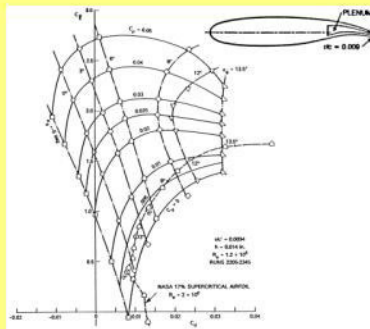
Comparisons Between CCW and Blown Flap Airfoil Lift at $\alpha = 0^\circ$



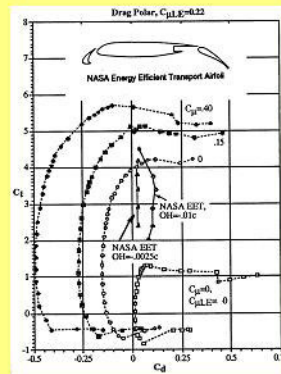
2-D SUPERCRITICAL CCW DUAL-RADIUS FLAPS, LIFT VARIATION WITH BLOWING, α



Drag Polars for Blown CCW Airfoils



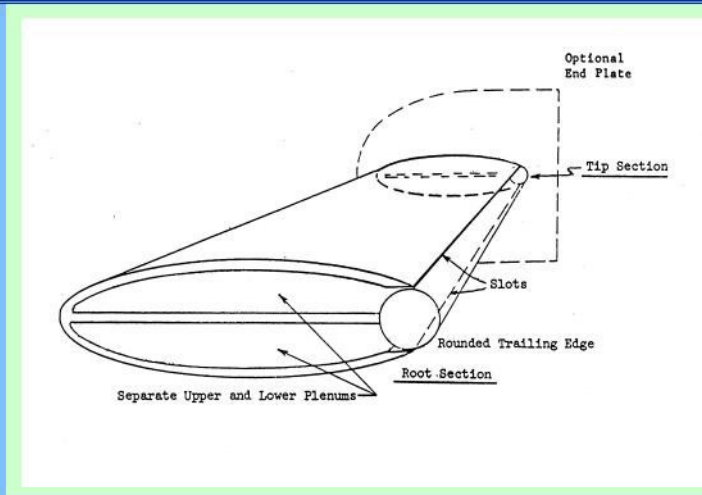
CCW Supercritical



Dual-Radius CCW vs Mechanical Flap

RE-67

“Pneumatic” Dual-Slotted Underwater Marine Surface Design Using Blowing of Water Jets in Water



RE-76

3D Channel Wing Configuration Being Developed by GTRI for NASA LaRC

Technology Goal:

Merging Custer Channel Wing Circulation Control & CCW/USB to provide simple, reliable and effective SuperSTOL (VSTOL) aircraft, with ample Low-Speed Controllability



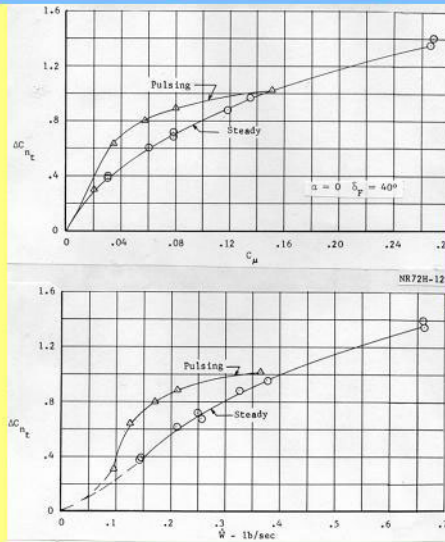
Operations:

Remote or small sites, as well as increasingly dense urban environments- Military, PAV and Commercial Applications



RE-50

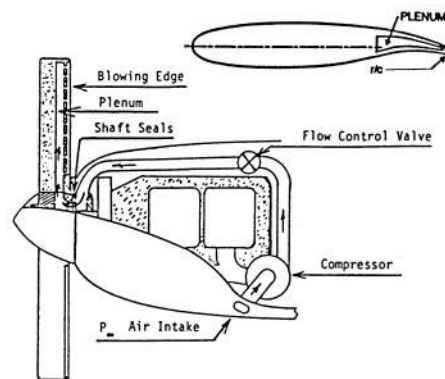
Pulsed Blowing for Reduced Required Mass Flow



North American Rockwell
Pulsed Blowing Tests on
Conventional Blown Flap

RE-18

Circulation Control Propeller System for Mechanical Simplicity and Pneumatic Pitch Control



Joint with
NASA LaRC

RE-67

Experimental Development and Evaluation of Pneumatic Powered-Lift Super-STOL Aircraft

Robert J. Englar*
Georgia Tech Research Institute (GTRI)
Aerospace, Transportation and Advanced Systems Laboratory
Atlanta, GA 30332-0844
and
Bryan A. Campbell**
NASA Langley Research Center (LaRC)
Configuration Aerodynamics Branch, MS 286
Hampton, VA 23681-2199

Abstract

The powered-lift Channel Wing concept has been combined with pneumatic Circulation Control aerodynamic and propulsive technology to generate a Pneumatic Channel Wing (PCW) configuration intended to have Super-STOL or VSTOL capability while eliminating many of the operational problem areas of the original Channel Wing vehicle. Wind-tunnel development and evaluations of a PCW powered model conducted at Georgia Tech Research Institute (GTRI) have shown substantial lift capabilities for the blown configuration (C_L values of 10 to 11). Variation in blowing of the channel was shown to be more efficient than variation in propeller thrust in terms of lift generation. Also revealed was the ability to operate unstalled at very high angles of attack of 40° - 45° , or to achieve very high lift at much lower angle of attack to increase visibility and controllability. In order to provide greater flexibility in Super-STOL takeoffs and landings, the blown model also displayed the ability to interchange thrust and drag by varying blowing without any moving parts. A preliminary design study of this pneumatic vehicle based on the two technologies integrated into a simple Pneumatic Channel Wing configuration showed very strong Super-STOL potential. This paper presents these experimental results, discusses variations in the configuration geometry under development, and addresses additional considerations to extend this integrated technology to advanced design studies of PCW-type vehicles.

Introduction / Background

The ability to achieve Super-STOL or V/STOL capability with fixed-wing aircraft has been an attractive goal in the aerospace community for over 50 years. The impetus toward its achievement has historically been the numerous benefits associated with very-short to zero-field-length operations of non-rotary-wing aircraft. While such capability has direct application for military missions such as those of a tilt-rotor or tilt-wing aircraft, there also exists an additional need for simple/reliable/effective personal and business-sized Super-STOL or VSTOL aircraft operating from remote or small sites as well as increasingly dense

* Principal Research Engineer; GTRI

** Principal Investigator; NASA LaRC

urban environments. The development of simple, efficient aeropropulsive technology and corresponding low-speed control systems to make this possible is a goal which now seems practical due to technical breakthroughs in pneumatic and powered-lift aerodynamic technologies. This paper, presented at the NASA/ONR CC Workshop in March 2004, will discuss recent progress in the integration of high-lift, propulsive, and control systems, all employing common pneumatic techniques using Circulation Control blowing, into a promising Super-STOL configuration.

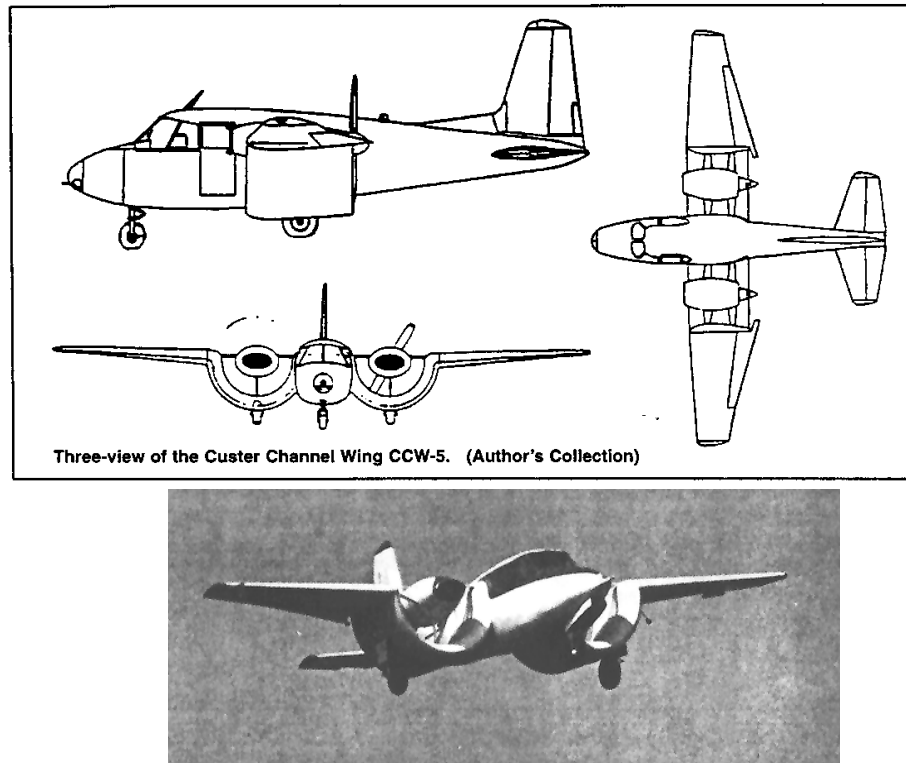


Figure 1– 3-View and in-flight photo of 1960s Custer Channel Wing Aircraft (Refs.1, 2 and 3)

Two promising technologies to evolve from earlier STOL/VSTOL research are the Custer Channel Wing powered-lift configuration and the Circulation Control Wing (CCW) pneumatic high-lift concept. Through innovative use of the propeller slipstream, the Channel Wing airplane developed by Willard Custer (Figure 1 and Refs. 1, 2, 3) was able to achieve significant lift coefficient and efficient downward thrust deflection without varying the high-lift configuration geometry. This powered-lift technology, tunnel-tested by NACA in 1953, (Ref. 1) and then flight-tested and further developed by Custer in the mid 1960's (Ref. 2), employed the Channel Wing concept shown in the sketch of Figure 2 (from Ref. 3). In essence, the propeller located at the very trailing edge of the 180°-arc circular channel in the wing further increased the velocity over the channel's upper surface and augmented the circulation and lift there in much the same manner as a deflected flap, but perhaps to a greater extent. Lift was also augmented by the deflected slipstream behind the channel such that

$$\Delta C_L = C_T \sin (\alpha + \delta_{\text{slipstream}})$$

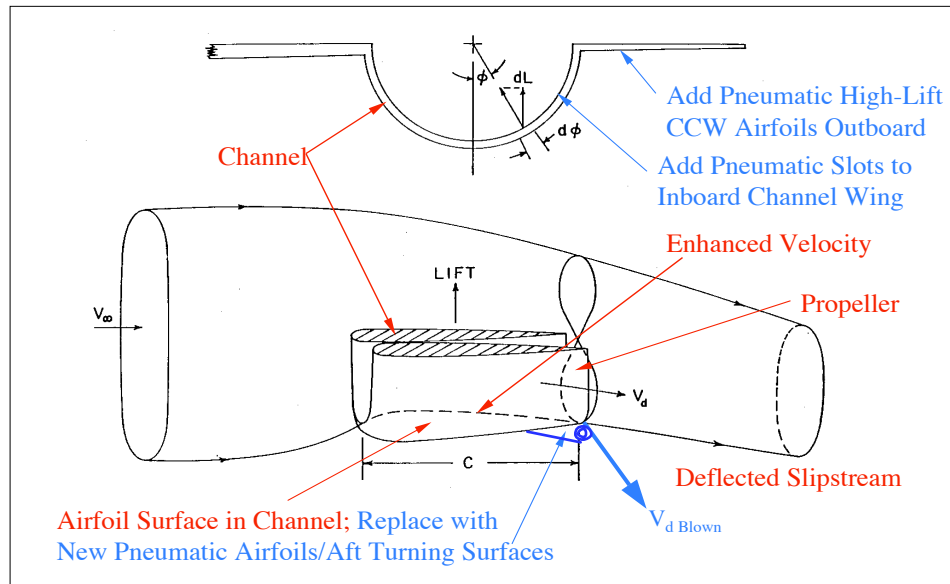


Figure 2- Basis of the Channel Wing Concept and Current Pneumatic Improvements (Blue)

However, while in-flight lift coefficients nearing 5 were generated by thrust coefficients also nearing 5 (Ref. 3), the flight-tested Custer Channel Wing aircraft demonstrated a number of drawbacks associated with low-speed handling, cruise drag, stability & control, high-incidence operation, and one-engine-out scenarios, including:

- much of the high C_L was from redirected thrust, less was from circulation lift augmentation
- high cruise drag could result from the channel's extra surface area
- asymmetric thrust yields asymmetric moments & instability
- channel leading-edge and trailing-edge separation could occur at high angle of attack, α
- poor low-speed control from conventional aerodynamic surfaces at low speeds
- nose-down pitch from aft propeller loading on the wing
- non-uniform flow around the prop at high α
- poor lift/drag ratio
- high-angle-of-attack operation could cause poor visibility and control
- one-engine-out control problems

To alleviate these shortcomings, preliminary research has been accomplished under a NASA-Langley-sponsored program at Georgia Tech Research Institute (GTRI) which has investigated adapting Circulation Control pneumatic technology (Figure 3 and Refs. 4 and 5, for example) to dramatically improve the Channel Wing configuration. As Figure 2 shows, the new pneumatic configuration (in blue) thus developed combines blowing on curved surfaces at the channel trailing edge to greatly augment the lift and thrust deflection without using high angle of attack. It also employs blown Circulation Control Wing technology on the

POSSIBLE LEADING EDGE BLOWING



TANGENTIAL BLOWING OVER ROUNDED TRAILING EDGE SURFACE

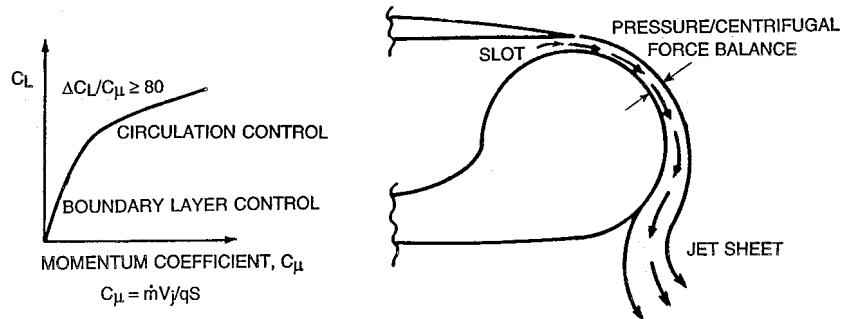
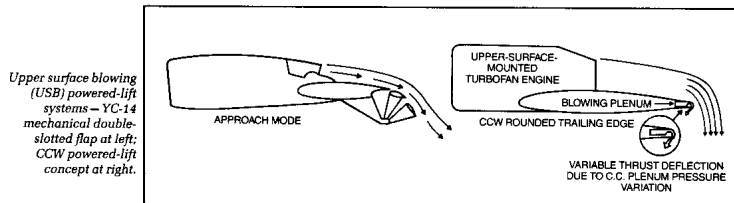
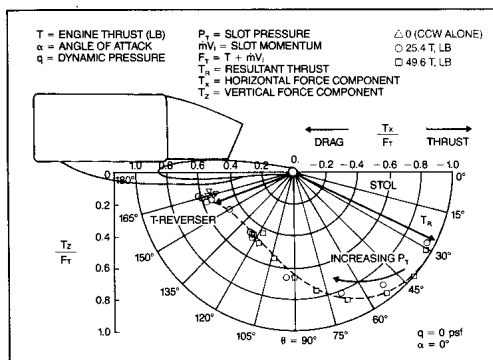


Figure 3-Basics of Circulation Control Pneumatic Technology



Upper surface blowing (USB) powered-lift systems – YC-14 mechanical double-slotted flap at left; CCW powered-lift concept at right.



Static thrust deflection of CCW/USB wind tunnel model.



Fig. 4 – Previously Developed Circulation Control Wing/ Upper Surface Blowing Powered-Lift Concept (Ref. 6)

outboard wing panels to further augment lift and low-speed controllability while providing additional drag when needed for slow-speed approaches down steep glide slopes for Super-STOL.

This channel thrust turning and lift augmentation are based on the CCW/Upper Surface Blowing (USB) concept of Figure 4, where tangential blowing on a highly curved trailing edge behind a jet engine augments flow field entrainment, increases circulation and

deflects thrust to add more incremental lift. Thrust deflection angles of 165° produced by blowing were measured experimentally on wind-tunnel models (Refs. 5 and 6). This concept provides pneumatic STOL, VSTOL and thrust-reversing capabilities without any moving parts. CCW alone (Figure 3) employs a similar tangential-blowing configuration but without the pneumatic thrust deflection. CCW airfoils have generated measured 2-D lift augmentations of 80 times the input blowing momentum (Refs. 4 and 5). When flight-tested on an A-6 flight demonstrator, CCW showed a 140% increase in useable high-lift, employing only half of the bleed air available from the aircraft's standard turbojet engines (Ref. 8). Figure 2 shows how these blown flow-entrainment devices would be arranged to enhance the effectiveness of the Pneumatic Channel Wing (PCW) configuration. In addition, the CCW lift capability can be applied differentially outboard to generate very large rolling and yawing moments, which are essential for controlled flight at the very low speeds of Super-STOL.

Based on earlier CCW/USB wind-tunnel and full-scale data (Figure 4 and Refs. 6 and 7) and CCW flight test data from the A-6 STOL-demonstrator program (Ref. 8), the predicted lift and drag capabilities for the Pneumatic Channel Wing configuration were expected to offer great Super-STOL promise. Reference 9 details these early predictions before the current wind-tunnel test data were available; these implied C_L values approaching 9-10 for a Pneumatic Channel Wing aircraft with blowing on outboard CCW wing panels at relatively low aircraft angle of attack. Higher C_L values were possible at higher thrust coefficients if higher α values were used due to the additional vectored thrust component. Again, for comparison, the Custer Channel Wing aircraft generated in-flight C_L of 4.9; a conventional slotted flap on this wing geometry would generate C_L from 2 to 3. Initial takeoff predictions (Ref. 9) showed that these PCW capabilities could produce very-short hot-day takeoff ground rolls for typical mission weights, and even zero ground roll under certain conditions.

As part of an ongoing program for NASA Langley Research Center to develop this Pneumatic Channel Wing concept, GTRI and NASA have teamed in an experimental development program being conducted at GTRI, which has provided aerodynamic and propulsive data input for design studies being conducted at both NASA and GTRI. This current paper will summarize these experimental results and discuss effects deriving from variations in PCW geometry, propeller thrust and channel blowing.

Experimental Apparatus and Test Techniques

A wind-tunnel development/evaluation program was conducted at GTRI on a generic twin-engine Super-STOL-type transport configuration, Figure 5, using the 0.075-scale semi-span model shown in Figure 6. Here, a variable-speed electric motor was installed in the nacelle, which could be located at various positions in the channel, and which drove interchangeable 2-bladed, 3-bladed or 4-bladed propellers of various diameters and pitch. Also variable was the height of the blowing slot located at 95% of the channel chord length, as well as the blowing momentum coefficient and portions of the slot arc length which were blown. Behind the slot, the rounded trailing edge curved only 90° (rather than the more conventional 180° of typical CCW configurations) for an anticipated maximum thrust deflection of around $(90^\circ + \alpha)$. It was already known (Fig. 4) that thrust deflections up to 165° yielded by blowing were a possibility. Here, the momentum coefficient is defined as

$$C_{\mu} = (\text{mass flow rate} * \text{jet velocity}) / (\text{dynamic pressure} * \text{wing planform area}) \\ = m V_j / (qS).$$

This semi-span model configuration (Fig. 6) was mounted on an under-floor balance with air supplies and automated pitch table in the GTRI Model Test Facility 30" x 43" x 90" test section. Tunnel wall boundary layer near the test section floor was eliminated by use of tangential floor blowing. In a follow-on version of this configuration, both the leading edge and the trailing edge of the outboard CCW wing section were also blown for separation control. The emphasis in the following data is on the performance of the inboard blown Pneumatic Channel Wing configuration, but performance of the outboard CCW sections to further augment lift is also shown.

Wind-Tunnel Evaluations and Results

Test techniques employed in the subsonic tunnel evaluation of this pneumatic powered-lift model are similar to those employed and described in Refs. 10 and 11 for blown airfoil and semi-span models, except that special additional techniques were employed to account for the installation of the active propeller in the channel (see below). Some 980 wind-tunnel runs (including propeller calibrations) have now been conducted during three test programs at GTRI to develop these blown-configuration geometries and to evaluate their aeropropulsive, flight-trim and control characteristics. A typical run consisted of a sweep (incremental variation) of prop thrust or blowing pressure at constant angle of attack and wind speed. Also, angle of attack sweeps or dynamic pressure (velocity) sweeps were run at constant thrust and blowing coefficients, C_T and C_{μ} . Numerous runs were made with varying tail configurations to evaluate pitch trim and control. Typical test results are presented in the following sections to demonstrate how these various parameters affected overall performance.

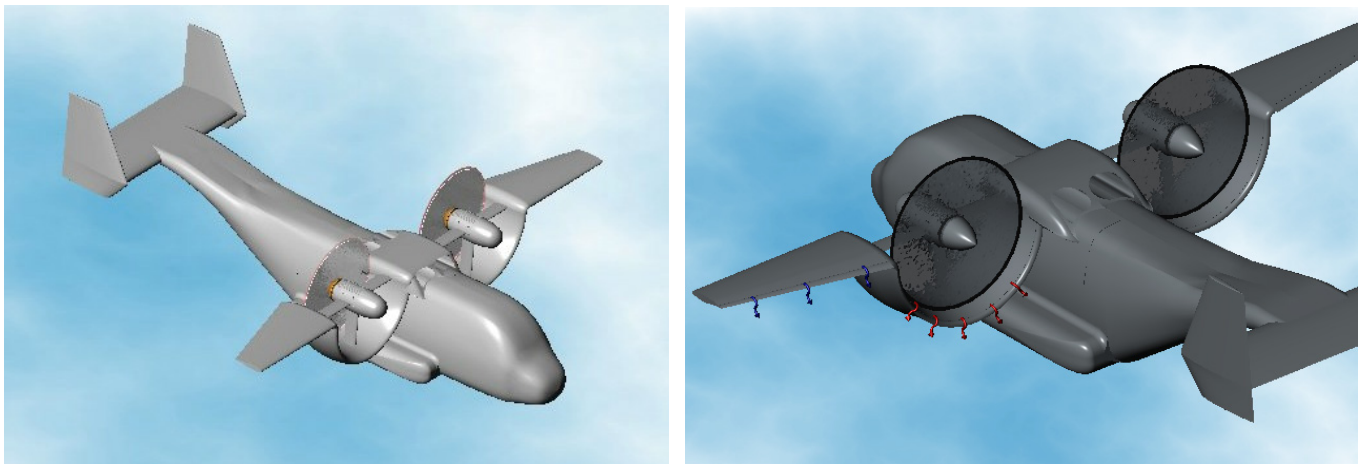


Fig. 5 – Conceptual Pneumatic Channel Wing Super-STOL Transport Configuration

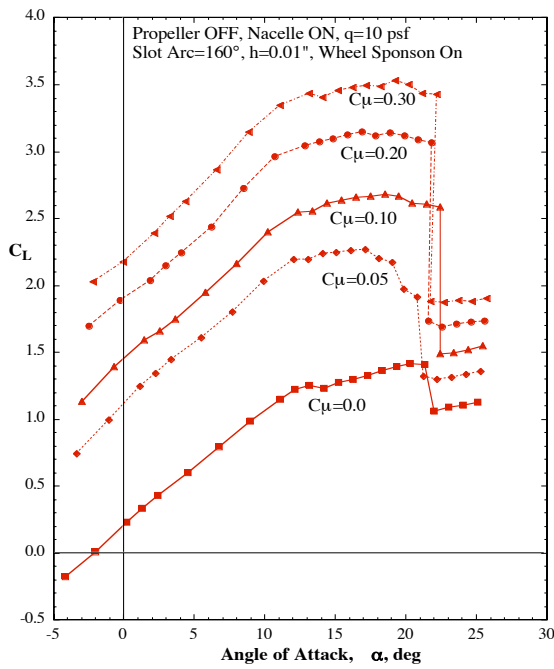


Fig. 6 – Pneumatic Channel Wing/CCW Semi-span Model Installation in GTRI Model Test Facility Research Tunnel (3-bladed prop with Unblown Outboard CCW), plus Jet Flow Turning in Channel (black tufts)

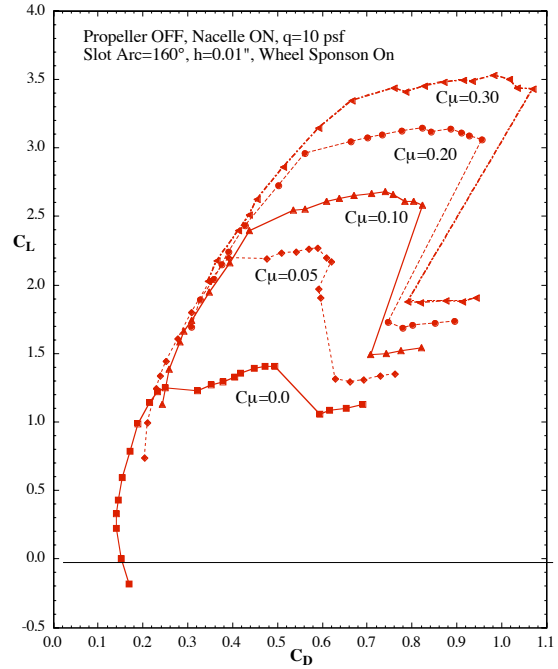
Tunnel Test Results, Outboard Wing ON

In Figures 7a and 7b are shown the effects on lift and drag coefficients of blowing the channel trailing edge without the prop installed (i.e., $C_T = 0$), but with the engine nacelle in place, Fig. 6. Notice the ability of the blowing to more than double the C_{Lmax} of the unblown configuration with virtually no reduction in the stall angle, α_{stall} . The C_L values shown are comparable to or greater than those which would normally be generated by more-complex moving mechanical flaps. Notice also the ability of the blowing at $\alpha = 0^\circ$ to increase C_L by a factor of nearly 10 over the unblown value. At $\alpha = 0^\circ$, blowing at $C_\mu = 0.30$ yields 50% more C_L than the C_{Lmax} of the unblown configuration. In Figure 7b, the drag polars at constant C_μ are typically quadratic in C_L . Earlier in α than where the stall begins, they follow essentially the same single curve, using blowing to progress to each successive higher C_L region.

Addition of the propeller to the channel brings into play the powered-lift characteristics of the Pneumatic Channel Wing configuration. Figure 8, for $\alpha = 0^\circ$, shows the variations in C_L and C_D with thrust coefficient C_T for fixed values of blowing coefficient. Here, in order to recognize the direct thrust component to lift and drag, thrust coefficient is defined as $C_T = T/(qS)$, where T is the calibrated uninstalled wind-on prop-alone (not-in-the-channel) thrust at the proper advance ratio, i. e., representative test dynamic pressure, q . The reference area S is the wing semi-planform area. These thrust values were determined prior to installation in the channel by testing the prop alone in the tunnel at various RPMs and tunnel speeds.



(a) Lift vs α



(b) Lift-Drag Polars

Fig. 7– Measured Blown Lift and Drag Capabilities of the Pneumatic Channel Wing Model Without the Propeller Installed

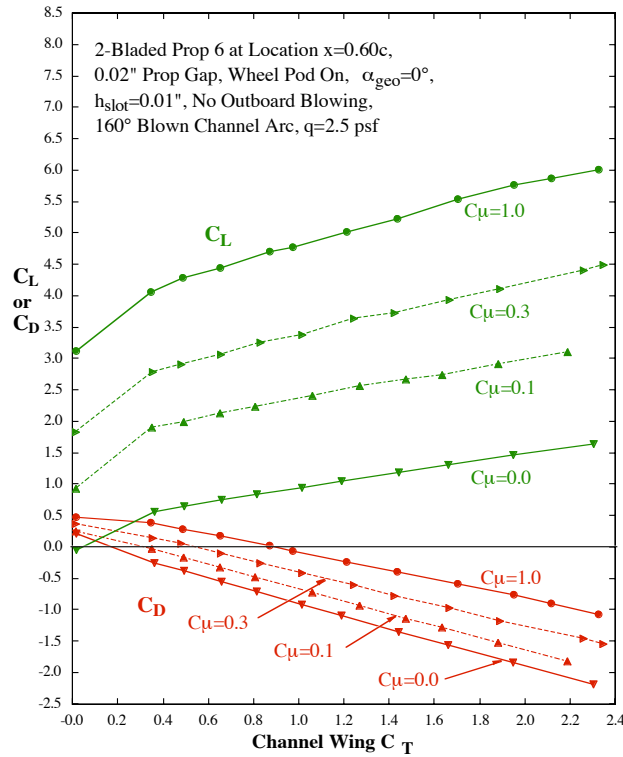


Fig. 8– Effects of Prop Thrust Variation on Lift and Drag at Constant Blowing (C_μ) and $\alpha = 0^\circ$

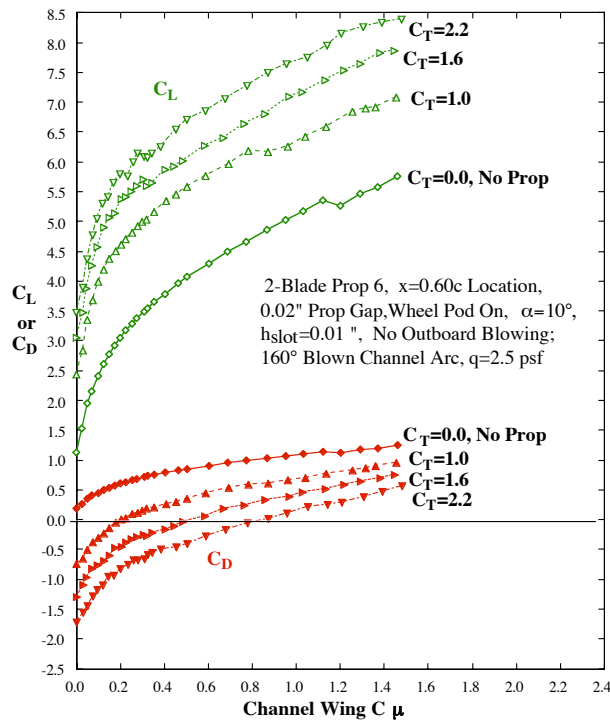


Fig. 9 – Effects of Blowing Variation on Lift and Drag at Constant C_T and $\alpha=10^\circ$

Then, calibration curves of T vs RPM were input to the data reduction program at given test wind speeds. Thus C_T , C_L and C_D are directly comparable on a common reference basis to determine force contributions from installed thrust. This avoids the difficulty which would be caused by using the standard helicopter thrust coefficient, based on rotor (or prop) geometry rather than wing area. Also, note that measured C_D thus obviously includes the input thrust, which cannot reasonably be separated from the aerodynamic drag alone once the prop is in the channel. Measured C_D can thus be (and sometimes is) negative. After the initial low values of C_T are exceeded, C_L increases nearly linear with C_T , and C_D reduces nearly linearly. (This implies that at a constant C_μ , the thrust deflection angle is nearly constant.)

Figure 9 shows that incremental lift augmentation due to blowing (C_μ) is much greater than due to C_T (Figure 8). Here at $C_T = 2.2$, the blown configuration generates C_L around 8.5 at $\alpha = 10^\circ$. The flight-tested Custer Channel Wing (Ref. 3) generated roughly 1/3 this C_L at this C_T , but also required $\alpha = 24^\circ$ - 25° . Note also that increased blowing at a constant C_T yields increased drag (rather than thrust recovery), which can be quite essential for Super-STOL approaches and short landings. These lift comparisons in Figures 8 and 9 show that lift increases more efficiently by increasing blowing than by increasing thrust. In the Figure 10 plot is shown the variation in lift and drag with angle of attack for the blown powered-lift configuration in comparison to the unblown baseline configuration without the prop. Here, flow visualization showed that the initial stall ($\alpha=15^\circ$ - 17°) seen for most of the lift

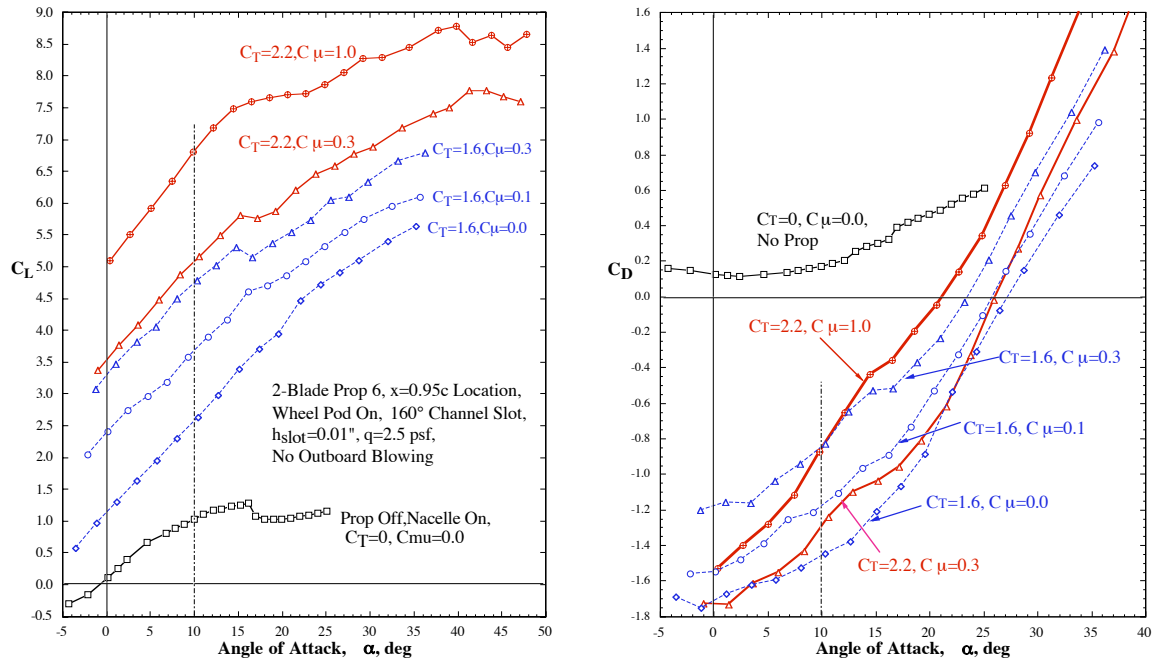
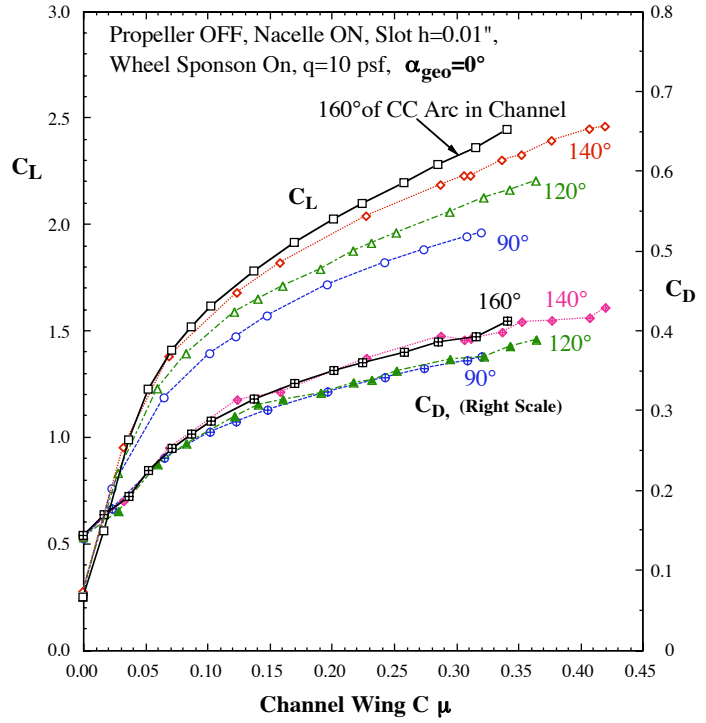
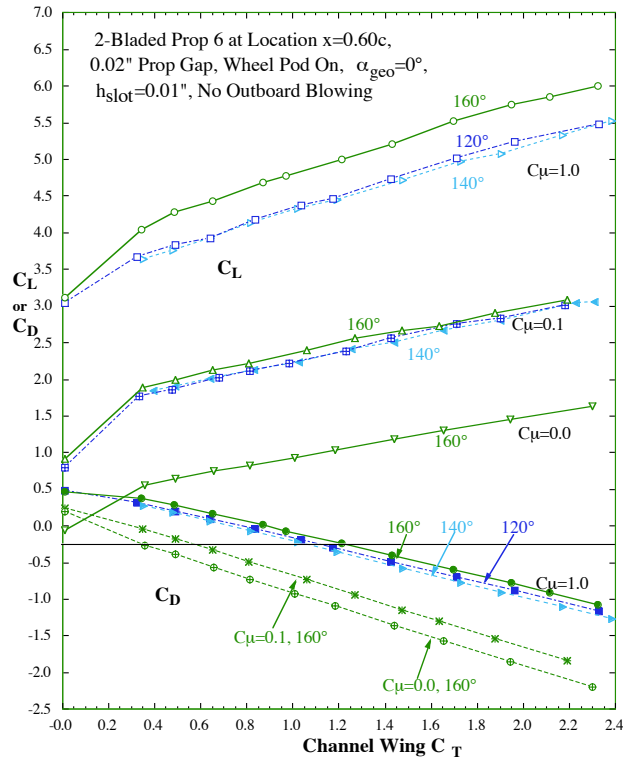


Fig. 10 – Effects of Blowing, C_T , and α on Lift Coefficient, Stall Angle and Drag Coefficient for Pneumatic Channel Wing Model with Unblown Outboard Wing

curves corresponded to stall of the outboard unblown wing section, while the blown channel wing section then continued on to stall angles of 40° - 45° and C_L values of 8.5 to 9. Notice that C_D (including thrust) increases from negative to positive values as incidence increases.

Figure 11 shows the effect on lift and drag of increasing the circular arc length of the blown slot around the channel at a given prop longitudinal location ($x/c = 0.95$), where the maximum slot arc of 160° was most effective. Blowing of more than 160° of channel arc was not appropriate on this model because the last 20° of inboard arc was along the channel right next to the fuselage, and blowing there would do little more than bounce off the fuselage.

The effect on increased tail-off pitching moment caused by suction loading on the aft of the channel (either by blowing, prop slipstream, or both) is shown in Figure 12 as a function of C_T and C_{μ} , all at $\alpha = 0^\circ$. These moments are referred to the channel's quarter-chord location ($c/4$), and confirm the typical trend of this type of blown configuration: large nose-down C_M which, while it does make the aircraft much more stable longitudinally, causes concern with pitch trim. It is for this reason that additional experimental evaluations were conducted tail-on to investigate increased longitudinal trim capabilities. All data presented so far have been tail-off. Also a second investigation was conducted with leading-edge blowing installed on the outboard wing CCW portion to provide counteracting nose-up pitch for trim, as well as for leading-edge separation prevention.



(a) Prop & Nacelle Installed (b) Prop OFF but nacelle installed
 Fig. 11 – Effects on Lift and Drag of Varying Blown Channel Slot Arc Length at Constant C_μ and at $\alpha=0^\circ$

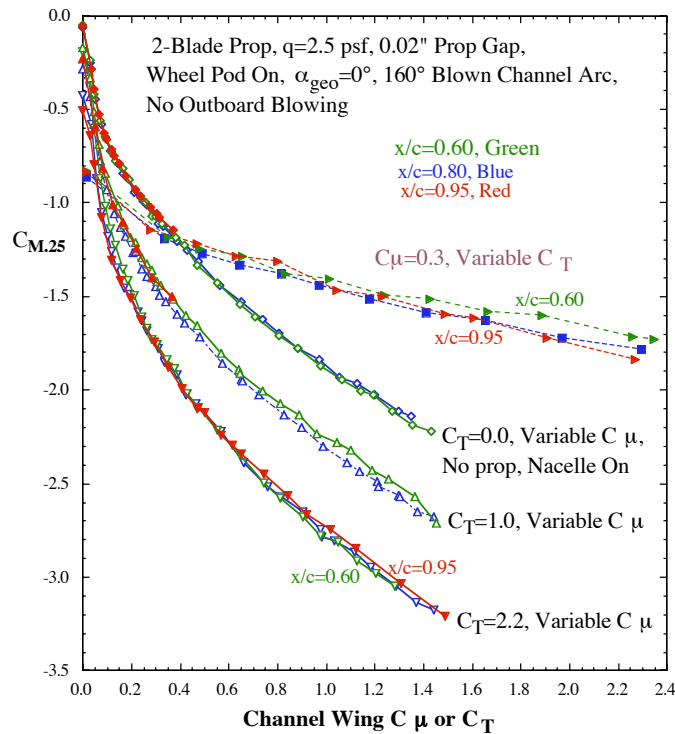


Fig. 12 – Effects of Prop/Nacelle Location, Blowing and Thrust on Quarter-Chord Pitching Moment, $\alpha=0^\circ$

Tunnel Test Results, Channel Wing Only

Higher non-dimensional thrust coefficient values were available when the channel-only configuration was tested (fuselage, blown channel and prop, but with no outboard CCW panels) since the reference planform area of the wing was also reduced. This allowed C_T of ~ 3 for the channel-only vehicle, and as Figure 13 shows, lift coefficients nearing 11 were measured with a conventional horizontal tail installed at the mid-vertical location on the aft fuselage. Needless to say, not all of the lift values shown in Figure 13 (right plot) are trimmed longitudinally. Furthermore, for the $C_T = 3$ case with blowing on, the conventional tail of the aircraft stalled experimentally over much of the lower α range (more on this below).

The possible inability to longitudinally trim these Super STOL aircraft was pointed out as a problem of blown systems in Refs. 7 and 8. It is further emphasized in Figure 13,

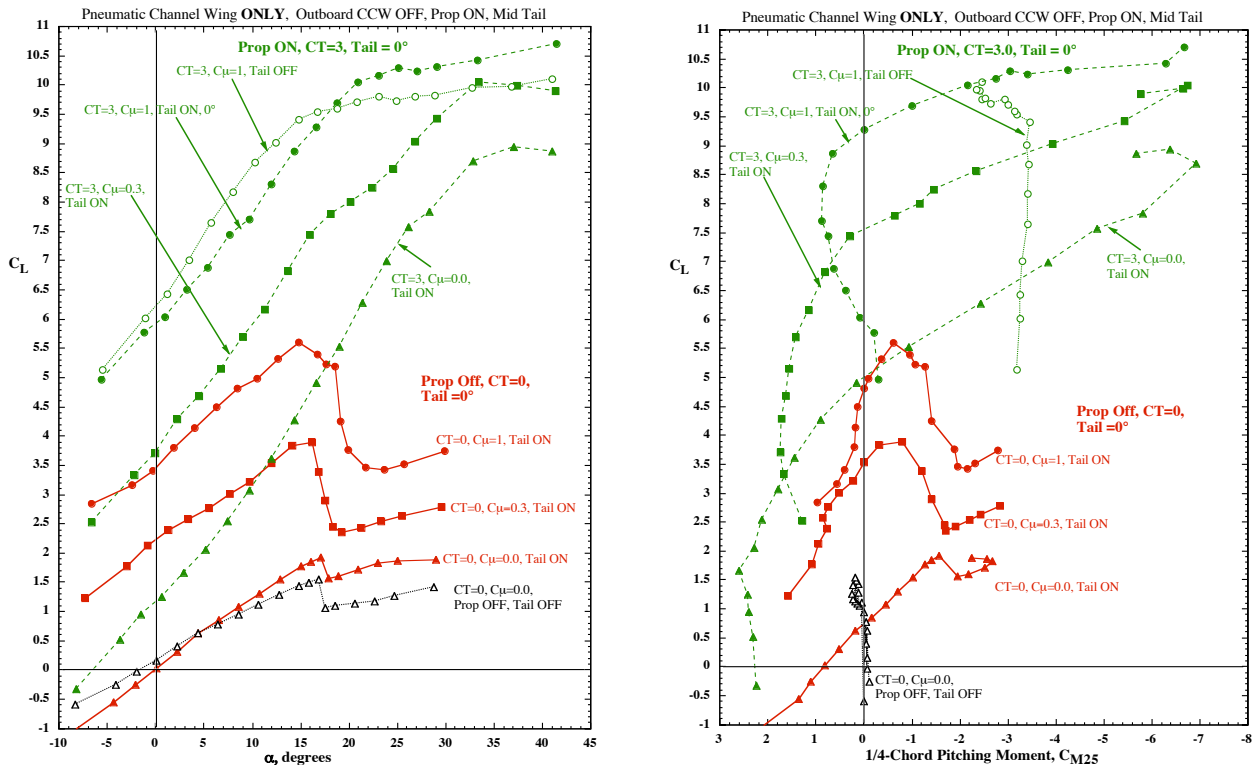


Figure 13 –Effect of Thrust and/or Blowing Increase on Lift & Pitching Moment Variation with α for Channel-Wing-Only Configuration (No Outboard Wing Panels) with Tail at Mid-location, $i_T=0^\circ$

where the large suction on the aft-loaded blown channel (and blown wing, if present) produces very large nose-down pitching moments (see the tail-off curve). Even though this can produce improved longitudinal stability, these moments must also be trimmed. Horizontal tail investigations were conducted as part of this 3-D model development plan in hopes of determining tail location and configuration to provide enough nose-up pitch to trim the vehicle. Several horizontal tail configurations (one without an elevator, a second with a 20° -up elevator [$\delta_{\text{elev}} = +20^\circ$], and a third with an inverted leading edge droop) were designed and fabricated. As Figure 14 shows, these could be mounted on a vertical center plate yielding variation in both tail incidence (i_T) and vertical position in the propeller slipstream. High, mid-fuselage, and low-tail positions were tested. Testing of these tail-on configurations over a range of tail parameters revealed that a low-tail position immersed in

the prop slipstream and dynamic pressure was more effective than the higher tail (Figure 15), but the lower tail also experienced more leading-edge stall for the same reason. This tail stall prevents the vehicle from being trimmed at this higher blowing condition (here with the outboard CCW wing on again). Considerable videotaping of flow visualization tufts on the tail revealed these problem areas and led to the development of the inverted-droop (drooped upward) leading-edge modification for the tail. Keeping the tail LE attached allows positive nose-up pitch and thus trim to be generated for the vehicle over a much wider range of lower α values. For the Channel-Wing-Only model with the modified tail, trimmed C_L values greater than 9 are thus seen (Figure 16), but much of this data is still untrimmed, and again the low tail with no LE mods is fully stalled. Thus, this data implies that further tail development (perhaps including LE blowing to prevent the tail stall without mechanical LE fixes) is needed to trim in this high C_L range at all vehicle angles of attack.



Figure 14 – Horizontal Tail Configurations Evaluated: High Tail; Low Tail; Mid-fuselage Tail, Outboard CCW ON

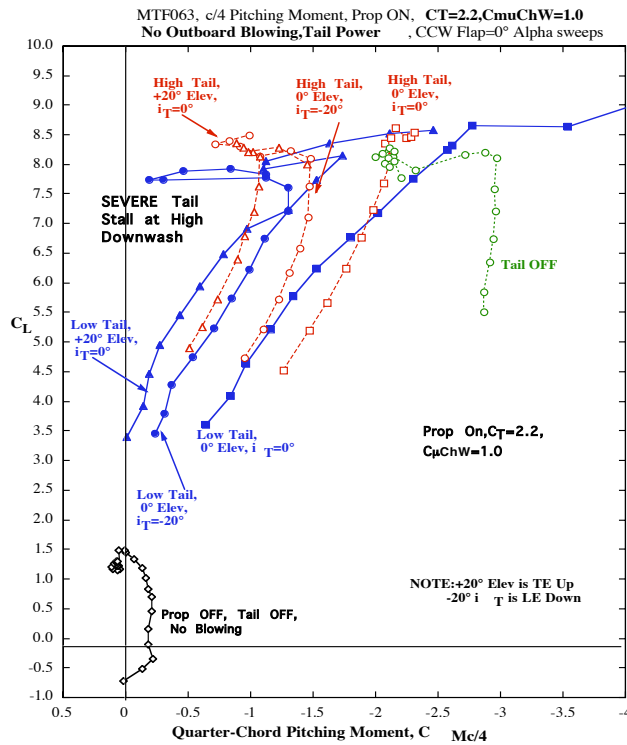


Figure 15 – Comparison of High and Low Tail Position on Pneumatic Channel Wing Configuration with **Unblown Outboard Wing** and Horizontal Tail

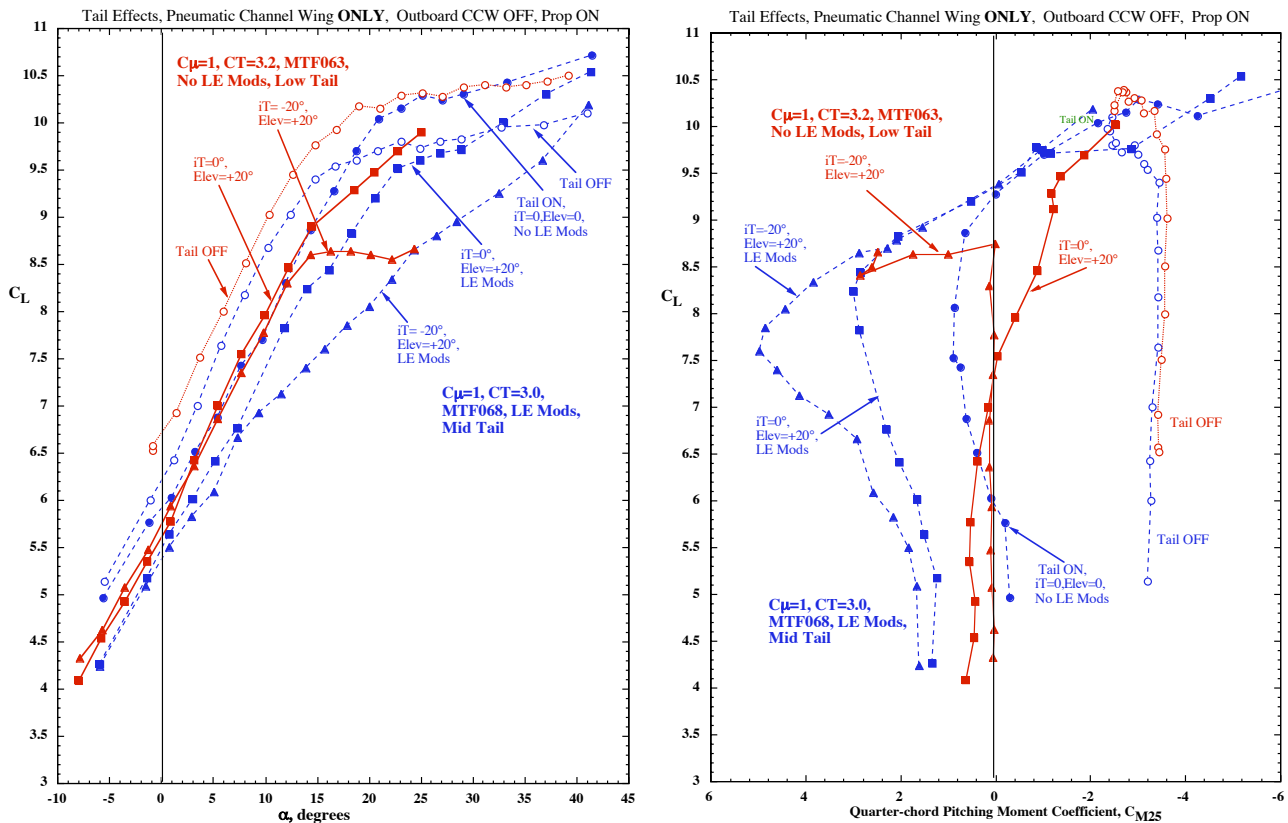


Figure 16 – Comparative Lift and 1/4-Chord Pitching Moment Coefficients of Pneumatic Channel Wing; **No Outboard CCW**, with and without Tail LE Modifications

Tunnel Test Results: Flow Attachment

An additional series of flow visualizations was conducted to further identify means to prevent separated flow fields on the wing during high-lift generation. Figure 17 data show that the flow at the channel leading edge is entrained to the point where LE separation is prevented up until $\alpha=35-40^\circ$ or more, but that the outboard CCW is prone to stall there. Leading-edge blowing on this outboard CCW wing panel greatly entrained this flowfield as well. Figure 18 flow visualization shows this severe separation at $\alpha = 20^\circ$ for the unblown case (left photo), while blowing the leading edge completely re-attached the flowfield there.

An additional means of trim and control was investigated for the Pneumatic Channel Wing. This means merely offsets these large nose-down pitching moments (seen in Figures 13, 15, and 16) by moving the aircraft center of gravity aft to trim, with no tail installed. Aft cg movement was previously performed for flight tests of the A-6/CC Wing aircraft, but with the tail on, Ref. 8. Figure 19 shows data for the $C_T=3$ case of a tailless Pneumatic Channel Wing without outboard wing. At $C_\mu = 0$, moving the cg aft from $x/c = 0.25$ to 0.375 gives the aircraft neutral longitudinal stability but does produce trim over most of the angle of attack range. Similar reduction in pitching moment can be produced by aft cg shift as blowing is increased (Figure 19b), but this requires further aft cg to trim at lower α , and the C_L vs C_M curves are now unstable ($dC_M / dC_L = +$). Some small control surface (such as a blown canard to provide nose-up pitch and positive lift to trim) could perhaps be incorporated with a state-of-the-art control system and control laws to make this a feasible pitch-trim device without lift loss due to tail download.

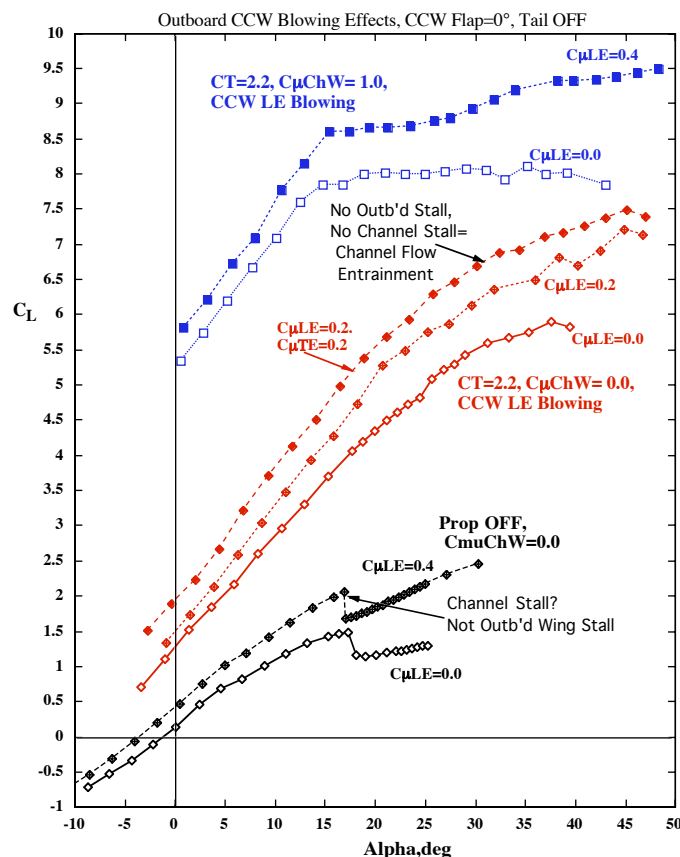


Figure 17 – Leading-edge Blowing and Channel Flow Entrainment Prevent Flow Separation over Both Channel and Outboard CCW Leading Edges



(a) Outboard LE slot unblown



(b) Outboard LE Slot blown

Figure 18 – Flow Attachment Caused by Leading-edge Blowing on Outboard CCW and Channel Flow Entrainment at $\alpha=20^\circ$, Channel LE not Blown

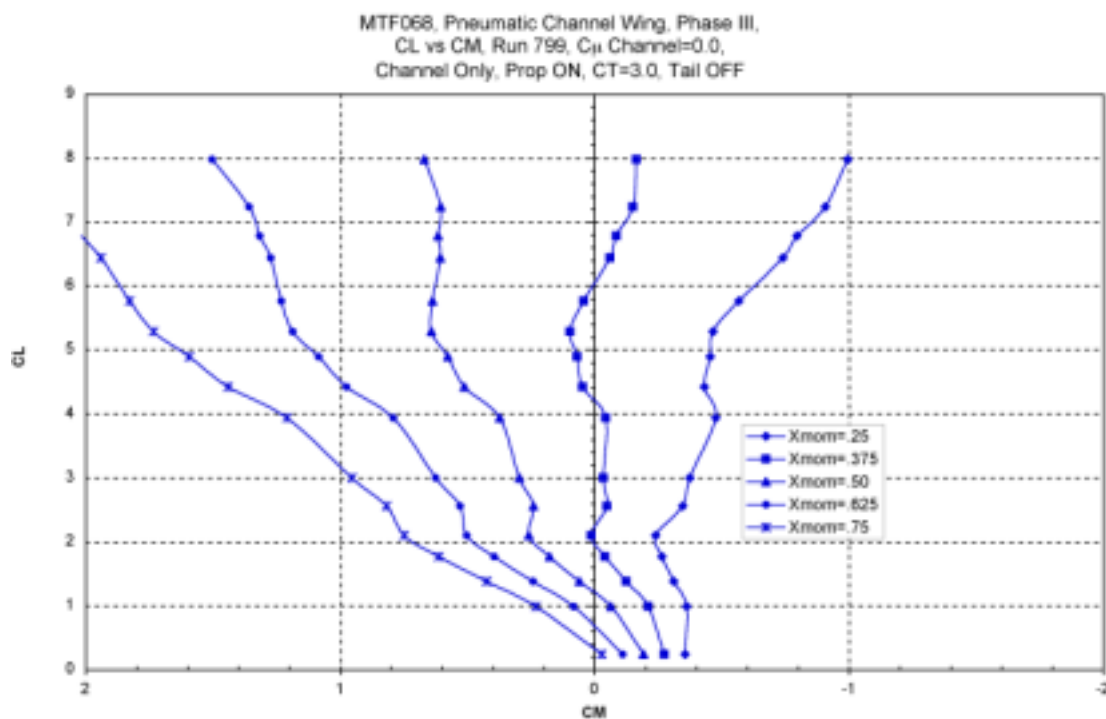


Fig. 19 (a) $C_T=3$, $C_{\mu}=0$

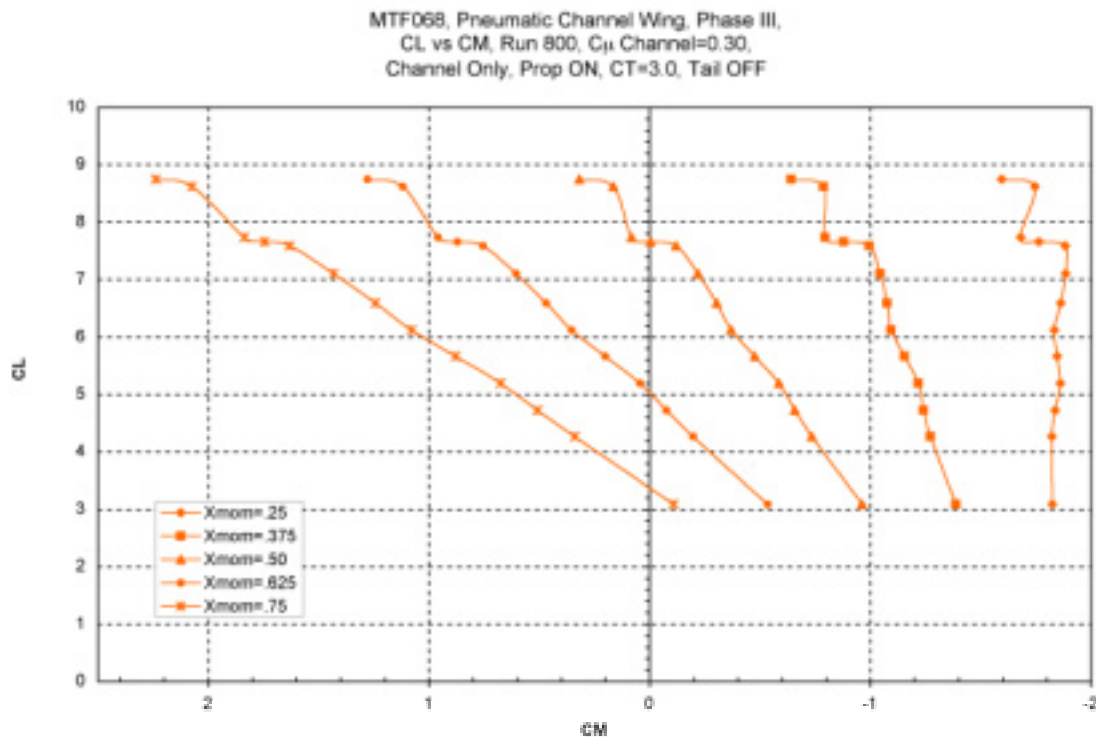


Fig. 19 (b) $C_T=3$, $C_{\mu}=0.3$

Figure 19 – Effect of Aft CG Location on Pitching Moment Curves for the Tail-less Pneumatic Channel Wing at $C_T=3$, $X_{mom}=X_{cg}/c$

Comparison of Measurements and Predictions

In Figure 20 are compared the results of these investigations with previously-predicted lift and drag data which were estimated from existing CCW/USB wind-tunnel data and from A-6/CCW flight-test data. Whereas the prop/electric motor currently available did not allow higher C_T values than about 2.2 (outboard wing ON), this lower-thrust wind-tunnel data considerably surpasses the predicted lift data (Fig. 20a). If the ratio of measured-to-predicted holds linearly up to $C_T=10$, then C_L values over 14 are to be expected at $\alpha = 10^\circ$. The experimental drag data (Fig. 20b) is similar to the predicted values at lower C_{μ} but shows less drag than predicted at higher blowing. These estimated data had been used to predict Super-STOL takeoff distances on a hot day at 3000 ft altitude to be less than 100 feet and in some instances, zero feet (see Reference 9 and Fig. 21 below). The measured-versus-predicted results in Figure 20 seem to suggest that even better takeoff performance might be obtained (higher lift, lower drag). However, the lower measured drag values indicate that additional attention will need to be paid to obtaining greater drag values for steeper glide slopes on STOL approaches (when desired and chosen by the pilot).

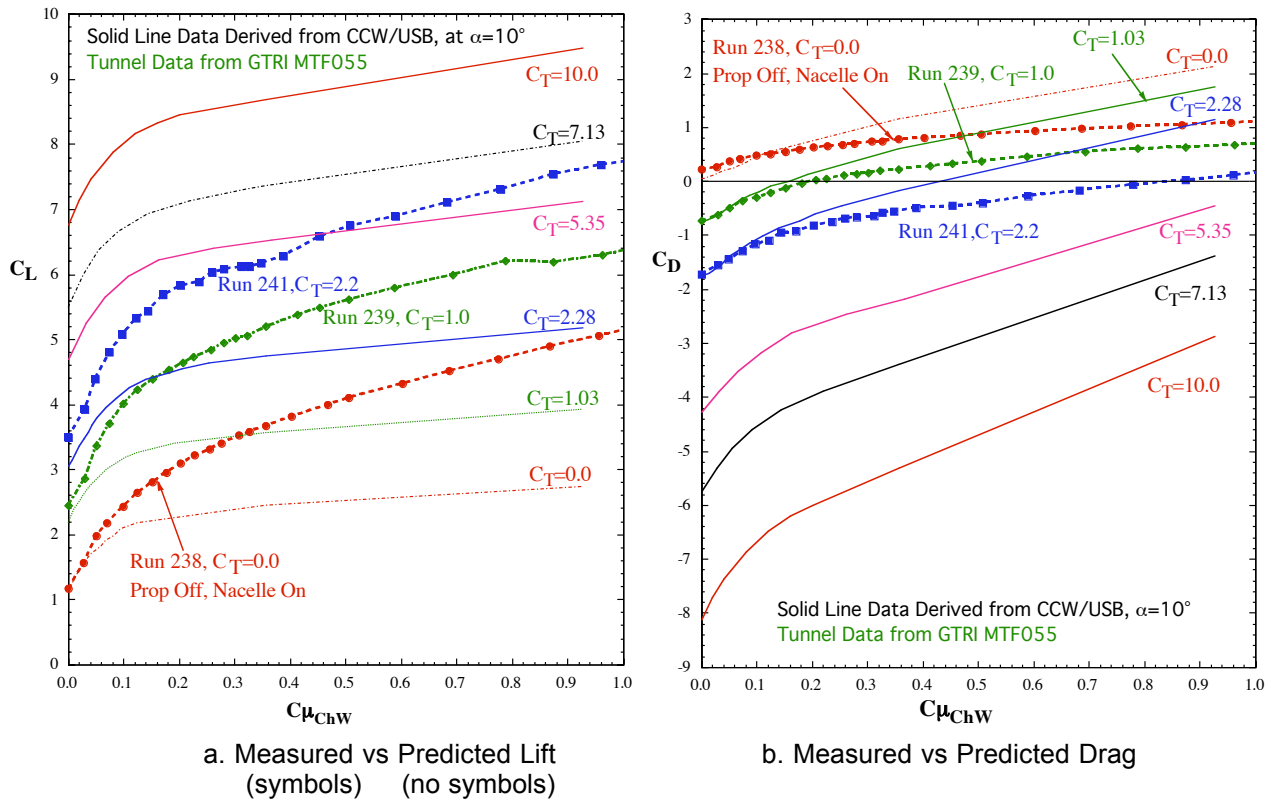
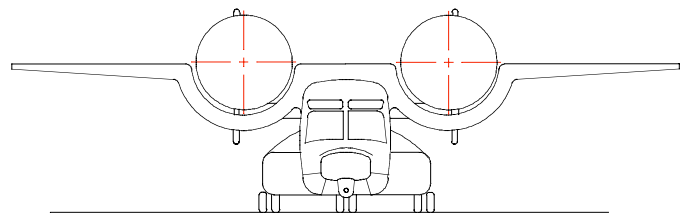
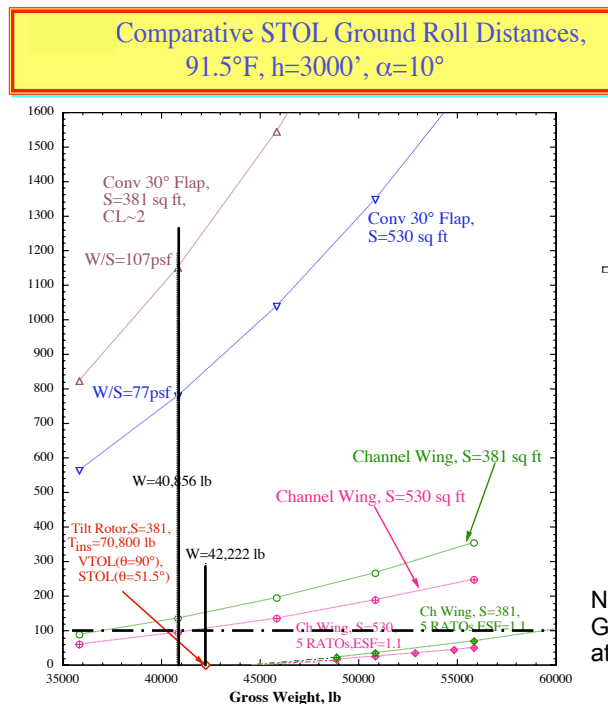


Fig. 20 – Comparisons of Predicted and Experimental PCW Lift & Drag Data at Constant C_T , $\alpha=10^\circ$, Outboard CCW ON



NOTE: ~17,000 lb Increase in TO Gross Wt over Baseline Tilt Rotor at 100' ground roll

Fig. 21- Pneumatic Channel Wing Predicted Super-STOL Takeoff Performance

Potential Applications

Design and mission studies conducted at NASA LaRC based on the above tunnel data have lead to consideration of several new pneumatic powered-lift PCW-type configurations. The capability of the Pneumatic Channel Wing to significantly augment lift, drag, and stall angle to the levels reported herein demonstrates that this technology has the potential to enable simple/reliable/effective STOL and possibly VTOL operations of personal and business-sized aircraft operating from remote or small sites as well as increasingly dense urban environments. Such capability now opens the way for alternate visions regarding civilian travel scenarios, as well as both civilian and military aerial missions. One such vision is represented by the Personal Air Vehicle Exploration (PAVE) activity at NASA Langley Research Center. Another vision, a military Super-STOL transport, is discussed in the mission study of Reference 9 and Figure 21 above.

Summary and Conclusions

Results from subsonic wind-tunnel investigations conducted at GTRI on a 0.075-scale powered semi-span model of a conceptual Pneumatic Channel Wing (PCW) transport have confirmed the potential aerodynamic payoffs of this possible Super-STOL configuration, including very high lift and overload capability. These results include:

- Lift and drag augmentations and/or reductions as desired for Super-STOL operation have been confirmed, with $C_L=9$ measured at $\alpha=10^\circ$ ($C_L=10-11$ at higher α), and drag coefficient (including thrust) varying between -2 and $+2$, depending on blowing and thrust levels. C_L 's nearing 14 are predicted if higher C_T is available, say on takeoff
- Blowing (C_μ) and thrust (C_T) variations were both found to significantly enhance circulation, thrust deflection and lift; but, if evaluated as incremental lift per unit of input thrust or momentum (C_T or C_μ), blowing was far more efficient than thrust.
- By varying only C_μ and/or C_T , all the aircraft's aerodynamic characteristics (forces and moments) can be augmented or reduced as desired by the Super-STOL aircraft's pilot or it's control system without mechanical moving parts (such as tilting rotors or wings) and without resorting to high α to acquire larger vertical thrust components for lift.
- The blown channel wing itself, without thrust applied, was able to double the C_{Lmax} capability of the baseline aircraft configuration, and multiply its lift at $\alpha=0^\circ$ by a factor of 10. Addition of blowing on the outboard CCW section can increase this further, and can also add drag as needed for Super-STOL approaches.
- Even with the unblown outboard wing stalling at $\alpha=15^\circ-17^\circ$, the blown and thrusting channel continued to increase lift up to a stall angle of $40^\circ-45^\circ$ due to channel flow entrainment. While this high α may not prove practical as a takeoff/landing operational incidence, it does show significant improvement over the asymmetric LE separation of

the conventional channel wing's stalled channel and the resulting low-speed control problems.

- PCW conversion of thrust into either drag decrease or drag increase without moving parts is also quite promising for STOL operation.
- Large nose-down pitching moments are produced by these blown configurations, and thus longitudinal trim capability needs to be addressed in future evaluations.
- Unlike a tilt rotor, in Super-STOL or VSTOL, there is no download on the wing from prop thrust since the PCW props don't tilt
- PCW's potential for an integrated lift, thrust/drag interchange and control system all from one set of devices holds promise in terms of simplicity, weight reduction and reliability/maintainability

Thus far, the projected operational benefits based on these early data suggest Super-STOL and possible VSTOL capability with significantly increased payload, reduced noise signatures, and increased engine-out control, all without variable geometry or mechanical engine/prop tilting. A Pneumatic Channel Wing aircraft thus equipped could provide a simpler, less costly way of achieving the Super-STOL/VSTOL capability without the complexity, weight or reliability issues of rotating the propulsion system, carrying large engines and rotors on the wing tips, or thrusting downwards on fixed wings during hover. Additionally, the integration of pulsed-blowing technology with Circulation Control (currently being investigated by GTRI and NASA, Ref. 12) may further increase lift efficiency and reduce already low blowing requirements by up to 50% or more, while further enhancing stability and control. Successful application of these results can lead to positive technology transfer to personal, business, and military sized aircraft. In addition to the military Super-STOL transport discussed above, NASA LaRC has included these experimental data and pneumatic technology results in preliminary design studies of other possible pneumatic powered-lift configurations, including smaller personal and business-type aircraft

Recommendations

Future testing, evaluation and development still need to be accomplished to address possible pitch-trim problems, performance at higher C_T and lower C_μ , and associated stability and control. In the future, the existing model or larger 3-D models should be modified to include blown tail surfaces and additional improvements to the pneumatic thrust deflection system. The following should be experimentally investigated:

- Use of pulsed blowing to further reduce required blowing mass flows (both inboard on the channel and outboard on the CCW).
- Higher propulsor solidity for greater thrust and powered lift, or improved propeller characteristics for greater C_T availability.

- Further evaluation of low-speed controllability and trim, including evaluation of improved tail surfaces, which might even be blown to reduce tail area and drag.
- Further evaluation of low-speed controllability and trim by novel aerodynamic/ pneumatic trim and control devices (blown canards, for example.)

The earlier mission analyses should be revised to incorporate the experimentally developed aeropropulsive and stability & control characteristics of the Pneumatic Channel Wing concept. If the projected benefits are confirmed, and further benefits come to light, then larger-scale, higher-Reynolds-number testing on a full-3-D Pneumatic Channel Wing model with variable yaw capability should be conducted to facilitate greater strides toward this pneumatic powered-lift technology's maturation .

References

1. Pasamanick, Jerome, "Langley Full-Scale-Tunnel Tests of the Custer Channel Wing Airplane," NACA RM L53A09, National Advisory Committee for Aeronautics, April 1953.
2. Mitchell, Kent A., "Mr. Custer and His Channel Wing Airplanes," *Journal of American Aviation Historical Society*, Spring 1998.
3. Blick, Edward. F, and Vincent Homer, "Power-on Channel Wing Aerodynamics," *AIAA Journal of Aircraft*, Vol. 8, No. 4, pp. 234-238, April 1971.
4. Englar, Robert J., "Circulation Control Pneumatic Aerodynamics: Blown Force and Moment Augmentation and Modification; Past, Present and Future," AIAA Paper 2000-2541, AIAA Fluids 2000 Meeting, Denver, CO, June 19-22, 2000.
5. Englar, R. J. and C. A. Applegate, "Circulation Control - A Bibliography of DTNSRDC Research and Selected Outside References (Jan. 1969 through Dec. 1983)," DTNSRDC-84/052, September 1984.
6. Englar, R. J., "Development of Circulation Control Technology for Powered-Lift STOL Aircraft," NASA CP-2432, "Proceedings of the 1986 Circulation Control Workshop".
7. Englar, R. J., J. H. Nichols, Jr., M. J. Harris, J. C. Eppel, and M. D. Shovlin, "Development of Pneumatic Thrust-Deflecting Powered-Lift Systems," AIAA Paper No. 86-0476, AIAA 24th Aerospace Sciences Meeting, Reno, Nevada, January 6-9, 1986.
8. Pugliese, A. J. (Grumman Aerospace Corporation) and R. J. Englar (DTNSRDC), "Flight Testing the Circulation Control Wing," AIAA Paper No. 79-1791, AIAA Aircraft Systems and Technology Meeting, August 1979.
9. Hines, N., A. Baker, M. Cartagena, M. Largent, J. Tai, S. Qiu, N. Yiakas, J. Zentner and R. J. Englar, "Pneumatic Channel Wing Comparative Mission Analysis and Design Study, Phase I," GTRI Technical Report, Project A-5942, March 22, 2000.

10. Englar, R. J. and R.M. Williams, "Test Techniques for High Lift Airfoils with Boundary Layer and Circulation Control for Application to Rotary Wing Aircraft," *Canadian Aeronautics and Space Journal*, Vol. 19, No. 3, pp. 93-108, March, 1973.
11. Englar, R. J., Niebur, C. S., and Gregory, S. D., "Pneumatic Lift and Control Surface Technology for High Speed Civil Transport Configurations," *AIAA Journal of Aircraft*, Vol. 36, No.2, pp. 332-339, March-April, 1999.
12. Jones, G. S., and R.J. Englar, "Advances in Pneumatic-Controlled High-Lift Systems Through Pulsed Blowing", AIAA 2003-3411, AIAA 21st Applied Aerodynamics Conference, Orlando, June 23-26, 2003.

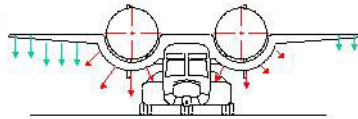
Experimental Development and Evaluation of Pneumatic Powered-Lift Super-STOL Aircraft ~ 2004 Circulation Control Workshop ~



Pneumatic High-Lift Technology,
Circulation Control Wing



Custer Channel Wing Aircraft



Pneumatic Channel Wing Aircraft
Powered-Lift Configuration with
Pneumatic Control Surfaces



Pneumatic Channel Wing Aircraft
Semi-span Model Configuration

Robert J. Englar

Georgia Tech Research Institute
Atlanta, GA



Bryan A. Campbell

NASA Langley Research Center
Hampton, VA

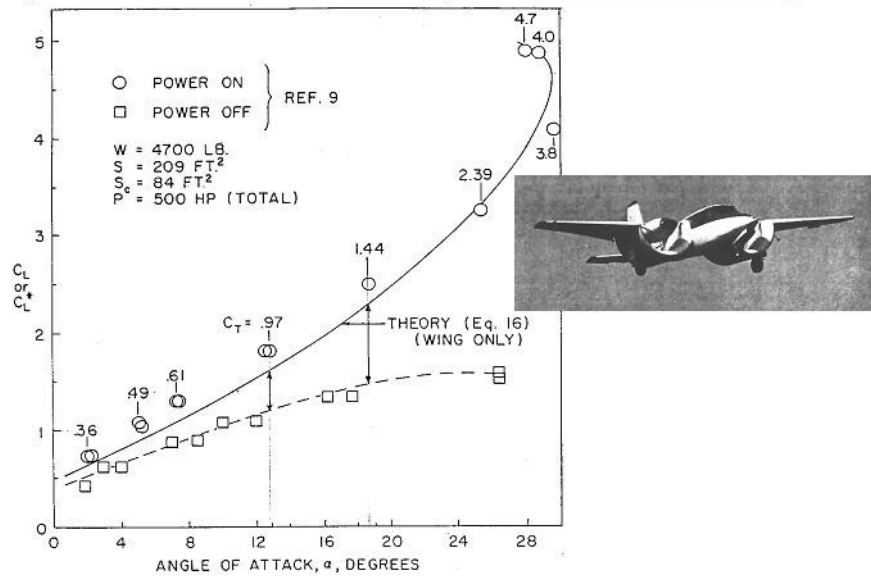


Outline of Presentation

- Introduction & Background
 - Custer Channel Wing
 - Circulation Control Wing (CCW)
 - CCW /Upper Surface Blowing
- Pneumatic Channel Wing Concept
- Current Pneumatic Channel Wing Configuration
- Test Apparatus, Models, Techniques and Setup
- Experimental Results
- SuperSTOL Performance
- Predicted Payoffs and Benefits
- Summary and Conclusions

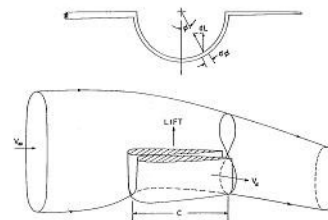


Reference: Flight Test Data from Full-Scale Custer CCW-5 Channel Wing Aircraft



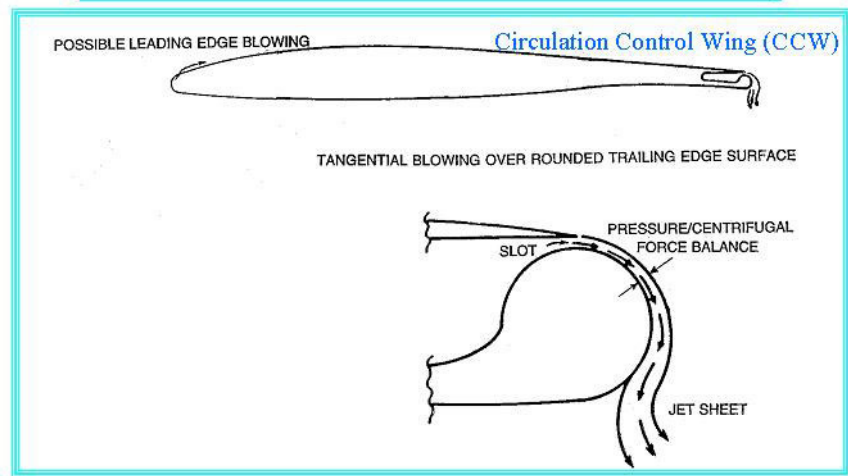
Disadvantages of Conventional Channel Wing Configuration

- Much of High C_L is from **Redirected Thrust**, little augmentation
- **High Drag** from Channel Surface Area
- **Asymmetric Thrust** yields Asymmetric Moments & Instability
- Channel Leading-edge and Trailing-edge **Separation** at High α
- **Poor low-speed control** from conventional aerodynamic surfaces
- **Nose-down Pitch** from Aft Propeller
- **Non-Uniform Flow** around Prop at High α
- **Poor Lift/Drag** ratio
- **High angle of attack** operation: poor visibility, control
- **One-engine-out** control problems



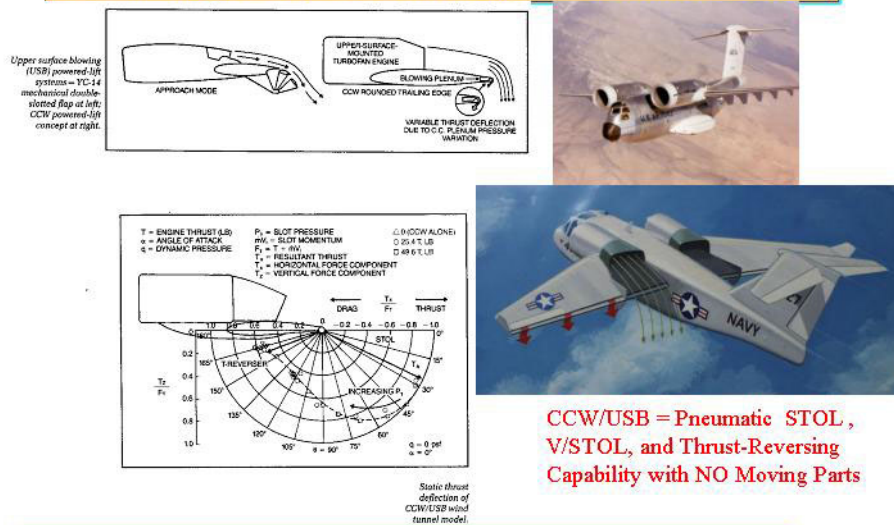
- ALL ARE SOLVABLE BY PNEUMATIC SYSTEMS APPLICATION, and ADDITIONAL SYNERGIES WILL RESULT

Basis of Circulation Control Pneumatic Aerodynamics



Basis for Outboard CCW and Inboard Pneumatic Channel Wing

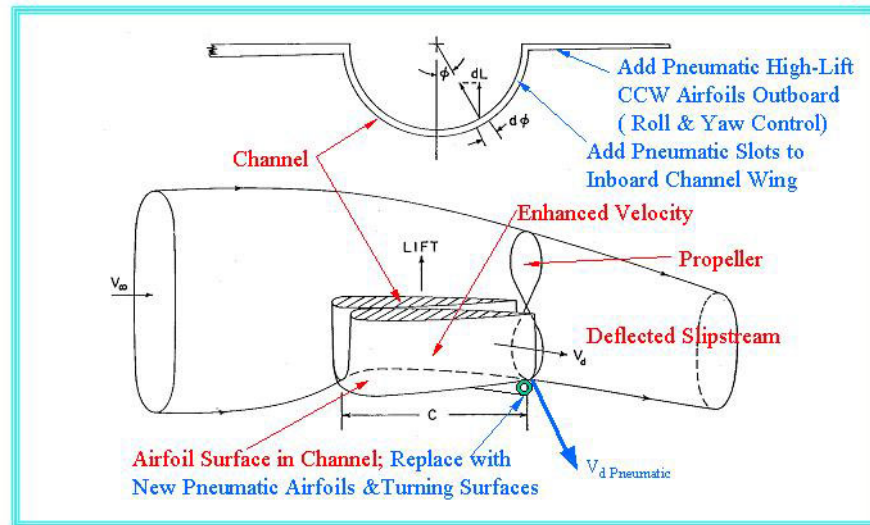
Demonstrated Static Thrust-Turning Capability of CCW/Upper Surface Blowing Wind Tunnel Model



CCW/USB = Pneumatic STOL ,
V/STOL, and Thrust-Reversing
Capability with NO Moving Parts

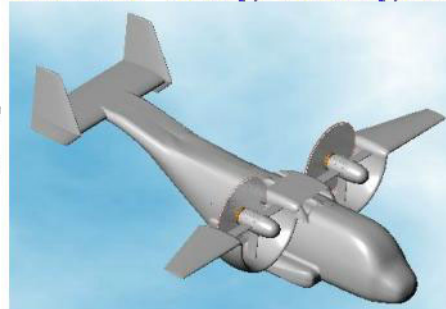
Basis for Pneumatic Channel Wing Concept Developed in this NASA Program :
Augment Channel-Flow Lift and Produce Greater Thrust Turning

Basis of Channel Wing Propulsive Aerodynamics and Current Pneumatic Developments

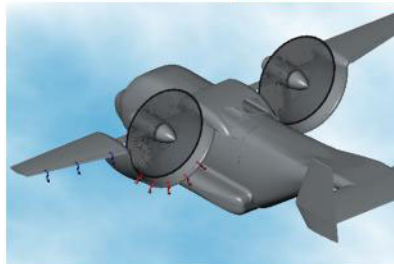


3D Channel Wing Configuration

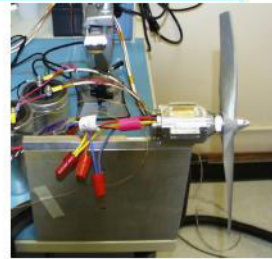
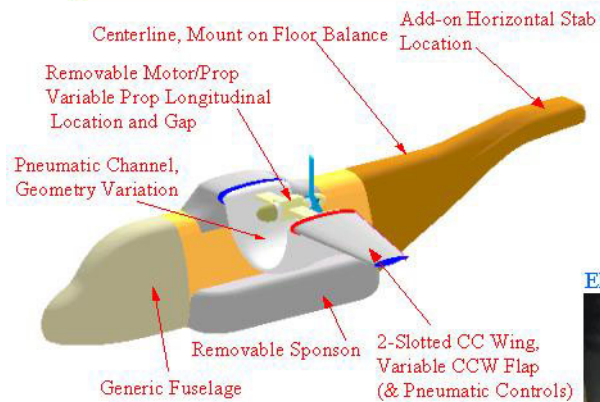
Technology Goal:
Merging Custer Channel Wing and Circulation Control to provide simple, reliable and effective SuperSTOL (VSTOL) aircraft, with ample control



Operations:
Remote or small sites, as well as increasingly dense urban environments-
Military, PAV and Commercial Applications



Pneumatic Channel Wing/CCW Model Design and Associated Experimental Propulsion Unit



Electric Motor and Prop Cal Setup



Half-span 0.075-scale Powered Pneumatic Channel Wing
Model with 3 Air Supply Sources: Channel TE,
Wing LE & TE

0.075-Scale Channel Wing Model Installed in GTRI Model Test Facility, and Jet Flow Turning

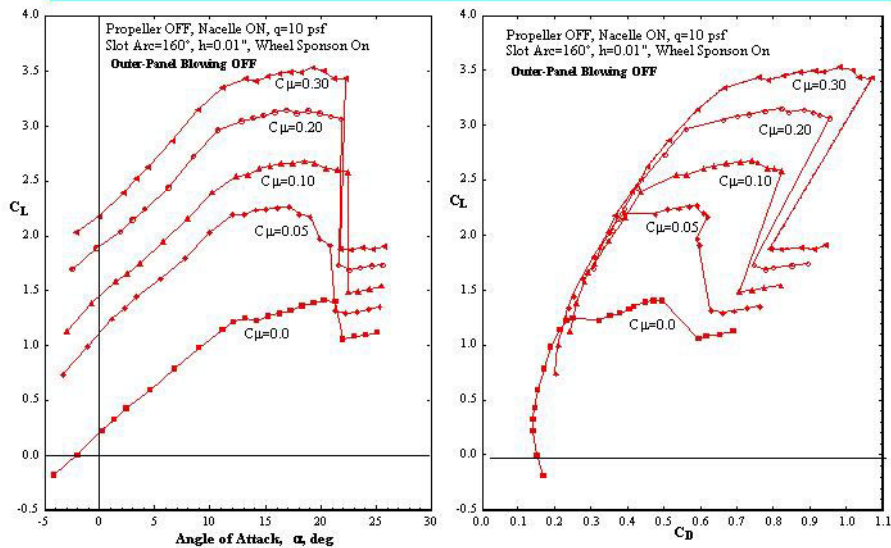


Semi-Span Pneumatic Model with
Prop Installed at Aft Location



Assembled Pneumatic Channel with
Blowing and Flow Turning

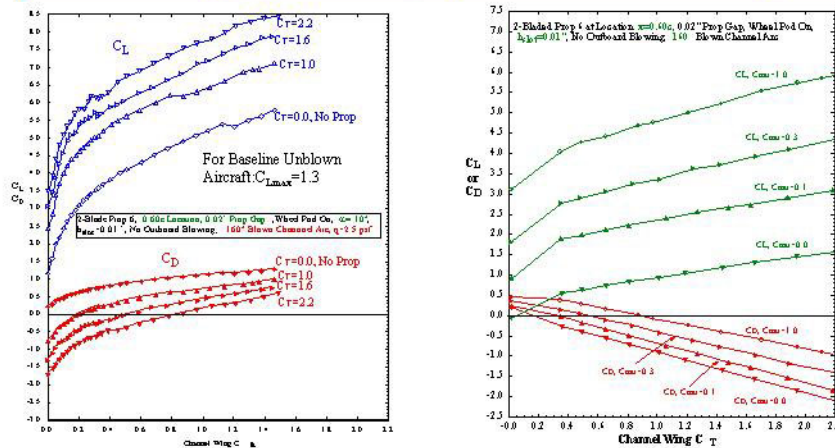
GTRI Test Results: Blown Channel Wing Lift and Drag Variation with Incidence without the Propeller Installed



Lift Increase due to Channel Blowing

Drag Polars due to Channel Blowing

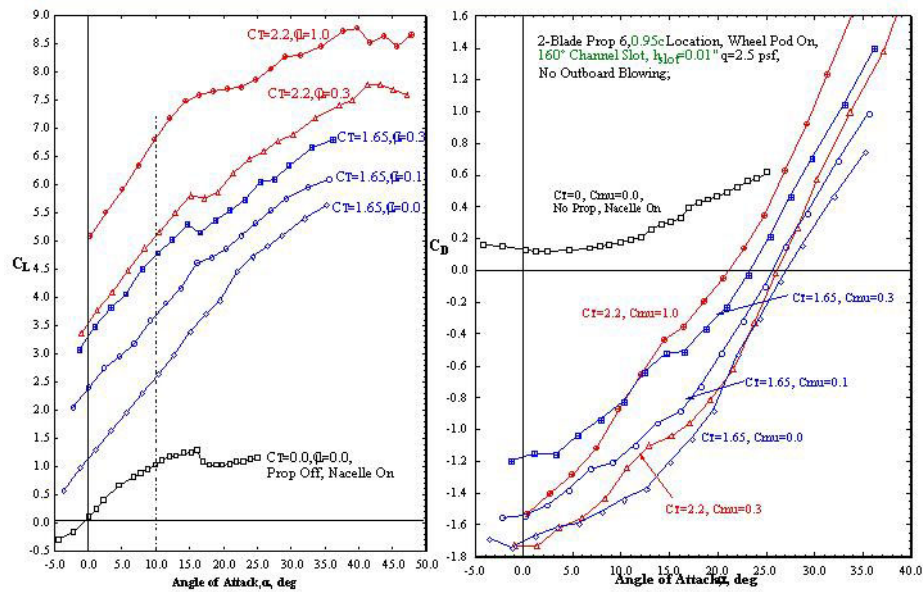
GTRI Proof-of-Concept Wind-Tunnel Test Results: Effects of Blowing (C_μ) & Thrust (C_T) Variation on Lift & Drag



C_μ Variation: Note that Lift Augmentation from Blowing is much greater than linear in C_μ ; C_D varies with Blowing. Very Useful on STOL Approaches ($\alpha=10^\circ$)

C_T Variation: Note that Lift from Thrust is nearly linear in C_T ; C_D is mostly Thrust recovery & Linear $C_D = C_{horizontal}$ includes horizontal C_T component $C_T = T/(qS)$, where T is calibrated thrust at test speed, ($\alpha=0^\circ$)

Effects of Blowing and C_T on Lift Coefficient, Stall Angle, and Drag Coefficient



Addition of Outboard LE & TE Blowing for Extra C_L & LE Flow Attachment, (Channel Thrust and Blowing Off)



Outboard CCW Jet Turning, 90° Flap
to Yield Extra C_L & Control
(Photo is inverted)



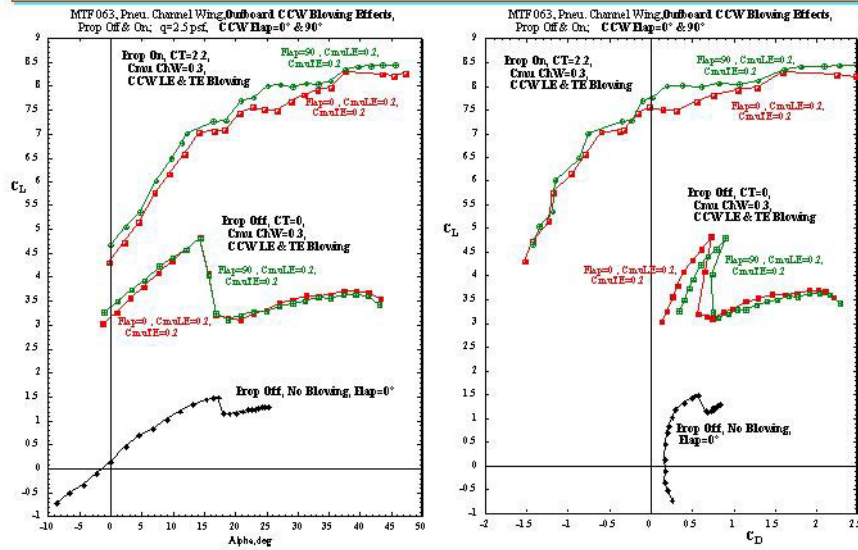
$\alpha=25^\circ$, LE Blowing Only, Flap=0°



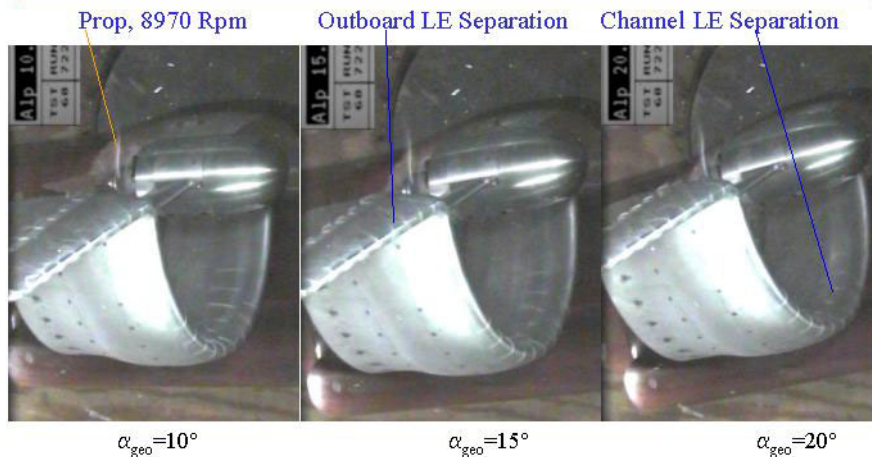
$\alpha=25^\circ$, LE Blowing Only, Flap=90°

Outboard LE Blowing for LE
Flow Attachment through $\alpha=45^\circ$,
Plus additional BL Entrainment
And TE attachment

Outboard CCW Trailing-Edge Blowing, Comparison of 0° and 90° CCW Flaps



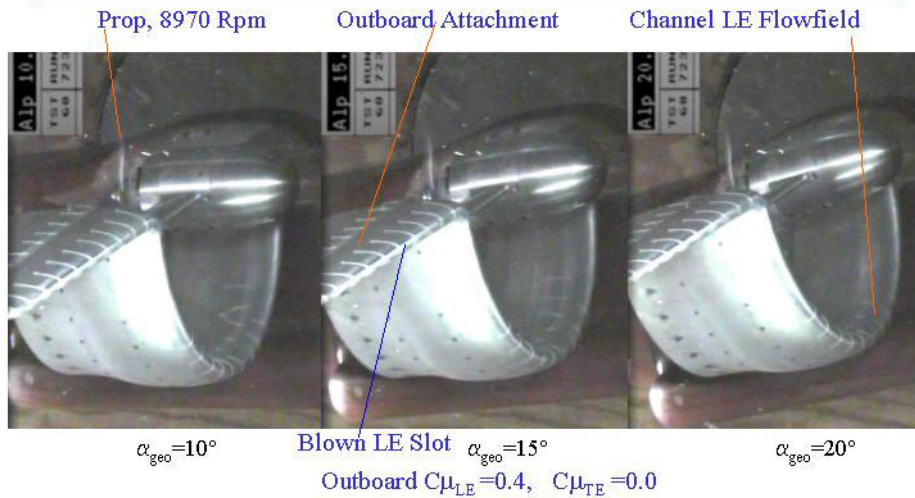
Flow Visualization showing Leading-Edge Separation at Higher Lift and α ($C_T=2.2$, $C_{\mu_{channel}}=1.0$, LE Blowing OFF)



Outboard $C_{\mu_{LE}}=0.0$, $C_{\mu_{TE}}=0.0$

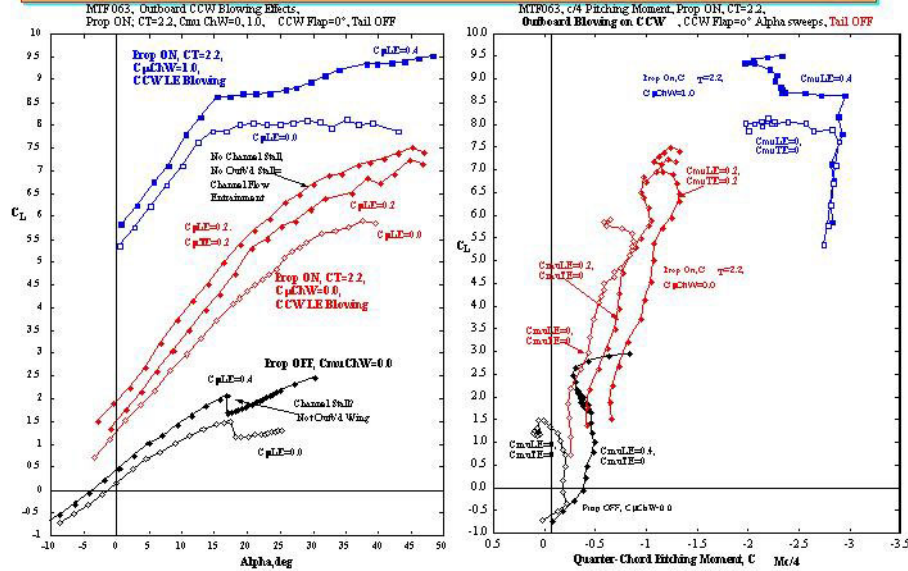
Tuft fuzziness or reversal indicates flow separation
(Video Still Frames, Video Available from GTRI)

Flow Visualization showing Leading-Edge Attachment
at Higher Lift and α ($C_T=2.2$, $C_{\mu_{channel}}=1.0$, LE Blowing ON)



Tuft steadiness indicates full attachment Outboard (up to $\alpha=45^\circ$)
but partial flow separation near Channel inlet
(Video Still Frames, Video available from GTRI)

Leading-Edge Blowing Prevents LE Stall on Outboard CC Wing;
Channel Flow Entrainment Allows Very High α and C_L

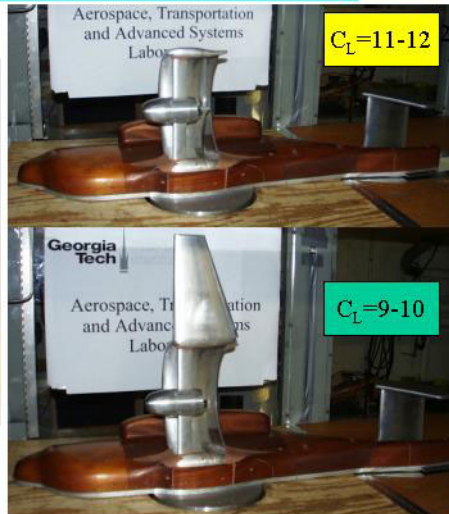


$\alpha_{\text{stall}} = 45^\circ - 50^\circ$ due to LE Blowing and Channel LE Entrainment; Stable, but C_M must be Trimmed

Pneumatic Channel Wing Configurations Tested, with and without Outboard CCW



Basic Blown Channel Wing & Unblown
CCW Outboard, No Tails



Blown Channel Wing Alone & Outboard Unblown
CCW, Both with H-Tail, Plus Outboard LE and TE
CCW, New Tails, New Props

Evaluations of Horizontal Tail Positions for Longitudinal Trim



High Tail (out of downwash, minimum drag)



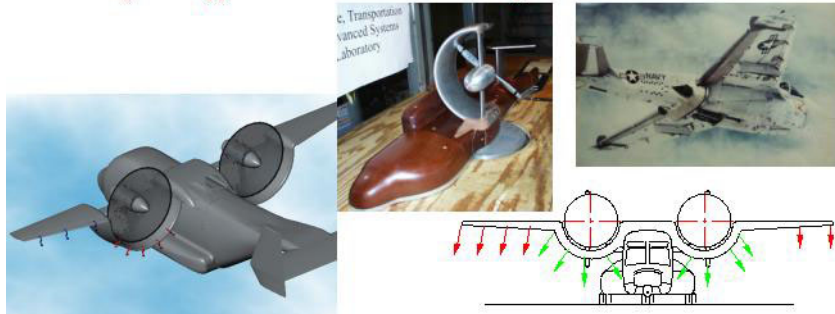
Mid Tail (fuselage installation)

Low Tail (in Prop downwash, max. trim tail
power, but tail LE Stall a problem)

Note: Pneumatic Canard an Excellent
Alternative to Aft Tail, but not yet tested

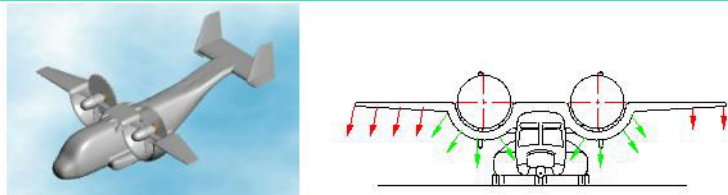
SUMMARY & CONCLUSIONS

- Blown/Powered Tunnel & Flight Investigations have confirmed CCW and/or the Pneumatic Channel Wing concepts for High Lift, Super STOL & Overload capabilities
- Lift, Drag, all 3 Moments are all variable (+ or -) by both C_T and C_{μ} , and without moving elements~ More or Less C_L , C_D , and C_M are available as required by Pilot or control system
- For Lift Augmentation and SuperSTOL, C_{μ} more effective than C_T ; High α Not Needed
- No Moving Parts are necessary for Blowing Benefits: Weight reduction
- C_T can be converted to Thrust Recovery, C_D increase, or even Thrust Reversal
- Trim and Low-speed Control ALWAYS Need to be addressed for SuperSTOL aircraft
- Wind-Tunnel and Flight-Test Data lead to significant Super STOL or VSTOL benefits, advantages and applications for Pneumatic Military, Commercial or Private Aircraft



Projected Operational Benefits & Advantages of Pneumatic Channel Wing

- **Pneumatic/Propulsive High Lift** Generated with Thrust Deflection and No Moving Parts: $C_L = 10 - 11$ or greater at $\alpha=10^\circ$; avoids high α operation, flow separation, loss of control
- Additional Lift from **Outboard CCW surfaces**: Yields high Overload Capability- No tilting rotors or tilting engines necessary!
- Non-moving Augmented **Blown Control Surfaces** yield **Low-Speed Control**: Pitch, Roll&Yaw; Increased One-engine-out Control; **High Response Rates** from variable blowing
- **Integrated** Lift, Propulsion, and Control Systems yield **Simplicity, Low Weight & Increased Performance**; **Systems Synergy** yields inter-related multi-function components
- Pneumatic Channel Wing Provides Significant Powered Lift **Without Rotor Tilt**: **Increased Lifiable Weight and Payload** are possible with very short field length
- **Super STOL and VSTOL** Potential, with Possibility for **Hover** without Engine Tilt
- Channel Wing can "**Hide**" **Propulsion System** from Acoustic & Infrared Detection
- **No Download** Impacting on Fixed Wing in Low speed or Hover; **High DL= Higher Cruise V**
- **Signature Reduction**; **Payload Fraction Increase**, **Cost Reduction** relative to Tilt Rotor
- These Benefits should be **Quantified and Confirmed** in Future research



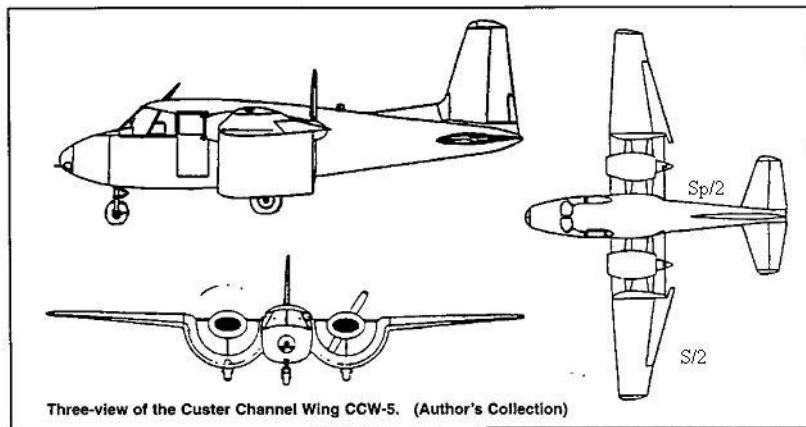
Recommendations for Advanced Pneumatic Aircraft

- Continue Analytical & Experimental Development of 2-Engine Pneumatic Channel Wing Aircraft as SuperSTOL or V/STOL transport
- Analytically & Experimentally Develop a 4-Engine Pneumatic Aircraft as an Advanced Transport with SuperSTOL or V/STOL and Overload capabilities (turboprop or jet driven)
- Develop CCW on a Pneumatic Fighter/Attack Aircraft with SuperSTOL and Overload Potential plus High Maneuverability
- Develop a CCW-only STOL Transport with Gross-Weight-Overload capability on unprepared runways (Runway Independent Aircraft)
- Apply to Personal Air Vehicles and/or ESTOL vehicles for Small- or No-Runway Operation

Georgia Tech Research Institute and NASA Langley Research Center **can help!!**
~36+ years pneumatic technology development & expertise; unique test facilities;
flight-test experience; related analytical capabilities and programs; and the
Enthusiasm to develop and employ this technology on future advanced aircraft

Backup Slides

Custer Channel Wing, CCW-5, Flown in
Powered-Lift Flight in Early 1960's



Channel Wing Model with Variable Nacelle Locations, to Determine Effect of Prop Position on Flow Entrainment

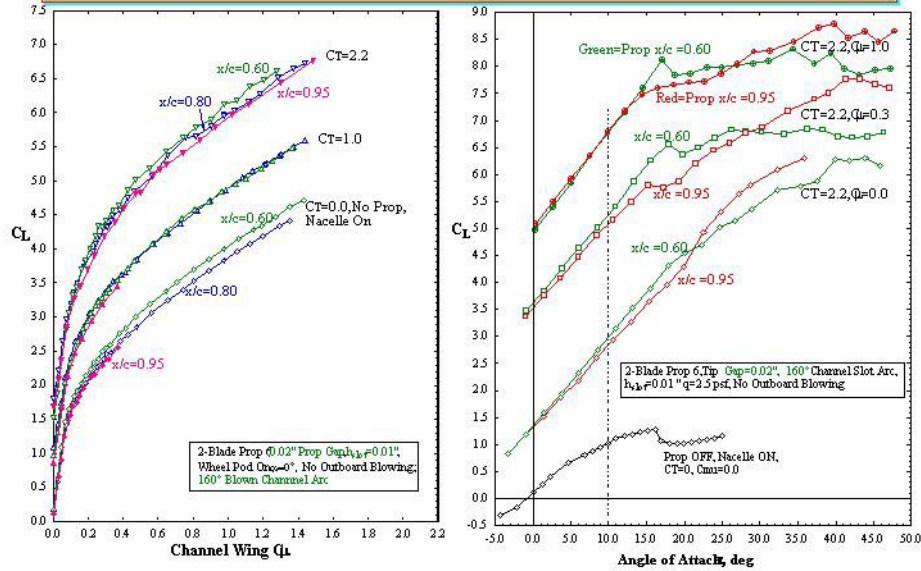


Channel Wing Configuration with Aft Prop/Nacelle Location, $x/c=0.95$



Channel Wing Configuration with Forward Prop/Nacelle Location, $x/c=0.60$

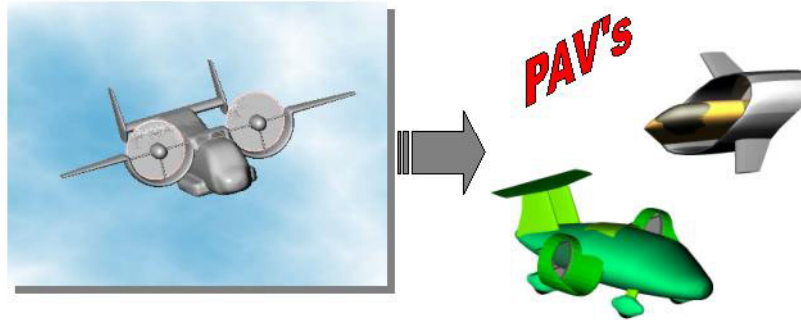
GTRI Test Results: Effects of Prop/Nacelle Location on Lift & Stall Angle: Less-aft Prop is Better



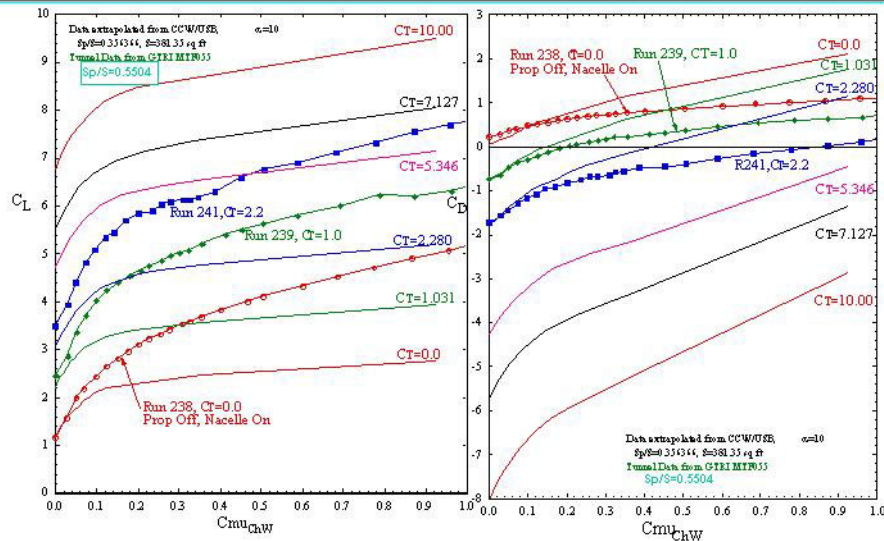


Connection to Other Programs

Pneumatic channel wing provides enabling technology for conceptual Personal Air Vehicles



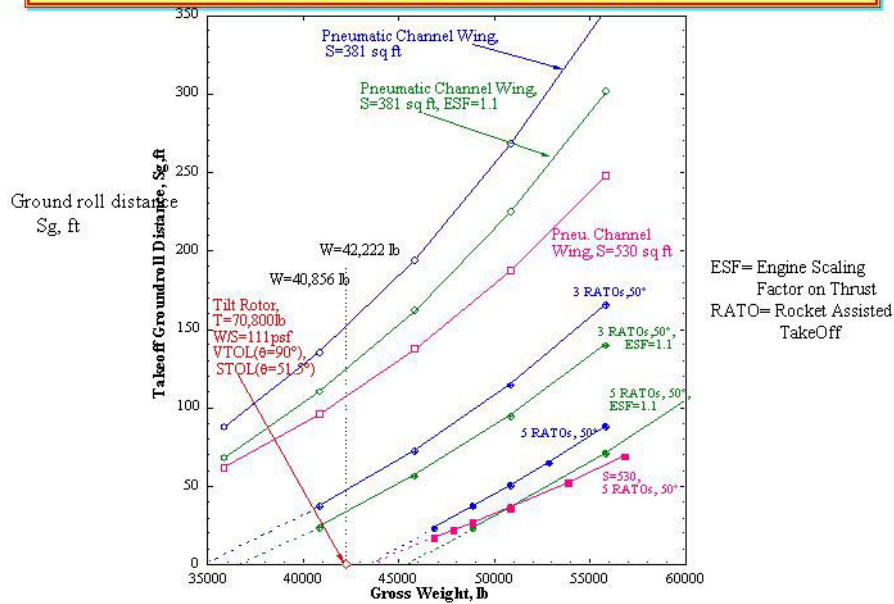
Comparison of Predicted & Experimental Pneumatic Channel Wing
Lift and Drag due to Blowing and Thrust Deflection, $\alpha = 10^\circ$, No Outbd CCW



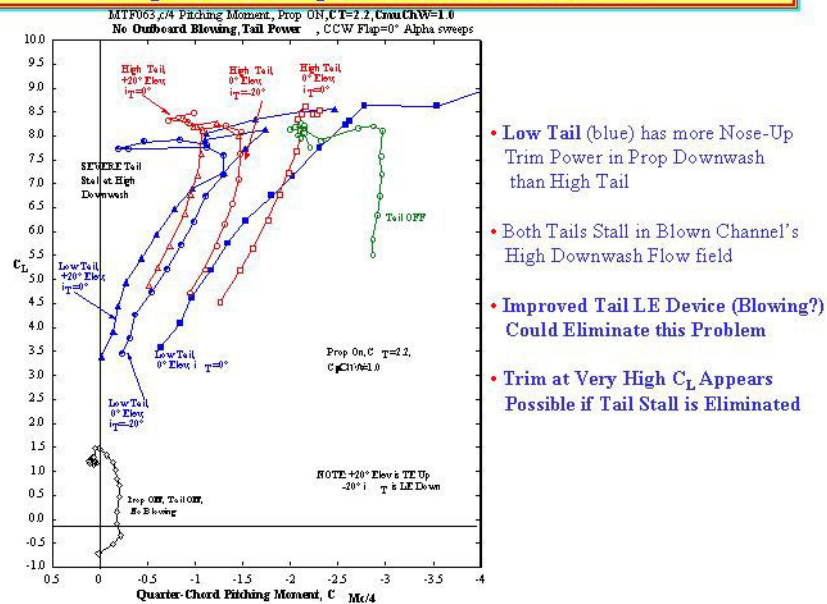
Lift Generated by Pneumatic Channel Wing
At Higher C_T , $C_L > 10$ & Higher T Recovery Probable

Drag (Including C_T) Generated by
Pneumatic Channel Wing

Pneumatic Channel Wing Predicted Ground Roll Distances, 91.5°F, h=3000', $\alpha=10^\circ$, S=381.4 ft²



Tail Stall Problem With Channel Blowing ON; Comparison of High and Low Tail Locations



Full-Reynolds Stress Modeling of Circulation Control Airfoils

Peter A. Chang, III, Joseph Slomski, Thomas Marino, Michael P. Ebert and Jane Abramson

Hydromechanics Directorate

Carderock Division—Naval Surface Warfare Center

9500 MacArthur Blvd., West Bethesda, Maryland 20817-5700, USA

ABSTRACT

The flow about the NCCR 1510-7067N elliptical circulation control (CC) airfoil is computed with compressible Navier-Stokes equations and full Reynolds Stress turbulence modeling (FRSM). This airfoil, with a slot on its upper surface at 97% chord, has been run with both circular and logarithmic spiral trailing edges. The hybrid structured/unstructured grids, consisting primarily of quadrilaterals, with triangles in the slot region, have between 100,000 and 150,000 cells. The free stream Reynolds number, based on chord, is 5.45×10^5 with a free stream Mach number of 0.12. We run three variations in the slot height to chord (h/c) of 0.0015, 0.0022 and 0.0030. The non-dimensional blowing rates are varied from 0.05 to 0.20. For $h/c = 0.0030$ we run 0° , -4° and -8° angles of attack.

Results show that the FRSM predicts the correct jet detachment behavior for the circular trailing edge. For the largest slot height, the behavior of the lift coefficient with change in blowing rate and angle of attack are well-predicted as compared with experiments. However, the absolute values are consistently low due to under-prediction of the global circulation. This may be due to discrepancies in the exact location of jet detachment. The FRSM method correctly captures the variation in leading edge stagnation point as the blowing rate is varied. Performing calculations on smaller slot heights, $h/c = 0.0015$ and 0.0022, we show some correct trends in the variation of lift with slot height, but have found the compressible calculations difficult to converge for high blowing rates.

The logarithmic spiral is a geometry that continually increases its radius of curvature with increasing distance from the slot. As such, it has proven to be a more challenging test case for the FRSM. We show our results for one slot height and three blowing rates.

We compare results from FRSM with those from isotropic eddy viscosity models, including the $k - \epsilon$ and $k - \omega$ models and investigate the conditions necessary for physically correct coanda jet detachment.

We have also begun simulation of the aspect ratio 2 CC wing that was recently tested in the Large Cavitation Channel (LCC) in Memphis, TN.[1] The LCC test model is a semi-span wing with a taper ratio of 0.76. The model has both upper and lower trailing edge blowing slots with a $h/c = 0.0019$.

INTRODUCTION

Recently, low speed maneuverability has become an important design requirement for aircraft, ships, and submarines. At low speed, the control authority (that is, the normal, or lifting force) associated with conventional hinged control surfaces is often insufficient to perform certain maneuvers. As a result, designers have begun to investigate the use of circulation control airfoils to achieve the required control authority at low speeds.

Circulation control technology has been investigated both experimentally[2, 3] and analytically[4, 5] over the past twenty five years. True circulation control airfoils typically have bluff trailing edges. These airfoils employ the coanda effect to obtain lift augmentation by tangentially ejecting (blowing) a sheet of fluid near the trailing edge on the upper surface. Because of the coanda effect, the jet sheet remains attached to the bluff trailing edge and provides a mechanism for boundary layer control. The blowing can be thought of as a movement of the stagnation point, producing an increase in circulation around the airfoil. Experimental results for coanda type trailing edge blowing[6] have shown lift coefficient increases of as much as a factor of four when compared to the case of no blowing.

Because of the difficulty and expense involved in experimentally investigating different circulation control configurations for parametric design studies, researchers and designers have begun to focus on the use of computational fluid dynamics (CFD) to analyze circulation control devices. Although the majority of the computational problem of the circulation control airfoil is straightforward, complications arise in the area of the coanda jet itself. This jet is bounded

by a curved wall on one side and a free shear layer on the other, and contains very high momentum fluid. This high momentum enables the jet to remain attached to the curved trailing edge. The extent to which the jet remains attached controls the circulation, and, hence, the lift generated by the airfoil. Thus, any computational technique, in order to be successfully applied to the circulation control problem, must be able to accurately predict the spreading rate of the jet and the location at which the coanda jet finally separates from the curved trailing edge of the airfoil. To accomplish this, the computational flow solver must be able to correctly predict the exchange of momentum between the coanda jet and the surrounding fluid, the entrained upstream boundary layer from the airfoil. Consequently, the computational mesh in the vicinity of the jet must be fine enough to adequately resolve the boundary layer between the wall and the jet, and the shear layer between the jet and the surrounding fluid. In addition, the type of turbulence model chosen for the problem will be crucial to successful modeling of the coanda jet and its interaction with the surrounding fluid, and subsequent prediction of the lift force generated by the circulation control airfoil.

A recent paper[7] reports good results from numerical solutions for circulation control airfoils using algebraic[8] and one-equation[9] eddy-viscosity turbulence models. However, the circulation control for these airfoils was essentially a blown flap method, where the jet separated from a sharp, rather than bluff, trailing edge, which fixes the separation point. The general circulation control airfoil problem requires the jet to separate at some point along a curved wall (the blunt trailing edge). Figure 1 depicts the streamlines around such an airfoil at zero degrees angle-of-attack and some finite free stream velocity. In the figure, the flow is from left to right, and the jet emerges from a slot above the curved trailing edge on the right hand side of the airfoil. The jet remains attached to the trailing edge for some distance before finally separating. Also, the circulation increase caused by the jet has moved the leading edge stagnation point to a position below the leading edge. In general, curved wall jets like those on the circulation control airfoil have been problematical for simple eddy viscosity based turbulence models to predict. While eddy-viscosity models can often be modified to improve their predictive accuracy for curved wall jets, these modifications are largely ad hoc, and cannot be easily generalized for arbitrary flows and configurations[9]. For example, Slomski, Gorski, Miller and Marino[10] demonstrated that standard isotropic, two-equation turbulence models yielded non-physical solutions for a CC airfoil as blowing rate increased, whereas a full Reynolds-stress turbulence model reproduced the correct lift/blowing rate behavior for the same airfoil. Recently, however, Paterson and Baker[11] reported a successful

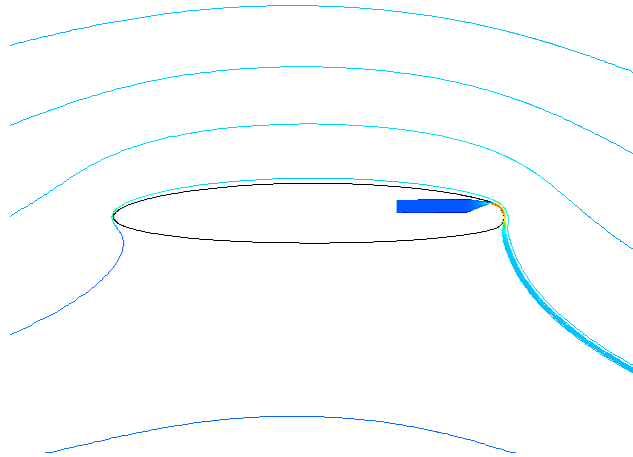


Figure 1: Typical circulation control airfoil showing coanda jet and surrounding streamlines. Flow is from left to right. The jet is depicted by the thick group of streamlines at the trailing edge of the airfoil. Streamlines are colored by increasing velocity magnitude from blue to red.

simulation of the highest blowing rate case reported in Slomski *et al.*[10], using a blended $k - \omega/k - \epsilon$ SST (shear stress transport) two-equation turbulence model.

The current paper explores the performance of the FRSM turbulence model for two-dimensional CC airfoils beyond the cases investigated in Slomski *et al.*[10] and Paterson and Baker[11]. Specifically, we investigate varying blowing slot heights, airfoil angles-of-attack, and varying airfoil trailing edge shapes. Based on the encouraging results reported in Paterson and Baker[11], we also investigate the performance of the $k - \omega/k - \epsilon$ SST model in some of these new conditions. Finally, we report on the initial results of three-dimensional simulations of a low-aspect ratio CC wing that was recently tested in the LCC. These three-dimensional simulations use both the FRS and $k - \omega/k - \epsilon$ SST turbulence models.

MATHEMATICAL DEVELOPMENT

We solve the two- and three-dimensional Navier-Stokes equations using the commercially-available code, Fluent, which solves the steady state problem implicitly using a finite volume-based segregated solver with SIMPLE pressure-velocity coupling. Second order upwinding is used to discretize the convective terms in the momentum equations with second order central differencing used on the viscous terms. First order upwinding is used on density, energy, k , ϵ and Reynolds stress equations,

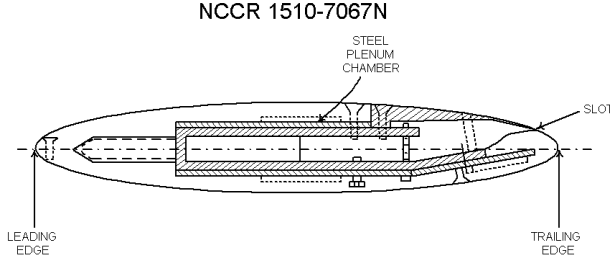


Figure 2: Geometry of the NCCR 1510-7067N airfoil.

where k is the turbulent kinetic energy and ϵ is the turbulence dissipation rate.

The effect of turbulent flow on the steady state solution is obtained using the Full Reynolds Stress turbulence model, as well as the $k - \omega$ SST model. In two dimensions, the RSM introduces an additional five equations — 3 equations for each of the correlations $\overline{u'u'}$, $\overline{u'v'}$ and $\overline{v'v'}$; equations for k and ϵ are solved in order to evaluate $\overline{u_i u_j}$ at the walls. A wall reflection term is invoked which damps the normal stresses at the wall while enhancing the stresses parallel to the wall.

Enhanced wall treatment is utilized which solves to the wall where $y^+ \leq 3$ and uses wall functions valid in buffer region ($3 < y^+ < 10$) including the effect of pressure gradients. The wall function is important because of the wide range of velocities over the foils where upstream of the slot the grid had $y^+ \approx 1$ while in the coanda jet, $y^+ \approx 3 - 10$.

2-D Airfoil

Numerical simulations of airfoils with 15% thickness to chord ratio, 1% camber, with a slot located at 97% chord, with a 6.7% thickness at the slot location, and two coanda trailing edge shapes[6] are undertaken. Both the “nominal” circular trailing edge foil, NCCR 1510-7067N, shown in Figure 2, and the logarithmic spiral TE foil, NCCR 1510-7067S, are used. The logarithmic spiral has a constantly increasing radius of curvature with the smallest radius at the slot exit. The slot-height-to-chord (h/c) ratios include 0.0015, 0.0022 and 0.0030. Incidence angles are 0, -4 and 8 degrees.

The computational grids have between 100,000 – 150,000 cells, depending on slot height. An O-grid topology is used near the body with an H-grid in the wake extending approximately 13 chord lengths downstream. The leading and trailing edge regions are shown in Figures 3 and 4, respectively. The hybrid mesh consists of quadrilaterals with triangular elements in the slot exit as shown Figure 5.

The flow is assumed to be compressible in order to validate the wind tunnel experiments. Obtaining

a well-converged solution is difficult because of the large range of length and velocity scales (*e.g.*, the ratio of the jet to free stream velocities is as high as 6.). The following routine is developed and automated using journal files:

1. Incompressible, $k - \epsilon$ - initial coanda jet development
2. Incompressible, RSM - develop coanda and set approximate separation point
3. Compressible, $k - \epsilon$ - incorporate compressibility effects
4. Compressible, RSM - final jet development
5. Compressible, RSM, larger under-relaxation factors (URFs) - ensure convergence to stable solution 30,000-50,000 iterations necessary for converged solution

On the body, boundary conditions were specified as no-slip except at the upstream end of the plenum where \dot{m} (mass flow rate) and pressure were specified. For the incompressible startup conditions, the upstream, outer boundary is set to a velocity inlet condition where the freestream speed is set to 41.65m/sec, $\nu_T/\nu = 5$ and $k/U_o^2 = 0.05$. Also, for the incompressible startup conditions, the downstream boundary was set to a pressure outlet with zero pressure. When the flow is assumed to be compressible, the air is assumed to be governed by the ideal gas law with the Sutherland law applied to the evaluation of molecular viscosity; the outer boundaries are set to far-field pressure with $M_\infty = 0.12$ and zero pressure. It is assumed that the freestream temperature is 288K, with a freestream kinematic viscosity $\nu_\infty = 1.462 \times 10^{-5} \text{m}^2/\text{sec}$ and density, $\rho_\infty = 1.224 \text{kg}/\text{m}^3$. The chord length of the airfoil, c , is 0.203m, giving a freestream Reynolds number, $Re = 5.8 \times 10^5$.

In order to change α , the freestream velocity was rotated appropriately. The mass flow rate is non-dimensionalized as the jet momentum coefficient,

$$C_\mu = \frac{\dot{m} V_j}{\frac{1}{2} \rho_\infty V_\infty^2 c} \quad (1)$$

where ρ_∞ and V_∞ are the freestream density and velocity, respectively, and c is the airfoil chord length. The experimental \dot{m} values were measured using a calibrated venturi meter which is inserted in the air supply line and the jet velocity, V_j , was calculated as an isentropic expansion from duct pressure to freestream static pressure[6].

The flow about a logarithmic spiral trailing edge is also run. A comparison between the circular and logarithmic spiral trailing edge geometries is shown

Table 1: 2-D runs, C: circular TE, LS: log-spiral TE.

Case[6]	C_μ	h/c	$\alpha(^{\circ})$	TE
293	0.050	0.0030	0	C
289	0.092	0.0030	0	C
283	0.209	0.0030	0	C
311	0.048	0.0030	-4	C
307	0.093	0.0030	-4	C
302	0.189	0.0030	-4	C
330	0.047	0.0030	-8	C
326	0.090	0.0030	-8	C
321	0.184	0.0030	-8	C
60	0.052	0.0015	0	C
57	0.104	0.0015	0	C
53	0.201	0.0015	0	C
229	0.053	0.0022	0	C
227	0.103	0.0022	0	C
223	0.198	0.0022	0	C
56	0.054	0.0022	0	LS
53	0.107	0.0022	0	LS
51	0.140	0.0022	0	LS

in Figure 6. The logarithmic spiral curve has a constantly increasing radius of curvature with the smallest radius at the slot. The rationale for a logarithmic spiral TE is that for a given blowing rate the coanda jet may stay attached a longer distance around the TE due to the decreasing curvature where the jet would tend to detach for a circular TE. This would reduce the power requirement necessary to obtain a given lift augmentation ratio.¹

Table 1 lists the 2-D cases for which runs that have been completed.

3-D Airfoil

For the 3-D calculation, the incompressible RANS equations are solved, consistent with the use of water as the test medium in the LCC experiments. As was done for the 2-D airfoil studies, turbulence is modeled using both FRS transport model, and Menter's $k - \omega$ SST model.

To date, the volume mesh has been completed. The multi-element unstructured grid is developed using SolidMesh[12]. The volume grid is generated using an advancing normal methodology for the boundary layer prism elements and an Advancing Front/Local Reconnection (AFLR) technique to develop high quality isotropic elements[13]. It contains

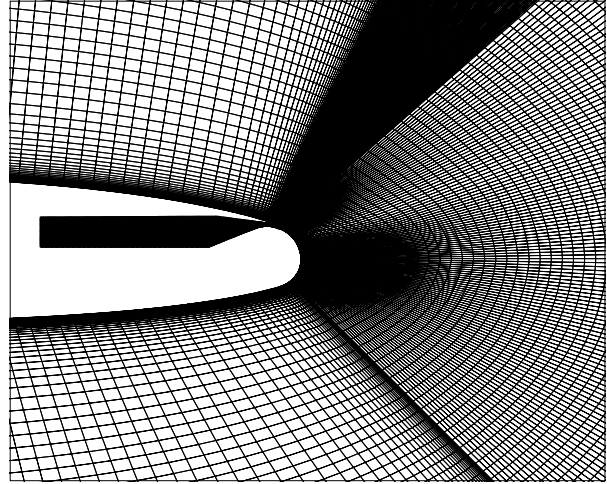


Figure 3: Grid for $h/c = 0.0030$ airfoil showing detail of leading edge.

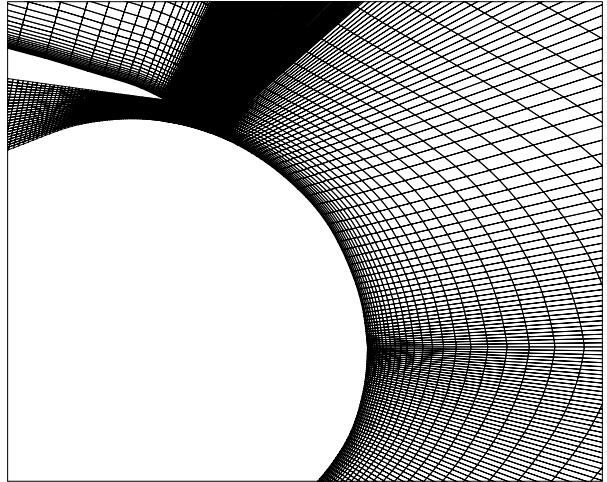


Figure 4: Grid for $h/c = 0.0030$ airfoil showing detail of coanda jet region.

18.5×10^6 cells, composed of tetrahedra in the far-field, and triangular and pentahedral prisms above the no-slip surface. Only the upper blowing slot has been accounted for in this mesh, since most of the LCC experiments were performed using single-slot blowing. Details of this volume mesh are shown in Figures 7, 8 and 9.

¹Rogers, E., personal communication 3/2004.

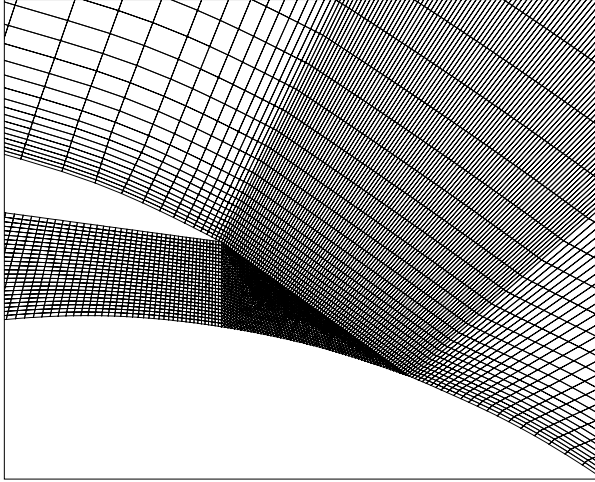


Figure 5: Grid for $h/c = 0.0030$ airfoil showing detail of slot region.

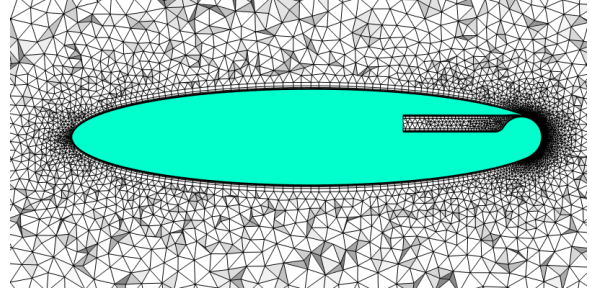


Figure 8: Cross-sectional cut of 3-D grid.

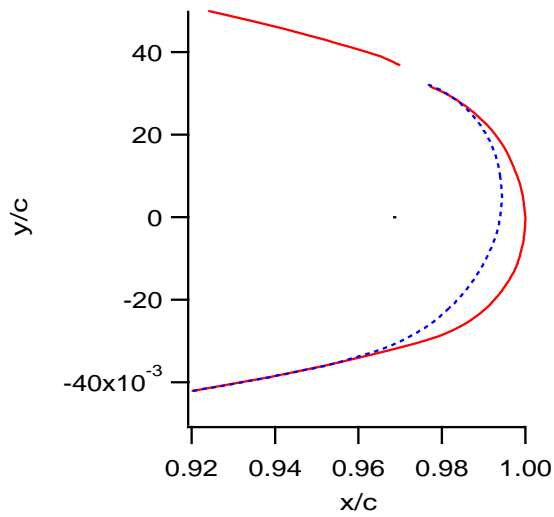


Figure 6: Comparison of circular and logarithmic spiral TE geometry; — : circular TE; - - - : logarithmic spiral TE.

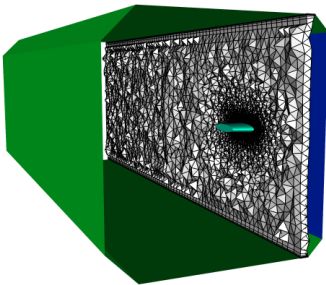


Figure 7: 3-D grid and computational domain.

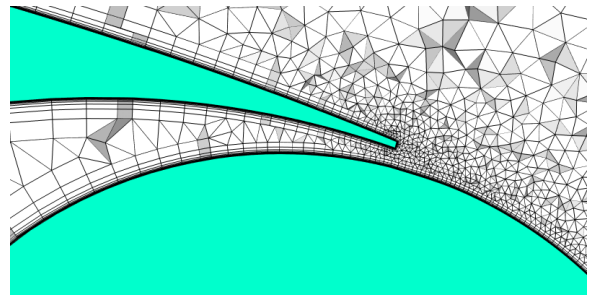


Figure 9: Cross-sectional cut of 3-D grid showing detail of slot region.

RESULTS

In this section we first show the qualitative flows that are computed, we compare integrated lift vs. AOA curves and surface pressure distributions about foil with experimental data.

The lift and drag coefficients are computed by

$$C_{D,L} = \frac{F_{x,y}}{\frac{1}{2}\rho_\infty U_\infty^2 A} \quad (2)$$

where $F_{x,y}$ is the force in the x or y direction, ρ_∞ and U_∞ are the freestream values of density and velocity magnitude, respectively, and A is the reference surface area, cS , where c is the chord length and S the 1 meter span (since for the 2-D calculations, the forces are given in terms of force/unit span).

The coanda jet changes the location of the detachment point on the trailing edge and with it, the circulation around the airfoil. As can be seen in Figure 10 the TE detachment point and the LE stagnation point migrate around to the pressure side of the foil as C_μ increases. It can be clearly seen that the coanda jet detaches at the TE which is the correct behavior as is evident in the surface pressure distributions, discussed later in the paper. The jet does not wrap around to the suction side as was shown by Slomski *et al.*[10] for isotropic turbulence models. Figures 11

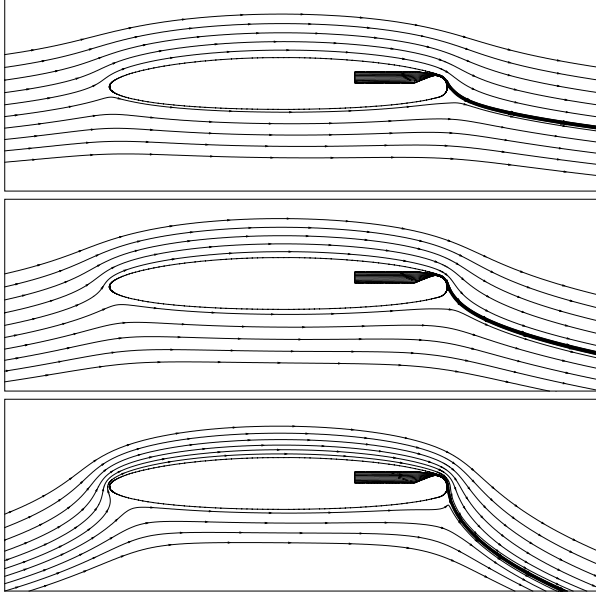


Figure 10: Streamlines for $h/c = 0.0030$ and $\alpha = 0^\circ$; upper: $C_\mu = 0.050$, middle: $C_\mu = 0.092$ and bottom: $C_\mu = 0.209$.

and 12 show the streamlines for $\alpha = -4^\circ$ and -8° , respectively. For both cases it can be seen that at the lower blowing rate the stagnation point is at the LE or on the upper surface. As C_μ is increased, the coanda

jet induces the stagnation point to migrate around to the bottom, in essence modifying the AOA.

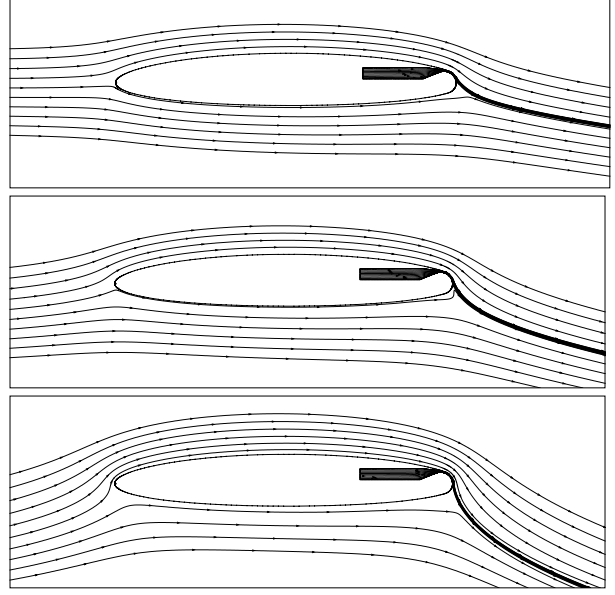


Figure 11: Streamlines for $h/c = 0.0030$ and $\alpha = -4^\circ$; upper: $C_\mu = 0.048$, middle: $C_\mu = 0.093$; bottom: $C_\mu = 0.189$.

The integrated lift coefficients for the circular TE with $h/c = 0.0030$ vs. α for $\alpha = 0^\circ, -4^\circ, -8^\circ$ are shown in Figure 13. The experimental data shows an almost constant difference between the curves of constant α and a slight decrease in slope with increase in C_μ . The computational FRSM results show similar behavior although they are low by about $\Delta C_L \approx 0.5$. This can be explained by the differences in surface pressure distributions. Lift coefficient vs. C_μ for curves of constant h/c are shown in Figure 14. The experimental results show that at the lower values of C_μ there is very little change in C_L with variation in slot height. As C_μ increases, the C_L for $h/c = 0.0030$ falls away from the two smaller slot heights. The FRSM results show that for the lower two values of C_μ the smaller h/c values come closer to the experimental values, with $h/c = 0.0015$ right on the experimental data. At the higher value of C_μ the FRSM values show a decrease in slope matching the behavior in the experiments.

Surface pressure distributions for $h/c = 0.0030$ at $\alpha = 0^\circ$ for three values of C_μ are shown in Figure 15. Here, we see that the overall circulation, as indicated by the mid-chord pressure difference, is under-predicted by the computations. The leading and trailing edge suction peaks are overestimated, due, in part, to the under prediction of airfoil circulation. In general, the pressures upstream of the slot are well-predicted although the under-prediction

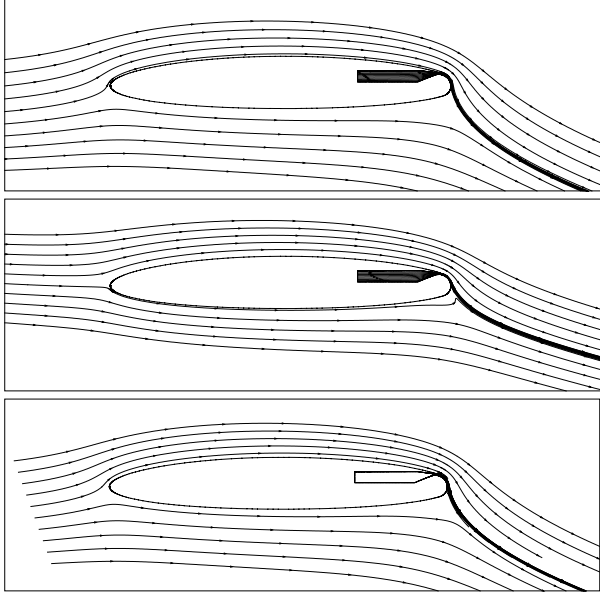


Figure 12: Streamlines for $h/c = 0.0030$ and $\alpha = -8^\circ$; upper: $C_\mu = 0.047$, middle: $C_\mu = 0.090$; bottom: $C_\mu = 0.184$.

of the TE pressure may be the cause of the underprediction of the LE pressure peak. Figures 16 and 17 show the pressure distributions for $h/c = 0.0030$ at -4° and -8° , respectively. The results are consistent with the streamline plots, Figures 11 and 12, which showed that at the low C_μ cases the stagnation point (*i.e.*, the point of maximum positive pressure) is on the upper surface, migrating around to the lower surface as the C_μ increases. In all cases, the pressure at the TE is underpredicted. This will be discussed in more detail later in this paper.

Logarithmic-Spiral TE

Figure 18 shows the streamlines for the three C_μ cases run on the logarithmic spiral TE. Figure 18(b) and (c) show that the coanda jet does not detach from the TE, but instead at about a third of a chord length forward of the TE on the pressure side. Figure 19 shows that for $C_\mu = 0.054$, the pressure at the lower TE is correctly predicted. However, the predicted suction side pressures are low. For the $C_\mu = 0.107$ and $C_\mu = 0.140$ cases, the pressures on the lower side of TE do not increase to their constant suction-side values due to the attachment of the coanda jet. The pressure amplitudes at the LE are overpredicted indicating excessive circulation.

Effect of turbulence modeling

Figure 21 compares with Case 283 results with $k - \omega$ SST model with FRSM and experimental re-

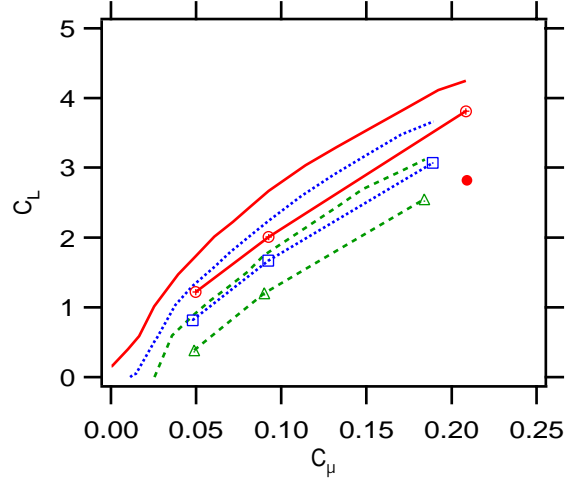


Figure 13: Lift coefficient vs. C_μ at $h/c = 0.0030$ for three angles of attack, comparing FRSM results to experimental results. FRSM: — : $\alpha = 0^\circ$; : $\alpha = -4^\circ$; - - - - : $\alpha = -8^\circ$. Experiment[6] symbols: \circ : $\alpha = 0^\circ$; \square : $\alpha = -4^\circ$; \triangle : $\alpha = -8^\circ$.

sults. The $k - \omega$ SST results are similar to previous computations[11]. The $k - \omega$ SST predicts the coanda jet detachment at the TE, rather than the trailing edge pressure drawdown effect typical for isotropic models[10]. However, the $k - \omega$ results predict lower airfoil circulation as evidenced by a smaller difference in surface pressure magnitudes between the upper and lower surfaces of the airfoil. This results in a lower $C_L = 2.82$ as compared with 4.25 from experiments and 3.81 from FRSM.

Results for the logarithmic spiral TE using the $k - \omega$ SST model are shown in Figure 21(b). In this case, the pressure drawdown effect is not as severe as for the RSM model, with pressure profile on the lower side of the TE much closer to the experimental results. This generates a pressure distribution which is much closer to the experimental values at the TE and along mid-chord. The TE peak pressure is not as well predicted however. This comparison is an example of how the change in the jet detachment point determines the overall pressure levels around the foil.

SUMMARY

An extensive series of RANS calculations have been performed on two-dimensional circulation control airfoils with circular arc and logarithmic spiral trailing edges. It is shown that for a circular arc TE, the full Reynolds stress turbulence closure can predict the Coanda jet detachment point fairly well for a range of angles-of-attack, jet slot heights, and

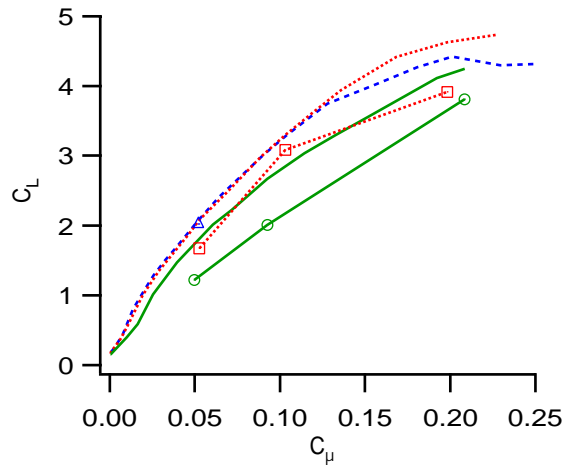


Figure 14: Lift coefficient vs. C_D at $\alpha = 0^\circ$ for three values of slot height, h/c , comparing FRSM results to experimental results. FRSM: — : $h/c = 0.0030$; : $h/c = 0.0022$; - - - - : $h/c = 0.0015$. Experiment[6] symbols: \circ : $h/c = 0.0030$; \square : $h/c = 0.0022$; \triangle : $h/c = 0.0015$.

jet blowing coefficients. For most cases the lift is low in comparison to experimental values. However, the trends in lift due to angle-of-attack and jet blowing coefficient are correctly predicted. The logarithmic spiral TE is a much more challenging case: for higher jet blowing rates, the Coanda jet detaches upstream on the pressure (lower) side of the airfoil and the lift is overpredicted.

References

- [1] E. O. Rogers and M. J. Donnelly, Characteristics of a dual-slotted circulation control wing of low aspect ratio intended for naval hydrodynamic applications, in *AIAA 42nd Aerospace Sciences Meeting*, number 2004-1244, Reno, NV, 2004.
- [2] R. Englar and G. Huson, Development of advanced circulation control wing high lift airfoils, Number 83-1847, 1983.
- [3] R. Englar, M. Smith, S. Kelley, and R. Rover, Development of circulation control technology for application to advanced subsonic aircraft, in *AIAA Aerospace Sciences Conference*, number 93-0644, 1993.
- [4] G. Shrewsbury, Analysis of circulation control airfoils using an implicit navier-stokes solver, Number 85-0171, 1985.
- [5] G. Shrewsbury, *Dynamic Stall of Circulation Control Airfoils*, Ph.d., Georgia Institute of Technology, 1990.
- [6] J. Abramson, Two-dimensional subsonic wind tunnel evaluation of two related cambered 15-percent-thick circulation control airfoils, Technical report, DTNSRDC, 1977.
- [7] Y. Liu, L. Sankar, R. Englar, and K. Ahuja, Numerical simulations of the steady and unsteady aerodynamic characteristics of a circulation control wing airfoil, in *39th AIAA Aerospace Sciences Meeting*, number 2001-0704, Reno, NV, 2001.
- [8] B. Baldwin and H. Lomax, Thin layer approximation and algebraic model for separated turbulent flows, in *AIAA Aerospace Sciences Conference*, number 78-0257, 1978.
- [9] P. Spalart and S. Allmaras, A one-equation turbulence model for aerodynamic flows, in *AIAA*, number 92-0439, 1992.
- [10] J. F. Slomski, J. J. Gorski, R. W. Miller, and T. A. Marino, Numerical simulation of circulation control airfoils as affected by different turbulence models, in *40th AIAA Aerospace Sciences Meeting & Exhibit*, number 2002-0851, Reno, NV, 2002.
- [11] E. G. Paterson and W. J. Baker, Simulation of steady circulation control for marine-vehicle control surfaces, in *42nd AIAA Aerospace Sciences Meeting*, number 2004-0748, Reno, NV, 2004.
- [12] A. J. Gaither, *A Solid Modeling Topology Data Structure for General Grid Generation*, Master's, Mississippi State University, 1997.
- [13] D. L. Marcum and A. Gaither, Mixed element type unstructured grid generation for viscous flow applications, in *AIAA*, number 99-3252, 1999.

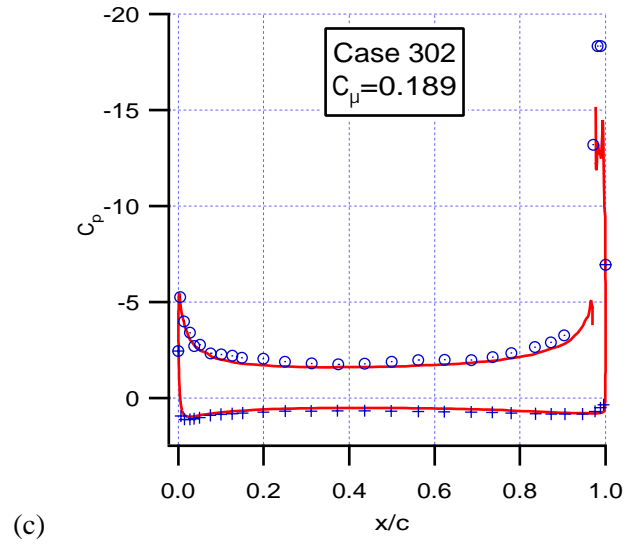
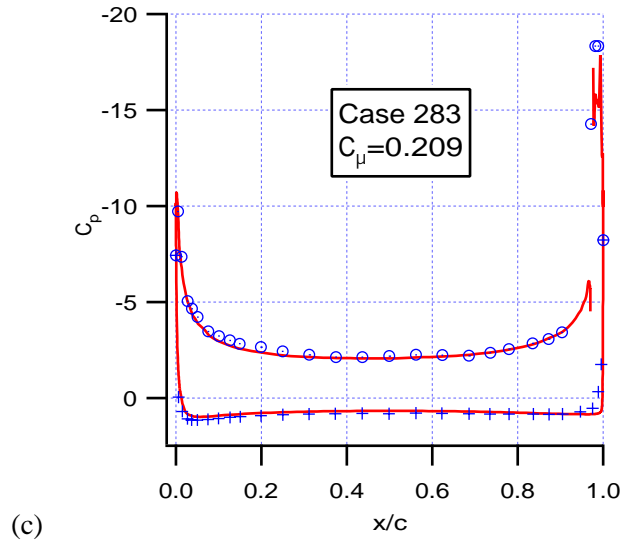
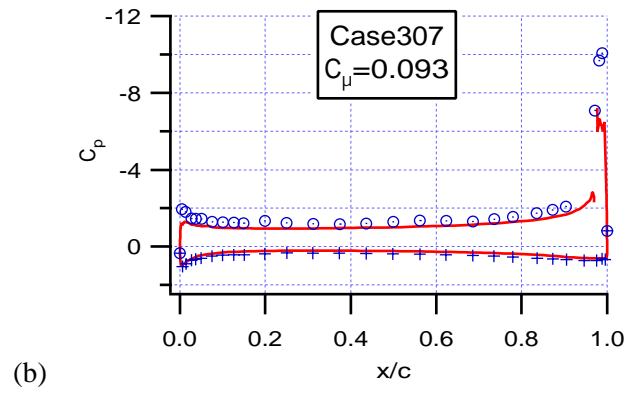
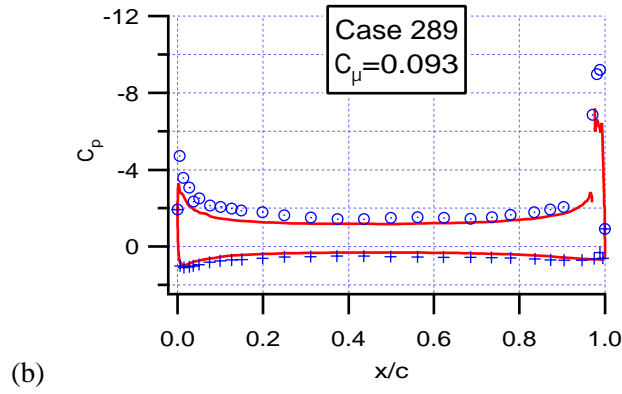
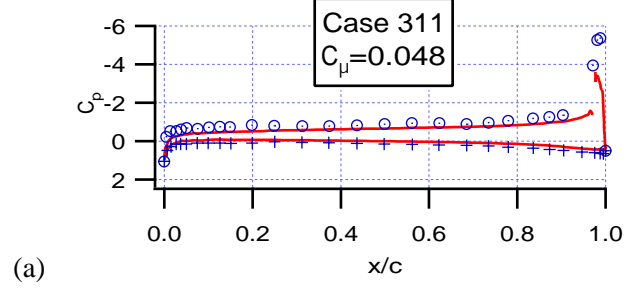
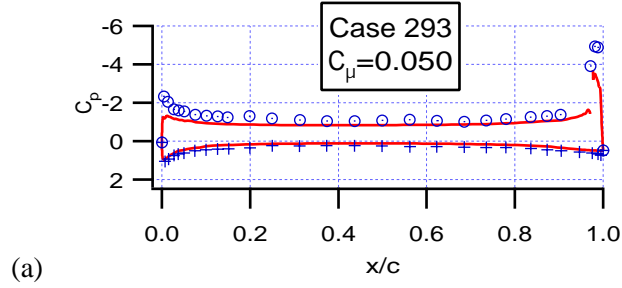


Figure 15: Surface pressure distributions for $h/c = 0.0030$ at $\alpha = 0^\circ$; — : FRSM, \circ : experiment—top, + : experiment—bottom; (a): $C_\mu = 0.050$, (b): $C_\mu = 0.093$, (c): $C_\mu = 0.209$.

Figure 16: Surface pressure distributions for $h/c = 0.0030$ at $\alpha = -4^\circ$; — : FRSM, \circ : experiment—top, + : experiment—bottom; (a): $C_\mu = 0.048$, (b): $C_\mu = 0.093$, (c): $C_\mu = 0.189$.

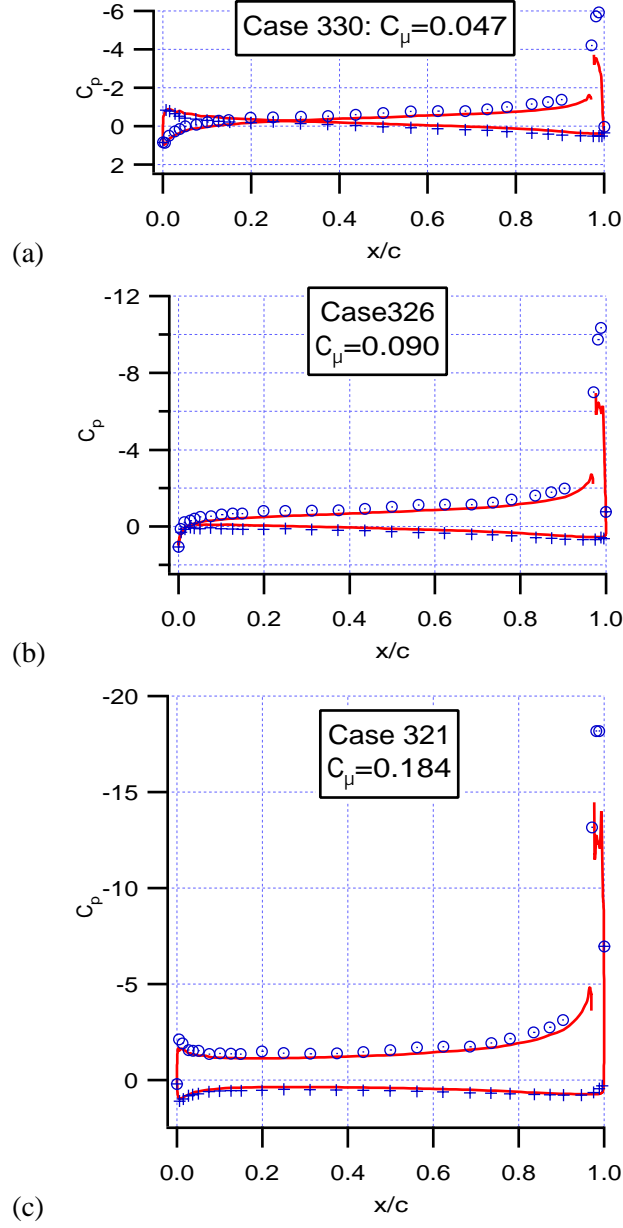


Figure 17: Surface pressure distributions for $h/c = 0.0030$ at $\alpha = -8^\circ$; — : FRSM, \circ : experiment—top, + : experiment—bottom (a): $C_\mu = 0.047$, (b): $C_\mu = 0.090$, (c): $C_\mu = 0.184$.

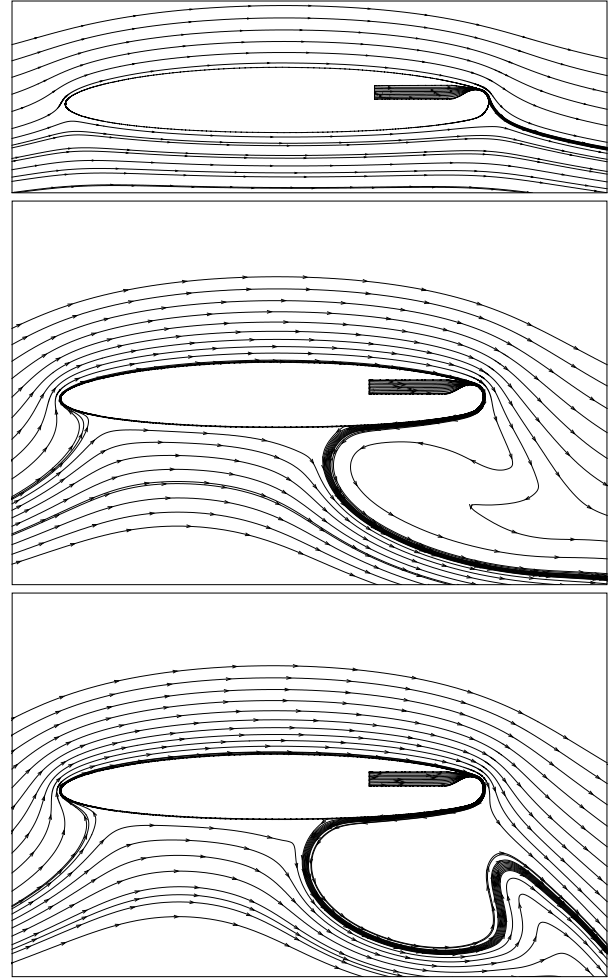
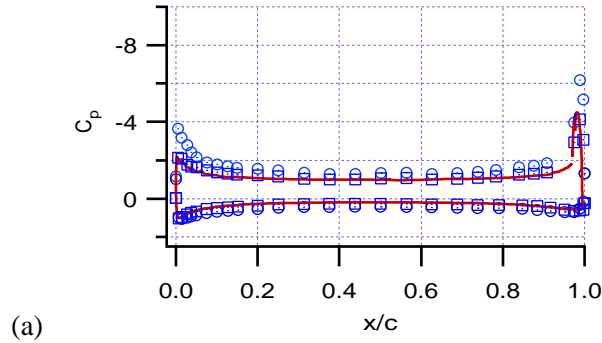
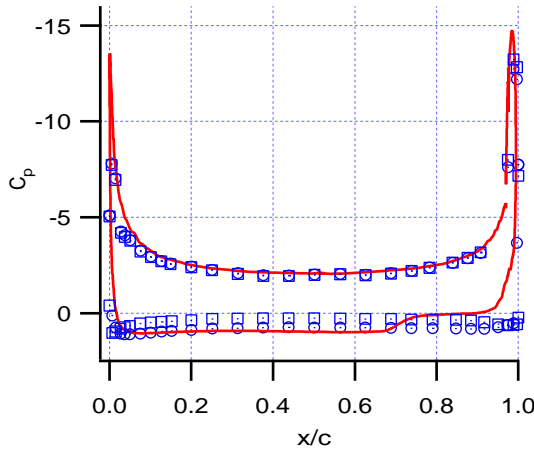


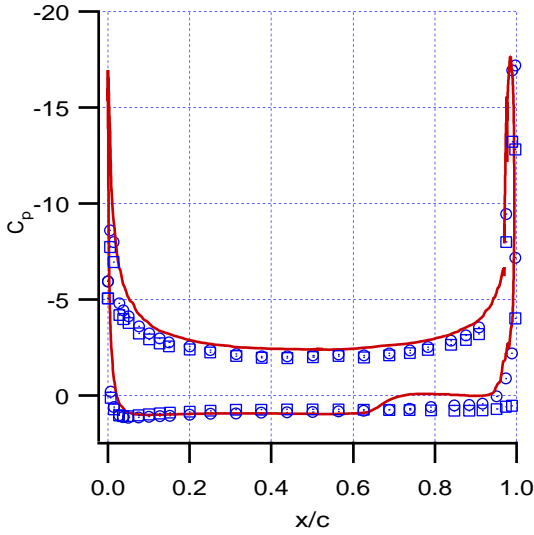
Figure 18: Streamlines for logarithmic spiral TE; $C_\mu = 0.054$, middle: $C_\mu = 0.107$ and bottom: $C_\mu = 0.140$.



(a)



(b)



(c)

Figure 19: Surface pressure distributions for logarithmic spiral cases; — : FRSM, \circ : experiment—top, + : experiment—bottom (a): $C_\mu = 0.054$, (b): $C_\mu = 0.107$, (c): $C_\mu = 0.140$.

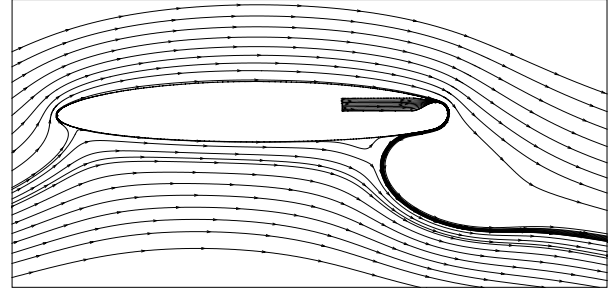


Figure 20: Streamlines for logarithmic spiral TE using $k - \omega$ turbulence model (Case 51, $C_\mu = 0.140$).

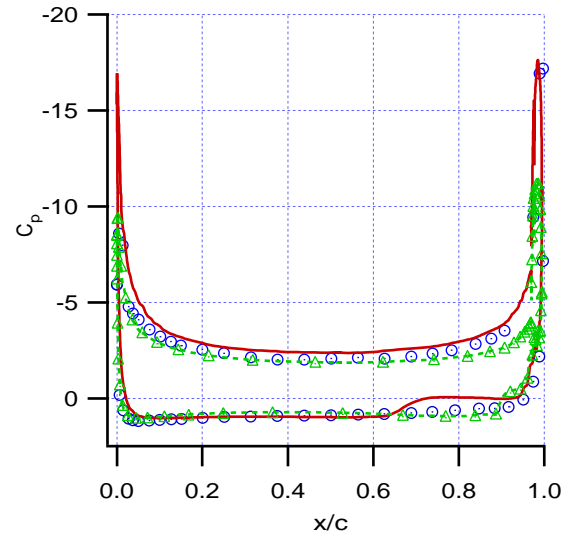
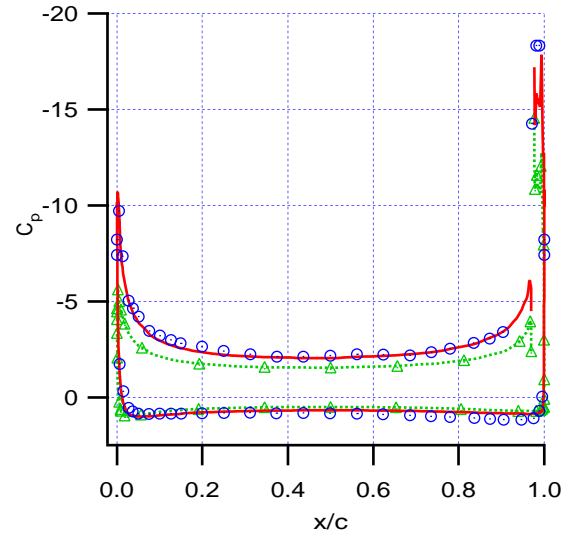
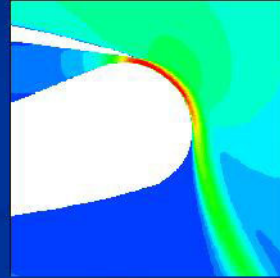


Figure 21: Surface pressure distributions comparing turbulence models. (a) Circular TE Case 283 ($h/c = 0.0030$, $\alpha = 0^\circ$, $C_\mu = 0.209$) (b) logarithmic spiral TE Case 51 ($C_\mu = 0.140$) — : FRSM, \triangle : $k - \omega$ SST, \circ : experiment.

Full Reynolds Stress Modeling of Circulation Control Airfoils



P.A. Chang ChangPA@nswccd.navy.mil 301-227-7059
J. F. Slomski SlomskiJF@nswccd.navy.mil 301-227-1935
T. A. Marino MarinoTA@nswccd.navy.mil
M. Ebert EbertMP@nswccd.navy.mil
J. Abramson AbramsonJS@nswccd.navy.mil

Hydromechanics Directorate
Carderock Division, Naval Surface Warfare Center
West Bethesda, MD 20817-5700

Acknowledgements: This work funded by ONR (Ron Joslin, program manager). Thanks to Ernest Rogers for help in explaining CC foil physics.

16-17 Mar 2004

Chang, Slomski, Marino, Ebert & Abramson
ONR-NASA CC Foil Workshop

1

Outline



- Motivation and introduction
- 2-D problem and results
 - Circular TE
 - Log-spiral TE
 - 2-D Conclusions
- 3-D problem

16-17 Mar 2004

Chang, Slomski, Marino, Ebert & Abramson
ONR-NASA CC Foil Workshop

2

Motivation



- Circulation-control (CC) offers the promise of improved maneuverability through higher lift producing control surfaces, *especially at low speeds (e.g., maneuvering in the littoral).*
 - Up to factor of 4 lift increase has been shown experimentally.
- Accurate CFD simulation of CC may offer a time- and expense-saving tool to augment and focus CC experimental techniques.
- CFD data (flow, pressure etc.) can be used to increase understanding of CC physics which can help in selection and design of CC foils.

Background



- Slomski, et al (AIAA 2002-0851) showed that CFD could accurately simulate the trailing edge (TE) coanda jet and its separation point from a BLUFF trailing edge.
 - Full Reynolds stress turbulence modeling.
- Patterson and Baker (AIAA 2004-0748) showed that Menter's $k-\omega$ SST isotropic turbulence model was promising for simulation of CC airfoil performance.

Objectives



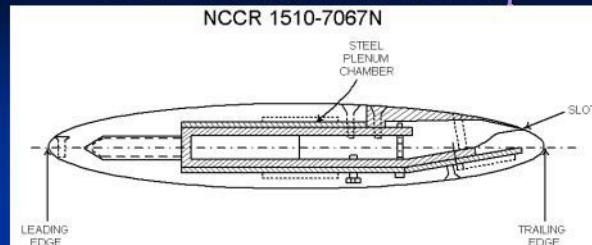
- Confirm that use of the full Reynolds Stress turbulence model (FRSM) will permit accurate CFD simulations of **general** CC airfoil/hydrofoil configurations and operating conditions.
 - AIAA 2002-0851 addressed one airfoil at 0° AOA
- Further investigate the performance of Menter's $k-\omega$ SST turbulence model for prediction of CC airfoil performance over a wider range of configurations and operating conditions.
 - NCCR 1510-7567S log-spiral trailing edge airfoil
- Extend 2-D conclusions to 3-D case.
 - Simulation of low-aspect ratio CC wing as tested in the LCC.
- Mature CFD as a design tool for CC, which would augment and focus experimental design techniques.
 - Accurate simulations over ranges of angle of attack (AOA), slot heights, trailing edge (TE) geometry and blowing rate.
 - Would be the first useful design tool for CC airfoils/hydrofoils based on first principles.

16-17 Mar 2004

Chang, Slomski, Marino, Ebert & Abramson
ONR-NASA CC Foil Workshop

5

2-D Problem Setup



- Steady, turbulent flow over a two-dimensional, circulation control airfoil, NCCR 1510-7067
 - 15% thickness, 1% camber
 - $X/c=0.97$ slot location, 6.7% thickness at slot
 - $Re_c = 5.45 \times 10^5$ ($M_\infty = 0.12$)
 - Blowing rates $0.05 \leq C_\mu \leq 0.20$
 - $C_\mu = (\text{Jet thrust force})/(\text{free stream stagnation force})$
 - Wind tunnel data available for all cases (Abramson, 1977).
 - Surface C_p data and integrated forces

16-17 Mar 2004

Chang, Slomski, Marino, Ebert & Abramson
ONR-NASA CC Foil Workshop

6

Mathematical Formulation



- Flow assumed to be governed by the compressible, Reynolds-averaged, two-dimensional Navier-Stokes equations
- Fluent - Segregated solver, steady state, implicit
- Ensemble-average turbulence models
 - Full Reynolds Stress turbulence model
 - 5 additional equations - RS (3 eqns.) , k , ε
 - $K-\omega$ model
 - Flow assumed to be turbulent over entire foil
- Enhanced wall treatment
 - Includes wall function valid in buffer region ($3 < y^+ < 10$)
 - Includes pressure gradients effects

16-17 Mar 2004

Chang, Slomski, Marino, Ebert & Abramson
ONR-NASA CC Foil Workshop

7

Test Matrix

Circular TE



Circular TE

Case	C_μ	H/c	α°
293	0.050	0.0030	0
289	0.092	0.0030	0
283	0.209	0.0030	0
311	0.048	0.0030	-4
307	0.090	0.0030	-4
302	0.189	0.0030	-4
330	0.047	0.0030	-8
326	0.090	0.0030	-8
321	0.184	0.0030	-8

Case	C_μ	H/c	α°
60	0.052	0.0015	0
57	0.104	0.0015	0
53	0.201	0.0015	0
229	0.053	0.0022	0
227	0.103	0.0022	0
223	0.198	0.0022	0

Log-Spiral TE

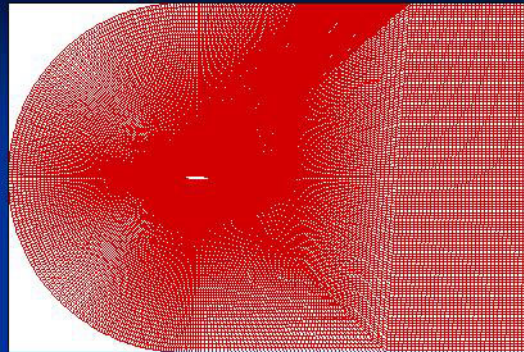
Case	C_μ	H/c	α°
56	0.054	0.0022	0
53	0.107	0.0022	0
51	0.140	0.0022	0

16-17 Mar 2004

Chang, Slomski, Marino, Ebert & Abramson
ONR-NASA CC Foil Workshop

8

Computational Grids



Click for 4 add'l graphics

- O-H topology
- 100k-150k cells, depending on slot height
- Downstream boundary 13 chord lengths
- Hybrid quad, tri mesh
- Wall-normal grid spacing
 - $y^+ < 2$ upstream of slot
 - $y^+ > 4$ in coanda jet
- Mass flow BC at plenum
- No-slip BC on walls
- Far-field pressure/velocity BC on outer boundaries
 - Characteristic, non-reflecting
- Inflow conditions:
 - 5% inflow turbulence intensity
 - $v_x/v_y=10$

16-17 Mar 2004

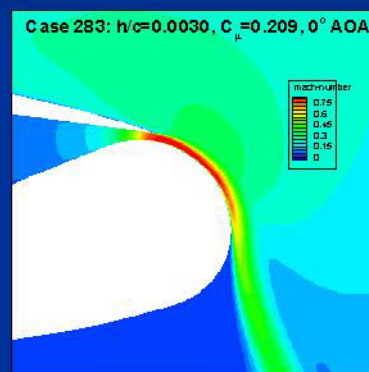
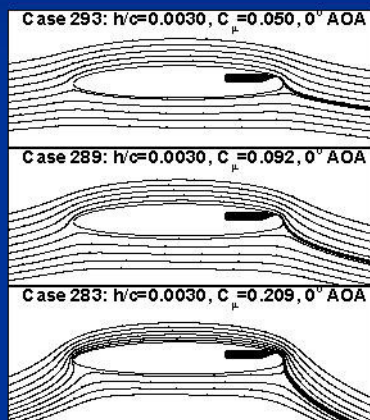
Chang, Slomski, Marino, Ebert & Abramson
ONR-NASA CC Foil Workshop

9

Streamlines as a function of C_μ $h/c = 0.0030, 0^\circ$ AOA



- Qualitatively correct detachment points



16-17 Mar 2004

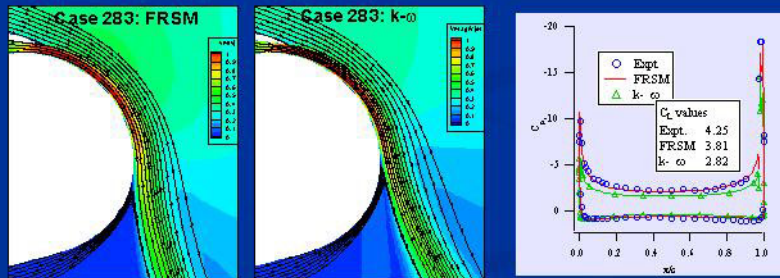
Chang, Slomski, Marino, Ebert & Abramson
ONR-NASA CC Foil Workshop

10

Comparison of FRSM and $k-\omega$ turbulence models Circular TE Case 283



- Detachment point for $k-\omega$ is earlier than FRSM
- Pressure over foil is less, resulting in smaller C_L .



16-17 Mar 2004

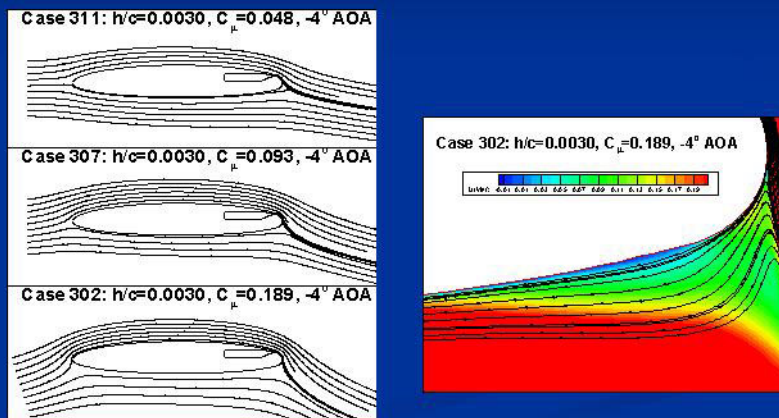
Chang, Slomski, Marino, Ebert & Abramson
ONR-NASA CC Foil Workshop

11

Streamlines as a function of C_μ for -4° AOA



- No TE pressure drawdown
- Small separation zones are found on pressure side of TE



16-17 Mar 2004

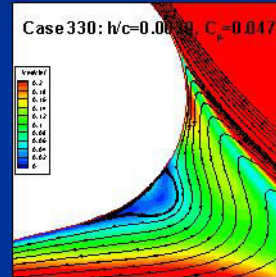
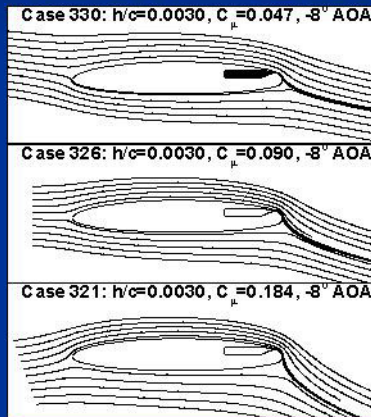
Chang, Slomski, Marino, Ebert & Abramson
ONR-NASA CC Foil Workshop

12

Streamlines as a function of C_{μ} -8° AOA



- No signs of TE pressure drawdown
- Separated flow on pressure side of TE



16-17 Mar 2004

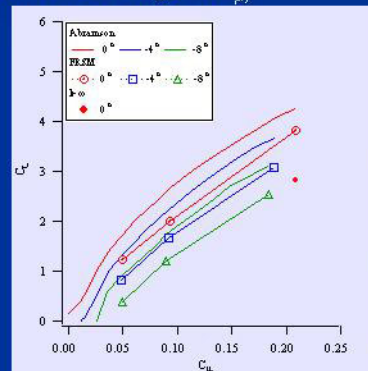
Chang, Slomski, Marino, Ebert & Abramson
ONR-NASA CC Foil Workshop

13

Lift as a function of angle of attack Circular TE, $h/c=0.0030$



- Experimental trends:
 - Blowing allows negative angle of attack to provide positive lift while avoiding suction-side separation
 - C_L decreases by constant amount over range of C_{μ}
- FRSM results:
 - Correctly predicts constant decrease in C_L with change in AOA
 - C_L values are consistently low



[Click for CFD results](#)

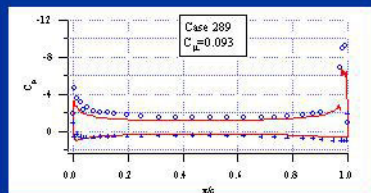
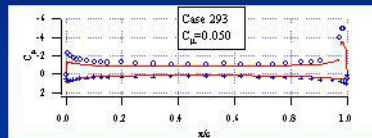
16-17 Mar 2004

Chang, Slomski, Marino, Ebert & Abramson
ONR-NASA CC Foil Workshop

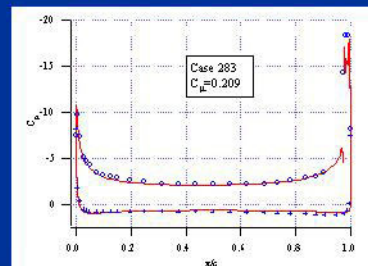
14

Pressure distributions

0° AOA, $h/c=0.0030$



- Pressure is slightly under-predicted in all cases
- Probable cause is relative location of jet detachment point
 - Experimental pressure and velocity field data is necessary in coanda jet region



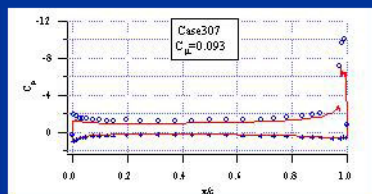
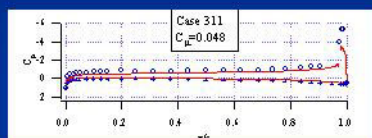
16-17 Mar 2004

Chang, Slomski, Marino, Ebert & Abramson
ONR-NASA CC Foil Workshop

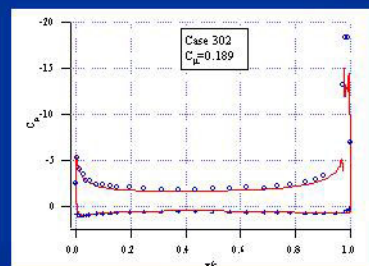
15

Pressure distributions

-4° AOA, $h/c=0.0030$



- For all cases, predicted pressures are lower than experiment
- Qualitative trends in pressure, especially as LE stagnation point migrates to bottom, are predicted correctly.



16-17 Mar 2004

Chang, Slomski, Marino, Ebert & Abramson
ONR-NASA CC Foil Workshop

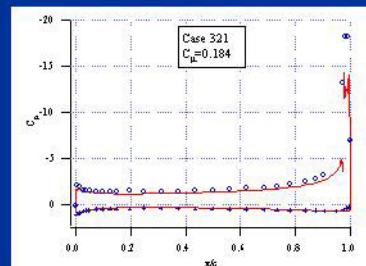
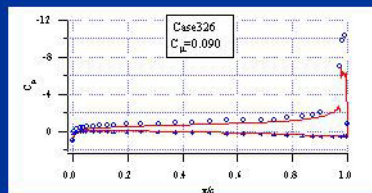
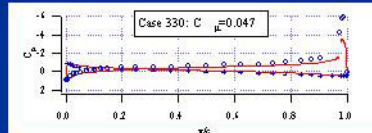
16

Pressure distributions for -8° AOA

$h/c=0.0030$



- Slight under-prediction of pressure for all cases



16-17 Mar 2004

Chang, Slomski, Marino, Ebert & Abramson
ONR-NASA CC Foil Workshop

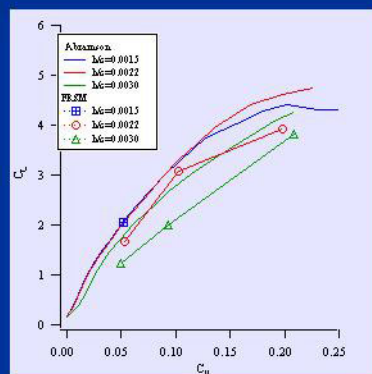
17

Lift as a function of slot height

0° AOA



- Three slot heights: $h/c=0.0030, 0.0022, 0.0015$
- At equal values of C_{μ} , mass flow- V_{jet} product must remain constant
 - As h/c decreases, mass flow decreases and jet velocity increases, supposedly increasing turbulent entrainment of outer fluid and jet stability
 - At low values of C_{μ} decreasing h/c results in negligible change in C_L
 - At higher values of C_{μ} C_L curve flattens out, indicative of over-blowing or "TE pressure drawdown."



- FRSM results
 - Low C_{μ} values and small slot heights have close agreement with experiments
 - Small slot cases are transonic and very hard to converge
 - Higher loading cases for $h/c=0.0015$ never converged – so, only lowest loading case shown.

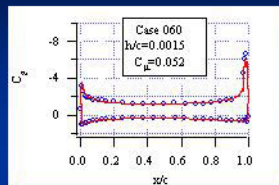
Click on graph for CFD and expt. comparison.

16-17 Mar 2004

Chang, Slomski, Marino, Ebert & Abramson
ONR-NASA CC Foil Workshop

18

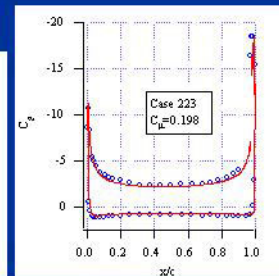
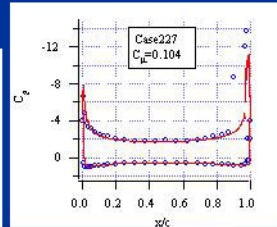
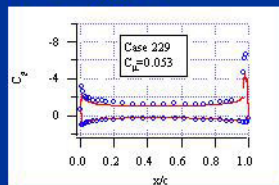
Pressure Distributions as a function of slot height



- Pressure for lowest velocity $h/c=0.0015$ case compares very well with experiment
- $H/c=0.0022$ cases have lower pressure than experiment
- Higher jet velocities cases compare best with experimental data

$H/c=0.0015$

$H/c=0.0022$



16-17 Mar 2004

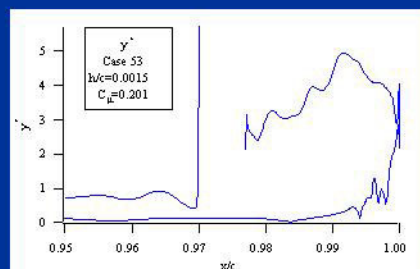
Chang, Slomski, Marino, Ebert & Abramson
ONR-NASA CC Foil Workshop

19

Wall Jet Mesh Resolution Issue for High Jet Velocity (small h/c) ?



- Wall jet may be under-resolved.
 - Shear stress at wall under-estimated \rightarrow coanda jet loses less momentum \rightarrow separation postponed?
 - Mesh resolution issue needs to be addressed in future work.



16-17 Mar 2004

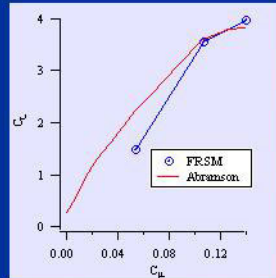
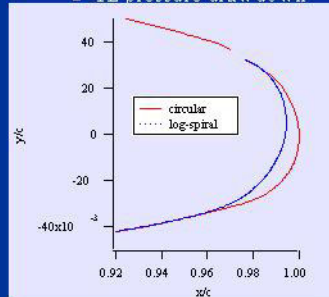
Chang, Slomski, Marino, Ebert & Abramson
ONR-NASA CC Foil Workshop

20

Log-spiral TE

- Log-spiral radius of curvature increases with distance from jet
- Purportedly minimizes blowing power requirement for given lift augmentation
 - FRSM under-predicts lift at low C_{μ} , over-predicts at higher C_{μ}

■ TE pressure drawdown



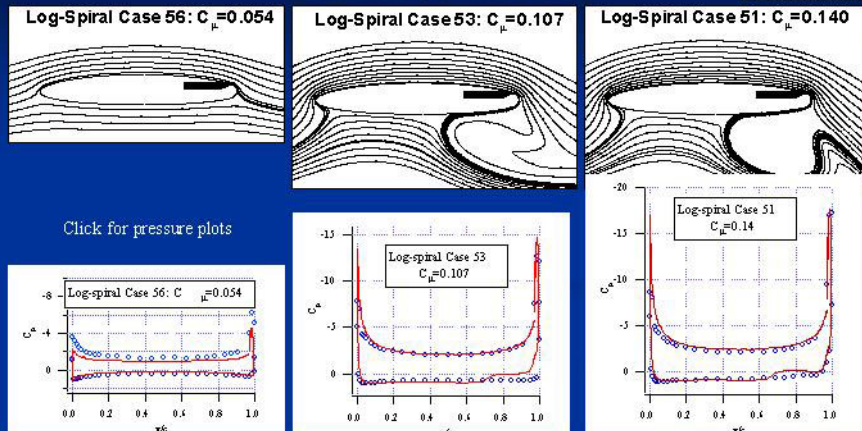
16-17 Mar 2004

Chang, Slomski, Marino, Ebert & Abramson
ONR-NASA CC Foil Workshop

21

Log-Spiral TE: Results

FRSM, 0° AOA



- Higher loading cases have TE pressure drawdown

16-17 Mar 2004

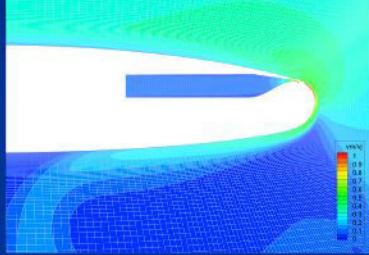
Chang, Slomski, Marino, Ebert & Abramson
ONR-NASA CC Foil Workshop

22

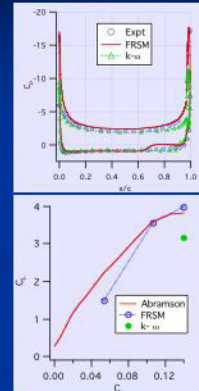
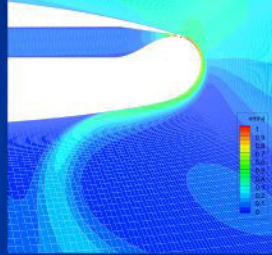
Comparison of FRSM and $k-\omega$ turbulence models - log-spiral TE



Log Spiral Case 51: FRSM



Log Spiral Case 51: $k-\omega$



- $K-\omega$ SST correctly predicts detachment point
 - Expt is slightly overblown
 - Under-predicts pressure directly upstream of slot
 - Under-predicts entrainment effect?
 - Recall circular arc TE results – separated earlier than FRSM – same thing happens here.

16-17 Mar 2004

Chang, Slomski, Marino, Ebert & Abramson
ONR-NASA CC Foil Workshop

23

2-D Conclusions



- For **circular** trailing edge, FRSM provides improved predictions (vice most isotropic eddy viscosity methods) for range of C_{μ} , AOA and h/c
 - All cases show qualitatively correct jet behavior with no TE pressure drawdown
 - C_L is uniformly low in most cases (e.g., $h/c=0.0030$) getting closer to experimental values as jet velocity increases.
- For **log-spiral** trailing edge, curvature is much less in detachment region and FRSM results are less consistent
 - Lowest C_{μ} case compares well with experiments
 - Higher C_{μ} cases have TE pressure drawdown
- $K-\omega$ turbulence model gives qualitatively good results for one circular and one log-spiral case
 - In both cases, C_L is quite low
 - Jet detachment point is earlier than FRSM
- We plan to explore the wall jet profiles and TKE profiles for each turbulence model to try to determine what makes the FRSM and $k-\omega$ SST models work, while the $k-\varepsilon$ model fails.

16-17 Mar 2004

Chang, Slomski, Marino, Ebert & Abramson
ONR-NASA CC Foil Workshop

24

Ongoing Work 3-D CC Foil



- Computational simulation of low aspect ratio CC wing as tested in the LCC:
 - Investigate the performance of FRSM and Menter's $k-\omega$ SST turbulence models.

16-17 Mar 2004

Chang, Slomski, Marino, Ebert & Abramson
ONR-NASA CC Foil Workshop

25

Low Aspect Ratio CC Wing



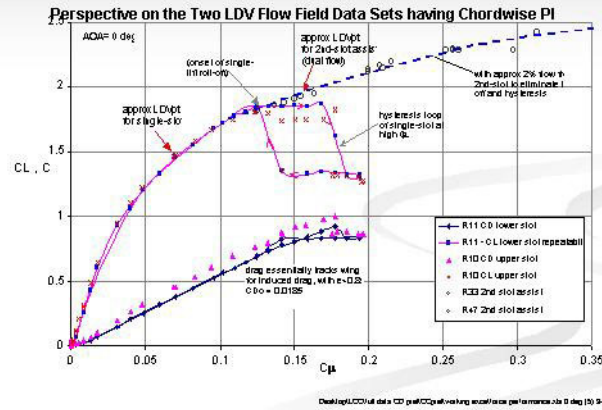
- Steady flow over a three-dimensional, circulation control wing, $AR = 2$.
 - 2 foot semi-span model
 - Elliptical cross-section, 20% thickness, 15° leading edge sweep.
 - $X/c=0.97$ slot location.
 - $Re_c = 2.1 \times 10^6$ ($V_\infty = 10$ ft/sec)
 - Blowing rates $0.0 \leq C_\mu \leq 0.20$ (some points out to 0.50).
 - LCC data available (Rogers and Donnelly, AIAA 2004-1244).
 - Forces and moments.
 - Limited LDV in the wake.

16-17 Mar 2004

Chang, Slomski, Marino, Ebert & Abramson
ONR-NASA CC Foil Workshop

26

Focus on C_L - C_μ Range from Experiment

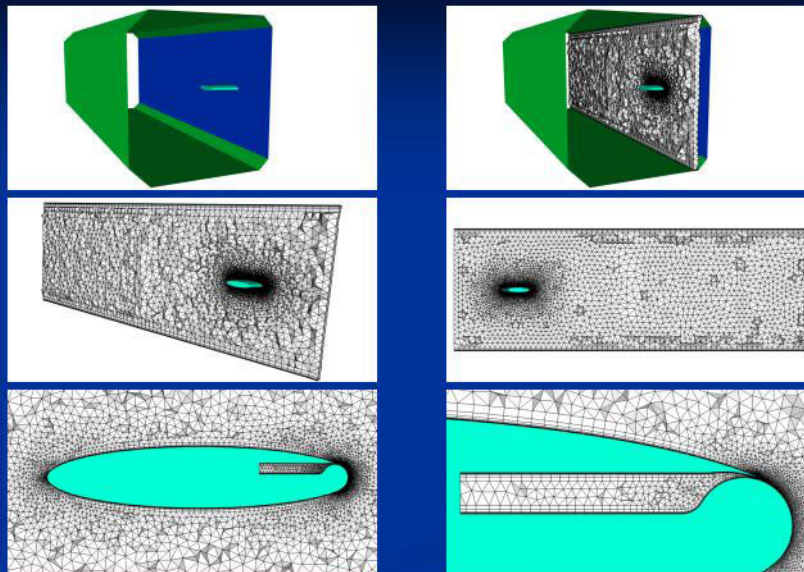


16-17 Mar 2004

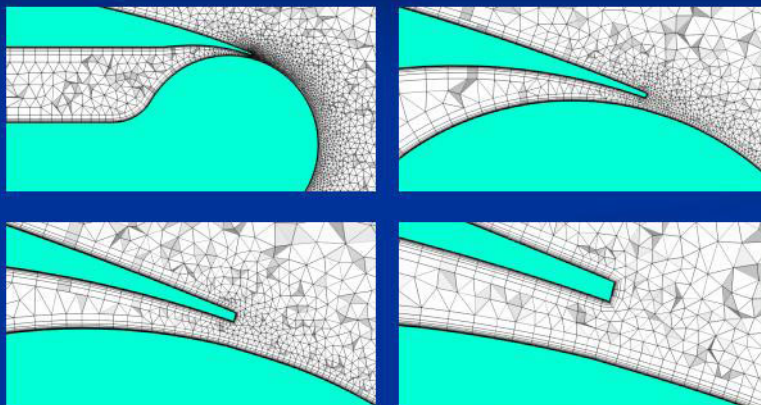
Chang, Slomski, Marino, Ebert & Abramson
ONR-NASA CC Foil Workshop

27

Volume Mesh Details for CC Wing



Volume Mesh Details in Slot Region



16-17 Mar 2004

Chang, Slomski, Marino, Ebert & Abramson
ONR-NASA CC Foil Workshop

29

RANS AND DETACHED-EDDY SIMULATION OF THE NCCR AIRFOIL

Eric G. Paterson* and Warren J. Baker†
The Pennsylvania State University
University Park, PA 16804

A circulation control foil is studied using incompressible Reynolds-averaged Navier Stokes and detached-eddy simulation CFD methods. Contrary to expectations, it is shown that Reynolds-averaged Navier-Stokes simulations of two large jet-momentum coefficient cases with a linear Reynolds-stress closure and a blended $k-\omega/k-\epsilon$ turbulence model is able to successfully predict the pressure-distribution trends in comparison to benchmark data. This implies that higher-order curvature-corrected models may only be required to resolve localized details such as the maximum suction peak on the Coanda surface. Details of the simulated flow are presented through analysis of the integral forces and moment, velocity field, and turbulent kinetic energy. However, given the lack of data and CFD grid studies, these results lack validation. Detached-eddy simulation is undertaken for the unblown case, and demonstrates that the method is capable of resolving turbulent vortex shedding. Statistical and spectral analysis is used to explain the simulation results, however, as with the RANS simulations, lack of data precludes validation for this problem. Nonetheless, results are encouraging and suggest further application of DES to both circulation control studies as well as other trailing-edge applications. Finally, implications for cavitation-free operation of circulation-control devices are discussed.

NOMENCLATURE

C_d	Section drag coefficient $\left(= \frac{F_d}{\frac{1}{2}\rho U_\infty^2 S}\right)$
C_l	Section lift coefficient $\left(= \frac{F_l}{\frac{1}{2}\rho U_\infty^2 S}\right)$
C_m	Section moment coefficient $\left(= \frac{M_s}{\frac{1}{2}\rho U_\infty^2 S c}\right)$
C_p	Pressure coefficient $\left(= \frac{p-p_\infty}{\frac{1}{2}\rho U_\infty^2}\right)$
C_μ	Jet momentum coefficient $\left(= \frac{\dot{m} U_j}{\frac{1}{2}\rho U_\infty^2 S}\right)$
c	Chord length
h	Slot height
k	Turbulent kinetic energy
\dot{m}	Mass flow rate
M	Mach number $\left(= \frac{U}{a}\right)$
p	Pressure
Re	Reynolds number $\left(= \frac{\rho U_\infty c}{\mu}\right)$
S	Planform area
U, V, W	Velocity components
x, y, z	Cartesian coordinates
α	Angle of attack, deg
Δt	Time step
μ	Dynamic viscosity
ω	Turbulent dissipation rate
ρ	Density

Subscripts

∞	Freestream
j	At jet orifice

Superscripts

r	resolvable scale
-----	------------------

s sub-grid scale

INTRODUCTION

CIRCULATION control (CC) for lift augmentation via the Coanda effect has been studied for many years.^{1,2} In comparison to mechanical means of circulation control (e.g., shape change and leading- and trailing-edge flaps), the use of a wall jet on a convex curved trailing-edge surface is attractive for many reasons including simplification of actuation, reduction in weight and number of parts, dual-mode operation (i.e., cruise and high-lift scenarios), contribution to novel design options such as placing control surfaces at non-traditional locations and arrangement of sensors and payloads on control surfaces, and improved shock resistance.

As with all flow control schemes,³⁻⁵ there are technical as well as economic and operational issues which must be overcome for systems to be transitioned into practical application. For example, for CC schemes to be incorporated in the marine environment, they must address the inherent drag penalty of a blunt trailing edge at cruise condition, overcome operator reluctance to fixed control surfaces, not suffer from orifice fouling or shock damage, and limit impact on hydroacoustics. Research such as that presented herein are motivated by these issues.

Continued development of new actuation methods⁶ potentially leads to novel solution of issues. Actuators such as high-performance solenoid valves, smart materials, zero-net-mass actuators, synthetic jet actuators, and plasma control actuators find application to CC as well as other forms of flow control. Of particular interest here are high-performance solenoid valves⁷ which can achieve efficient pulsed blowing, a mode of CC which has been known to reduce mass-flow re-

*Senior Research Associate, Applied Research Laboratory, and Associate Professor of Mechanical and Nuclear Engineering.

†Graduate Research Assistant, Department of Aerospace Engineering

quirements.^{8–10} However, application to the aqueous environment and detailed understanding of the unsteady flow physics is lacking.

Even for steady blowing CC, there are important flow physics which must be incorporated into CFD models if such tools are to be used in design. Most notable are streamwise curvature effects on the turbulent boundary layer and spanwise coherence of the wall jet. Nearly the entire range of RANS turbulence models from algebraic to full Reynolds-Stress transport equations have been modified for curvature effects.^{11–13} Unfortunately, the state of affairs is poor in that modifications to algebraic and one- and two-equation models are limited in range due to empiricism, whereas Reynolds-stress transport models (RSTMs) have yet to convincingly demonstrate capability to resolve subtleties in the way curvature impacts mean flow and turbulence structure.¹² Nonetheless, numerical experiments for a CC configuration¹⁴ have demonstrated that baseline RSTMs significantly improve simulation results in comparison to baseline two-equation models, especially at large jet momentum coefficients. Moreover, the simulations using two-equation models demonstrated non-physical behavior with a dramatic reduction in lift and a wall jet which remained attached to the surface for $1\frac{1}{2}$ revolutions around the foil.¹⁴

Detailed understanding of the high Reynolds number turbulent boundary layer on the Coanda surface would best be facilitated by DNS or possibly LES. For the usual reasons, i.e., lack of computer power, this is not yet realizable. Therefore, the approach pursued here is one based upon the detached-eddy simulation (DES)¹⁵ which is a hybrid RANS/LES method. In this approach, the foil forebody and the near-wall region is treated as URANS and the outer regions of the aftbody boundary layer and near wake are treated as LES. DES has been shown to improve accuracy for massively separated flows^{16,17} and has been applied to an active flow control application with zero-net-mass actuation¹⁸ albeit with inconclusive results. Ability of DES to resolve curvature effects, or the need for curvature modifications in the RANS portion of the DES model, is unknown.

Although the objective of our research is to develop validated simulation tools using recently acquired incompressible water-tunnel data for a low-aspect-ratio tapered control surface¹⁹ and wind-tunnel data for a pulsed CC configuration,^{7,10} the work presented herein represents our initial efforts to apply URANS and DES to a simpler steady-blowing CC configuration.²⁰ It has been selected as a preliminary validation exercise due to the fact that it can be treated as a 2D geometry and has previously been studied using RANS CFD.¹⁴ Our progress is reported in the following sections: Geometry, conditions, and data; Computational methods; Grid generation; Initial and boundary conditions; Results; and Conclusions.

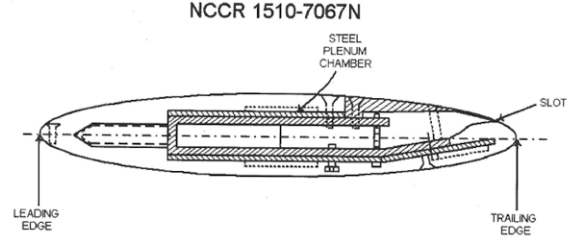


Fig. 1 Cross sectional geometry of NCCR 1510–7067N.

GEOMETRY, CONDITIONS, AND DATA

The NCCR-1510-7067N CC foil was wind tunnel tested at the David Taylor Naval Ship Research and Development Center in 1977.²⁰ The geometry is a 15% thick elliptical cambered foil with a single jet orifice on the upper surface at $\frac{x}{c}=0.967$. The model chord length is $c = 8$ inches, the slot height-to-chord ratio is $h/c = 0.003$, and the Coanda surface is a nominal circular arc. A cross section of the model is shown in Figure 1.

While a wide range of C_μ and α were studied in the original experiment, two cases are studied here. For the first, which is designated as Case 283, $C_\mu=0.209$ and $\alpha=0^\circ$. For the second, which is designated as Case 321, $C_\mu=0.184$ and $\alpha=-8^\circ$. Both are assumed to have the following common parameters: free-stream velocity $U_\infty=128.54 \frac{ft}{sec}$, free-stream density $\rho_\infty=0.07654 \frac{lbm}{ft^3}$, and kinematic viscosity $\mu = 3.7373 \times 10^{-7} \frac{slug}{ft \cdot sec}$. This yields a $Re=5.45 \times 10^5$ and $M_\infty=0.12$. Assuming that the jet is incompressible (i.e., $\frac{\rho_j}{\rho_\infty} = 1$), the non-dimensional jet-orifice velocities can be computed as $U_j/U_\infty = \sqrt{\frac{1}{2} \frac{\rho_j}{\rho_\infty} \frac{c}{h} C_\mu} = 5.90$ and 5.54 for Case 283 and 321, respectively.

Available experimental data is somewhat limited in comparison to modern experiments. Data consists of surface pressure measured via pressure taps placed at mid-span. Experimental lift and moment were computed by integrating surface pressure, and drag was evaluated using a wake survey and a momentum-deficit method. In addition, the magnitude of experimental uncertainty is not available, however, several sources have been identified such as slot-height growth due to plenum pressure, and interaction with tunnel walls, especially at large C_μ , such that the effective α is different from the geometric α .

COMPUTATIONAL METHODS

Unsteady RANS

CFDSHIP-IOWA²¹ is a general-purpose parallel unsteady incompressible Reynolds-averaged Navier-Stokes (RANS) CFD code. The computational approach is based upon structured overset-grid, higher-order finite-difference, and pressure-implicit split-operator (PISO) numerical methods. Production turbulence model uses a linear closure and the blended

$k - \omega/k - \varepsilon$ SST 2-equation model.²² Efficient parallel computing is achieved using coarse-grain parallelism via MPI distributed computing. For time-accurate unsteady simulations, global solution of the pressure-Poisson equation is achieved using pre-conditioned GMRES and the PETSc libraries.^{23–25}

Detached-Eddy Simulation

Detached-eddy simulation (DES) is a three-dimensional unsteady numerical method using a single turbulence model, which functions as a subgrid-scale model in regions where the grid density is fine enough for a LES, and as a RANS model in all other regions. Implementation of DES in CFDSHIP-IOWA was accomplished by modifying the turbulence model and convective-term discretization.

The turbulence model is modified by introducing a DES length scale

$$\tilde{\ell} = \min(\ell_{k\omega}, C_{DES}\Delta) \quad (1)$$

which compares the sub-grid length scale to the local grid size where the former can be written as

$$\ell_{k\omega} = \frac{k^{1/2}}{\beta^*\omega} \quad (2)$$

C_{DES} is a model constant with a value between 0.78 and 0.61 weighted by the Menter $k - \omega/k - \varepsilon$ blending function,²² and Δ is based on the largest dimension of the local grid cell

$$\Delta = \max(\delta_x, \delta_y, \delta_z) \quad (3)$$

The new length scale $\tilde{\ell}$ replaces $\ell_{k\omega}$ in the the dissipative term of the k-transport equation

$$D_{RANS}^k = \rho\beta^*k\omega = \frac{\rho k^{3/2}}{\ell_{k\omega}} \quad (4)$$

which results in a new dissipation term

$$D_{DES}^k = \frac{\rho k^{3/2}}{\tilde{\ell}} \quad (5)$$

The effect of this modification is to increase dissipation in LES regions such that the turbulence budget shifts energy from sub-grid, or modeled, scales to resolvable scales as defined by the filter width $C_{DES}\Delta$.

The second modification aims to reduce numerical dissipation inherent in the upwind convective-term discretization scheme. The implemented approach is based upon a hybrid central/upwind approximation of the convective terms (or fluxes).

$$F_{inv} = (1 - \sigma) F_{ctr} + \sigma F_{upw} \quad (6)$$

where σ is defined as

$$\sigma = \max \left\{ \tanh \left(\frac{C_{DES}\Delta}{\ell_{k\omega}} \right)^n, \tanh \left(\frac{|U|\Delta t}{\Delta} \right)^m \right\} \quad (7)$$

The result is that σ smoothly transitions between 1.0 in the RANS regions, resulting in an "almost upwind" scheme, and 0.0 in the LES regions, resulting in an "almost centered" scheme. In addition, a Courant-number constraint of 1.0 has been imposed which requires that time step be sufficiently small to support turbulent eddies. The coefficients n, m permit the interface between RANS and LES regions to be arbitrarily "sharpened", however, currently we use $n = m = 1$ due to the fact that higher-order coefficients have resulted in unstable simulations. It is also noted that Equation 7 was developed since implementation of Strelets function for σ^{15} was unsuccessful.

In CFDSHIP-IOWA the convective terms are discretized with the following higher-order upwind formula

$$U^k \frac{\partial \phi}{\partial \xi_k} = \frac{1}{2} (U^k + |U^k|) \delta_{\xi_k}^- \phi + \frac{1}{2} (U^k - |U^k|) \delta_{\xi_k}^+ \phi \quad (8)$$

where

$$\delta_{\xi_i}^- \phi = w_{mm}\phi_{i-2} + w_m\phi_{i-1} + w_n\phi_i + w_p\phi_{i+2} + w_{pp}\phi_{i+2} \quad (9)$$

$$\delta_{\xi_i}^+ \phi = -w_{pp}\phi_{i-2} - w_p\phi_{i-1} - w_n\phi_i - w_m\phi_{i+2} - w_{mm}\phi_{i+2} \quad (10)$$

DES implementation is accomplished by redefining these equations

$$\delta_{\xi_i}^- \phi = W_{mm}\phi_{i-2} + W_m\phi_{i-1} + W_n\phi_i + W_p\phi_{i+2} + W_{pp}\phi_{i+2} \quad (11)$$

$$\delta_{\xi_i}^+ \phi = -W_{pp}\phi_{i-2} - W_p\phi_{i-1} - W_n\phi_i - W_m\phi_{i+2} - W_{mm}\phi_{i+2} \quad (12)$$

where $W_{mm}, W_m, W_n, W_p, W_{pp}$ are hybrid coefficients defined as the blending between the 2nd-order upwind and the 4th-order central schemes.

$$\begin{aligned} W_{pp} &= (1 - \sigma) w_{pp}^{4c} + \sigma w_{pp}^{2u} \\ W_p &= (1 - \sigma) w_p^{4c} + \sigma w_p^{2u} \\ W_n &= (1 - \sigma) w_n^{4c} + \sigma w_n^{2u} \\ W_m &= (1 - \sigma) w_m^{4c} + \sigma w_m^{2u} \\ W_{mm} &= (1 - \sigma) w_{mm}^{4c} + \sigma w_{mm}^{2u} \end{aligned} \quad (13)$$

Finally, as discussed in the following section, it is noted that CFDSHIP-IOWA is an overset-grid capable CFD code with an interface to PEGASUS 5.1.²⁶ This capability will be exploited to perform local grid refinement and flow adaptation in the wall-jet, wake, and LES regions.

GRID GENERATION

Overset grids are generated primarily using hyperbolic extrusion, although transfinite interpolation and elliptic smoothing is used for blocks which don't lend themselves to that approach. Overset interpolation coefficients and holes are computed using Pegasus 5.1.²⁶ CFDSHIP-IOWA employs double-fringe outer and hole boundaries so that the 5-point discretization stencil (i.e., in each curvilinear coordinate direction)

and order-of-accuracy does not have to be reduced near overset boundaries. Level-2 interpolation capability of PEGASUS 5.1 is also used so as to achieve optimal match between donor and interpolant meshes.

Grid design is based upon a domain size of $-2 \leq x/c \leq 4$ and $-2 \leq y/c \leq 2$ and $0 \leq z/c \leq 0.2$ and a near-wall spacing of 1.0×10^{-5} , the latter of which aims to resolve the sub-layer of the turbulent boundary layer with a wall spacing of $y^+ = 1$.

Grid system used for RANS simulations is shown in Figure 2. Nested orthogonal uniform box grids are used for the far-field and a simple O-grid is used for the foil. Preliminary solutions were used to locate streamlines, and wake-refinement blocks were built off of these streamlines for subsequent higher-fidelity simulations. RANS simulations were computed in a pseudo-2D fashion which requires 5-points in the spanwise direction. Overall grid consists of 323,000 points and is comprised of 8 blocks ranging in size from 30,000 to 51,000 points.

For DES, the approach is the same as described above, except that the spanwise resolution must be increased in regions where turbulent eddies are to be resolved. Overset grids are effectively used to locally refine the simulation. As shown in Figure 3, forebody and far-field, which is in the RANS region, is resolved with 5-points in the spanwise direction. In contrast, the trailing-edge and near-wake blocks are resolved with 41-points in the spanwise direction. Wake refinement mesh shown in Figure 3 is designed for unblown $C_\mu = 0$ simulations and has an isotropic spacing of $\Delta = 0.005$. Overall grid consists of 855,000 points and is comprised of 15 blocks ranging in size from 31,000 to 67,000 points. It is noted that translational periodicity is imposed in the spanwise direction and that the extent of the domain in this direction is 20% of chord length. It is acknowledged that this can potentially affect flow structures in wake, particularly if this dimension is smaller than spanwise turbulent correlation length scales, which for this problem are unknown. However, other trailing-edge flows²⁷ have shown correlation lengths of 4 foil thicknesses, which in this case would be $0.60c$. Since periodic boundaries are used, domain size in the spanwise direction would need to be $1.2c$. As such, our domain may be $\frac{1}{6}$ the required size.

INITIAL AND BOUNDARY CONDITIONS

Initial conditions for the steady RANS simulations are straight-forward: $U = U_\infty, V = V_\infty, k = k_\infty, \omega = \omega_\infty$, and $p = 0$. For unsteady RANS and DES, a cubic polynomial is used to accelerate the foil from rest over a non-dimensional time of 2.0.

No-slip boundary conditions were applied on all surfaces of the foil and the top and bottom walls of the plenum. On the inlet face of the plenum, a top-hat velocity profile was prescribed using $\frac{U}{U_\infty}$ and the plenum

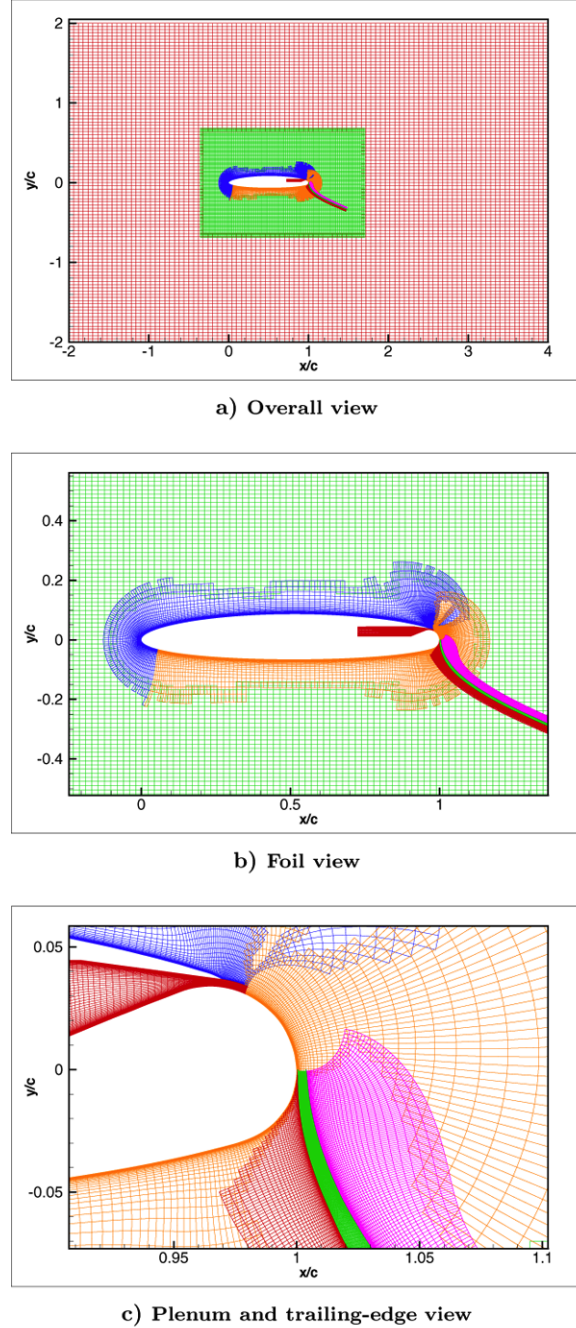
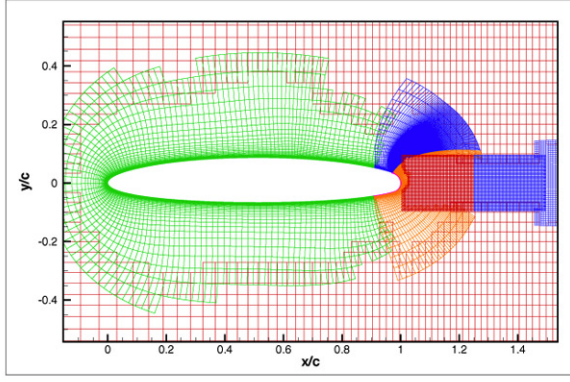
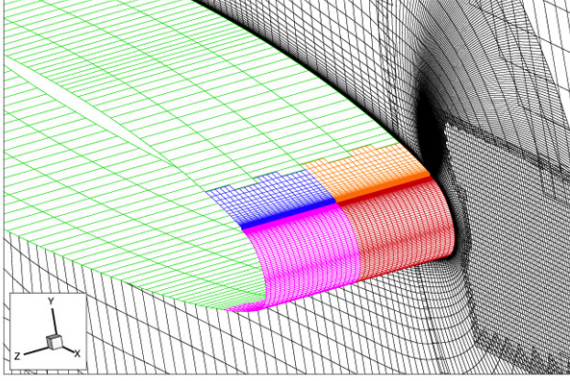


Fig. 2 Overset grid system for RANS simulation.



a) Side view



b) Trailing-edge detail, showing spanwise resolution

Fig. 3 Overset grid system for DES.

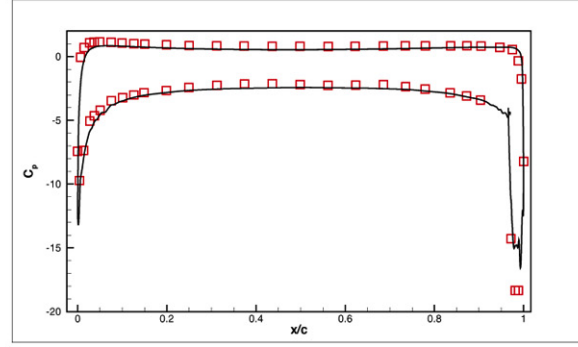
contraction of 10.63. For Case 283 and 321, this velocity magnitude corresponds to 0.555 and 0.521, respectively. Inlet, far-field, and exit conditions were applied on the outer boundaries of the largest box grid and translational periodicity was applied on all spanwise faces. Neumann conditions were used for pressure on all boundaries. As already mentioned, outer and hole boundary trilinear interpolation coefficients are computed using Pegasus 5.1.²⁶ Mathematical formulation of all boundary conditions are described by Paterson et al.²¹ Finally, it is noted that boundary conditions are set and input file created using the CFDSHIP-IOWA filter in the GRIDGEN software from Pointwise, Inc.

RESULTS

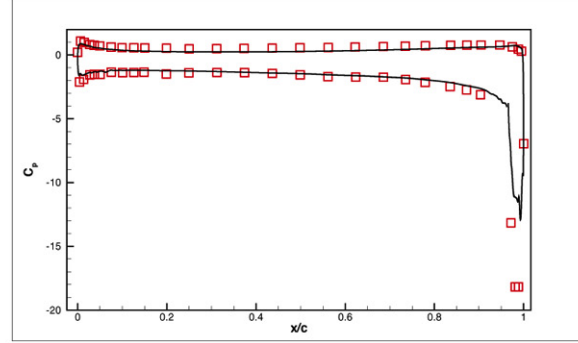
Research has been undertaken along two paths, both of which are presented. First, RANS simulations for Cases 283 and 321 will be presented. Second, DES results for the unblown $C_\mu = 0$ case will be shown and discussed.

Steady RANS Simulation

A comparison of experimental and simulated surface pressure is shown in Figure 4. Relatively good agreement is demonstrated for both cases. Largest discrepancy is the underprediction of the suction peak aft



a) Case 283, $C_\mu=0.209$, $\alpha=0^\circ$



b) Case 321, $C_\mu=0.184$, $\alpha=-8^\circ$

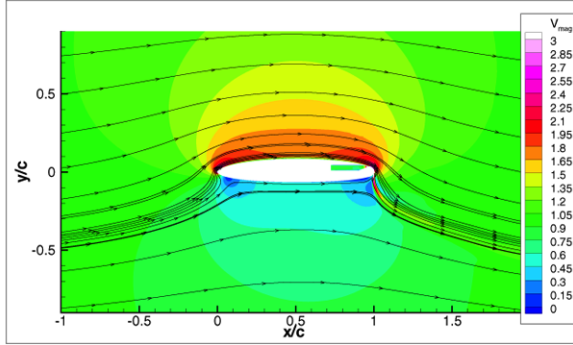
Fig. 4 Comparison of experimental (symbols) and computational (lines) surface pressure.

of the jet orifice. Case 283 shows a strong leading-edge low pressure, relatively uniform loading over the majority of the chord, and a $C_{p,min}$ of -17 and -18 at the trailing-edge for the simulation and experiment, respectively. Due to the negative angle-of-attack, Case 321 lacks the leading-edge low pressure. It also shows larger error in comparison to the data across the chord, but especially on the Coanda surface. The predicted and experimental $C_{p,min}$ is -13 and -18, respectively.

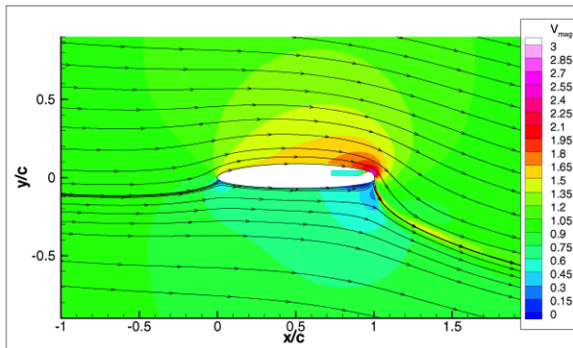
Lift, drag, and moment about the z -axis centered at mid-chord were computed by integrating C_p and wall shear stress on all external surfaces, i.e., all plenum surfaces were neglected. Results are tabulated in Table 1. Experimental values were computed²⁰ by directly integrating the discrete (and fairly coarse) surface-pressure data. Lift coefficient for Case 283 is within 5% of the data, whereas Case 321 shows a discrepancy of 30% due to the larger underprediction of the suction peak on the Coanda surface. Drag for both cases show a very large difference from the data. The data, which was measured using a wake profile corrected by the jet momentum, shows a negative drag, whereas the CFD values are positive and substantially larger in magnitude. Moment coefficient C_m is positive (leading-edge down, trailing-edge up) for both cases due to the large suction peak on the Coanda surface. Data for C_m is not available for this case.

	C_l		C_d		C_m	
	Data	CFD	Data	CFD	Data	CFD
Case 283	4.2	4.0	-0.05	0.18	-	2.07
Case 321	3.1	2.4	-0.08	0.12	-	1.21

Table 1 Lift, Drag, and Moment Coefficients



a) Case 283, $C_\mu=0.209$, $\alpha=0^\circ$



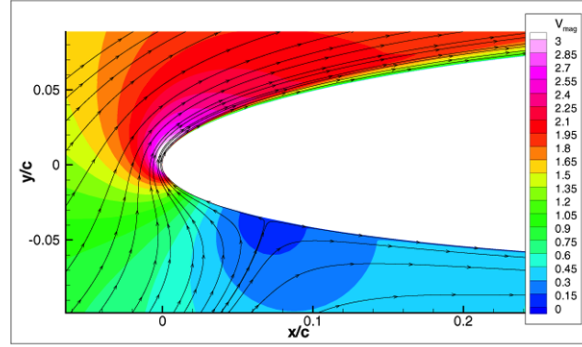
b) Case 321, $C_\mu=0.184$, $\alpha=-8^\circ$

Fig. 5 Overall view of velocity magnitude contours and streamlines.

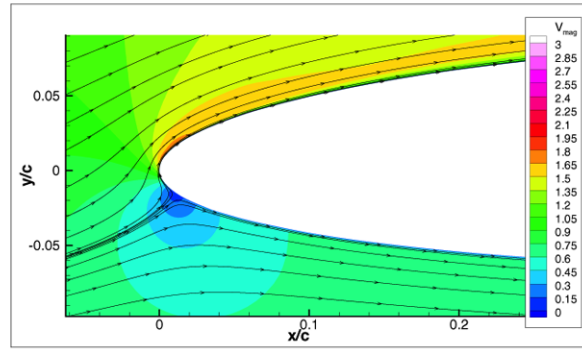
Figure 5 illustrates the impact of the Coanda effect upon the overall circulation. For both cases, velocity-magnitude contours show high velocity on the top surface that is consistent with surface pressure shown in Figure 4. Streamlines show effect of angle-of-attack and locations of stagnation points.

A close-up view of the leading-edge flow field is shown in Figure 6. For Case 283, the stagnation point is located at $x/c = 0.07$ on the foil bottom surface. For Case 321, the stagnation point is located at $x/c = 0.01$ on the foil bottom surface, despite the negative angle-of-attack. Comparing the two cases, the relative magnitudes of velocity are shown to be consistent with the differences in the leading-edge suction peak shown in Figure 4.

A close-up of the trailing-edge flow field is shown in Figure 7. Both cases are similar: they demonstrate a high-velocity jet emanating from the plenum; increased velocity around the initial curvature of the Coanda surface; clean jet detachment; and flow separation on the bottom surface upstream of the jet. For



a) Case 283, $C_\mu=0.209$, $\alpha=0^\circ$



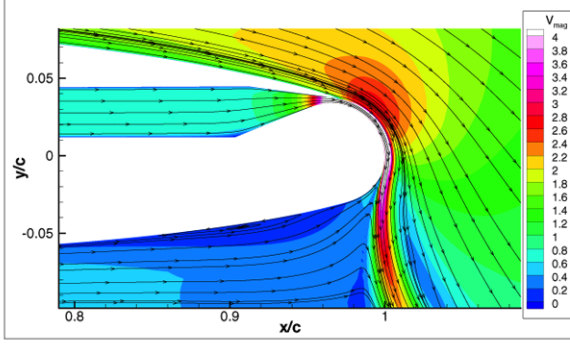
b) Case 321, $C_\mu=0.184$, $\alpha=-8^\circ$

Fig. 6 Leading-edge view of velocity magnitude contours and streamlines.

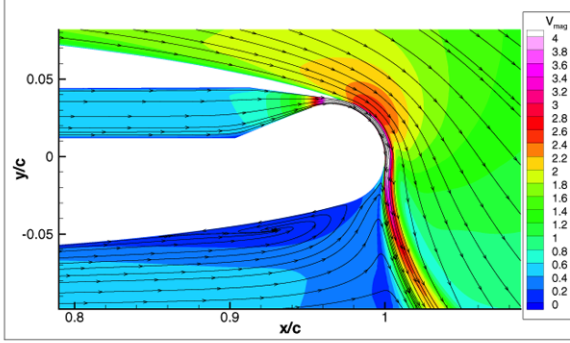
Case 283, the wall jet stays attached longer and the thickness of the separated region is smaller in comparison to Case 321.

Contours of turbulent kinetic energy near the trailing-edge are shown in Figure 8. Again, both cases demonstrate similar behavior. Contours show two primary sources of kinetic energy, both of which correspond to regions of high mean shear. The first is downstream of the jet-slot knife edge and grows along the wall-jet shear layer. The second, which is larger in magnitude, starts at the point of wall jet separation and grows into the wake. It is noted that the maximum $k \approx 0.7$, is two orders-of-magnitude larger than k in the turbulent boundary layer.

Details of the velocity magnitude and turbulent kinetic energy are shown by extracting profiles at two locations for Case 283 as shown in Figure 9. Location A is slightly aft of the jet orifice, and Location B is along a $y = 0$ line. At A, the wall jet and strong shear layer are clearly shown. The turbulent kinetic energy shows spikes downstream of the plenum walls, the outer of which merges with k from the suction-side boundary layer. At B, the peak velocity magnitude is close to that at A, however, the wall-jet shape has greatly thickened due to viscous and turbulent stresses near the wall and along the shear layer. The turbulent kinetic energy has significantly grown in both magni-



a) Case 283, $C_\mu=0.209$, $\alpha=0^\circ$



b) Case 321, $C_\mu=0.184$, $\alpha=-8^\circ$

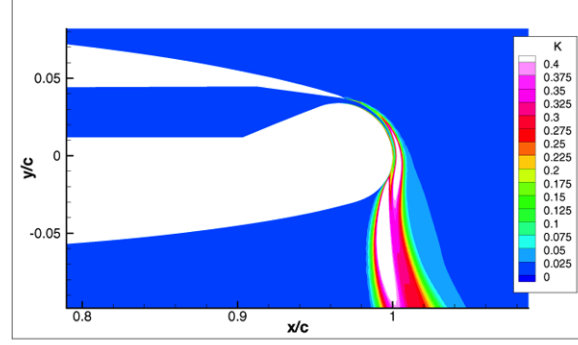
Fig. 7 Trailing-edge view of velocity magnitude contours and streamlines.

tude and thickness, both of which are consistent with velocity profiles and k contours shown in Figure 8.

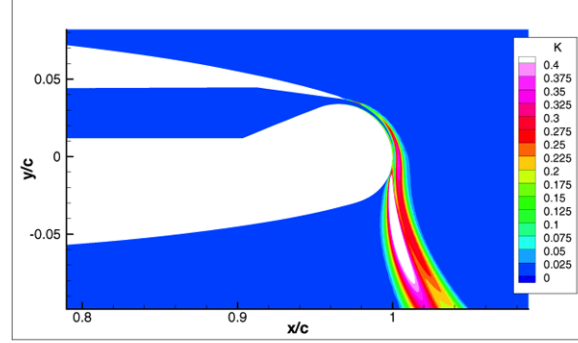
In preparation for future DES of the blown cases, the length scale in Equation 2 was computed for Case 283 and is shown in Figure 10. This shows that the largest eddies in the boundary layer and near wake are on the order of $0.02c$. However, the length scale is much smaller (i.e., $\ell_{k\omega} \leq 0.002$) in the near orifice region. Therefore, target grid spacing in this area should be approximately $\Delta = 0.001$.

Detached-Eddy Simulation

DES was performed for 10,000 time steps with $\Delta t = 0.001$ (or 10 flow-through periods). Animations of the instantaneous iso-surface of vorticity colored by spanwise velocity were made and snapshots are shown in Figure 11. Side view clearly shows the dominant vortex shedding of spanwise eddies. The overset grid is also shown in the background to illustrate the effect of switching from high-to-low, i.e., LES-to-RANS, grid resolution. All spanwise structure is filtered and only the "2D" vortex passes through this interface. The top view clearly displays the longitudinal vortices which are intertwined with the spanwise vortices. Again, the impact of switching from high-to-low grid resolution is shown. The lack of spurious numerical reflections at this overset boundary is noted.



a) Case 283, $C_\mu=0.209$, $\alpha=0^\circ$

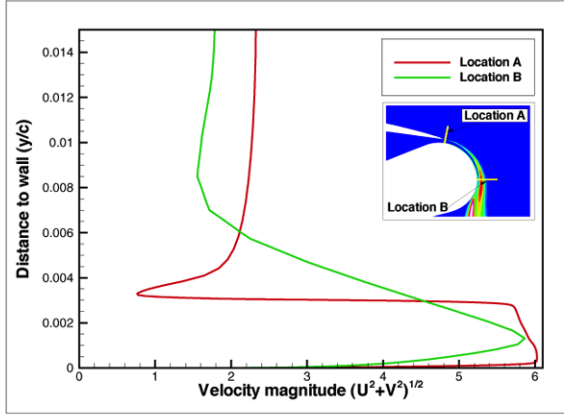


b) Case 321, $C_\mu=0.184$, $\alpha=-8^\circ$

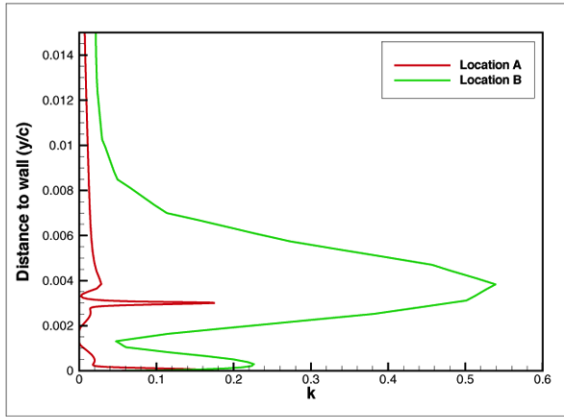
Fig. 8 Contours of turbulent kinetic energy.

Mean and RMS statistics for all dependent variables were computed over 6000 time steps. Figure 12 shows the contours of the mean axial velocity \bar{U} , streamlines through the mean field, and RMS axial velocity $\sqrt{u'^2}$. Mean flow field shows a typical wake with two eddies. Root-mean-square also shows a typical wake pattern²⁷ with two peaks across the wake corresponding to vortices shed off the top and bottom sides of the foil. It is noted that computed statistics were not yet fully two-dimensional, thus indicating that a larger integration time is needed to reduce uncertainty in the computed statistics.

Analysis of the turbulent kinetic energy is shown in Figure 13. Sub-grid turbulence k^s is computed from the modified $k - \omega$ turbulence model, whereas the resolvable turbulence is computed from the velocity correlations $k^r = \frac{1}{2}(\overline{uu} + \overline{vv} + \overline{ww})$. Total kinetic energy is the sum of these two parts. These figures show that k^s is significant only in the boundary layer upstream of the separation. Downstream, total k is comprised of resolvable scales only. A region of particular interest is the potential "gray region" where the solution switches from RANS to LES. Total k does show a slight decrease as the trailing-edge is approached. Whether or not this is physical is unknown, but it remains a topic for future research, especially for problems with smooth-body separation which is



a) Velocity magnitude



b) Turbulent kinetic energy

Fig. 9 Extracted profiles.

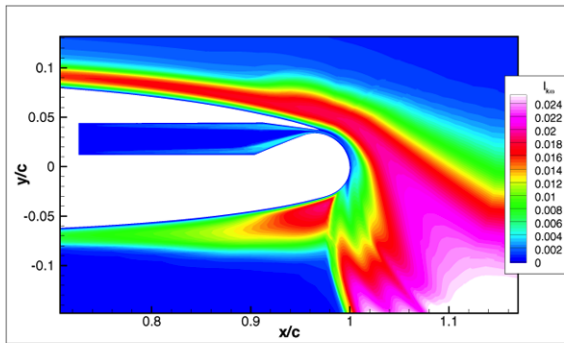
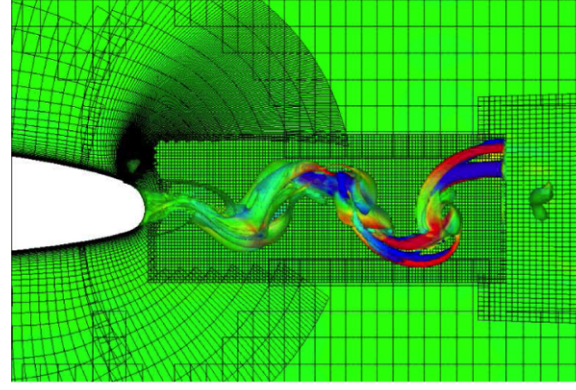
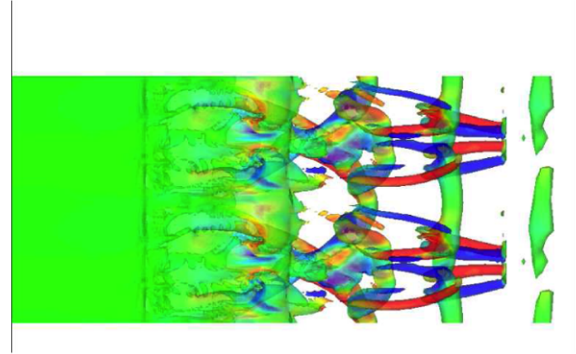


Fig. 10 $k - \omega$ length scale for Case 283



a) Side view.



b) Top view.

Fig. 11 Instantaneous iso-surface of vorticity colored by spanwise velocity component.

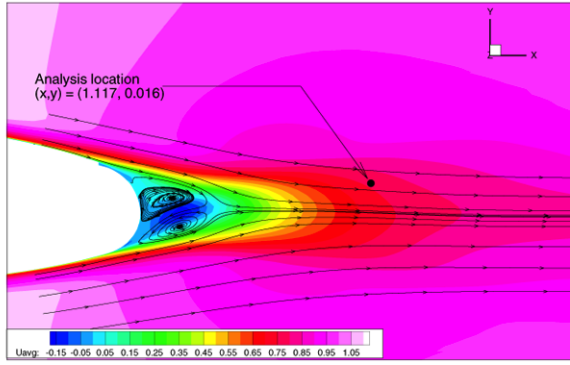
sensitive to boundary-layer characteristics.

Finally, Figure 14 shows spectral analysis of velocity at a single point $(x/c, y/c) = (1.117, 0.016)$, location of which was shown in Figure 12. Time history and FFT show a shedding frequency at $f_0^* = \frac{f c}{U_\infty} = 3.8$. If a new length scale is defined as the vertical distance between points of mean separation at the trailing edge, which is $d/c = 0.052$, a more appropriate shedding frequency is computed to be $\tilde{f} = \frac{f d}{U_\infty} = 0.198$, which is consistent with a typical Strouhal number of 0.2. FFT shows superharmonics at $f_1^* = 7.5$ and $f_2^* = 12$, which are $2f_0^*$ and $3f_0^*$, respectively, and a decay of the higher frequencies at $-5/3$ slope up to a frequency of about 30, the latter of which is consistent with a grid spacing of 0.005 and the assumption of 10 grid points per wavelength.

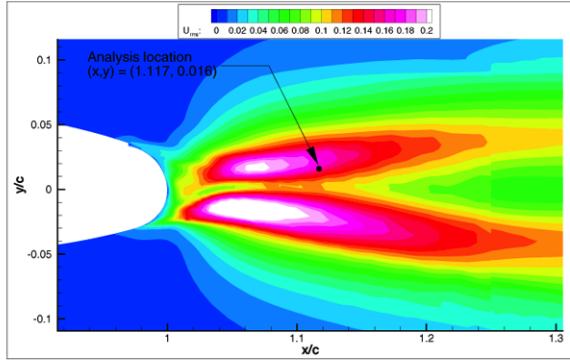
Cavitation-Free Operating Depth and Speed

Given the low pressure on the Coanda surface, cavitation is a concern. As a rough estimate, cavitation occurs when the magnitude of minimum pressure coefficient exceeds the cavitation number.

$$-C_p \geq \sigma \quad (14)$$



a) Mean velocity, \bar{U}



b) Root-mean-square velocity, $\sqrt{u^2}$

Fig. 12 Statistical analysis of axial velocity.

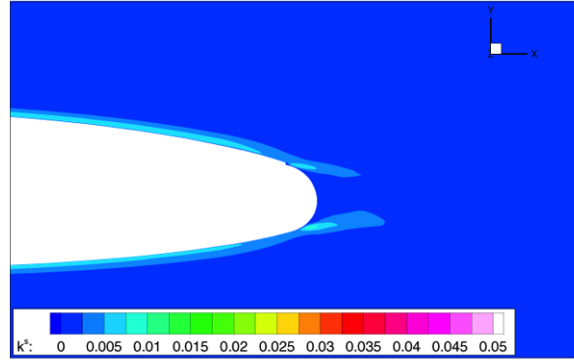
$$-C_p \geq \frac{p_\infty - p_v}{\frac{1}{2}\rho U_\infty^2} \quad (15)$$

Given that $p_\infty = \rho g z$, an expression for cavitation-free operation relating $C_{p,min}$, depth z , and vehicle speed U_∞ can be derived.

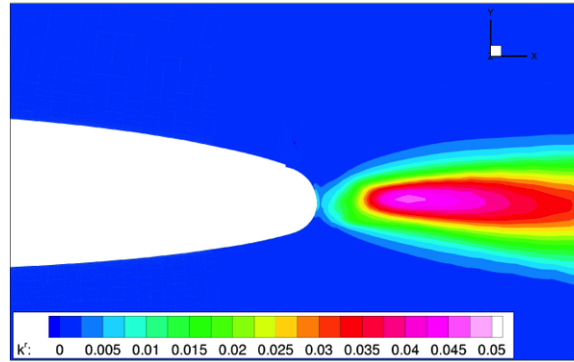
$$\frac{\rho g z - p_v}{\frac{1}{2}\rho U_\infty^2} = -C_{p,min} \quad (16)$$

Using properties of water at 15°C ($\rho = 1000 \frac{\text{kg}}{\text{m}^3}, p_v = 1.7 \text{ kPa}$), a family of curves can be computed which relates the three variables. Such a figure is shown in Figure 15. It illustrates, for example, that for a $C_{p,min} = -20$, cavitation can be avoided at all depths greater than 50 feet as long as speed remains lower than 10 knots.

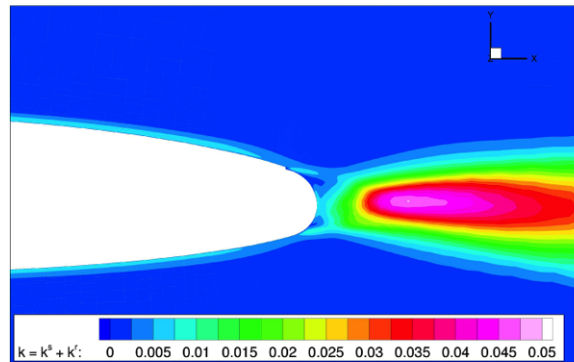
Since CC is envisioned for low-speed operation in the littorals, an operation point where traditional control surfaces lose control authority, this is a favorable observation. On the other hand, speed of 30 kts would require a depth of 750 ft to achieve cavitation-free operation, at least for the C_μ studied herein. Fortunately, since dynamic pressure increases with U_∞^2 , lower C_μ and C_L , and therefore decreased $C_{p,min}$, would be required at high speed thus permitting CC to be used throughout the operation envelope.



a) Sub-grid, k^s

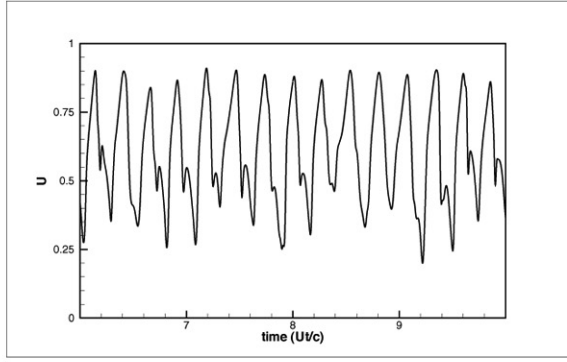


b) Resolvable, k^r

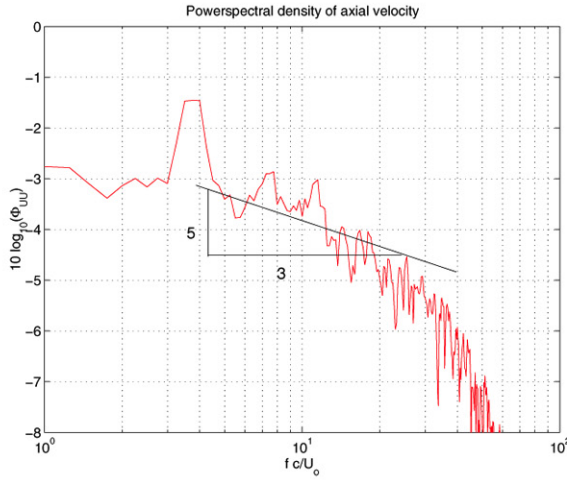


c) Total, $k^s + k^r$

Fig. 13 Statistical analysis of turbulent kinetic energy.



a) Time history.



b) Fourier transform.

Fig. 14 Frequency analysis of axial velocity at $(x/c, y/c) = (1.117, 0.016)$.

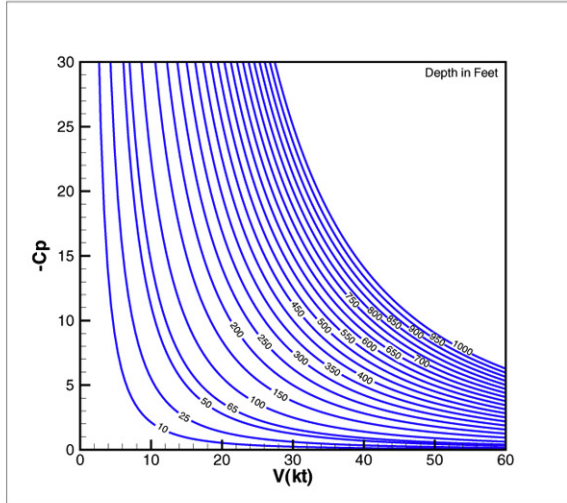


Fig. 15 Cavitation-free operation curves.

CONCLUSIONS

A circulation control foil was studied using incompressible RANS and DES CFD methods. RANS simulations of large jet-momentum coefficient cases demonstrated that a linear closure with blended $k - \omega/k - \epsilon$ turbulence model was able to successfully predict the pressure distribution trends in comparison to benchmark data. This is contrary to expectations and other published results¹⁴ which indicate the need for higher-order curvature-corrected models such as a full Reynolds-stress model. The reason for this discrepancy is unknown but suggests that such models may only be required to resolve localized details such as the maximum suction peak on the Coanda surface. Details of the simulated flow were presented through analysis of the integral forces and moment, velocity field, and turbulent kinetic energy. However, given the lack of data and CFD grid studies, these results lack validation.

Detached-eddy simulation was undertaken for the unblown case, and demonstrated that the method is capable of resolving turbulent vortex shedding. Statistical and spectral analysis was undertaken to explain the simulation results, however, as with the RANS simulations, lack of data precludes validation for this problem. Nonetheless, results are encouraging and suggest further application of DES to both circulation control studies as well as other trailing-edge applications (e.g., propulsor blades and nozzles).

Future work will focus on validation using modern water-tunnel data for a low-aspect-ratio tapered control surface¹⁹ and wind-tunnel data for a pulsed CC configuration.^{7,10} In addition to providing high-fidelity flow field data, these cases will permit study of three-dimensional effects and pulsed blowing, both of which are important issues for practical application and improved understanding of basic CC flow physics.

ACKNOWLEDGMENTS

The authors gratefully acknowledge support from both the Office of Naval Research through Grant Number N00014-03-1-0122 (Program Officer: Dr. Ron Joslin) and NAVSEA SUB-RT (Program Manager: Ms. Meg Stout), the latter of which was in the form of a graduate student fellowship for the second author. The DoD High Performance Computing Modernization Office (HPCMO) and Army Research Laboratory-Major Shared Resource Center are acknowledged for providing computing resources through a DoD HPCMO Challenge Project. Finally, it is noted that this paper is a re-representation of AIAA 2004-0748, which was published in the proceedings of the 42nd AIAA Aerospace Sciences Meeting held January 5–8, 2004 in Reno, NV.

REFERENCES

- ¹Englar, R., "Circulation Control Pneumatic Aerodynamics: Blown Force and Moment Augmentation and Modifications; Past, Present, and Future," AIAA Paper 2000-2541, June 2000.
- ²Wood, N. and Nielson, J., "Circulation Control Airfoils Past, Present, and Future," AIAA Paper 1985-0204, Jan. 1985.
- ³Bushnell, D., "Application Frontiers of "Designer Fluid Mechanics" – Visions versus Reality or An Attempt to Answer the Perennial Question "Why Isn't It Used?," AIAA Paper 1997-2110, June 1997.
- ⁴Joslin, R., Kunz, R., and Stinebring, D., "Flow Control Technology Readiness: Aerodynamic versus Hydrodynamic," AIAA Paper 2000-4412, Denver, CO, June 2000, In AIAA 18th Applied Aerodynamics Conference Proceedings.
- ⁵Hess, D. and Fu, T., "Impact of Flow Control Technologies on Naval Platforms," AIAA Paper 2003-3568, Orlando, FL, June 2003, In 33rd AIAA Fluid Dynamics Conference.
- ⁶Schaeffler, N., Hepner, T., Jones, G., and Kegerise, M., "Overview of Active Flow Control Actuator Development at NASA Langley Research Center," AIAA Paper 2002-3159, St Louis, MO, June 2002, In AIAA 1st Flow Control Conference Proceedings.
- ⁷Jones, G., Viken, S., Washburn, A., Jenmins, L., and Cagle, C., "An Active Flow Circulation Controlled Flap Concept for General Aviation Aircraft Applications," AIAA Paper 2002-3157, St Louis, MO, June 2002, In AIAA 1st Flow Control Conference Proceedings.
- ⁸Oyler, T. and Palmer, W., "Exploratory Investigation of Pulse Blowing for Boundary Layer Control," Tech. Rep. NR72H-12, North American Rockwell Report, January 1972.
- ⁹Walters, R., Myer, D., and Holt, D., "Circulation Control by Steady and Pulsed Blowing for a Cambered Elliptical Airfoil," Aerospace Engineering TR-32, West Virginia University, July 1972.
- ¹⁰Jones, G. and Englar, R., "Advances in Pneumatic-Controlled High-Lift Systems Through Pulsed Blowing," AIAA Paper 2003-3411, Orlando, FL, June 2003, In 33rd AIAA Fluid Dynamics Conference.
- ¹¹Wallin, S. and Johansson, A., "Modelling Streamline Curvature Effects in Explicit Algebraic Reynolds Stress Turbulence Models," *International Journal of Heat and Fluid Flow*, Vol. 23, 2002, pp. 721-730.
- ¹²Patel, V. and Sotiropoulos, F., "Longitudinal Curvature Effects in Turbulent Boundary Layers," *Progress in Aerospace Science*, Vol. 33, 1997, pp. 1-70.
- ¹³Gatski, T. and Speziale, C., "On Explicit Algebraic Stress Models for Complex Turbulent Flows," *Journal of Fluid Mechanics*, Vol. 254, 1993, pp. 59-78.
- ¹⁴Slomski, J., Gorski, J., Miller, R., and Marino, T., "Numerical Simulation of Circulation Control Airfoils as Affected by Different Turbulence Models," AIAA Paper 2002-0851, Reno, NV, Jan. 2002, In 40th AIAA Aerospace Sciences Meeting and Exhibit Proceedings.
- ¹⁵Strelets, M., "Detached-Eddy Simulation of Massively Separated Flows," AIAA Paper 2001-0879, Reno, NV, Jan. 2001, In 39th AIAA Aerospace Sciences Meeting and Exhibit Proceedings.
- ¹⁶Squires, K., Forsythe, J., Morton, S., Strang, W., Wurtzler, K., Tomaro, R., Grismer, M., and Spalart, P., "Progress on Detached-Eddy Simulation of Massively Separated Flows," AIAA Paper 2002-1021, Reno, NV, Jan. 2002, In 40th AIAA Aerospace Sciences Meeting and Exhibit Proceedings.
- ¹⁷Forsythe, J., Squires, K., Wurtzler, K., and Spalart, P., "Detached-Eddy Simulation of Fighter Aircraft at High Alpha," AIAA Paper 2002-0591, Reno, NV, Jan. 2002, In 40th AIAA Aerospace Sciences Meeting and Exhibit Proceedings.
- ¹⁸Spalart, P., Hedges, L., Shur, M., and Travin, A., "Simulation of active flow control on a stalled airfoil," Tech. rep., Toulouse, France, 2002, Proceedings of IUTAM Sympo. on Unsteady Separated Flows.
- ¹⁹Rogers, E. and Abramson, J., "Low-aspect ratio CC hydrofoil investigation in the LCC, August 2002," unpublished.
- ²⁰Abramson, J., "Two-Dimensional Subsonic Wind Tunnel Evaluation of Two Related Cambered 15-Percent Circulation Control Airfoils," DTNSRDC ASED-373, Sept. 1977.
- ²¹Paterson, E., Wilson, R., and Stern, F., "General-Purpose Parallel Unsteady RANS Ship Hydrodynamics Code: CFDSHIP-IOWA," Tech. Rep. 432, IIHR Hydroscience and Engineering, The University of Iowa, Iowa City, IA, Nov 2003.
- ²²Menter, F., "Two-Equation Eddy Viscosity Turbulence Models for Engineering Applications," *AIAA Journal*, Vol. 32, No. 8, 1994.
- ²³Balay, S., Buschelman, K., Gropp, W. D., Kaushik, D., Knepley, M., McInnes, L. C., Smith, B. F., and Zhang, H., "PETSc home page," <http://www.mcs.anl.gov/petsc>.
- ²⁴Balay, S., Buschelman, K., Gropp, W. D., Kaushik, D., Knepley, M., McInnes, L. C., Smith, B. F., and Zhang, H., "PETSc Users Manual," Tech. Rep. ANL-95/11 - Revision 2.1.5, Argonne National Laboratory, 2002.
- ²⁵Balay, S., Gropp, W. D., McInnes, L. C., and Smith, B. F., "Efficient Management of Parallelism in Object Oriented Numerical Software Libraries," *Modern Software Tools in Scientific Computing*, edited by E. Arge, A. M. Bruaset, and H. P. Langtangen, Birkhauser Press, 1997, pp. 163-202.
- ²⁶Suhs, N., Dietz, W., Rogers, S., Nash, S., and Onufer, J., T., "PEGASUS User's Guide, Version 5.1e," Tech. rep., NASA, 2000.
- ²⁷Blake, W., "A Statistical Description of Pressure and Velocity Fields at the Trailing-Edges of a Flat Strut," Report 4241, David W. Taylor Naval Ship Research and Development Center, Bethesda, MD 20084, December 1975.



RANS and Detached-Eddy Simulation of the NCCR Airfoil

Eric Paterson and Warren Baker

Computational Mechanics Division
Applied Research Laboratory
The Pennsylvania State University
University Park, PA U.S.A.

2004 NASA-ONR Circulation Control Workshop – p. 1/34



Acknowledgements

- Office of Naval Research, Dr. Ron Joslin
- NAVSEA SUB-RT, Ms. Meg Stout
- DoD HPCMP and Army Research Lab MSRC, Challenge Program



2004 NASA-ONR Circulation Control Workshop – p. 2/34



Outline

- Objective
- Geometry
- Flow Conditions
- Data
- Computational Methods
- Grid Generation
- Initial and Boundary Conditions
- Results
- Conclusions and Future Work

2004 NASA-ONR Circulation Control Workshop – p. 3/34



Objective

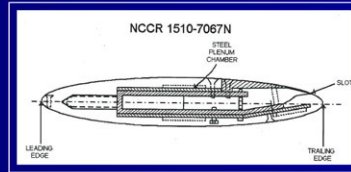
- Develop validated simulation tools using
 - *wind-tunnel data for a pulsed CC configuration (Jones et al., 2002) \implies Baker and Paterson (2004)*
 - *incompressible water-tunnel data for a low-aspect-ratio tapered control surface (Rogers and Abramson, 2003)*
- The work presented herein represents initial efforts to apply RANS and DES to a simpler steady-blowing CC configuration (Abramson, 1977)
 - can be treated as a 2D geometry
 - other RANS CFD studies (Slomski et al., 2002)
 - March 2004 NASA/ONR circulation control workshop

2004 NASA-ONR Circulation Control Workshop – p. 4/34



Geometry

- 15% thick elliptical cambered foil
- Chord length is $c = 8$ inches
- Single jet orifice on the upper surface at $\frac{x}{c} = 0.967$
- Slot height-to-chord ratio is $h/c = 0.003$
- Coanda surface is a nominal circular arc



Flow Conditions

- Three cases studied
 - Unblown, $C_\mu = 0.0$ and $\alpha = 0^\circ$ (DES)
 - Case 283, $C_\mu = 0.209$ and $\alpha = 0^\circ$ (RANS)
 - Case 321, $C_\mu = 0.184$ and $\alpha = -8^\circ$ (RANS)
- Common parameters
 - $Re = 5.45 \times 10^5$
 - $M_\infty = 0.12$
- Jet velocities, $U_j/U_\infty = \sqrt{\frac{1}{2} \frac{\rho_j}{\rho_\infty} \frac{c}{h} C_\mu}$
 - incompressible RANS solver $\Rightarrow \frac{\rho_j}{\rho_\infty} = 1$
 - Case 283: $U_j/U_\infty = 5.90$
 - Case 321: $U_j/U_\infty = 5.54$

Data



- The NCCR-1510-7067N CC model was wind tunnel tested at the David Taylor Naval Ship Research and Development Center in 1977
- Limited in comparison to modern experiments
 - surface pressure measured via pressure taps
 - lift computed by integrating surface pressure
 - drag evaluated using a wake survey and a momentum-deficit method
- Sources of uncertainty include:
 - slot-height growth due to plenum pressure
 - interaction with tunnel walls \Rightarrow change in effective α

2004 NASA-ONR Circulation Control Workshop – p. 7/34

Computational Methods



- CFDShip-IOWA (Paterson et al., 2003) is a general-purpose parallel unsteady incompressible Reynolds-averaged Navier-Stokes (RANS) CFD code
 - structured overset grids
 - higher-order finite-difference discretization
 - pressure-implicit split-operator (PISO) algorithm
 - blended $k - \omega / k - \varepsilon$ SST 2-equation model
 - coarse-grain parallelism via MPI distributed computing
 - pre-conditioned GMRES solver for pressure-Poisson equation

2004 NASA-ONR Circulation Control Workshop – p. 8/34



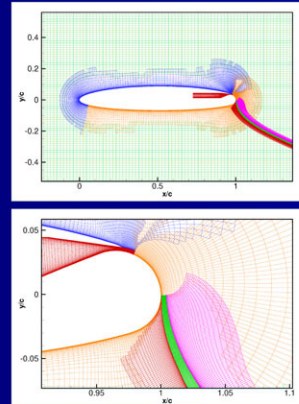
Computational Methods

- Detached-eddy simulation (DES)
 - three-dimensional unsteady numerical method
 - single turbulence model, which functions as a subgrid-scale model in regions where the grid density is fine enough for a LES, and as a RANS model in all other regions
- Modifications to turbulence model and convective-term discretization.
 - k -equation dissipation term $D_{DES}^k = \frac{\rho k^{3/2}}{\tilde{\ell}}$ where $\tilde{\ell} = \min(\ell_{kw}, C_{DES}\Delta)$
 - hybrid central/upwind approximation of the convective terms
 $F_{inv} = (1 - \sigma) F_{ctr} + \sigma F_{upw}$ where
 $\sigma = \max \left\{ \tanh \left(\frac{C_{DES}\Delta}{\ell_{kw}} \right)^n, \tanh \left(\frac{|U|\Delta t}{\Delta} \right)^m \right\}$



RANS Grid Generation

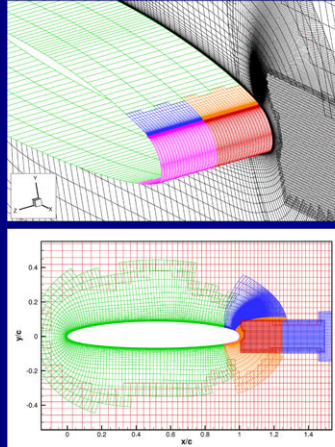
- Overset structured grids
 - nested orthogonal box grids
 - simple O-grid for the foil
 - wake-refinement blocks
 - Pegasus 5.1
- Near-wall spacing of 1.0×10^{-5}
- Pseudo-2D
- Overall grid
 - 323,000 points
 - 8 blocks ranging in size from 30,000 to 51,000 points





DES Grid Generation

- Spanwise resolution must be increased
- Overset grids are used for local refinement
- Wake refinement designed for $C_\mu = 0$ and has an isotropic spacing of $\Delta = 0.005$
- Overall grid
 - 855,000 points
 - 15 blocks ranging in size from 31,000 to 67,000 points



2004 NASA–ONR Circulation Control Workshop – p. 11/34



Initial and Boundary Conditions

- Initial Conditions
 - steady flow: free-stream values
 - unsteady flow: cubic-polynomial acceleration from rest
- Boundary Conditions
 - no-slip
 - inlet, far-field, exit
 - overset interpolation coefficients
 - top-hat profile on plenum inlet
 - Neumann conditions for pressure

2004 NASA–ONR Circulation Control Workshop – p. 12/34

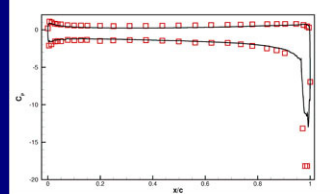
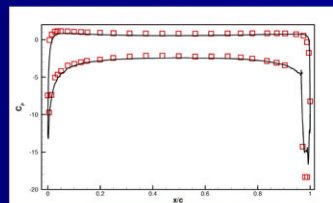


RANS Simulations



Surface Pressure

- Relatively good agreement
- Underprediction of the suction peak aft of the jet orifice
- Case 283
 - strong leading-edge low pressure
 - relatively uniform loading
 - $C_{p,min}$ is -17 and -18
- Case 321
 - lacks leading-edge low pressure
 - $C_{p,min}$ is -13 and -18





Forces and Moments

- C_l , C_d , C_m computed by integrating C_p and C_f on all external surfaces, i.e., all plenum surfaces were neglected
- Differences in sign of C_d suggest definition problem
- Given discrepancy in C_d , computation of CC efficiency is premature

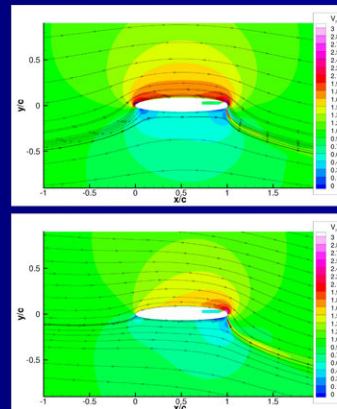
	C_l		C_d		C_m	
	Data	CFD	Data	CFD	Data	CFD
Case 283	4.2	4.0	-0.05	0.18	-	2.07
Case 321	3.1	1.9	-0.08	0.12	-	1.21

2004 NASA-ONR Circulation Control Workshop – p. 15/34



Flow Field

- Contours of velocity magnitude and streamlines
- Impact of the Coanda effect upon the overall circulation is clearly shown
- Contours are consistent with surface pressure
- Streamlines show effect of angle-of-attack and locations of stagnation points

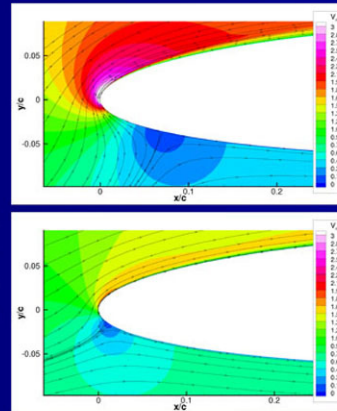


2004 NASA-ONR Circulation Control Workshop – p. 16/34



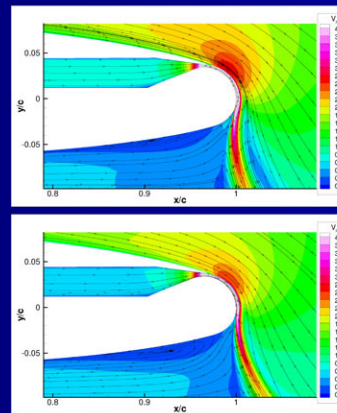
Leading-Edge Flow Field

- Case 283: stagnation point is located at $x/c = 0.07$
- Case 321, stagnation point is located at $x/c = 0.01$
- Comparing the two cases, the relative magnitudes of velocity are shown to be consistent with the differences in the leading-edge suction peak



Trailing-Edge Flow Field

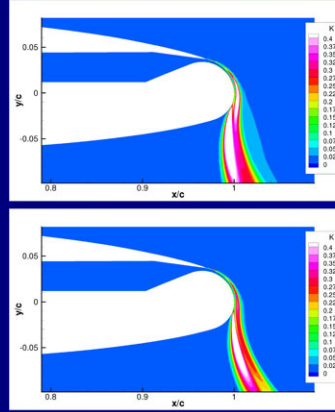
- Both cases are similar
 - high-velocity jet emanating from the plenum
 - increased velocity around the Coanda surface
 - clean jet detachment
 - flow separation on bottom surface
- For Case 283, jet stays attached longer and thickness of separated region is smaller in comparison to Case 321





Turbulence

- Contours of turbulent kinetic energy near the trailing edge
- Both cases demonstrate similar behavior
- Two primary sources of kinetic energy
 - shear-layer downstream of the jet-slot knife edge
 - shear-layer downstream of wall-jet separation
- Maximum $k \approx 0.7$, two orders-of-magnitude larger than k in the turbulent boundary layer

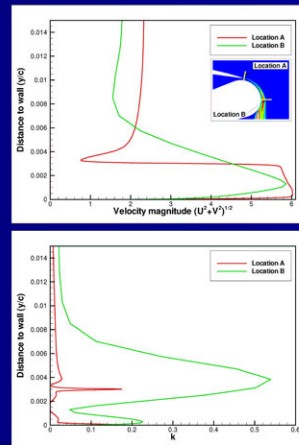


2004 NASA-ONR Circulation Control Workshop - p. 19/34



Extracted Profiles

- Location A
 - wall jet and strong shear layer are clearly shown
 - $\delta_1/R \approx 0.01$ (weak);
 - $\delta_2/R \approx 0.16$ (moderate);
 - k shows spikes downstream of the plenum walls, but jet core is \approx laminar
- Location B
 - wall-jet shape has greatly thickened
 - k has significantly grown in both magnitude and thickness



2004 NASA-ONR Circulation Control Workshop - p. 20/34



PENNSTATE

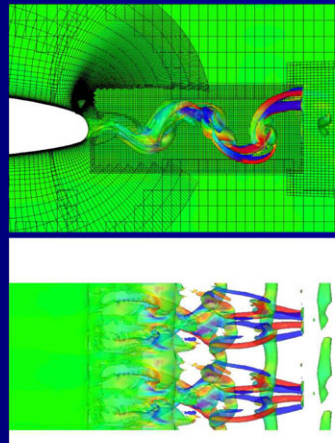


Detached-Eddy Simulation

2004 NASA-ONR Circulation Control Workshop – p. 21/34

Wake Visualization

- Iso-surface of vorticity colored by spanwise velocity
- Side view shows the dominant vortex shedding of spanwise eddies
- Top view displays longitudinal vortices
- Overset grid shows effect of switching from high-to-low grid resolution
- Spanwise structure is filtered

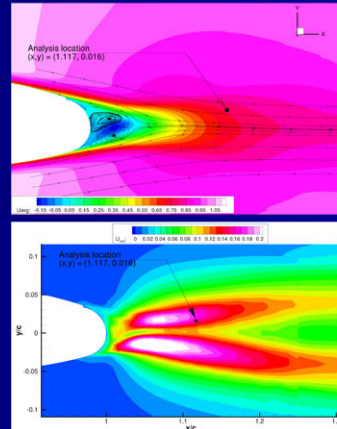


2004 NASA-ONR Circulation Control Workshop – p. 22/34



Statistical Analysis

- Mean and RMS statistics computed over 6000 time steps
- Mean field shows a typical wake with two eddies
- $\sqrt{u^2}$ shows a typical pattern with two peaks across the wake corresponding to vortices shed off the top and bottom sides of the foil
- Computed statistics were not exactly two-dimensional, indicating larger integration time needed to reduce uncertainty



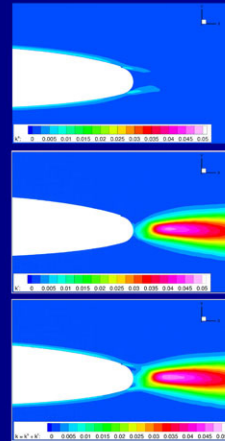
2004 NASA-ONR Circulation Control Workshop - p. 23/34



Turbulence

- Sub-grid turbulence k^s is computed from the modified $k - \omega$ turbulence model
- Resolvable turbulence is computed from the velocity correlations

$$k^r = \frac{1}{2} (\overline{uu} + \overline{vv} + \overline{ww})$$
- $k_{total} = k^s + k^r$
- k^s is significant only in the boundary layer upstream of the separation
- Downstream, k_{total} is comprised of resolvable scales only
- "Gray region" where the solution switches from RANS to LES

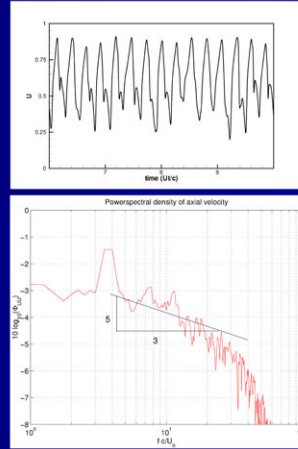


2004 NASA-ONR Circulation Control Workshop - p. 24/34



Spectral Analysis

- Analysis at $(x/c, y/c) = (1.117, 0.016)$
- Shedding frequency at $f_0^* = \frac{f c}{U_\infty} = 3.8$
- Using $d/c = 0.052$, $\tilde{f} = \frac{f d}{U_\infty} = 0.198$
- Superharmonics at $f_1^* = 7.5$ and $f_2^* = 12$, which are $2f_0^*$ and $3f_0^*$
- Decay of higher frequencies at -5/3 slope up to $f^* = 30$. Consistent with $\Delta = 0.005$ and 10 points/wavelength





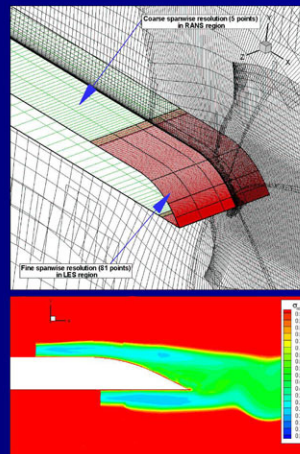
Detached-Eddy Simulation, Flat Strut

2004 NASA-ONR Circulation Control Workshop – p. 26/34



Approach

- Simulation of Blake (1977) experiment
- Extensive database for flat strut with trailing-edge variants
- Grid generation approach similar to NCCR
- Detailed study of RANS-LES transition
- To appear ASME FEDSM 2004.

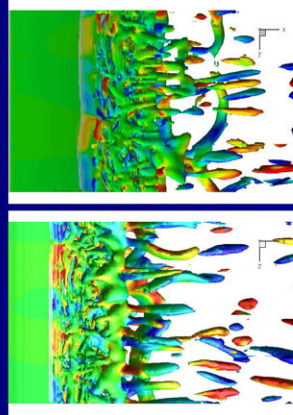
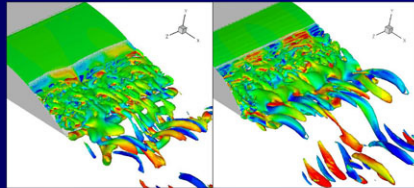


2004 NASA-ONR Circulation Control Workshop – p. 27/34



Instantaneous Flow Field

- Swirl parameter colored by helicity.
- Perspective and top views.
- "Ribs and rollers"
- Eddy length scales \propto size of separated flow region

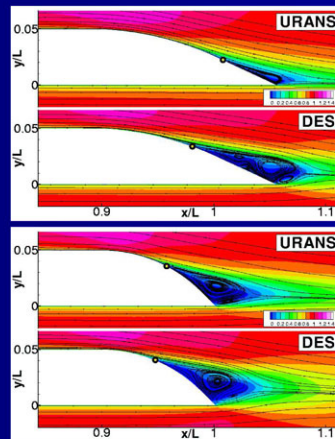


2004 NASA-ONR Circulation Control Workshop - p. 28/34



Mean Flow Field

- Statistics computed over 2000 time steps
- URANS and DES flow patterns similar
- Location and size of separated flow region: better agreement for 45° bevel than for 25° bevel
- Transition from RANS-to-LES identified as critical issue.

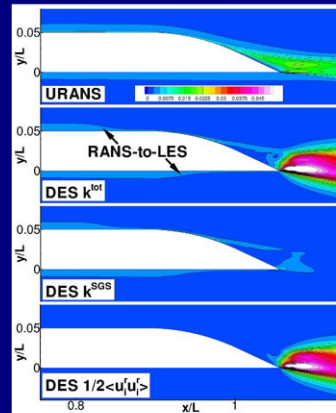


2004 NASA-ONR Circulation Control Workshop - p. 29/34



Turbulent kinetic energy

- Increase in grid resolution \Rightarrow decrease in k^s
- However, k^r does not respond instantaneously
- Model required: stochastic forcing of buffer layer, synthetic turbulence, or zonal approach
- Similar model required at LES-to-RANS locations

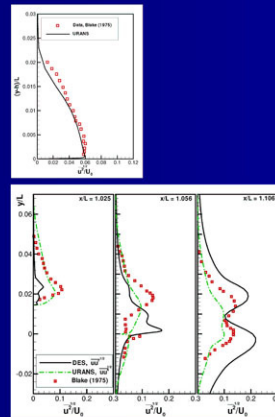


2004 NASA-ONR Circulation Control Workshop - p. 30/34



RMS Velocity, comparison to data

- Good agreement upstream of bevel
- Immediately downstream of RANS-to-LES, underprediction of $\overline{uu}^{1/2}$
- Under-resolution of k^{tot} causes premature separation and subsequent over-energization of near wake
- Nonetheless, trends and profile shapes are encouraging

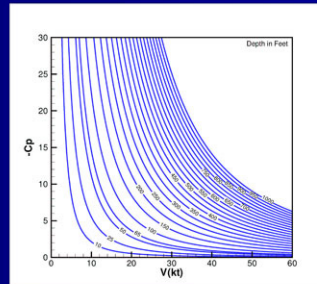


2004 NASA-ONR Circulation Control Workshop - p. 31/34



Cavitation

- Given low C_p , cavitation is a concern
- Roughly, cavitation occurs
 $-C_p \geq \sigma$
- Expression for cavitation-free operation relating $C_{p,min}$, depth z , and vehicle speed U_∞ can be derived
$$\frac{\rho g z - p_v}{\frac{1}{2} \rho U_\infty^2} = -C_{p,min}$$
- For shallow-water ops, speed must be reduced for high C_μ



Conclusions

- RANS with linear closure demonstrate relatively good performance
 - Need for higher-order RANS model unclear. Look to Chang et al. (2004) for guidance.
 - Hydroacoustics of CC requires turbulence simulation \Rightarrow DES
- DES was undertaken for the unblown NCCR and Blake's strut
 - Turbulent structures resolved
 - Transition from RANS-to-LES isolated as important issue. "Gray-region" modeling required.
 - Results nonetheless promising



Future Work

- Validation using modern benchmark experiments
 - wind-tunnel data for a pulsed CC configuration (NASA LaRC GACC Foil)
 - water-tunnel data for a low-aspect-ratio tapered control surface (NSWC-CD CC Foil)
- Understanding of basic CC flow physics
 - three-dimensional effects
 - pulsed blowing
- Prediction of flow-induced hydroacoustics using ARL CHAMP (Combined Hydroacoustic Modeling Program)

Numerical Analysis of Circulation Control on a NCCR 1510-7607N Airfoil using RANS Models

Aroon K. Viswanathan
Danesh K Tafti
Mechanical Engineering Department
Virginia Polytechnic Institute and State University
Blacksburg, VA 24061-0238

ABSTRACT

Numerical predictions of the lift augmentation and circulation control have been presented for a NCCR 1510-7607N airfoil using Reynolds-Averaged Navier Stokes (RANS) equations. Computations have been carried out for an airfoil at 0° angle-of-attack with the Reynolds number (based on chord length, c) of 5.45×10^5 . The effects of trailing edge wall jets have been studied and two different blowing rates have been simulated to show the effect of the jet momentum on the lift characteristics. Computations have been carried out for a fixed slot height ($h/c = 0.003$). Numerical solutions obtained using a $k-\omega$ RANS model are compared with experimental results. The results show very good agreement of the pressure and the lift coefficients with the experimental values, at the low blowing rate case, while showing reasonable agreement at the high blowing ratio.

INTRODUCTION

Motivation

The basic objective of circulation control is to augment the lift characteristics of the airfoil by blowing a moderate to high pressure jet of fluid through a narrow slot tangentially to the trailing edge surface. The wall jet stays attached to the

trailing edge surface and delays separation. This phenomenon due to which the fluid stays attached to the surface when injected tangentially to the surface is known as the Coanda effect. Coanda effect was discovered in the early 20th century by Henri Coanda. It has been observed by various earlier studies that irrespective of the angle of attack the lift characteristics can be controlled by adjusting the characteristics of the jet.

Experimental Studies

An extensive experimental database is available for circulation control at low Mach number (incompressible) flows. Significant augmentation in the lift characteristics has been observed by the introduction of the jet in the free-stream. The trailing edge geometry, the jet blowing coefficient and the jet slot height are observed to affect the lift characteristics.

Detailed experimental analysis of the lift characteristics in a NCCR 1510-7067N and NCCR 1510-7067S airfoils were carried out for incompressible flows by Abramson (1977). The effect of various parameters such as the trailing edge geometry, the slot height to chord ratio, angle of attack of the airfoil and the duct pressure (which directly affects the momentum of the jet) were studied. The pressure distributions and the lift coefficients obtained were used for comparison in the current simulations.

Englar *et al.* (1983, 1993) studied the effect of variations of the blowing rate, angle-of-attack, flap deflections and blowing slot heights on circulation control wing airfoils. Jones *et al.* (2002, 2003) studied the effects of the effects of dual

blowing and pulsed blowing on General Aviation Circulation Control (GACC) airfoils. Abramson (1983) studied the compressibility effects on the lift characteristics of circulation control airfoils, in transonic flows.

Computational Studies

To complement the experimental work, several computational studies have also been reported in the field of circulation control. Slomski *et al.* (2002) carried out computations on NCCR-1510N airfoils using $k-\varepsilon$, $k-\varepsilon-A$ and RSM models. The computations were carried out for various jet momentum coefficients. All the models showed good agreement for low momentum coefficients. However, at higher momentum coefficients the $k-\varepsilon$ and the $k-\varepsilon-A$ models failed to predict the flow characteristics accurately.

Liu *et al.* (2002) used the Baldwin - Lomax and Spalart - Allmaras turbulence models to study the flow in circulation control airfoils. The effect of various parameters such as angle of attack, jet momentum coefficient, jet slot height and jet free stream velocity were studied for steady and pulsed jets. Jones *et al.* (2002, 2003) also studied numerically the effects of steady and pulsed blowing on GACC airfoils. Spalart – Allmaras model was used to simulate the flow and the results when compared with the experiments showed reasonable agreement. Shrewsbury (1989) used eddy viscosity models to successfully predict the overall behavior of the jet on CCW airfoils. Promising results were also obtained by Williams *et al.* (1992) who used Baldwin - Lomax model to

study circulation control in 103RE airfoils. However most of the computations carried out in the earlier studies were for low momentum jets.

The current work is an effort to simulate the effect of a high momentum coanda jet or the wall jet on the lift characteristics of a NCCR 1510-7067N airfoil. The capability of the $k-\omega$ RANS model to predict the flow has been tested and comparisons of the pressure coefficient have been made with experimental data.

COMPUTATIONAL MODEL AND THE GOVERNING EQUATIONS

The governing flow and energy equations are non-dimensionalized by a characteristic length scale which is chosen to be the chord length (c) and a characteristic velocity scale given by the freestream velocity. Therefore the non-dimensional time dependent Navier-Stokes and energy equations in transformed coordinates are

Continuity:

$$\frac{\partial}{\partial \xi_j} (\sqrt{g} \bar{U}^j) = 0 \quad (2)$$

Momentum:

$$\frac{\partial}{\partial t} (\sqrt{g} \bar{u}_i) + \frac{\partial}{\partial \xi_j} (\sqrt{g} \bar{U}^j \bar{u}_i) = - \frac{\partial}{\partial \xi_j} \left(\sqrt{g} (\bar{a}^j)_i \bar{p} \right) + \frac{\partial}{\partial \xi_j} \left(\left(\frac{1}{\text{Re}_\tau} + \frac{1}{\text{Re}_{t\tau}} \right) \sqrt{g} g^{jk} \frac{\partial \bar{u}_i}{\partial \xi_k} \right) \quad (3)$$

where \vec{a}^i are the contravariant basis vectors¹, \sqrt{g} is the Jacobian of the transformation, g^{ij} is the contravariant metric tensor, and $\sqrt{g}U^j = \sqrt{g}(\vec{a}^j)_i u_i$ is the contravariant flux vector and u_i is the Cartesian velocity vector.

Turbulence model

***k*- ω equations (1988 Wilcox Model)**

The equations for the turbulent kinetic energy (k) and the rate of dissipation of energy per unit volume and time (ω) are:

$$\frac{\partial(k)}{\partial t} + \frac{\partial(U_j k)}{\partial x_j} = \tau_{ij} \frac{\partial U_i}{\partial x_j} - \beta^* k \omega + \frac{\partial}{\partial x_j} \left[\left(\frac{1}{\text{Re}} + \frac{\sigma^*}{\text{Re}_t} \right) \frac{\partial k}{\partial x_j} \right]$$

$$\frac{\partial(\omega)}{\partial t} + \frac{\partial(U_j \omega)}{\partial x_j} = \gamma \frac{\omega}{k} \tau_{ij} \frac{\partial U_i}{\partial x_j} - \beta \omega^2 + \frac{\partial}{\partial x_j} \left[\left(\frac{1}{\text{Re}} + \frac{\sigma}{\text{Re}_t} \right) \frac{\partial \omega}{\partial x_j} \right]$$

The turbulent kinetic energy and the dissipation rate are needed to define the eddy viscosity as

$$\frac{1}{\text{Re}_\tau} = \frac{k}{\omega}$$

The Boussinesq approximation is used to define the Reynolds stress tensor in terms of the mean strain rate tensor (S_{ij}) as

$$\tau_{ij} = \frac{2}{\text{Re}_\tau} \left[S_{ij} - \frac{1}{3} \frac{\partial U_k}{\partial x_k} \delta_{ij} \right] - \frac{2}{3} k \delta_{ij}.$$

¹ The notation $(\vec{a}^j)_i$ is used to denote the i -th component of vector \vec{a}^j . $(\vec{a}^j)_i = \partial \xi_j / \partial x_i$

The closure coefficients and the auxiliary relations are defined as

$$\begin{aligned}\gamma &= 5/9, & \beta_0 &= 3/40. \\ \beta^* &= 0.09, & \sigma &= \sigma^* = 1/2\end{aligned}$$

Boundary conditions

A no-slip boundary condition is imposed on the airfoil. The conditions set at the solid wall are:

$$\begin{aligned}\bar{u} &= 0 \\ \nabla p \cdot \bar{n} &= 0\end{aligned}$$

$k = 0$, and $\omega \rightarrow 6/\text{Re} \beta_1 y^2$ as $y \rightarrow 0$, which is derived from a molecular diffusion and dissipation balance on smooth surfaces.

Numerical method

The governing equation for momentum is discretized with a conservative finite-volume formulation using a non-staggered grid topology. The Cartesian velocities and pressures are calculated and stored at the cell center, whereas contravariant fluxes are stored and calculated at the cell faces. For the time integration of the discretized continuity and momentum equations, a projection method is used. The temporal advancement is performed in two steps, a predictor step, which calculates an intermediate velocity field, and a corrector step, which calculates the updated velocity at the new time step by satisfying discrete continuity. A third order upwind scheme is used in the momentum equation.

The equations for the turbulent kinetic energy and the dissipation rate are solved using a third order upwind scheme with a TVD limiter. Typically the k - ω equations are stiff and so the equations are rearranged to obtain a diagonally dominant system. The sink terms ($\beta^* k\omega$ and $\beta\omega^2$), in the turbulence equations are solved implicitly along with the diffusion terms. These terms fortify the diagonal of the system matrix to add stability to the system. A BiCGSTAB Krylov method is used to solve the linear system of equations.

The computer program GenIDLEST (**Generalized Incompressible Direct and Large Eddy Simulations of Turbulence**) used for these simulations has been applied extensively to study air-side heat transfer augmentation in compact heat exchangers and internal cooling of turbine blades. Details about the algorithm, functionality, and capabilities can be found in Tafti (2001).

Computational Details

A two dimensional turbulent flow is considered around an 8 inch, 15% thick cambered NCCR 1510-7067N airfoil. The airfoil is placed at an angle-of-attack of 0° . The flow Reynolds number is 5.45×10^5 based on the chord which corresponds to a Mach number of 0.12. The coanda jet or the wall jet emerges from a slot of height $h = 0.024$ inches ($h/c = 0.003$) located above the trailing edge of the airfoil ($x/c = 0.967$). The jet mass flow rate per unit span is 0.196 kg/sec/m, which corresponds to a jet momentum coefficient (C_{μ}) of 0.204. A lower mass flow rate jet is also simulated which corresponds to a C_{μ} of 0.025. A uniform flow has been specified at the plenum inlet with a TKE value equal to

10% of the free-stream value and the flow is allowed to develop into a highly turbulent jet as it exits the slot.

Computations are carried out on a domain that extends 10 chord lengths upstream and downstream of the airfoil. A structured grid (Figure 1) is used to mesh the domain. The grid consists of around 78,000 cells. An initial wall normal spacing of $(y^+_1) < 1$ is used on the airfoil and in the injection slot. The domain is divided into 23 blocks to facilitate parallel processing. The results are compared with the experimental measurements carried out by Abramson *et al.* (1977).

RESULTS AND DISCUSSION

Numerical results for the two blowing rate cases are computed using a $k-\omega$ RANS model. Figure 2 shows that the fluid gains momentum as it passes through the plenum and reaches the slot exit. As the jet exits out of the slot, it encounters the solid wall on one side and free-stream on the other side, forming a non-symmetric nozzle. The momentum of the jet keeps the inner region attached to the wall while the outer region of the jet expands out, entraining the ambient fluid. This prevents separation at the trailing edge. As the jet separates from the surface the downwash penetrates into the free-stream thereby deflecting the streamlines on the pressure side. This provides an artificial camber and shifts the stagnation point in the leading edge towards the pressure side as shown in Figure 3 and Figure 4. This shift effectively increases the angle-of-attack on the airfoil. These phenomena at the leading and the trailing edges augment the lift on the airfoil. Figure 5 shows the comparison of the pressure

coefficients on the airfoil surface. The pressure distribution shows good agreement with the experimental measurements. The airfoil sectional lift coefficient on the airfoil is observed to be $C_L = 3.60$ which agrees reasonably with the experimental values of around 4.20.

Figure 6 shows the velocity contours in the vicinity of the trailing edge and the effects of the jet on the flow in the region. The region inside the slot shows the increase in the momentum of the flow as it flows through the plenum and enters the mainstream. The low momentum fluid just upstream of the slot gets entrained by the high momentum jet resulting in an increase in the ambient fluid velocities near the slot. The momentum of the jet keeps the jet attached to the trailing edge surface while the outer region of the jet entrains the outer fluid, delaying separation.

Velocity profiles are plotted at the trailing edge at 3 locations: (a) upstream of the slot (b) at the slot exit and (c) downstream of the slot at around 90° from slot exit. The velocity profiles in Figure 7(a) show that the momentum of the fluid is low at the trailing edge. The flow inside the plenum develops and the velocity of the jet is high at the slot exit owing to the constricted slot width as shown in Figure 7(b). The smooth geometry of the airfoil at the slot exit keeps the jet attached to the surface. Figure 7(c) shows the increase in the velocities in the free shear layer of the jet and this region is observed to become thicker as the jet moves down the trailing edge owing to the entrainment of the ambient fluid.

The turbulent kinetic energy (TKE) contours in Figure 8 show the increase in the TKE values in the trailing edge owing to the presence of the jet. The contours

show the two peaks in the TKE values corresponding to the two zones in the flow – the inner region that stays attached to the wall and the outer region that interacts with the ambient fluid. As the jet flows out of the slot the TKE in the outer region increases more rapidly as compared to the near wall region, due to the interaction of the jet with the free-stream.

A comparison of the TKE values upstream and downstream of the slot shows the increase in the TKE values in the flow as a result of the jet. As the jet exits out of the plenum two peaks are observed in the regions near the plenum walls as shown in Figure 7(b). As the jet travels downstream the TKE peaks are influenced by the ambient flow and the presence of the wall. The plot of the TKE values, in Figure 7(c), downstream of the slot shows a large increase in the TKE values in the outer region as it exits from the slot. The region of the high TKE values is observed to spread outwards as the jet propagates down the trailing edge. The TKE values in the near-wall region stay fairly constant as long as the jet stays attached to the airfoil. As soon as the flow separates the TKE in this region of the jet is observed to increase significantly due to the interaction of the vertically downward moving jet with the free-stream fluid in the pressure side of the airfoil.

Computations for a lower jet momentum coefficient ($C_\mu = 0.025$) were also carried out to study the effect of the jet momentum on the lift characteristics. Figure 9 shows the TKE values and the streamlines in the trailing edge of the airfoil. The TKE values in the trailing edge region are observed to be smaller due to lesser entrainment of the ambient fluid as compared to the higher momentum

jet. The streamlines also show that the jet separates earlier at the trailing edge. Figure 10 shows that at the leading edge the stagnation point is observed to shift downwards towards the pressure side, but to a lesser extent than the earlier case studied. The pressure coefficients, shown in Figure 11, are in good agreement with the values measured in the experiments. The airfoil sectional lift coefficient (C_L) is observed to be 1.25 which is in good agreement with the experimental value of around 1.1.

CONCLUSIONS AND FUTURE WORK

The presence of the jet delays the separation at the trailing edge of the airfoil. It provides an effective camber to the airfoil resulting in a shift of the stagnation point at the leading edge towards the pressure side. These effects augment the lift of the airfoil. The momentum of the jet is observed to affect the separation at the trailing edge and consequently the lift characteristics of the airfoil. The effect of the wall jet is captured reasonably by the $k-\omega$ RANS model, for both high and low momentum jets. The lift coefficient and the pressure distribution around the airfoil show very good agreement with the experimental measurements at low blowing rates while underpredicting the lift coefficient at high blowing rates.

Based on these preliminary computations it is proposed to extend the work to Large Eddy Simulations (LES). LES would provide a comprehensive knowledge of the mean and the turbulence characteristics of the flowfield. It is also proposed to extend the scope of this work to pulsed jets using both RANS as well as LES.

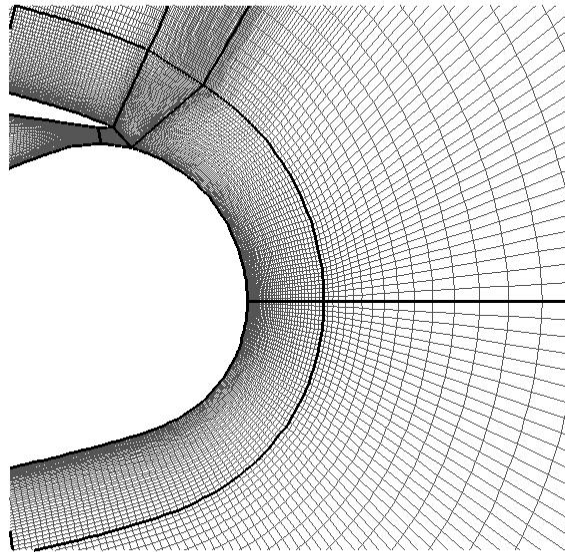
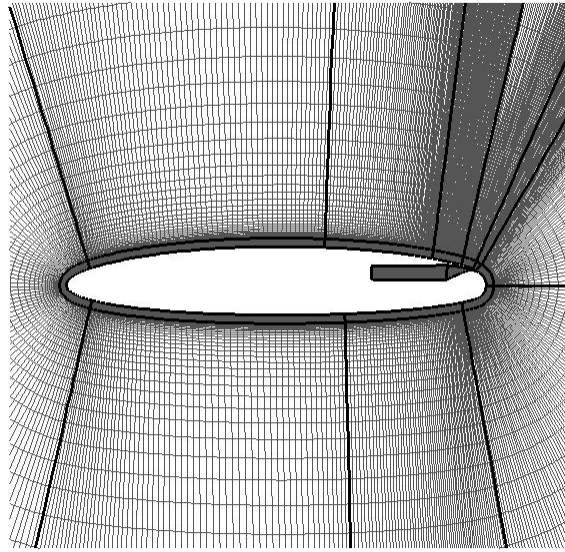


Figure 1: NCCR 1510-7067N Airfoil grids (a) complete airfoil (b) Grids in the vicinity of the slot exit.

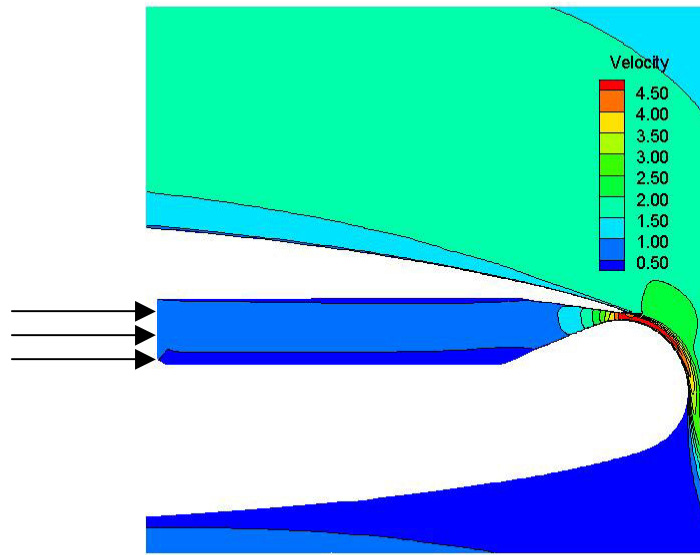


Figure 2: Development of the uniform flow in the plenum into a turbulent flow in the slot exit.

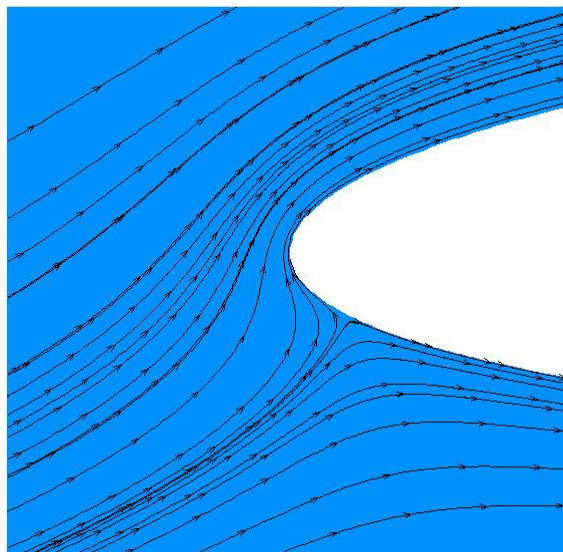


Figure 3: Effect of the Coanda jet on the stagnation point in the leading edge.

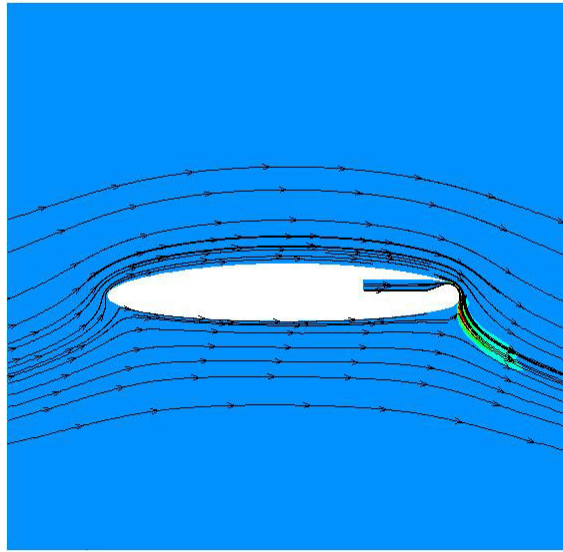


Figure 4: Complete flow field around the airfoil. The trailing edge wall jet augments the lift in the airfoil.

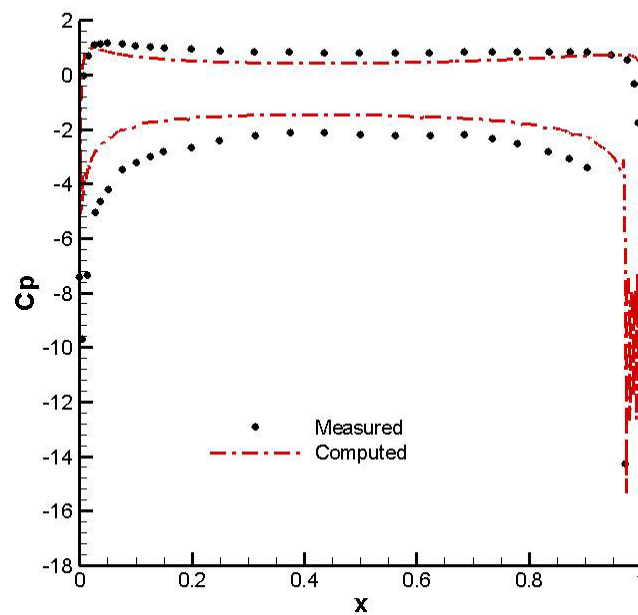


Figure 5: Comparison of the pressure coefficient around the airfoil for the jet momentum coefficient of 0.204.

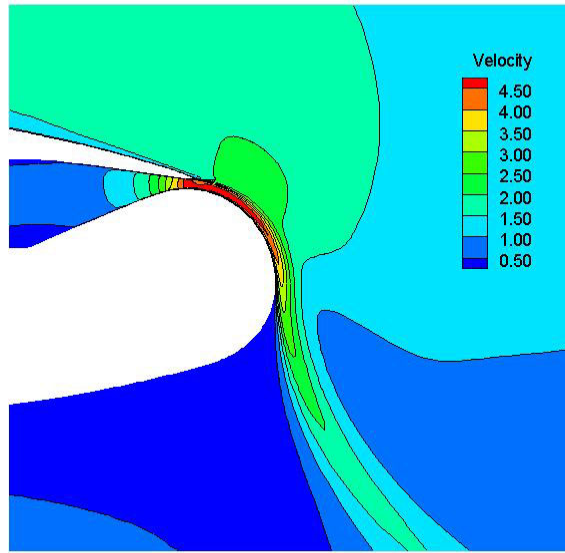
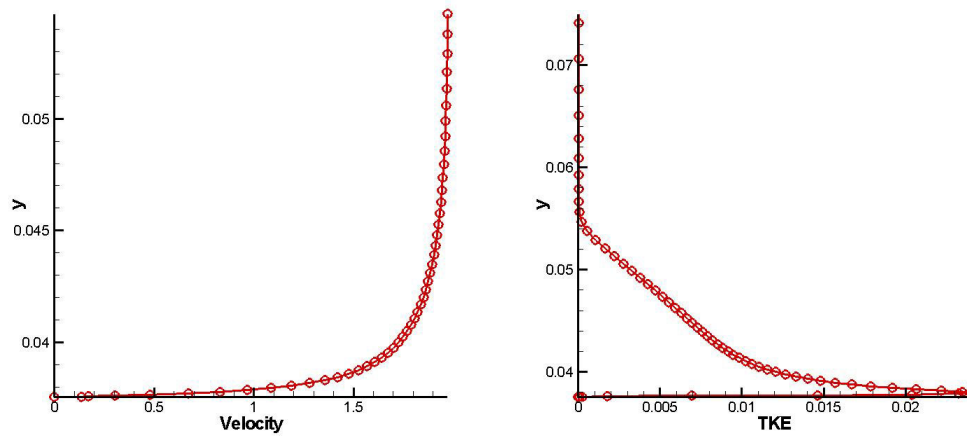
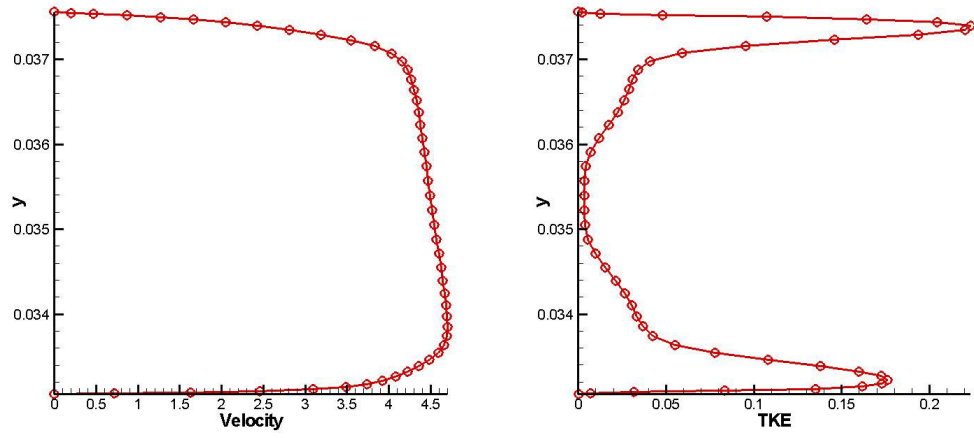


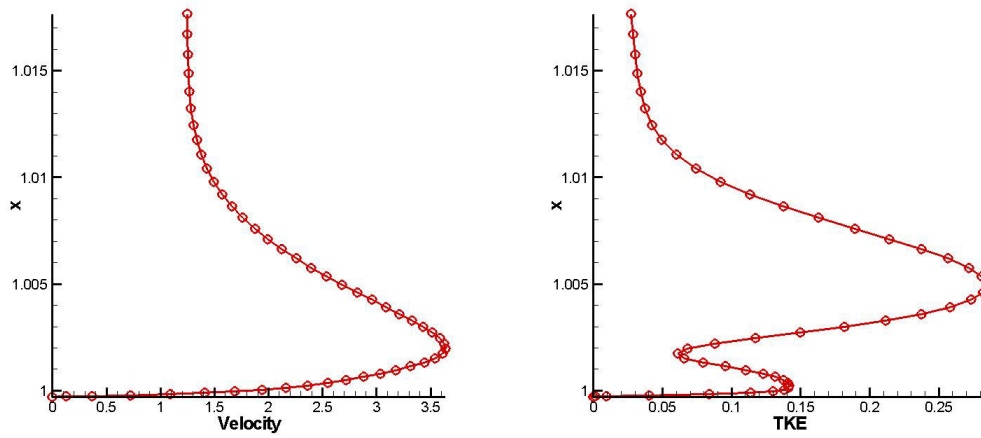
Figure 6: Velocity contours in the trailing edge for $C_\mu = 0.204$. The entrainment of the ambient fluid by the jet prevents the flow separation.



(a)



(b)



(c)

Figure 7: Velocity and TKE values (a) upstream of the slot (b) At the slot exit (c) downstream of the slot (90 degrees from slot exit)

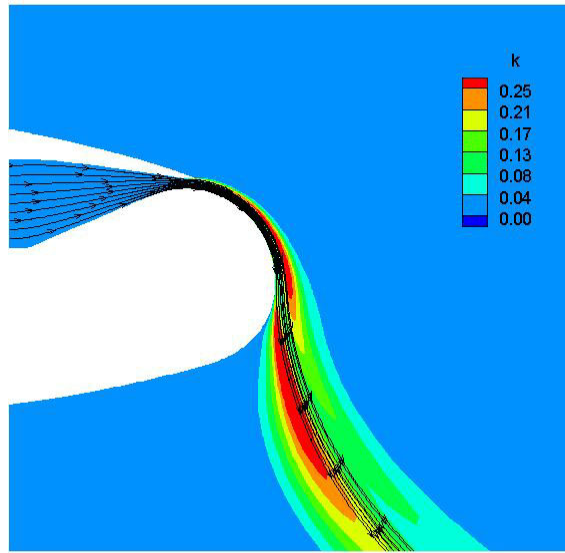


Figure 8: TKE contours and streamlines in the trailing edge of the airfoil.

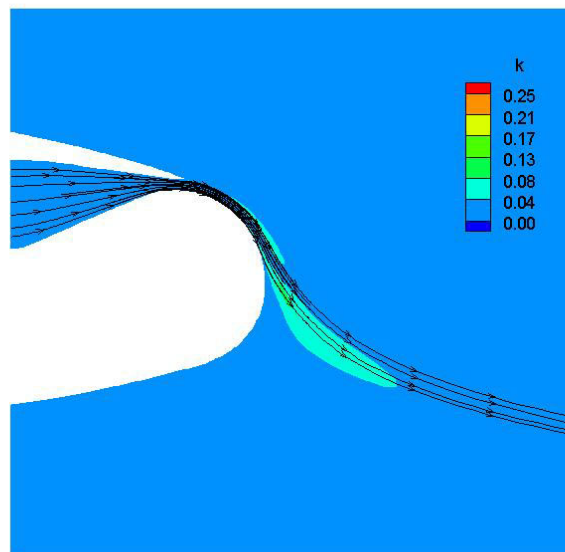


Figure 9: TKE contours and streamlines for a low momentum jet.

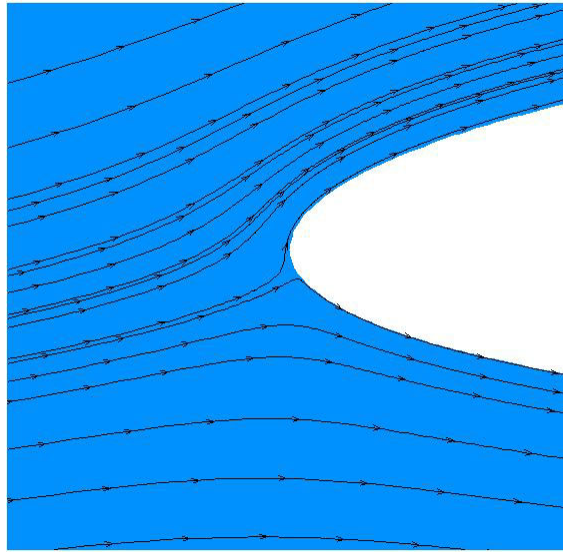


Figure 10: Effect of the Coanda jet on the stagnation point in the leading edge of the airfoil for $C_\mu = 0.025$.

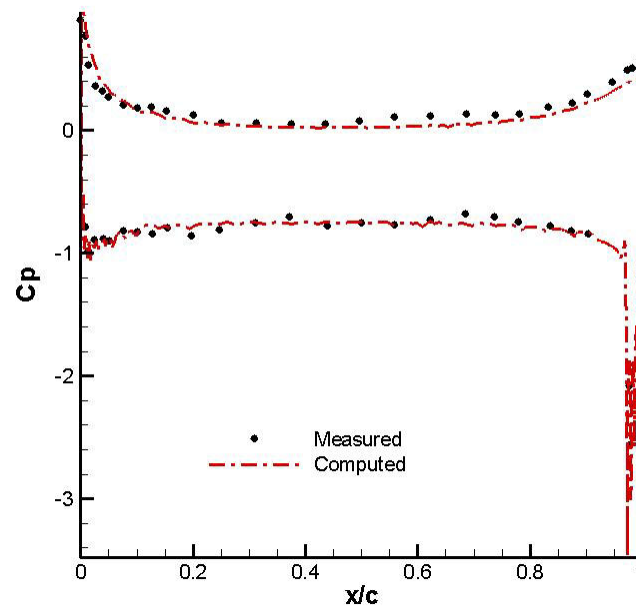


Figure 11: Comparison of pressure coefficients around the airfoil for a blowing rate (C_μ) of 0.025

REFERENCES

1. Abramson. J., "Two-dimensional Subsonic Wind Tunnel Evaluation of Two Related Cambered 15-percent thick Circulation Control Airfoils", DTNSRDC ASED-373, September 1977.
2. Englar. R.J., Smith. M.J., Sean. M., River. R.C III, "Application of Circulation Control to Advanced Subsonic Transport Aircraft, Part I: Airfoil Development", Journal of Aircraft, Vol 31, No. 5, pp 1160-1168, Sep 1994.
3. Englar. R.J., Smith. M.J., Sean. M., River. R.C III, "Application of Circulation Control to Advanced Subsonic Transport Aircraft, Part II: Airfoil Development", Journal of Aircraft, Vol 31, No. 5, pp 1169-1177, Sep 1994.
4. Jones. G.S., Viken. S.A., Washburn. A.E., Jenkins. L.N., Cagle. C.M., "An Active Circulation controlled Flap Concept for General Aviation Aircraft Applications", AIAA 2002-3157.
5. Cagle. C.M., Jones. G.S., "A Wind Tunnel Model to Explore Unsteady Circulation Control for General Aviation Applications", AIAA 2002-3240, June 2002.
6. Jones. G.S., Englar. R.J., "Advances in Pneumatic-Controlled High Lift Systems through Pulsed Blowing", AIAA 2003-3411.
7. Abramson. J., Rogers. E.O., "High-Speed Characteristics of Circulation Control Airfoils", AIAA 83-0265, January 1983.
8. Slomski. J.K., Gorski. J.J., Miller. R.W., Matino. T.A., "Numerical Simulation of Circulation Control Airfoils as Affected by Difference Turbulence Models", AIAA 2002-0851, January 2002.

9. Liu. Y., "Numerical Simulation of the Aerodynamic Characteristics of Circulation Control Wing Sections", Ph. D Thesis, Georgia Institute of Technology, April 2003.
10. Shrewsbury. G.D., "Numerical Study of a Research Circulation Control Airfoil Using Navier-Stokes Methods", *Journal of Aircraft*, Vol 26, No.1, pp 29-34, 1989.
11. Williams. S.L., Franke. M.E., "Navier-Stokes Methods to Predict Circulation Control Performance", *Journal of Aircraft*, Vol. 29, No. 2, pp 243-249, March – April 1992.
12. Wilcox, D.C., Reassessment of the Scale-Determining Equation for Advanced Turbulence Models, *AIAA Journal*, Vol 26 (11), pp 1299-1310. Nov 1988.
13. Tafti, D.K., GenIDLEST – A Scalable Parallel Computational Tool for Simulating Complex Turbulent Flows, Proc. ASME Fluids Engineering Division, FED – Vol. 256, ASME-IMECE, New York, 2001.

Numerical Analysis of Circulation Control on a NCCR 1510-7607N Airfoil using RANS Models

Aroon K Viswanathan

Danesh K Tafti

Virginia Polytechnic Institute and State University



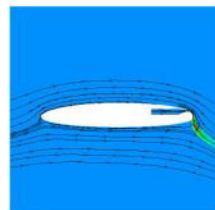
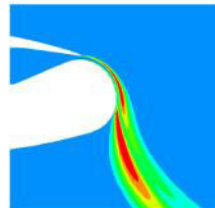
2004 Circulation Control Workshop
March 16 - 17, 2004
Raglan Hotel
Hampton, VA



High Performance Computational Fluid-Thermal Sciences & Engineering Lab

Outline

- Objective
- Coanda Effect
- Geometry and Grid
- Flow conditions
- Flow solver
- Computational details
- Results
- Conclusions



High Performance Computational Fluid-Thermal Sciences & Engineering Lab

Objectives and scope of the study

- **Simulate the effect of a coanda jet (wall jet) on the lift characteristics of a NCCR 1510-7067N airfoil.**
- **Preliminary studies carried out with RANS models are reported.**
- **Comparison with experimental data from Abramson (1977).**
- **Qualitative comparisons of the effect of the characteristics of the jet on the point of separation.**
- **Future implementation using LES based on the results.**



High Performance Computational Fluid-Thermal Sciences & Engineering Lab

Coanda Effect - Discovery by accident

- **Discovered by Henri-Marie Coanda**
 - Discovered while testing an aircraft without propellers (COANDA-1910).
 - Observed that the flames from the engine adhered to the sides of aircraft.
- **Tendency of moving fluid to stay attached to surface.**
- **Phenomena used to partially explain lift in airfoils.**



High Performance Computational Fluid-Thermal Sciences & Engineering Lab

Characteristics of Coanda Jets

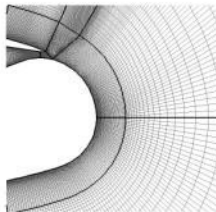
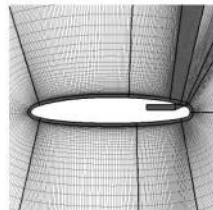
- **Highly turbulent jets generated by blowing moderate to high pressure fluids through a narrow slot over a surface.**
- **The jet has a wall on one side and a free shear layer on the other, forming a non-symmetrical nozzle.**
- **The smoothness of the geometry keeps the jet attached to the surface.**
- **Point of separation depends on the characteristics of the jet.**
- **Entrainment of ambient air is also greater than a conventional symmetric jet.**



High Performance Computational Fluid-Thermal Sciences & Engineering Lab

Geometry and Grid

- **NCCR 1510-7067N airfoil**
- **8 inch cambered elliptical section**
- **Thickness-to-chord ratio – 15%**
- **Blowing slot (x/c) = 0.967**
- **Slot height to chord ratio (h/c) = 0.003**



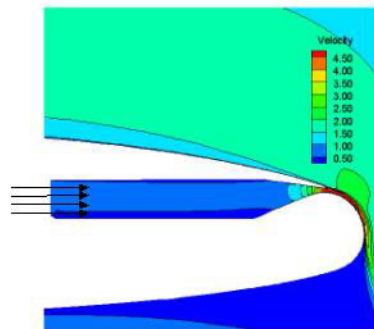
- **Domain extends 10 chord lengths upstream and downstream of the airfoil.**
- **Structured Grid – 78,000 cells**
- **$\Delta y^+_1 < 1$**
- **Domain discretized into 23 blocks.**



High Performance Computational Fluid-Thermal Sciences & Engineering Lab

Flow Conditions

- Bulk Reynolds number (based on chord length) – 5.45×10^5
- Angle of attack – 0.0°
- Jet mass flow rate per unit span – 0.196 kg/sec/m
- Jet blowing coefficient (C_m) – 0.209
- Uniform velocity specified at the slot inlet.
- Turbulence intensity (u_{rms}/u_∞) of the jet – 19.4%
(Value used in computation)



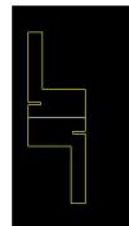
Velocity contours inside and in the vicinity of the slot



High Performance Computational Fluid-Thermal Sciences & Engineering Lab

Generalized Incompressible Direct and Large Eddy Simulations of Turbulence (GenIDLEST)

- Non-staggered finite volume code used to solve turbulent flows in complex geometries.
- Time integration
 - Unsteady problems : Fractional step algorithm used with explicit and semi-implicit time advancement.
 - Steady problems : Pseudo-compressibility.
- Applications – multi-louvered fins, internal cooling of turbine blades, electro-kinetics/MHD, applications for micro-fluidic chips.



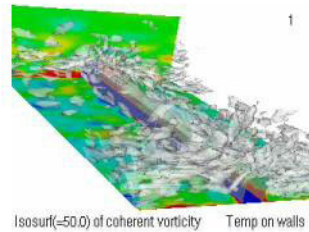
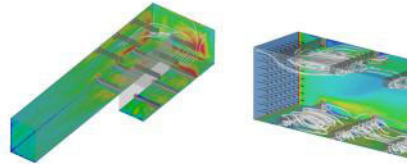
Electrokinetic micro-mixing



High Performance Computational Fluid-Thermal Sciences & Engineering Lab

Capabilities of GenIDLEST

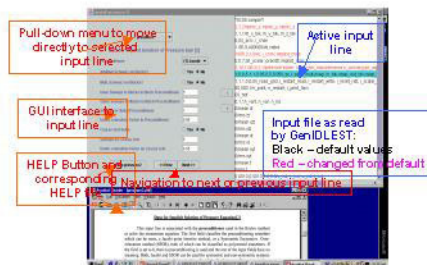
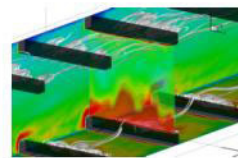
- **Parallel processing for maximum portability.**
- **Load balancing capabilities.**
 - Binary dissection algorithm
 - Genetic algorithm
- **Convection term discretizations.**
 - Second Order Central difference
 - Third order Upwind biased Approximation
 - TVD and Universal limiters
- **Turbulence modeling**
 - LES
 - Smagorinsky Eddy Viscosity
 - Germano's Dynamic Model
 - RANS, DES
 - $k-\omega$ – 1988, 1994, 1998
 - Menter's BSL, SST



High Performance Computational Fluid-Thermal Sciences & Engineering Lab

Capabilities of GenIDLEST

- **Linear System Solvers**
 - Krylov Methods
 - Conjugate Gradient
 - BiCGSTAB
 - GMRES(m)
 - Preconditioners (based on 2 level additive or multiplicative Schwarz domain decomposition)
 - Jacobi
 - SSOR
 - Störmer strongly implicit
- **Vortex identification methods incorporated.**
- **Capability to handle non-matching or non-conformal boundaries.**
- **GUI used to create the input file.**



High Performance Computational Fluid-Thermal Sciences & Engineering Lab

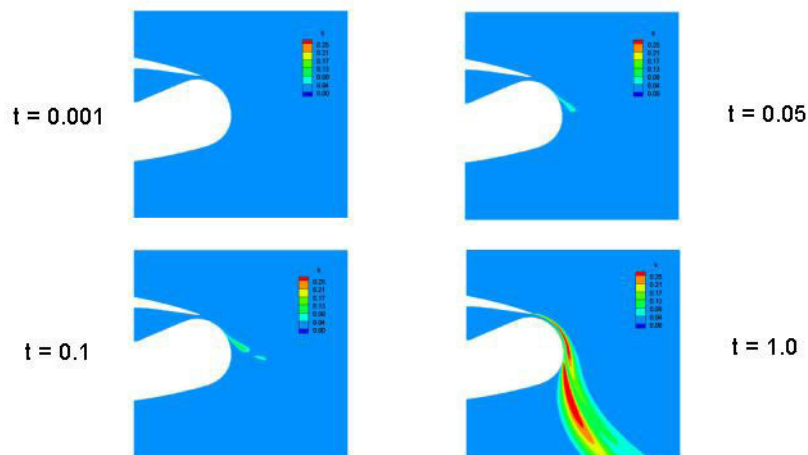
Computational Details

- **Semi-implicit solution of the pressure and the momentum equations.**
- **A third-order upwind scheme with TVD used for computations.**
- **k- ω and Menter's SST RANS models used for closure.**
- **BICGSTAB used to solve the linear systems.**
- **Genetic algorithm used to distribute blocks evenly to the processors.**



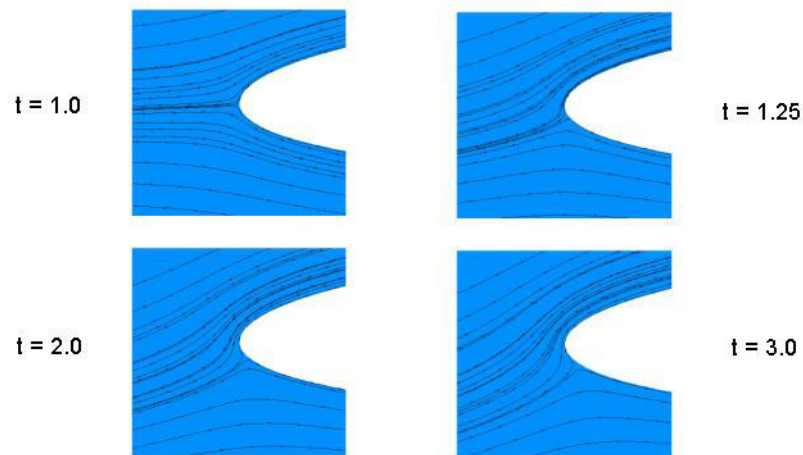
High Performance Computational Fluid-Thermal Sciences & Engineering Lab

TKE contours showing the evolution of the jet



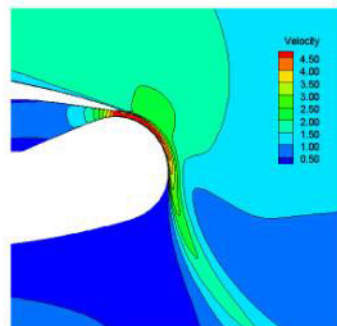
High Performance Computational Fluid-Thermal Sciences & Engineering Lab

Effect of the jet on the stagnation point

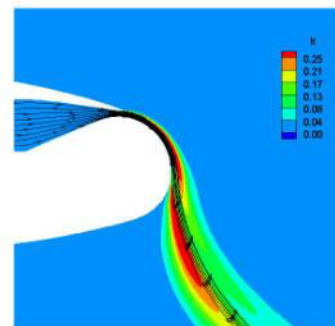


High Performance Computational Fluid-Thermal Sciences & Engineering Lab

Effect of the jet on the velocities and the TKE near the aft-body



Velocity contours near the jet

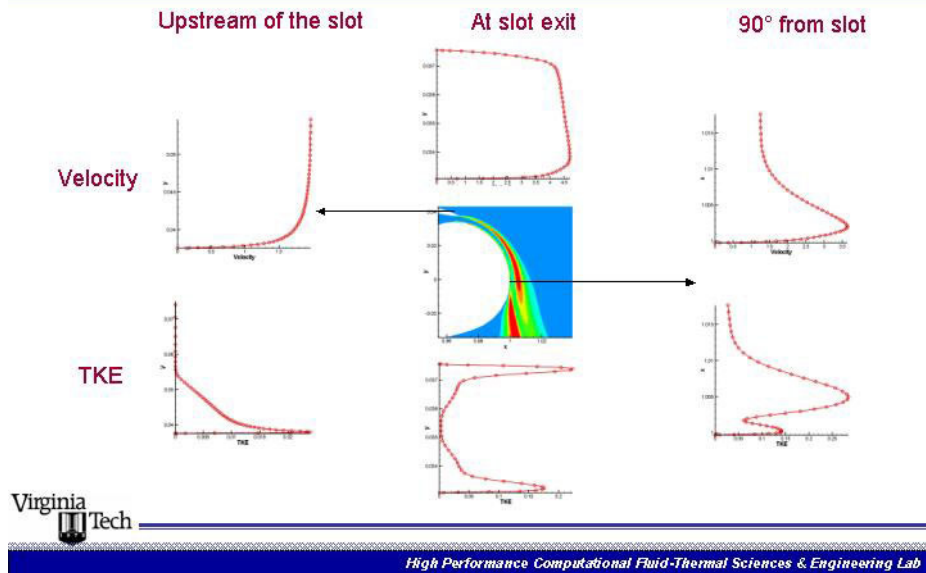


TKE contours and streamlines of the jet

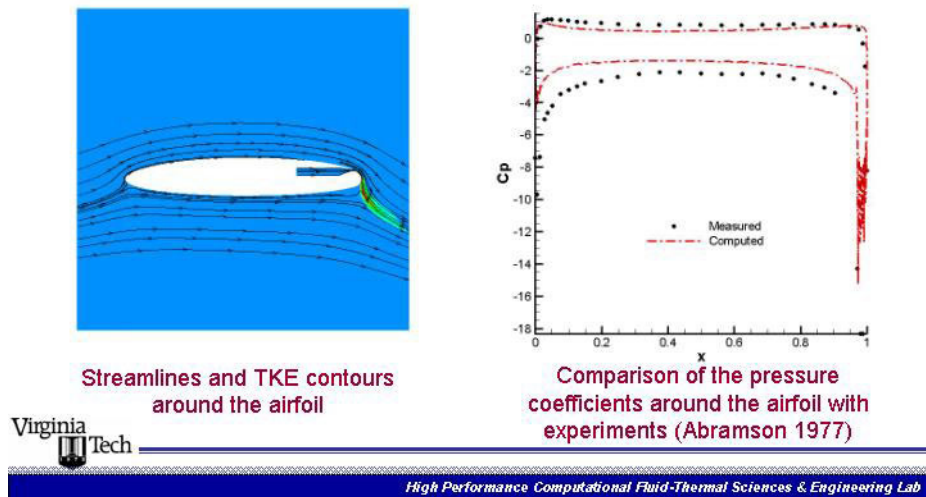


High Performance Computational Fluid-Thermal Sciences & Engineering Lab

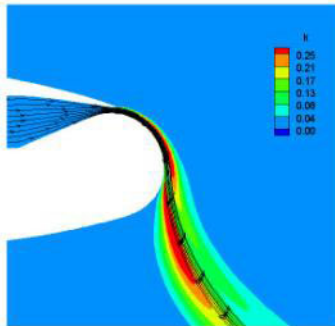
Effect of the jet near the wall



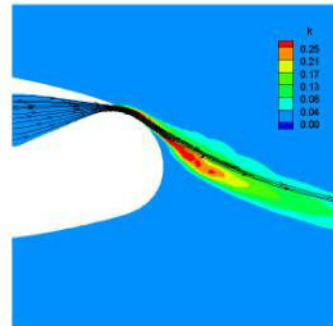
Overall effect of the jet on the airfoil



Comparison of the flow predicted by the turbulence models



Streamlines and TKE for the k- ω (1988) RANS case

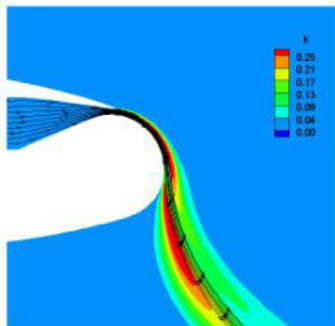


Streamlines and TKE for the Menter's SST case

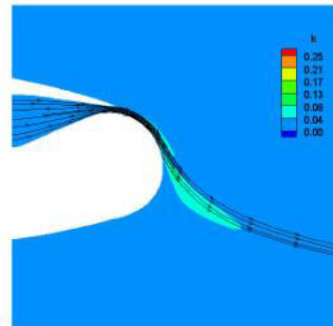


High Performance Computational Fluid-Thermal Sciences & Engineering Lab

Effect of the variation of the jet momentum on the point of separation



TKE for the High blowing rate ($C_m = 0.208$) case



TKE for the Low blowing rate ($C_m = 0.052$) case



High Performance Computational Fluid-Thermal Sciences & Engineering Lab

Conclusions

- Presence of the jet prevents the flow separation behind the airfoil and increases the lift.
- The effects of the coanda jet on the flow is predicted reasonably well by the k- ω model, but the SST predictions fail to reproduce the effect.
- Point of separation affected by the momentum of the jet.
- Ongoing computation on a denser grid (140,000 cells) using k- ω RANS model.



High Performance Computational Fluid-Thermal Sciences & Engineering Lab

Future work

- Computations using LES - Finer grid resolution near the walls, both in stream-wise direction and the wall normal direction. Estimated grid size – 15-20 million
 - Need detailed experimental measurements of mean and turbulent flow field for validation.
- Virginia Tech's Terascale computing facility and NCSA's Teragrid will be used for computations.
- Effects of 3D wall jets and other separation control mechanisms.



Virginia Tech's
Terascale Computing
Facility



QUESTIONS?

High Performance Computational Fluid-Thermal Sciences & Engineering Lab

Aspects of Numerical Simulation of Circulation Control Airfoils

R. C. Swanson, C. L. Rumsey, S. G. Anders
NASA Langley Research Center
Hampton, VA

Abstract

The mass-averaged compressible Navier-Stokes equations are solved for circulation control airfoils. Numerical solutions are computed with a multigrid method that uses an implicit approximate factorization smoother. The effects of flow conditions (e.g., free-stream Mach number, angle of attack, momentum coefficient) and mesh on the prediction of circulation control airfoil flows are considered. In addition, the impact of turbulence modeling, including curvature effects and modifications to reduce eddy viscosity levels in the wall jet (i.e., Coanda flow), is discussed. Computed pressure distributions are compared with available experimental data.

Introduction

Conventional high-lift systems use slats and flaps to create the necessary airfoil camber to achieve the desired circulation, and thus lift. There is a weight penalty and increased maintenance associated with these systems. For a number of years [1] aerodynamicists have been seeking alternative high-lift systems that can reduce the weight and complexity of the conventional systems. One such system for circulation control (CC) involves the Coanda effect. By controlling a jet discharged from a slot on the upper surface of the airfoil, the trailing edge stagnation point is moved forward on the lower surface, and the leading edge stagnation point is moved rearward. In this way the effective camber of the airfoil can be increased, resulting in the augmentation of lift. Previously, the weight and operational requirements of such systems have been unacceptable. The potential benefits of these CC systems in terms of reduced take-off and landing speeds as well as increased maneuverability have encouraged aerodynamicists to reconsider such systems. Moreover, the benefits of using pulsed jets offer the genuine possibility of significantly mitigating the obstacles preventing the implementation of these CC systems [2].

Computational methods will play a vital role in designing effective CC configurations. Certainly, detailed experimental data, such as velocity profiles and Reynolds stresses, will be absolutely essential for validating these prediction tools. Due to the cost of flow control experiments, design and parametric studies will strongly depend on accurate and efficient prediction methods. These methods must have the potential to treat pulsating jets, even multiple jets, for a broad range of flow conditions (e.g., Mach number, Reynolds number, angle of attack). In general, the numerical methods must be extendable to time-dependent and three-dimensional flows.

A number of computational methods have been applied to CC airfoil flows. In 1985 Pulliam et al. [3] used ARC2D [4], an implicit Navier-Stokes solver, to compute solutions for two of the CC configurations tested by Abramson and Rogers [5]. A spiral grid that begins in the plenum and wraps around the airfoil several times was used for the computations. Turbulence modeling of the flow over the airfoil and Coanda surface was done by applying a modified form of the zero-equation model of Baldwin and Lomax [6]. A term was introduced in the model to account for streamline curvature effects. The modification includes a constant C_c . This constant was modified for each set of experimental conditions, and a set is defined by Coanda geometry, free-stream Mach number (M_∞), angle of attack (α), and a range of jet momentum coefficient C_μ . The C_c was adjusted so that the computed C_L matched the experimental value for one of the C_μ values. Then this C_c was used in computing all of the cases for the given set of conditions. Certainly, this approach is not satisfactory in general for modeling the turbulence. Nevertheless, Pulliam et al. were able to obtain good comparisons with experimental data for all cases considered. This work demonstrated that accurate Navier-Stokes simulation of CC airfoil flows is possible, and turbulence modeling is the key issue.

In 2002 Slomski et al. [7] considered the effects of turbulence modeling on the prediction of CC airfoil flows. Calculations were performed for the NCCR 1510-7067 airfoil, which is a cambered, 15 percent thick, CC airfoil with a jet slot located on the upper surface just upstream of the trailing edge. The airfoil was at zero degree angle of attack. Two variations of a two-equation transport model ($k - \epsilon$ model) and a Reynolds stress model were used for modeling turbulence. Predictions of surface pressures with the two-equation model compared favorably with the experimental data at low blowing rates. At high rates of blowing only the Reynolds stress model provided predictions that compare well with the data. A principal conclusion of Slomski et al. is that non-isotropic turbulence models are probably required for the simulation of circulation control airfoils or lifting surfaces.

Recently, Paterson and Baker [8] used an incompressible Navier-Stokes code to calculate the flow over the same CC airfoil considered by Slomski et al. They obtained solutions for the high blowing rate case that Slomski et al. computed and a case with the same free-stream conditions but an α of -8 degrees. The shear stress transport (SST) model of Menter [16] was used to model turbulence. Using this isotropic turbulence model their predicted surface pressure distributions compared favorably with experiment, even though an incompressible simulation was performed. However, it should be pointed out that the variation in the ratio of the jet density to the free-stream density for the α of zero degree case can vary roughly from 0.8 to 1.2. Thus, there are compressibility effects, and these may be quite important when attempting to predict the characteristics of the jet.

In the current work various aspects of simulating CC airfoil flows are examined. These aspects include the following: 1) flow conditions, 2) grid density, 3) turbulence modeling. The primary purpose of this paper is to provide some guidelines for accurate solutions and to delineate improvements needed in numerical techniques to reliably predict CC flows, eventually including pulsed jets. The compressible, mass-averaged Navier-Stokes equations are solved with a finite-volume approach for discretization. The equations are solved on a multi-block, patched grid, and a multigrid method with an implicit approximate factorization scheme is used to integrate the equations. Numerical solutions are obtained for flow over the CC geometry tested by Abramson and Rogers [5]. Several turbulence models are considered, including models based on one transport equation and two transport equations. A two-equation explicit algebraic Reynolds stress model is also considered. The influence of turbulence modeling is revealed by comparing computed and experimental pressure

Case	M_∞	Re_c	α (deg.)	C_μ
302	0.6	5.2×10^6	0	0.0032
283	0.12	5.45×10^5	0	0.2090
321	0.12	5.45×10^5	-8	0.1840

Table 1: Flow conditions for CC airfoil flows.

distributions, as well as Coanda jet streamlines.

The initial sections of the paper concern the CC airfoil geometry and flow conditions, description of grids, numerical method, and boundary conditions. This is followed by a section on turbulence modeling, where particular emphasis is given to modifications introduced into the models, and also, implementation details of the models that can significantly affect their performance. In the final sections the numerical results are discussed and concluding remarks are given.

Geometry and Grid

The CC geometry for the 2004 Circulation Control Workshop held at NASA Langley Research Center is the CC elliptical airfoil, which is designated NCCR 1510-7067N. This airfoil has a chord of 8 inches, thickness ratio of 15 percent, and a camber ratio of 1 percent. The jet slot height-to-chord ratio is 0.0030, which corresponds to a slot height of 0.024 inches.

Previously, we performed calculations for the CC airfoil which was tested by Abramson and Rogers [5]. This airfoil, which is designated as 103RE, has a chord of 18 inches, thickness ratio of 16 percent, and a camber ratio of 1 percent. The jet slot height-to-chord ratio is 0.0021, which corresponds to a slot height of 0.0378 inches. This CC airfoil is compared with the NCCR 1510-7067N airfoil in Fig. 1. The most significant differences between the two configurations are the size of the plenum and the jet slot height. Since the computational grid for the 103RE airfoil was available, and this geometry is quite similar to the one of the workshop, we elected to use the 103RE airfoil in simulating the workshop cases. In order to compute solutions for the workshop cases, we applied the free-stream conditions for these cases and matched the corresponding jet momentum coefficients.

In this paper we consider CC airfoil flows for high and low free-stream Mach numbers. The designated case numbers, which are associated with the experiments, and the flow conditions are given in Table 1. The definition of C_μ is given in a later section. For Case 302 the testing was done by Abramson and Rogers [5], and for Cases 283 and 321 the experimental data was obtained by Abramson [9]. Surface pressure distributions are available from the experiments. There are no velocity profiles or Reynolds stresses to allow a detailed assessment of turbulence models. Nevertheless, pressure data provides an opportunity for initial evaluation of the models. The experimental lift coefficients were determined by integrating the surface pressures, and the drag coefficients were computed from wake survey data using a momentum deficit method. Thus, the drag values include the propulsion effects due to the Coanda jet. Several sources of error in the experimental data were reported by Abramson [9]. While the experiments were generally two dimensional, there were three-dimensional effects produced at the high blowing rates. Also, there

were changes in the slot height caused by the higher pressures required for the high blowing rates. We have not accounted for these effects on the experimental data.

For the numerical computations the domain surrounding the CC airfoil extended 20 chords away from the airfoil. This domain was partitioned with three blocks. At the interface boundary on the lower airfoil surface the grid is patched, as seen in Fig. 2, which displays the near field of a medium resolution grid. This grid includes 235 grid points around the airfoil and 49 points in the normal direction over the forward part of the airfoil. Over the aft part of the airfoil there are 101 points in the normal direction, and this number includes the points in the plenum for the jet. For the fine grid the number of cells in the medium grid is doubled in each coordinate direction, resulting in 70,563 points. The clustering of the grid at the airfoil leading edge and jet slot is clearly seen in Fig. 3 and Fig. 4. In the normal direction the grid is clustered at the surface so that the normalized coordinate y^+ is less than one for the first point off the wall. The quantity y^+ is defined by $y\sqrt{\tau_w/\rho}/\nu$, where τ_w is the shear stress at the wall, ρ is density, and ν is the kinematic viscosity.

Numerical Method

Numerical solutions were computed with CFL3D, a multi-zone mass-averaged Navier-Stokes code developed at NASA Langley [10]. It solves the thin-layer form of the Navier-Stokes equations in each of the (selected) coordinate directions. It can use one-to-one, patched, or overset grids, and employs local time step scaling, grid sequencing, and multigrid to accelerate convergence to steady state. In time-accurate mode, CFL3D has the option to employ dual-time stepping with subiterations and multigrid, and it achieves second-order temporal accuracy.

The code CFL3D is based on a finite-volume method. The convective terms are approximated with third-order upwind-biased spatial differencing, and both the pressure and viscous terms are discretized with second-order central differencing. The discrete scheme is globally second-order spatially accurate. The flux difference-splitting (FDS) method of Roe is employed to obtain fluxes at the cell faces. Advancement in time is accomplished with an implicit approximate factorization method (number of factors determined by number of dimensions).

In CFL3D, the turbulence models are implemented uncoupled from the mean-flow equations. The turbulent transport equations are solved using a two-factor implicit approximate factorization approach. The advection terms are discretized with first-order upwind differencing. The production source term is treated explicitly, while the advection, destruction, and diffusion terms are treated implicitly. For the explicit algebraic Reynolds stress (EASM-ko) model, the nonlinear terms are added to the Navier-Stokes equations explicitly.

Boundary and Initial Conditions

Boundary conditions are required at the inflow (internal and external), outflow, and solid surface boundaries. For numerical computations the physical boundary conditions must be supplemented with numerical boundary conditions, which generally involve extrapolation of flow quantities or combinations of them (e.g., Riemann invariants) from the interior of the domain. Discussion of the numerical boundary conditions is given in the user's manual for CFL3D [10]. At the far-field inflow boundary a Riemann invariant, entropy, and flow inclination angle are specified. A Riemann

invariant is specified at the far-field outflow boundary. For the plenum the mass flow rate and flow inclination angle are prescribed. If the mass flow rate is not known from the experiment, it is determined with an iterative process where it is changed until the experimental C_μ at the jet exit is matched. At the surface boundaries the no-slip and adiabatic wall conditions are specified. Boundary conditions for the various turbulence models considered herein are given in [10]. The initial solution is defined by the free-stream conditions.

Turbulence Modeling

Several turbulence models for computing CC airfoil flows are considered. The three principal models are the one-equation Spalart-Allmaras (SA) model [11], the Spalart-Allmaras rotation/curvature (SARC) model [12, 13], and the two-equation shear-stress transport (SST) model of Menter [14, 15, 16]. In addition, the zero-equation Baldwin-Lomax (BL) model [6] and the explicit algebraic stress (EASM) model in k - ω form (EASM-ko) [17] are used. The three primary models and the BL model are all linear eddy-viscosity models that make use of the Boussinesq eddy-viscosity hypothesis, whereas the EASM-ko model is a nonlinear model. The equations describing these four models can be found in their respective references. However, there are certain details concerning the implementation of the SARC and SST models that should be given here in order to facilitate the discussion of the numerical results.

The SA model can be written in general form as

$$\frac{D\tilde{\nu}}{Dt} = \mathcal{P} + \mathcal{D}_{diff} + \mathcal{D}_{diss} \quad (1)$$

where $\tilde{\nu} \sim \nu_t$, and \mathcal{P} , \mathcal{D}_{diff} , and \mathcal{D}_{diss} are the contributions associated with turbulence due to production, diffusion, and dissipation, respectively. The production term is given by

$$\mathcal{P} = c_{b1}[1 - f_{t2}]W\tilde{\nu}. \quad (2)$$

In the SARC model \mathcal{P} is replaced by

$$\mathcal{P}' = c_{b1}[f_{r1} - f_{t2}]W\tilde{\nu}, \quad (3)$$

$$f_{r1} = (1 + c_{r1})\frac{2r^*}{(1 + r^*)} [1 - c_{r3}\tan^{-1}(c_{r2}\tilde{r})] - c_{r1}, \quad (4)$$

where the function r^* is the ratio of scalar measure of strain rate to the scalar measure of rotation, the function \tilde{r} depends on the Lagrangian derivative of the strain-rate tensor principal axes angle (see [13] for details), and $c_{r1} = 1$, $c_{r2} = 12$, and $c_{r3} = 0.6 - 1.0$. As c_{r3} is increased, the turbulence production will decrease near convex surfaces. Later, we will exploit this behavior to reduce the production of turbulence in the Coanda flow.

The production term \mathcal{P}_k in the turbulent kinetic energy equation of the Menter SST model can be written as

$$\mathcal{P}_k = \tau_{ij} \frac{\partial u_i}{\partial x_j}, \quad (5)$$

where the stress tensor τ_{ij} is defined as

$$\tau_{ij} = \mu_t \left(\frac{\partial u_i}{\partial x_j} + \frac{\partial u_j}{\partial x_i} - \frac{2}{3} \frac{\partial u_k}{\partial x_k} \delta_{ij} \right) - \frac{2}{3} \rho k \delta_{ij}, \quad (6)$$

and μ_t is the turbulent viscosity, the partial derivatives are strain rates, and k is the turbulent kinetic energy. The production term \mathcal{P}_ω in the ω equation of the SST model is proportional to \mathcal{P}_k . Generally, in the computations with the SST model, the incompressible assumption is imposed, and the turbulent kinetic energy contribution is neglected. Thus,

$$\mathcal{P}_k = \mu_t \left(\frac{\partial u_i}{\partial x_j} + \frac{\partial u_j}{\partial x_i} \right) \frac{\partial u_i}{\partial x_j} = 2\mu_t S_{ij} S_{ij}, \quad (7)$$

where S_{ij} is the strain-rate tensor, and $S_{ij} S_{ij}$ represents the double dot product of two tensors. When the strain-rate tensor is used for \mathcal{P}_k , the SST model will be designated SST(1994). In some versions of the SST model, also referenced as SST(baseline) model herein, the vorticity is substituted for the strain rate (see Menter [14]). In this case the production term is written as

$$\mathcal{P}_k = 2\mu_t W_{ij} W_{ij} = \mu_t |\Omega|^2, \quad (8)$$

where $|\Omega|$ is the magnitude of the vorticity vector. The vorticity is used with the default SST model in the CFL3D code. Certainly, one would not expect much difference in boundary-layer type flows between using strain rate or vorticity in the production terms.

The eddy viscosity determined with the SST model is defined as

$$\nu_t = \frac{a_1 k}{\max(a_1 \omega; \Omega F_2)}, \quad (9)$$

where a_1 is a constant, ω is equal to the ratio of the turbulent dissipation rate to the turbulent kinetic energy, $\Omega = \sqrt{2W_{ij}W_{ij}}$, and F_2 is a blending function. In the recent paper by Menter et al. [18], the Ω in Eq. 8 is replaced by $S = \sqrt{2S_{ij}S_{ij}}$. In the default SST model in CFL3D the Ω is used. Attempts to use S instead of Ω in this work resulted in nonphysical behavior of the solution for high blowing rates.

Jet Momentum Coefficient

A frequently used parameter in circulation control is the jet momentum coefficient, which is defined as

$$C_\mu = \frac{\dot{m}_j V_j}{\frac{1}{2} \rho_\infty V_\infty^2 A} = \frac{\rho_j V_j^2 h b}{\frac{1}{2} \rho_\infty V_\infty^2 c b},$$

where the quantity \dot{m} is mass flow rate, V is velocity, ρ is density, and the subscripts j and ∞ refer to jet and free-stream conditions, respectively. The quantities A , b and c are the wing planform area, span, and chord, respectively, and h is the jet slot height. Therefore,

$$C_\mu \sim \frac{1}{M_\infty^2}. \quad (10)$$

Assume the same jet conditions. Then (roughly) for $M_\infty = 0.12$ and $M_\infty = 0.6$

$$(C_\mu)_{M=0.6} \approx \frac{(C_\mu)_{M=0.12}}{25}$$

So, at higher Mach numbers, small values of C_μ can be, in some sense, equivalent to higher values of C_μ at lower Mach numbers. One must keep this in mind when interpreting C_μ as M_∞ increases.

Numerical Results

The computational method described in previous sections was applied first to the high Mach number flow over the CC airfoil 103RE, which is Case 302 in Table 1. Calculations were performed on the medium grid. A comparison of the surface pressure distributions computed with the BL, SA, SST(baseline), and the anisotropic EASM-ko models is shown in Fig. 5. There is a significant discrepancy between the calculated and experimental [5] pressures for all of the turbulence models. Moreover, the predicted lift coefficient (C_L) is about two times the experimental C_L of 0.191 for all models. Since all of the models predict separation on the Coanda surface downstream of the location indicated by the experiment, this means that each model is producing near wall eddy viscosity values on the Coanda surface that are too high. Thus, too much high momentum fluid is being transferred to the inner part of the shear layer. For the transport equation models this indicates that the production of turbulent kinetic energy (TKE) is too high. To determine the effect of reducing the TKE, we decided to use the curvature correction term in the SARC model as a vehicle for TKE reduction.

As discussed in the turbulence modeling section, the c_{r3} parameter in the curvature correction term of the SARC model can provide a means to reduce the TKE in the Coanda flow. In Fig. 6 the influence of this parameter on the computed variations in pressure is displayed. With $c_{r3} = 9.6$ there is good agreement with the experimental data. The calculated C_L is 0.177, which underpredicts the experimental value by approximately 7 percent. Figure 7 shows the effect of c_{r3} on the variation in the turbulent viscosity μ_t in the direction normal to the airfoil trailing edge (x -axis). The dashed line represents $c_{r3} = 0.6$, which is the standard value for curvature correction, and the thin solid line refers to $c_{r3} = 9.6$. With $c_{r3} = 9.6$ there is a maximum reduction factor in μ_t of about 3 in the shear layer near the surface.

Figures 8 - 10 reveal the basic physics of the flow. In Fig. 8 the initial entrainment of the upper surface flow produced by the jet flow is discernible. A shear layer develops due to the entrainment. The early and subsequent development of the shear layer is evident. The Mach contours (with an interval of 0.04) in Fig. 9 indicate the rather thick boundary layers that develop on the upper and lower surfaces of the airfoil. They also suggest the separation of the Coanda jet. In Fig. 10 the separation of the jet flow is delineated by the streamline pattern. The flow over the blunt trailing edge separates later, but still upstream of the trailing edge, with the jet than without the jet. This delay in separation results in one of the vortices normally appearing in the blunt trailing edge region being eliminated.

In the subsequent discussion we consider results for the same airfoil at low Mach number, with several different blowing coefficients. For the first group of cases solutions were obtained on the medium grid with the SA, SARC($c_{r3} = 9.6$), and SST(baseline) turbulence models for various C_μ values. Comparisons are made in Fig. 11 between the computed and experimental [9] pressure distributions for $C_\mu = 0.026$. With the SA model there is significant disagreement with the data on the lower and upper surfaces of the airfoil. There is improvement in the agreement with the SST(baseline) model. The solution with the SARC model and $c_{r3} = 9.6$ exhibits relatively good agreement with the data. Figure 12 shows the Coanda jet streamlines for the SARC($c_{r3} = 9.6$) model. The vortex pair usually occurring behind the blunt trailing edge is conspicuously absent.

To provide some indication of convergence behavior of the computations, the variation with multigrid cycles in the L_2 norm of the residual (for density equation) is presented in Fig. 13. Roughly 7500 cycles are required to reduce the residual four orders of magnitude. A major contribution

to this slow convergence is the slowly converging plenum solution, which is a consequence of the very low-speed flow in the plenum. The implementation of low-speed preconditioning [19, 20, 21], especially in the plenum, should result in a significant acceleration of convergence. Recently, we tested preconditioning for this particular case. Without any attempt to optimize the performance of the preconditioning, the number of cycles required to attain the same level of convergence obtained previously was reduced by a factor of two. It should be mentioned that the need for preconditioning to achieve accurate solutions in very low-speed regions has been demonstrated [20].

In Fig. 14 the computed pressures when $C_\mu = 0.093$ are shown. Generally, the trends described for $C_\mu = 0.026$ are exhibited here as well. For this case solutions with both the SA and SST(baseline) models indicate jet wraparound (i.e., Coanda jet moves onto the lower surface of the airfoil), as supported by the reduced pressures on the airfoil lower surface. These reduced pressures are associated with the occurrence of recirculation. The jet wraparound with the SA model is seen in Fig. 15. With the SARC($c_{r3} = 9.6$) model there is generally good agreement with the data. However, a thin separation region (about 0.01 chord in maximum thickness) occurs just downstream of the airfoil leading edge. This separation results in a barely discernible plateauing effect on the calculated pressures, which is not consistent with the experimental data. Figure 16 shows the jet streamlines for the SARC model and the stronger jet penetration (relative to that in Fig. 12) into the flow field due to the increased C_μ .

The final two cases, which are Case 283 and Case 321, are those considered in the 2004 Circulation Control Workshop held at NASA Langley Research Center. Flow conditions for these cases are given in Table 1. For Case 283, where $C_\mu = 0.209$, the computed pressure distributions on the medium grid are compared with the experimental data in Fig. 17. There is considerable reduction in the computed lower surface pressures with the SA and SST(baseline) models relative to the experimental values. Such behavior indicates extensive flow separation on the lower surface with these models. In fact, the Coanda jet in these cases wraps around the trailing edge and moves even further upstream than shown in Fig. 15, a completely unphysical situation. The result with the SARC($c_{r3} = 9.6$) model exhibits fairly good agreement with the data on the lower airfoil surface, but it shows a plateau behavior over more than 50 percent of the airfoil on the upper surface. Thus, there is a large separation bubble on the upper surface. Numerical tests confirmed that this is a consequence of the large c_{r3} value being used for the SARC model in the airfoil leading edge region. By simply setting $c_{r3} = 9.6$ on the Coanda surface and taking it to be zero elsewhere, relatively good agreement with the data is again obtained for the SARC($c_{r3} = 0 - 9.6$) model.

The jet streamlines for the SARC($c_{r3} = 0 - 9.6$) model on the fine grid are presented in Fig. 18. In the Mach contours of Figs. 19 and 20 the rearward movement of the leading edge stagnation point, due to the Coanda effect, and the acceleration of the Coanda flow are seen. Details of the Mach contours at the jet exit, along with the corresponding fine grid, are displayed in Figs. 21 and 22. The jet flow is accelerated to a Mach number exceeding 0.9, indicating the compressible character of the jet.

There is only a small effect of mesh refinement on the solution calculated with the SARC($c_{r3} = 0 - 9.6$) model. Although not shown, the fine grid solution for the surface pressures nearly coincides with the medium grid solution. In addition, the velocity fields for the two grids are quite similar, as evident in velocity profiles shown in Figs. 23 and 24. Table 2 compares the predicted lift coefficient and drag coefficient (C_D) with the experimental values. In addition, the change in aerodynamic coefficients with further increases in C_μ are indicated. It must be kept in mind that there is some effect, although it may be small, on these low-speed predictions due to the differences between the

Case	C_μ	Grid	$(C_L)_{\text{exp}}$	C_L	$(C_D)_{\text{exp}}$	C_D
283	0.209	med.	4.20	3.26	-0.050	0.1140
283	0.209	fine	4.20	3.15	-0.050	0.1090
	0.281	med.		3.62	-0.050	0.1560
	0.342	med.		4.05	-0.050	0.2100
321	0.184	med.	3.10	2.17	-0.080	0.0957
321	0.184	fine	3.10	2.03	-0.080	0.0922

Table 2: Comparison of computed, with SARC($c_{r3} = 0 - 9.6$) model, and experimental lift and drag coefficients for circulation control airfoil.

103RE and the NCCR geometries.

As indicated in the section on turbulence modeling, Menter [15] has considered two ways to define the turbulence production terms of the SST model. For all of the previous SST(baseline) results that we have shown the production term was computed with vorticity (see Eq. 8). Now, we consider the impact of evaluating the production term using the principal strain-rate tensor (Eq. 7), as presented by Menter in his 1994 paper [16]. As mentioned earlier, we refer to this form of the SST model as SST(1994).

A comparison of the pressure distributions calculated with the SST(baseline) and SST(1994) turbulence models is shown in Fig. 25 for Case 283. Both medium and fine grid results are given. There is relatively good agreement with the data when applying the SST(1994) model, whereas the SST(baseline) results exhibit poor agreement. Thus, although use of Eq. 8 for the SST model has proven to be satisfactory for many aerodynamic flows of interest, it does not appear to be appropriate for the Coanda jet flows being considered here.

There is greater sensitivity to mesh refinement with the SST(1994) model than that experienced with the SARC($c_{r3} = 0 - 9.6$) model. The effect of mesh refinement on the Coanda surface skin-friction distributions calculated with these two models is shown in Fig. 26. Comparing Figs. 18 and 27, the jet streamlines with the SST(1994) model exhibit less spreading than those with the SARC($c_{r3} = 0 - 9.6$) model. Mesh refinement effect on the predicted C_L and C_D with the SST(1994) model is given in Table 3. While there is a reduction in C_L as the mesh is refined, as shown in Fig. 28, the lift augmentation (slope of C_L versus C_μ) appears to remain about the same for SST(1994) with mesh refinement. In the C_L predictions with both models shown in Fig. 28 there is a monotonic increase in C_L with increasing C_μ . The two-equation $k - \epsilon$ models considered by Slomski et al. [7] result in a nonphysical decrease in C_L beyond a C_μ of 0.093 (i.e., jet wraparound predicted).

For the second case (Case 321, angle of attack of -8 degrees) of the workshop, computed surface pressures for the medium and fine grids are presented in Figs. 29 and 30. Results with both the SST(1994) and SARC($c_{r3} = 0 - 9.6$) models compare favorably with the experimental data. Nevertheless, the experimental C_L is underpredicted by more than 22 percent (see Tables 2 and 3). Paterson and Baker [8] obtained the same value for the C_L of this case using the SST(1994) model and performing an incompressible simulation for flow over the NCCR-1510-7067N geometry. With the SARC($c_{r3} = 0 - 9.6$) model there is again greater spreading of the jet than with SST(1994), as

Case	C_μ	Grid	$(C_L)_{\text{exp}}$	C_L	$(C_D)_{\text{exp}}$	C_D
283	0.209	med.	4.20	4.19	-0.050	0.0966
283	0.209	fine	4.20	3.88	-0.050	0.0746
321	0.184	med.	3.10	2.96	-0.080	0.0655
321	0.184	fine	3.10	2.41	-0.080	0.0559

Table 3: Comparison of computed, with SST(1994) model, and experimental lift and drag coefficients for circulation control airfoil.

revealed by comparing Figs. 31 and 32 depicting the jet streamlines and Mach contours. There is an extremely small recirculation region, which occurs only for the SST(1994) model, on the lower surface that centers near the 0.92 chord location, but it is not visible in Fig. 32.

Concluding Remarks

A computational method (CFL3D) has been applied to both low and high subsonic Mach number CC airfoil flows. Several turbulence models have been investigated. These models include the one-equation SA model with curvature correction (SARC) and two variations of the two-equation shear stress transport (SST) model of Menter. For the high subsonic Mach number CC flow (Case 302), all models have predicted separation downstream of the experimental location, resulting in a significant overprediction of lift. In other words, all of the models have produced near wall eddy viscosity levels that are too high in the Coanda flow. A parameter (c_{r3}) in the curvature correction term of the SARC model has been used as a vehicle to explore the effect of reducing the turbulent kinetic energy in the Coanda flow. In so doing, relatively good agreement with the experimental pressure distribution of Case 302 has been obtained.

In the simulation of low Mach number CC airfoil flows a set of calculations has been performed for a range of values of C_μ . The two cases of the 2004 Circulation Control Workshop have also been considered. Relatively good agreement with experimental pressure data has been obtained when modeling turbulence with the SARC($c_{r3} = 0 - 9.6$) and the SST(1994) models. The SST(1994) model uses principal strain rate for the shear stress in the modeling of the turbulence production. The SST(baseline) model, which uses vorticity in the turbulence production term, has not been satisfactory when computing Coanda jet flows. An indication of the effects of grid refinement on the results computed with the turbulence models has been given. The SST(1994) model has shown greater sensitivity to mesh refinement than the SARC(0 - 9.6) model. Lift and drag coefficients have also been determined in the calculations.

Clearly, turbulence modeling is the major component in determining the success of a computational method for predicting CC airfoil flows. Further investigation of models is essential to achieving a reliable prediction technique that can be used for a broad range of flow conditions.

In addition, improvements in computational efficiency must also be considered quite important if the prediction method is to be applied on a routine basis with a high degree of reliability. Some rather straightforward numerical algorithm features such as low-speed preconditioning should be included in the method. Potential benefits of this preconditioning have been indicated in this paper.

Another possible improvement in computational performance can be achieved by full coupling of the fluid dynamic and turbulence transport equations, which is not done currently with the CFL3D code. These and other improvements in computational efficiency are especially important as the hierarchy (i.e., complexity) of the turbulence modeling is increased. For example, if a full Reynolds stress model is used instead of a two-equation model, such as SST(1994), one must anticipate that there will be a reduction in computing efficiency, due to a lower degree of numerical compatibility of the more complex model. In the case of steady flows, numerical compatibility can be defined as a measure of the effect on solution convergence of the complete system of flow equations due to turbulence modeling.

References

- [1] Englar, R. J., and Williams, R. M., "Test Techniques for High Lift Two-Dimensional Airfoils with Boundary Layer and Circulation Control for Application to Rotary Wing Aircraft," *Canadian Aeronautics and Space J.*, vol. 19, No. 3, pp. 93–108, 1973.
- [2] Jones, G. S., Viken, S. A., Washburn, A. E., Jenkins, L. N., Cagle, C. M., "An Active Flow Circulation Controlled Flap Concept for General Aviation Aircraft Applications," *AIAA Paper* 03-3157, 2003.
- [3] Pulliam, T. H., Jespersen, D. C, Barth, T. J., "Navier-Stokes Computations for Circulation Control Airfoils," *AIAA Paper* 85-1587, 1985.
- [4] Pulliam, T. H., "Euler and Thin Layer Navier-Stokes Codes: ARC2D, ARC3D," *Notes for Computational Fluid Dynamics User's Workshop*, The University of Tennessee Space Institute, Tullahoma, Tennessee, March 12–16, 1984.
- [5] Abramson, J., and Rogers, E., "High-Speed Characteristics of Circulation Control Airfoils," *AIAA Paper* 83-0265, 1983.
- [6] Baldwin, B. S., and Lomax, H., "Thin Layer Approximation and Algebraic Model for Separated Flows," *AIAA Paper* 78-257, 1978.
- [7] Slomski, J. F., Gorski, J. J, Miller, R. W., Marino, T. A., "Numerical Simulation of Circulation Control Airfoils as Affected by Turbulence Models," *AIAA Paper* 02-0851, 2002.
- [8] Paterson, E. G, and Baker, W. J., "Simulation of Steady Circulation Control for Marine-Vehicle Control Surfaces," *AIAA Paper* 04-0748, 2004.
- [9] Abramson, J., "Two-Dimensional Subsonic Wind Tunnel Evaluation of Two Related Cambered 15-Percent Circulation Control Airfoils," DTNSRDC ASED-373, 1977.
- [10] Krist, S. L., Biedron R. T. and Rumsey, C. L., "CFL3D User's Manual," *NASA TM* 1998-208444, 1998.
- [11] Spalart, P. R. and Allmaras, S. R., "A One-Equation Turbulence Model for Aerodynamic Flows," *La Recherche Aerospatiale*, vol. 1, pp. 5–21, 1994.

- [12] Spalart, P. R. and Shur, M., “On the Sensitization of Turbulence Models to Rotation and Curvature,” *Aerospace Sci. Technol.*, vol. 5, pp. 297–302, 1997.
- [13] Rumsey, C. L., Gatski, T. B., Anderson, W. K. and Nielsen, E. J., “Isolating Curvature Effects in Computing Wall-Bounded Turbulent Flows,” *Inter. J. of Heat and Fluid Flow*, vol. 22, pp. 573–582, 2001.
- [14] Menter, F. R., “Improved Two-Equation $k - \omega$ Turbulence Model for Aerodynamic Flows,” *NASA TM* 103975, 1992.
- [15] Menter, F. R., “Zonal Two Equation $k - \omega$ Turbulence Model for Aerodynamic Flows,” *AIAA Paper* 93-2906, 1993.
- [16] Menter, F. R., “Two-Equation Eddy-Viscosity Turbulence Models for Engineering Applications,” *AIAA J.* vol. 32, No. 8, pp. 1598–1605, 1994.
- [17] Rumsey, C. L., Gatski, T. B. and Morrison, J. H., “Turbulence Model Predictions of Strongly Curved Flow in a U-Duct,” *AIAA J.*, vol. 38, No. 8, pp. 1394–1402, 2000.
- [18] Menter, F. R., Kuntz, M. and Langtry, R., “Ten Years of Industrial Experience with the SST Turbulence Model,” *Turbulence, Heat and Mass Transfer 4*, K. Hanjalic, Y. Nagano, and M. Tummers (editors), Begell House, Inc., pp. 625–632, 2003.
- [19] Turkel, T., Vatsa, V. N. and Radespiel, R., “Preconditioning Methods for Low-Speed Flow,” *AIAA* , 96-2460, 1996.
- [20] Turkel, T., Radespiel, R. and Kroll, N., “Assessment of Two Preconditioning Methods for Aerodynamic Problems,” *Computers and Fluids*, vol. 26, no. 6, pp. 613–634, 1997.
- [21] Turkel, T., “Preconditioning Techniques in Computational Fluid Dynamics,” *Annual Review of Fluid Mechanics*, vol. 31, pp. 385–416, 1999.

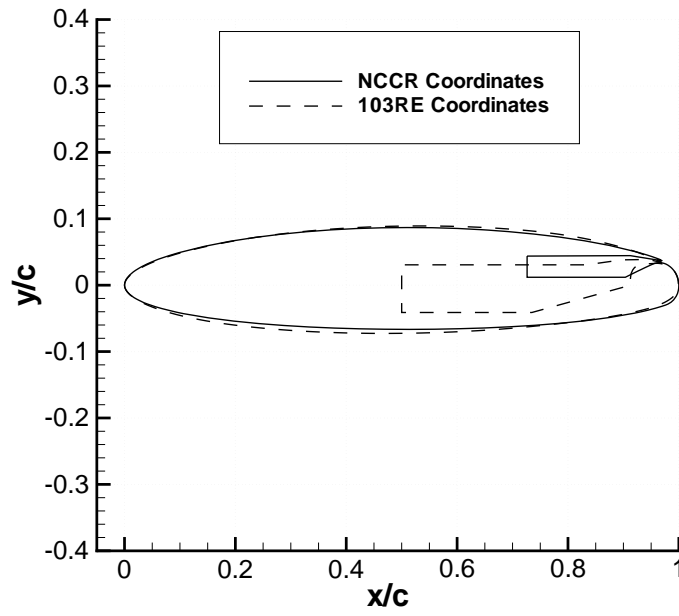


Figure 1: Geometry of airfoils.

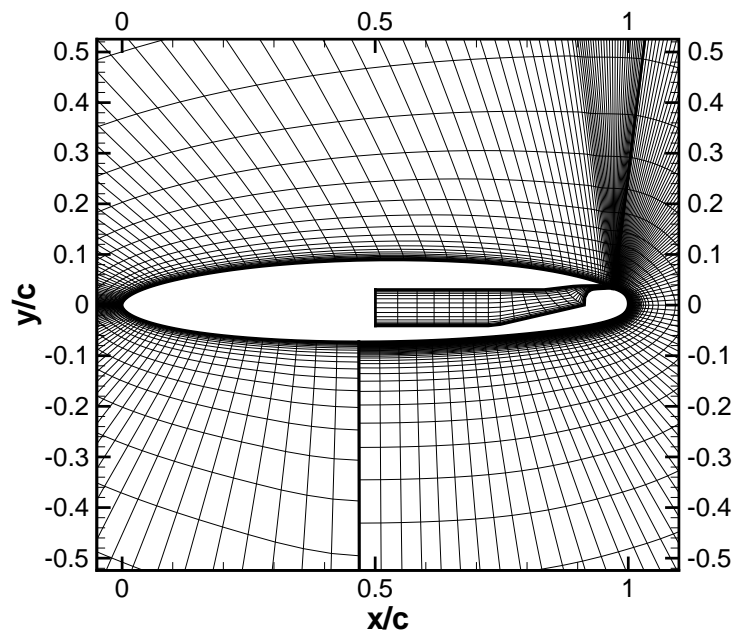


Figure 2: Near field of medium grid for circulation control airfoil.

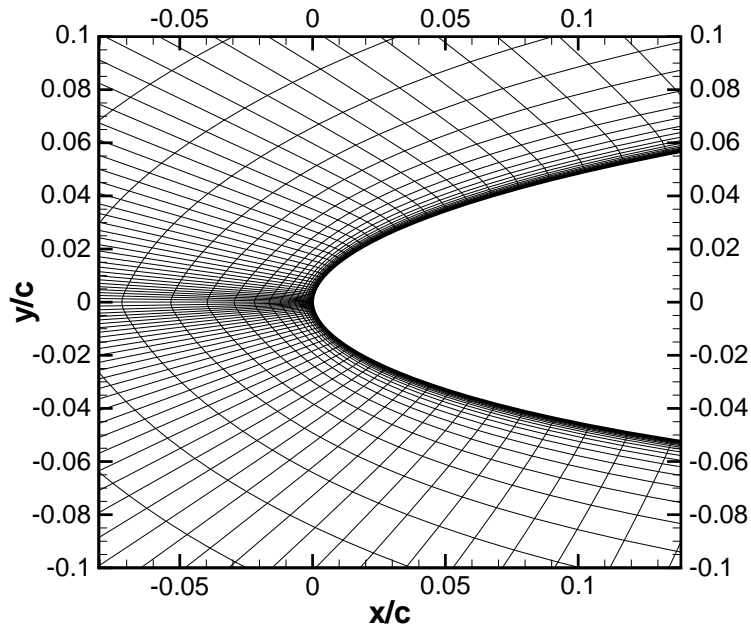


Figure 3: Leading edge region of medium grid for circulation control airfoil.

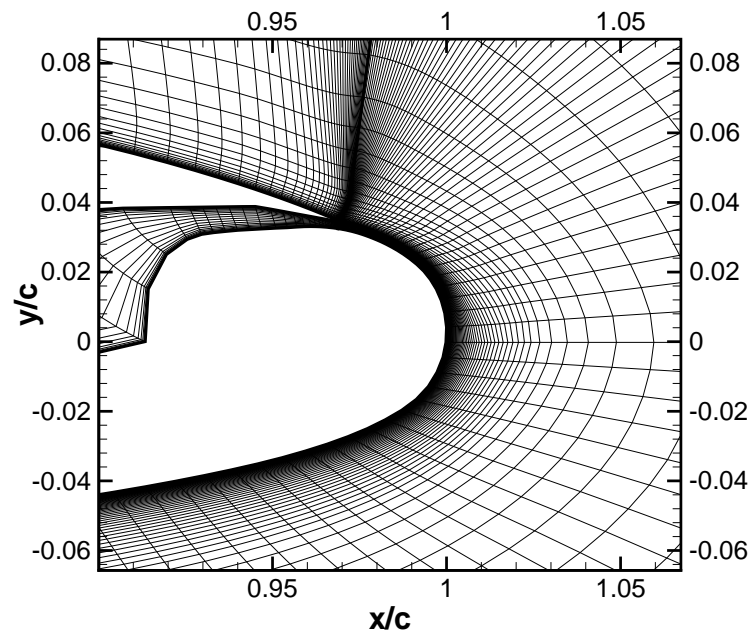


Figure 4: Trailing edge region of medium grid for circulation control airfoil.

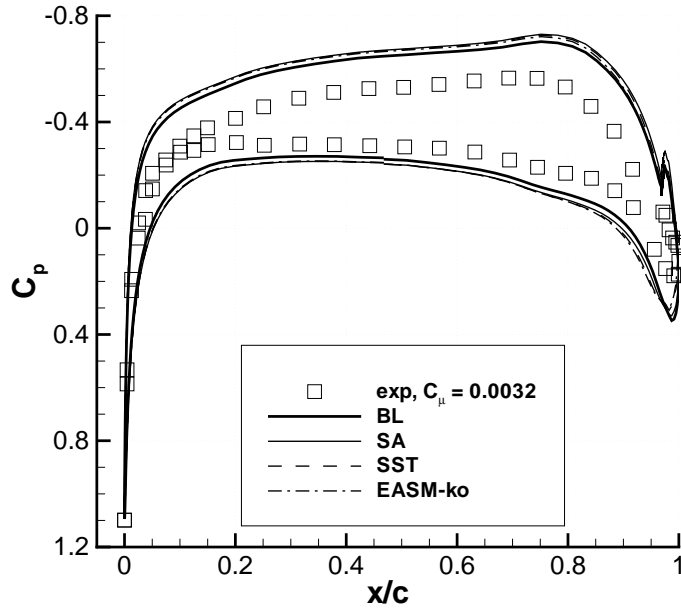


Figure 5: Comparison of surface pressures computed with several turbulence models ($M_\infty = 0.6$, $\alpha = 0^\circ$, $Re_c = 5.2 \times 10^6$, $C_\mu = 0.0032$, medium grid).

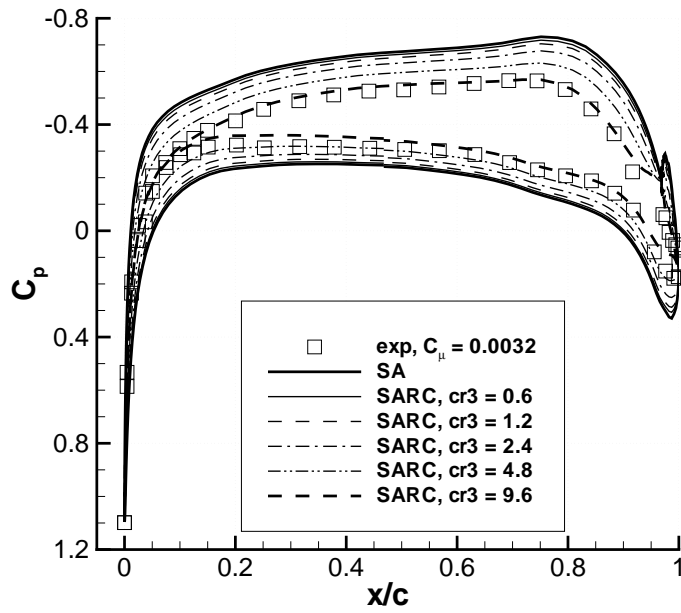


Figure 6: Effect of turbulence production parameter c_{r3} of SARC model on surface pressures ($M_\infty = 0.6$, $\alpha = 0^\circ$, $Re_c = 5.2 \times 10^6$, $C_\mu = 0.0032$, medium grid).

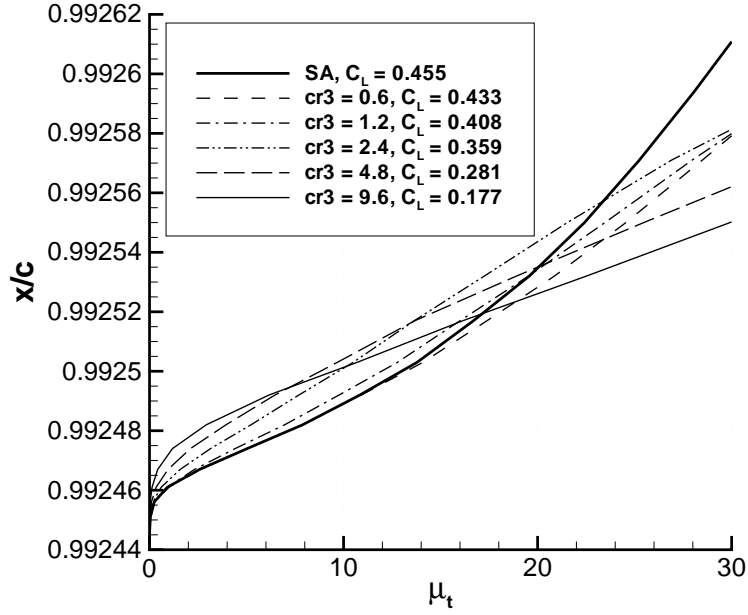


Figure 7: Effect of turbulence production parameter c_{r3} of SARC model on turbulent viscosity ($M_\infty = 0.6$, $\alpha = 0^\circ$, $Re_c = 5.2 \times 10^6$, $C_\mu = 0.0032$, medium grid).

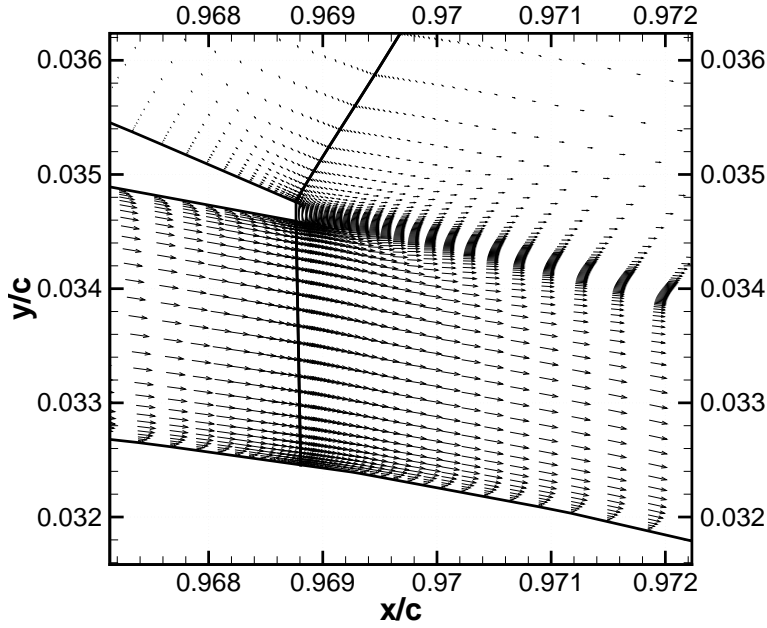


Figure 8: Velocity vectors near jet exit computed with SARC model and $c_{r3} = 9.6$ ($M_\infty = 0.6$, $\alpha = 0^\circ$, $Re_c = 5.2 \times 10^6$, $C_\mu = 0.0032$, medium grid).

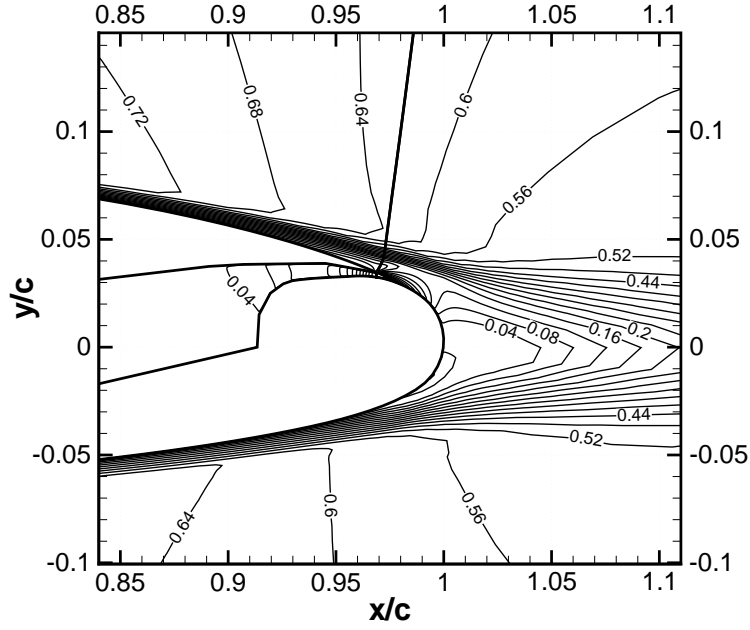


Figure 9: Mach contours at trailing edge computed with SARC model and $c_{r3} = 9.6$ ($M_\infty = 0.6$, $\alpha = 0^\circ$, $Re_c = 5.2 \times 10^6$, $C_\mu = 0.0032$, medium grid).

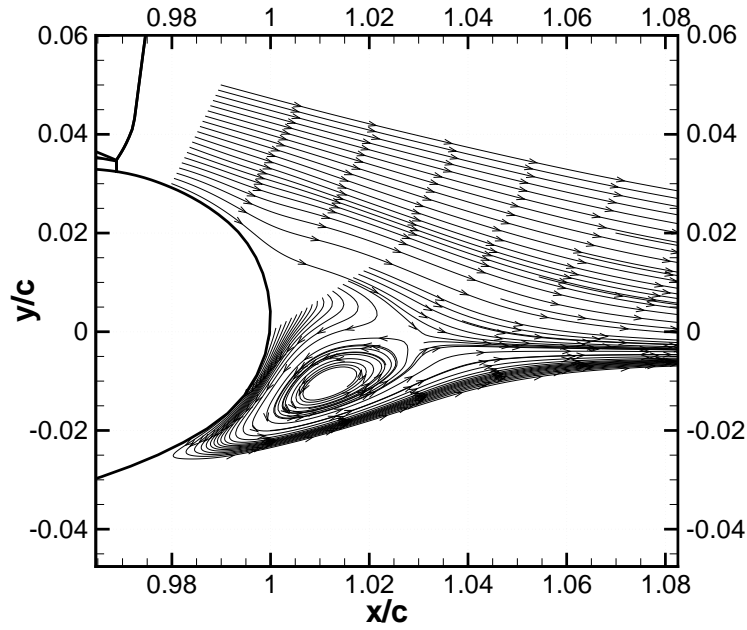


Figure 10: Streamline pattern at trailing edge computed with SARC model and $cr3 = 9.6$ ($M_\infty = 0.6$, $\alpha = 0^\circ$, $Re_c = 5.2 \times 10^6$, $C_\mu = 0.0032$, medium grid).

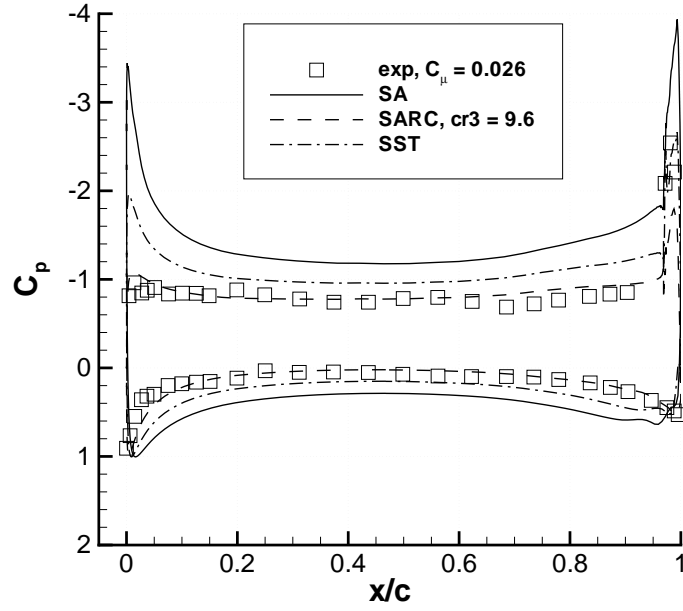


Figure 11: Surface pressures computed with SA, SARC($c_{r3} = 9.6$), and SST turbulence models ($M_\infty = 0.12$, $\alpha = 0^\circ$, $Re_c = 5.45 \times 10^5$, $C_\mu = 0.026$, medium grid).

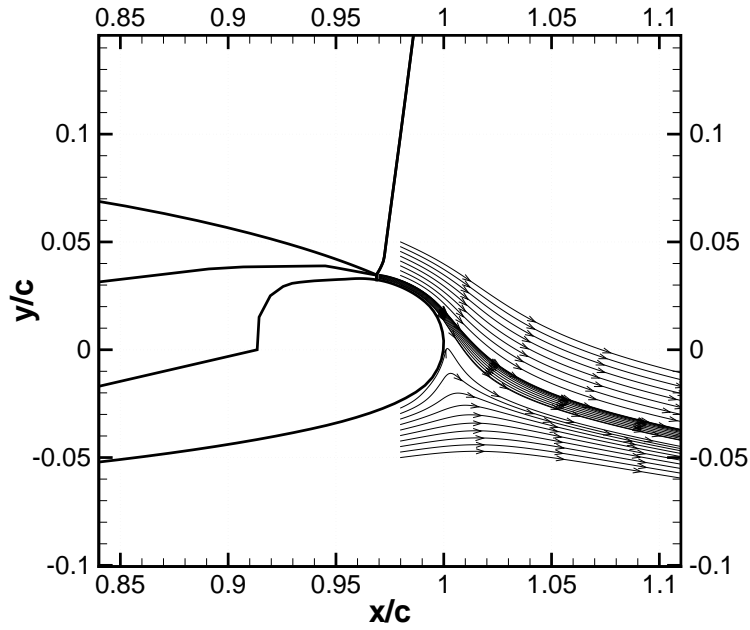


Figure 12: Jet streamlines computed with SARC($c_{r3} = 9.6$) turbulence model ($M_\infty = 0.12$, $\alpha = 0^\circ$, $Re_c = 5.45 \times 10^5$, $C_\mu = 0.026$, medium grid).

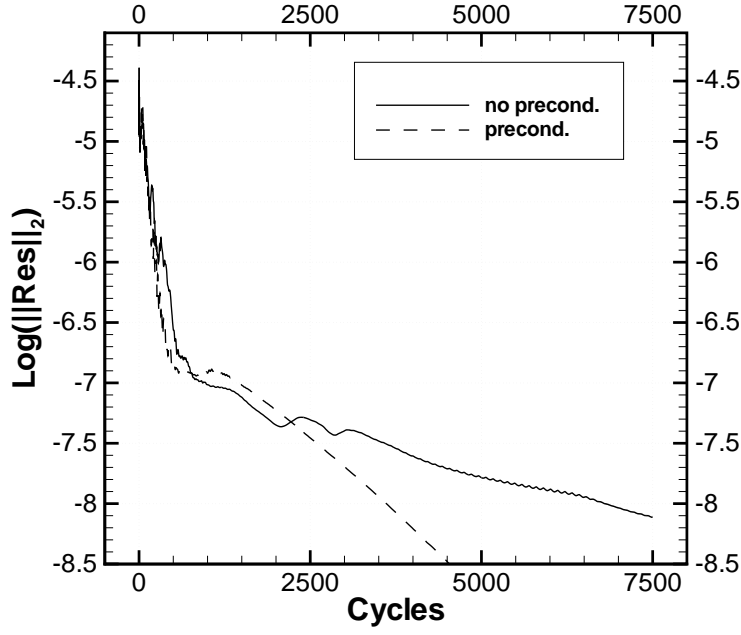


Figure 13: Residual histories with SA turbulence model, without and with preconditioning ($M_\infty = 0.12$, $\alpha = 0^\circ$, $Re_c = 5.45 \times 10^5$, $C_\mu = 0.026$, medium grid).

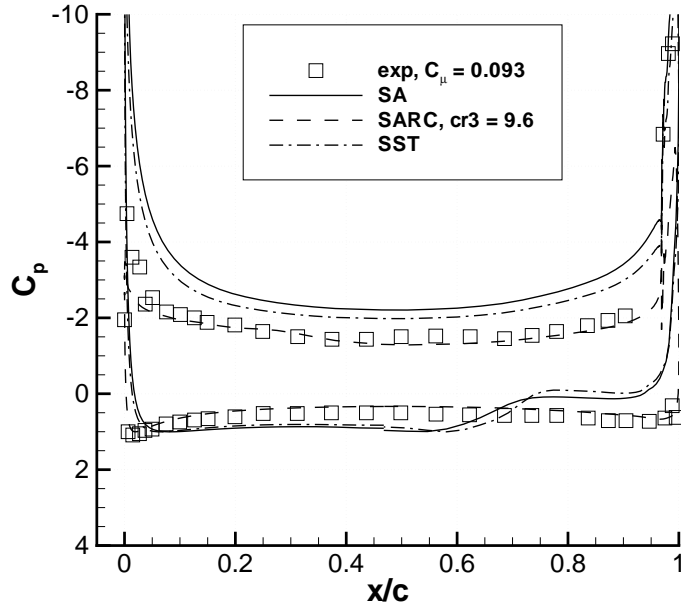


Figure 14: Surface pressures computed with SA, SARC($c_{r3} = 9.6$), and SST turbulence models ($M_\infty = 0.12$, $\alpha = 0^\circ$, $Re_c = 5.45 \times 10^5$, $C_\mu = 0.093$, medium grid).

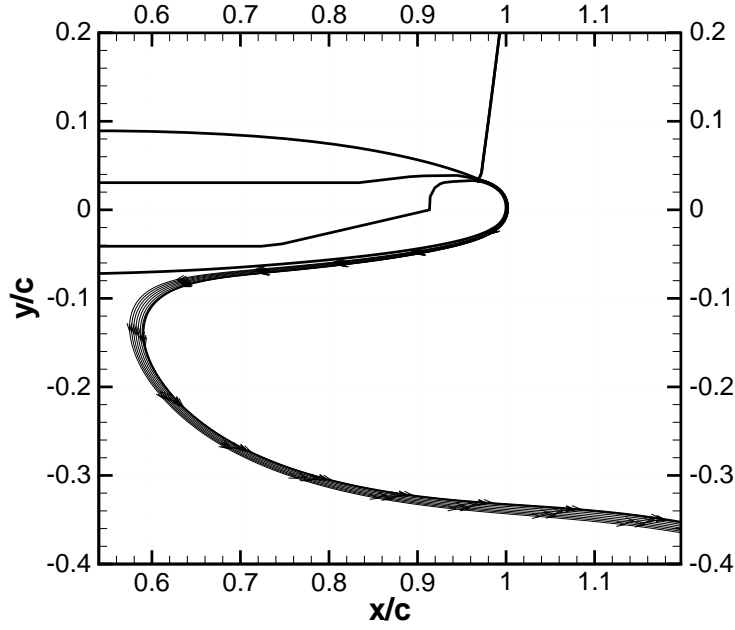


Figure 15: Jet streamlines computed with SA turbulence model ($M_\infty = 0.12$, $\alpha = 0^\circ$, $Re_c = 5.45 \times 10^5$, $C_\mu = 0.093$, medium grid).

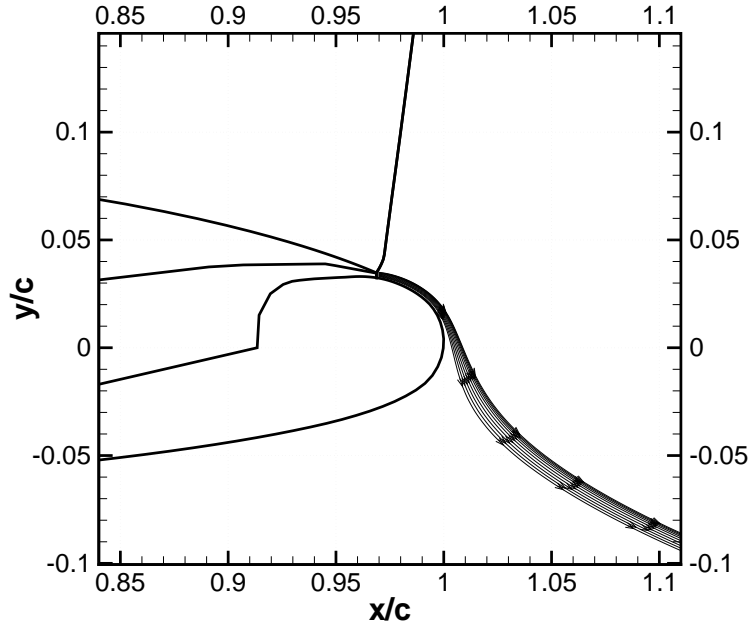


Figure 16: Jet streamlines computed with SARC($c_{r3} = 9.6$) turbulence model ($M_\infty = 0.12$, $\alpha = 0^\circ$, $Re_c = 5.45 \times 10^5$, $C_\mu = 0.093$, medium grid).

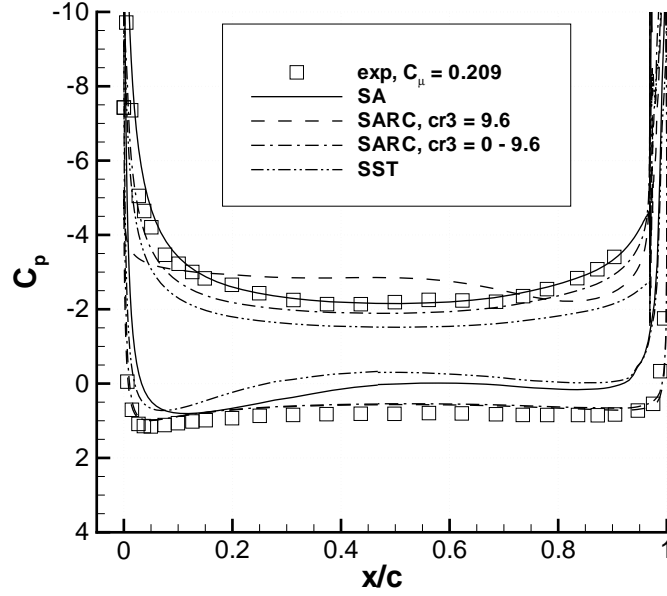


Figure 17: Surface pressures computed with SA, SARC($c_{r3} = 9.6$), SARC($c_{r3} = 0 - 9.6$), and SST turbulence models ($M_\infty = 0.12$, $\alpha = 0^\circ$, $Re_c = 5.45 \times 10^5$, $C_\mu = 0.209$, medium grid).

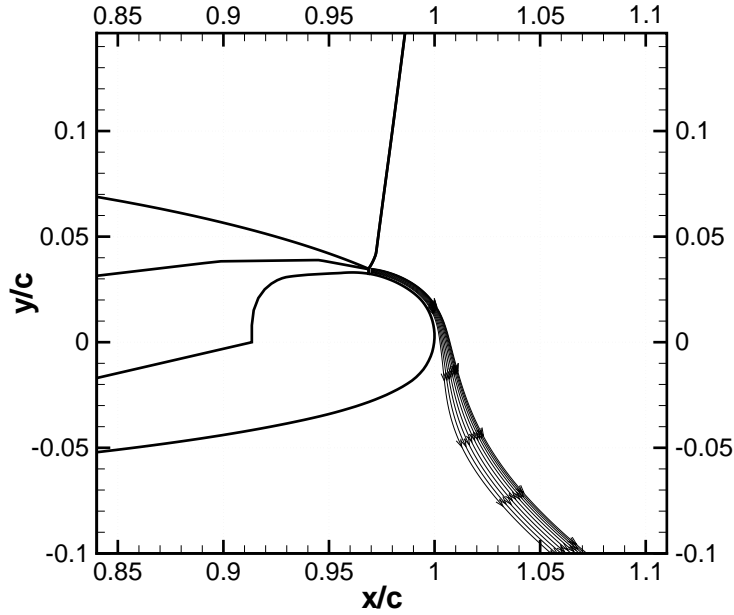


Figure 18: Jet streamlines computed with SARC($c_{r3} = 0 - 9.6$) turbulence model ($M_\infty = 0.12$, $\alpha = 0^\circ$, $Re_c = 5.45 \times 10^5$, $C_\mu = 0.209$, fine grid).

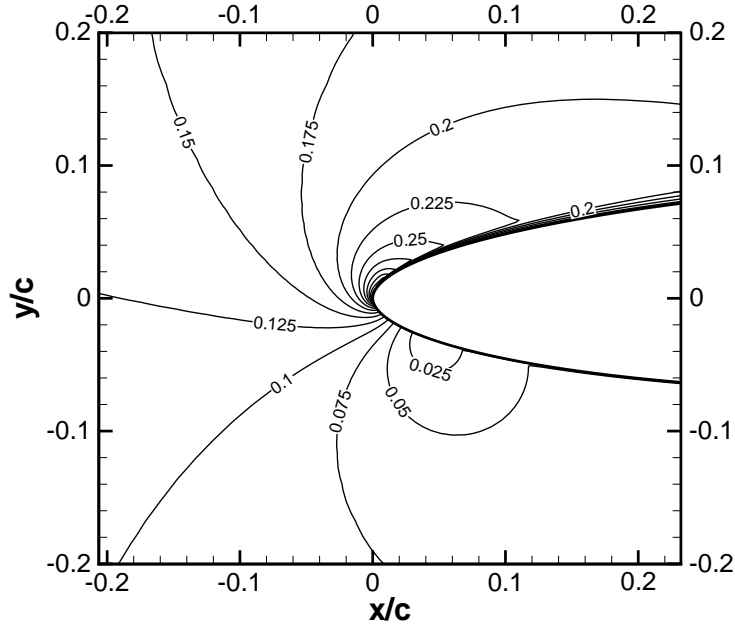


Figure 19: Mach contours computed at leading edge with SARC($c_{r3} = 0 - 9.6$) turbulence model ($M_\infty = 0.12$, $\alpha = 0^\circ$, $Re_c = 5.45 \times 10^5$, $C_\mu = 0.209$, fine grid).

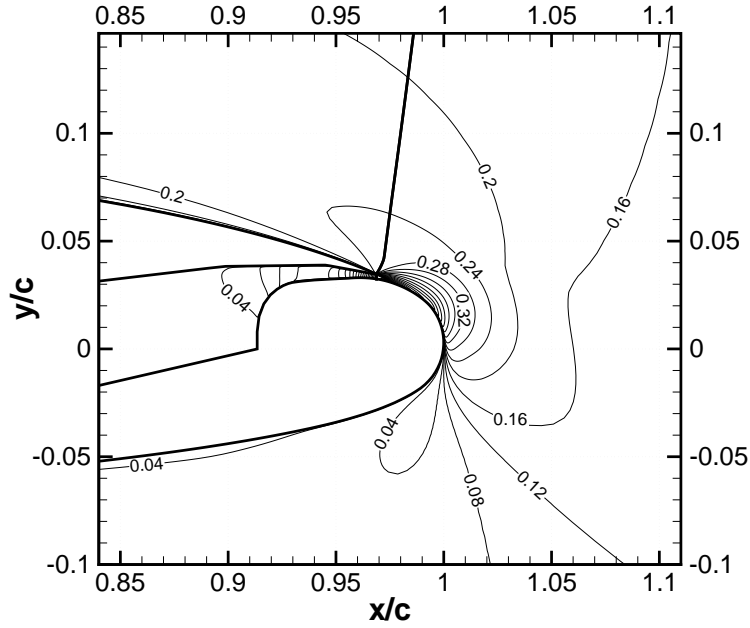


Figure 20: Mach contours computed at trailing edge with SARC($c_{r3} = 0 - 9.6$) turbulence model ($M_\infty = 0.12$, $\alpha = 0^\circ$, $Re_c = 5.45 \times 10^5$, $C_\mu = 0.209$, fine grid).

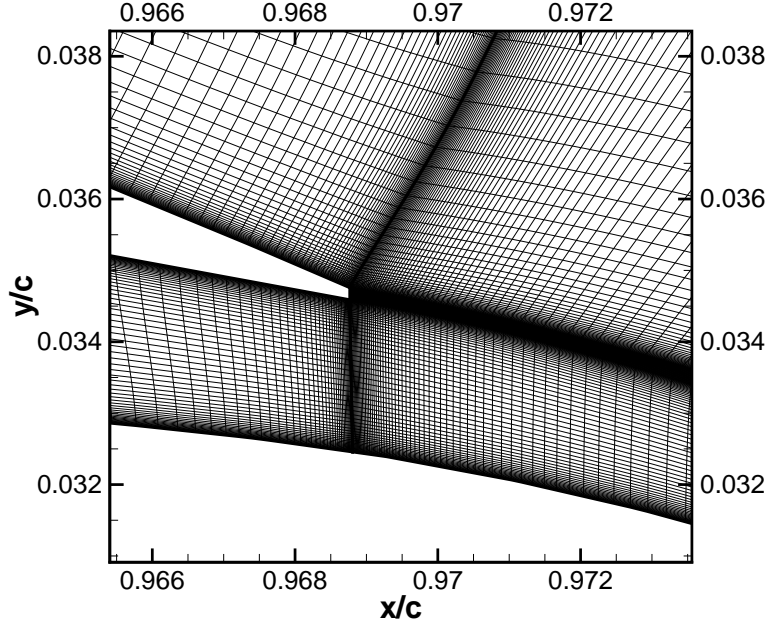


Figure 21: Fine grid in jet exit region.

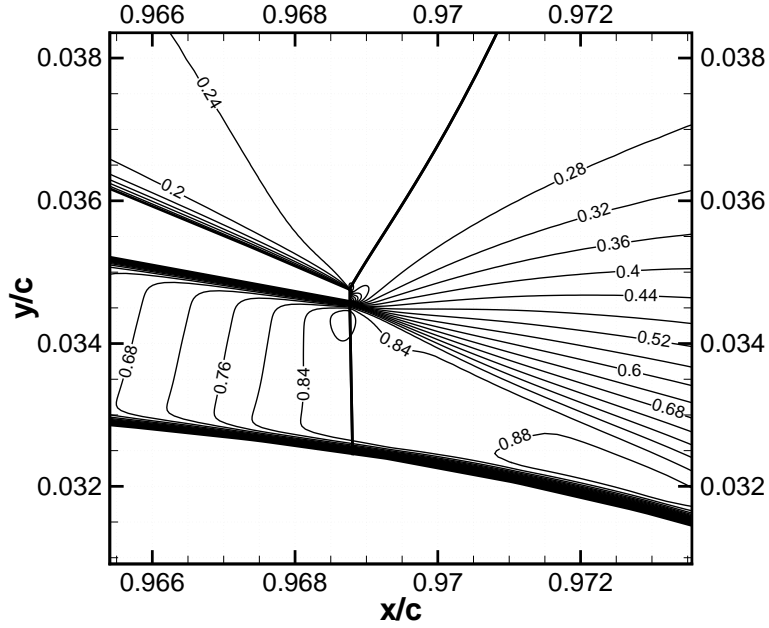


Figure 22: Mach contours in the vicinity of jet exit computed with SARC($c_{r3} = 0 - 9.6$) turbulence model ($M_\infty = 0.12$, $\alpha = 0^\circ$, $Re_c = 5.45 \times 10^5$, $C_\mu = 0.209$, fine grid).

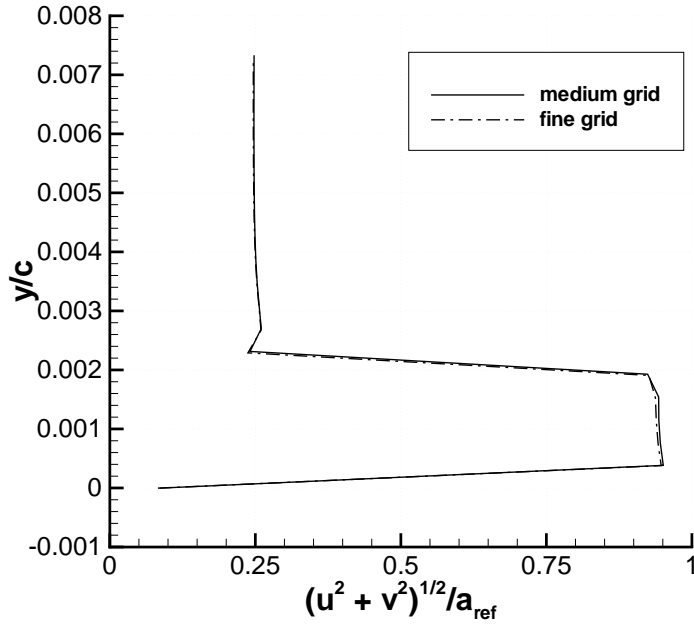


Figure 23: Effect of mesh density on velocity profiles computed at jet exit with SARC($c_{r3} = 0 - 9.6$) turbulence model ($M_\infty = 0.12$, $\alpha = 0^\circ$, $Re_c = 5.45 \times 10^5$, $C_\mu = 0.209$).

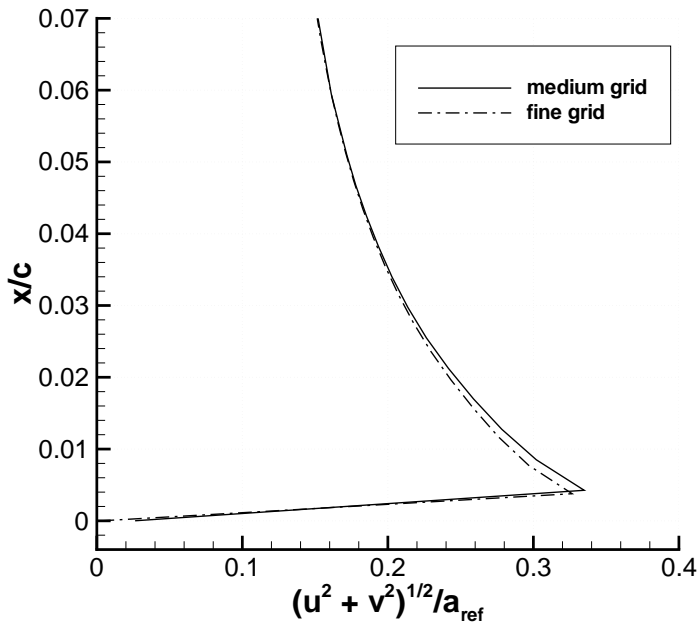


Figure 24: Effect of mesh density on velocity profiles computed at trailing edge with SARC($c_{r3} = 0 - 9.6$) turbulence model ($M_\infty = 0.12$, $\alpha = 0^\circ$, $Re_c = 5.45 \times 10^5$, $C_\mu = 0.209$).

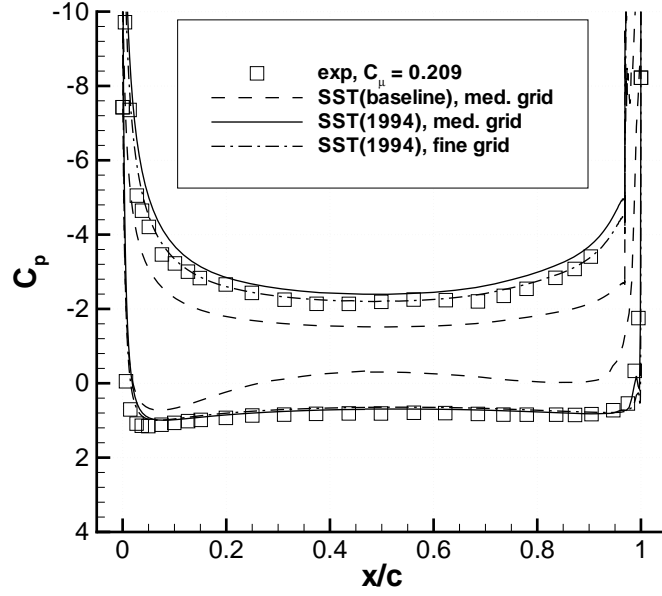


Figure 25: Surface pressures computed with SST(1994) turbulence model ($M_\infty = 0.12$, $\alpha = 0^\circ$, $Re_c = 5.45 \times 10^5$, $C_\mu = 0.209$).

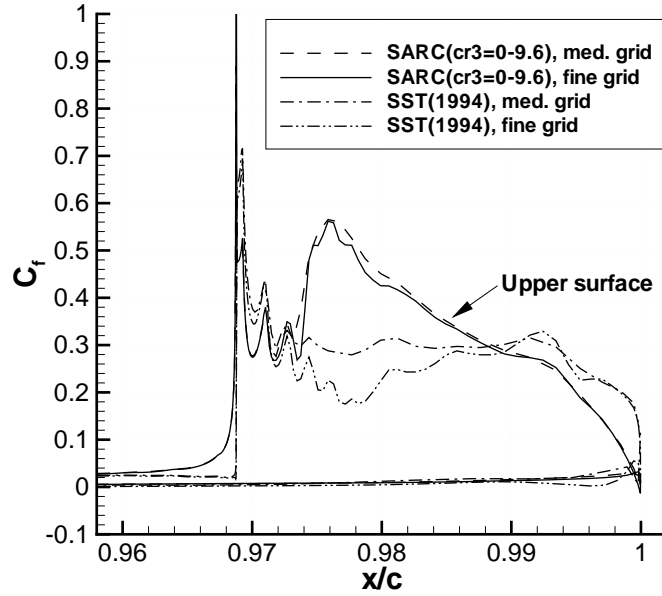


Figure 26: Comparison of surface skin-friction distributions at the trailing edge computed with SARC($c_{r3} = 0 - 9.6$) and SST(1994) turbulence models ($M_\infty = 0.12$, $\alpha = 0^\circ$, $Re_c = 5.45 \times 10^5$, $C_\mu = 0.209$).

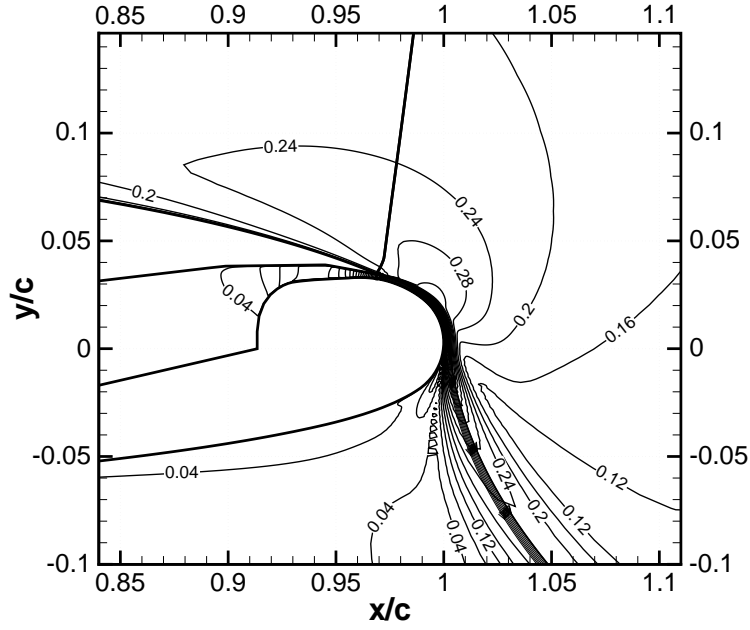


Figure 27: Jet streamlines and Mach contours computed with SST(1994) turbulence model ($M_\infty = 0.12$, $\alpha = 0^\circ$, $Re_c = 5.45 \times 10^5$, $C_\mu = 0.209$, fine grid).

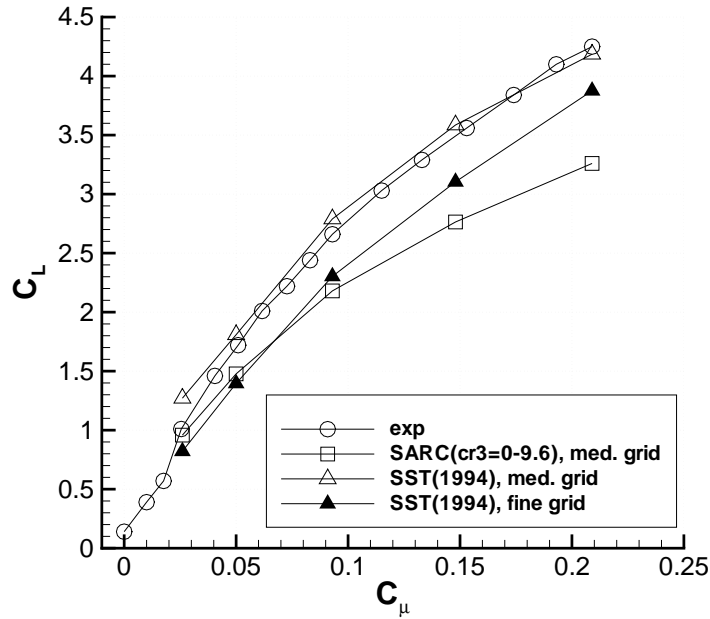


Figure 28: Variation of lift coefficient with jet momentum coefficient using SARC($c_{r3} = 0 - 9.6$) and SST(1994) turbulence models ($M_\infty = 0.12$, $\alpha = 0^\circ$, $Re_c = 5.45 \times 10^5$).

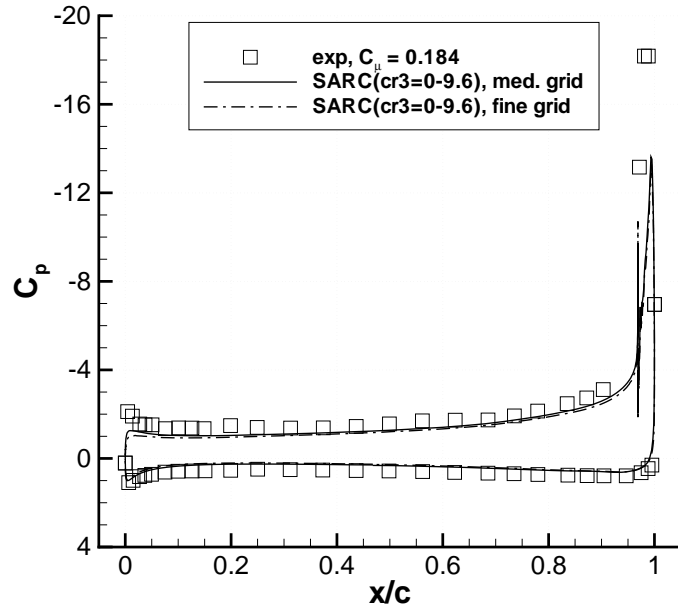


Figure 29: Surface pressures computed with SARC($c_{r3} = 0 - 9.6$) turbulence model ($M_\infty = 0.12$, $\alpha = -8^\circ$, $Re_c = 5.45 \times 10^5$, $C_\mu = 0.184$).

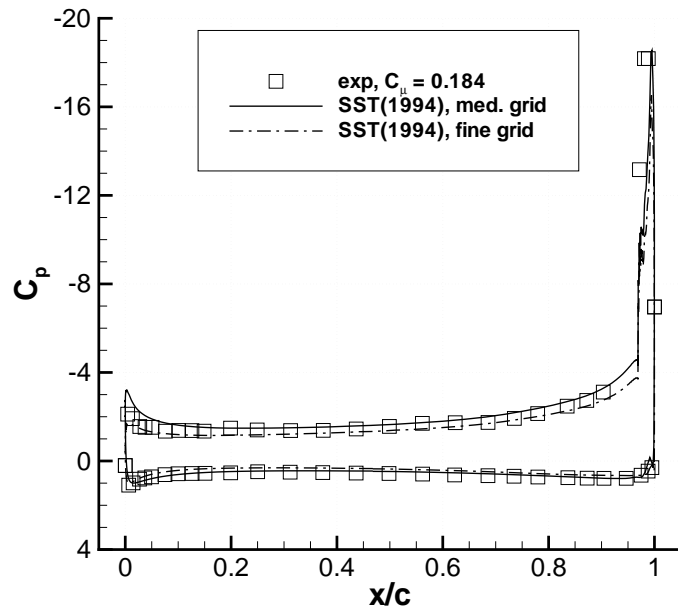
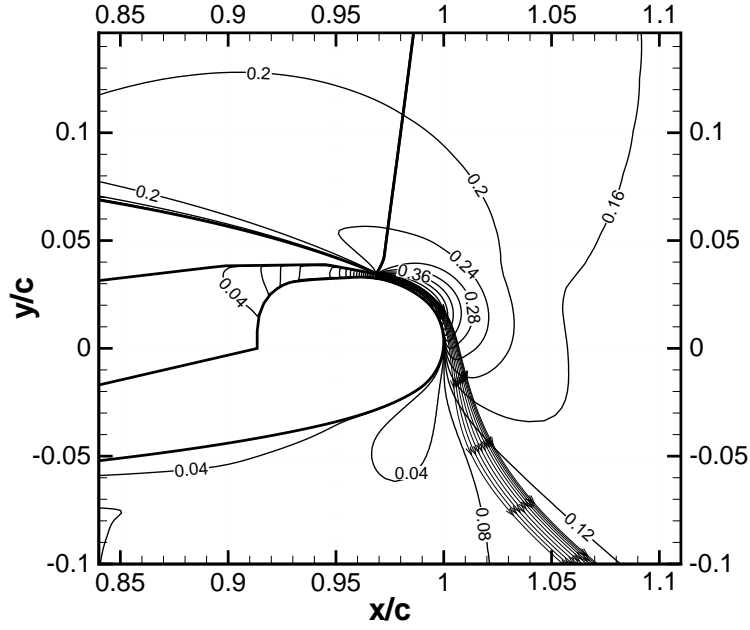


Figure 30: Surface pressures computed with SST(1994) turbulence model ($M_\infty = 0.12$, $\alpha = -8^\circ$, $Re_c = 5.45 \times 10^5$, $C_\mu = 0.184$).



Aspects of Numerical Simulation of Circulation Control Airfoils

R. C. Swanson, C. L. Rumsey, S. G. Anders
NASA Langley Research Center

2004 Circulation Control Workshop (March 16 - 17)

Outline

- Introduction
 - Motivation and objectives
 - Definition of jet momentum coefficient
- Computational Method
- Turbulence Modeling
- Geometry, flow conditions, grid
- Computational Results
 - Initial effort ($M_\infty = 0.6$, $Re_c = 5.2 \times 10^6$)
 - Workshop cases ($M_\infty = 0.12$, $Re_c = 5.45 \times 10^5$)
- Conclusions

Introduction

- Some possible benefits of circulation control airfoils (e.g., for general aviation)
 - Reduced weight and complexity (maintenance) relative to conventional high lift systems
 - Slower takeoff and landing speeds
 - Increased maneuverability
- There is a need to develop reliable flow prediction capability.
- Key issue for computing circulation control airfoil flows is turbulence modeling.

Introduction (Cont.)

- Previous work (on the workshop cases), indicates uncertainty in required turbulence model complexity.
 - Full Reynolds stress model (Slomski et al., 2002)
 - Two transport equations (Paterson and Baker, 2004)
- Computational efficiency and reliability is another important issue for computing circulation control airfoil flows.
 - Convergence acceleration (steady flows)
 - Improved efficiency of time integration scheme (unsteady flows)
 - Numerical compatibility of turbulence model

Introduction (Cont.)

- Capability of flow prediction tool must include:
 - Accurate prediction of details of flow (i.e., velocity profiles, Reynolds stresses, TKE, jet characteristics)
 - Pulsating jets, multiple jets
 - Amenable to broad range of flow conditions (i.e., M_∞ , Re_∞ , α)
 - 3-D effects
- In current effort various aspects of computing circulation control airfoils are considered.
 - Turbulence modeling
 - Flow conditions
 - Grid density
 - Variation of lift with jet momentum coefficient (C_μ)
 - Convergence behavior

Jet Momentum Coefficient

- Definition

$$C_\mu = \frac{\dot{m}_j V_j}{\frac{1}{2} \rho_\infty V_\infty^2 S} = \frac{\rho_j V_j^2 h b}{\frac{1}{2} \rho_\infty V_\infty^2 c b}$$

- $C_\mu \sim M_\infty^{-2}$
- Assume the same jet conditions. Then (roughly) for $M_\infty = 0.12$ and $M_\infty = 0.6$

$$(C_\mu)_{M=0.6} \approx \frac{(C_\mu)_{M=0.12}}{25}$$

- One must keep this in mind when interpreting C_μ as M_∞ increases.

Computational Method

- Computer Code: CFL3D (developed at NASA Langley)
- Solves mass-averaged Navier-Stokes equations
- Allows multi-zone domain
- Grids: one-to-one, patched, or overset
- Finite-volume discretization method
 - Flux difference splitting scheme of Roe
 - 3rd-order upwind biased differencing, convective terms
 - central differencing, pressure and viscous terms
- Time advancement: implicit AF scheme

Computational Method (cont)

- Solves steady and unsteady flows
 - Steady flows: Convergence acceleration with multigrid (FMG)
 - Unsteady flows: dual time stepping with subiterations and multigrid

Turbulence Modeling

- Baldwin-Lomax (BL): Zero equation (algebraic eddy viscosity model)
- Spalart-Allmaras (SA)
 - One equation model (1994)
 - Transport equation for eddy viscosity
- Spalart-Allmaras with curvature effects (SARC)
- Shear stress transport (SST)
 - Two equation model (1992, Menter)
 - Transport of TKE and ω (\sim dissipation rate)
- Explicit algebraic stress (EASM-ko)
 - Two equation model + algebraic eqns. (1993, Gatski and Speziale)

SARC Turbulence Model

- The SA model can be written in general form as

$$\frac{D\tilde{\nu}}{Dt} = \mathcal{P} + \mathcal{D}_{diff} + \mathcal{D}_{diss} \quad (1)$$

where $\mathcal{P} = c_{b1}[1 - f_{t2}]W\tilde{\nu}$ and $\tilde{\nu} \sim \nu_t$.

- In the SARC model \mathcal{P} is replaced by

$$\mathcal{P}' = c_{b1}[f_{r1} - f_{t2}]W\tilde{\nu} \quad (2)$$

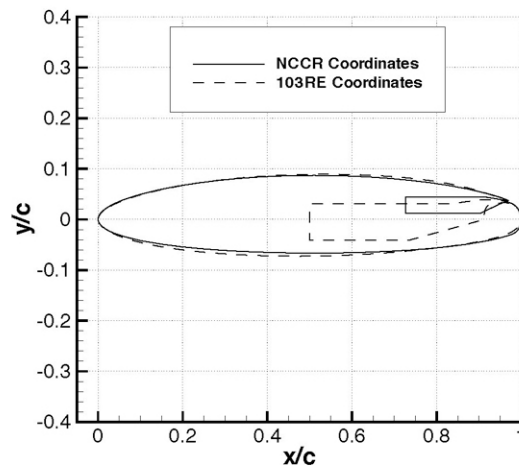
$$f_{r1} = (1 + c_{r1})\frac{2r^*}{(1 + r^*)} [1 - c_{r3}\tan^{-1}(c_{r2}\tilde{r})] - c_{r1}, \quad (3)$$

Airfoil Geometry

- Workshop geometry: Elliptical airfoil (designated NCCR 1510-7067N),
 - Chord of 8 inches
 - 15% thickness ratio, 1% camber ratio
 - Slot height-to-chord ratio: $h/c = 0.0030$ ($h = 0.024$ inches)
- Geometry: Elliptical airfoil (designated 103RE or 103XW)
 - Chord of 18 inches
 - 16% thickness ratio, 1% camber ratio
 - Slot height-to-chord ratio: $h/c = 0.0021$ ($h = 0.0378$ inches)

Geometry of Elliptical Airfoils

Circulation Control Airfoils



Flow Conditions

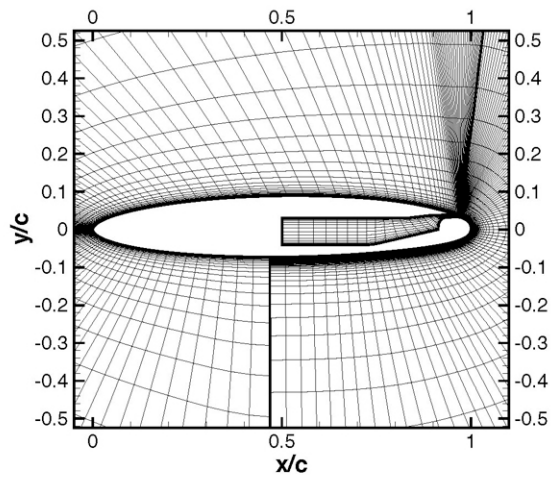
- High free-stream Mach number
 - $M_\infty = 0.6$, $Re_c = 5.2 \times 10^6$, $\alpha = 0^\circ$
 - Case 302: $M_{jet} = 0.519$, $C_\mu = 0.0032$
- Low free-stream Mach number
 - $M_\infty = 0.12$, $Re_c = 5.45 \times 10^5$, $\alpha = 0^\circ$
 - Case 283: $C_\mu = 0.209$
 - $M_\infty = 0.12$, $Re_c = 5.45 \times 10^5$, $\alpha = -8^\circ$
 - Case 321: $C_\mu = 0.184$

Computational Grid

- Medium grid
 - Multiblock domain with 3 blocks
 - 235 grid points around the airfoil
 - 49 points in the normal direction over forward part of the airfoil
 - 101 points in the normal direction over aft part of the airfoil (includes points in nozzle)
- Fine grid: number of grid cells doubled in each coordinate direction (70,563 points)

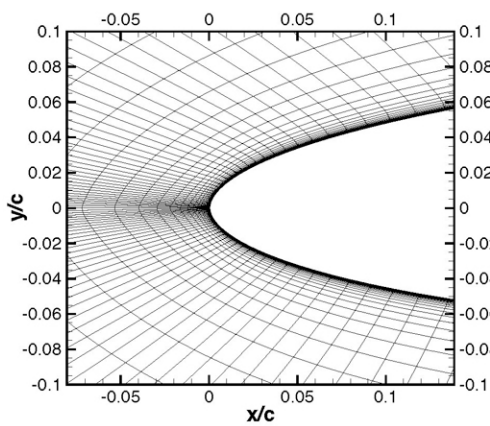
Computational Grid

Circulation Control Airfoil

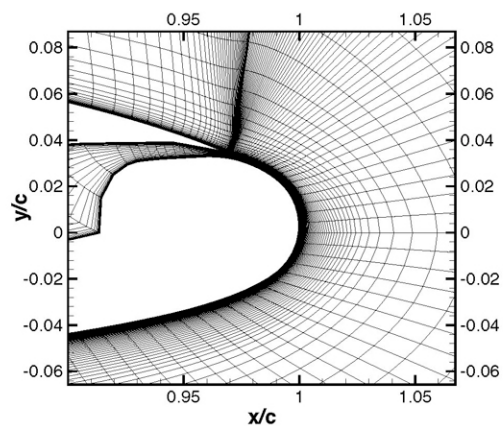


Computational Grid

Medium Grid, Leading and Trailing Edges



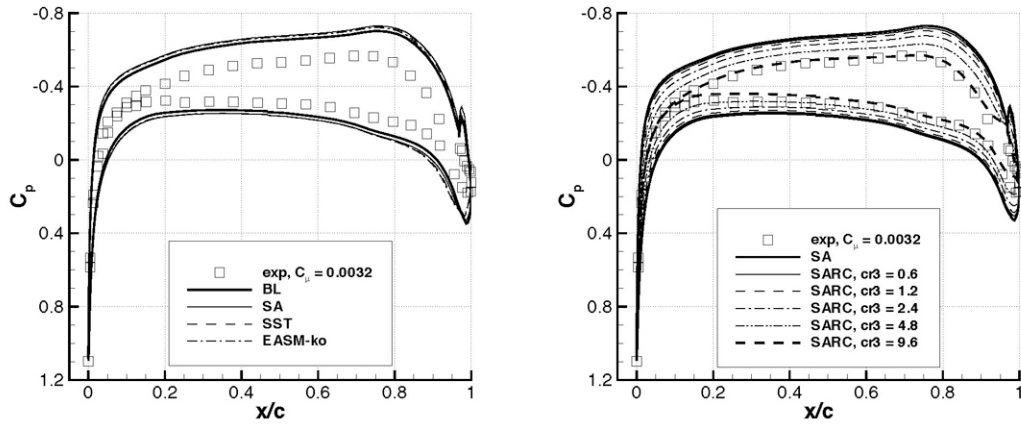
(a) Leading edge



(b) Trailing edge

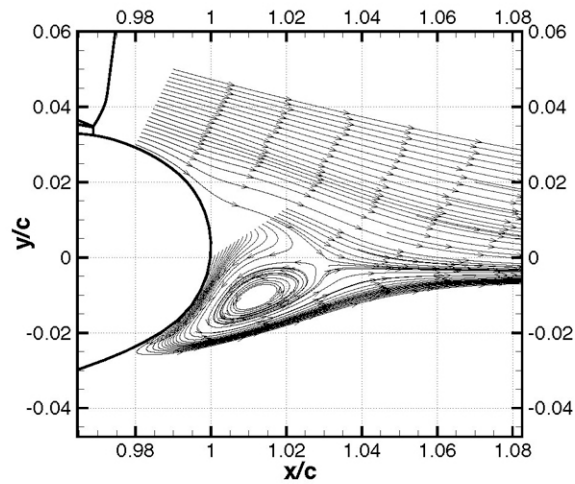
Surface Pressures (Case 302)

$$M_\infty = 0.6, \alpha = 0^\circ, Re_c = 5.2 \times 10^6, C_\mu = 0.0032, C_L = 0.191$$



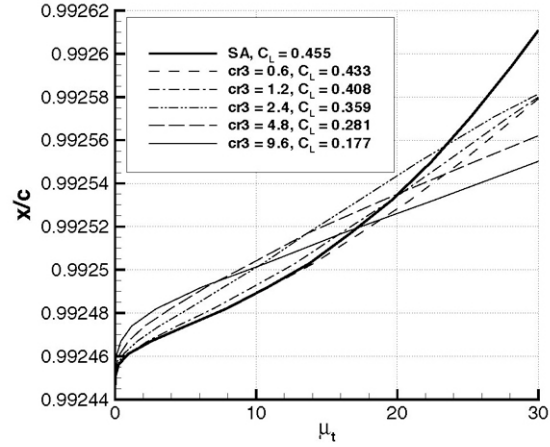
Streamline Pattern at Trailing Edge

$$M_\infty = 0.6, \alpha = 0^\circ, Re_c = 5.2 \times 10^6, C_\mu = 0.0032$$



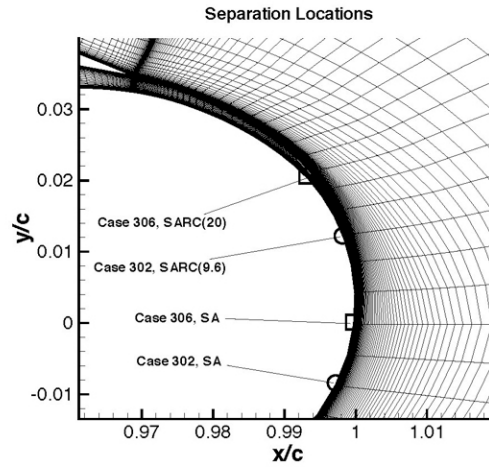
Effect of Model Constant on Turbulent Viscosity

$$M_\infty = 0.6, \alpha = 0^\circ, Re_c = 5.2 \times 10^6, C_\mu = 0.0032$$



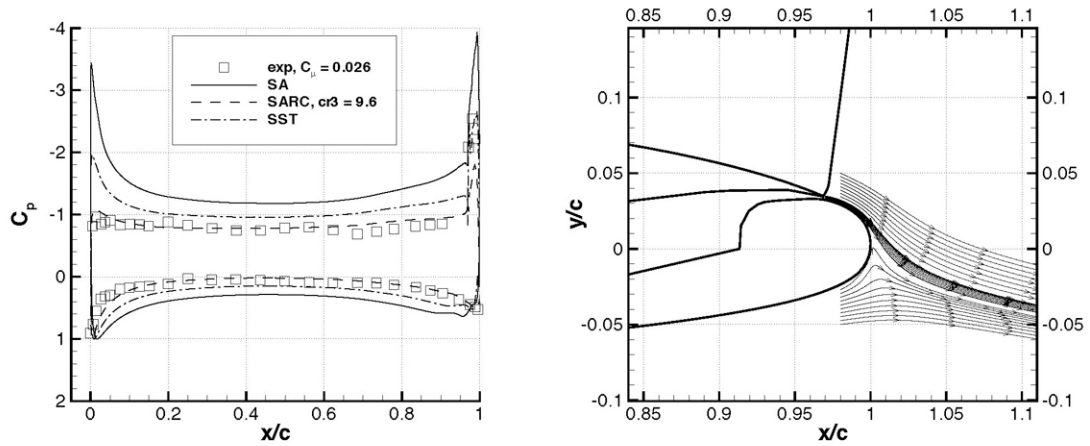
Influence of Turbulence Model on Separation

$$M_\infty = 0.6, \alpha = 0^\circ, Re_c = 5.2 \times 10^6$$



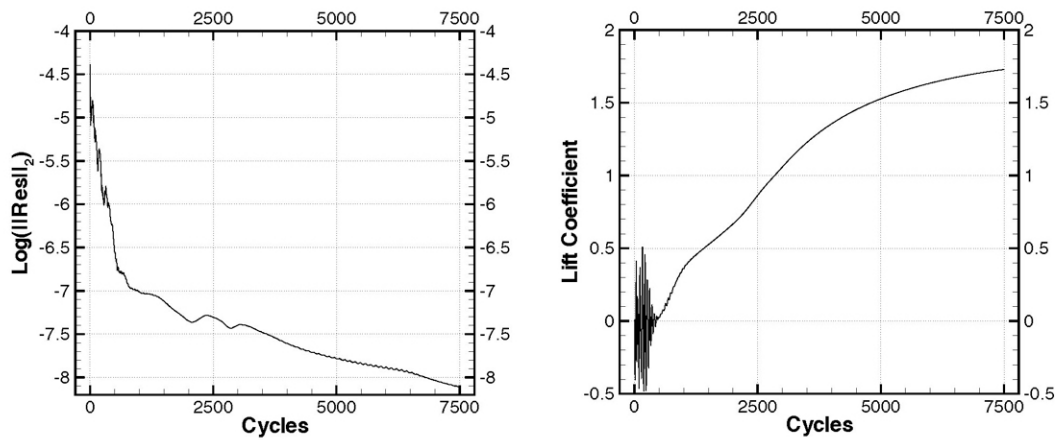
Surface Pressures and Jet Streamlines

$$M_\infty = 0.12, \alpha = 0^\circ, Re_c = 5.45 \times 10^5, C_\mu = 0.026$$



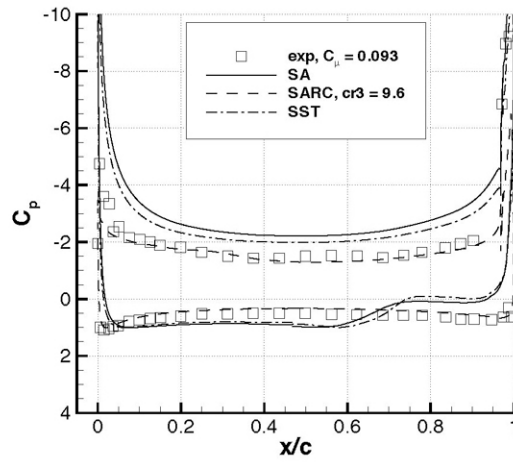
Convergence Behavior with SA Model

$$M_\infty = 0.12, \alpha = 0^\circ, Re_c = 5.45 \times 10^5, C_\mu = 0.026$$



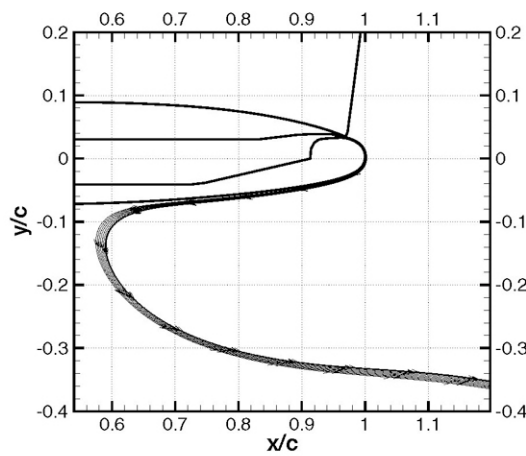
Surface Pressures

$$M_\infty = 0.12, \alpha = 0^\circ, Re_c = 5.45 \times 10^5, C_\mu = 0.093$$

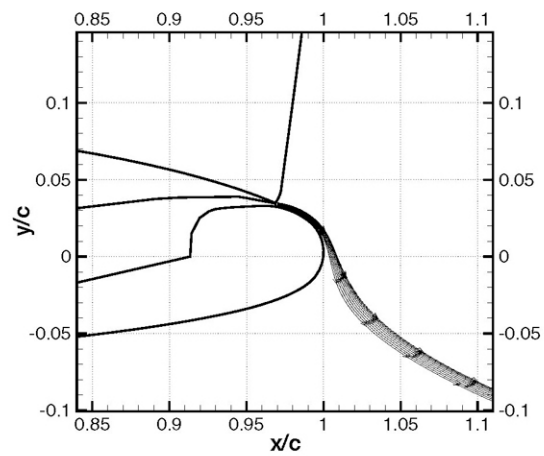


Jet Streamlines - SA and SARC Models

$$M_\infty = 0.12, \alpha = 0^\circ, Re_c = 5.45 \times 10^5, C_\mu = 0.093$$



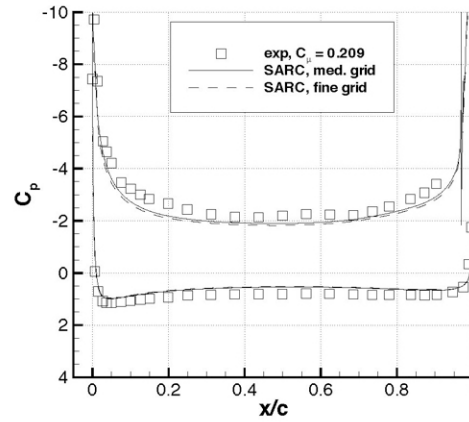
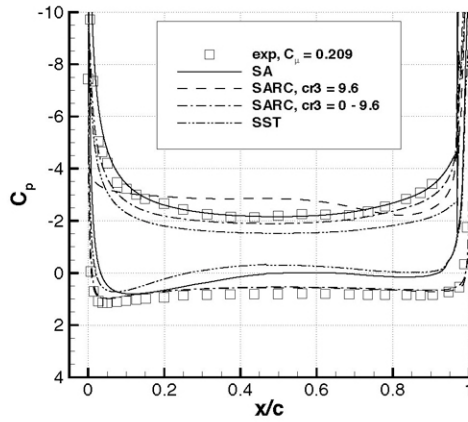
(a) SA



(b) SARC($cr3 = 9.6$)

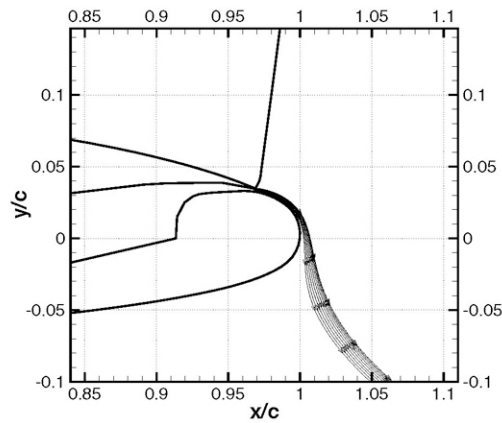
Surface Pressures and Jet Streamlines (Case 283)

$$M_\infty = 0.12, \alpha = 0^\circ, Re_c = 5.45 \times 10^5, C_\mu = 0.209$$

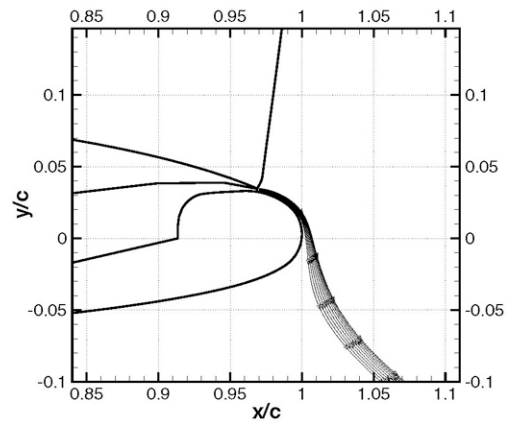


Jet Streamlines (Case 283)

$$M_\infty = 0.12, \alpha = 0^\circ, Re_c = 5.45 \times 10^5, C_\mu = 0.209$$



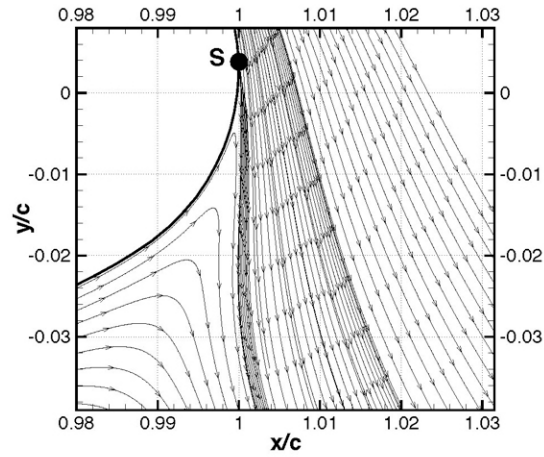
(a) Medium grid



(b) Fine grid

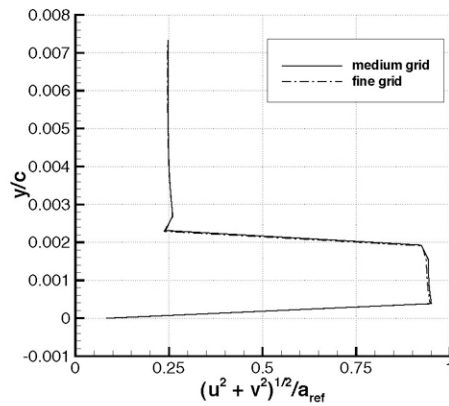
Streamline Pattern at Trailing Edge

$$M_\infty = 0.12, \alpha = 0^\circ, Re_c = 5.45 \times 10^5, C_\mu = 0.209$$

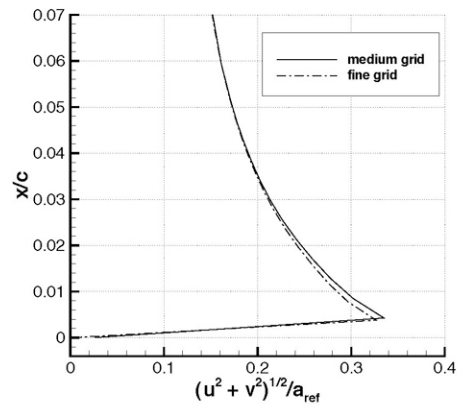


Effect of Mesh Density on Velocity Profiles

$$M_\infty = 0.12, \alpha = 0^\circ, Re_c = 5.45 \times 10^5, C_\mu = 0.209$$



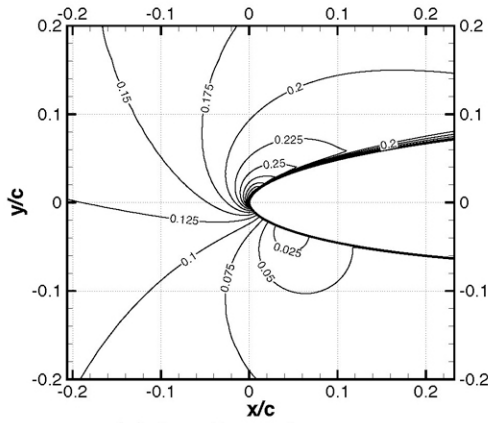
(a) Jet exit



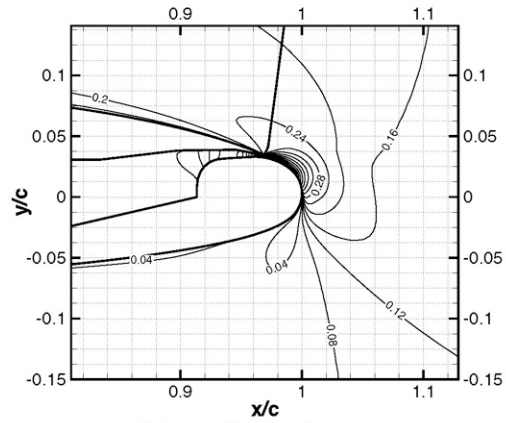
(b) Trailing edge

Mach Contours in Leading and Trailing Edge Regions

$$M_\infty = 0.12, \alpha = 0^\circ, Re_c = 5.45 \times 10^5, C_\mu = 0.209$$



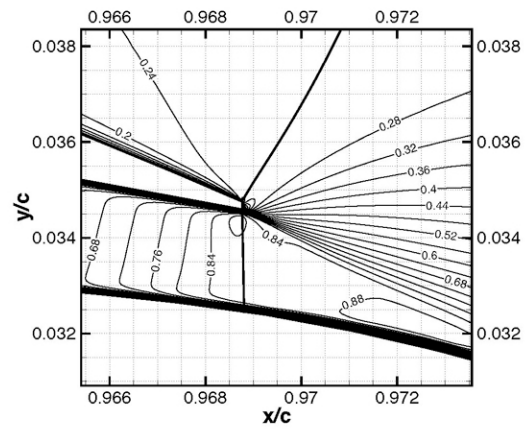
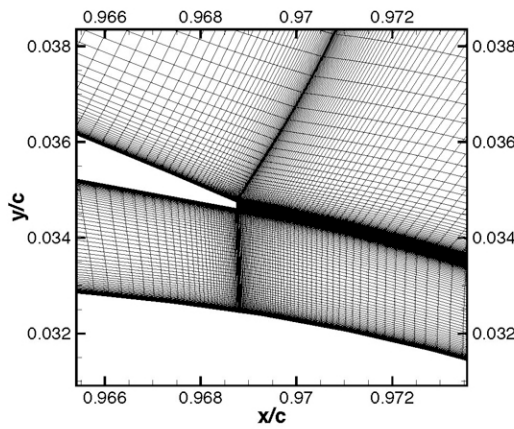
(a) Leading edge



(b) Trailing edge

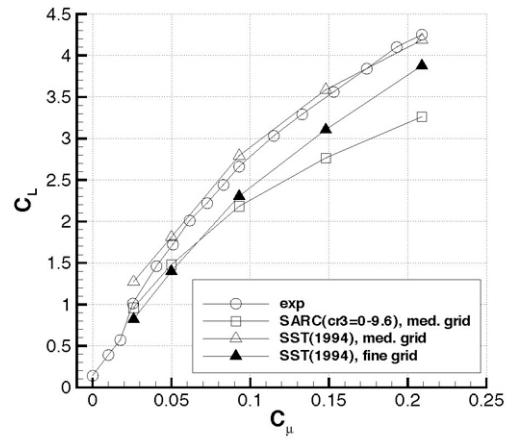
Mach Contours in Jet Exit Region

$$M_\infty = 0.12, \alpha = 0^\circ, Re_c = 5.45 \times 10^5, C_\mu = 0.209$$



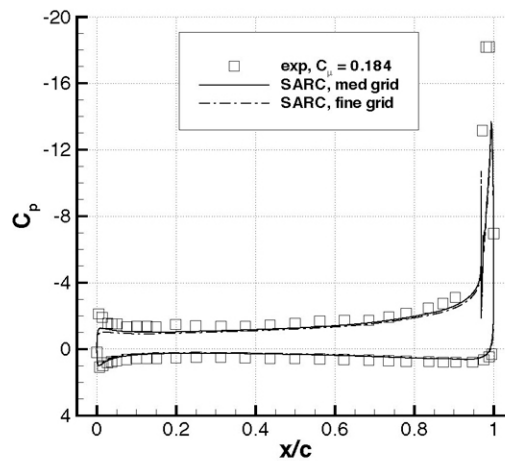
Variation of Lift with Jet Momentum

$$M_\infty = 0.12, \alpha = 0^\circ, Re_c = 5.45 \times 10^5$$



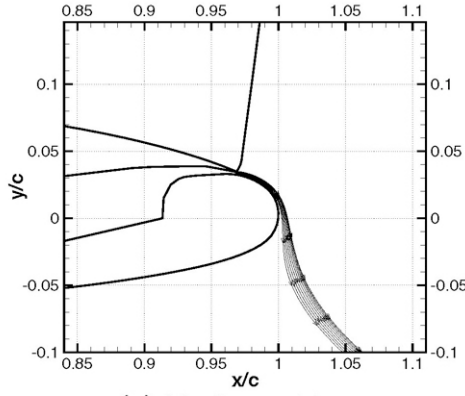
Surface Pressures (Case 321)

$$M_\infty = 0.12, \alpha = -8^\circ, Re_c = 5.45 \times 10^5, C_\mu = 0.184$$

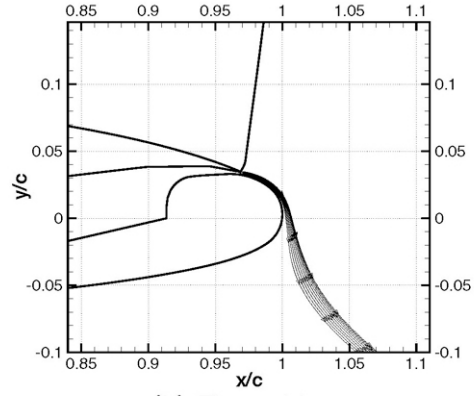


Jet Streamlines (Case 321)

$$M_\infty = 0.12, \alpha = -8^\circ, Re_c = 5.45 \times 10^5, C_\mu = 0.184$$



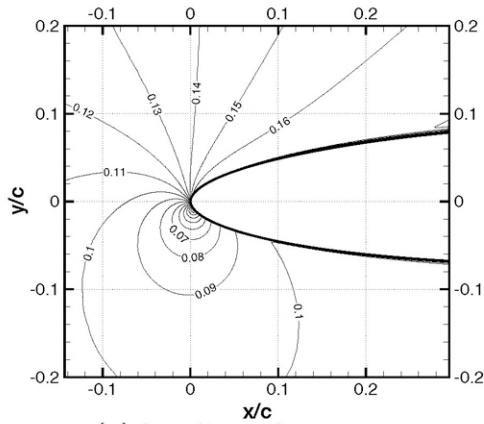
(a) Medium grid



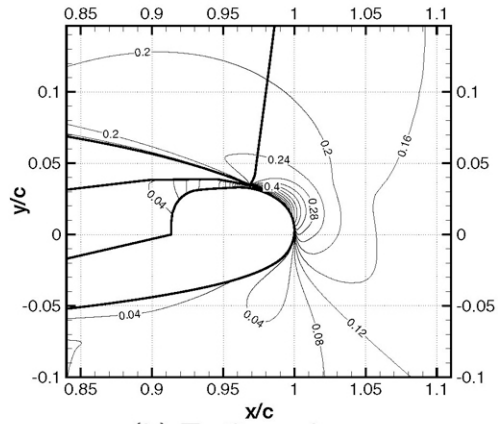
(b) Fine grid

Mach Contours in Leading and Trailing Edge Regions

$$M_\infty = 0.12, \alpha = -8^\circ, Re_c = 5.45 \times 10^5, C_\mu = 0.184$$



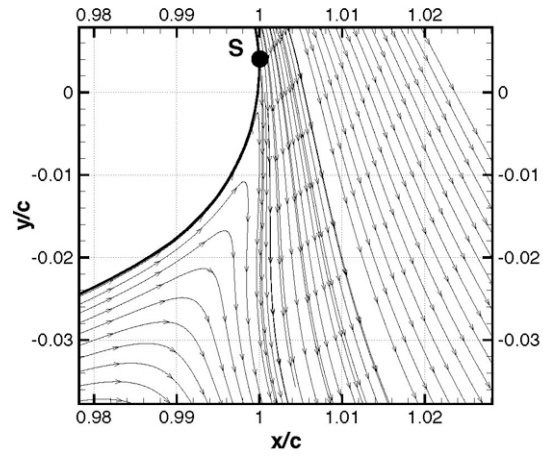
(a) Leading edge



(b) Trailing edge

Streamline Pattern at Trailing Edge

$$M_\infty = 0.12, \alpha = -8^\circ, Re_c = 5.45 \times 10^5, C_\mu = 0.184$$



Lift and Drag Coefficients

Case	C_μ	Grid	$(C_l)_{\text{exp}}$	C_l	$(C_d)_{\text{exp}}$	C_d
283	0.209	med.	4.20	3.26	-0.050	0.1140
283	0.209	fine	4.20	3.15	-0.050	0.1090
	0.281	med.		3.62	-0.050	0.1560
	0.342	med.		4.05	-0.050	0.2100
321	0.184	med.	2.40	2.17	-0.080	0.0957
321	0.184	fine	2.40	2.03	-0.080	0.0922

Comparison of computed and experimental lift and drag coefficients for circulation control airfoil.

Conclusions

- Circulation control airfoil flows at different conditions have been considered.
- Various turbulence models based on one and two transport equations have been considered.
- A calibration of the Spalart-Allmaras model with curvature effects (SARC) has resulted in good predictions of pressure distributions.
- Relatively small effects of mesh density have been demonstrated for results with SARC($\nu = 0 - 9.6$) model.

Role of Turbulence Modeling in Flow Prediction of Circulation Control Airfoils

by

G. McGowan, A. Gopalarathnam, X. Xiao, and H. Hassan
Mechanical and Aerospace Engineering
North Carolina State University, Raleigh, NC 27695-7910

Abstract

The k - ζ turbulence model and the k - ζ transitional/turbulence model are used to investigate the flow past 103RE(103 XW) circulation control airfoil, at a Mach number of 0.6, a Reynolds number of 5.2×10^6 and a range of momentum coefficients. Preliminary results suggest that the nature of the flow in the cavity plays a major role in determining the flow over the airfoil.

Introduction

The work was motivated by a presentation by Swanson, et al. at a workshop conducted at NASA Langley Research center on October 14, 2003 in which they presented results for the 103 RE (103 XW) circulation control airfoil tested by Abramson and Rogers², using the CFL3D code. Eight turbulence models were used to calculate the flow. None of the turbulence models gave good agreement with experiment.

Calculations were presented at this workshop using the k - ζ model³ and the k - ω model. The k - ω model gave essentially results similar to those presented in Ref. 1 and are included to provide reference to the predictions of the other models. The grid and input parameters used in Ref.1, were used in an older version of CFL3D (version 5) which was modified to incorporate the k - ζ turbulence and the k - ζ transitional/turbulence models. Thus, the goal of this work is to assess the role of existing turbulence models in predicting flows over circulation control (CC)

airfoils using the same code, grid and input parameters. Moreover, an attempt will be made to explain observed discrepancies between theory and experiment.

The k - ζ model^{3,4} differs from other traditional models used in Ref. 1 by the fact that it is derived by modeling the exact equations that govern the variance of velocity, or turbulence kinetic energy, k , and the variance of vorticity, or enstrophy, ζ . As a result, the k - ζ model contains all the relevant physics in the k and ζ equations, is tensorially consistent and Galilean invariant, coordinate-system independent, and is free of wall or damping functions. It correctly predicts wall-bounded shear flows and the growth of all free shear layers⁴ (Jets, wakes and mixing layers). According to Wilcox⁵, this is a minimum requirement for any turbulence model that is proposed for use in complex flows. It is to be noted that none of the turbulence models used in Ref. 1 satisfy the requirements suggested by Wilcox.

The k - ζ transitional/turbulence model, which is another option in our version of CFL3D was implemented after the workshop. In this model one has the option to treat the flow in each block as laminar, transitional or turbulent. The model requires that the transitional mechanism and freestream turbulent intensity be specified and is capable of predicting the onset and extent of transition. In this work, the transition over the external surface of the airfoil is deemed to be a result of the growth of Tollmien-Schlichting waves. The code has no transitional mechanism suited for internal flows, such as the cavity flow or subsonic nozzle employed here.

Results and Discussion

The grid employed is shown in Fig. 1. It consists of 235 grid points around the airfoil, 49 points in the normal direction over forward part (block 2) and 101 points in the aft part (block 3) including points in the cavity (block 1). The airfoil is elliptical in shape, 16% thick and 1%

comber. The chord C is 1.5 ft. It employs a single upper slot with height $h/C = 0.0021$. A summary of the flow condition employed is given in Table 1, with $C\mu$ defined as

$$C\mu = \dot{m}_j V_j / \frac{1}{2} \rho_\infty V_\infty^2 C \quad (1)$$

where \dot{m}_j is the jet mass flux per unit span, V_j is the jet velocity, ρ_∞ and V_∞ are the freestream density and velocity and M_j the jet Mach number. The effective angle of attack, α_{eff} , was determined by matching pressure coefficient distribution forward of mid-chord with a potential code that used C_l and angle of attack as inputs².

Figure 2 compares calculated and measured pressure distribution in the absence of injection (case 301). As is seen from the figure, both model predictions are in good agreement with experiment. Figure 3 compares predictions with experiment for case 302. As is seen from the figure, the k - ζ turbulence model predictions are in better agreement with experiment than those given by the k - ω model. Figures 4-5 compare the streamline patterns in the injection region.

Figure 6 compares the prediction of a steady k - ω solution and a provisional time-accurate k - ζ solution for the 306 case. It was not possible to obtain a steady solution using local time stepping for the k - ζ model. This is an indication that the flow is unsteady. The solution is a result of over 280,000 time-accurate steps. It was terminated before arriving at a statistically steady solution. Thus, it should be treated as a provisional solution.

The following results were obtained after the workshop. In this work, the k - ζ transitional/turbulence model was employed to analyze the flow for the 306 case. The model, as coded in CFL3D, allows the user to specify laminar, transitional or turbulent flow in each block.

Further, it requires the user to specify the transitional mechanism and the freestream turbulence intensity.

The transitional mechanism considered in the code is a result of the growth of Tollmien-Schlichting waves. This mechanism is not the correct mechanism for triggering transition in cavities. As a result, two cases were run. In the first, the flow in block 2 and 3 were specified transitional and turbulent, respectively, while the flow in the cavity was specified to be laminar. In the second case the flow in the cavity was assumed to be turbulent. It is seen from Figs. 7 and 8 that the results are dependent on whether the flow in the cavity is laminar or turbulent. A slight oscillation was noted in both solutions. It is not clear whether the shape of the cavity has any influence on the results.

Concluding Remarks

It is to be emphasized that the results presented in this work are preliminary. Additional investigation is required to assess the role of using a cavity in analyzing CC airfoils. In addition, other grids need to be investigated.

There is a need to develop new approaches to determine the effective Mach number and effective angle of attack for such flows. In addition, measurements other than the pressure distribution, such a velocity profiles and turbulent stresses are needed to further validate turbulence models.

Acknowledgements

The authors would like to acknowledge the assistance of Dr. Chris Rumsey of NASA Langley for providing us, for the 103 RE (103 XW) airfoil, the grid, input data and advice; and Dr. Charlie Swanson, of NASA Langley for sharing with us the results presented at the October 16, 2003 workshop. Further, the authors would like to acknowledge many helpful discussions

during and after the workshop with Dr. Jane Abramson of the David Taylor Naval Ship Research and Development Center.

References

1. Swanson, C., Rumsey, C., and Anders, S., Private Communications.
2. Abramson, J., and Rogers, E. O., “High-Speed Characteristics of Circulation Control Airfoils,” AIAA Paper 83-0265, January 1983.
3. Robinson, D. F., and Hassan, H. A., “Further Development of the k - ζ (Enstrophy) Turbulence Closure Model,” *AIAA Journal*, Vol. 36, No. 10, October 1998, pp. 1825-1833.
4. Robinson, D. F., Harris, J. E., and Hassan, H. A., “Unified Turbulence Closure Model for Axisymmetric and Planar Free Shear Flows,” *AIAA Journal*, Vol. 33, No. 12, December 1995, pp. 2324-2331.
5. Wilcox, D. C., *Turbulence Modeling for CFD*, DCW Industries, Inc., La Canada, CA, 2nd Edition, 1998.
6. Warren, E. S., and Hassan, H. A., “Transition Closure Model for Predicting Transition Onset,” *Journal of Aircraft*, Vol. 35, No. 5, 1998, pp. 769-775.

Table 1

Case	C_μ	M_j	α_{eff}
301	0.0	0.0	– 0.0540
302	0.0032	0.519	– 0.2865
306	0.0110	0.979	– 0.7980

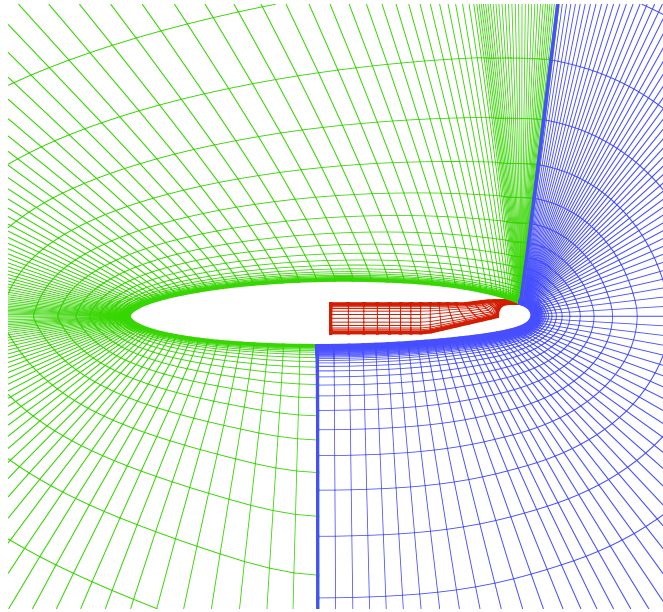


Fig.1 Closeup of the grid employed

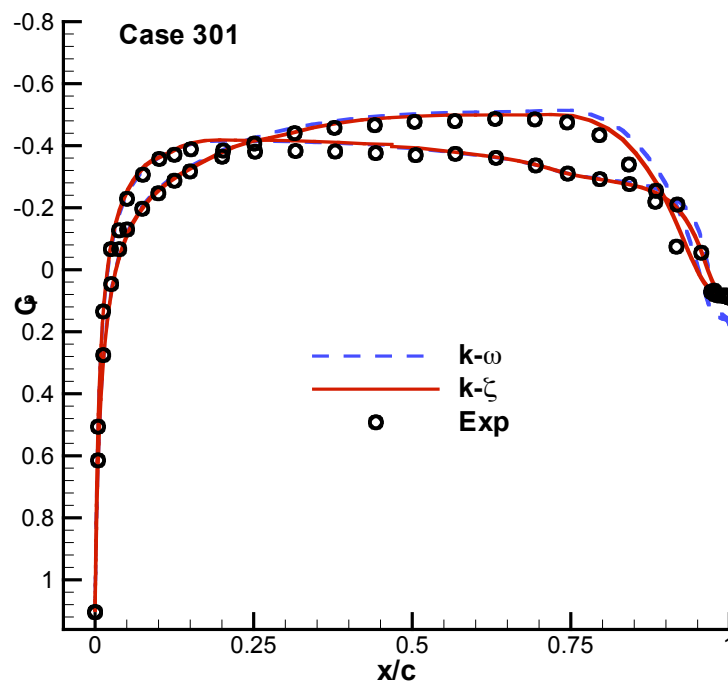


Fig.2 Comparison of C_p for $k-\zeta$ and $k-\omega$

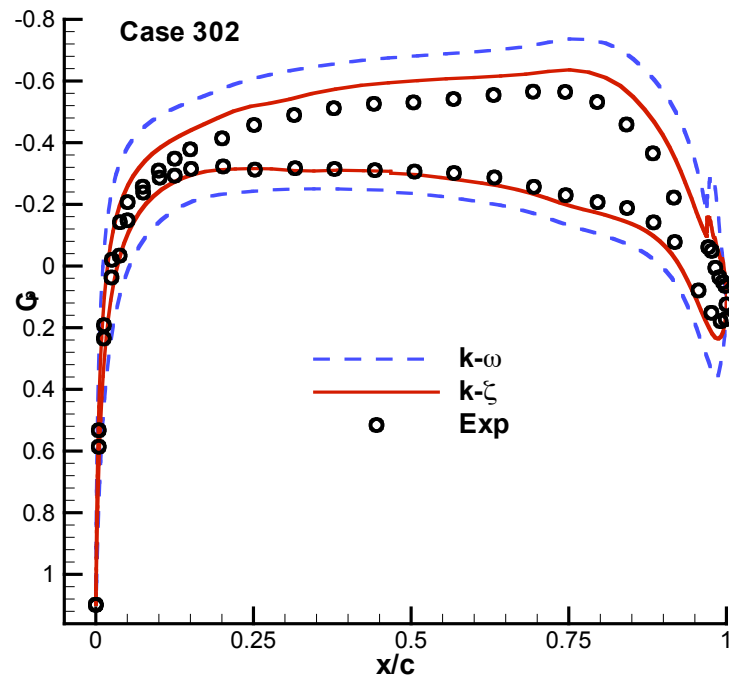


Fig.3 Comparison of C_p for $k-\zeta$ and $k-\omega$

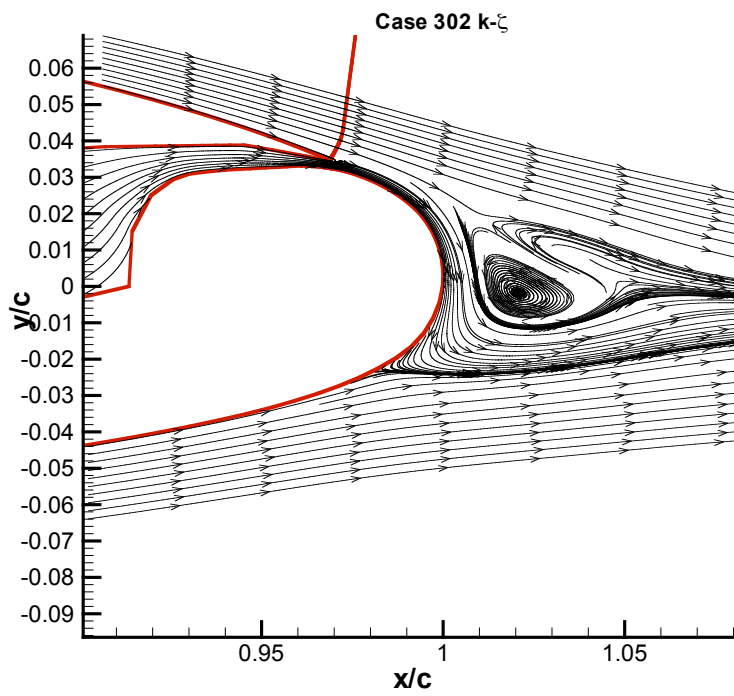


Fig.4 Streamline pattern around separate point ($k-\zeta$)

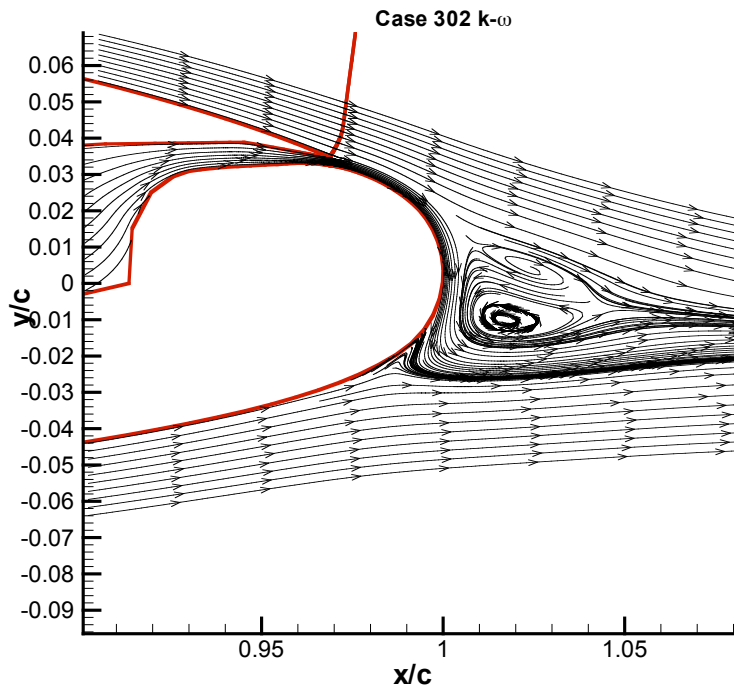


Fig.5 Streamline pattern around separate point ($k-\omega$)

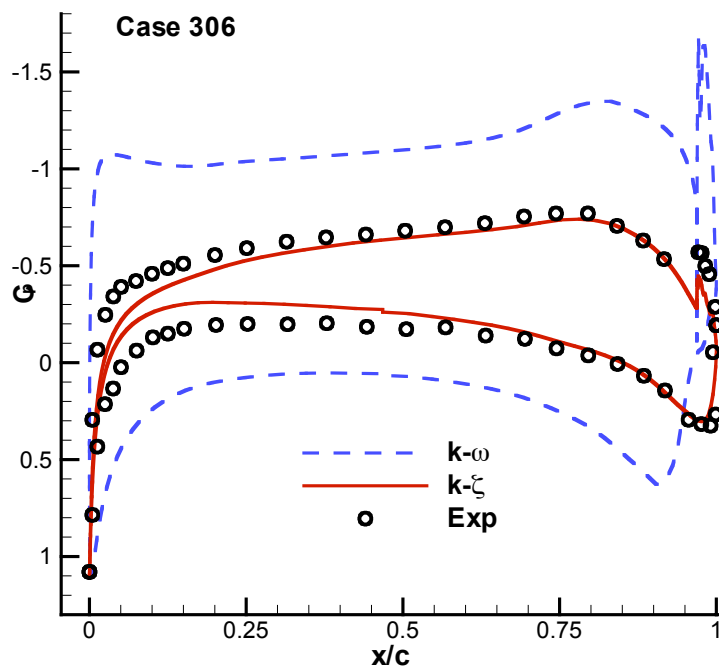


Fig.6 Comparison of C_p for $k-\zeta$ and $k-\omega$

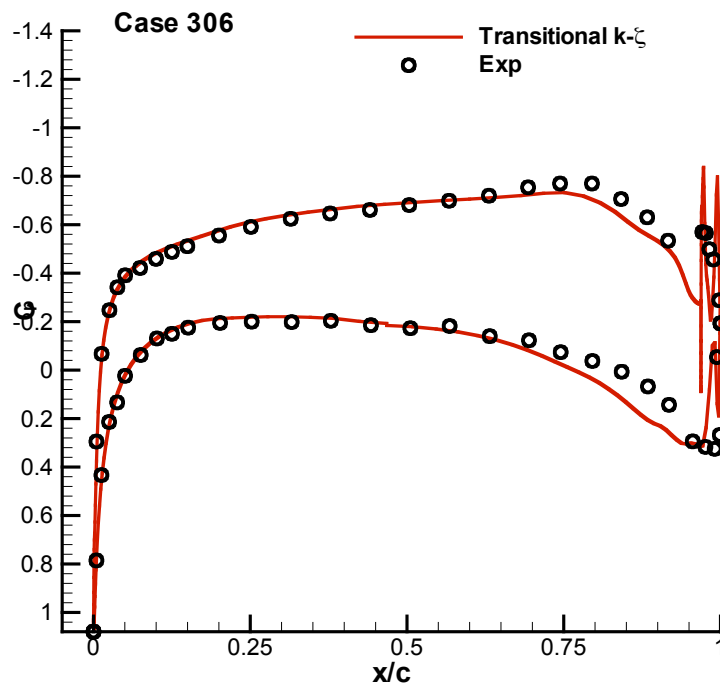


Fig.7 Prediction of C_p using transitional $k-\zeta$
(Laminar cavity)

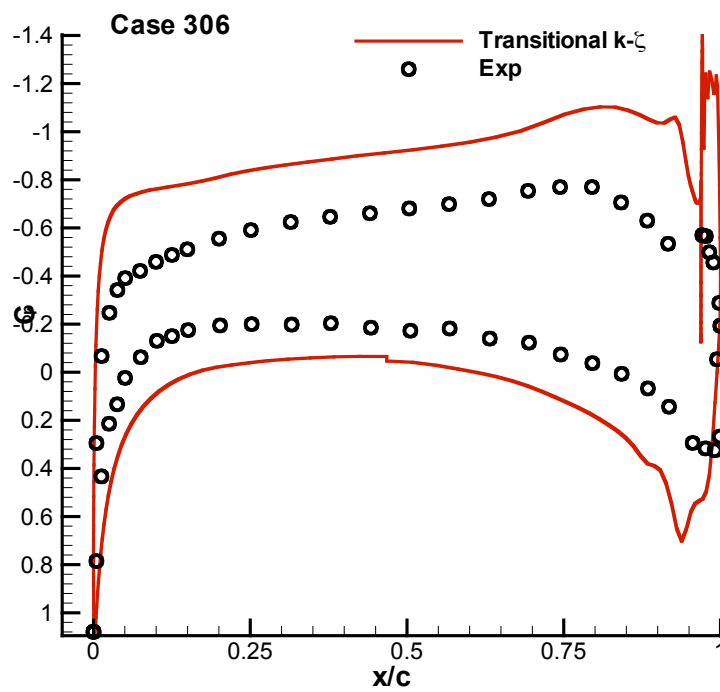


Fig.8 Prediction of C_p using transitional $k-\zeta$
(Turbulent cavity)

Role of Turbulence Modeling in Flow Prediction
Of Circulation Control Airfoils

by

G. McGowan, A. Gopalarathnam, X. Xiao, and H. Hassan

North Carolina State University
Raleigh, NC 27695-7910

2004 Circulation Control Workshop
March 16-17, 2004

Acknowledgement

The authors would like to acknowledge the assistance of Dr. Chris Rumsey for providing us, for the 103RE (103XW) airfoil, with the grid, input data, and advice, and Dr. Charlie Swanson for sharing with us the results presented at the October 16, 2003 Workshop.

Outline

1. Motivation
2. Comparison with Experiment
3. Concluding Remarks
4. Future Work

Motivation

1. Swanson, Rumsey and Anders made a presentation in the Workshop on October 14, 2003, in which they presented results for the 103RE (103 XW) airfoil which was tested by Abramson and Rogers
2. Cases considered where for $M = 0.6$, $Re_c = 5.2 \times 10^6$

<u>Case</u>	<u>C_μ</u>	<u>M_j</u>	<u>α_{eff}</u>
301	0.0	0.0	-0.0540
302	0.0032	0.519	-0.2865
306	0.0110	0.979	-0.7980

Motivation (Cont.)

3. Bulk of the calculations used CFL3D and eight different turbulence models.
4. Results for the non-injection case were in good agreement with experiment but the ones with injection were not.
5. Calculations will be presented for two additional models:
The $k-\omega$ model and the $k-\zeta$ model
6. The $k-\omega$ model performance is essentially similar to the other models discussed by Swanson et al. and is included to provide reference to the other models.

Motivation (Cont.)

7. The $k-\zeta$ model is employed because it differs from other models in two distinct ways
 - A. The ζ -equation is derived by modeling all the terms in the equation that governs the variance of vorticity or enstrophy. As a result, the $k-\zeta$ model has the following features:
 - a. Contains all the relevant physics in the k and ζ equations
 - b. Tensorially consistent and Galilean invariant
 - c. Coordinate-system independent
 - d. Free of wall and damping functions

Motivation (Cont.)

- B. In addition to correctly predicted wall-bounded shear flows, the $k-\zeta$ model correctly predicts the growth rate of all free shear layers (Jets, Wakes and Mixing Layers). None of the models used by Swanson, et al. have similar characteristics.

According to Wilcox (p. 122), this is a minimum requirement for any turbulence model that is proposed for use in complex flows.

- 8. The $k-\zeta$ was incorporated into version 5.0 of CFL3D. All calculations presented here use this version
- 9. We used the same grid and same inputs employed by Swanson et al.

Motivation (Cont.)

- 10. It is to be noted that the effective angle of attack was determined by matching pressure distribution forward of the mid-chord with a potential code that uses C_ℓ and angle of attack as input.

The procedure is questionable in the presence of flow separation.

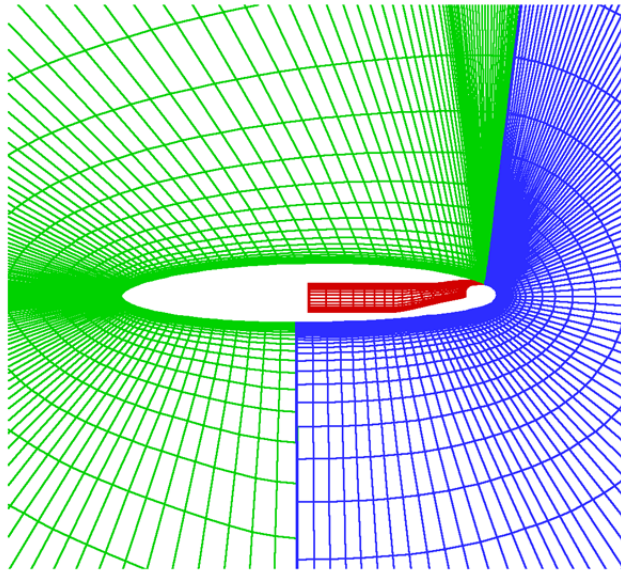


Fig.1 closeup of the grid employed

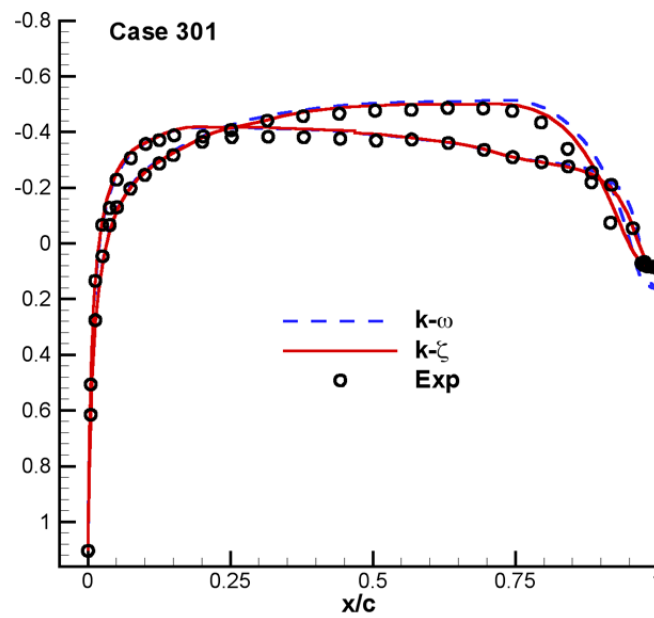


Fig. 2 Comparison of C_p for $k-\zeta$ and $k-\omega$

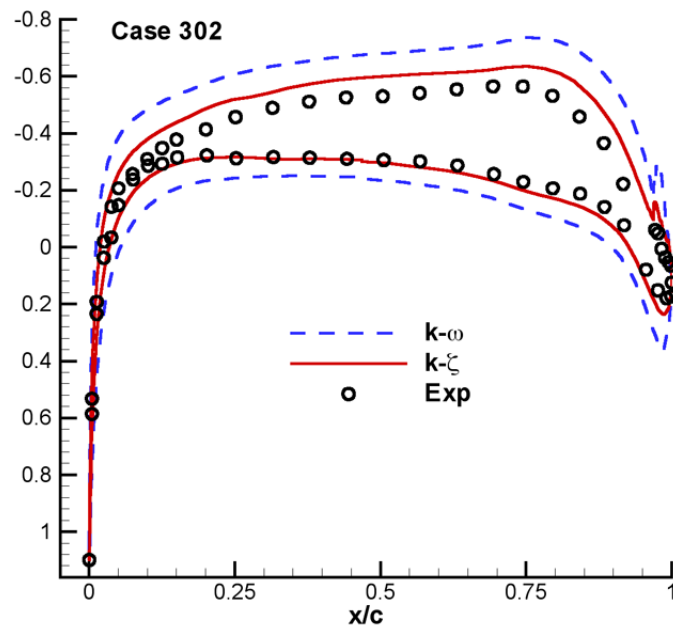


Fig. 3 Comparison of C_p for $k-\zeta$ and $k-\omega$

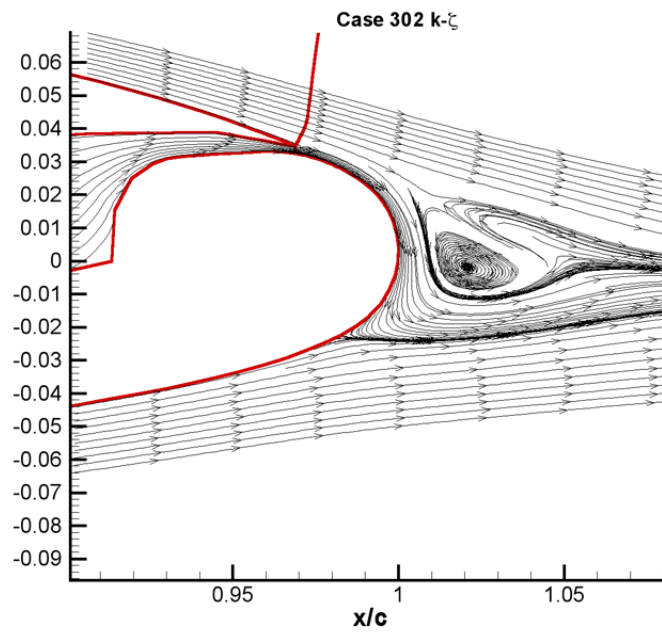


Fig. 4 Streamline pattern around separate point ($k-\zeta$)

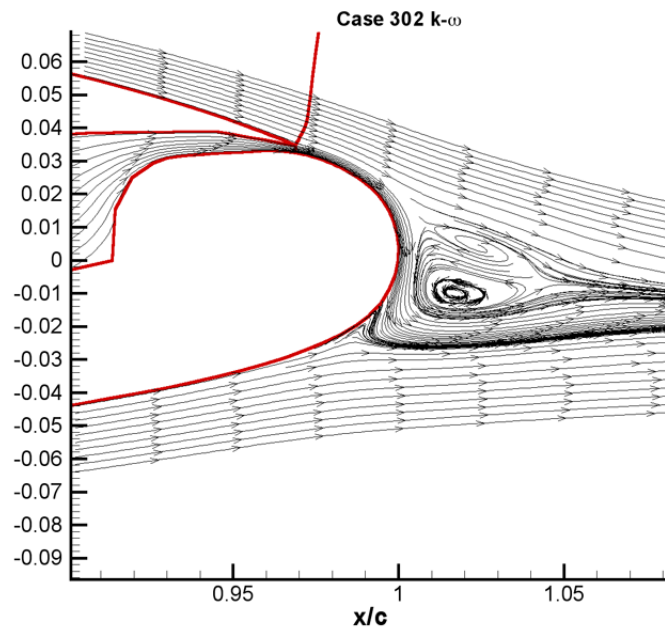


Fig. 5 Streamline pattern around separate point ($k-\omega$)

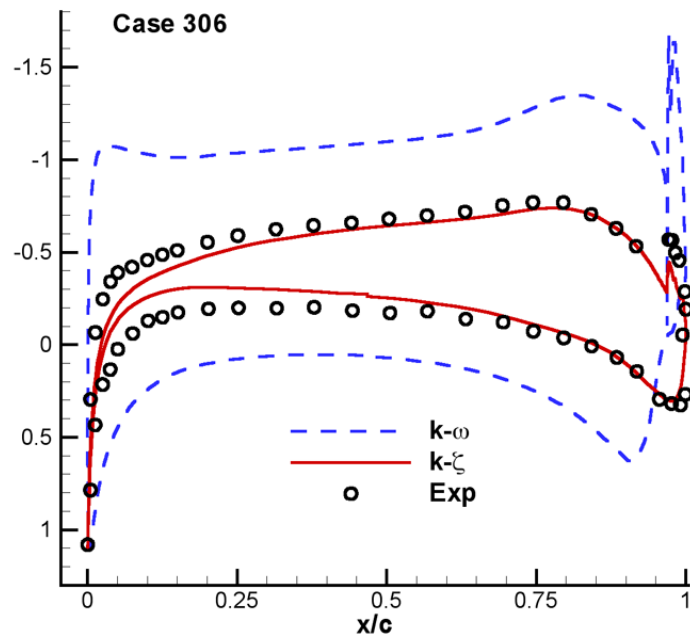


Fig. 6 Comparison of C_p for $k-\zeta$ and $k-\omega$

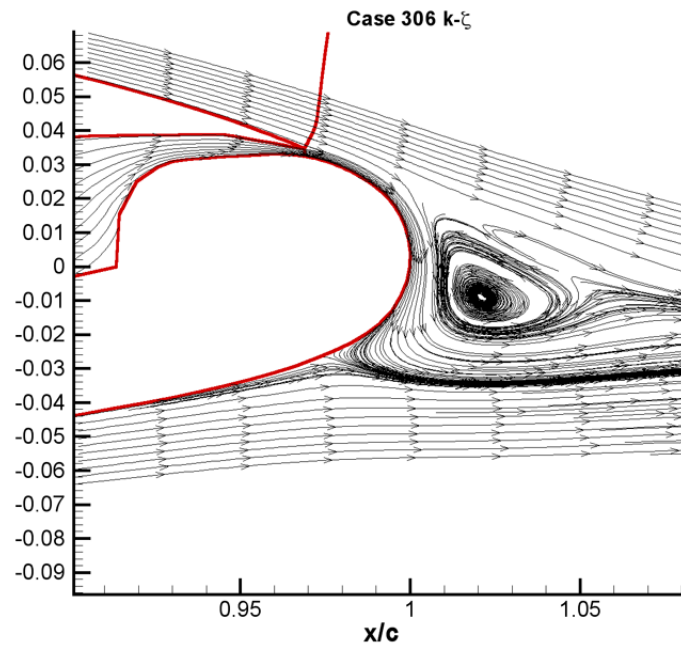


Fig. 6 Streamline pattern around separate point ($k-\zeta$)

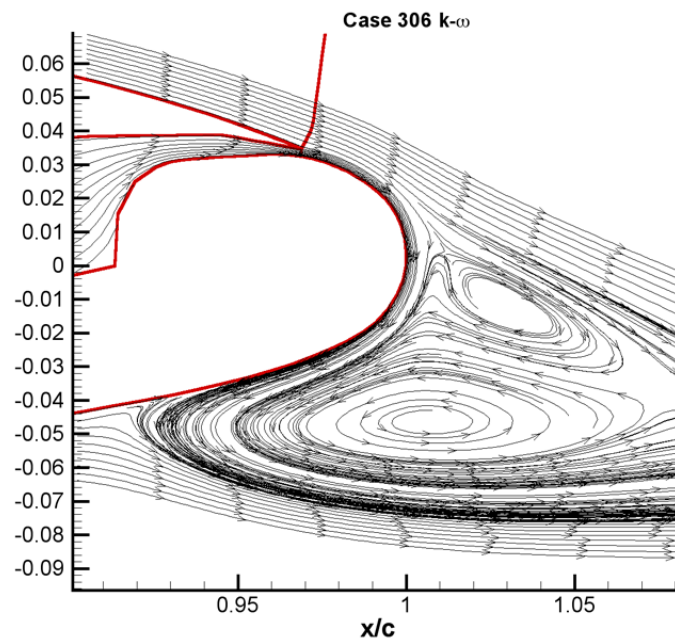
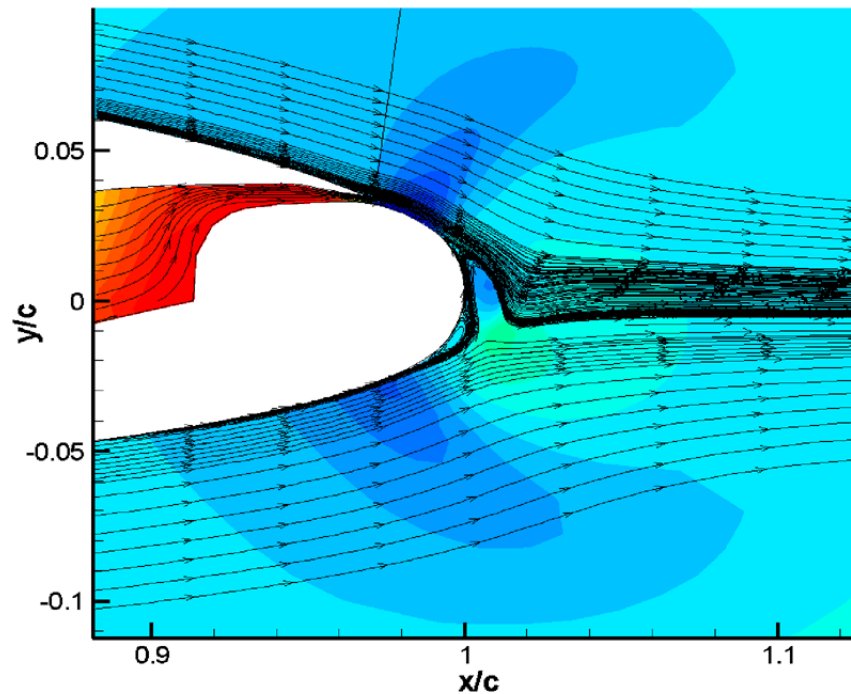


Fig. 5 Streamline pattern around separate point ($k-\omega$)



Concluding Remarks

1. It appears that Wilcox observation regarding using turbulence models that are capable of predicting both wall-bounded and free shear flows to study complex flows has some merit.
2. There is a need to develop new approaches to determine the effective Mach number and effective angle of attack.
3. Prediction of pressure distribution is not sufficient to validate a turbulence model. Measurements of velocity profiles and turbulent stresses are needed to further validate models.

Future Work

1. It would be desirable to undertake a well-coordinated experimental/computational program where the experiment is well-documented and where a variety of relevant measurements are taken.
2. There is a need to investigate the role of transition on the performance of circulation control airfoils.

Computational Evaluation of the Steady and Pulsed Jet Effects on the Performance of a Circulation Control Wing Section

Yi Liu, Lakshmi N. Sankar, Robert J. Englar, Krishan K. Ahuja, R. Gaeta

Georgia Institute of Technology, Atlanta, GA 30332-0150

ABSTRACT

Circulation Control technology is a very effective way of achieving high lift forces required by aircraft during take-off and landing. This technology can also directly control the flow field over the wing. Compared to a conventional high-lift system, a Circulation Control Wing (CCW) can generate comparable or higher lift forces during take-off/landing with fewer or no moving parts and much less complexity. In this work, an unsteady three-dimensional Navier-Stokes analysis procedure has been developed and applied to Circulation Control Wing configurations. The effects of 2-D steady jets and 2-D pulsed jets on the aerodynamic performance of CCW airfoils have been investigated. It is found that a steady jet can generate very high lift at zero angle of attack without stall, and that a small amount of blowing can eliminate vortex shedding at the trailing edge, a potential noise source. It is also found that a pulsed jet can achieve the same high lift as a steady jet at lower mass flow rates, especially at a high frequency, and that the Strouhal number has a more dominant effect on the pulsed jet performance than just the frequency or the free-stream velocity.

INTRODUCTION

During the past several decades, there has been a significant increase in air travel and a rapid growth in commercial aviation. At the same time, environmental regulations and restrictions on aircraft operations have become issues that affect and limit the growth of commercial aviation. In particular, the noise pollution from aircraft, especially around the airport, has become a major problem that needs to be solved. Reducing aircraft noise has become a priority for airlines, aircraft manufacturers, and NASA researchers.

Current generation large commercial aircraft are dependent on components that generate high levels of lift at low speeds during take-off or landing from existing runways. Conventional high-lift systems include flaps and slats, with the associated flap-edges and gaps that are significant noise sources. Furthermore, these high-lift systems also add to the weight of the aircraft, and are costly to build and maintain. An alternative to the conventional high-lift systems is the Circulation Control Wing (CCW) technology. This technology and its aerodynamic benefits have been extensively investigated over many years by Englar et al at Georgia Tech through experimental studies [1, 2]. A limited number of numerical analyses [1, 3, 4] have also been done. Work has also been done on the acoustic characteristics of Circulation Control Wings [5]. These studies indicate that very high C_L values (as high as 8.5 at $\alpha=0^\circ$) may be achieved with Circulation Control wings. Because many mechanical components associated with the high-lift system are no longer needed, the wings can be lighter and less expensive to build. Major airframe noise sources such as flap-edges, flap-gaps, and trailing/leading edge flow-separation can all be eliminated with the use of CCW systems.

Earlier designs of CCW configurations used airfoils with a large radius rounded trailing edge to maximize the lift production. However, these designs also produced very high drag [6]. Such high drag levels associated with a blunt, large radius trailing edge can be prohibitive under cruise conditions when Circulation Control is no longer necessary. To overcome this difficulty, an advanced CCW section, called a circulation hinged flap [1, 2], has been developed that replaces the traditional rounded trailing edge CC airfoil. This concept originally developed by Englar is shown in Figure 1. The upper surface of the CCW flap is a large-radius arc surface, but the lower surface of the flap is flat. The flap could be deflected from 0 degrees to 90 degrees. When an aircraft takes-off or lands, the flap is deflected as in a conventional high lift system, and Circulation Control is deployed. The large curvature of the upper surface produces a large jet turning angle, leading to high lift. When the aircraft is in cruise, the flap is retracted and a conventional sharp trailing edge shape results, greatly reducing the drag. This kind of flap does have some moving elements that increase the weight and complexity over the earlier CCW design. But overall, the hinged flap design still maintains most of the advantages of the Circulation Control, while greatly reducing the drag in cruising condition associated with the rounded trailing edge CCW design.

To understand and quantify the aeroacoustic characteristics and benefits of the Circulation Control Wing, Munro, Ahuja and Englar [7, 8, 9, 10] have recently conducted several acoustic experiments comparing the noise levels of a conventional high-lift system with that of an advanced CC wing at the same lift setting. The present Computational Fluid Dynamics (CFD) study [11] is intended to complement this work, and numerically investigate the aerodynamic characteristics and benefits associated with the CC airfoil. CFD studies

such as the one presented here can also help in the design of future generation CCW configurations.

SCOPE OF PRESENT WORK

The present work is an extension of a previous work where 2-D studies of the effects of steady and pulsed jets on the CCW configuration shown in figure 1 were done [12]. The objective of this study is to isolate and quantify the effects of the parameters such as leading edge blowing, free-stream velocity, jet slot-height, and frequency, on the performance of 2-D steady and pulsed Circulation Control jets. The unsteady Navier-Stokes methodology used here has also been applied to study 3-D Circulation Control Wing and to model tangential blowing effects. These 3-D results have not been included here, and reader is referred to the Ph. D dissertation of the first author [11] for details.

MATHEMATICAL AND NUMERICAL FORMULATION

Governing Equations

In the present work, Reynolds-averaged Navier-Stokes equations were solved using an unsteady three-dimensional viscous flow solver. This solver can model flow fields over isolated wing-alone configurations. This solver has been validated for clean and iced wings by Kwon et al [13] and Bangalore et al [14]. As part of the first author's Ph. D work, modifications to this solver have been made to model Circulation Control jets. Both 3-D finite wings and 2-D airfoils may be simulated with the same solver. Two turbulence models have been used: the Baldwin-Lomax [15] algebraic model and Spalart and Allmaras [16] one

equation model. In this work, all the calculations were done using the Baldwin-Lomax model. The effects of turbulence model are discussed in Ref. 11.

Computational Grid

Construction of a high-quality grid about the CCW airfoil is made difficult by the presence of the vertical jet slot. In this solver, the jet slot is treated as part of the airfoil surface as done by Shrewsbury [17, 18] and Williams and Franke[19]. A hyperbolic three-dimensional C-H grid generator is used in all the calculations. The three-dimensional grid is constructed from a series of two-dimensional C-grids with an H-type topology in the spanwise direction. The grid is clustered in the vicinity of the jet slot and the trailing edge to accurately capture the jet behavior over the airfoil surface.

The grid generation and the surface boundary condition routines are general enough so that one can easily vary the slot location, slot size, blowing velocity and the direction of blowing.

Boundary Conditions

In Circulation Control Wing studies, the driving parameter is the momentum coefficient, C_μ , defined as follows.

$$C_\mu = \frac{\dot{m}V_{jet}}{\frac{1}{2}\rho_\infty V_\infty^2 S} \quad (1)$$

Here, the jet mass flow rate is given by:

$$\dot{m} = \rho_{jet} V_{jet} A_{jet} \quad (2)$$

Conventional airfoil boundary conditions are applied everywhere except at the jet slot exit. Non-reflection boundary conditions are applied at the outer boundaries of C grid. On the airfoil surface, adiabatic and no-slip boundary conditions are applied, and the normal derivative of the pressure is set to zero.

At the jet slot exit, the jet is assumed to be subsonic, and the following conditions are specified: total temperature of the jet, momentum coefficient C_μ as a function of time, and the flow angle at the exit. In this simulation, the jet was tangential to the airfoil surface at the exit. All other parameters were computed using ideal gas law, and by equating the static pressure at the slot exit to the static pressure field over the airfoil, in the immediate vicinity of the jet slot.

RESULTS AND DISCUSSION

The CCW configuration studied in the present work is shown in Figure 2. The flap setting angle may be varied both in the experiments and the simulations. The studies presented here are all for the 30 degree flap setting. In both the experiments [1] and the present studies, the free-stream velocity was approximately 94.3 ft/sec at a dynamic pressure of 10 psf and an ambient pressure of 14.2 psia. The free-stream density is 0.00225 slugs/ft³. These conditions translate into a free-stream Mach number 0.0836. The airfoil chord was 8 inch and the Reynolds number was 395,000.

Validation Studies

Prior to its use in studying CCW configurations, the Navier-Stokes solver was validated by modeling the viscous subsonic flow over a small aspect-ratio wing made of NACA 0012 airfoil sections [12], and the results were in good agreement with the experimental measurement of Bragg and Spring [20]. These validation studies have been previously documented in Ref. 11 and 12, and are not reproduced here.

Figure 3 shows the variation of lift coefficient with respect to C_μ at a fixed angle of attack ($\alpha=0$ degree) for the CCW configuration with a 30-degree flap. Excellent agreement with measured data from the experiments by Englar [1] is evident. It is seen that very high lift can be achieved by Circulation Control technology with a relatively low C_μ . A lift coefficient as high as 4 can be obtained at a C_μ value of 0.33, and the lift augmentation $\Delta C_l / \Delta C_\mu$ is greater than 10 for this 30-degree flap configuration.

Figure 4 shows the computed C_l variation with the angle of attack, for a number of C_μ values, along with measured data. It is found that the lift coefficient increases linearly with angle of attack until stall, just as it does for conventional sharp trailing edge airfoils. However, the increase of lift with angle of attack breaks down at high enough angles. This is due to leading edge static stall, and is much like that experienced with a conventional airfoil, but occurs higher $C_{l,max}$ values, thanks to the beneficial effects of Circulation Control. The calculations also correctly reproduce the decrease in the stall angle observed in the experiments at high momentum coefficients. Unlike conventional airfoils that experience stall due to the progressive growth of trailing edge separation, CCW configurations stall due to leading edge separation. Figure 5 shows typical streamlines around the CC airfoil at an angle of attack of 6 degrees, and $C_\mu = 0.1657$ at a typical instance in time. In this case, a

leading edge separation bubble forms, that spreads over the entire upper surface resulting in a loss of lift. However, the flow is still attached over the trailing edge because of the strong Coanda effect.

Leading Edge Blowing

Functioning like a slat, leading edge blowing is an effective way of alleviating leading edge stall and for achieving the desired performance at high angles of attack. To understand the effects of leading edge blowing, a dual-slot CC airfoil was designed, and simulations of both leading edge (LE) and trailing edge (TE) blowing were done. Figure 6 shows lift coefficient variations with angle of attack for three different combinations of LE and TE blowing. In the first case, there is only a TE blowing with $C_{\mu} = 0.08$, and it is seen that the stall angle is very small, at approximately 5 degrees. If a small amount of LE blowing is used ($C_{\mu} = 0.04$), while keeping the TE blowing at $C_{\mu} = 0.08$ as before, the stall angle is greatly increased from 5 degrees to 12 degrees. If even higher levels of LE blowing is used, e.g. a LE blowing with $C_{\mu} = 0.08$ and a TE blowing with $C_{\mu} = 0.04$, the stall angle is increased to more than 20 degrees, but the total lift is decreased at the same angle of attack compared to the previous case even when the total momentum coefficients ($C_{\mu,LE} + C_{\mu,TE}$) of the both cases are the same, equal to 0.12 here.

In conclusion, the leading edge blowing is seen to increase the stall angle, replacing the slat, while the trailing edge blowing is effective in producing high levels of lift. Leading edge blowing can also reduce the large nose down pitch moment associated with high lift and the suction pressure peak in the vicinity of the slot. In general, operating at high angles of attack is not necessary for CC airfoils since high lift can be readily achieved with low

angles of attack and a moderate amount of blowing. But in situations where the CCW configuration must operate at high angles of attack, a combination of leading edge and trailing edge blowing may be necessary to achieve the best performance.

Effects of Free-stream Velocity on Lift Production

As a follow up to previous studies [12], numerical simulations have also been done where the free-stream velocities (and the Reynolds number) were systematically varied. The purpose of these studies was to determine and isolate how free-stream velocities and the Reynolds number affect the beneficial effects of Circulation Control at a fixed momentum coefficient.

In this case, the jet momentum coefficient, C_{μ} , is fixed at 0.1657, and the jet slot height is also fixed at 0.015 inch. The free-stream velocities vary from 0.5 to 1.8 times the experimental free-stream velocity, equal to 94.3 ft/sec as stated earlier. The jet velocity also varies with the free-stream velocity to maintain a constant C_{μ} . As shown in Figures 7 and 8, for a given momentum coefficient, the lift and drag coefficients are not significantly affected by the variation of the free-stream velocity except at very low free-stream velocities. At very low free-stream velocities, degradation of lift and the generation of high drag are seen. This is because the jet velocity is too low to generate a sufficiently strong Coanda effect that eliminates trailing edge separation and vortex shedding. At sufficiently high free-stream velocities, the performance of CC airfoils is independent of the free-stream velocity and the Reynolds number under the fixed C_{μ} and fixed jet slot height conditions. Thus the momentum coefficient is an appropriate driving parameter for CC blowing if the jet slot-height is fixed.

Effects of Jet Slot Height

According to recent acoustic measurements [7, 8], the jet slot height has a strong effect on the noise produced by the CC airfoil. These studies indicate that a larger jet slot will reduce the noise at the same momentum coefficient compared to a smaller slot. To investigate the effect of jet slot heights on the aerodynamic characteristics of CCW sections, simulations at several slot heights (varied from 0.006 inch to 0.018 inch) have been done, at a fixed low C_{μ} ($C_{\mu} = 0.04$) and a fixed high C_{μ} ($C_{\mu} = 0.1657$) value, and at a constant free-stream velocity of 94.3 ft/sec.

From Figure 9, it is seen that a higher lift coefficient can be achieved with a smaller slot height even for the same momentum coefficient, and that the lift coefficient is decreased by 20% as the slot height is increased from 0.006 inch to 0.018 inch. A similar behavior is seen for the drag coefficient as shown in Figure 10. The L/D characteristics of the airfoil, which is computed here as $C_l/(C_d+C_{\mu})$ by adding C_{μ} to the drag coefficient in order to consider the rate of change of momentum associated by the jet flow, does not vary much with the change of the jet slot height. As shown in Figure 11, when the slot height is increased, the efficiency decreases approximately by 7.6% for $C_{\mu} = 0.1657$ case, and increases by about 5.3% for the $C_{\mu} = 0.04$ case. However, as shown in Figure 12, the jet mass flow rate increases by ~60% when the slot height is increased from 0.006 inch to 0.018 inch, due to the larger jet slot area.

As it is always preferable to obtain higher lift with as low a mass flow rate as possible, a thin jet is aerodynamically more beneficial than a thick jet. However, the large stagnation pressure losses associated with small orifices or slots means that a higher

stagnation pressure is required to generate a jet issuing through a smaller slot than through a larger slot at the same momentum coefficient. The higher power consumption of compressors needed to produce the required high stagnation pressures can negate the beneficial effects of Circulation Control for very thin jets.

In summary, a smaller jet slot height is preferred from an aerodynamic design perspective. However, as mentioned above, a larger jet slot height is preferred from an aeroacoustic perspective. Thus, an optimum choice must be made for the jet slot height from aerodynamic, acoustic, and compressor power consumption considerations.

Pulsed Jet Effects

In earlier work [12], it has been shown that the pulsed jet with square-wave form is more efficient than the traditional sinusoidal form and that the square-wave form pulsed jet can generate the same lift of the steady jet at a much lower mass flow rate. In this work, we describe the studies done to isolate the effects of free-stream velocity, frequency, and chord length on pulsed jet behavior.

Figures 13 and 14 show the variation of the time-averaged incremental lift coefficient ΔC_l over and above the base-line unblown configuration at three frequencies, 40 Hz, 120 Hz and 400 Hz. Figure 13 shows the variation with the average momentum coefficient, $C_{l,0}$ and Figure 14 shows the variation with the average mass flow rate.

At first glance, Figure 13 and Figure 14 will appear to show opposite trends. Figure 14 appears to favor high frequencies – i.e. ΔC_l increases as frequency increases, and pulsed jet produces a higher ΔC_l than a steady jet. This appears to be consistent with experiments [21]. However, Figure 13 appears to show the opposite trend – steady jet appears to be

always more efficient than a pulsed jet, and produces a large ΔC_l . To resolve this “apparent” inconsistency between Figure 13 and 14, four points A, B, C, D are shown in Figure 13. These points are all at the same mass flow rate of 0.00088 slug/sec. It is seen that point A is above point B. That is, a steady jet is indeed able to produce a higher ΔC_l than a low frequency 40 Hz jet. This is because the flow separates over a period of time before a new cycle of blowing begins, destroying the lift generation. However, points C and D (120 and 400 Hz jets) are higher than point A. In these cases, bound circulation over the airfoil has not been fully shed into the wake before a new cycle begins. The time-averaged lift at the same specified averaged mass flow rate is thus higher compared to a steady jet. This is consistent with Figure 14.

It has also been found that high frequencies have the beneficial effect of decreasing the time-averaged mass flow rate of the pulsed jet [12]. For example, as shown in Figure 15, when the frequency is equal to 400 Hz, the pulsed jet requires only 73% of the steady jet mass flow rate while it can achieve 95% of the average lift achieved with a steady blowing. Examination of the flow field over an entire cycle indicates that it takes some time after the jet has been turned off before all the beneficial circulation attributable to the Coanda effect is completely lost. If a new blowing cycle could begin before this occurs, the circulation will almost instantaneously reestablish itself. At high enough frequencies, as a consequence, the pulsed jet will have all the benefits of the steady jet at considerably lower mass flow rates.

For aerodynamic and acoustic studies, the frequency is usually expressed as a non-dimensional quantity called the Strouhal number. Simulations has been done to calculate

the average lift generated by the pulsed jet at fixed Strouhal numbers, which is defined as follows:

$$St = \frac{f L_{ref}}{V_{\infty}} \quad (3)$$

In the present study, for the baseline case, the L_{ref} is 8 inches, and the V_{∞} is equal to 94.3 ft/sec. For a 200 Hz pulsed jet, the Strouhal number is equal to 1.41.

From the above equation, besides the frequency, there are other two parameters that could affect the Strouhal number- the free-stream velocity V_{∞} and L_{ref} (Chord of the CC airfoil). To isolate these effects, as shown in Tables 1-3, three cases have been studied. In the first case (Table 1) the free-stream velocity and the chord of the CC airfoil are fixed, and the Strouhal number varies with the frequency. In the second case, as shown in Table 2, the Strouhal number is fixed at 1.41 and the chord of the CC airfoil is also fixed. The frequency varies with the free-stream velocity to achieve the same Strouhal number. In the third case, as shown in Table 3, the Strouhal number is fixed at 1.41 and the free-stream velocity is also fixed, while the frequency varies along with the chord of the CC airfoil. The Mach number and Reynolds number are also functions of the free-stream velocity and the airfoil chord, and were changed appropriately. The time-averaged momentum coefficient, $C_{\mu,0}$, is fixed at 0.04 in these studies. Figure 16 shows the lift coefficient variation with the frequency for these three cases.

From tables 2 and 3, it is seen that the computed time-averaged lift coefficient varies less than 2% when the Strouhal number is fixed, and the chord and/or the free-stream velocity is varied. Table 2 indicates that the same C_l can be obtained at a much lower frequency with a smaller free-stream velocity as long as the Strouhal number is fixed. Table

3 shows that for a larger configuration, the same C_l can be obtained at a lower frequency provided the Strouhal number is fixed. Table 1, on the other hand, shows that varying the frequency and Strouhal number while holding the other variables fixed can lead to a 12% variation in C_l . Thus, it is concluded the Strouhal number has a more dominant effect on the average lift coefficient of the pulsed jet than just the frequency.

CONCLUDING REMARKS

Navier-Stokes simulations are necessary for modeling flow over the CCW configurations due to the complexity of the flow field and the strong viscous effects. The results indicate that this approach is an efficient and accurate way of modeling CCW flows with steady and pulsed jets.

The Circulation Control Technology is a useful way of achieving very high lift at even zero angle of attack. It can also eliminate the vortex shedding in the trailing edge region, a potential noise source. The lift coefficient of the CC airfoil is also increased with angle of the attack as with the conventional sharp trailing edge airfoil. However, the stall angle of the CC airfoil decreases rapidly with an increase in the blowing momentum coefficient. This stall phenomenon occurs in the leading edge region, and may be suppressed by leading edge blowing. In practice, because high C_L values are achievable at low angles of attack, it may seldom be necessary to operate CC wings at high angles of attack. However, because there is always a large nose down pitch moment for the CC airfoil, leading edge blowing may be necessary to reduce this pitch moment at high C_{μ} values, even at zero angle of attack.

At a fixed momentum coefficient, the performance of the CC airfoil does not vary significantly with free-stream velocity and the Reynolds number. However, at a fixed C_{μ} , the lift coefficient is influenced by the jet slot height. A thin jet from a smaller slot is preferred since it requires much less mass flow, and has the same efficiency in generating the required C_l values as a thick jet. From a practical perspective, a much higher plenum pressure may be needed to generate thin jets for a given C_{μ} . This may increase the power requirements of compressors that provide the high-pressure air.

A square wave shape pulsed jet configuration gives larger increments in lift over the baseline unblown configuration, when compared to the steady jet at the same time-averaged mass flow rate. Pulsed jet performance is improved at higher frequencies due to the fact that the airfoil has not fully shed the bound circulation into the wake before a new pulse cycle begins.

The Strouhal number, has a more dominant effect on the performance of the pulsed jet than just the frequency. Thus, the same performance of a pulsed jet could be obtained at lower frequencies for a larger configuration or at smaller free-stream velocities provided the Strouhal number is kept the same.

ACKNOWLEDGEMENT

This work was supported by NASA Langley Research Center under the Breakthrough Innovative Technology Program, Grant-NAG1-2146.

REFERENCES

1. Englar, Robert J., Smith, Marilyn J., Kelley, Sean M. and Rover, Richard C. III., "Application of Circulation Control to Advanced Subsonic Transport Aircraft, Part I: Airfoil Development," Journal of Aircraft, Vol.31 No.5, pp. 1160-1168, Sep. 1994.
2. Englar, Robert J., Smith, Marilyn J., Kelley, Sean M. and Rover, Richard C. III., "Application of Circulation Control to Advanced Subsonic Transport Aircraft, Part II: Transport Application," Journal of Aircraft, Vol.31, No.5, pp. 1169-1177, Sep. 1994.
3. Shrewsbury, G. D. and Sankar, L. N., "Dynamic stall of an oscillating circulation control airfoil," International Symposium on Nonsteady Fluid Dynamics, Toronto, Canada, June 4-7, 1990, Proceedings. New York, American Society of Mechanical Engineers, pp. 15-22, 1990.
4. Shrewsbury, G. D. and Sankar, L. N., "Dynamic Stall of Circulation Control Airfoils," AIAA Paper 90-0573, January 1990.
5. Salikuddin, M., Brown, W. H. and Ahuja, K. K., "Noise From a Circulation Control Wing with Upper Surface Blowing," Journal of Aircraft, Vol.24, pp55-64, Jan. 1987.
6. Englar, R. J. and Huson, G. G., "Development of Advanced Circulation Control Wing High Lift Airfoils," AIAA paper 83-1847, presented at AIAA Applied Aerodynamics Conference, July, 1983.
7. Munro, S., Ahuja, K., and Englar, R., "Noise Reduction Through Circulation Control Technology," AIAA Paper 2001-0666, Jan. 2001.

8. Munro, S. and Ahuja, K. K., "Aeroacoustics of a High Aspect-Ratio Jet," AIAA paper 2003-3323, 2003, presented at the 9th AIAA/CEAS Aeroacoustics Conference and Exhibit, Hilton Head, South Carolina, 12-14 May 2003.
9. Munro, S. and Ahuja, K. K., "Fluid Dynamics of a High Aspect-Ratio Jet," AIAA paper 2003-3129, 2003, presented at the 9th AIAA/CEAS Aeroacoustics Conference and Exhibit, Hilton Head, South Carolina, 12-14 May 2003.
10. Munro, S. and Ahuja, K. K., "Development of a Prediction Scheme for Noise of High-Aspect Ratio Jets," AIAA paper 2003-3255, 2003, presented at the 9th AIAA/CEAS Aeroacoustics Conference and Exhibit, Hilton Head, South Carolina, 12-14 May 2003.
11. Liu, Y., "Numerical Simulations of the Aerodynamic Characteristics of Circulation Control Wing Sections," Ph.D Thesis, Georgia Institute of Technology, 2003.
12. Liu, Y., Sankar, L. N., Englar, R. J. and Ahuja, K. K., "Numerical Simulations of the Steady and Unsteady Aerodynamic Characteristics of a Circulation Control Wing Airfoil," AIAA paper 2001-0704, January 2001.
13. Kwon, J. and Sankar, L.N., "Numerical Study of the Effects of Icing on Finite Wing Aerodynamics," AIAA Paper 90-0757.
14. Bangalore, A., Phaengsook, N. and Sankar, L. N., "Application of a Third Order Upwind Scheme to Viscous Flow over Clean and Iced Wings," AIAA Paper 94-0485.
15. Baldwin, B. S., and Lomax, H., "Thin Layer Approximation and Algebraic Model for Separated Turbulent Flows," AIAA Paper 78-257, Jan. 1978.
16. Spalart, P. R., and Allmaras, S. R., "A One-Equation Turbulence Model for Aerodynamic Flows," AIAA Paper 92-0439, Jan. 1992.

17. Shrewsbury, G. D., "Numerical Evaluation of Circulation Control Airfoil Performance Using Navier-Stokes Methods," AIAA paper 86-0286, January 1986.
18. Shrewsbury, G. D., "Numerical Study of a Research Circulation Control Airfoil Using Navier-Stokes Methods," Journal of Aircraft, Vol. 26, No. 1, pp.29-34, 1989.
19. Williams, S. L. and Franke, M. E., "Navier-Stokes Methods to Predict Circulation Control Airfoil Performance," Journal of Aircraft, Vol. 29, No.2, pp.243-249, March-April 1992.
20. Bragg, M. B., and Spring, S. A., "An Experimental Study of the Flow Field about an Airfoil with Glaze Ice," Presented at the AIAA 25th Aerospace Science Meeting, Reno, Nevada, AIAA paper 87-0100, Jan 12-15, 1987.
21. Oyler, T.E., and W.E. Palmer, "Exploratory Investigation of Pulse Blowing for Boundary Layer Control," North American Rockwell Report NR72H-12, Jan. 1972.

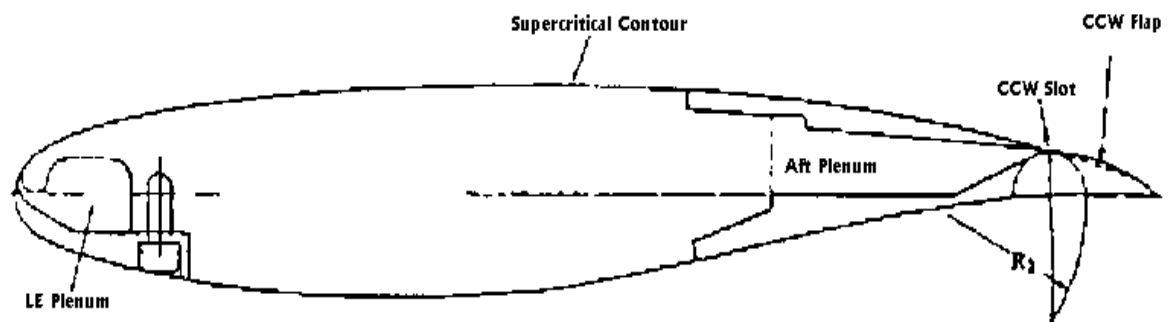


Figure 1 Dual Radius CCW Airfoil with LE Blowing [2]

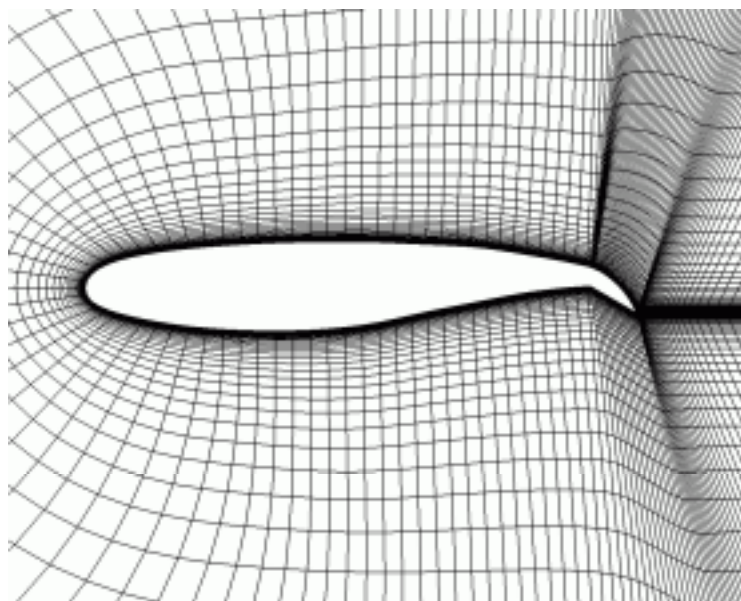


Figure 2 Body-fitted C Grid near the CC Airfoil Surface.

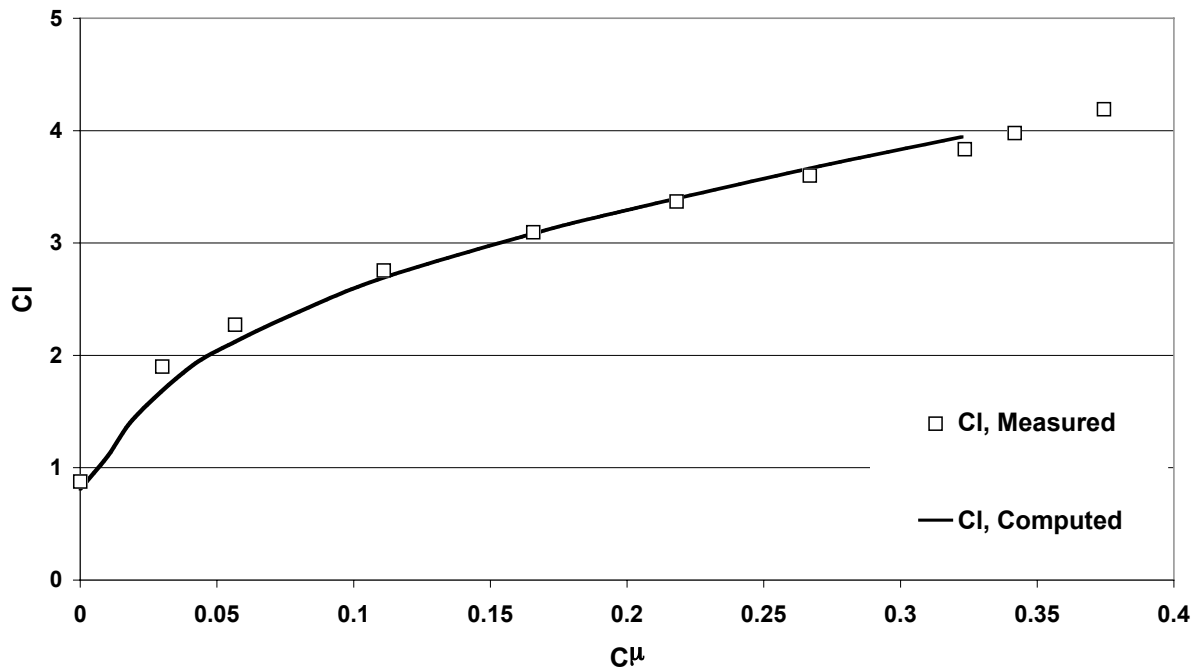


Figure 3 Variation of the Lift Coefficient with Momentum Coefficients at $\alpha=0^\circ$

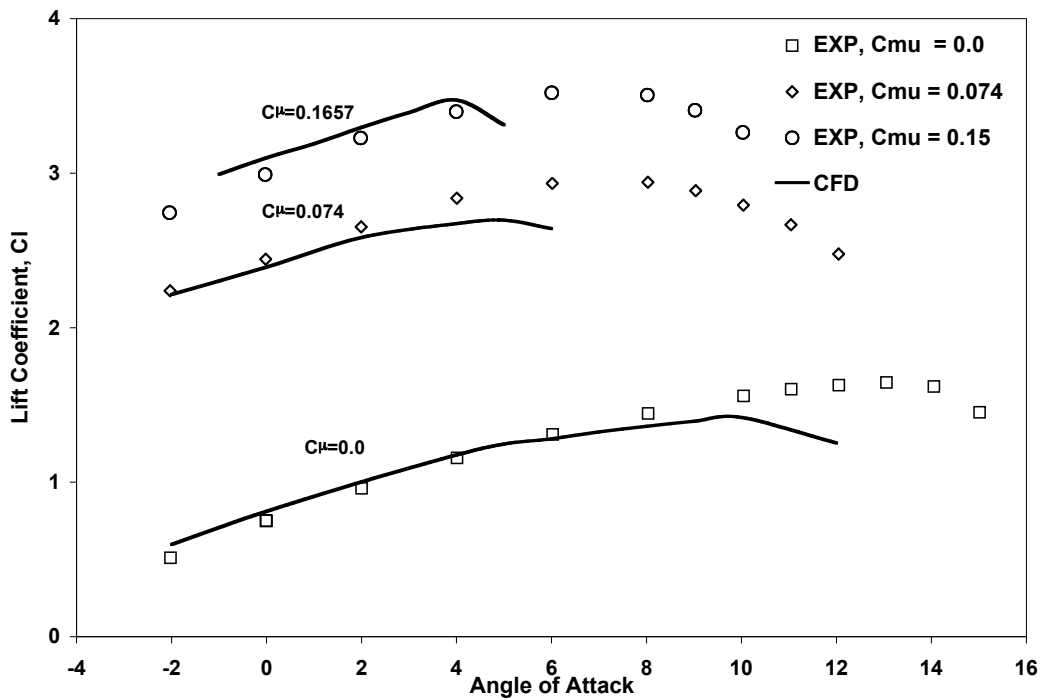


Figure 4 Variation of the Lift Coefficient with Angle of Attack

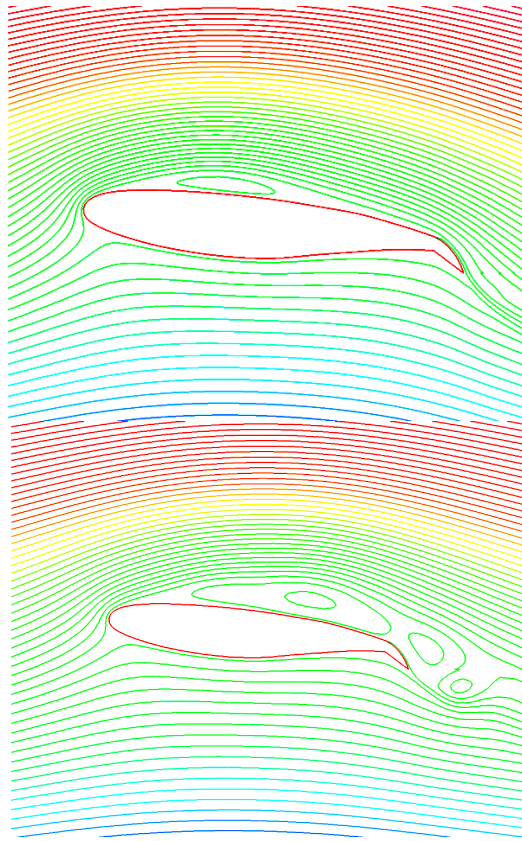


Figure 5 Streamlines over the CC airfoil at Two Instantaneous Time Levels ($C_{\mu} = 0.1657$, Angle of Attack = 6°)

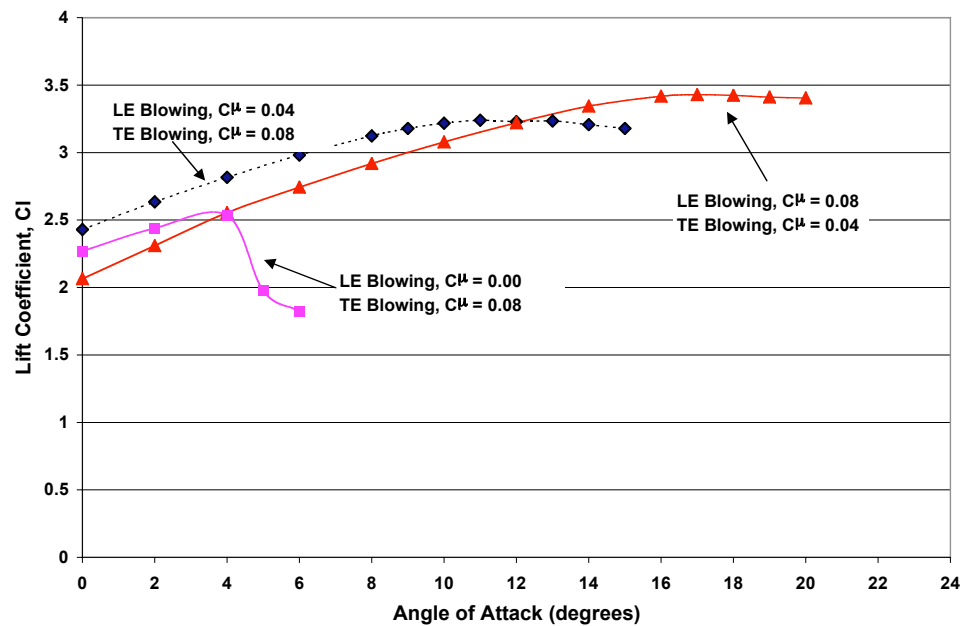


Figure 6 Lift Coefficient vs. the Angle of Attack for the Leading Edge Blowing Case

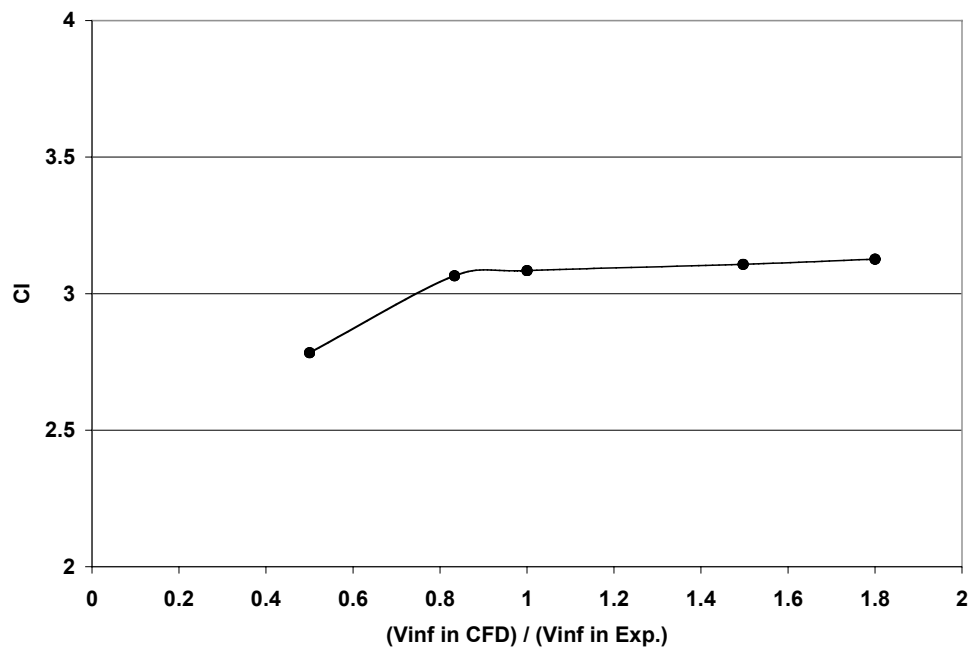


Figure 7 Lift Coefficient vs. Free-stream Velocity
($C_\mu = 0.1657$, $h = 0.015$ inch and $V_{\infty, \text{exp}} = 94.3$ ft/sec)

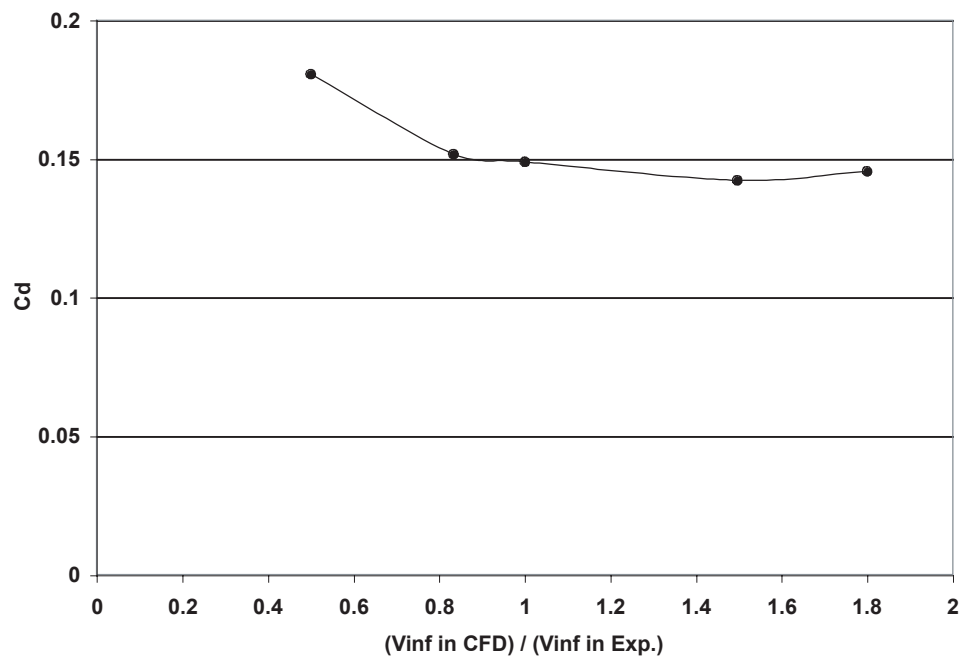


Figure 8 Drag Coefficient vs. Free-stream Velocity
($C_\mu = 0.1657$, $h = 0.015$ inch and $V_{\infty, \text{exp}} = 94.3$ ft/sec)

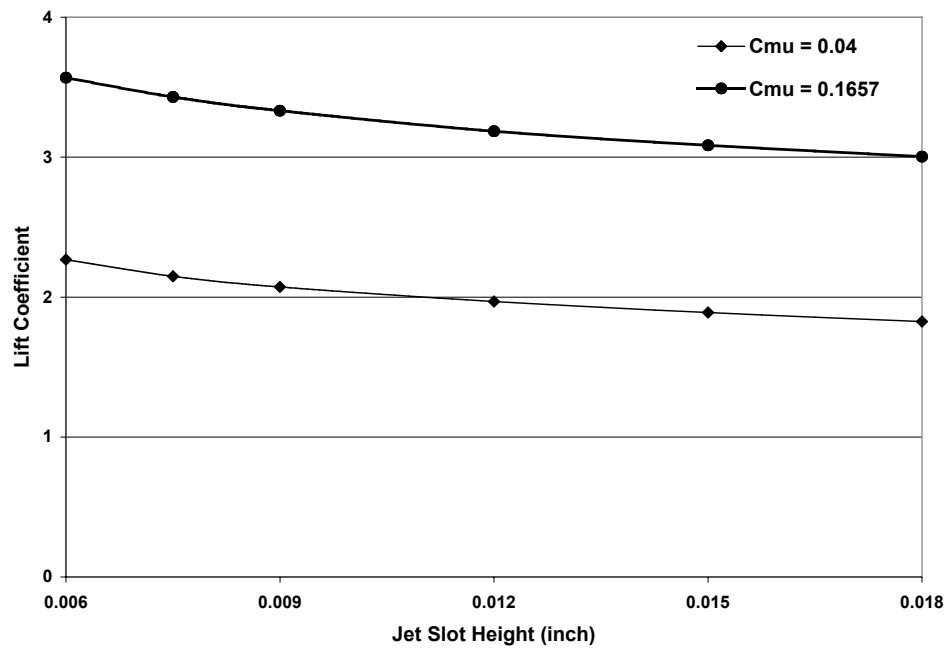


Figure 9 Lift Coefficient vs. Jet Slot Height
($V_{\infty} = 94.3$ ft/sec)

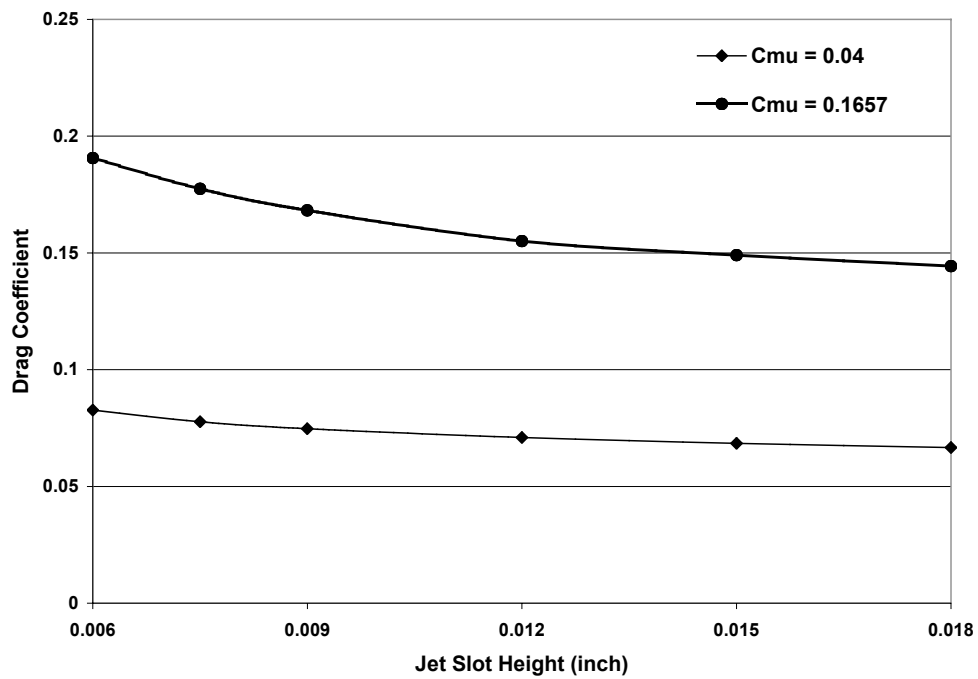


Figure 10 Drag Coefficient vs. Jet Slot Height
($V_{\infty} = 94.3$ ft/sec)

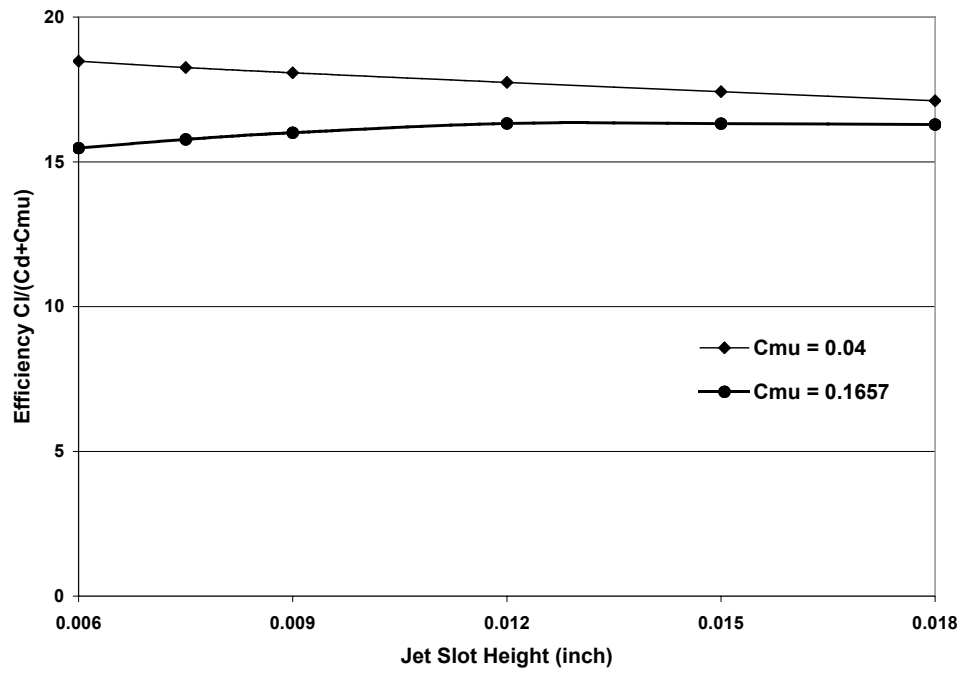


Figure 11 Variations of the L/D characteristics of with Jet Slot Height ($V_{\infty} = 94.3$ ft/sec)

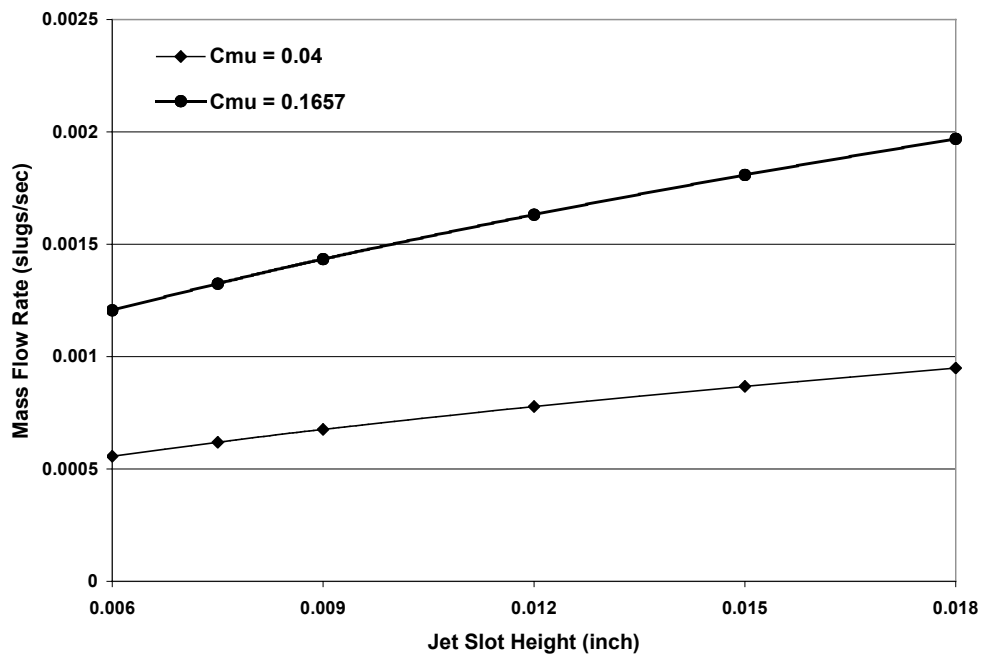


Figure 12 Mass Flow Rate Requirements of the Jet per foot of span vs. Jet Slot Height ($V_{\infty} = 94.3$ ft/sec)

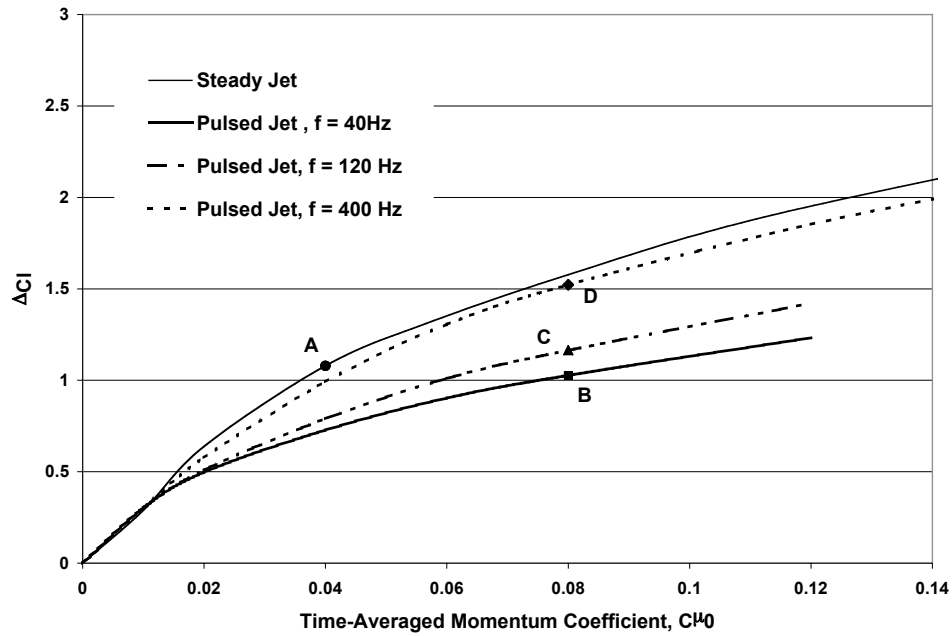


Figure 13 Incremental Lift vs. the Time-averaged Momentum Coefficient

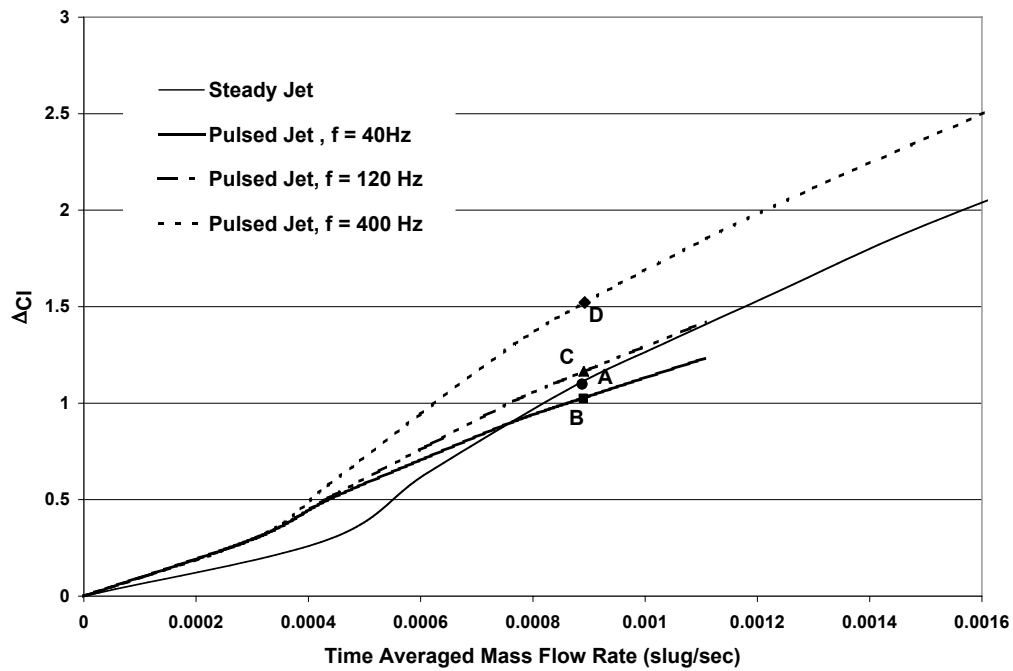


Figure 14 Incremental Lift Coefficient vs. Time-averaged Mass Flow Rate

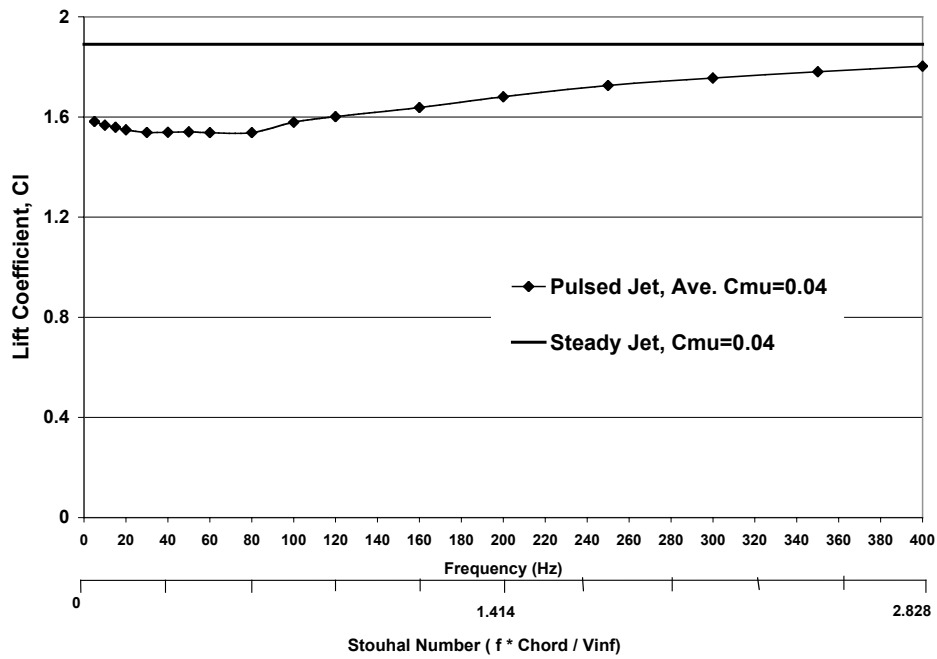


Figure 15 Time-averaged Lift Coefficient vs. Frequency & Strouhal Number

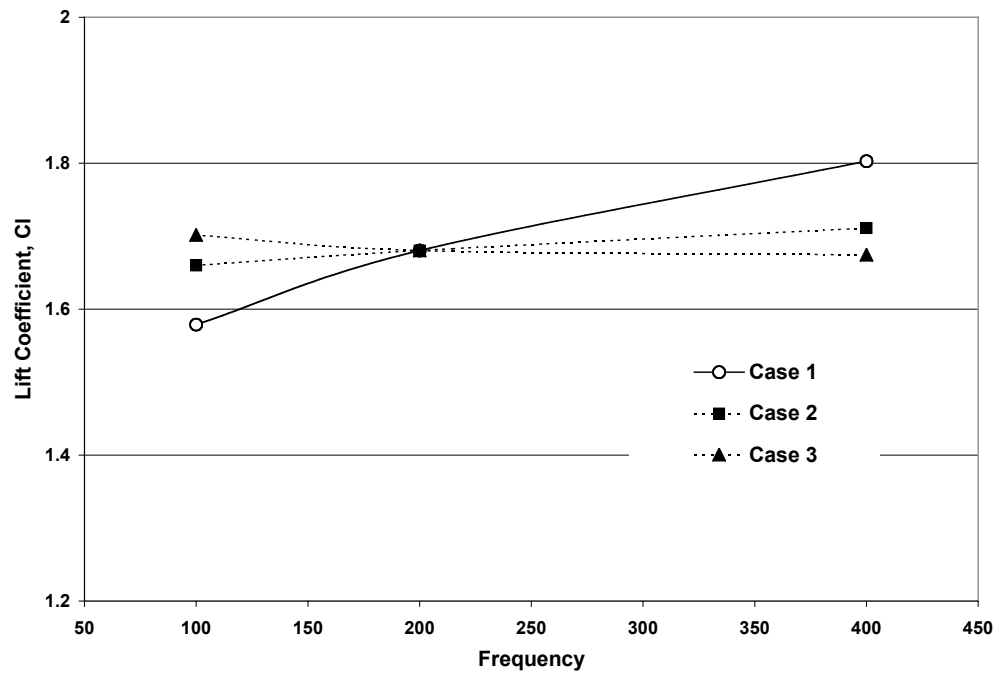


Figure 16 Time-averaged Lift Coefficient vs. Frequency

(Case 1. Strouhal number was not fixed; U_{∞} and L_{ref} were fixed)

(Case 2. Strouhal number and L_{ref} were fixed; U_{∞} was not fixed)

(Case 3. Strouhal number and U_{∞} were fixed; L_{ref} was not fixed)

Table 1 Computed Time-averaged Lift Coefficient for the Case where U_∞ and L_{ref} are fixed, and the Strouhal number is varied by varying with the frequency

	Baseline	Half Frequency	Double Frequency
Frequency (Hz)	200	100	400
Free-Stream Velocity U_∞ (ft/sec)	94.3	94.3	94.3
Chord of the Airfoil L_{ref} (inch)	8	8	8
Strouhal Number	1.41	0.705	2.82
Computed Average Lift Coefficient (C_l)	1.6804	1.5790	1.8026

Table 2 Computed Time-averaged Lift Coefficient for the Case where Strouhal number and L_{ref} fixed, and U_∞ and the frequency are varied.

	Baseline	Half Velocity	Double Velocity
Frequency (Hz)	200	100	400
Free-Stream Velocity U_∞ (ft/sec)	94.3	47.15	118.6
Chord of the Airfoil L_{ref} (inch)	8	8	8
Strouhal Number	1.41	1.41	1.41
Computed Average Lift Coefficient (C_l)	1.6804	1.6601	1.7112

Table 3 Computed Time-averaged Lift Coefficient for the Case where Strouhal number and U_∞ fixed, and L_{ref} and frequency are varied.

	Baseline	Double Chord	Half Chord
Frequency (Hz)	200	100	400
Free-Stream Velocity U_∞ (ft/sec)	94.3	94.3	94.3
Chord of the Airfoil L_{ref} (inch)	8	16	4
Strouhal Number	1.41	1.41	1.41
Computed Average Lift Coefficient (C_l)	1.6804	1.7016	1.6743



Numerical Simulations of the Aerodynamic Characteristics of Circulation Control Wing Sections

Y. Liu, L. N. Sankar
School of Aerospace Engineering
Georgia Institute of Technology, Atlanta GA 30332-0150

Supported by NASA Langley Research Center



Outline of Presentation

- Motivation and Objectives
- Circulation Control Wing Technology
- Mathematical and Numerical Formulation
- 2D Simulation Results and Discussion
 - Steady Blowing Results
 - Pulse Blowing Results
- Concluding Remarks



Motivation and Objectives

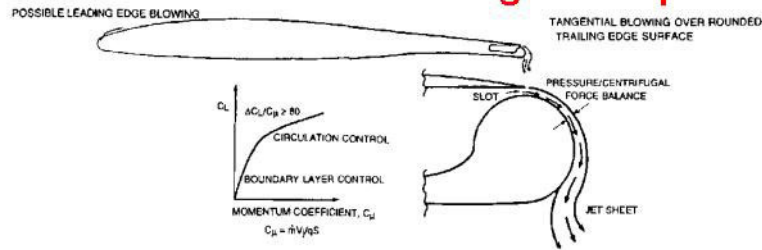
- Noise pollution from the large aircraft has become a major problem that needs to be solved. NASA proposed a plan to reduce the noise by a factor of four (20dB) by 2025.
- A major source of large aircraft airframe noise during take-off and landing is the high-lift system - namely flaps, slats, associated with flap-edges and gaps.
- The high-lift system also contains many moving parts, which add to the weight of the aircraft, and are costly to build and maintain.
- These devices for generating high lift are necessary for large aircraft that use existing runways.



- An alternative to conventional high-lift systems is the Circulation Control Wing (CCW) technology.
- The CC wing can generate the same high lift with much less complexity compared to the high-lift system, and many noise sources such as flaps and slats, can also be eliminated by the CC wing.



Circulation Control Wing Concept



- Circulation Control Aerodynamics: In this approach a tangential jet is blown over a highly curved aerodynamic surface (the Coanda surface) to increase or modify the aerodynamic forces and moment with few or no moving surfaces.
- Figure (Taken from paper by Englar) shows a traditional Circulation Control Airfoil with a rounded trailing edge.



Circulation Control Wing Concept

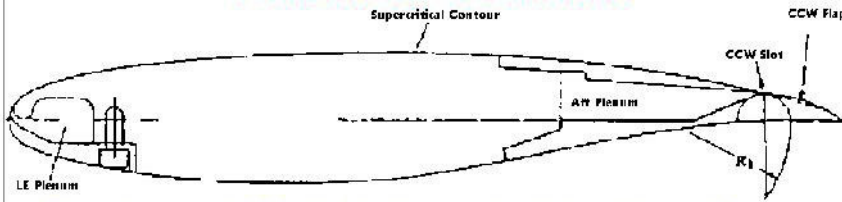
- In general, the driving parameter of Circulation Control is the jet momentum coefficient, C_{μ} , which is defined as:

$$C_{\mu} = \frac{\dot{m}_{jet} V_{jet}}{qS}$$

- At very low momentum coefficients, the tangential blowing will add energy to the slow moving flow near the surface. This will delay or eliminate the separation, and is called Boundary Layer Control.
- When the momentum coefficient is high, the lift of the wing will be significantly increased. This is called Circulation Control.
- The lift augmentation, which is defined as $\Delta CL / \Delta C_{\mu}$, can exceed 80 as shown in previous figure.



Advanced CC Airfoil



- The advanced CC airfoil, i.e. a circulation hinged flap, was developed by Englar et al to replace the traditional CC airfoil.
- This advanced CC airfoil use a small trailing edge flap with a large-radius arc upper surface and a flat low surface. The flap can be deflected $0^\circ < \delta_f < 90^\circ$.
- During take-off / landing, the flap is deflected, thus generating very high lift like a traditional rounded trailing edge CC airfoil.
- During cruise, $\delta_f = 0^\circ$, leading to a conventional airfoil shape with a sharp trailing edge that significantly reduces the drag.



Mathematical and Numerical Formulation

- Three-dimensional compressible unsteady Reynolds Averaged Navier-Stokes equations are solved in a strong conservation form on curvilinear coordinates.
- This solver can be used in both a 2D mode and a 3D mode in this study for different applications.
- The scheme is second or fourth order accurate in space and first order accurate in time.
- Baldwin-Lomax and Spalart-Allmaras one-equation turbulence models have been used.
- The jet slot location, slot size, blowing velocity and direction of blowing can easily be varied in the analysis.



Initial and Boundary Conditions

- Initial flow conditions are set to free stream values inside the flow field.
- Boundary Conditions
 - Outer Boundary
 - Solid Surface Boundary
 - Wake Cut Boundary
 - Jet Slot Exit Boundary



Jet Slot Boundary Conditions

- The driving parameter for jet blowing is the momentum coefficient, C_μ , defined as follows:

$$C_\mu = \frac{\dot{m} V_{\text{jet}}}{\frac{1}{2} \rho_\infty V_\infty^2 S}$$

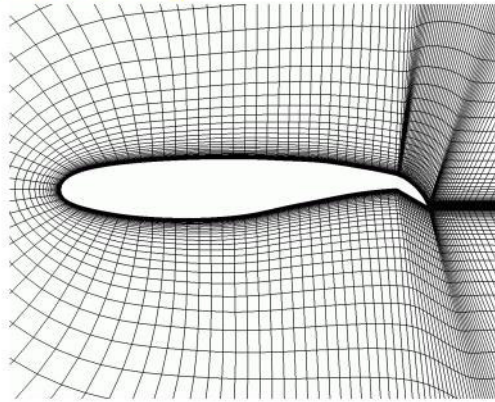
Where $\dot{m} = \rho_{\text{jet}} V_{\text{jet}} A_{\text{jet}}$ is the mass flow rate of jet flow

- The C_μ , orientation of the jet and the total temperature of jet are specified in the analysis.
- Other quantities such as pressure and density are found by extrapolation and /or Ideal Gas Law.
- The total jet pressure can also be specified as the boundary condition instead of the momentum coefficient.

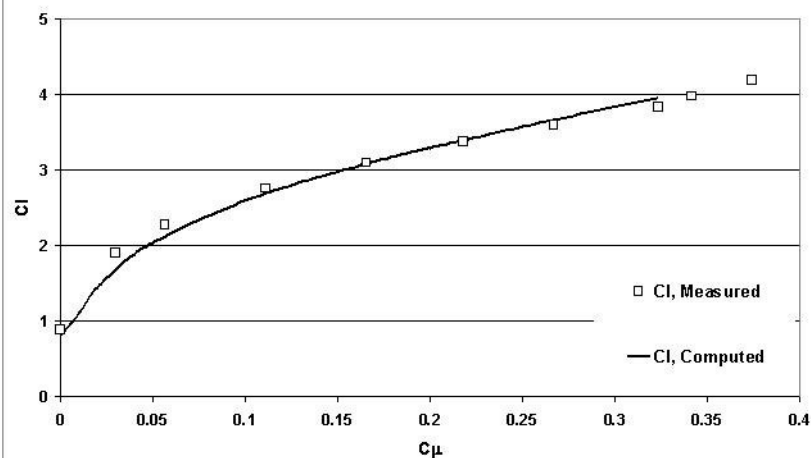


2D Steady Blowing Results

- Steady blowing performance at different C_{μ} values, and at different angles of attack
- Leading Edge Blowing



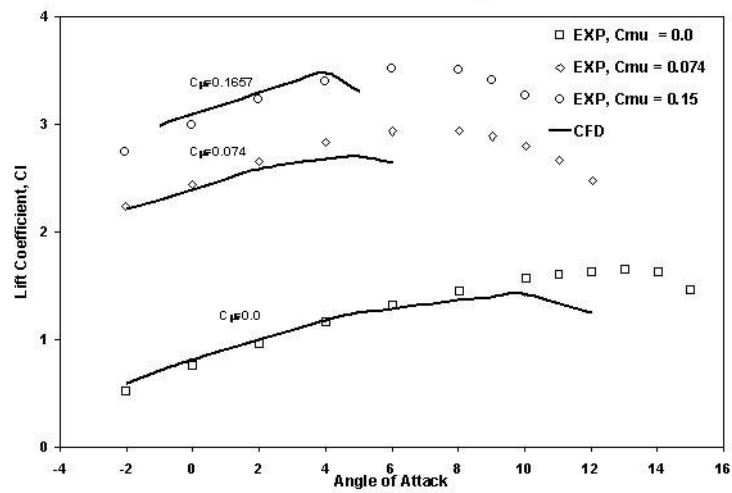
Lift Coefficient vs. C_{μ}



Angle of Attack 0 degrees, Integral Flap at 30 degrees



Lift Coefficient vs. Angle of Attack

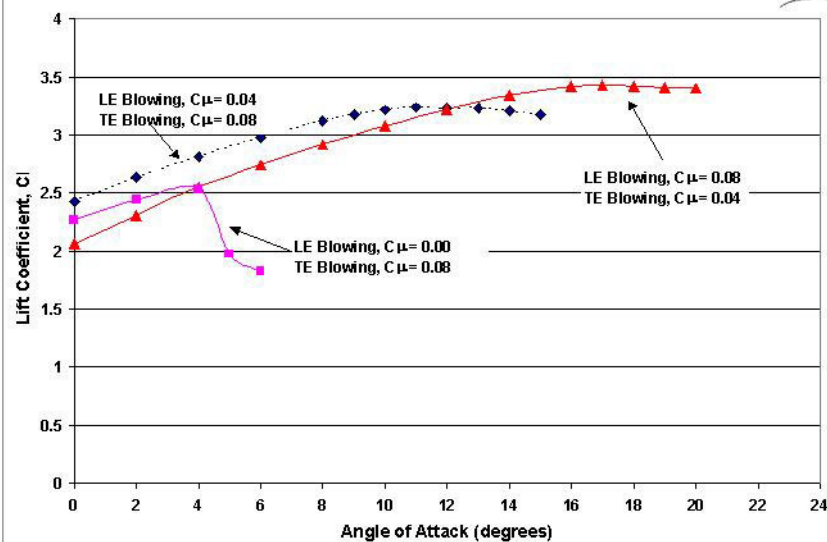


The Stream lines over CC airfoil, $C_{\mu} = 0.1657$, $\alpha = 6^\circ$



Leading Edge Blowing

- At high angles of attack, the leading edge separation and stall can occur for the CC airfoil, due to the large pressure gradients.
- The stall angle is decreased quickly with the increase of the jet momentum coefficient of the trailing edge blowing.
- Leading edge Coanda blowing can eliminate this and increase the stall angle.
- In reality, because CCW airfoils can achieve very high lift even at zero angle of attack with a small amount of blowing, there is no real need for operation at high angles of attack unless maneuver requires it.



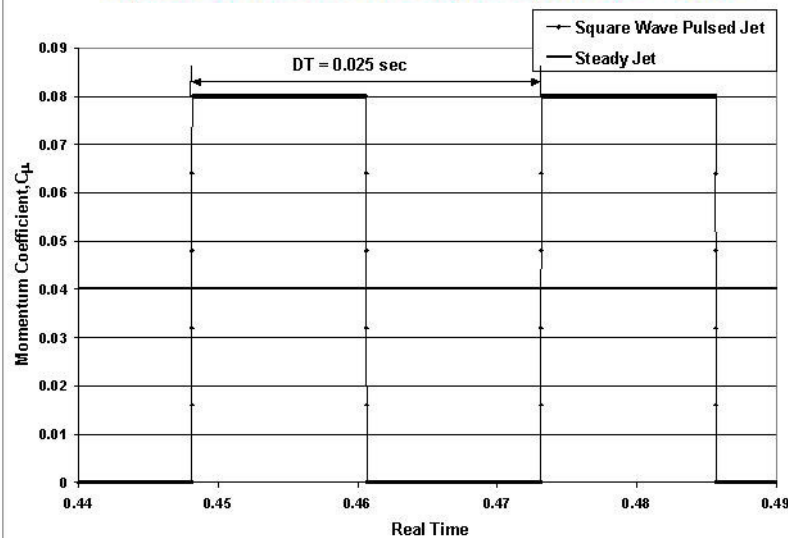


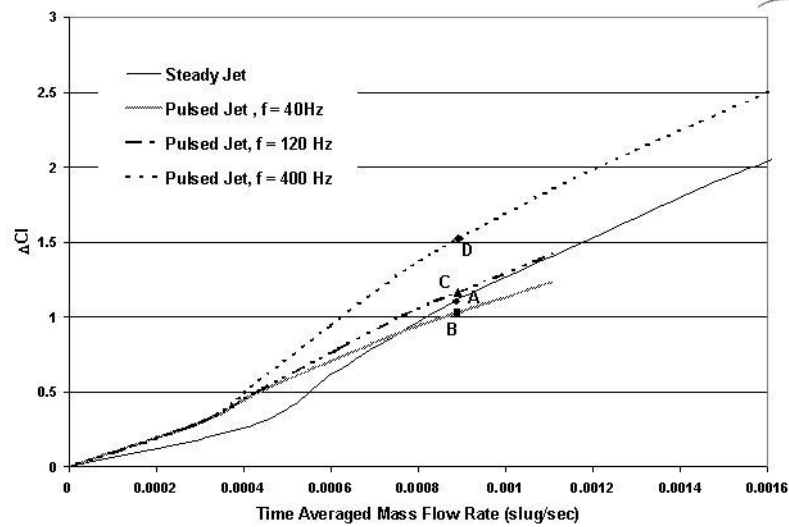
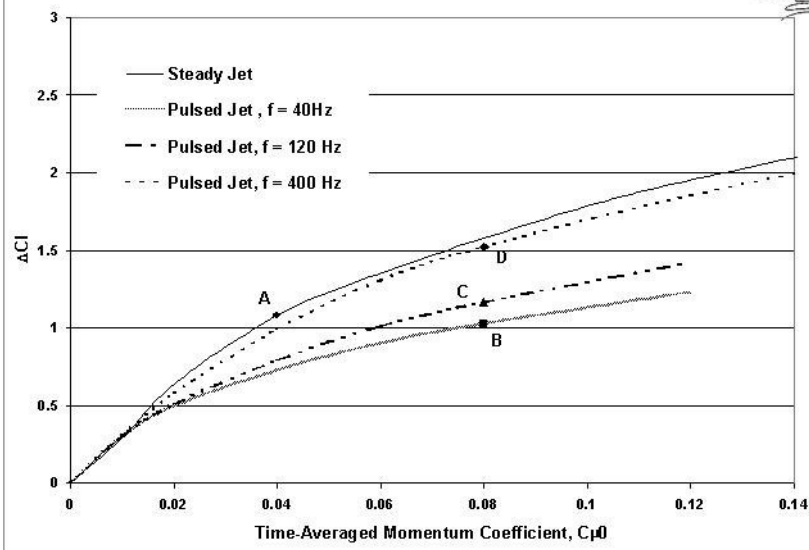
2D Pulsed Jet Results

- Pulsed jet studies were done to answer:
 - Can pulsed jets be used to achieve desired increases in the lift coefficient at lower mass flow rates relative to a steady jet?
 - What is the optimum wave shape for the pulsed jet, ie, how should it vary with time?
 - What are the effects of the pulsed jet frequency on the lift coefficient?
- $C_{\mu}(t) = C_{\mu,0} + C_{\mu,0}F(f,t)$
- Sinusoidal and Square wave form variations were considered. Sinusoidal forms were found ineffective.



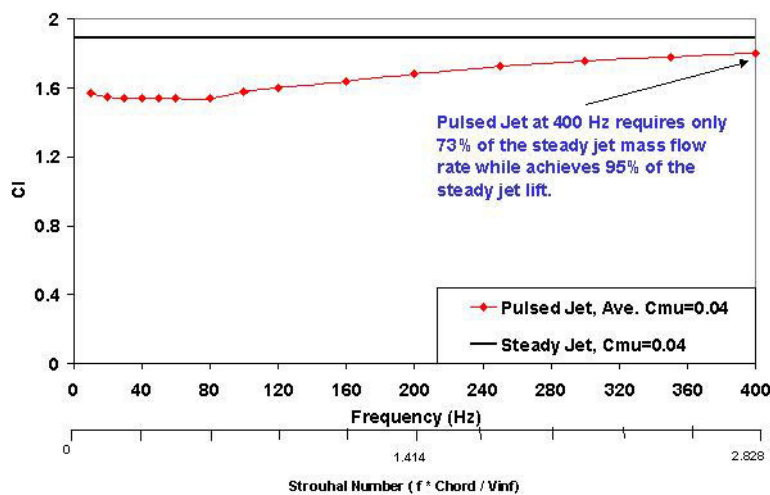
Square Wave Pulsed Jet, Frequency = 40 Hz





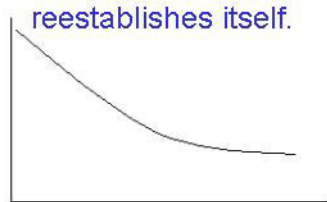


Average Lift Coefficient Vs. Frequency For Pulsed Jet

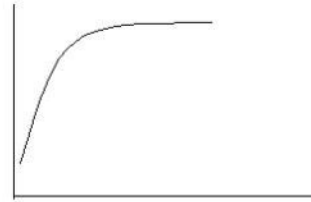


Effect of Frequency at Fixed C_{μ}

- High Frequencies were more effective.
- This is explained as follows:
 - When the jet is turned off, the beneficial Coanda effect persists for several chord lengths of travel.
 - If a new cycle starts soon, the Coanda effect quickly reestablishes itself.



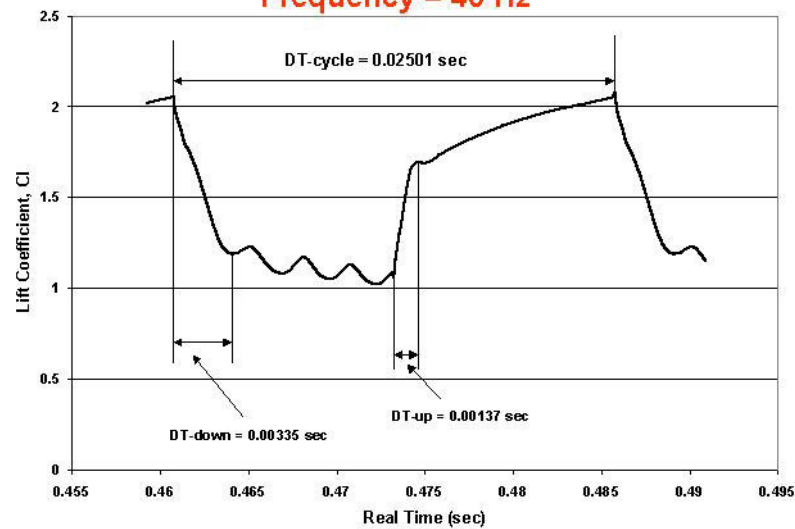
Long time for lift to decay



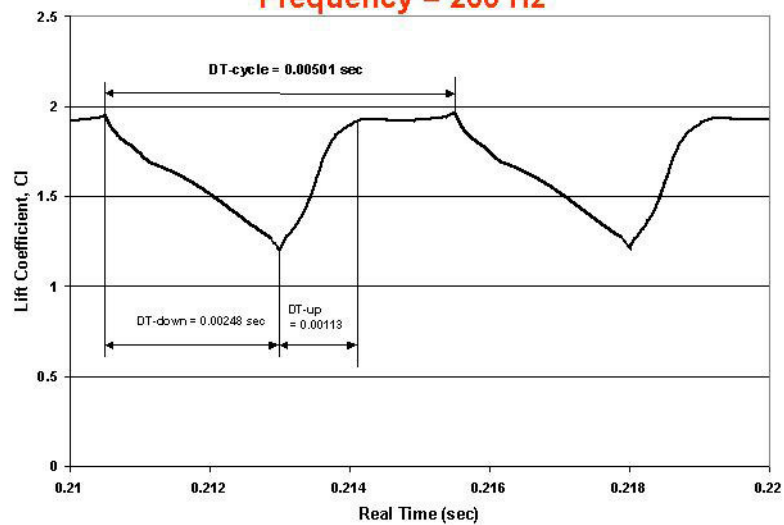
Lift rapidly builds back up



Time History of the Lift Coefficient Frequency = 40 Hz

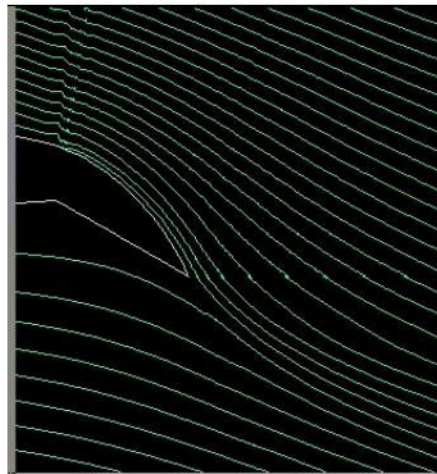


Time History of the Lift Coefficient Frequency = 200 Hz





Pulsed Jet Frequency = 120 Hz



Pulsed Jet Frequency = 400 Hz





Strouhal Number Effects

- The non-dimensional frequency, Strouhal number is defined as :

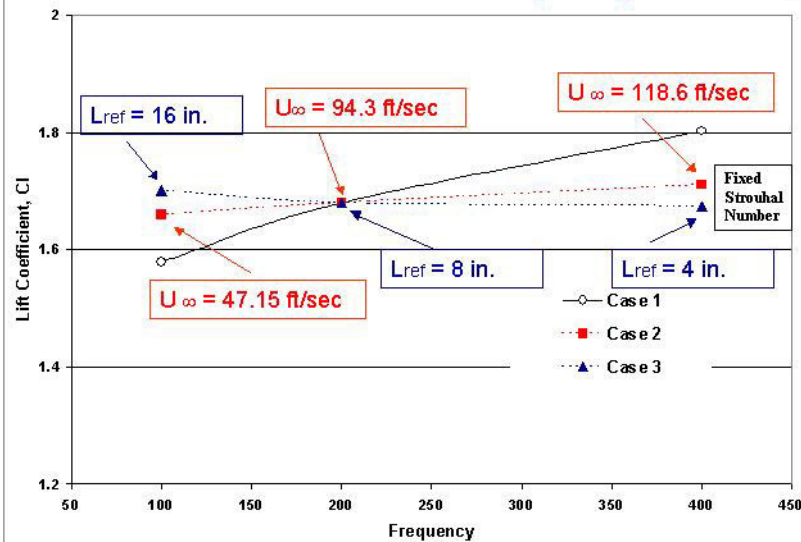
$$\text{Str} = \frac{f * L_{\text{ref}}}{U_{\infty}}$$

Where, L_{ref} is the chord of airfoil, and U_{∞} is the free-stream velocity.

- Three Cases have been studied:
 - Case 1: Strouhal number was not fixed; U_{∞} and L_{ref} were fixed
 - Case 2: Strouhal number and L_{ref} were fixed; U_{∞} was not fixed
 - Case 3: Strouhal number and U_{∞} were fixed; L_{ref} was not fixed
 - Strouhal number = 1.41 for Case 2 and 3



Lift Coefficient vs. Frequency





Concluding Remarks - I

- CCW concept is an extremely effective way of achieving high C_{Lmax} , without the drawbacks of conventional high-lift systems. Navier-Stokes simulations are necessary for modeling flow over CCW configurations.
- The stall angle of the CC airfoil is decreased quickly with the increase of the momentum coefficient. It is a leading edge stall, and can be significantly delayed by leading edge blowing.



Concluding Remarks - II

- The pulsed jet configuration can give larger increments in lift coefficient compared to the steady jet at the same mass flow rate.
- The Strouhal number has a more dominant effect on the performance of the pulsed jet than just the frequency. Thus, for a larger configuration or at a smaller free-stream velocity, the same lift can be obtained with a lower frequency pulsed jet.
- There are other potential applications for the Circulation Control technology beyond what has been studied in this work, such as Circulation Control Nacelle, Highly Loaded Compressor studies etc.

Investigation of Turbulent Coanda Wall Jets Using DNS and RANS

NASA/ONR 2004 Circulation Control Workshop

16-17 March 2004

Hampton, VA

H. Fasel, A. Gross, S. Wernz

The University of Arizona
Tucson, AZ 85721

1 Introduction

Wall jets over curved surfaces have great potential for technical applications. Coanda wall jets over convex surfaces can effectively provide aerodynamic side forces or change the circulation of an airfoil. An existing application is the NOTAR helicopter, prospective applications are the enhancement of low-speed maneuverability of underwater vehicles or high-lift wings for STOL aircraft. However, without profound understanding of the mechanisms that keep the wall jet attached to the surface for large downstream distances, any implementation of Coanda flow technology must rely on empiricism and hence requires excessive safety margins to account for unknowns. In this paper results from numerical investigations of two separate Coanda flow experiments are presented that may help to shed some light on the relevant physical mechanisms.

One of the most intriguing phenomena of the Coanda wall jet is the competition/interaction of naturally occurring streamwise and spanwise vortical structures which are a consequence of a centrifugal, Görtler-type instability (leading to streamwise coherent structures) and a Kelvin-Helmholtz-type instability (leading to spanwise coherent structures), respectively. It can be conjectured that the intensity of these structures, both absolute and relative to each other, will significantly influence the separation location, and, as a consequence, will have a key effect on the side forces that can be generated and thus on the effectiveness and reliability of this technique. The amplitudes and wave lengths of the coherent structures will also determine the intensity and frequency spectrum of the associated aerodynamic/hydrodynamic noise. In addition, since both, the streamwise and spanwise structures are a consequence of hydrodynamic instabilities, instability mechanisms may be exploited advantageously for active flow control strategies.

Tani was among the first to report on streamwise vortices in a turbulent boundary layer along a concave wall [2]. In his experiments he observed regularly spaced spanwise modulations of the velocity profiles which he attributed to a Görtler instability mechanism. To compare with stability theory results for a laminar boundary layer, he assumed a constant eddy viscosity of $0.018u_\infty\delta^*$ and a displacement thickness δ^* of 1.3θ (θ is the momentum thickness). Moser and Moin performed direct numerical simulations (DNS) of a curved turbulent channel flow to reveal the effects of curvature in wall-bounded turbulent flows [3]. They found stationary Görtler vortices which had

a significant impact on the mean Reynolds shear stresses and which enhanced the asymmetry of the channel flow. Sufficiently close to the wall, the mean velocity profiles followed the law of the wall. For a curvature of $\delta/r=0.1$ the turbulence intensities and shear stresses were, in some cases, twice as large for the curved wall than for a plane wall.

In the RANS calculations considered in the present paper, the prediction of the spreading rate depends on the turbulence model employed. Pajayakrit and Kind [4] used the Baldwin-Lomax, the Dash et al. $k-\varepsilon$, the Wilcox $k-\omega$, and the Wilcox multiscale turbulence models for the calculation of plane and curved turbulent wall jets. They tuned the model constants to obtain better agreement of skin friction and spreading rate with experimental data. They also pointed out that the Boussinesq-approximation mandates zero shear stress at the velocity peak while it is well known that the zero shear stress location in wall jets occurs substantially closer to the wall. For the curved wall jet the nondimensional velocity profile predicted by the $k-\varepsilon$ model matched the experimental profile while the profile predicted by the $k-\omega$ model had the velocity peak slightly closer to the wall.

2 Geometries

First, in collaboration with an experimental effort by Wygnanski and coworkers [1] a turbulent wall jet on a circular cylinder was investigated. For this geometry extensive numerical simulations, including direct numerical simulation (DNS), large eddy simulation (LES), and unsteady Reynolds averaged Navier-Stokes (URANS) were conducted [5, 6]. The cylinder had a diameter $d=0.1016m$, and nozzle height $h=2.34 \cdot 10^{-3}m$. The jet exit velocity was $48m/s$. The Reynolds number based on jet exit velocity and cylinder diameter was $6.15 \cdot 10^5$. The experiment was conducted in a quiescent environment.

Second, the NCCR 1510-7067N circulation control airfoil was computed using steady RANS. The experimental results were documented by Abramson (1977). The airfoil has 15% relative thickness (maximum thickness to cord length c) and a Coanda trailing edge. A blowing slot is located at $x/c=0.967$, the slot height h being $0.003c$. The tests were conducted at a freestream Mach number of $M_\infty=0.12$ for various angles of attack α_∞ .

The flow for this geometry was computed by Slomski et al. [7] using the commercial flow software Fluent on computational grids with approximately $1.6 \cdot 10^5$ points. Computations with the standard and the realizable $k-\varepsilon$ turbulence model did only yield realistic results for the jet momentum coefficient $c_\mu=0.026$. The jet momentum coefficient was defined as

$$c_\mu = \frac{v_{jet}^2 \rho_{jet} h}{\frac{1}{2} \rho_\infty v_\infty^2 c} \quad (1)$$

with jet exit velocity v_{jet} , jet mass flux $\dot{m}_{jet}=v_{jet}\rho_{jet}h$, and freestream dynamic pressure $1/2\rho_\infty v_\infty^2$. For a higher momentum coefficient, $c_\mu=0.093$, the same two turbulence models predicted the wall jet separation slightly farther downstream than observed in the experiment. At the even higher momentum coefficient, $c_\mu=0.209$, the jet wraps around the entire elliptic airfoil 1 1/2 times if the realizable $k-\varepsilon$ model was used. Only the full Reynolds stress model predicted the correct separation locations and hence the correct overall circulation for all momentum coefficients studied. In general, turbulence models based on the Boussinesq assumption predicted separation too far downstream.

Another simulation for the same geometry was carried out by Paterson and Baker [8]. They studied the two workshop CFD challenge cases (Tab. 1), using the incompressible CFDSHOP-IOWA code. For two-dimensional (2-D) RANS the SST two-equation turbulence model was employed. The

	case 283	case 321
α_∞ [°]	0	-8
\dot{m}_{jet} [kg/(ms)]	0.196	0.182
c_μ	0.209	0.184

Table 1: Elliptic airfoil CFD challenge cases.

prediction of wall jet separation location and wall pressure distribution (and therefore circulation) was in good agreement with the experiment by Abramson.

3 Numerical Approach

For the computational results presented in this paper two different numerical approaches were used. Since each of these approaches is tailored and optimized for certain subtasks, computational resources can be focused effectively. When combined, they will help to understand the different physical mechanisms involved.

3.1 Direct Numerical Simulations (DNS)

An existing incompressible Navier-Stokes code [9, 10] was adopted to allow for highly accurate direct numerical simulations (DNS) of turbulent Coanda wall jets for Reynolds numbers in the range of the laboratory experiments by Wygnanski and coworkers. In this code the incompressible Navier-Stokes equations in vorticity-velocity formulation are solved. The governing equations are discretized using 4th-order accurate compact differences in the streamwise (x) and wall-normal (y) directions. The spanwise direction is assumed to be periodic and is discretized using a pseudo-spectral Fourier method. A 4th-order accurate Runge-Kutta scheme is employed for time integration. Metric terms were included to allow for computations on orthogonal curvilinear grids. The velocity Poisson equations are solved using an iterative solver with multigrid acceleration.

3.2 Reynolds-Averaged Navier-Stokes (RANS) calculations

A multi-domain, compressible, finite volume Navier-Stokes code with high-order accurate upwind schemes was developed to allow for robust computations of complex geometries. The convective terms are discretized with 5th-order upwind schemes based on a WENO extrapolation and the Roe scheme [11], the viscous terms are 4th-order accurate. A 2nd-order accurate Adams-Moulton method is used for time integration. Various turbulence models were implemented. The standard 1988 and 1998 k - ω models and the k - ϵ model [12] can be combined with both, a Reynolds stress based on the Boussinesq assumption, and an explicit algebraic stress model (EASM) [13]. The Menter SST [14] and Spalart-Allmaras [15] models were included as well.

4 Geometry 1: Turbulent Wall Jet on a Circular Cylinder

4.1 Direct Numerical Simulations (DNS)

The computational grid used for the DNS results is shown in Fig. 1. The resolution was 673x193 streamwise and wall-normal grid size points. Between 20 and 80 modes were used in the spanwise direction. At the inflow boundary a Glauert wall jet profile was prescribed. At the outflow a buffer domain was employed to damp out fluctuations and prevent reflections from the outflow boundary. Volume forcing was used to transition the wall jet near the inflow and to generate spanwise and streamwise structures for the controlled cases.

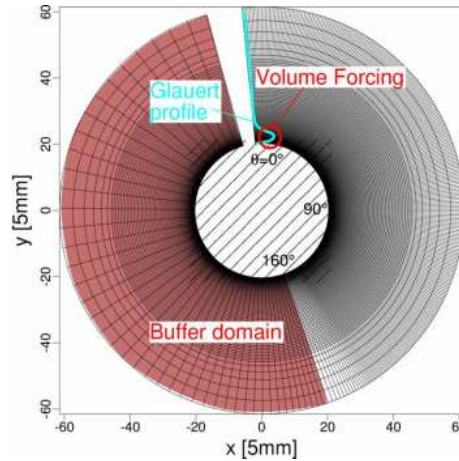


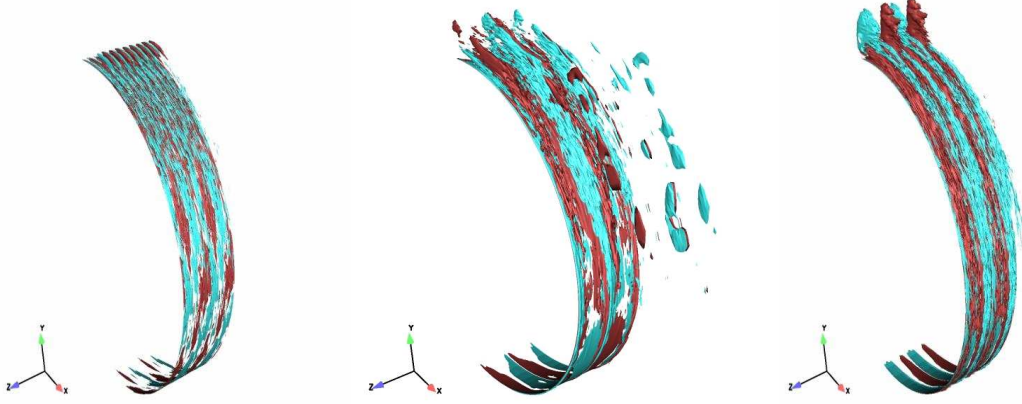
Figure 1: Computational grid used for DNS.

Visualizations of the DNS flow data (Fig. 2) clearly reveal both, spanwise and streamwise coherent structures in the turbulent Coanda wall jet [5]. The streamwise structures are caused by a centrifugal, Görtler-type instability while the spanwise structures originate from an inviscid, Kelvin-Helmholtz-type instability (inflection point of velocity profile). It appears that the spreading and, as a consequence thereof, the separation behavior are both governed by the complicated interaction/competition between these two instability mechanisms and the resulting vortical structures. Individually, both, streamwise and spanwise structures facilitate entrainment of low momentum fluid from the freestream into the wall boundary layer, causing a more rapid spreading and velocity decay of the jet, ultimately leading to earlier separation.

It may be conjectured, that in the natural (unforced) turbulent Coanda wall jet (under “clean” experimental conditions) the two instability mechanisms balance each other. For example, the Görtler-type, centrifugal instability and the resulting Görtler vortices may inhibit the spatial growth of the spanwise coherent structures that result from the inflectional instability. To probe this conjecture DNS were performed, where deliberate forcing was introduced to enhance certain structures, or where the simulations were set up such that certain instability mechanisms were weakened.

The DNS results have provided clear evidence that with 2-D forcing the intensity of the spanwise coherent structures could be enhanced strongly (Fig. 2) while the intensity of the naturally occurring streamwise coherent structures was not significantly affected (possibly slightly weakened; however, more research is required to substantiate this). On the other hand, by forcing the

I. time-averaged streamwise vorticity



II. instantaneous spanwise vorticity, spanwise average

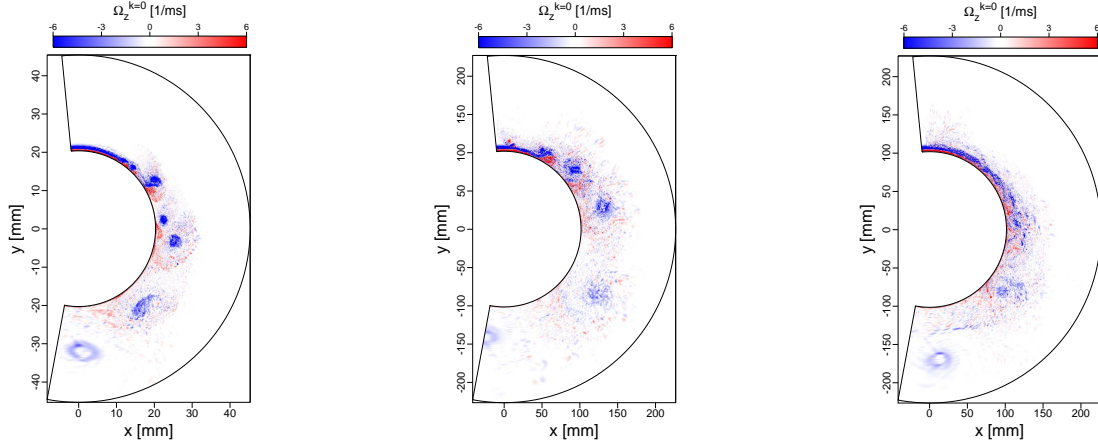
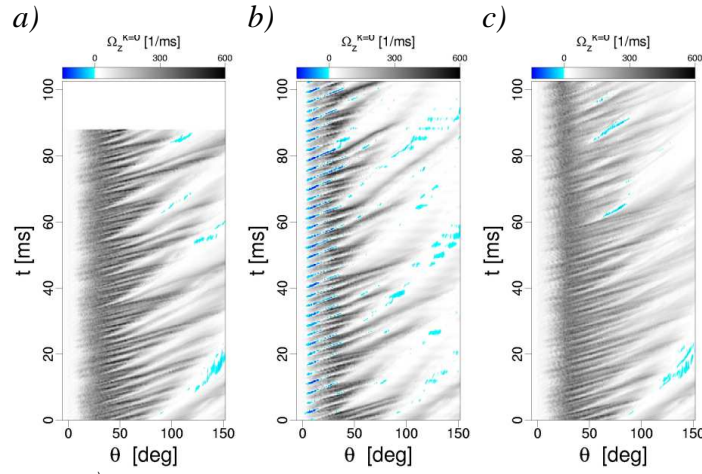


Figure 2: DNS of turbulent Coanda wall jet. *Top*: Streamwise vorticity (time-averaged) and *bottom*: spanwise vorticity (instantaneous), spanwise average. Shown are on the *left*: the unforced reference case, in the *center*: a case with 2-D harmonic forcing to enhance the spanwise vortical structures, and on the *right*: a case with steady 3-D forcing to enhance the streamwise vortices.

streamwise structures the intensity of the naturally occurring Görtler vortices could be significantly increased, while the intensity of the spanwise structures was weakened (Fig. 2).

The time-development of the spanwise coherent structures can be illustrated nicely with a time-space diagram of the spanwise averaged spanwise vorticity (Fig. 3). Figures 3a-c, which correspond to the cases in Fig. 2, illustrate the downstream propagation of the spanwise coherent structures and their mergings into larger structures (subharmonic cascade). Blue areas represent local flow separation. On the bottom part of Figure 3 the corresponding time-averaged streamwise wall vorticity is shown. When the spanwise coherent structures were forced, the intensity of the spanwise wall vorticity fluctuations in the time-trace became larger but the coherence of the streamwise coherent structures was not diminished noticeably. When the streamwise vortices were forced the strength of the spanwise coherent structures was decreased and the coherence of the streamwise structures was increased.

I. time-space
diagrams



II. time-averaged
wall footprint

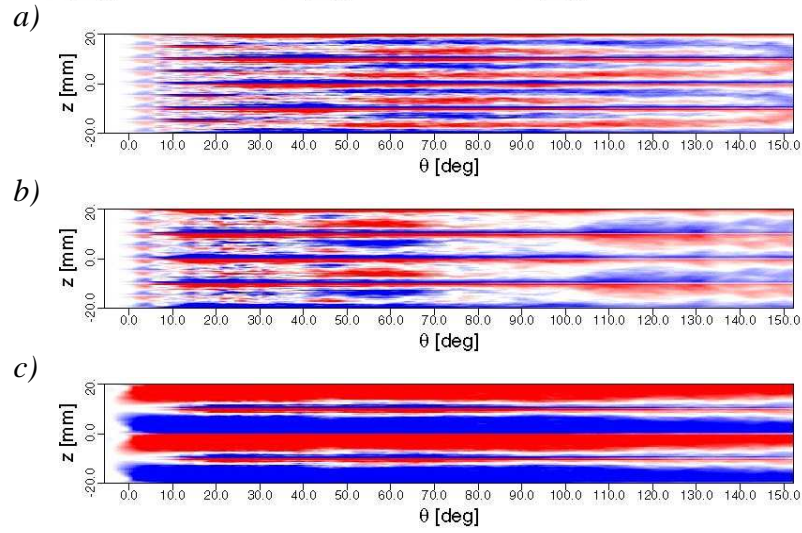


Figure 3: DNS of turbulent Coanda wall jet. *Top*: Spanwise averaged wall vorticity (time-signal) and *bottom*: streamwise wall vorticity (time-averaged). Shown are *a*): the unforced reference case, *b*): a case with 2-D harmonic forcing to enhance the spanwise vortical structures, and *c*): a case with steady 3-D forcing to enhance the streamwise vortices.

The results from the DNS also confirmed that a strengthening or weakening of the streamwise or spanwise structures changes the downstream development of the Coanda wall jet. For example, the spreading rate and the downstream decay of the streamwise mean velocity is significantly increased as a result of the forcing (Fig. 4). While the separated flow region is not computed in our DNS, it may be conjectured that the wall jet will separate from the wall farther upstream as a direct result of the increased spreading and decay of the turbulent mean flow. This, in turn, has an effect on the side force that is being generated. However, most of the interacting mechanisms between spanwise and streamwise vortical structures have to be investigated in considerably more detail as numerous physical aspects are not yet fully understood. This understanding is essential for the implementation of the Coanda technology for practical applications.

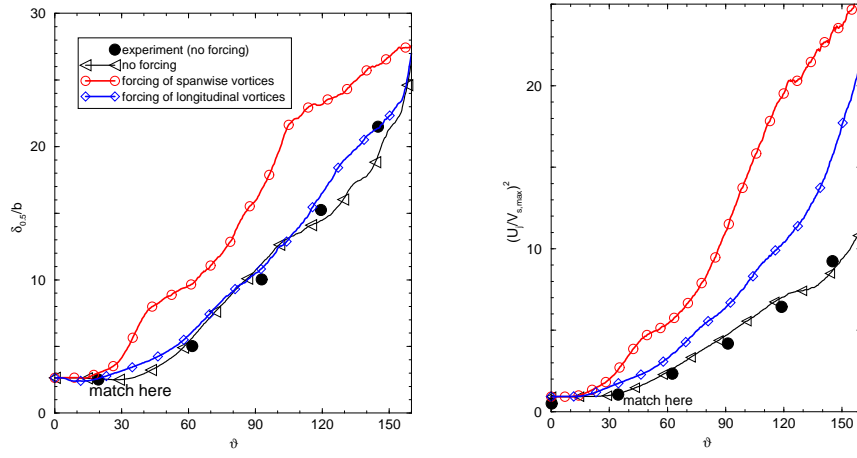


Figure 4: DNS of turbulent Coanda wall jet. Effect of forcing on the mean-flow development. Shown versus downstream angle are wall jet half-thickness (*left*) and inverse square of streamwise mean-velocity maximum (*right*).

4.2 Reynolds-Averaged Navier-Stokes (RANS)

Prior to investigating the fundamental mechanisms, the available turbulence models were scrutinized with respect to their applicability for Coanda flow calculations. The computational grid used for these investigations is shown in Fig. 5 and consisted of 3 blocks. The block resolutions were 200x75, 50x50, and 150x20. At the nozzle inflow a top-hat velocity profile is prescribed. The ambient is quiescent. The flow was assumed to be laminar at the nozzle inflow and in the ambient.

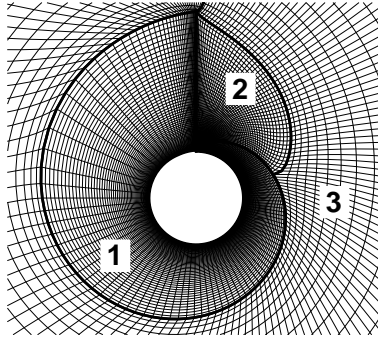


Figure 5: Computational grid used for 2-D RANS computations. Close-up.

Generally, most turbulence models gave disappointing results, some to a larger degree than others. Typical results in form of iso-contours of eddy-viscosity from such RANS calculations are given in Fig. 6. The 1988 $k-\omega$ model facilitates the strongest turbulent mixing across the wall jet and hence leads to the fastest jet velocity decay and largest jet spreading and the earliest separation. When the $k-\varepsilon$ or the Spalart-Allmaras model was used the jet wrapped around the cylinder more than once.

For some of these turbulence models the jet velocity decay and jet-half-thickness over downstream angle ϑ are plotted in Fig. 7. When the 1988 $k-\omega$ model was used in conjunction with the EASM model a close match of the jet velocity decay with the measured data was achieved. However,

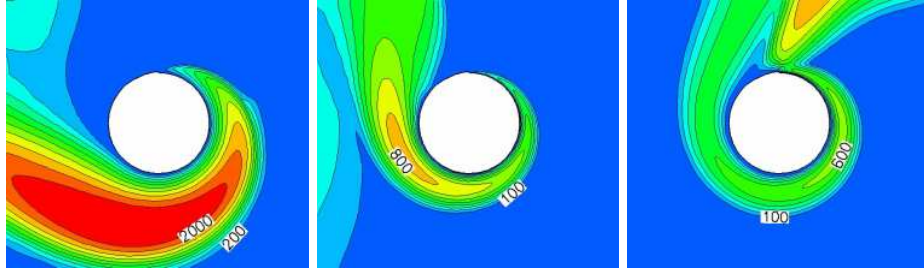


Figure 6: 2-D RANS computations of Coanda flow. Ratio of eddy viscosity normalized by laminar viscosity. *Left*: 1988 $k-\omega$ model, *center*: $k-\epsilon$ model, and *right*: Spalart-Allmaras model. The $k-\epsilon$ and S-A results are transient.

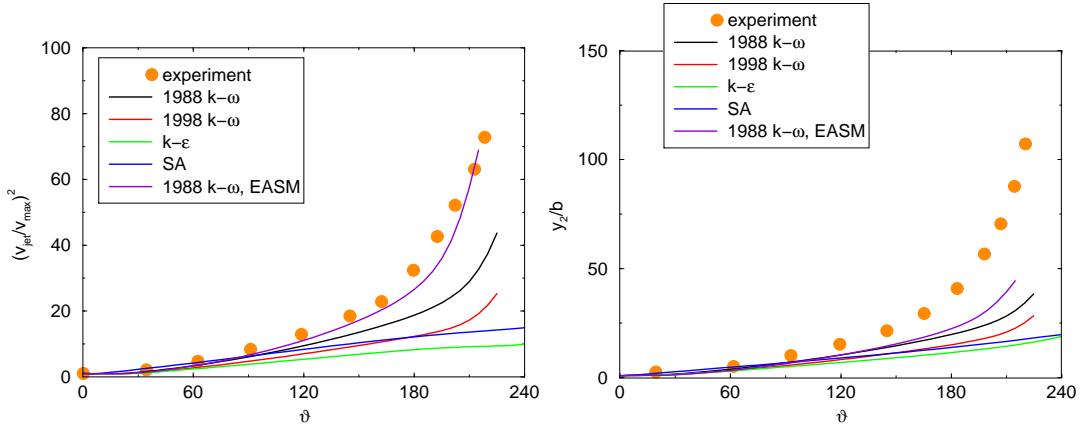


Figure 7: 2-D RANS computations of Coanda flow. Jet-velocity decay (*left*) and jet half-thickness (*right*) versus downstream angle.

even with this model the downstream development of the jet half-thickness distribution was poorly predicted. The second best model was the 1988 $k-\omega$ model.

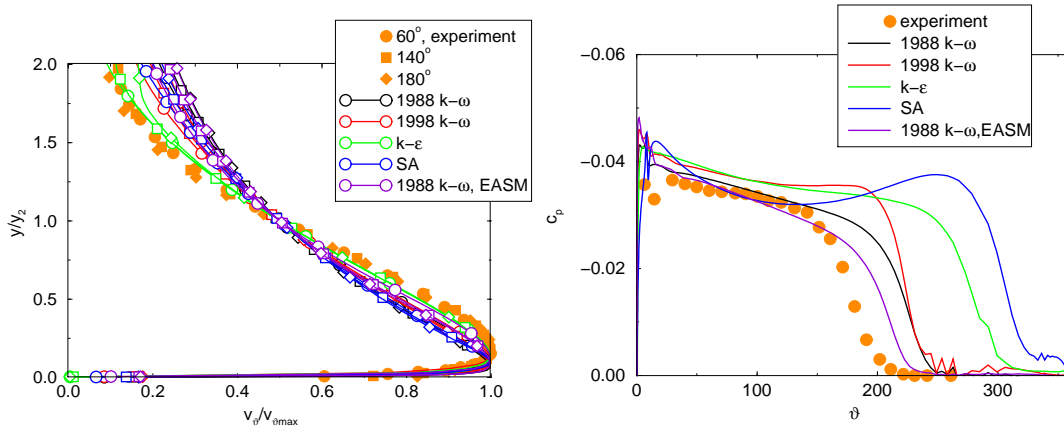


Figure 8: 2-D RANS computations of Coanda flow. Velocity profiles at three downstream stations (*left*) and wall pressure coefficient $c_p = 2(p - p_a)/(\rho_{jet}v_{jet}^2)$ (*right*).

The shape of the normalized velocity profiles is predicted best by the $k-\varepsilon$ model (Fig. 8). The second best results were obtained from the 1988 $k-\omega$ model with EASM. However, since the predicted half-thickness was too small for all models (Fig. 7), the non-normalized velocity profiles still did not match the experimental velocity profiles. With the 1988 $k-\omega$ model (with Boussinesq or EASM Reynolds stress) very good predictions of the wall pressure distribution were possible (Fig. 8). For the EASM model the separation location was slightly closer to the experiment. When the $k-\varepsilon$ and Spalart-Allmaras models were used the jet did stay attached to the cylinder for more than 360° . The data shown for these two models are not from steady state solutions but from transient solutions at time instants when the wall jet still separated at downstream locations smaller than 360° . This was done to allow for a comparison with the $k-\omega$ model results.

For all but the 1988 $k-\omega$ model with EASM, jet spreading and velocity decay were underpredicted. Based on the DNS results one may assume that the turbulence models failed to account for (or underpredicted) the additional mixing facilitated by the strong coherent turbulence structures that are present in the flow. Since the separation location was predicted within 10% of the experimental result when the standard 1988 $k-\omega$ turbulence model was used, this model was then chosen for subsequent three-dimensional (3-D) RANS stability investigations [6]. For these 3-D computations the computational grid was extended in the spanwise direction by 48 cells ($48/k$ cells per wave length $\lambda_z(k)=0.3d/k$, where k is the spanwise wave number and d is the cylinder diameter).

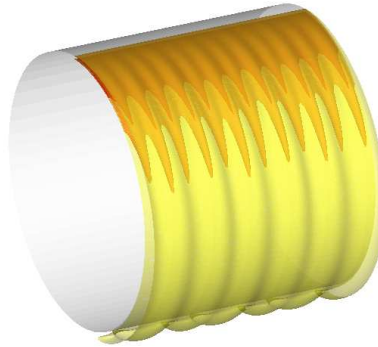


Figure 9: RANS computation of Coanda wall jet. Spanwise Fourier modes $k=1, 2$ forced at non-linear amplitudes of 0.01 and $0.1v_{jet}$ (mode 2 phase-shifted by $\pi/2$ relative to mode 1). Iso-surfaces of azimuthal velocity component. As the jet passes along the cylinder in downstream direction the structures with a higher spanwise wave number disappear, while the structures with a lower spanwise wave number emerge.

In these 3-D RANS simulations steady 3-D perturbations with different spanwise wave numbers k (wave length $\lambda_z(k)=0.3d/k$) were introduced at the nozzle exit with different amplitudes (one of these cases is shown in Fig. 9). Then their growth and interaction in downstream direction was computed.

Forcing at small amplitudes allows for a comparison with linear stability theory. From the experiment by Wygnanski and coworkers [1] it was found that the spanwise wave length of the locally predominant structures scales roughly with the local half-thickness of the jet (Fig. 10). This can be confirmed by the computation.

When the streamwise structures were forced at higher disturbance levels, nonlinear subharmonic resonances could be observed (Figs. 10 and 11). The results obtained at the nonlinear amplitudes

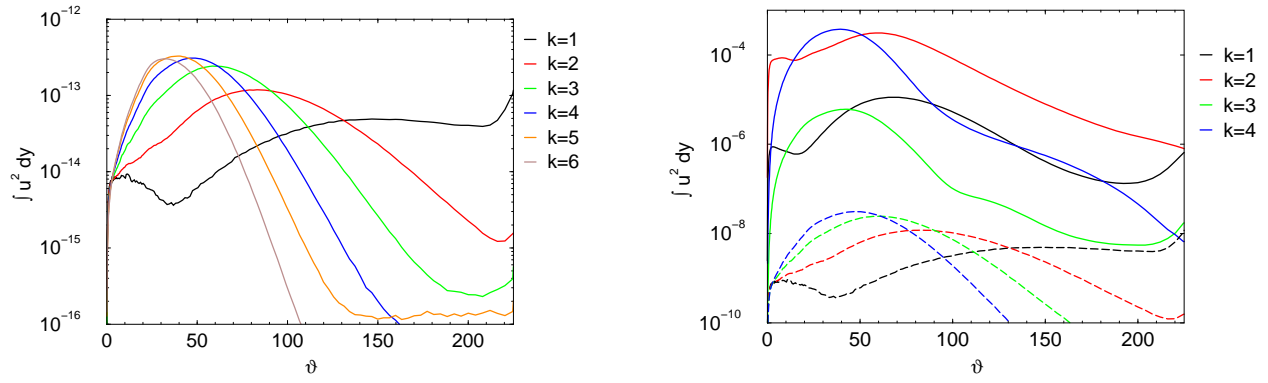


Figure 10: RANS computation of Coanda wall jet. Amplitude of spanwise Fourier modes k . *Left*: Linear case, all modes forced at small disturbance amplitudes. *Right*: Fourier modes $k=1, 2$ forced at large, non-linear amplitudes of 0.01 and $0.1v_{jet}$ (solid lines). Comparison with linear case (dashed lines). In particular close to the nozzle ($\vartheta=0^\circ$), the growth rates for the non-linear forcing deviate substantially from the growth rates for the linear forcing.

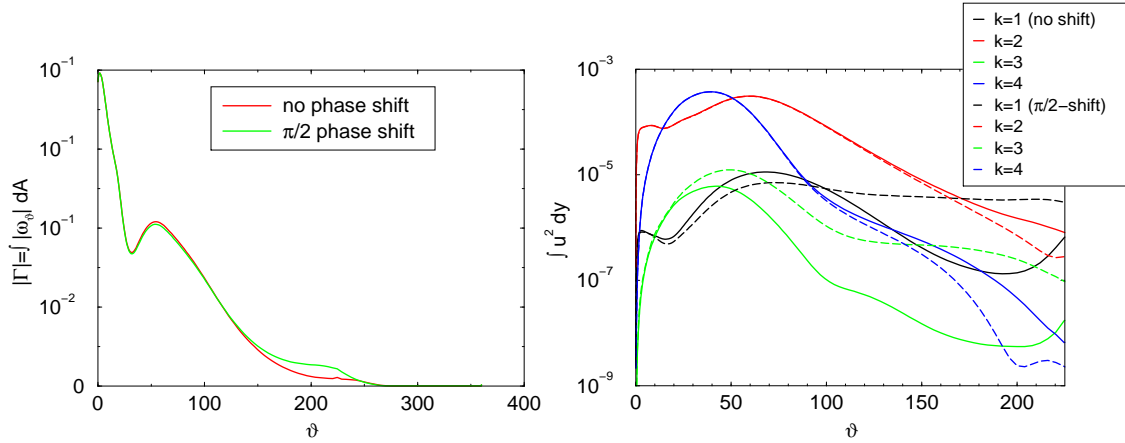


Figure 11: 2-D RANS computation of Coanda flow. Fourier modes $k=1, 2$ forced at amplitudes of 0.01 and $0.1v_{jet}$. Mode 1 and 2 forced in phase and with a relative phase shift of $\pi/2$. Total circulation $\Gamma(\vartheta) = \int |\omega_\vartheta| dA$ (*left*) and mode amplitudes (*right*).

depend on the relative phase between the modes. This becomes evident from the total circulation for $\vartheta > 150^\circ$. These preliminary investigations suggest that both, linear instability as well as non-linear subharmonic resonance are possible viable mechanisms for the merging of the longitudinal vortices that was observed in the experiments. Based on our calculations the linear process appears to be more likely for the present experimental conditions. However, for possible control of the Coanda wall jet behavior, the nonlinear resonance mechanisms might also be exploited.

Since RANS underpredicted the cross-stream mixing (and hence the jet velocity decay and jet spreading) and since our DNS results clearly indicate that strong turbulent coherent structures play a dominant role in the turbulence mixing, application of our flow simulation methodology (FSM) [16, 17] appeared to be a logical choice. With FSM, depending on the local turbulence characteristics and grid resolution, small turbulence motion is modeled while large scale turbulence coherent

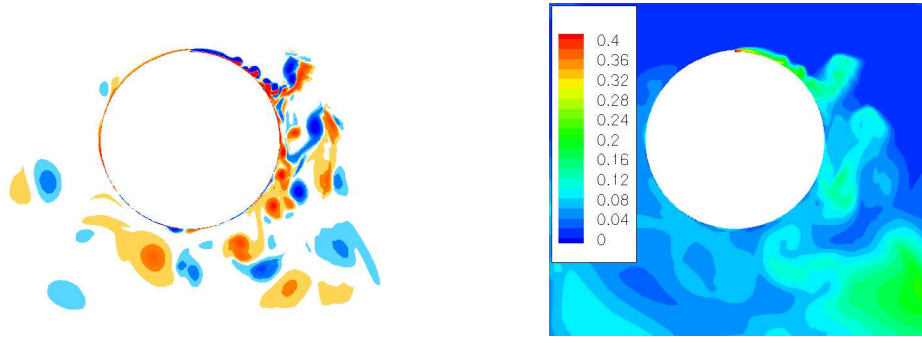


Figure 12: 2-D FSM computation of Coanda wall jet. Shown are vorticity (*left*) and contribution function (*right*). Since 3-D streamwise vortices are deliberately excluded the 2-D structures have a high intensity. The spatial distribution of the contribution function clearly correlates with dominant flow structures.

structures are simulated in a time-accurate fashion. Results from a preliminary 2-D FSM are shown in Figure 12. Large spanwise coherent structures arise as a consequence of the inflectional wall jet profile (left plot, Fig. 8). The turbulence model contribution is clearly linked to the flow structures as shown in the right plot of Fig. 12.

5 Geometry 2: Circulation Control Airfoil

5.1 Case Description

The airfoil chord length c was $8in$ or $0.2032m$. The freestream velocity was $v_\infty=39.18m/s$, the freestream density was $1.226kg/m^3$, and the freestream molecular viscosity was $1.790 \cdot 10^{-5} kg/(ms)$. Assuming a gas constant of $R=287.1J/(kgK)$ and a ratio of specific heats $\gamma=1.4$ the freestream temperature can be computed as $T_\infty = (v_\infty/M)^2/(\gamma R)=265.21K$. The Reynolds number based on freestream velocity and chord length was

$$Re = \frac{\rho_\infty v_\infty c}{\mu_\infty} = 5.455 \cdot 10^5. \quad (2)$$

If the assumption $\rho_\infty = \rho_{jet}$ is made, the jet blowing ratio $B=v_{jet}/v_\infty=\sqrt{c_\mu \rho_\infty c/(2\rho_{jet}h)}$ is 5.90 for case 283 and 5.54 for case 321. However, this results in a nozzle exit Mach number of ≈ 0.7 and requires the use of a compressible code. The nozzle inflow area is $A_{in}/c=0.03188$. The nozzle area ratio is 10.2.

5.2 Computational Grid

The computational grid used for the investigations discussed here is shown in Fig. 13. The number of cells around the airfoil was 500, the nozzle interior was resolved by 100×80 cells. The resolution of the individual blocks was: 700×80 (red block), 40×40 (green block), and 400×50 (blue block). This resulted in a total number of cells of 77600. The total extent of the grid was $10c$ in both x and y measured from the center of the airfoil. For the turbulence models used in these

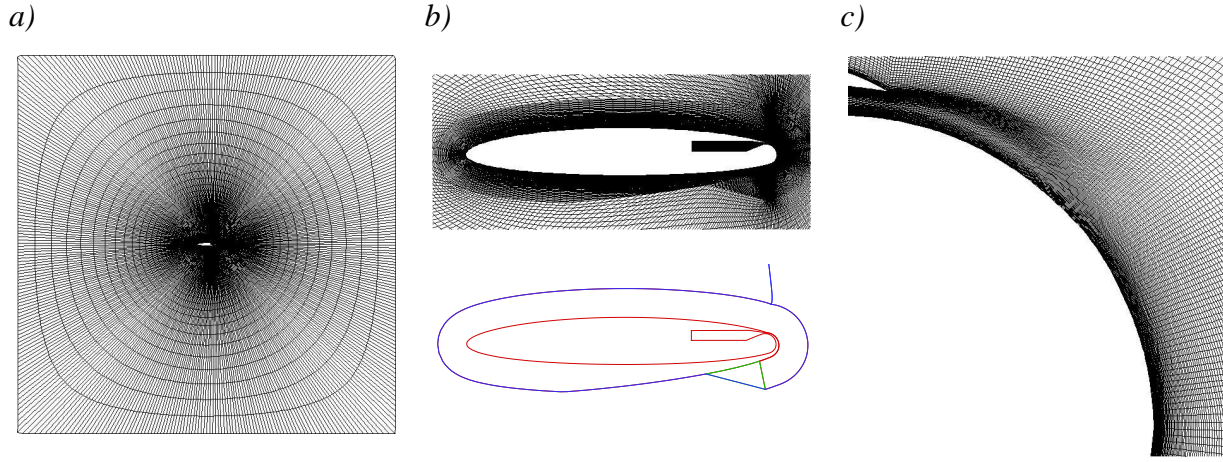


Figure 13: Computational grid for circulation control airfoil. *a)* Entire grid, *b)* close-up of airfoil and block boundaries, and *c)* close-up of Coanda flow region.

calculations the laminar sublayer needed to be resolved. The y^+ value of the wall next grid point was therefore set to be smaller than 1.

5.3 Boundary Conditions

Following common practice, velocities and temperature were set at the freestream inflow boundary, while the static pressure was extrapolated. At the outflow boundary all flow quantities were extrapolated, except for the static pressure which was prescribed. A stable and realistic nozzle inflow condition was found by extrapolating the static pressure and prescribing the mass flux $\dot{m}_{in} = \dot{m}_{jet} = \rho_{in} v_{in} A_{in}$ and the total temperature (the total temperature at the nozzle inlet was chosen to match the total temperature of the freestream). Inflow velocity v_{in} and temperature T_{in} were then obtained by solving

$$v_{in} = \frac{RT_{in} \dot{m}_{in}}{pA_{in}} \quad (3)$$

and

$$\frac{\gamma R}{\gamma - 1} T_{\infty} + \frac{1}{2} v_{\infty}^2 = \frac{\gamma R}{\gamma - 1} T_{in} + \frac{1}{2} v_{in}^2. \quad (4)$$

The wall was considered to be adiabatic and hydraulically smooth.

5.4 Results

With the 1988 $k-\omega$ model and the Menter SST model the wall jet stayed attached to the wall for far too long (Fig. 14). Shown therefore are transient solutions for these models. On the other hand, very good results could be obtained when the EASM model was used.

Case 321 was computed with the 1988 $k-\omega$ model and EASM only (Fig. 15). For both cases the jet exit velocity was about $6.7v_{\infty}$, resulting in a jet exit Mach number of about 0.85. The nozzle pressure ratio (nozzle inflow to nozzle exit) was approximately 1.6 and the nozzle density ratio was about 1.4. Wall pressure distributions are shown in Fig. 16. For both cases the prediction is in very

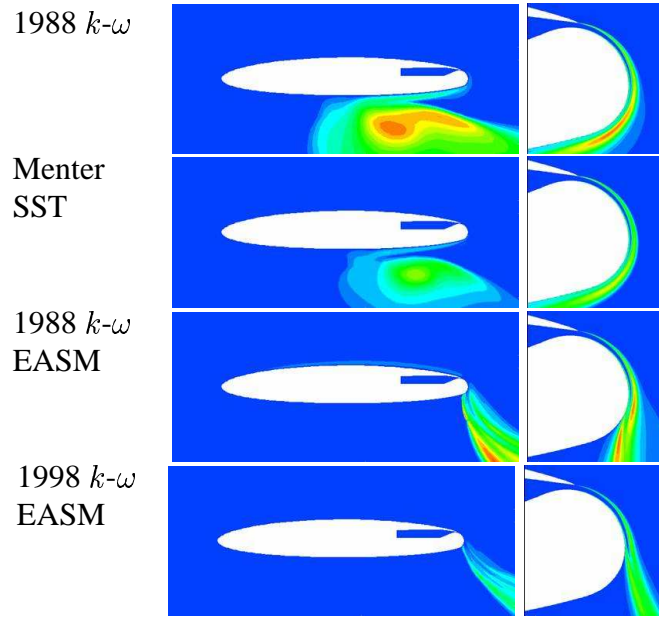


Figure 14: RANS calculation of circulation control airfoil. Case 283 ($\alpha=0^\circ$). Turbulence kinetic energy. (Result for 1988 $k-\omega$ and Menter SST model are transient).

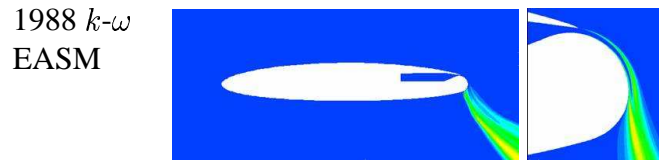


Figure 15: RANS calculation of circulation control airfoil. Case 321 ($\alpha=-8^\circ$). Turbulence kinetic energy.

good agreement with the experiment. When the 1998 $k-\omega$ model with EASM was used, the wall jet separated somewhat earlier, leading to a slightly smaller circulation augmentation and a slightly smaller area enclosed by the pressure coefficient curves. The leading edge stagnation point moved backward as a result of the increase in total circulation (Figs. 17, 18).

6 Summary and Conclusions

Coanda wall jets for two different geometries were investigated numerically: 1) The circular cylinder which was studied experimentally by Wygnanski and coworkers [1] and 2) the NCCR 1510-7067N circulation control airfoil (Abramson (1977) (the workshop CFD challenge). Geometry 1 was investigated using direct numerical simulations (DNS) and RANS computations. DNS showed that both spanwise and streamwise coherent structures were present in the flow. It was conjectured that in the natural unforced case both types of structures keep each other at bay and that if either one was favored or forced by active flow control (AFC) the other one would be weakened. This conjecture was probed by separately forcing the spanwise and streamwise coherent structures at

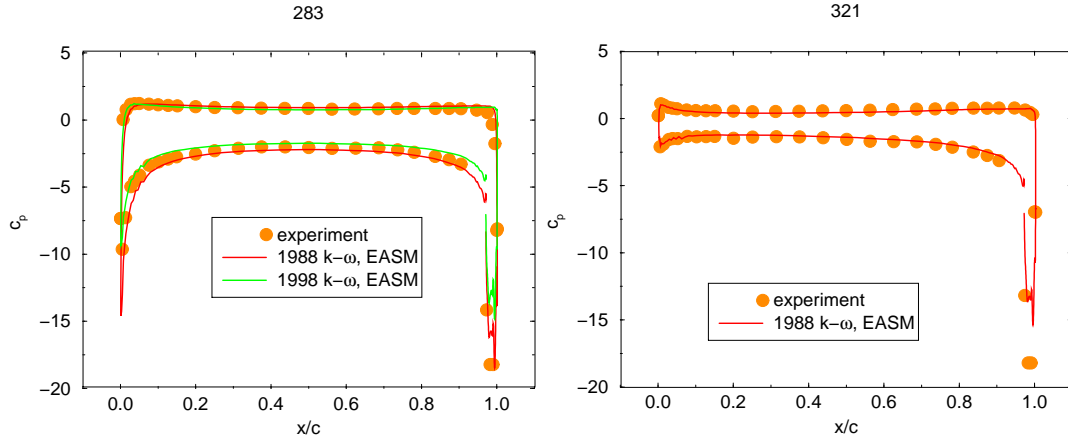


Figure 16: RANS calculation of circulation control airfoil. Wall pressure coefficient $c_p = 2(p - p_\infty)/(\rho_\infty v_\infty^2)$. *Left*: Case 283 ($\alpha=0^\circ$) and *right*: case 321 ($\alpha=-8^\circ$).

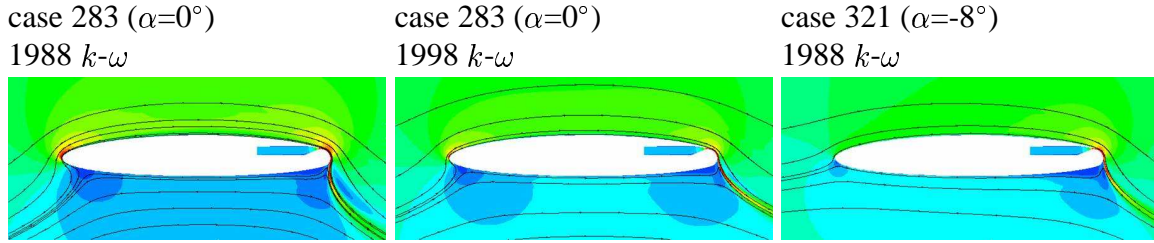


Figure 17: RANS calculation of circulation control airfoil. Total velocity ($\sqrt{u^2 + v^2}$) and streamlines.

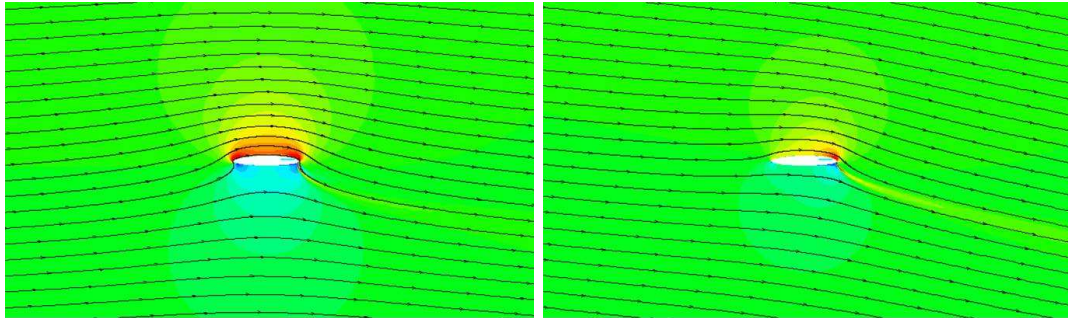


Figure 18: RANS calculation of circulation control airfoil. Total velocity ($\sqrt{u^2 + v^2}$) and streamlines. 1988 $k-\omega$ model. *Left*: Case 283 ($\alpha=0^\circ$) and *right*: case 321 ($\alpha=-8^\circ$).

the nozzle inflow. Forcing of the spanwise structures indeed strengthened their downstream coherence but did not noticeably weaken the streamwise structures. The reason for this is unclear and necessitates further research. Forcing of the streamwise structures weakened the spanwise structures and strengthened the streamwise structures, as expected. The downstream development and interaction of both types of structures and their influence on the turbulence dynamics are ultimately responsible for the downstream development of the wall jet. The goal here is to actively control the jet spreading and velocity decay by application of AFC at the nozzle exit.

Geometry 1 was also used to evaluate turbulence models for steady RANS of Coanda wall jets. None of the tested models correctly predicted all relevant aspects of the flow. Evidently, important physical mechanisms are not modeled. For example, none of the employed turbulence models had a curvature correction. Also, the strong turbulent coherent structures that are not captured in steady and 2-D RANS may significantly contribute to the mean flow and turbulence characteristics. By comparison, the models based on an EASM Reynolds stress model performed best. Geometry 1 was also used for steady RANS stability investigations. Steady streamwise structures were introduced at the nozzle, and their development in downstream direction was investigated. At low disturbance amplitudes (linear case) the local size of the dominant streamwise structures roughly scales with the local wall jet half-thickness, an observation that was also made in the experiment. Overall, the amplification of the streamwise coherent structures by the centrifugal Görtler instability was rather small. If the streamwise coherent structures observed in the experiment were of similar strength as in the linear 3-D RANS computation the vortex mergings observed in the experiment may be explainable by linear stability mechanisms.

Based on the experience gained from studying geometry 1 using RANS computations, the elliptic circulation control airfoil (geometry 2) was then computed using the 1988 and 1998 $k-\omega$ model and the Menter SST model. In our calculations, only use of the EASM Reynolds stress model resulted in good predictions of the wall jet separation from the airfoil. For both angles of attack, excellent agreement with the experimental data could be obtained with this model.

Acknowledgment

The authors gratefully acknowledge the Office of Naval Research for funding of this research under grant number N00014-01-1-09 with Dr. Ronald Joslin serving as program manager.

References

- [1] Neuendorf, R., Wygnanski, I., "On a turbulent wall jet flowing over a circular cylinder," *J. Fluid Mech.*, Vol. 381, pp. 1-25, 1999.
- [2] Tani, I., "Production of Longitudinal Vortices in the Boundary Layer along a Concave Wall," *J. Geophys. Res.*, Vol. 67, pp. 3075-3080.
- [3] Moser, R.D., Moin, P., "The effects of curvature in wall-bounded turbulent flows," *J. Fluid Mech.*, Vol. 175, 1987, pp. 479-510.
- [4] Pajayakrit, P., Kind, R.J., "Assessment and Modification of Two-Equation Turbulence Models," *AIAA Journal*, Vol. 38, No. 6, June 2000, pp. 955-963.
- [5] Wernz, S., Valsecchi, P., Groß, A., Fasel, H.F., "Numerical Investigation of Turbulent Wall Jets Over a Convex Surface," AIAA-2003-3727, June 2003.
- [6] Groß, A., Wernz, S., Fasel, H.F., "Numerical Investigation of Coherent Structures in a Turbulent Coanda Wall Jet," AIAA-2003-4020, June 2003.

- [7] Slomski, J.F., Gorski, J.J., Miller, R.W., Marino, T.A., "Numerical Simulation of Circulation Control Airfoils as Affected by Different Turbulence Models," AIAA-2002-0851, Jan. 2002.
- [8] Paterson, E.G., Baker, W., "Simulation of Steady Circulation Control for Marine-Vehicle Control Surfaces," AIAA-2004-0748, Jan. 2004.
- [9] Meitz, H.L., "Numerical Investigation of Suction in a Transitional Flat-Plate Boundary Layer," *Dissertation*, The University of Arizona, 1996.
- [10] Meitz, H.L., Fasel, H.F., "A compact-difference scheme for the Navier-Stokes equations in vorticity-velocity formulation," *Journal of Computational Physics*, Vol. 157, No. 1, 2000, pp. 371-403.
- [11] Gross, A., Fasel, H., "High-Order WENO Schemes Based on the Roe Approximate Riemann Solver," AIAA-2002-2735, June 2002.
- [12] Wilcox, D.C., "Turbulence Modeling for CFD," Second Edition, DCW Industries, 2000.
- [13] Rumsey, C.L., Gatski, T.B. "Recent Turbulence Model Advances Applied to Multielement Airfoil Computations" *J. of Aircraft*, Vol. 38, No. 5, Sept.-Oct. 2001, pp. 904-910.
- [14] Menter, F.R. "2-Equation eddy-viscosity turbulence models for engineering applications" *AIAA Journal*, Vol. 32, No. 8, Aug. 1994, pp. 1598-1605
- [15] Spalart, P.R., Allmaras, S.R., "A One-Equation Turbulence Model for Aerodynamic Flows," AIAA-92-0439, Jan. 1992.
- [16] Fasel, H.F., Seidel, J., Wernz, S., "A methodology for simulations of complex turbulent flows," *Trans. ASME, J. Fluid Eng.* Vol. 124, pp. 933-942, 2002.
- [17] Fasel, H.F., von Terzi, D.A., Sandberg, R.D., "A methodology for simulating compressible turbulent flows," FEDSM 2003-45334, 4th ASME/JSME Joint Fluids Engineering Conference, 6-11 July 2003 / Honolulu, Hawaii .

Investigation of Turbulent Coanda Wall Jets Using DNS and RANS

NASA/ONR 2004 Circulation Control Workshop

16-17 March 2004

Hampton, VA

supported by ONR grant N00014-01-1-09

H. Fasel, A. Gross, P. Valsecchi, S. Wernz
University of Arizona

overview

Coanda effect (attached wall jet on curved surface)

- ⇒ generating a **side force** on a cylindrical body
- ⇒ **low speed maneuvering, circulation control**, etc.
- ⇒ more efficient and quieter than conventional thrusters

for many technical applications wall jet is **turbulent**

- ⇒ understanding of the dynamics of large **coherent structures** is essential
- ⇒ effect of structures on separation location

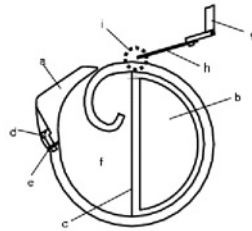
numerical simulations: **DNS** and **RANS**

2 cases:

- ⇒ experiment by Wygnanski and coworkers at UofA
- ⇒ workshop CFD challenge, NCCR 1510-7067N, cases 283, 321

case 1: Coanda cylinder in quiescent air

experiment by
Wynanski and
coworkers at
University of
Arizona



radius	$R=101.6\text{mm}$
slot width	$b=2.34\text{mm}$
spanwise extent	experiment: 914.4mm
jet	$u_{\text{jet}}=48\text{m/s}$, ambient temperature

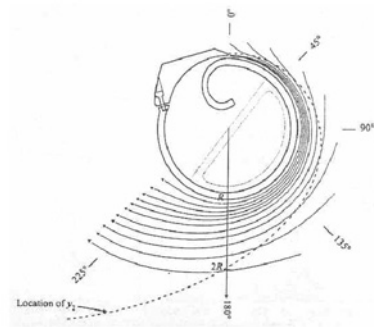
$$\text{Re}_N = \frac{u_{\text{jet}} \sqrt{\frac{bR}{2}}}{\nu} = 33,000$$

$$\text{Re}_D = \frac{u_{\text{jet}} D}{\nu} = \frac{2R}{\sqrt{\frac{bR}{2}}} \text{Re}_N = \sqrt{\frac{8R}{b}} \text{Re}_N = 615,032$$

experimental observations

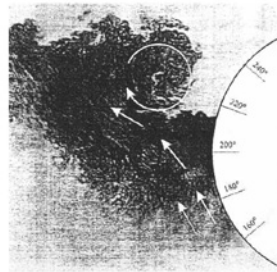
- flow is **turbulent** and **3-D**
- wall jet detaches from cylinder at about 240°
- flow displays **coherent structures**
 - ⇒ 3-D structures caused by **Görtler instability** mechanism
 - ⇒ 2-D structures due to **inflectional instability** of wall jet profile
- structures **enhance momentum transfer** across wall jet
 - ⇒ entrainment of low momentum free stream fluid
 - ⇒ structures counteract efforts to keep jet attached !?

experimental observations



time averaged streamlines

experiments by Wygnanski *et al.*



flow visualization

numerical methods

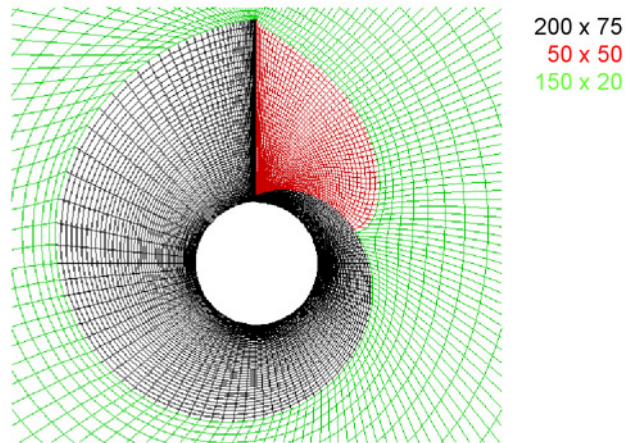
Reynolds Averaged Navier-Stokes (RANS):

- compressible Navier-Stokes equations solved with finite volume method
- 5th order accurate upwind method based on WENO approximation and Roe scheme
- 4th order accurate viscous terms
- 2nd order accurate Adams-Moulton time integration

Direct Numerical Simulation (DNS):

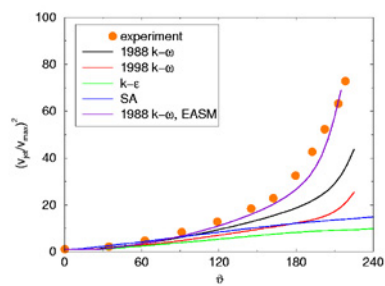
- incompressible Navier-Stokes equations are solved in vorticity-velocity formulation with finite difference method
- 4th order accurate compact differences and spectral method in spanwise direction
- 4th order accurate Runge-Kutta time integration

RANS, computational domain

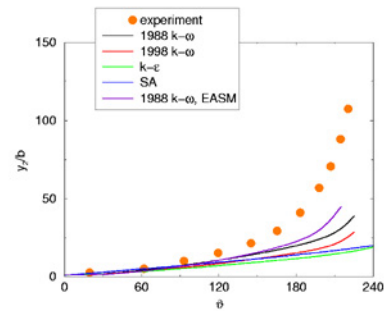


2-D RANS, comparison of turbulence models

jet velocity decay



jet half thickness

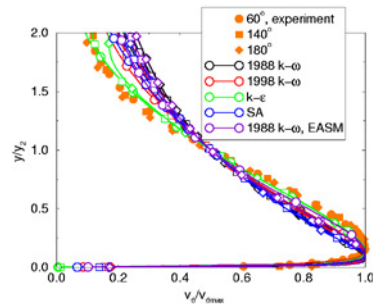


EASM by Rumsey and Gatski

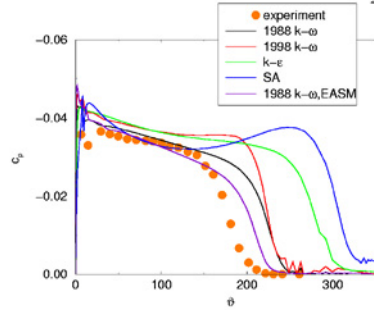
J. of Aircraft, Vol. 38, No. 5, Sept-Oct 2001, pp. 904-910

2-D RANS, comparison of turbulence models

velocity profiles

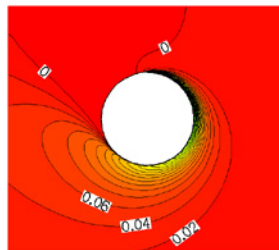


surface pressure distribution $c_p = \frac{p - p_{\infty}}{\frac{1}{2} \rho_{\infty} U_{\infty}^2}$

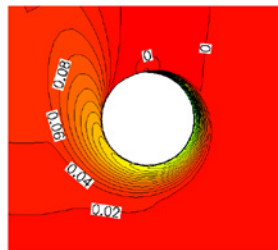


k- ϵ and SA data are **transient**

comparison of turbulence models

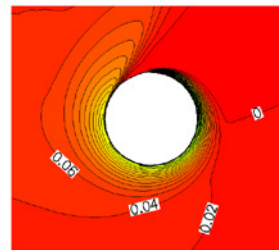


1988 k- ω



k- ϵ

transient solution



Spalart-Allmaras

transient solution

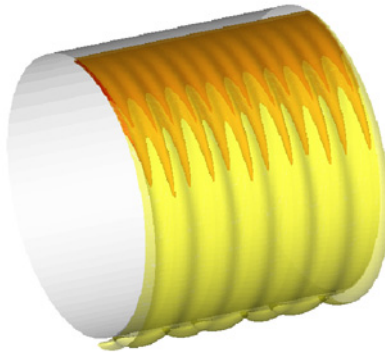
strongest spreading

flow separation at $\theta \approx 225^\circ$,
experiment 240°

weakest spreading

iso-contours of circumferential velocity

3-D RANS

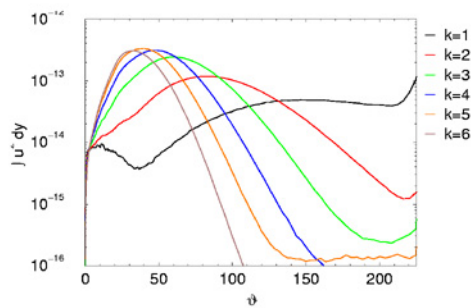


iso-surfaces of circumferential velocity

3-D RANS computation using 1988 $k-\omega$ model
spanwise Fourier modes 1 and 2 forced at amplitudes of 0.01 and 0.1 of u_{jet}
wavelength $\lambda_z(k)=0.3D/k$

3-D RANS, linear

mode amplitudes



integral of $v_\theta(k)^2$ in wall normal direction

linear case, all modes forced simultaneously at low disturbance amplitude

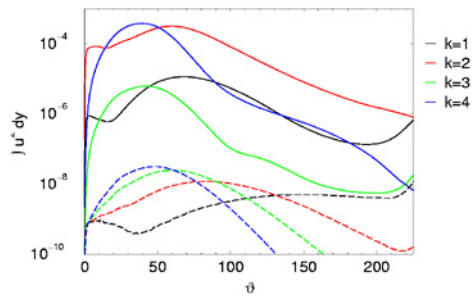
weak amplification due to centrifugal Görtler instability

half-wavelength of dominant mode scales roughly with local jet half-thickness

3-D RANS, nonlinear

mode amplitudes

comparison with linear result
(dashed lines)



significant nonlinear effects close
to slot where mode amplitudes are
high

mode 1 amplitude not clearly
linked to Görtler instability

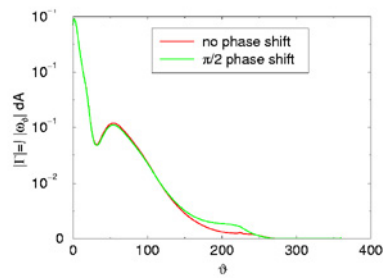
slower decay of modes 3, 4

modes 1 and 2 forced at
nonlinear amplitudes:

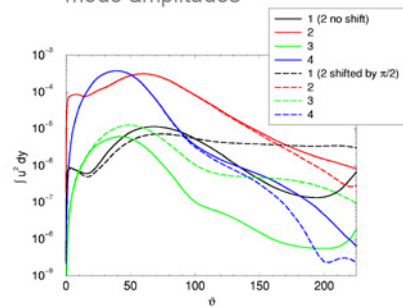
mode k	$w_{dis}^{(k)}$
1	0.01
2	0.1

3-D RANS, nonlinear, relative phase shift

circulation $\Gamma(\theta) = \int |\omega_\phi| dA$

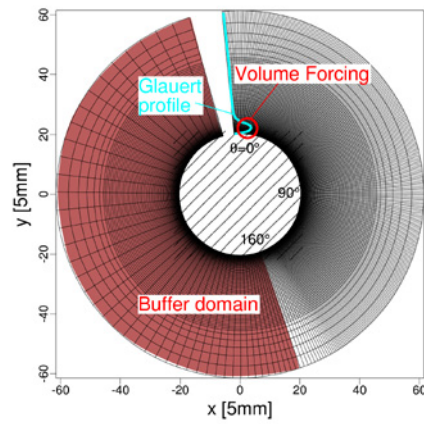


mode amplitudes



mode 2 phase-shifted by $\pi/2$
relative to mode 1

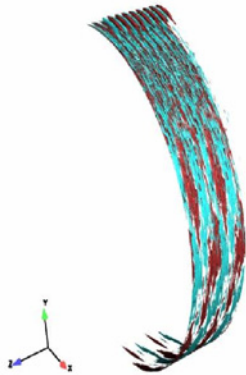
3-D DNS, computational domain



673x193 points, 20-80 modes in z

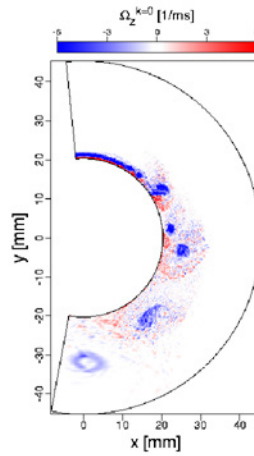
3-D DNS, natural case

time-averaged streamwise vorticity



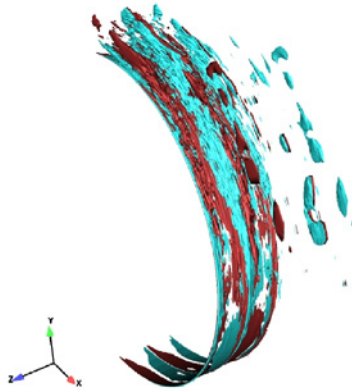
no forcing

instantaneous spanwise vorticity

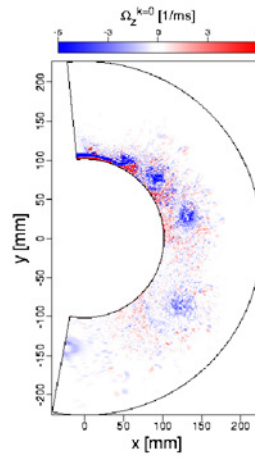


3-D DNS, weakening of streamwise structures

time-averaged streamwise vorticity



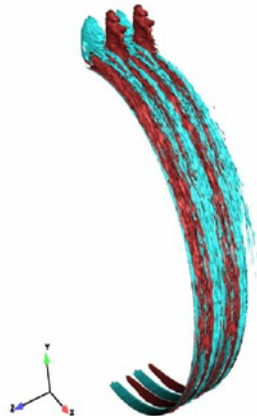
instantaneous spanwise vorticity



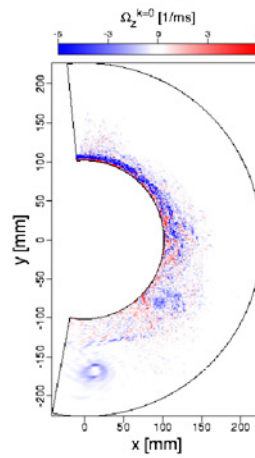
spanwise structures forced

3-D DNS, weakening of spanwise structures

time-averaged streamwise vorticity

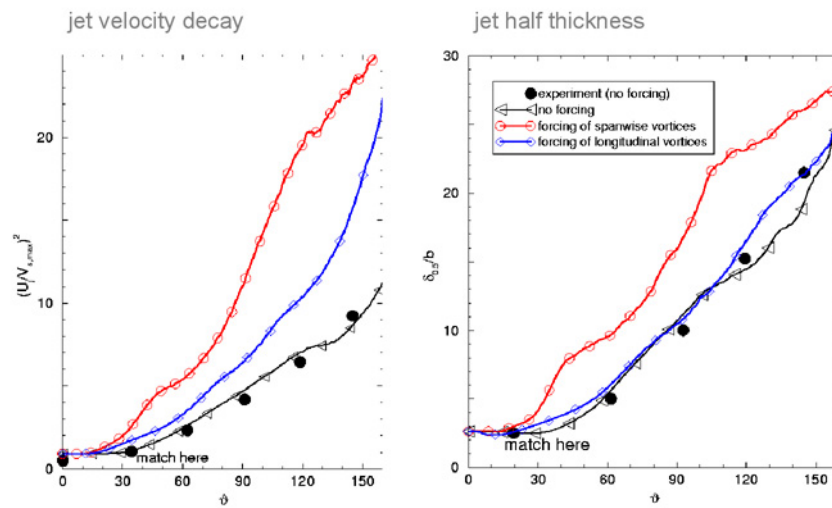


instantaneous spanwise vorticity



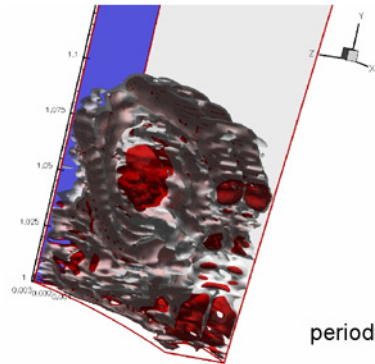
streamwise structures forced

3-D DNS, comparison

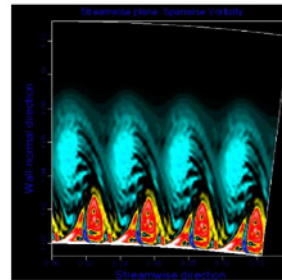


3-D temporal DNS

Instantaneous total velocity



instantaneous spanwise vorticity



periodic domain in stream- and spanwise direction

no downstream evolution,
but local effects of turbulence

small domain allows easier and faster investigations

computational domain

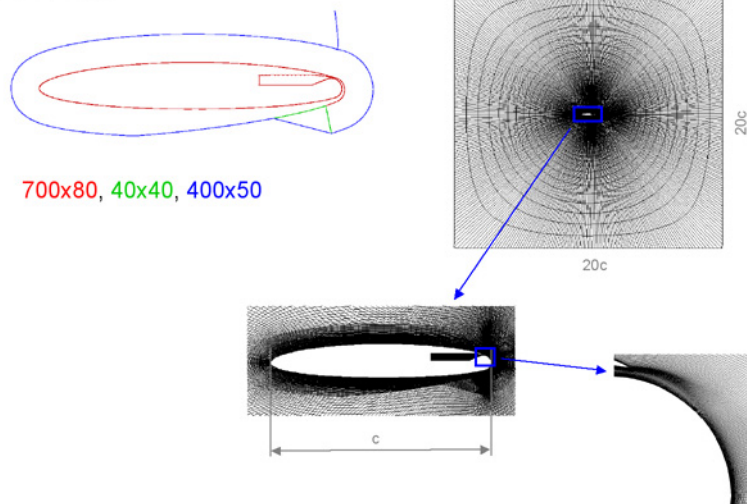
circulation control airfoil NCCR 1510-7067N tested at DTNSRDC

chord length	$c = 8 \text{ in} = 0.21032 \text{ m}$
slot height	$h = 0.003c$
nozzle area ratio	10.2
freestream	$u_\infty = 39.179 \text{ m/s} \quad \Rightarrow \text{Re}_c = 545501$
	$\rho_\infty = 1.2261 \text{ kg/m}^3$
	$\mu_\infty = 1.7894 \cdot 10^{-5} \text{ kg/ms}$

	angle of attack α_∞	mass flux $(dm/dt)_{\text{jet}}$
case 283	0°	0.196 kg/ms
case 321	-8°	0.1819 kg/ms

computational domain

grid topology



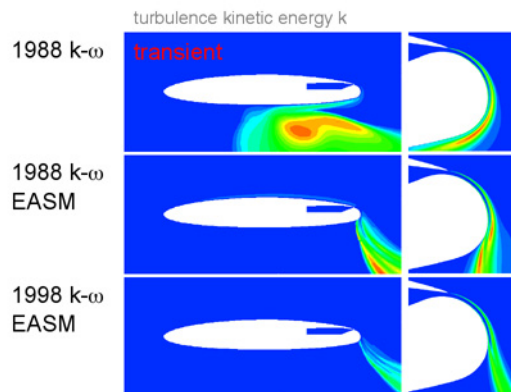
nozzle inflow boundary conditions

static pressure p is extrapolated,
mass flux dm/dt and total
temperature T_0 are prescribed

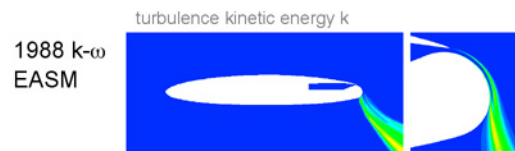
$$v_{in} = \frac{RT_{in}\dot{m}_{in}}{p_{in}A_{in}}$$

$$\frac{\gamma RT_{\infty}}{\gamma - 1} + \frac{1}{2}v_{\infty}^2 = \frac{\gamma RT_{in}}{\gamma - 1} + \frac{1}{2}v_{in}^2$$

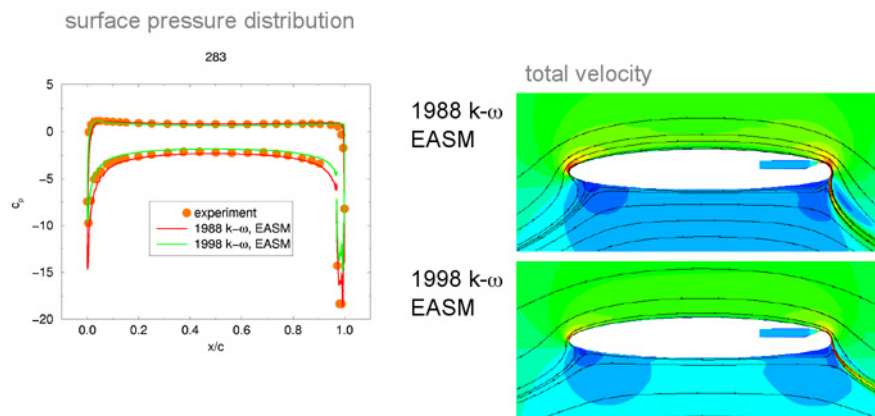
case 283, $\alpha_{\infty}=0^{\circ}$



case 321, $\alpha_\infty = -8^\circ$

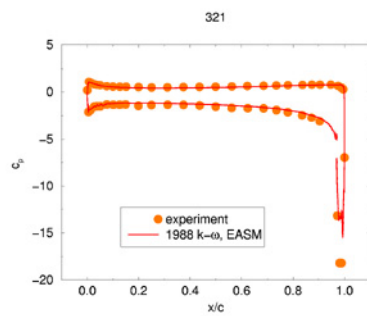


comparison with experiment, case 283, $\alpha_\infty = 0^\circ$



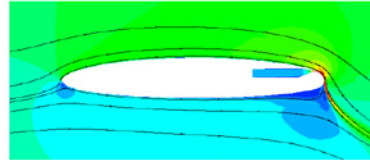
comparison with experiment, case 321, $\alpha_{\infty} = -8^\circ$

surface pressure distribution



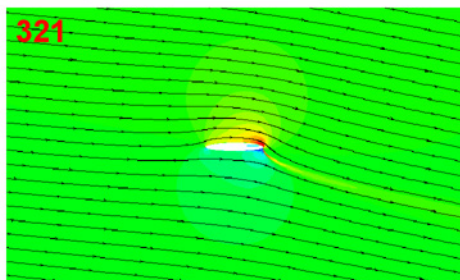
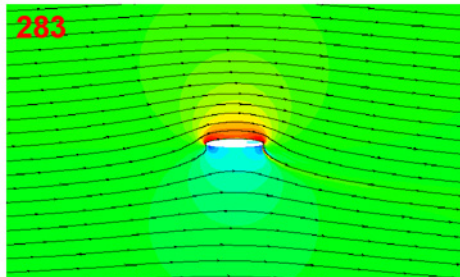
total velocity

1988 $k-\omega$
EASM



comparison cases 283 & 321

total velocity
1988 $k-\omega$
EASM



conclusions

Objective: understand Görtler instability mechanism for Coanda wall jets

3 approaches:

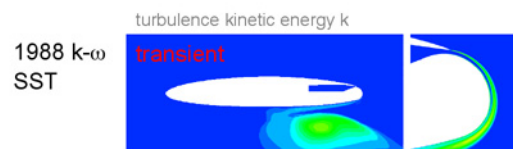
RANS

- for full geometry (2-D and 3-D steady RANS)
- understanding of "vortex merging"

DNS (spatial and temporal)

- interaction of spanwise and streamwise structures
- upstream and local effects
- use of selective forcing to isolate mechanisms

case 283, $\alpha_\infty = 0^\circ$



Some Circulation Control Experiments

D. Cerchie, L. Cullen, J. Goldstein, E. Halfon[‡], G. Han, L. Taubert, L. Trouve[†] & I. Wygnanski
Aerospace Mechanical Engineering, University of Arizona, Tucson, AZ, 85721, USA

[†]L'Ecole Nationale Supérieure de Mécanique et d'Aérotechnique, Poitiers, France

[‡]Faculty of Engineering, Tel Aviv University, Ramat Aviv 69978, Israel

Abstract

In this paper we examine a series of circulation control experiments using different control strategies such as steady blowing, suction and periodic excitation from a narrow slot. The latter is often referred to as Active Flow Control (AFC). The impact of flow control is discussed for the cylinder, a standard airfoil and an elliptic airfoil.

Nomenclature

c	chord length
C_L	lift coefficient: $L / q S$
C_p	pressure coefficient: $(p - p_\infty) / q$
C_μ	steady blowing coefficient: $(2h/c)(U_{\text{Slot}}/U)^2$
$\langle C_\mu \rangle$	oscillatory blowing coefficient: $(h/c)(U_{\text{SlotMax}}/U)^2$
d	reference length, diameter
F^+	non-dimensional frequency: $f d / U$
h	slot height
Re_θ	Reynolds number $U_e \theta / \nu$
U	Free Stream Velocity
U_{Slot}	Slot Velocity
U_{SlotMax}	Maximum Slot Velocity
α	Angle of attack
δ_f	Flap Deflection

1. Introduction

A thin jet being emitted tangentially from a slot milled in a circular cylinder, or other convex, highly curved surface, alters its direction and wraps itself around the surface. A circular cylinder can turn a jet around and alter its direction by more than 180° . The centrifugal force acting on the deflected jet is balanced by the pressure difference between the surface of the cylinder and the ambient fluid. Integrating this pressure results in a force that is approximately equal to twice the jet momentum emitted at the slot (**Figure 1**). Blunting a trailing edge of an airfoil and blowing over its upper surface will deflect the fluid downward changing the “Kutta condition” thus providing powerful means of increasing the usable lift. This is loosely being referred to as super-circulation. One may divert the flow around a blunt trailing edge by using suction, as it was aptly demonstrated by Prandtl⁽¹⁾, but suction (in particular distributed suction) was primarily used for

drag reduction by stabilizing the boundary layer on the upper surface of a wing⁽²⁾.

The integration of propulsion with lift-generation is a long sought dream advocated by many⁽³⁾. The advent of jet propulsion seemed to offer such an opportunity but it became quickly apparent that materials withstanding the heat were too heavy and too costly for aeronautical applications. In most instances, only the compressed air generated prior to combustion by turbo-jet engines was ducted to slots and blown over flaps to augment their lift. A number of aircraft used this form of lift augmentation (e.g. Lockheed F104 Starfighter, Blackburn NA39 Buccaneer, Dassault Etandard IVM).

In the application of blowing, a distinction is made between boundary-layer control and circulation control. The first function of the jet, as it blows over the surface, is to increase the mean kinetic energy of the fluid within the boundary layer so that the latter may advance without separation into a region of rising pressure, e.g., over the upper surface of a highly deflected trailing-edge flap. If the jet momentum is sufficient, the lift coefficient corresponding approximately to the potential flow predictions is obtained. In this régime of boundary-layer control, the lift increment is roughly proportional to the first power of the jet momentum ($\Delta C_L \propto C_\mu$). A further increase of jet momentum augments the lift further, but this augmentation is roughly proportional to the square root of the jet momentum ($\Delta C_L \propto \sqrt{C_\mu}$). This is the régime of super-circulation where the jet departs from the trailing edge with sufficient downward momentum to increase appreciably the circulation around the wing. Poisson-Quinton⁽⁴⁾ is credited for establishing these criteria as well as the critical value of $(C_\mu)_{\text{crit}}$ that empirically determined the momentum required to pass from one flow regime to the other over an airfoil with a deflected flap at arbitrary angle, δ_f . Circulation control may also be obtained by blowing the jet obliquely from the trailing edge of the wing, as it was done on pure “jet-flap” experiments, however there is a substantial gain in lift when the jet is blown over a suitably-designed solid flap⁽⁴⁾.

A number of theoretical methods have been developed for predicting the ΔC_L resulting from super-circulation. Stratford attempted to calculate the lift by assuming that

the “jet-flap” was equivalent to a physical flap⁽⁵⁾. More realistic assumptions were made by Helmbold⁽⁶⁾, Spence⁽⁷⁾, Legendre⁽⁸⁾ and Woods⁽⁹⁾, who replaced the jet by a vortex sheet originating at the trailing edge. Woods used the hodograph method while Spence and Malavard⁽¹⁰⁾ linearized the problem, assuming small incidence and small jet deflection. In all the theoretical models, the mixing of the jet with the ambient flow is neglected. In reality the jet entrains fluid from its surroundings and that entrainment is well represented by placing a suitable distribution of sinks along its path⁽¹¹⁾ (**Figure 2**). When a strong jet flows over a curved flap or the upper surface of an airfoil this sink distribution contributes to circulation⁽¹²⁾ that is also proportional to $C_\mu^{1/2}$. When the jet is emitted from the trailing edge of a bluff body (e.g. a circular or elliptic cylinders), the entrainment that takes place on both sides of the jet contributes to form drag⁽¹¹⁾.

In the present paper an attempt is made to compare the effects of steady blowing, suction or periodic excitation on circulation. This report is of ongoing research whose purpose is to improve our understanding of each technique and to classify the leading parameters that affect the flow, and our ability to control and manipulate it. We shall start by examining the flow over a flapped, symmetrical airfoil. The Kutta condition is fixed and the impact of the increased circulation is easily noticed when compared to the standard airfoil. We shall then examine the flow around the circular cylinder because it is the most widely researched flow even if it is perhaps the most difficult one to control. The Kutta condition is not fixed and the impact of the parameters affecting flow attachment are shown. We shall then proceed to a thick elliptical cylinder that has a maximum of 30% thickness to chord ratio and whose leading and trailing edges are approximated by circles. This geometry is a combination of the previous two in that it has the rounded trailing edge but the upstream pressure gradient set similar to a standard airfoil.

1. Flow Control on a NACA 0015 Airfoil

Most aerodynamic control of lift experiments begin with a standard NACA airfoil and then either progress towards more custom lofting, lift augmentation devices or flow control to achieve not only the desired loads, but a more favorable distribution of the load along the airfoil surface. We will discuss the impact of the total load and distribution of the load for a standard airfoil using both a trailing edge flap and flow control.

Data was collected using a NACA 0015 airfoil with a simple 26% chord flap at $Re < 5 \times 10^5$. A schematic drawing is included in **Figure 3**, showing a cross-section through the airfoil model. Some early

observations carried out by Greenblatt et al⁽¹³⁾ indicate that the flow over a deflected flap at $\delta_f = 20^\circ$ separates around $\alpha = -2^\circ$. Thus even at $\alpha = 0^\circ$ both steady blowing and periodic excitation are beneficial. Consider injection of momentum at $C_\mu = 3\%$ (**Figure 4**). For a flap deflection of $\delta_f = 20^\circ$, both steady blowing and periodic excitation at very low frequency generate a lift increment of $\Delta C_L = 0.5$ relative to the baseline airfoil performance, while periodic excitation at $F^+ = 1.1$ generated an inferior lift increment of only $\Delta C_L = 0.35$. Repeating the same experiment at lower $C_\mu = 1.2\%$ shows slightly less performance for periodic excitation and poorer performance of the steady blowing (see **Figure 5** for $\delta_f = 20^\circ$). At $\delta_f = 35^\circ$ and at the high $C_\mu = 3\%$, both steady blowing and low frequency excitation ($F^+ = 0.3$) peaked out by generating $\Delta C_L = 0.4$ & 0.52 relative to the baseline flapped airfoil respectively. An increase in the flap deflection beyond this angle results in a reduction in the lift increment generated by steady blowing, until at $\delta_f > 50^\circ$ the injection of steady momentum became detrimental to the generation of lift. The efficacy of the low frequency periodic excitation at $C_\mu = 3\%$ did not deteriorate with increasing flap deflection beyond $\delta_f = 35^\circ$, while the excitation at the higher frequency of $F^+ = 1.1$ improved with increasing flap deflection until the two curves crossed over around $\delta_f = 65^\circ$. At the lower level of $C_\mu = 1.2\%$ the increase in flap deflection beyond $\delta_f = 35^\circ$ rendered the steady blowing ineffective but not detrimental while even higher frequency excitation remained effective (**Figure 5**).

The pressure distribution associated with the three modes of flow control at $C_\mu = 3\%$ and $\delta_f = 35^\circ$ is plotted in **figure 6**. The change in the pressure distribution on the upper surface of the trailing edge indicates that the baseline flow was totally separated over the flap. The flow was partially attached by the periodic excitation at $F^+ = 1.1$ and completely attached by the low frequency excitation at $F^+ = 0.3$ and by the steady blowing. The reattachment of the flow over the flap changes the circulation around the airfoil and has a far-reaching effect on the pressure distribution all the way to the leading edge of the airfoil.

It seems reasonable to provide a comparison of various flow control mechanisms providing identical circulation and hence C_L . This approach is of practical interest since a potential designer is required to generate a prescribed lift by various techniques available to him and he should be familiar with the consequences, such as drag, pitching moment, momentum input, etc, associated with generating the required lift.

During the experiments discussed here the flap was deflected to an angle (δ_f) of 20° and 40° with periodic

excitation being applied through a 0.06" slot at the interface of the main element and the flap shoulder. **Figure 7** includes two pairs of angle of attack sweeps, showing the lift coefficient, obtained both with and without AFC (periodic excitation) at the two different flap deflections mentioned before. Some features are immediately apparent in this figure. All of the configurations share the same lift curve slope above $\alpha = 0^\circ$. The deflection of the flap on the model increases the effective camber of the model even if the flow over the flap is separated, causing a shift upward (or to the left) of the C_L versus α curve. At 20° flap deflection, the introduction of AFC at $F^+ = 0.9$, $C_\mu = 2.2\%$, causes the same change in effective circulation as an additional 20° of flap deflection to $\delta_f = 40^\circ$. In fact the curve for $\delta_f = 20^\circ$ with AFC falls on top of the curve for $\delta_f = 40^\circ$ without AFC until stall occurs. With the AFC applied and the flap deflected 20° stall is delayed by 2° beyond the value observed without AFC at either flap deflection but even the $C_{L_{max}}$ is approximately the same for both cases.

When the same AFC is applied to the model with the flap deflected to 40° a maximum lift coefficient of 2.25 is generated at an angle of attack of 10° . At negative angles of attack ($-8^\circ < \alpha < -4^\circ$), the additional lift generated by the application of the AFC is commensurate with that observed at 20° flap deflection, for angles of attack prior to stall. Beyond $\alpha = -4^\circ$ the flow on the upper surface of the highly deflected flap ($\delta_f = 40^\circ$) separates and the remainder of the α sweep falls onto a lower C_L versus α curve. Despite the flow separation on the upper surface, the deflected flap continues to generate enhanced lift and circulation relative to the $\delta_f = 20^\circ$ case, primarily due to the deflection of the flow by the lower surface.

In the discussion that follows, we examine pressure distributions measured on the surface of the airfoil model, which produced three different lift coefficients ($C_L = 1.0, 1.35, 1.5$). These 'sectional' cuts through the (C_L vs. α) curves show different approaches that a designer could select to produce a specific lift and are marked in **Figure 7** to aid the reader. We consider this to be an important technique to evaluate different flow control strategies, rather than simply looking at the relative benefit in performance that the control can provide at a fixed geometric configuration. **Figure 8** shows four pressure distributions, which all generate $C_L = 1.0$. In the absence of any AFC and the flap deflected to 40° , a slight pitch down attitude ($\alpha = -2^\circ$) will generate a small suction peak and mild adverse pressure gradient along the upper surface of the entire main element. The flap is undoubtedly separated and consequently there is a drag penalty associated with this configuration. When the flap is only deflected to 20° the

angle of attack must be increased ($\alpha = 2^\circ$) to generate the same lift, creating a larger suction peak, while separation on the flap is pushed slightly further downstream.

When the appropriate level of AFC is applied while the flap is deflected at $\delta_f = 20^\circ$ the angle of attack can once again be returned to ($\alpha = -2^\circ$), resulting in a more uniform pressure distribution and reduced suction peak. Since α is the same for the two flap deflections as is the circulation, the flow near the leading edge is identical over the upper surface as is the pressure distribution between $0 < x/c < 0.4$ for the two cases considered. At $x/c > 0.5$ and in the absence of AFC, the pressure remains constant over the upper surface of the airfoil and the deflected flap, since it is dominated by the "base pressure" ($C_p \sim -0.7$) of the re-circulating region downstream. On the other hand, when AFC is applied and the flap is only deflected at 20° an acceleration of the flow is noticeable upstream of the slot (i.e. for $0.6 < x/c < 0.74$). The flow over the flap is fully attached with a pressure coefficient at the trailing edge being positive ($C_p \sim 0.25$) suggesting that the flow downstream of the trailing edge continues with its downward momentum generating perhaps a "jet flap" effect. With the flap further deflected to 40° while AFC was being applied, it's possible to heavily load the flap region without causing separation, recovering a $C_p \sim 0$ at the trailing edge. This is achieved while maintaining a favorable pressure gradient over the entire upper surface of the main element, by placing the airfoil at ($\alpha = -8^\circ$). In this case the flow acceleration upstream of the slot is magnified. This behavior would be especially advantageous for laminar flow applications where delay of transition is important. It is easy to identify the upstream influence of the AFC along the upper surface of the main element.

Figure 9 shows the pressure distributions over the model that generated a lift coefficient equal to ($C_L = 1.35$). Focusing first on the two cases that share the same angle of attack and lift ($\alpha = 2^\circ$), ($\delta_f = 20^\circ$, $C_\mu = 2.2\%$ & $\delta_f = 40^\circ$, $C_\mu = 0\%$), indicate that the pressure distributions on both the upper and lower surfaces over the upstream half of the airfoil are almost identical. The case with AFC shows the flow over the flap as attached with a pressure coefficient close to zero at the trailing edge. The heavily deflected flap in the absence of AFC has the same $C_p \sim -0.7$ at the trailing edge as it did at $C_L = 1.0$, indicating that in both cases the re-circulating wake region has approximately the same dimension. It implies that the flow over the flap was completely separated at both angles of incidence and that the additional lift was generated on the main element. Once again the flow is accelerated on the upper surface of the main element, relative to a corresponding case without AFC. This reduces the adverse pressure gradient on the

upper surface making the airfoil less susceptible to stall at this value of C_L . The basic airfoil with the flap deflected at 20° also generates $C_L = 1.35$ at $\alpha = 8^\circ$. Under these conditions the flow is still separated over the flap but the wake is narrow as evidenced by the trailing edge C_p of -0.2 . One may reattach the flow to a deflected flap at 40° through AFC enabling $C_L = 1.35$ at $\alpha = -4^\circ$ due to the increase suction on the aft portion of the main element upstream of the slot (i.e. at $0.4 < x/c < 0.74$). In conclusion, the results described in **Figure 9** are similar to those associated with $C_L = 1$ but with the effect of AFC being accentuated. Therefore not only does the AFC prevent flow separation downstream, thereby increasing the circulation, but it also lowers pressure on the upper surface upstream resulting in an enhanced lift. The prime benefit is in the form-drag reduction that was reduced by a factor of four between $0.5 < C_L < 1$, and increased the performance of the airfoil, (L/D_p) , by the same factor.

The final sectional cut is performed at the maximum lift coefficient ($C_{L_{max}} = 1.5$), obtainable in the un-augmented mildly deflected flap configuration (**Figure 10**). In the absence of AFC the airfoil model must be pitched up to 12° to obtain this amount of lift at the milder flap deflection. This configuration, has a substantial suction peak, obtaining a large maximum negative pressure coefficient ($C_p = -5.3$). A strong adverse pressure gradient develops over the remainder the main element before the flow separates at some point over the flap. When the flap is deflected an additional 20° , the pitch of the airfoil can be reduced to ($\alpha = 4^\circ$) to produce the required lift. In this configuration the airfoil becomes more evenly loaded along the chord, but the flow over the flap is fully separated. In order to obtain this higher level of lift in the absence of AFC, it appears necessary to suffer the drag penalty associated with a large suction peak or a separated flap.

When we examine the two cases with the AFC applied, the angle of attack can be reduced by either 8° or 4° depending on the deflection of the flap needed to produce the same lift coefficient. For the lower flap deflection case, the suction peak is reduced by approximately 40% and the flow over the flap is fully attached with a trailing edge pressure coefficient close to that of the free stream. At the higher flap deflection, the suction peak is further attenuated when sufficient lift is generated at zero angle of attack. Although the flow over flap is no longer attached, the upstream effect of the AFC is strong enough to load the main element sufficiently to generate the necessary lift. This behavior is not unique to this airfoil, in the following section we will show the same mechanism at play on the upper surface of a more generic lifting body, with suction applied to generate enhanced lift.

One can conclude from the data presented that AFC contributes through three distinct mechanisms to airfoil performance. First, though a boundary-layer control mechanism, by preventing separation on a deflected flap. The same mechanism was investigated by Nishri & Wygnanski⁽¹⁴⁾ and Darabi & Wygnanski⁽¹⁵⁾. Second, by enhancing circulation in much the same manner that a jet flap increases lift by producing a virtual fluid flap extension to an existing flap or airfoil main element. The final mechanism is the one identified in the pressure distributions we have presented, namely an acceleration of the flow and a lowering of the static pressure along the upper surface of the airfoil, upstream from the location at which the control is applied. Lachmann⁽²⁾ identified the first two mechanisms using steady blowing. The final mechanism, while almost certainly present in those cases, appears to be more prominent when oscillatory zero net mass active flow control is used.

2. The Flow around a Circular Cylinder

In the absence of an external stream the wall jet wraps itself around a convex surface such as a circular cylinder following its surface up to and sometimes beyond $\frac{1}{2}$ of its circumference (**Figure 1**). In the example shown a jet of momentum J , emanating to the right from a slot located on top of the cylinder turns around it before separating to the left from its lower surface. The change in the direction of the flow generates a low-pressure region on the right hand surface that when integrated yields a side force whose magnitude is almost equal to twice the jet momentum. This force multiplier makes some applications of wall jets over curved surfaces very attractive arousing interest in improving the understanding of this flow. One of the unique characteristics of the curved wall jet is its phenomenal rate of spread and its high turbulence level that are attributed to the streamwise vortices generated by a centrifugal instability⁽¹⁶⁾. The cylinder over which these measurements were made was carefully designed with the jet emerging tangentially to the surface after passing through a smooth contraction. This jet characteristic is a consequence of an instability. Therefore, it is important to know how sensitive this flow is to the detailed jet characteristics leaving the nozzle, and to the width of the jet relative to the radius of the cylinder. Two additional cylinders were constructed that were more suitable to wind tunnel tests in which an external stream of variable velocity could be added. One of the cylinders (Number 2 in **Figure 11**) was machined from two parts and has a continuous nozzle. The figure shows that the nozzle design is an important part of the external flow characteristics. The best tangential flow design, Number 1, maintained

attached flow at least 40° further around the cylinder than the other two slot designs. Number 3, which had the slot cut through a cylinder demonstrated the worst performance.

Figure 12 compares the three flow control approaches over the cylinder. The slot location was rotated from the leading edge to the trailing edge and data plotted was for the best performance location. The data is presented similar to airfoil data in % chord rather than degrees around the cylinder. The two blowing cases illustrate a standard observation, the stronger the blowing the further into the adverse pressure region the flow can be applied for maximum performance. Notice also that the suction and oscillatory (AFC) flow control have nearly the same pressure distribution, while the AFC magnitude is only one-third the suction magnitude.

The effect of the input AFC frequency is shown in **Figure 13**. With the slot at 110° from the leading edge and the $C_\mu = 0.04$, the performance increased with increasing frequency in the test range of 100 to 200 Hz. The cylinder demonstrated the same linearity in performance to input blowing magnitude as shown in **Figure 14**. The sensitivity to slot location shows that the performance drops rapidly if the slot location is too far downstream (**Figure 15**).

Figure 16 is data from the symmetric dual slot cylinder. The pressure distribution appears to be insensitive to blowing magnitude. **Figure 17** provides the wake profiles for these conditions on the dual slot. If the blowing magnitude is taken to be totally downstream, then an efficiency can be calculated. It shows that the $C_\mu = 0.46$ produces a 14% reduction in drag for the entire system. The larger blowing condition, $C_\mu = 1.02$, produced a lower drag at the expense of C_μ . Therefore, it actually increased the system drag when the momentum required to produce the drag reduction is included.

3. The Flow around an Elliptical Airfoil

The final section represents an aerodynamic body that has the characteristics of both the previous two sections. **Figure 18** is the modified 30% ellipse with both leading and trailing edge cylinders that have adjustable slot widths and exhaust angles. The ellipse develops a pressure distribution similar to an airfoil with angle of attack. However, it has the adjustable circulation characteristics of the cylinder when flow control is introduced.

Steady suction, steady blowing and oscillatory flow control has been tested using the model. **Figure 19** presents the effectiveness of the three flow control types

at zero angle of attack. The slot location was varied around the trailing edge of the model to yield the presented data. The three flow types were run at a blowing coefficient of 1.9%. The oscillatory flow produced the best lift results, followed by suction and then blowing. It was typical of the data to reflect the trend shown between the blowing and suction data as effectiveness was increased. The angle where the flow provided the best lift moved towards the trailing edge. This was also true when the blowing coefficient was increased for a particular type of flow control.

Figure 20 shows the difference in the pressure distributions for the three control types at lift coefficient near 0.44. The pressure distribution over the elliptical body is nearly constant for the three cases from 15%c to 85%c. The real difference is at both the leading and trailing edges.

The AFC, or oscillatory flow control data represent the time averaged pressure data. The data was gathered at 600 Hz and 700 samples for each static port were used. Based on the number of static ports on the model the typical data runs was just over a minute in duration.

The AFC and steady suction produced the same characteristics at the leading when the control was applied at the trailing edge. The AFC and blowing looked similar at the trailing edge. The pressure peak associated with the slot flow was not present at the trailing for the suction case, as would be expected. The slot exhaust angle was 25 degrees from parallel to the local loft and directed down stream.

The effect on increasing the AFC blowing coefficient is shown in **Figure 21**. The AFC “off” condition is also plotted for reference. This AFC off baseline pressure distribution agrees well with the CFD results generated by A. Hassan from The Boeing Company using CFL3D. The three AFC magnitudes increased the lift by increase the velocity along the entire upper surface of the ellipse. The lower surface velocity is slightly reduced with AFC compared to the change on the upper surface. The other interesting characteristic to note is the AFC effect on the trailing edge.

Figure 22 is a closer look at the trailing edge region for these various AFC magnitudes. The baseline condition shows symmetrically separated flow on the upper and lower surface from around 97%c to the trailing edge. Once AFC is applied, there is a large time-averaged increase in the velocity on the upper surface very near the leading edge. The separation region shifts to an asymmetric region from the trailing edge to around 95%c on the lower surface. This region stays constant as AFC is increased further. However, the upper surface becomes more energized until the large velocity

increase is present all the way from the slot to the trailing edge.

Figure 23 presents the effectiveness of the AFC forcing at the trailing edge as a function of angle of attack. The tunnel speed was slightly lower for this data relative to the other data presented. The data shows a nearly constant benefit of the AFC control until near stall angles. The effectiveness increases for the higher blowing cases causing even an increased peak for the highest condition. The reason for this is under investigation but may provide some insight on better effectiveness for different configurations.

Angle of attack sweeps were performed with steady suction applied at the trailing edge (**Figure 24**). Rather than increasing the blowing coefficient, the slot angle was varied for these sweeps. The intent was to see how the data on **Figure 19** at zero angle of attack would present itself during an angle of attack sweep.

The initial run was with the slot angle at 120° , or 5° from the peak performance point on **Figure 19**. The lift benefit from steady suction was nearly constant until it dropped rapidly at 4 degrees angle of attack. The slot angle was then reduced by 10° , but the maximum lift angle of attack only increased by 3 degrees. Another 10° -degree reduction only increased the maximum lift point by one-degree angle of attack. From this data it is clear that the zero angle of attack data provides some very good insight to the optimum performance point. It also shows that the upstream pressure gradient associated with angle of attack has a very big influence on the maximum performance.

The same test was repeated for a larger slot angle and larger suction coefficient (**Figure 25**). The same trends seen at the smaller slot were recorded. The larger suction coefficient produced larger maximum lift points. However, the peak angle of attack was not directly proportional to the change in the suction slot location. **Figure 26** shows the effect of steady suction at zero angle of attack. The lower surface velocity is decreased slightly and almost at the same increment along the entire lower surface. The majority of the effect, similar to the AFC data shown in **Figure 21** is on the upper surface. The increase in velocity is constant near the leading edge, but increased even more near the trailing edge. The change in the trailing edge static pressure is very evident on this plot.

The steady suction effect on the pressure distribution at 4 degrees angle of attack is shown on **Figure 27**. Again, most of the impact is seen on the upper surface and there is an increase as the trailing edge is approached.

Figure 28 illustrates the real power of flow control, the ability to generate lift and dictate the pressure distribution. The plot shows two cases at a lift coefficient of 0.8. The suction off case is at 10 degrees angle of attack and has the typical large pressure rise at the leading edge and the strong adverse pressure gradient just down stream that will eventually lead to stall. The suction “on” case is only at 4° angle of attack and the lift is more evenly distributed along the span of the airfoil. The trailing edge also indicates that the suction condition generates a lower drag, or higher L/D.

AFC testing at the trailing edge was then conducted for a variety of slot angles, excitation frequencies and amplitudes. **Figure 29** shows the data plotted against the blowing coefficient. The data did not collapse to a single curve so data reduction methods were used to determine a new parameter for AFC trailing edge data.

Figure 30 is the result of that data reduction. This set of data appears collapse as a function of blowing coefficient and the square root of the non-dimensional excitation frequency and the trailing edge angle. The length scale for both the frequency and trailing edge angle terms was the length from the slot to the theoretical trailing edge of the ellipse.

4. Concluding Remarks **Acknowledgments**

The flow control testing of the three aerodynamic bodies has provided some additional insight to the benefits of flow control and aided our ability to manipulate the flow. A designer could use flow control to tailor the pressure distribution over the surface in a similar fashion to lofting or passive devices.

Flow control to obtain high lift conditions resulted in pressure distributions that would be more beneficial for high-speed penetration without encountering shocks and low drag relative to the use of a traditional trailing edge flap.

The cylinder data demonstrated the importance of a good slot design as well as the increased efficiency of oscillatory flow control relative to either steady blowing or suction.

The ellipse data showed many of the same features as the cylinder data with the added variable in the upstream pressure gradient. The trailing edge performance became less predictable as the pressure gradient along the forward section of the airfoil was increased. A new parameter was introduced to scale these results and make a rational comparison with other geometries that are creating trailing edge circulation.

We would like to thank Ahmed Hassan from The Boeing Company in Mesa, Arizona for the CFD results using CFL3D for the ellipse.

References

1. Prandtl, L. *Journal of the Royal Aeronautical Society*, Vol. 31, p. 735, 1927.
2. Lachmann, G.V.(editor), *Boundary layer and flow control Its Principles and application*. Pergamon Press, New York, 1961.
3. Goldschmied, F.R., Integrated Hull Design, Boundary Layer Control and Propulsion of Submerged Bodies. *J. Hydronautics* Vol.1, p.2, 1967
4. Ph. Poisson-Quinton Recherches Theoriques et Experimentales sur le controle de couche limits *VII International Congress of Applied Mechanics, London 1948*
5. Stratford, B.S. Early Thoughts on the Jet Flap. *Aeronautical Quarterly*, Vol. VII, p. 45, February 1956.
6. Helmbold, H.B. The Lift of a Blowing Wing in a Parallel Stream. *Journal of the Aeronautical Sciences*, Vol. 22, p. 341, 1955.
7. Spence, D.A. The Lift Coefficient of a Jet-Flapped Wing. *Proc. Roy. Soc. A* Vol. 238, p.46, 1956
8. Legendre, R. Influence de l'Emission d'un Jet au bord de Fuite d'un Profil sur l'Ecoulement autour de ce Profil. *Comptes Rendus, Académie des Sciences, Paris*, 1956.
9. Woods, L.C. Some Contributions to Jet-Flap Theory and to the Theory of Source Flow from Aerofoils. A.R.C. Current Paper 388, 1958
10. Malavard, L. Sur une Théorie Lineaire du Soufflage au bord de Fuite d'un Profil d'Aile. *Comptes Rendus, Académie des Sciences, Paris*, 1956.
11. Wygnanski, I., "The Effect of Jet Entrainment on Loss of Thrust on a Two-Dimensional Jet-Flap Aerofoil," *Aeronautical Quarterly* **17**, 31-51, 1966.
12. Wygnanski, I. & Newman, B. G. The effect of jet entrainment on lift and moment for a thin airfoil with blowing. *Aeronautical Quarterly*, Vol. XV, p.122, 1964.
13. Greenblatt, D. & Wygnanski, I. 2001 The control of flow separation by periodic excitation. *Progress in Aerospace Sciences* **36**, pp. 487-545.
14. Nishri B. & Wygnanski I. (1998) Effects of periodic excitation on turbulent flow separation from a flap. *AIAA Journal* **38** 4.
15. Darabi A. and Wygnanski, I, Active management of naturally separated flow over a solid surface, Part II: The separation process, *J. of Fluid Mech.* (2004).
16. Neuendorf, R., Lourenco, L., and Wygnanski, I., On large Streamwise structures in a wall jet flowing over a circular cylinder, *Physics of Fluids* **16**(6) 2004.

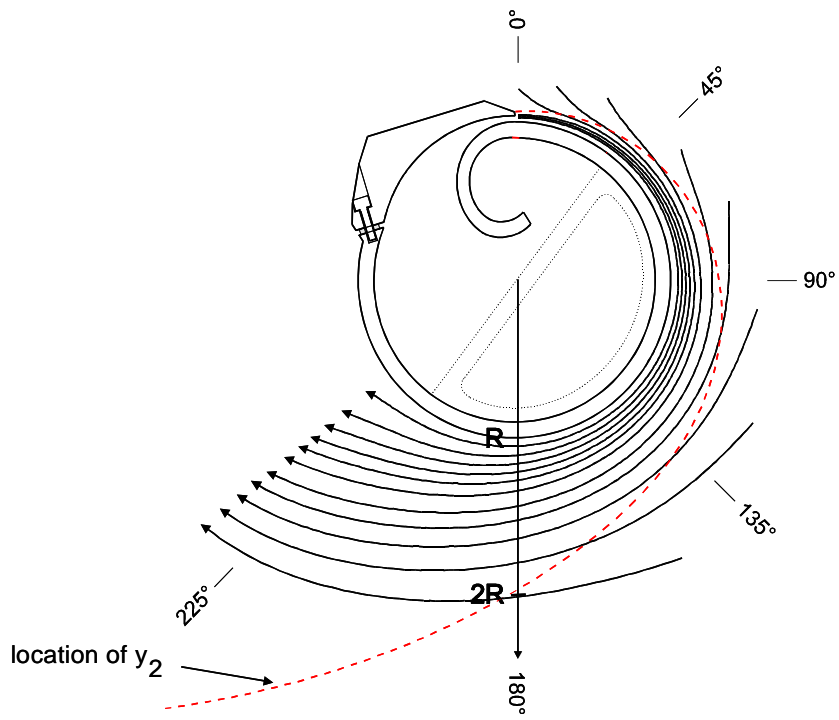
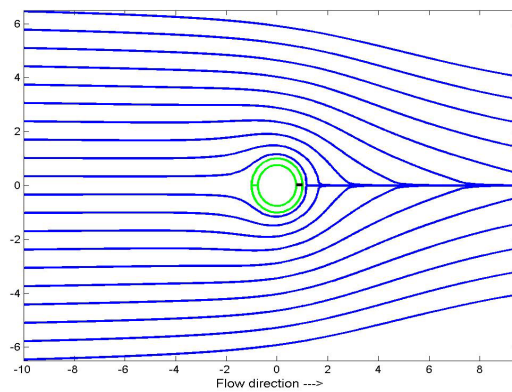
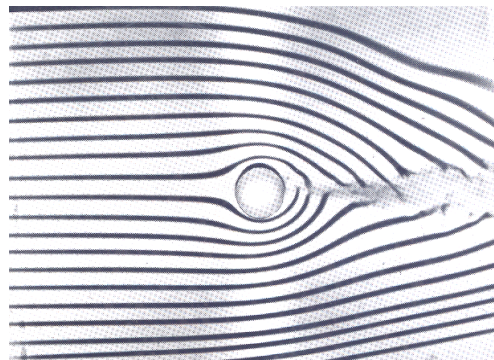


Figure 1 Slot Flow Around a Cylinder



$C\mu = 0.24$
Calculated using row of
sinks



$C\mu = 0.37$
Picture Ref()

Figure 2 Analytic and Real Stream lines around a Cylinder

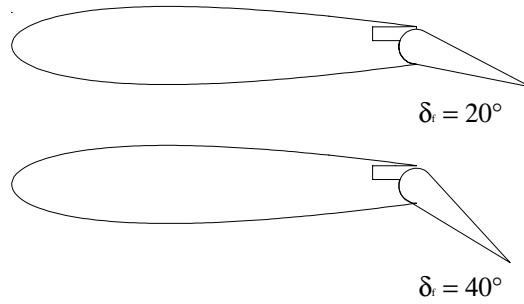


Figure 3 The NACA 0015 model with 26% simple flap

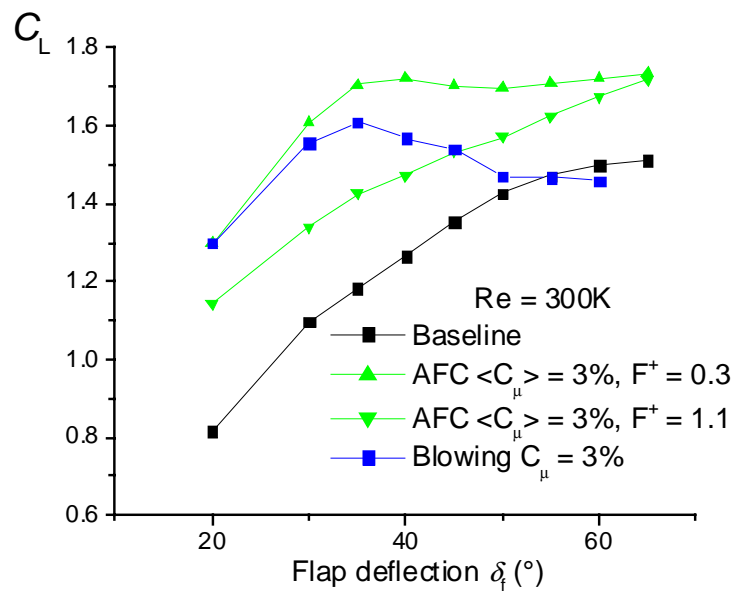


Figure 4 High flap deflection flow control using NACA 0015 with 26% chord simple flap

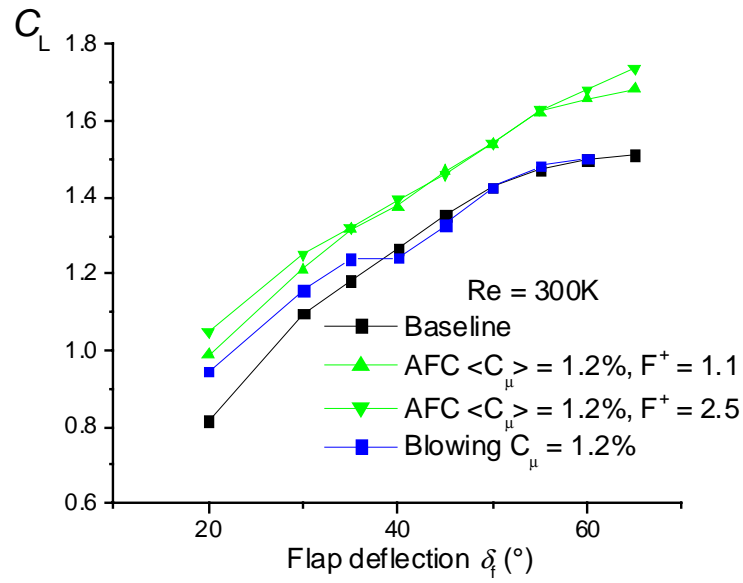


Figure 5 High flap deflection flow control using NACA 0015 with 26% chord simple flap

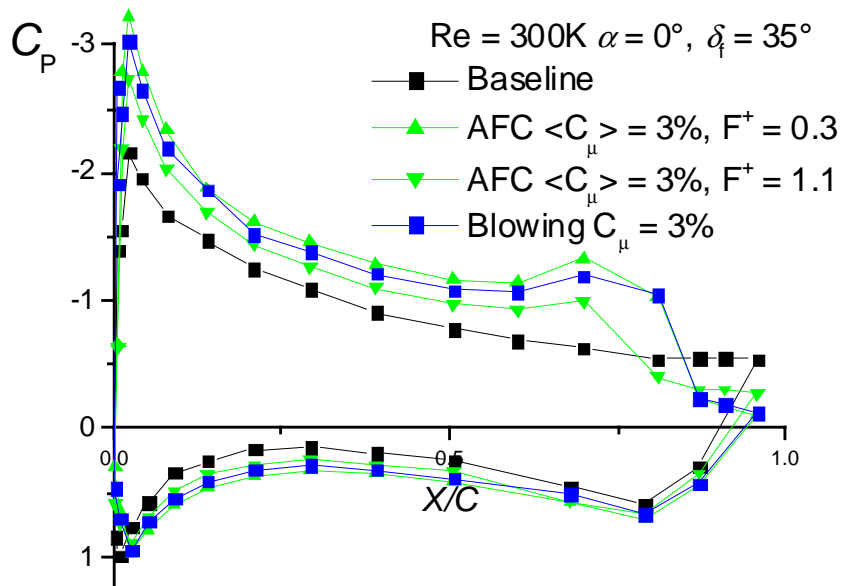


Figure 6 Pressure distribution over NACA 0015 with 26% chord simple flap

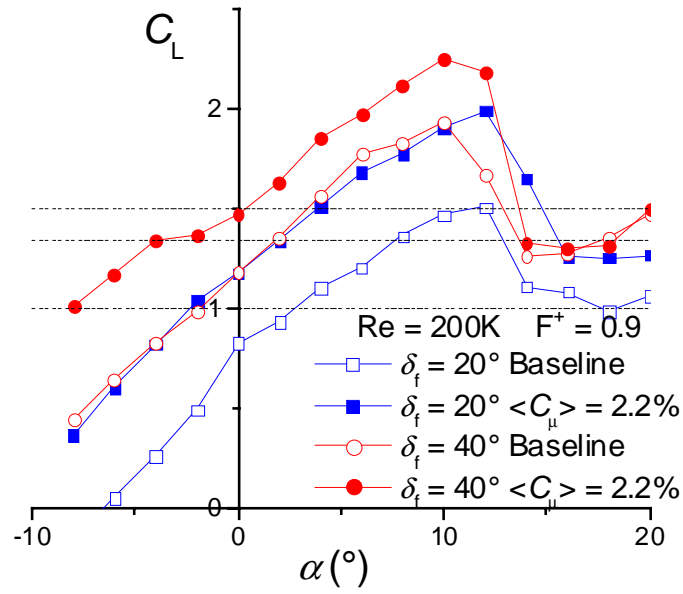


Figure 7 NACA 0015 airfoil performance with AFC

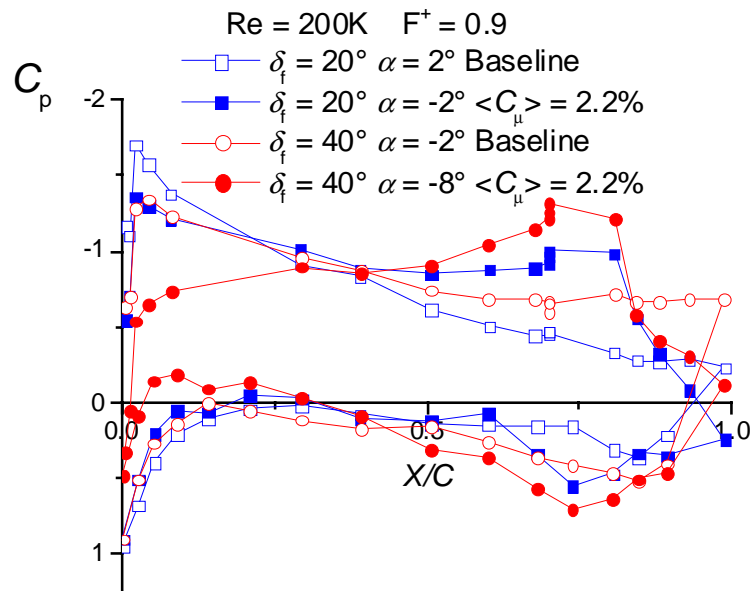


Figure 8 Pressure distribution that develop $C_L = 1.0$ for NACA 0015

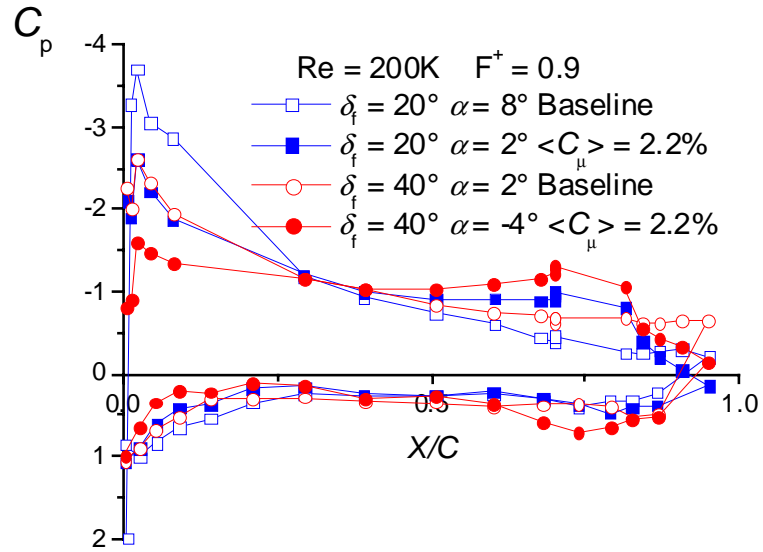


Figure 9 Pressure distributions that develop $C_L = 1.35$ for NACA 0015

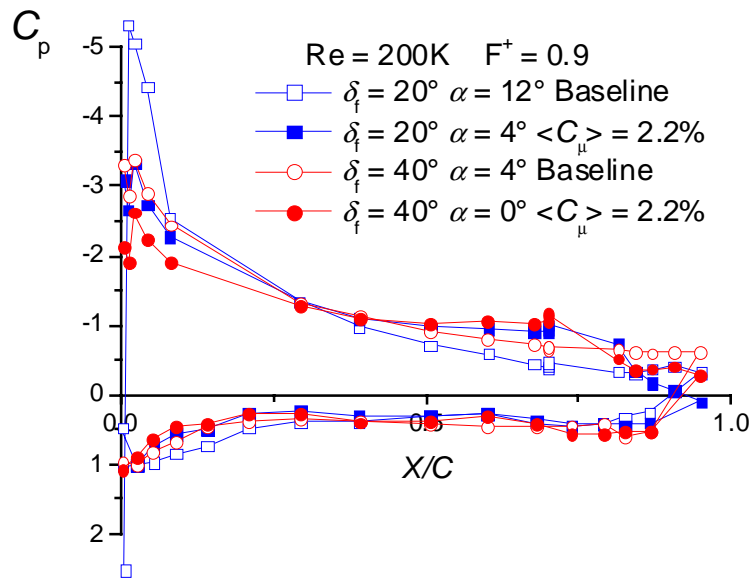


Figure 10 Pressure distributions that develop $C_L = 1.5$ for NACA 0015

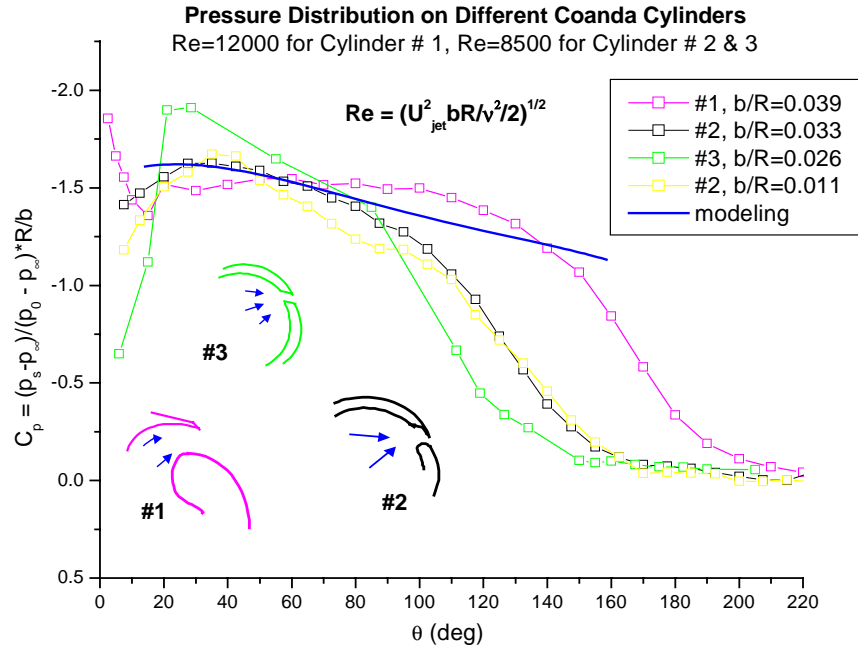


Figure 11 Pressure Distributions on a Cylinder in Distance from the Slot Location

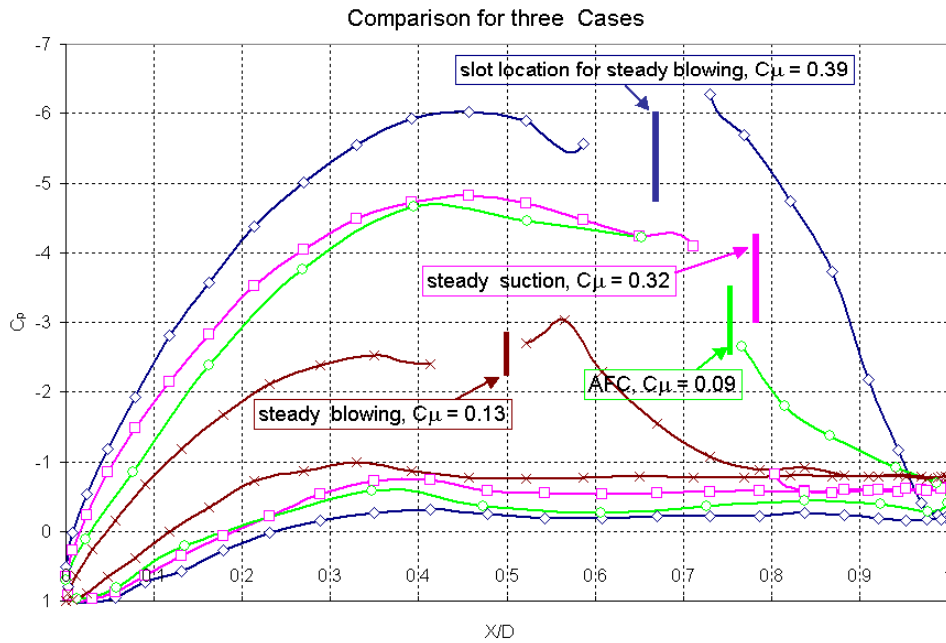
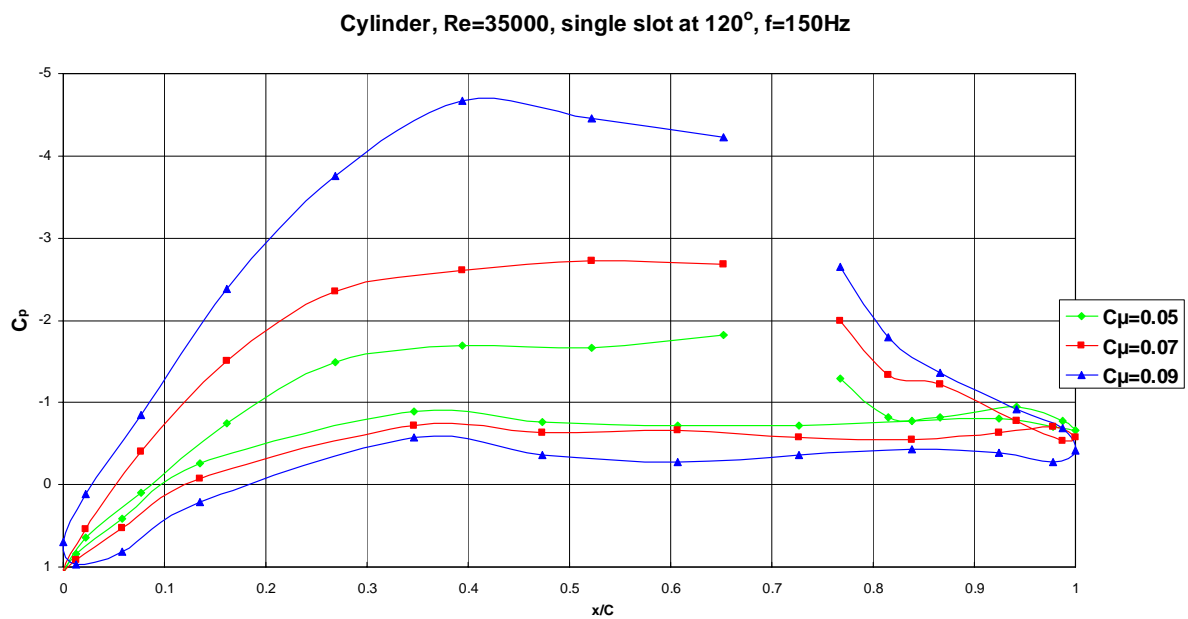
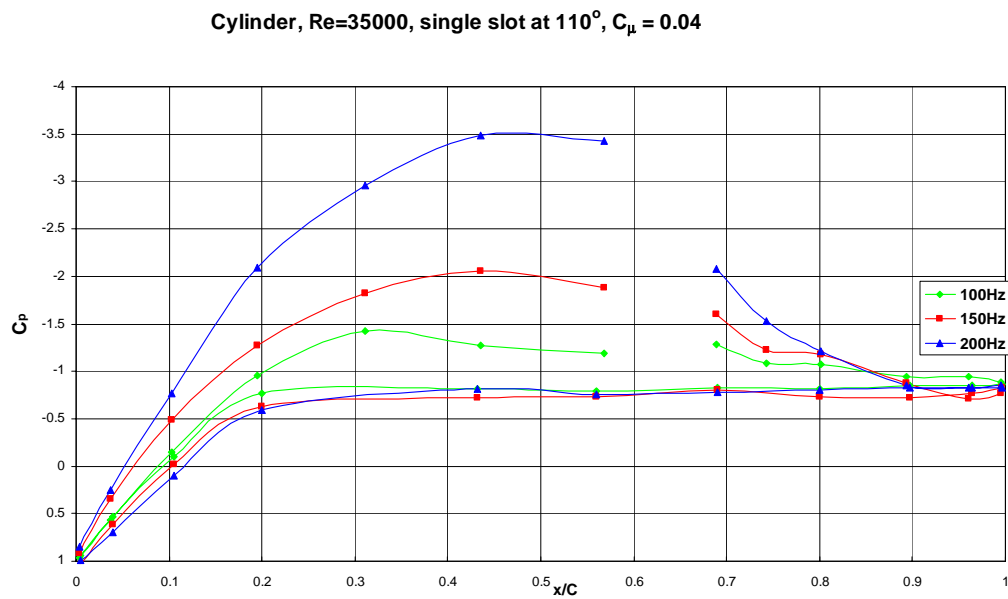


Figure 12 Pressure Distributions on a Cylinder for Three Different Flow Control Approaches



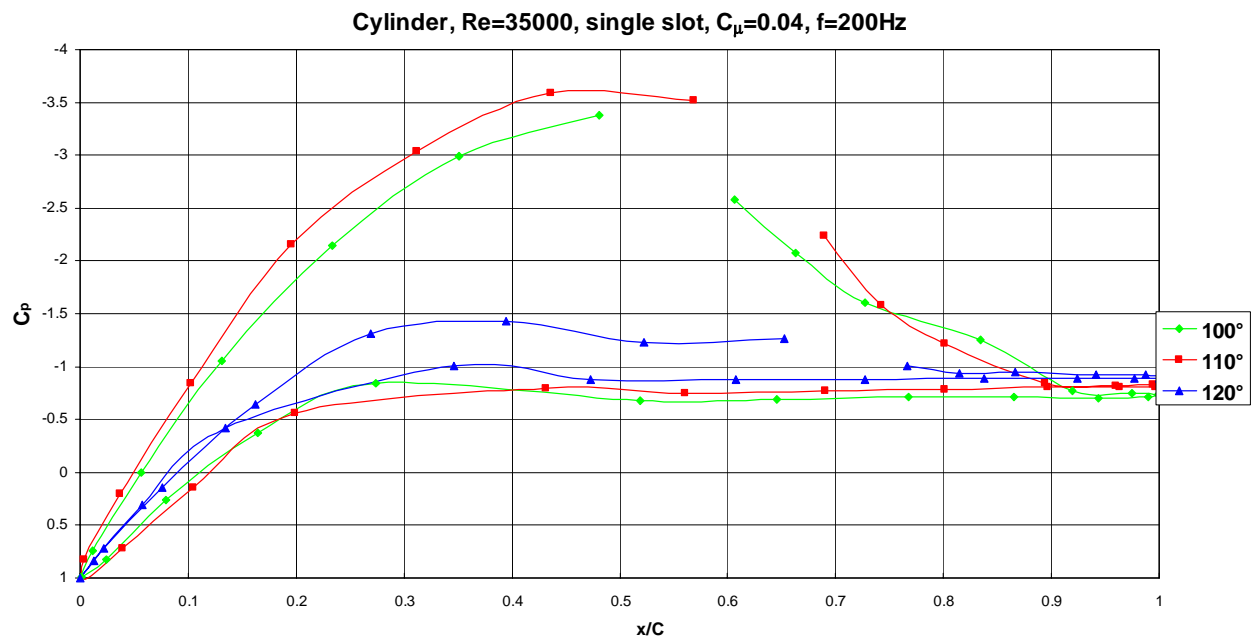


Figure 15 Pressure Distributions on a Cylinder for Different Slot Locations

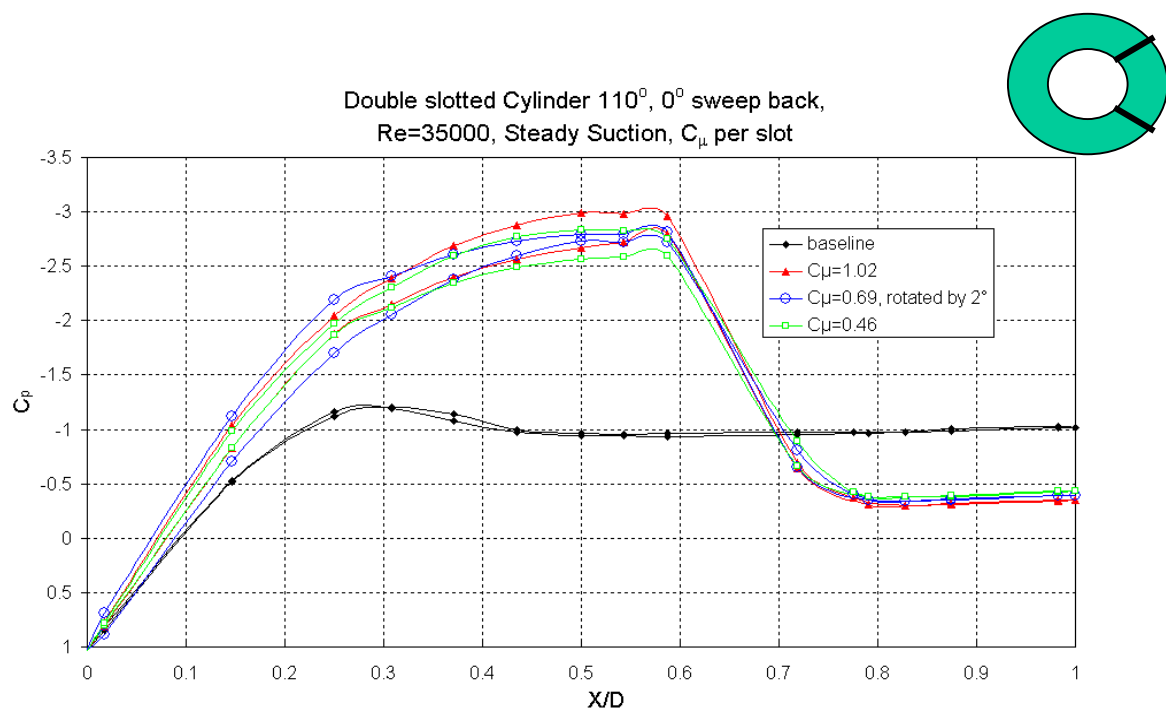


Figure 16 Pressure Distributions on a Dual Slot Cylinder for Different AFC Input Magnitudes

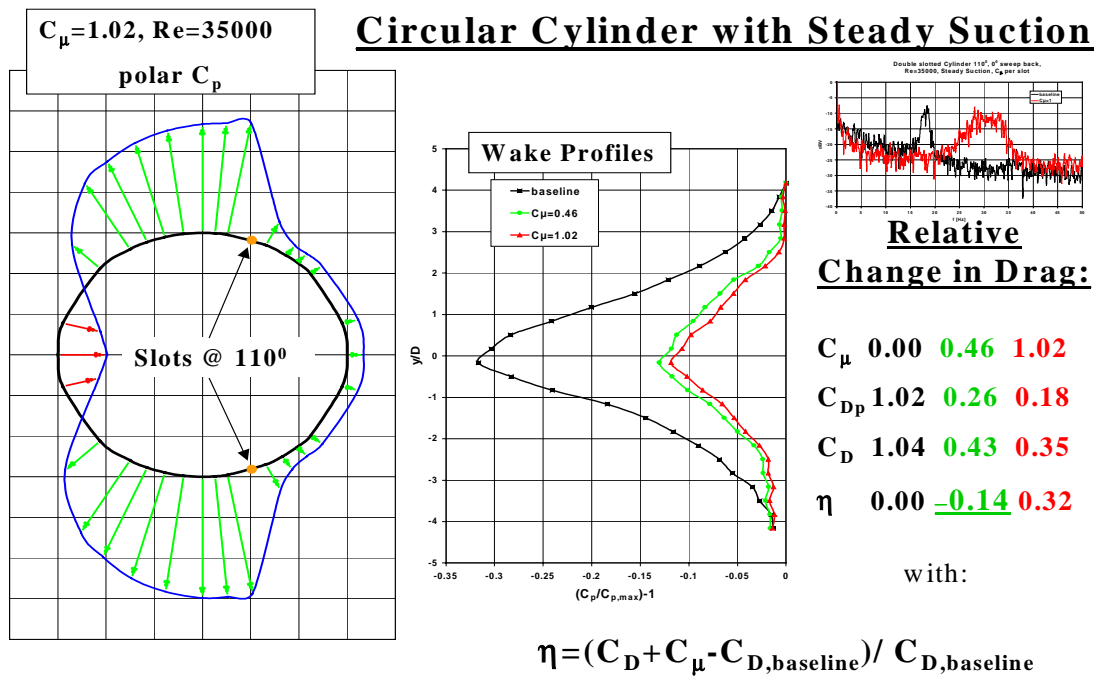


Figure 17 Pressure Distributions and Wake Profiles on a Dual Slot Cylinder

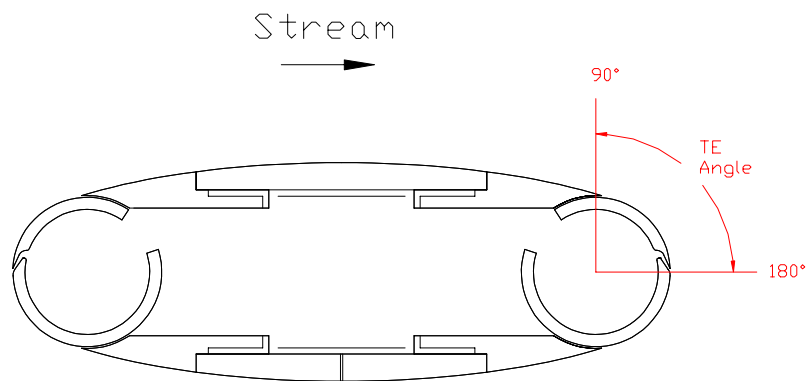


Figure 18 Cross-sectional drawing of the UA modified 30% thickness ellipse model

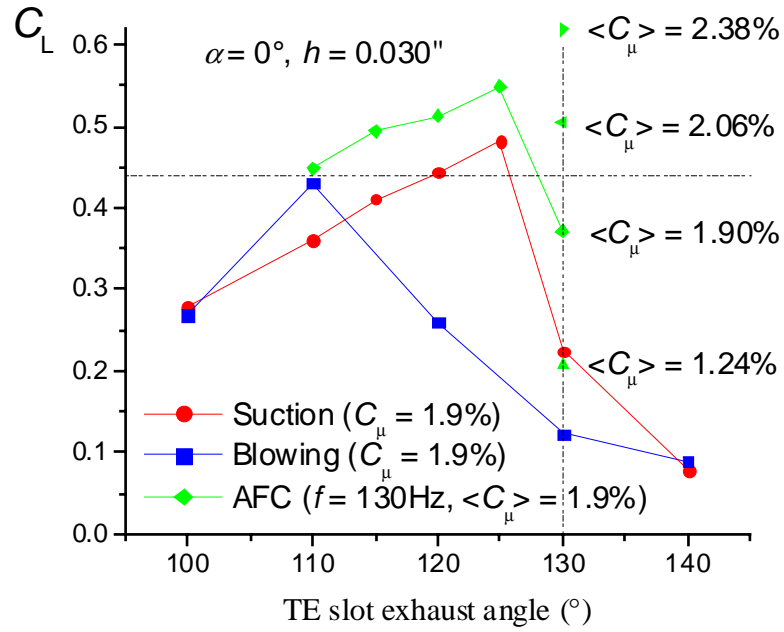


Figure 19 Comparison between three different types of flow control 30% thickness ellipse

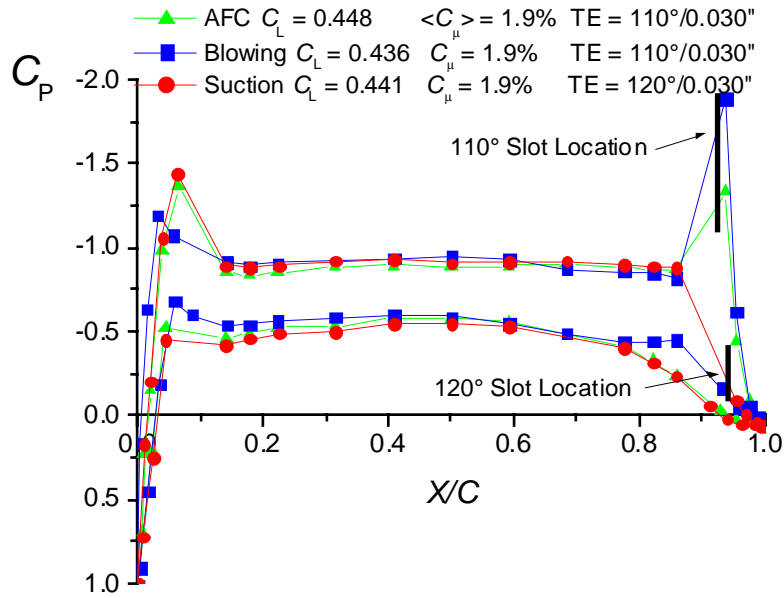


Figure 20 Comparison between different flow control techniques at constant C_L 30% thickness ellipse

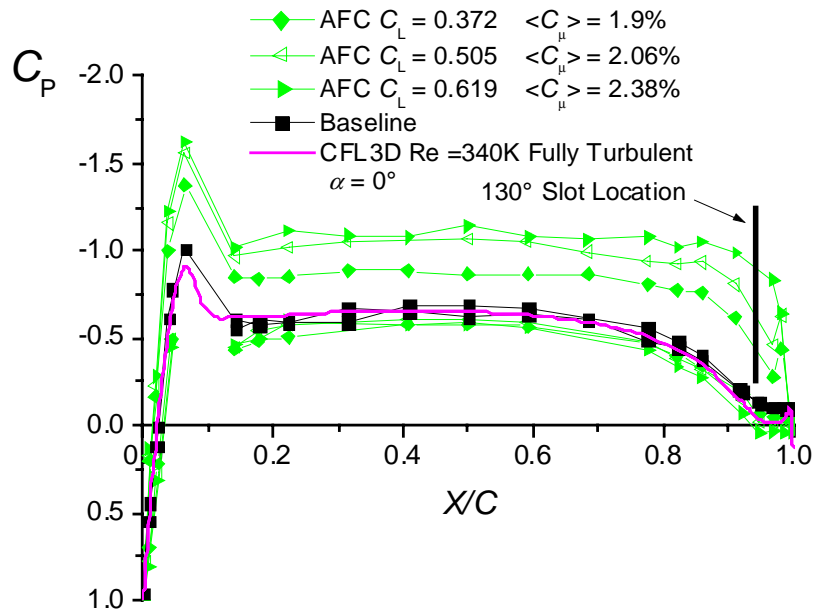


Figure 21 Super-circulation on 30% thickness ellipse using AFC (CFD courtesy of A. Hassan Boeing)

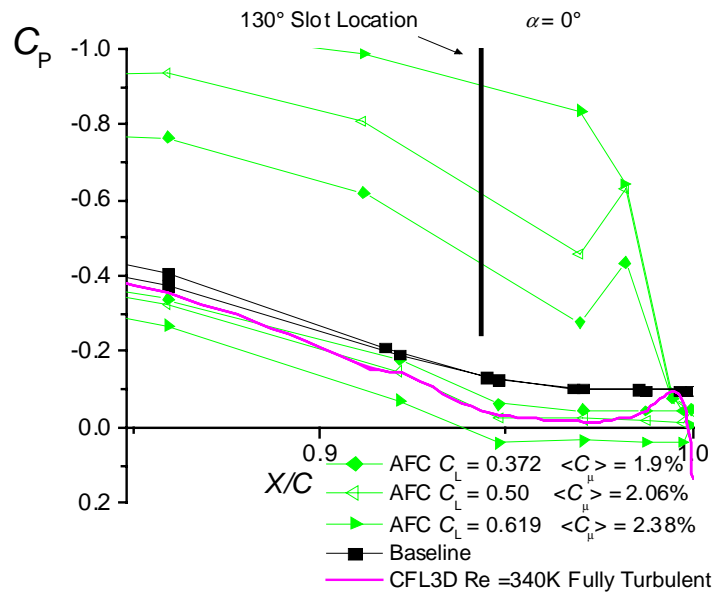


Figure 22 Zoom into TE region of Figure 11

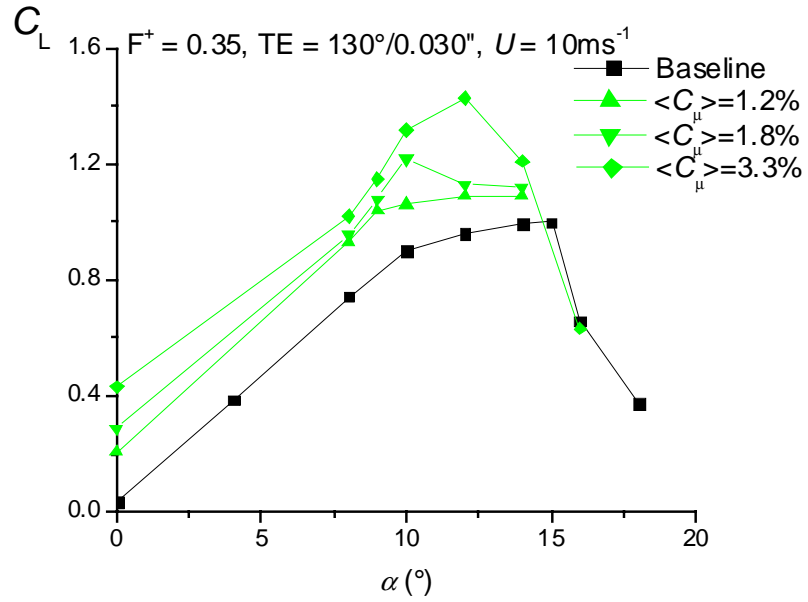


Figure 23 Angle of attack sweep using AFC on 30% thickness ellipse $U = 10\text{ms}^{-1}$

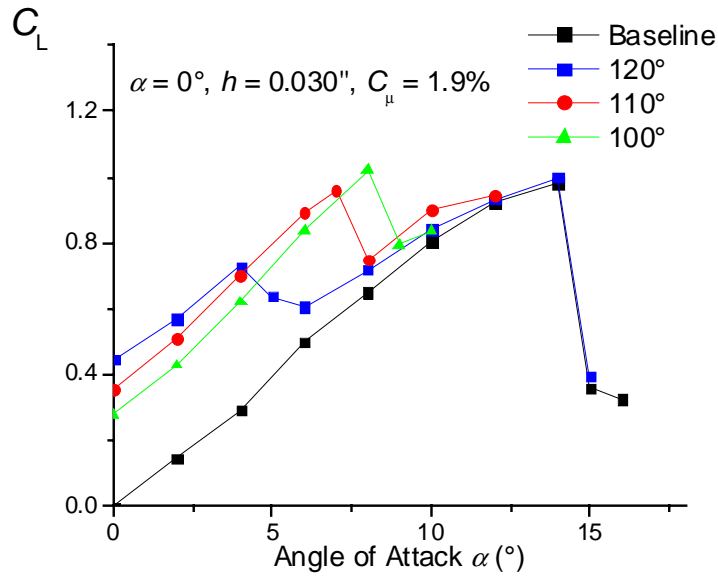


Figure 24 Suction on 30% Ellipse $C_\mu = 1.9\%$ and $0.030''$ slot

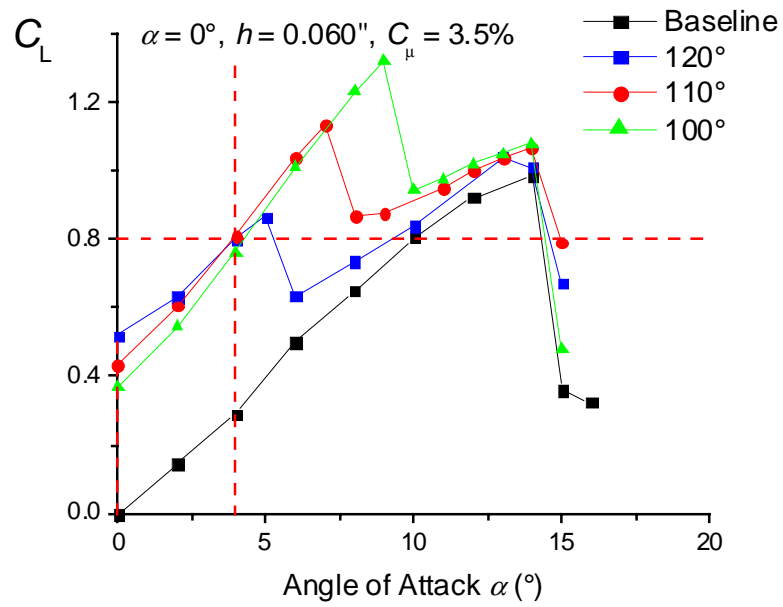


Figure 25 Suction on 30% Ellipse with $C_\mu = 3.5\%$ and 0.060" slot

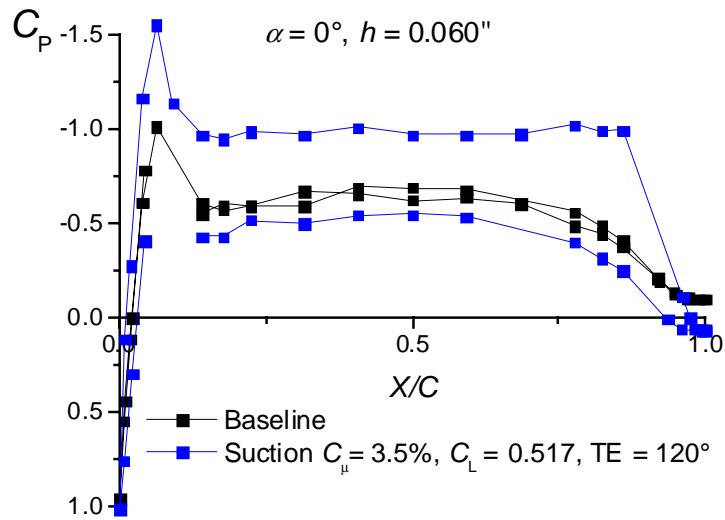


Figure 26 Super-circulation on the 30% Ellipse

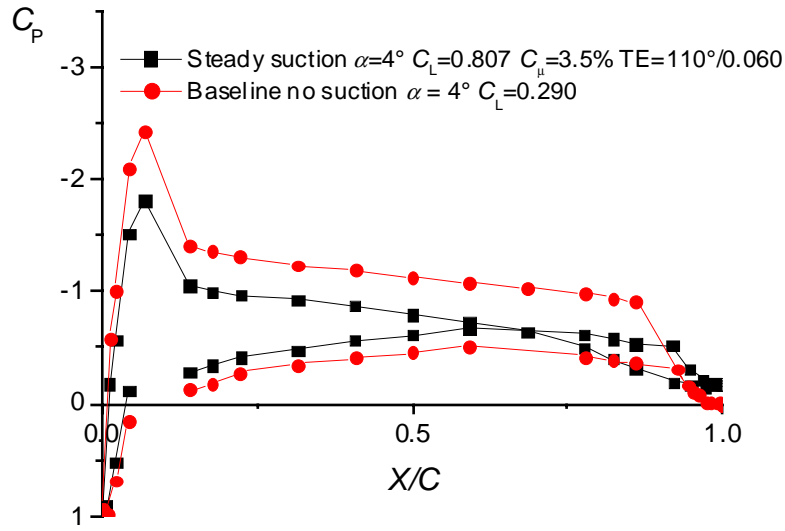


Figure 27 Pressure distribution over 30% thickness ellipse with suction

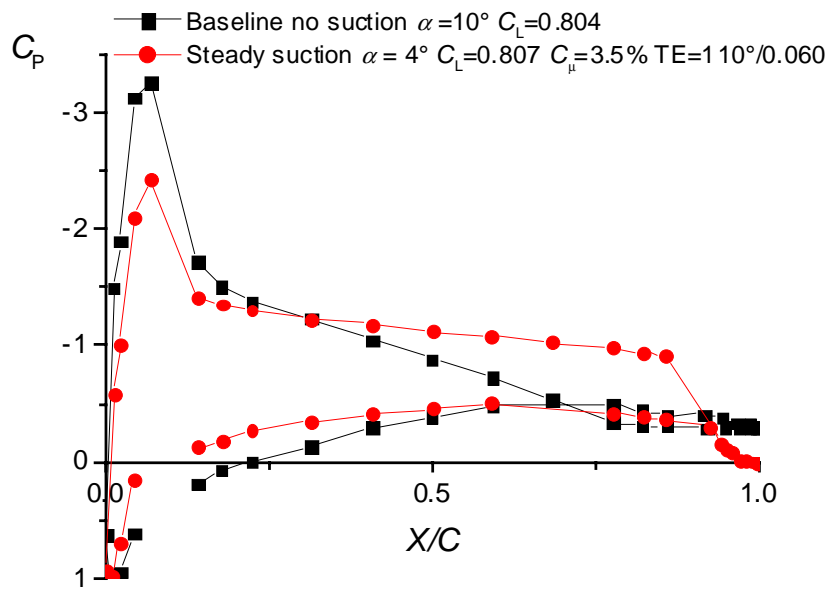


Figure 28 Pressure distribution over 30% ellipse with suction $C_L = 0.8$

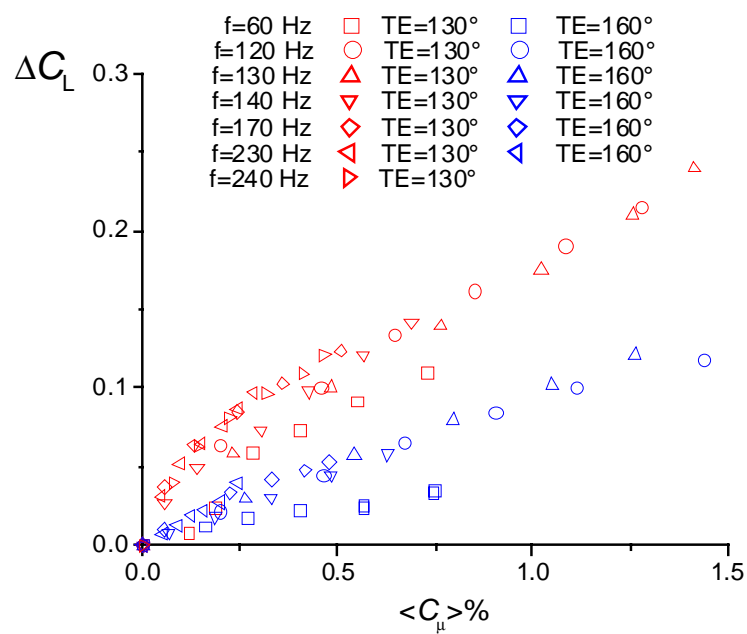


Figure 29 Scatter in data when C_μ used as parameter

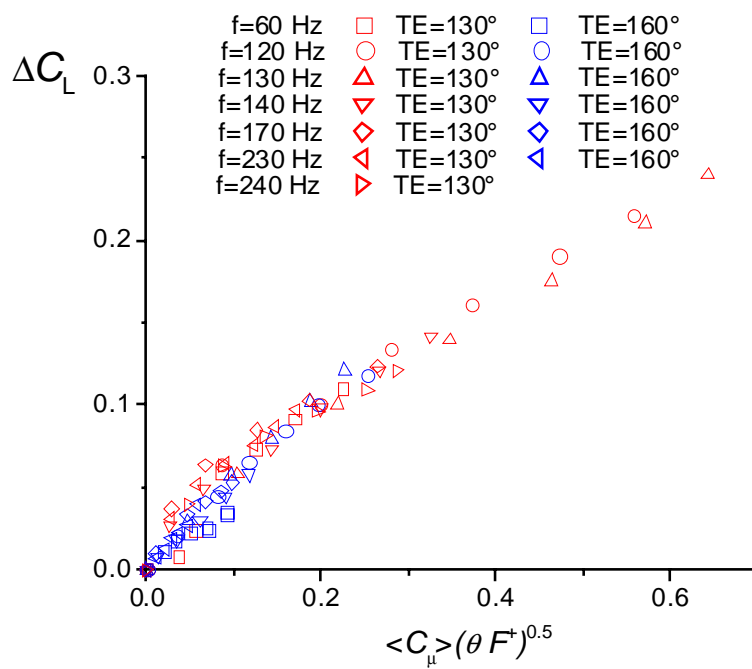


Figure 30 New empirically derived flow control parameter on 30% thickness ellipse TE AFC



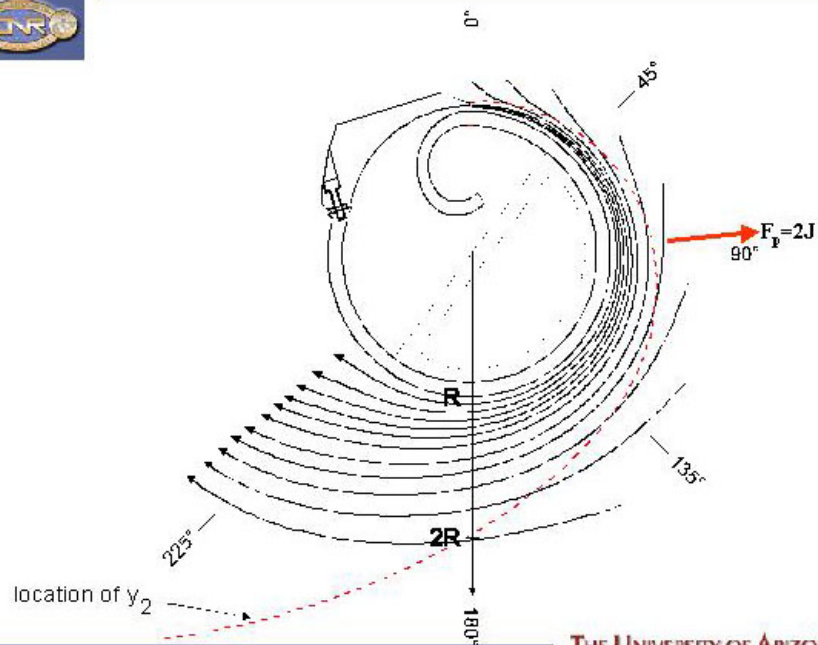
Some Circulation Control Experiments

D. Cerchie, L. Cullen, J. Goldstein, E. Halfon,
G. Han, L. Taubert, L. Trouve & I. Wygnanski

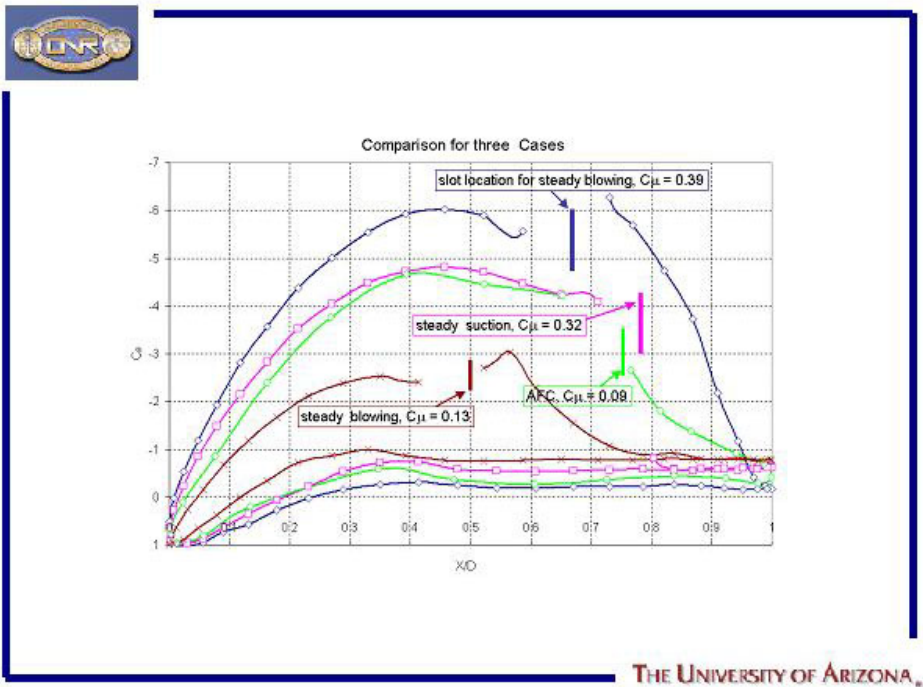
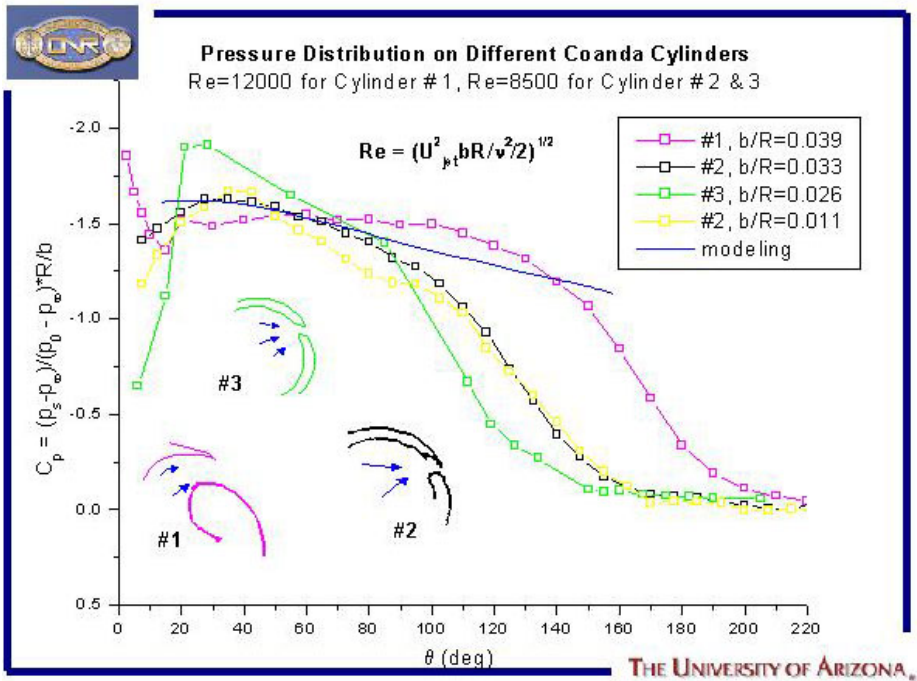
2004 Circulation Control Workshop

Hampton, Virginia
March 16, 2004

THE UNIVERSITY OF ARIZONA

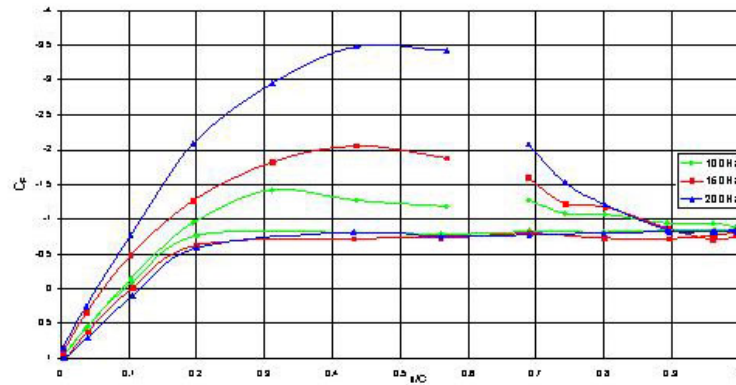


THE UNIVERSITY OF ARIZONA





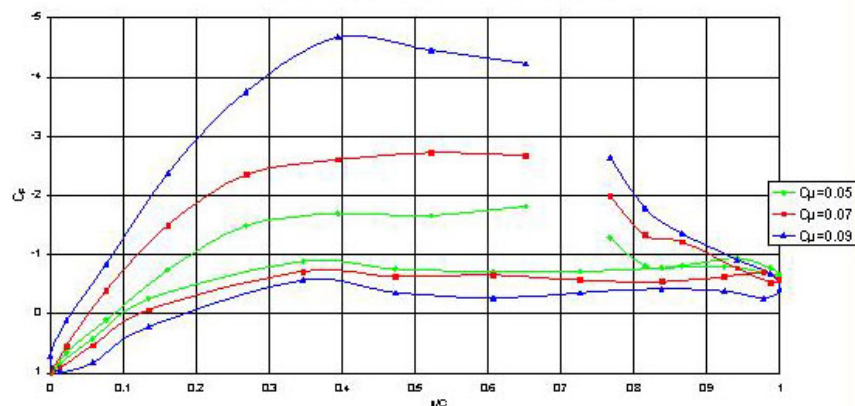
Cylinder, $Re=35000$, single slot at 110° , $C_\mu=0.04$



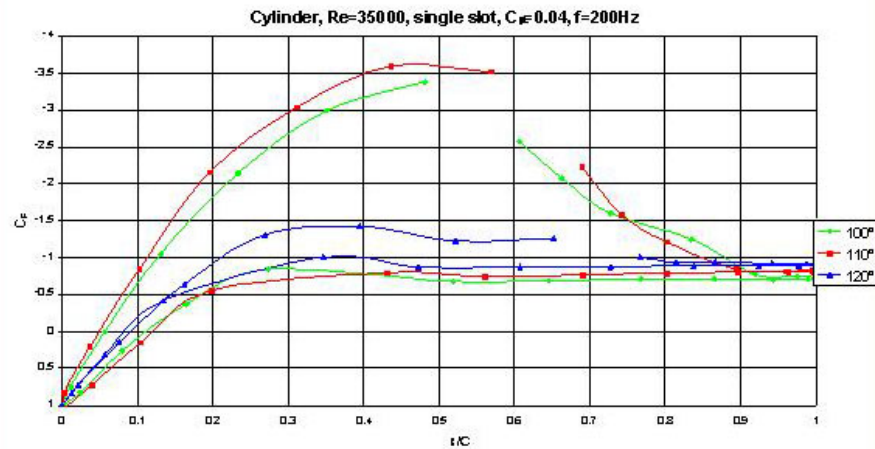
THE UNIVERSITY OF ARIZONA



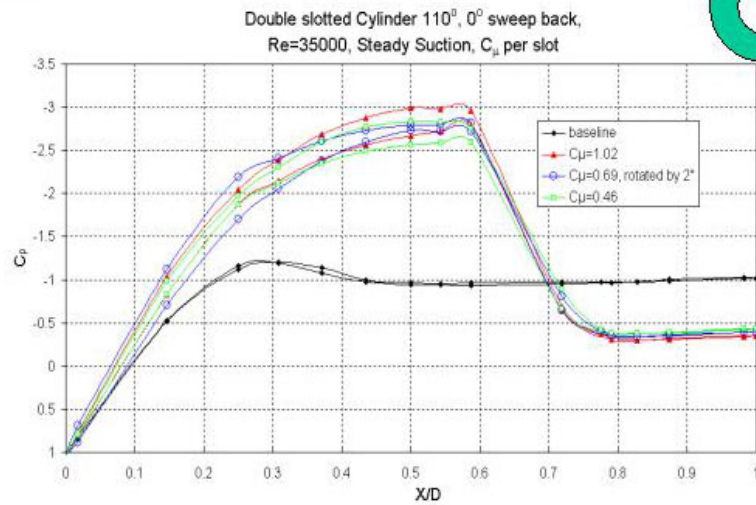
Cylinder, $Re=35000$, single slot at 120° , $f=150$ Hz



THE UNIVERSITY OF ARIZONA



THE UNIVERSITY OF ARIZONA

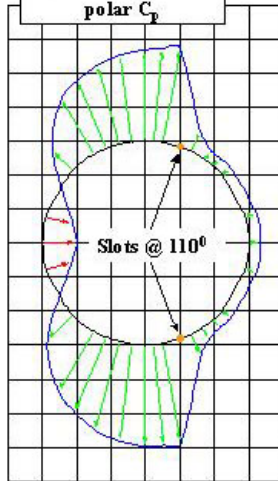


THE UNIVERSITY OF ARIZONA

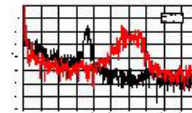
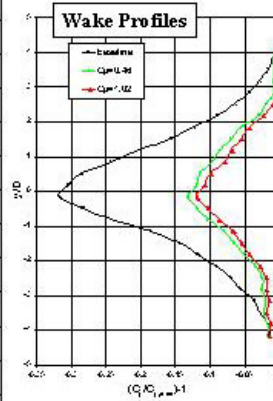


$C_{\mu} = 1.02, Re = 35000$

polar C_p



Circular Cylinder with Steady Suction



**Relative
Change in Drag:**

C_{μ} 0.00 **0.46** **1.02**
 C_{dp} 1.02 **0.26** **0.18**
 C_D 1.04 **0.43** **0.35**
 η 0.00 **-0.14** **0.32**

with:

$$\eta = (C_D + C_{\mu} - C_{D,baseline}) / C_{D,baseline}$$

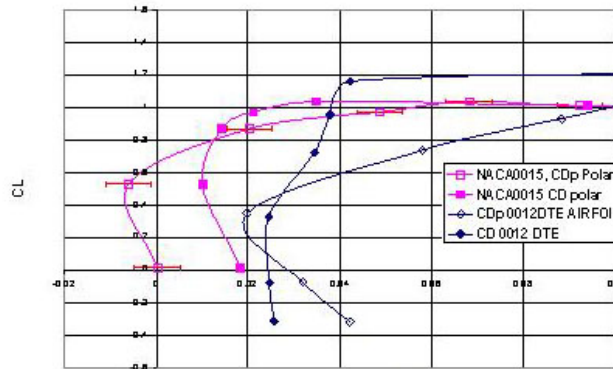
THE UNIVERSITY OF ARIZONA



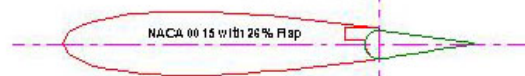
Divergent Trailing Edge Airfoil based on NACA 0012



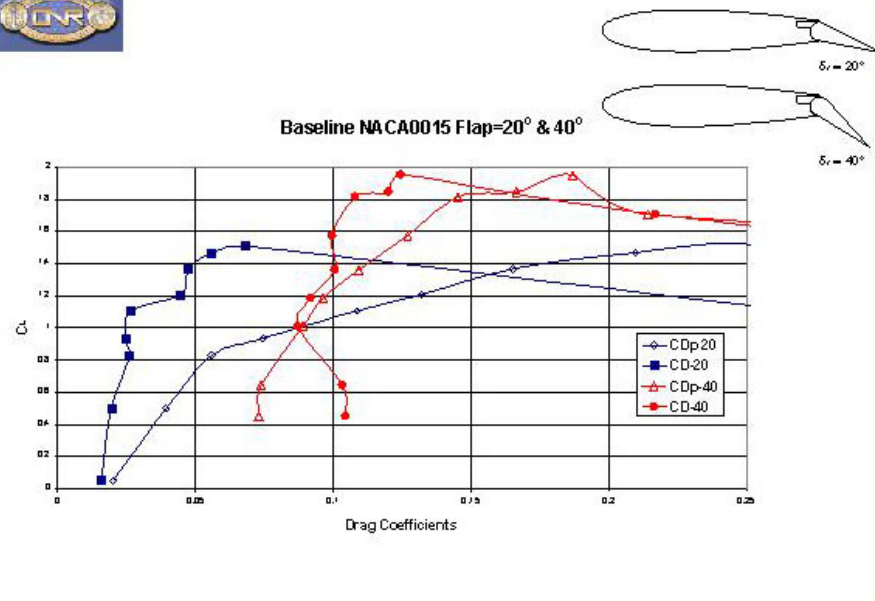
CD & CDp for two airfoils



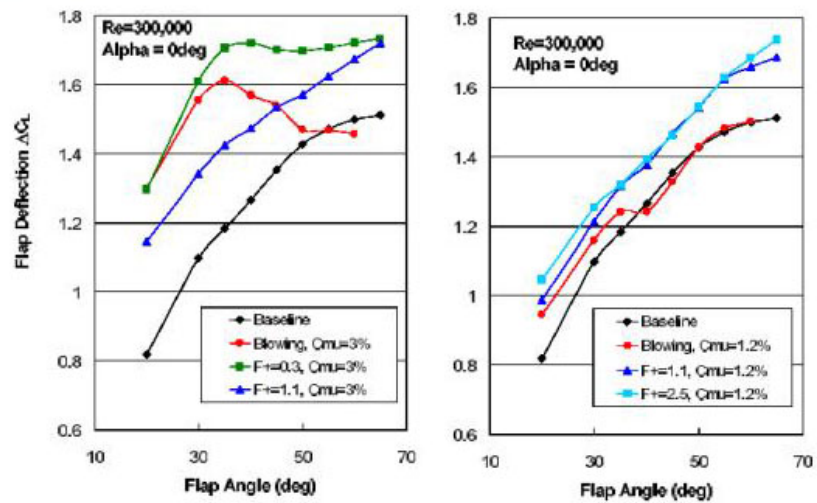
Drag Coefficient



THE UNIVERSITY OF ARIZONA

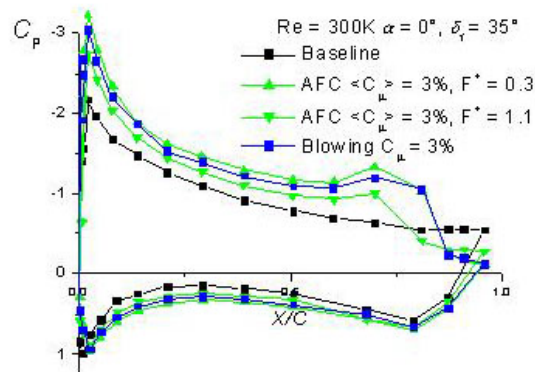


THE UNIVERSITY OF ARIZONA



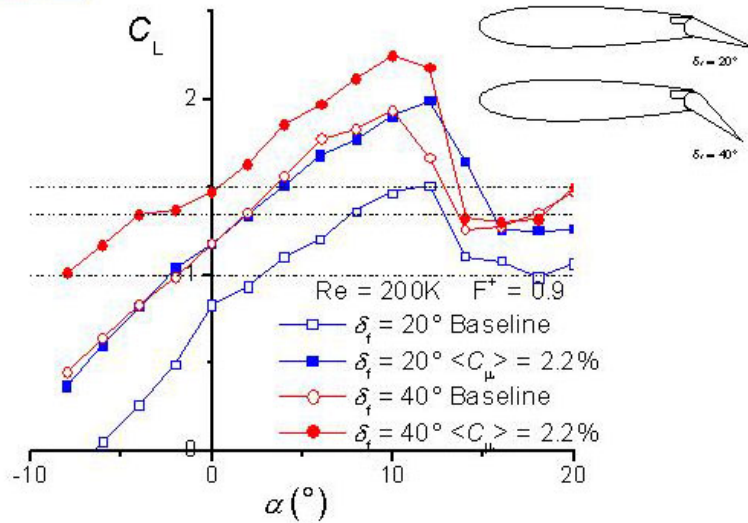
From Greenblatt & Wygnanski, PNAS, 36, 457 (2000)

THE UNIVERSITY OF ARIZONA

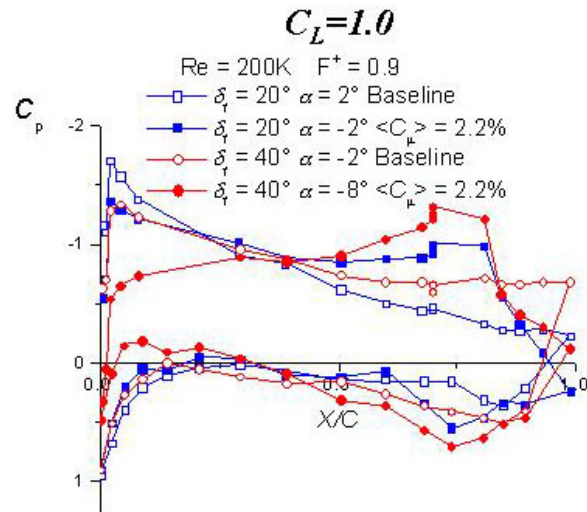


From Greenblatt & Wygnanski, PNAS, 36, 457 (2000)

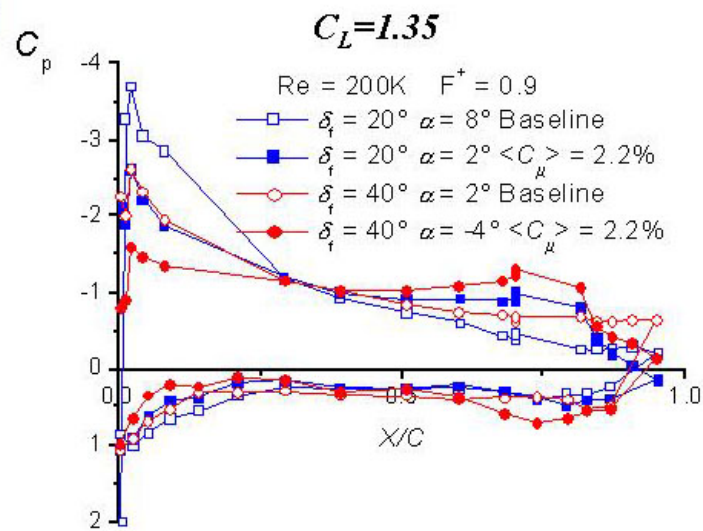
THE UNIVERSITY OF ARIZONA



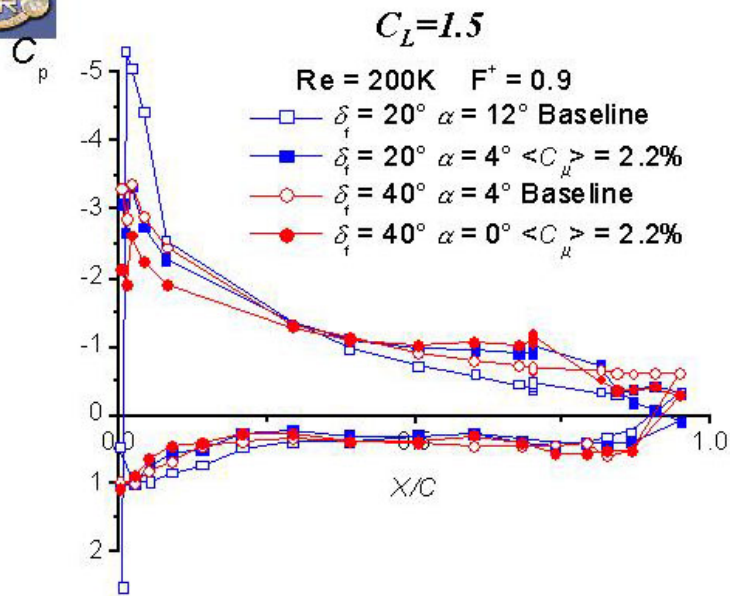
THE UNIVERSITY OF ARIZONA



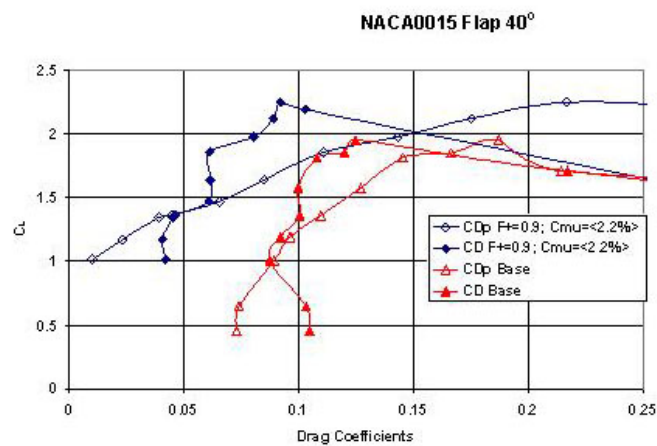
THE UNIVERSITY OF ARIZONA



THE UNIVERSITY OF ARIZONA



THE UNIVERSITY OF ARIZONA

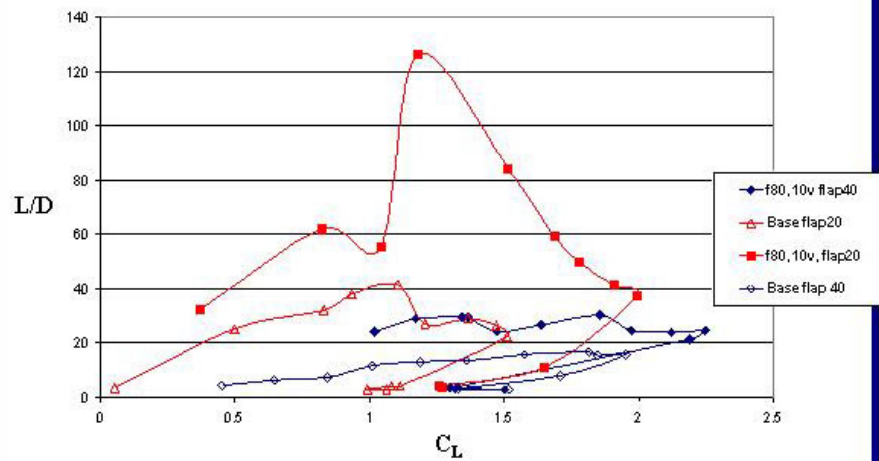


THE UNIVERSITY OF ARIZONA



L/D on NACA0015 for $\delta_f=20^\circ$ & 40°

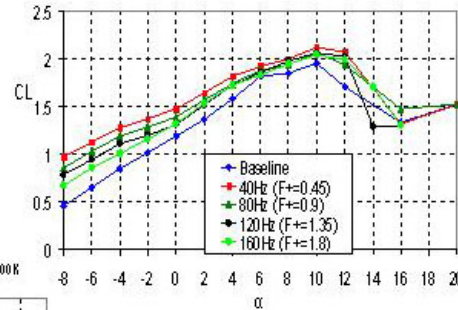
$Re=200,000$; $F^+=0.9$; $C_{\mu}=2.2\%$



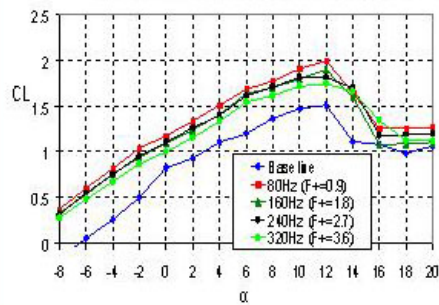
THE UNIVERSITY OF ARIZONA



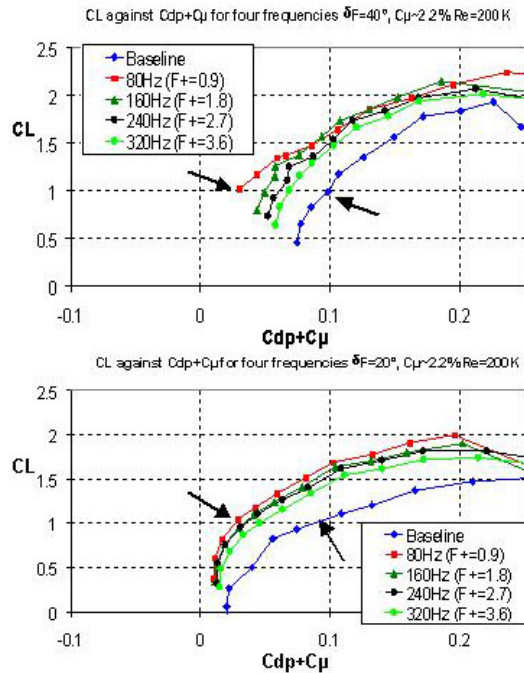
CL again sta for four frequencies $\delta_f=40^\circ$, $C_{\mu}=1\%$, $Re=200K$



CL again sta for four frequencies $\delta_f=20^\circ$, $C_{\mu}=2.2\%$, $Re=200K$



THE UNIVERSITY OF ARIZONA



For a given C_L excitation reduces C_{Dp} by a factor of 10 if C_{μ} is not accounted for and by a factor of 3 if one assumes that the entire C_{μ} should be accounted as thrust.

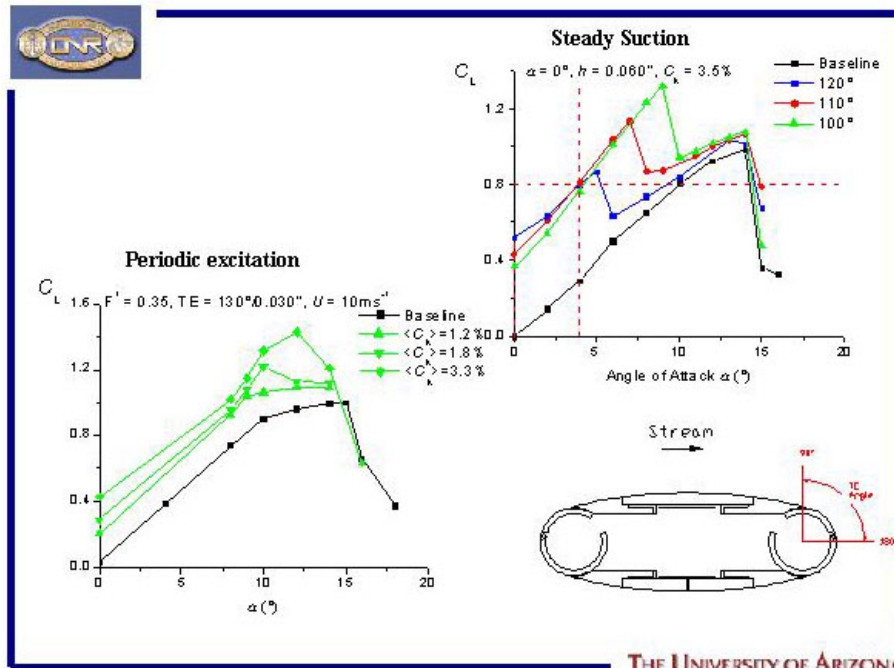
C_{Dp} at a given C_L is not affected by flap deflection

C_D at $C_L=1$

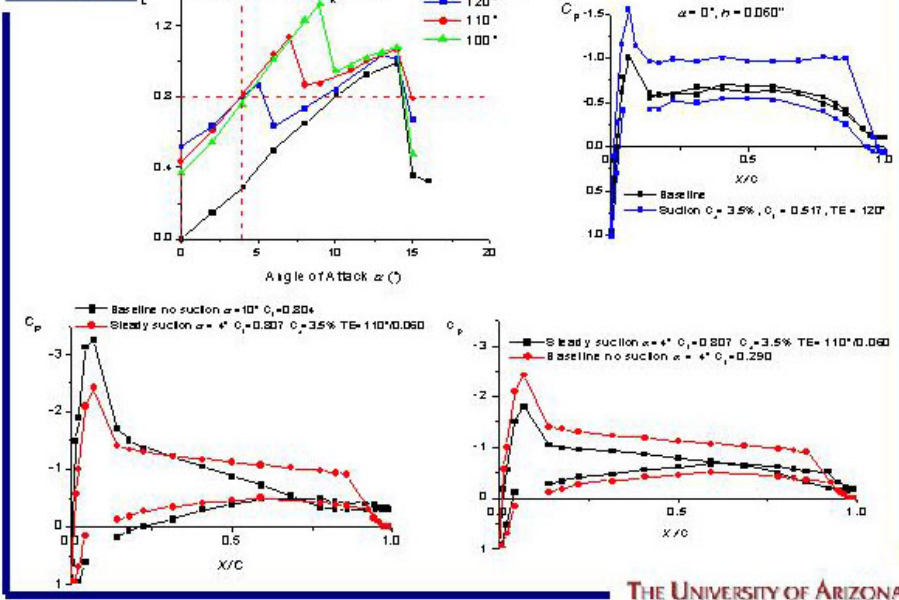
$\delta_f=20^\circ$ $C_{dbase}=0.025$ $C_{D80Hz}=0.018$ $\eta=60\%$

$\delta_f=40^\circ$ $C_{dbase}=0.085$ $C_{D80Hz}=0.040$ $\eta=27\%$

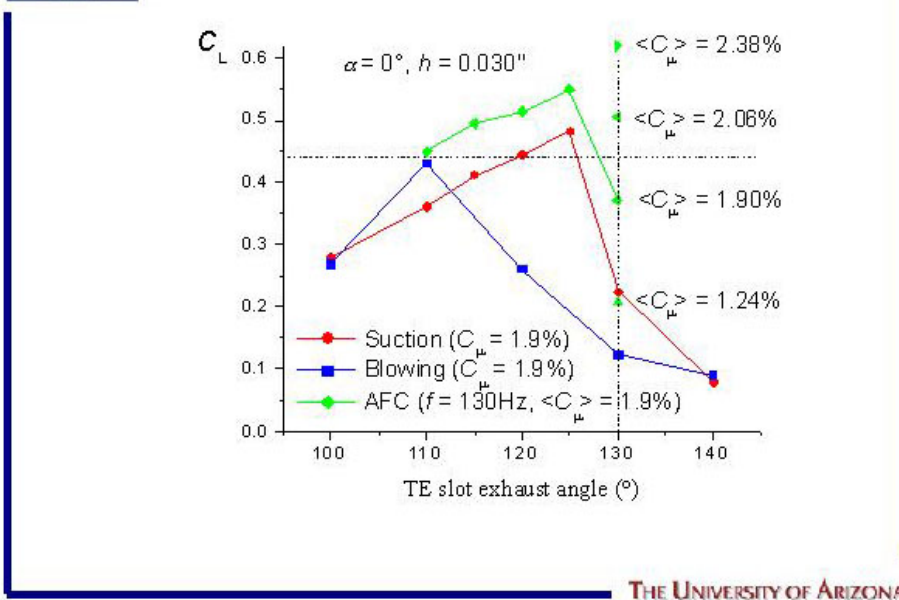
$$\eta = (C_{D80Hz} + C_{\mu} - C_{dbase}) / C_{Dbase}$$



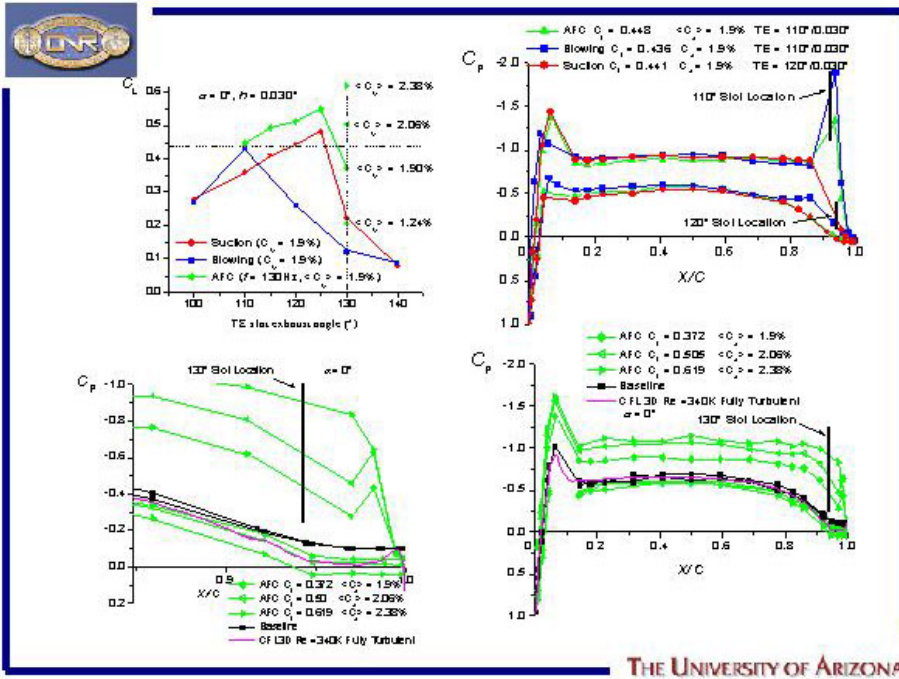
THE UNIVERSITY OF ARIZONA



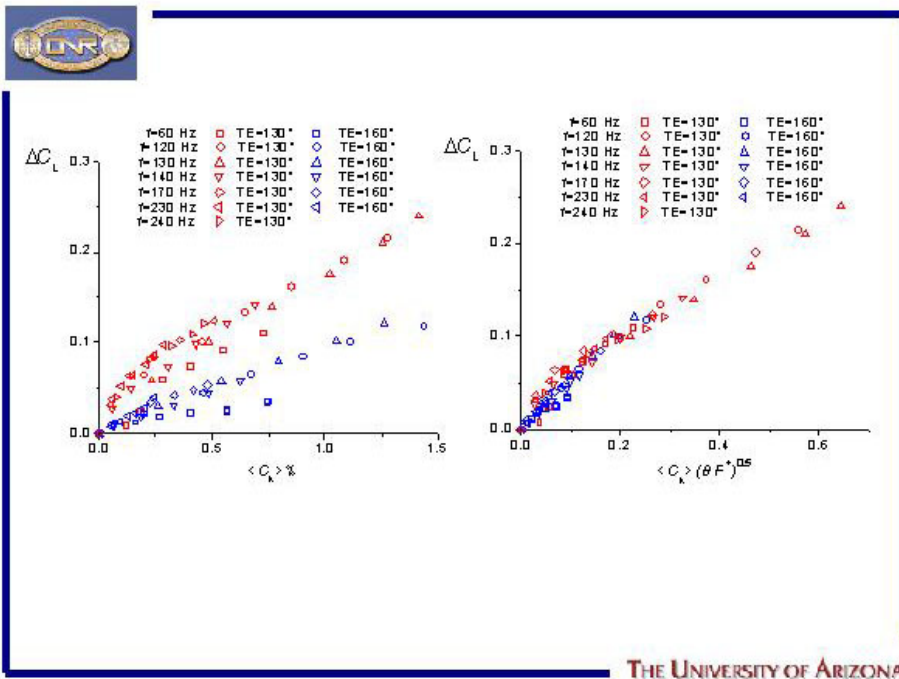
THE UNIVERSITY OF ARIZONA



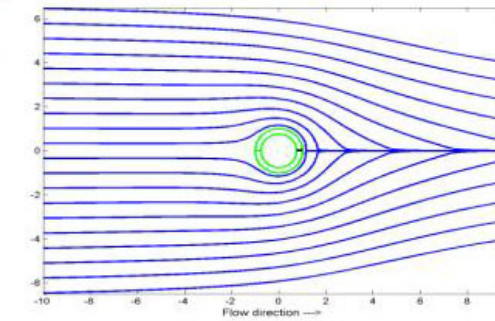
THE UNIVERSITY OF ARIZONA



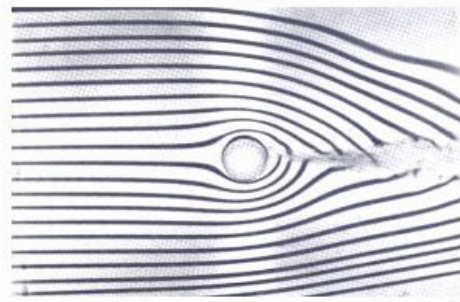
THE UNIVERSITY OF ARIZONA



THE UNIVERSITY OF ARIZONA



$$C_{\mu} = 0.24$$

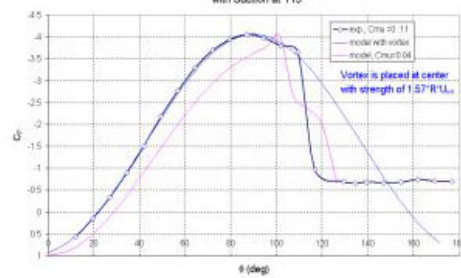


$$C_{\mu} = 0.37$$

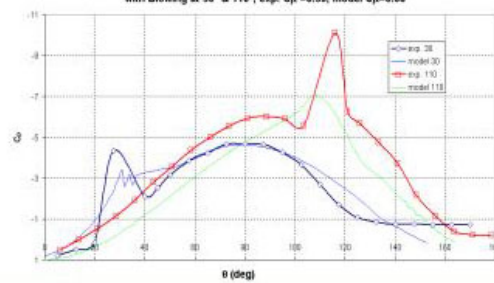
THE UNIVERSITY OF ARIZONA



Pressure Distribution on a Cylinder at $Re = 36000$
with Suction at 115°



Pressure Distribution on a Cylinder at $Re = 36000$
with Blowing at 30° & 110° , exp. $C_{\mu} = 0.39$, model $C_{\mu} = 0.08$



THE UNIVERSITY OF ARIZONA



CONCLUSIONS

- Periodic excitation (AFC) is more effective than either blowing or suction, but WHY?
- The efficacy of AFC depends on C_μ ; F^+ ; slot location; slot shape; Kutta Condition.
- The effects of AFC are most complex since they are felt both upstream and downstream of the actuation and they involve periodic generation of vortices next to the surface.
- One needs to define the criteria that will correlate the best input with the dominant result.

THE UNIVERSITY OF ARIZONA

A Wind Tunnel Experiment for Trailing Edge Circulation Control on a 6% 2-D Airfoil up to Transonic Mach Numbers

Michael G. Alexander, Scott G. Anders, Stuart K. Johnson

NASA-Langley Research Center
Hampton, VA. 23681-001

ABSTRACT

A wind tunnel test was conducted on a six percent thick slightly cambered elliptical circulation control airfoil with both upper and lower surface blowing. Parametric evaluations of jet slot heights and Coanda surface shapes were conducted at mass flow coefficients (C_μ) from 0.0 to 0.12. The test data was acquired in the NASA Langley Transonic Dynamics Tunnel at Mach numbers of 0.8 and 0.3 at Reynolds numbers per foot of 1.05×10^6 and 2.43×10^5 respectively.

For the transonic condition, (Mach = 0.8 at $\alpha = +3^\circ$), it was generally found that the smaller slot and larger Coanda surface were more effective overall than other slot/Coanda surface combinations.

Generally it was found at Mach = 0.3 at $\alpha = +6^\circ$ that the smaller slot and smaller Coanda surface were more effective overall than other slot/Coanda surface combinations.

INTRODUCTION

Circulation control is considered one of the most efficient methods for lift augmentation at low Mach numbers (ref. 1). The device augments an airfoil's lifting capability by tangentially ejecting a thin jet of high momentum air over a rounded trailing edge (ref. 2). The jet will remain attached to the surface as long as the low static pressures created by the jet are large enough to balance the centrifugal forces acting to detach the jet (ref. 3) (figure 1). The jet moves the separation point around the trailing edge toward the lower surface of the wing and entrains the external flow field. This entrainment and separation point movement produces a net increase in the circulation of the wing resulting in lift augmentation (ref 4.).

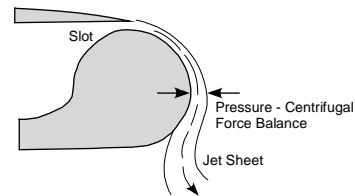


Figure 1 - Tangential Blowing Over a Coanda Surface

Numerous experimental circulation control tests using the Coanda effect to enhance lift have been conducted at subsonic velocities on relatively thick (15-percent) airfoil sections (ref. 5). The focus of this experiment is to evaluate the effectiveness of trailing edge circulation control on a thin airfoil section at transonic Mach numbers. A wind tunnel test was conducted on a six percent thick slightly cambered elliptical airfoil with both upper and lower surface slot blowing. Parametric evaluations of jet slot heights and Coanda surface shapes were conducted at mass flow coefficients (C_μ) from 0.0 to 0.12. The data was acquired in the NASA Langley Transonic Dynamics Tunnel at Mach = 0.8 at $\alpha = 3^\circ$ and Mach = 0.3 at $\alpha = 6^\circ$, at a Reynolds number per foot of 1.05×10^6 and 2.43×10^5 respectively.

SYMBOLS

α	Angle-of-attack, degrees
Δ	Delta, incremental change
ρ	Density; (lbm/ft ³)
γ	Ratio of specific heat
A	Area (ft ²)
b	Model span (inch)
c	Chord (inch)
c _{ref}	Reference chord (30-inch)
CD	Discharge coefficient
C _l	Sectional lift coefficient

C_m	Sectional 0.25c _{ref} pitching moment coefficient
CP or C _p	Pressure coefficient
C _μ	Blowing coefficient
$\Delta Cl/C_\mu$	Lift augmentation ratio
h	Average measured slot height (inch)
h/c	Non-dimensional slot height
\dot{m}	Mass flow (lbm/sec)
P _s	Free stream static pressure (psia)
P ₀	Total pressure (psia)
q	Dynamic pressure (psi)
r	Radius
Rn/ft	Reynolds number per foot
t	Airfoil thickness
T ₀	Total Temperature (R)
V	Velocity (ft/sec)
x	Chordwise distance (inch)
y	Span distance (inch)
y/b	Non-dimensional span location
<u>Subscripts</u>	
jet	Air flow that exits nozzle
l	Lower
s	Slot
TE	Trailing edge
u	Upper

MODEL DESCRIPTION

The configuration tested in this experimental investigation is a semi-span rectangular circulation control airfoil with zero leading and trailing edge sweep having a circular end plate at the tip. The model as shown in figure 2a, was mounted in the wind tunnel on a splitter plate located approximately 3-ft off the tunnel wall.



Figure 2a - CCA Model – (view from right rear quarter, looking upstream)

The model incorporated circulation control by blowing tangentially from spanwise rectangular slots located upstream of a trailing

edge “Coanda surface”. The model has two separate and isolated internal plenums that fed air to either the upper or lower rectangular slot nozzle. The rectangular slot exits are located at $x/c_{ref} = 0.9$ and extends the full span (60-inches) of the model. The model is instrumented with a total of 157 static and total pressure taps, one accelerometer, and a type J thermocouple located in each plenum. The model has a surface finish of 32 μ -inch, and the Coanda surface external finish from upper slot exit to lower slot exit was of 16 μ -inch.

Circulation Control Airfoil

The Circulation Control Airfoil (CCA) section is a simple six percent thick elliptical airfoil having 0.75-percent camber (figure 2b). The model span (b) was 60-inches with zero leading and trailing edge sweep. A reference chord (c_{ref}) of 30-inches gave the model an aspect ratio of two and a taper ratio of one. Common practice for testing semi-span models on a reflective plane is to refer to this as an aspect ratio four wing.

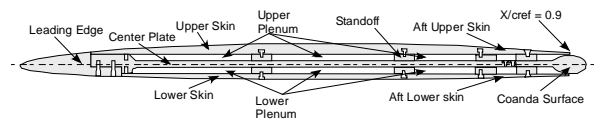


Figure 2b – CCA Airfoil Section

The CCA model tip is capable of accommodating either a 30-inch diameter circular end plate to promote 2-dimensional flow or a “t/2” tip used to evaluate 3-D effects. The model was tested with the end plate as shown in figure 2a.

Coanda Surface Definition

Three elliptical trailing edge surfaces (referred to as Coanda Surfaces) were manufactured with length-to-height ratios of 1.78:1, 2.38:1, and 2.98:1 as illustrated in Figure 3. The 2.38:1 Coanda surface installed on the CCA model with the end plate removed is shown in figure 4. The minor axis of the Coanda surface was aligned with the slot exit to ensure the minimum exit area occurred at $x/c_{ref} = 0.9$. The horizontal axis of the ellipse was then mapped to the camber line of the elliptical airfoil that formed a five-degree converging nozzle at the slot exit. The Coanda surface spanned the trailing edge of the model (60-inches).

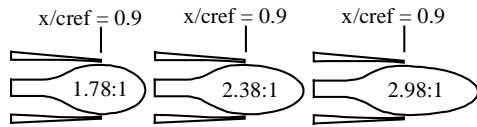


Figure 3 - Coanda Surfaces



Figure 4 - End View of a Coanda Surface and Aft Surfaces

Reference 6 provided guidelines for Coanda surface radius of curvatures as listed in table 1. It is not possible to meet the entire guideline radius of curvatures on a six percent thick airfoil. It was therefore decided that preference would be given to the slot radius of curvature in an effort to achieve initial jet attachment. As a result, a family of elliptical Coanda surfaces was chosen which have large slot radii of curvature and small trailing edge radii of curvature.

	Coanda		
	1.78 : 1	2.38 : 1	2.98 : 1
Chord (in)	27.82	28.09	28.36
r_s (in)	1.44	2.57	4.02
r_{TE} (in)	0.25	0.19	0.15
r_s/c	0.052	0.091	0.142
r_{TE}/c	0.009	0.007	0.005
Guidelines: r/c	0.02 to 0.06		
$h1/r_s$	0.024	0.014	0.009
$h2/r_s$	0.039	0.022	0.014
$h3/r_s$	0.051	0.028	0.018
$h1/r_{TE}$	0.14	0.18	0.23
$h2/r_{TE}$	0.22	0.30	0.37
$h3/r_{TE}$	0.29	0.38	0.48
Guidelines: h/r	0.01 to 0.08		

Table 1 – Coanda Radius and Slot Height Dimensions

Slot Definitions

Three upper and lower slot heights for each Coanda surface were possible for this wind tunnel investigation. The slot heights are given in table 2. A fourth slot height ($h4$) was constructed during the test using the upper surface small slot ($h/c = 0.0012$) aft skin by applying 4-layers of 0.0014-inch thick tape (0.0035-inches thick). The aft upper and lower removable surfaces were designed to set the slot heights by varying the internal mold line while not disturbing the outer mold line of the model. Average measured slot height (h) and chord lengths were used to determine the height to chord ratio (h/c) of each slot. Table 2 below lists the measured height and chords and the resulting h/c . Slot height to Coanda radius information is shown in table 1.

Slot	c (inches)	h (inches)	h/c
h1	27.82	0.035	0.0012
h2	28.09	0.056	0.0020
h3	28.36	0.073	0.0026
h4	28.36	0.0021	0.0007

Table 2 - Slot and Chord Measurements

Aft Surface

Three sets of aft surfaces were manufactured and attached to the main airfoil body which formed the upper and lower external airfoil contour as well as the internal five-degree convergent nozzle contour (figure 5).

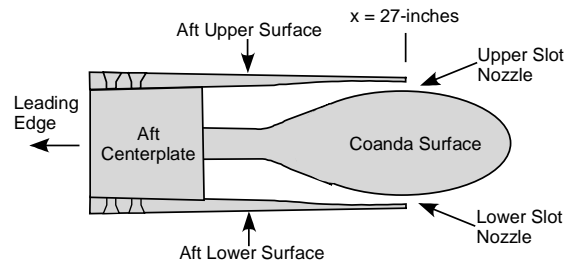


Figure 5 - Aft Surface Identification

The aft skins also contained chordwise surface static pressure taps at $y/b = 0.5$. Any aft surface in combination with any Coanda surface ensured the minimum nozzle area was located at the nozzle exit. Each aft surface also established a discrete slot height above the Coanda surface.

End Plate

The CCA model used a circular end plate to promote 2-D flow conditions. The end plate was

a 30-inch diameter circular plate constructed from a 0.25-inch thick aluminum plate with the outside edge beveled. The design of the end plate was based on sizing criteria found in reference 7. A removable cutout located at its trailing edge allowed for Coanda surface removal and replacement.

Internal Plenum

As seen in figure 2b, the airfoil section is divided into contiguous, separate, and isolated upper and lower plenums. The ratio of the slot height to plenum height ranged from 3.8 to 12.8 depending on the slot height. This ensured low flow velocities in the plenum that helped maintain uniform plenum flow.

Internal Plenum Screens

The model has the capability of holding six removable, 0.050-inch thick, high pressure-loss screens. The screens were fastened to the plenum floor and extended to the plenum ceiling. Each screen has a porosity of 30-percent and is capable of being placed in both upper and lower plenums at the three locations. The screen's porosity was sized using the method described in reference 8. It was determined through bench testing to use one screen in each plenum in the aft most position. The aft screen was located approximately $x/c_{ref} = 0.72$ and ran full spanwise and parallel to the slot nozzle.

Boundary Layer Trip

A boundary layer trip strip (ref. 9) was located 1.5-inches (measured along the surface) aft of the leading edge on the upper and lower surface. The trip strip used epoxy dots having a diameter of 0.038-inch, a thickness of 0.015-inch, and an edge-to-edge spacing distance between the epoxy dots of 0.098-inch.

INSTRUMENTATION

CCA Surface Static Pressures

A total of 83 external static surface pressure taps was located at $y/b = 0.5$ on the upper and lower airfoil surface (42 upper and 41 lower taps). There are two spanwise rows of 10-static pressures taps located at $x/c_{ref} = 0.5$ and 0.8 on each upper and lower airfoil surface.

Coanda Surface Static Pressures

Each Coanda surface had a total of 19-static surface pressure taps located at $y/b = 0.5$ every

10° radially from 0° to 180° with 0° and 180° at the nozzle exit (figure 6).

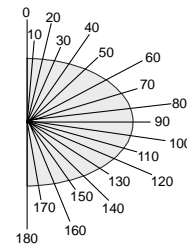


Figure 6 – Coanda Tap Placement

Total Pressures

Each plenum had six-total pressure taps. Their locations are given in table 3.

Taps	y/b	x/c _{ref}
1	0.2	0.3
2	0.2	0.8
3	0.45	0.8
4	0.5	0.8
5	0.55	0.8
6	0.8	0.8

Table 3 - Internal Plenum Tap Locations

Pressure taps at $x/c_{ref} = 0.8$ are located aft of the high loss screen and pressure taps $x/c_{ref} = 0.3$ are used to determine the total pressure entering the plenum from the intake nozzle. The total pressure for the plenum was averaged using taps 2, 3, 4, 5, and 6 to obtain the nozzle exit total pressure.

Thermocouples

The plenum has 2-iron-constantan, type J thermocouples located in each plenum to measure plenum total temperature.

FACILITY

This wind tunnel investigation was conducted in the NASA Langley Transonic Dynamics Tunnel (TDT) (ref. 10). The TDT is a closed circuit, continuous-flow, variable-pressure wind tunnel with a 16-foot square test section with cropped corners. The tunnel has the capability of using either air or R-134a gas as the test medium. The current investigation was conducted in air. The tunnel can operate up to Mach 1.2 and is capable of maximum Reynolds numbers of approximately three million per foot and dynamic pressures up to 2.29 psi in air.

Tunnel stagnation pressure can be varied from near vacuum to atmosphere.

Model Support

The TDT model support systems used for this test were a sidewall turntable and splitter plate as depicted in the figure 7. The splitter plate was located approximately 3-ft from the tunnel wall using wall standoffs. The rigid support and model instrumentation was placed inside an aerodynamic shape or “canoe” located between the splitter plate and the tunnel sidewall.

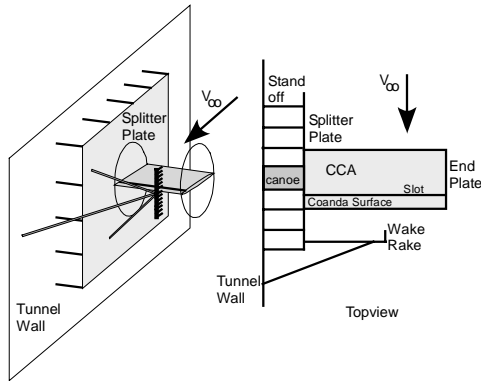


Figure 7 - CCA Model Installation in the TDT

Air Supply

Air was supplied to the test section via two 1-inch high-pressure flex lines delivering a maximum of 1-lbm/sec at 200-psia. Total temperature of the supply air was uncontrolled and ranged from -13°F to $+70^{\circ}\text{F}$. Each supply line was attached to a control valve that regulated total pressure to the CCA model. A manually operated crossover line located upstream of the control valve allowed mass flow to be diverted from one line to another. After the control valve, each line of the supply air went through its dedicated critical flow venturi and then entered the model plenum.

TEST PROCEDURES AND CONDITIONS

Lift and Pitching Moment

The sectional lift coefficient (equation 1) and quarter chord pitching moment coefficient (equation 2) were obtained by numerically integrating (with the trapezoidal method) the local pressure coefficient at each $y/b = 0.5$ chordwise orifice from the upper and lower surface of the model.

$$C_l = \int_0^1 \left(C_{p_l} - C_{p_u} \right) d\left(\frac{x}{c}\right) * \cos \alpha \quad (1)$$

$$C_{m_{.25}} = \int_0^1 \left(C_{p_l} - C_{p_u} \right) \left(0.25 - \left(\frac{x}{c}\right) \right) d\left(\frac{x}{c}\right) \quad (2)$$

Mass Flow

The mass flow coefficient is calculated using equation 3.

$$C_{\mu} = \left(\frac{\dot{m} V_{jet}}{q_{\infty} S} \right) \quad (3)$$

The ideal jet velocity (ft/s) was calculated (ref. 11) based on the assumption that the slot jet flow expands isentropically to the free-stream static pressure (equation 4).

$$V_{jet} = \sqrt{2 * R * T_o * g_c * \left(\frac{\gamma}{\gamma-1}\right) * \left[1 - \left(\frac{p_{\infty}}{P_{o_{plenum}}}\right)^{\frac{\gamma-1}{\gamma}} \right]} \quad (4)$$

Mass flow was determined using equation 5 below. The discharge coefficient was obtained from critical flow venturi calibrations conducted in the NASA Jet Exit facility.

$$\dot{m} = CD * (A * V * \rho)_{throat} \quad (5)$$

TEST CONDITIONS

The test conditions and ranges can be seen in table 4.

Mach	P _o (psia)	P _s (psia)	T _o (°F)	Rn/ft
0.3	2.7 - 4.1	2.6 - 3.8	67 - 94	3.6x10 ⁵ - 5.5x10 ⁵
0.8	3.0 - 4.1	2.0 - 2.7	95-125	7.8x10 ⁵ - 1.0x10 ⁶

Table 4 - CCA Test Range of Conditions

Data Corrections

No corrections were applied to account for tunnel flow angularity, wall interference effects, or end plate effects.

DISCUSSION OF RESULTS

Mach = 0.8; $\alpha = +3^{\circ}$

Coanda Surface Effect

In figures 8 and 9, Coanda surface effects are presented for the upper and lower slot blowing respectively. At Mach = 0.8 at $\alpha = 3^{\circ}$,

each Coanda surface was capable of generating incremental lift and pitching moment at each blowing condition. Upper slot blowing generated positive lift and negative pitching moment increments while the lower slot blowing generated negative lift and positive pitching moment increments. Generally, the data in figure 8 displays three distinct regions. The first region is characterized by an increasing lift increment with increasing C_{μ} followed by a plateau region in most cases and then finally, a region of negative lift increment with further increasing C_{μ} . As the Coanda surfaces lengthened, increasing C_{μ} stretched the regions further. The Coanda surface effect observed in this data indicates the longer Coanda surface is more effective over the mid to high C_{μ} range, while all three Coanda surfaces are equivocal at the low end of C_{μ} . The data suggests the jet on the longer Coanda surface remains attached longer over a larger range of blowing coefficients while, conversely, the jet separates much sooner on the smaller Coanda surfaces. This data trend is generally followed in figure 9 for lower surface blowing. However, the lower surface blowing is not as effective in producing lift increment as the upper surface blowing over the same range of blowing coefficients. Also, as seen in figure 9, none of the Coanda surfaces tested were capable of generating incremental lift or pitching moment for $h/c = 0.0026$.

The lift augmentation ratio ($\Delta C_l/C_{\mu}$) for upper and lower slot blowing is presented in figures 10 and 11 respectively. The upper and lower slot blowing data indicated the larger the Coanda surfaces, the greater the magnitudes of lift augmentation. It was observed that as C_{μ} increased, lift augmentation decreased in magnitude with the exception of the data obtained at $h/c = 0.0026$ (figure 11) which, as previously noted, generated insignificant lift increment. Maximum augmentation was typically achieved on each Coanda surface at mass flow coefficients less than 0.005. It appeared that the larger Coanda was more effective over a larger range of C_{μ} at any given h/c .

Slot Height Effect

In figures 12 and 13, slot height effects are presented for the upper and lower slot blowing. The data is the same data previously presented but replotted to better evaluate slot height effect. At Mach = 0.8 at $\alpha = +3^\circ$, the smallest slots were

most capable of generating incremental lift and pitching moment at each blowing condition.

The lift augmentation ratio for the upper surface slot blowing slot height effect is presented in figures 14 and 15. It is observed that the smaller the slot h/c on any given Coanda surface, the greater the lift augmentation. As stated earlier, as C_{μ} increased, the augmentation diminished.

Mach = 0.3 and $\alpha = +6^\circ$

Coanda Surface Effect

In figures 16 and 17, Coanda surface effects are presented for the upper and lower slot blowing respectively. At Mach = 0.3 at $\alpha = +6^\circ$, each Coanda surface was capable of generating incremental lift and pitching moment at each blowing condition. Increasing incremental lift and moments are observed with increasing blowing rate with upper slot blowing creating positive lift increments and negative pitching moment increments, while lower slot blowing created negative lift and positive pitching moment increments. Upper and lower slot blowing incremental lift and moment data trends for each Coanda surface displayed a marked decrease in effectiveness at higher blowing rates. Also observed is an apparent 'pinch down' in the $h/c = 0.0012$ and 0.0020 slot data from $C_{\mu} = 0.06$ to 0.08 that diminished as the Coanda surface increased. This may indicate a reattachment effect (in the immediate region of the slot) followed by a lull where there is little flow turning with C_{μ} increment. The lull is then followed by a period of flow turning around the Coanda Bulb due to the increased C_{μ} . On the upper surface blowing (figure 16), as the slot size (h/c) was increased, the preferred Coanda went from 1.78:1 at $h/c = 0.0012$ to 2.98:1 at $h/c = 0.0026$. It is observed in figure 17, the lower slot blowing force and moment increments followed the same trend as the upper slot blowing, but had reduced absolute values of force and moment increments than that of the upper surface blowing (figure 16). Differences in upper and lower slot blowing are probably due to angle-of-attack, camber, and jet exit angle. At Mach = 0.3 at $\alpha = +6^\circ$, the smaller slot ($h/c = 0.0012$) on the smaller Coanda surface 1.78:1 generated the largest increments over the largest C_{μ} range, making it the preferred surface at this test condition.

The lift augmentation ratio for upper and lower slot blowing is presented in figures 18 and

19 respectively. As was seen in the $M=0.8$ data, the lift augmentation decreased with increasing C_{μ} . Unlike the $M=0.8$ data, the smallest Coanda generated the largest augmentation ratio from all of the data shown. However, the smallest Coanda did not achieve the largest augmentation ratio for all slot heights. At $h/c=0.0012$ the 1.78:1 Coanda surface achieves the largest augmentation ratio. At $h/c=0.0026$, the 2.98:1 Coanda surface achieves the largest augmentation ratio.

Slot Height Effect

In figures 20 and 21 slot effects are presented for the upper and lower slot blowing. The data is the same data previously presented but replotted to better evaluate slot height effect. For each Coanda surface the data suggests that the smaller the h/c , the greater ΔC_l and ΔC_m generated for the upper (figure 20) and lower slot blowing (figure 21).

The lift augmentation ratio for the upper and lower slot blowing is presented in figures 22 and 23. In figure 22, at each Coanda surface tested, the smaller the slot, the greater its augmentation ratio becomes.

Nozzle Pressure Ratio

In figure 24, incremental lift data are presented at Mach numbers of 0.8 and 0.3 as a function of Nozzle Pressure Ratio (NPR). The surface and slot height noted in the figure was the best configuration for each Mach number. The NPR data are presented as an aid in interpreting the data. For NPR's greater than 1.893 the exit slot is choked and therefore the jet is supersonic.

Velocity Ratio

In figure 25, incremental lift data are presented at Mach numbers of 0.8 and 0.3 as a function of velocity ratio for the same configurations used in the NPR figures. These data are presented for reference purposes similar to the NPR data to orient the reader to the ranges of velocity ratios tested.

Pressure Distributions

Figure 26a presents data taken at Mach = 0.8 at $\alpha = +3^\circ$, for the (2.98:1) Coanda and $h/c=0.0012$ slot configuration. A C_{μ} effect was not observed on the leading edge of this airfoil. The data suggests a possible weakening of the upper surface shock with increasing C_{μ} . In figure 26b, which shows the Coanda surface

pressures, the pressure data suggested a shock just aft of the nozzle exit with flow re-attachment and pressure recovery. The surface pressure data indicated the shock moved aft with increasing C_{μ} . Also note at $C_{\mu} = 0.017$ and 0.02, the jet completely detaches from the surface.

Figure 27a presents data taken at Mach = 0.3 at $\alpha = +6^\circ$ for the 1.78:1 Coanda and $h/c=0.0012$ slot configuration. A C_{μ} effect is observed on the leading edge at this test condition. As C_{μ} was increased, the leading edge suction peak broadened further downstream up to a $C_{\mu} = 0.046$. The data indicated at $C_{\mu} \geq 0.046$ that no further enhancement of the leading edge suction are observed. In figure 27b, which shows the Coanda bulb pressures, the pressure data at $C_{\mu} \geq 0.046$ suggested a shock just aft of the nozzle exit followed by flow re-attachment. As C_{μ} is increasing an increasing negative pressure field is seen over the remaining length of the Coanda bulb surface. In addition, the surface pressure data suggests that the shock may be moving aft with increasing C_{μ} .

CONCLUSIONS

A wind tunnel experiment at Mach numbers 0.3 and 0.8 on a 2-D, six percent thick airfoil with a modified trailing edge to enhance the Coanda effect by tangential jet slot blowing was accomplished. Incremental sectional lift and quarter chord pitching moment and lift augmentation ratio data were presented to support any indications of slot height and Coanda surface effects.

At the transonic cruise condition, Mach = 0.8 at $\alpha = +3^\circ$, it was found that the effectiveness increased with decreasing slot height and increasing Coanda surface elliptical ratio.

At the low speed condition, Mach = 0.3 at $\alpha = +3^\circ$, it was found that the effectiveness increased with decreasing slot height and decreasing Coanda surface elliptical ratio.

ACKNOWLEDGMENTS

The authors would like to acknowledge the assistance of those individuals who efforts made this test possible. From the TDT, Mr. Chuck McClish, Mr. Don Keller, Ms. Jennifer P. Florance, and Mr. Wesley Goodman, from Lockheed-Martin, Mr. Jerome Cawthorn, and from the Naval Surface Warfare Center, Carderock Divison, Dr. Ernest Rogers and Ms. Jane Abramson.

REFERENCES

- 1) Novak, C.J.; Cornelius, K.C.; Road, R.K.: Experimental Investigations of Circular Wall Jet on a Circulation Control Airfoil. AIAA 87-0155.
- 2) Englar, R.J.: Investigations into and Application of the High Velocity Circulation Control Wall Jet for High Lift and Drag Generation on STOL Aircraft. AIAA 74-502.
- 3) Ahuja, K.K.; Sankar, L.N.; Englar, R.J.; Munro, S. Liu, Yi.: Application of Circulation Control Technology to Airframe Noise Reduction. GTRI Report: A5928/1, NASA Grant NAG-1-2146, February 15, 2000.
- 4) Abramson, J.: The Low Speed Characteristics of a 15-Percent Quasi-Elliptical Circulation Control Airfoil with Distributed Camber. David W. Taylor Naval Ship R&D Center Report DTNSRDC/ASED-79/07 (AD-A084-176), May 1979.
- 5) Nielsen, J. N.; and Bigger, J. C.: Recent Progress in Circulation Control Aerodynamics. AIAA Paper 87-0001, 1987.
- 6) Rogers, E.; and Abramson, J.: Selected Notes on Coanda Circulation Control Airfoils. unpublished notes, NSWC, 17 April 2002.
- 7) S.F. Hoerner; and H.V. Borst: Fluid-Dynamic Lift. 2nd edition (June 1992), ISBN: 9998831636.
- 8) Blevins, Robert, D.: Applied Fluid Dynamics Handbook. Van Nostrand Reinhold Company, New York, 1984.
- 9) Holmes, J. D.: Transition Trip Technique Study in the McAir Advanced Design Wind Tunnel. Technical Memorandum, May 1984.
- 10) Staff, Aeroelasticity Branch: *The Langley Transonic Dynamics Tunnel*. LWP-799 September 23, 1969.
- 11) Englar, Robert, J.: Two-Dimensional Transonic Wind Tunnel Test of Three 15-percent Thick Circulation Control Airfoils. Technical Note, AL-128, December 1970.

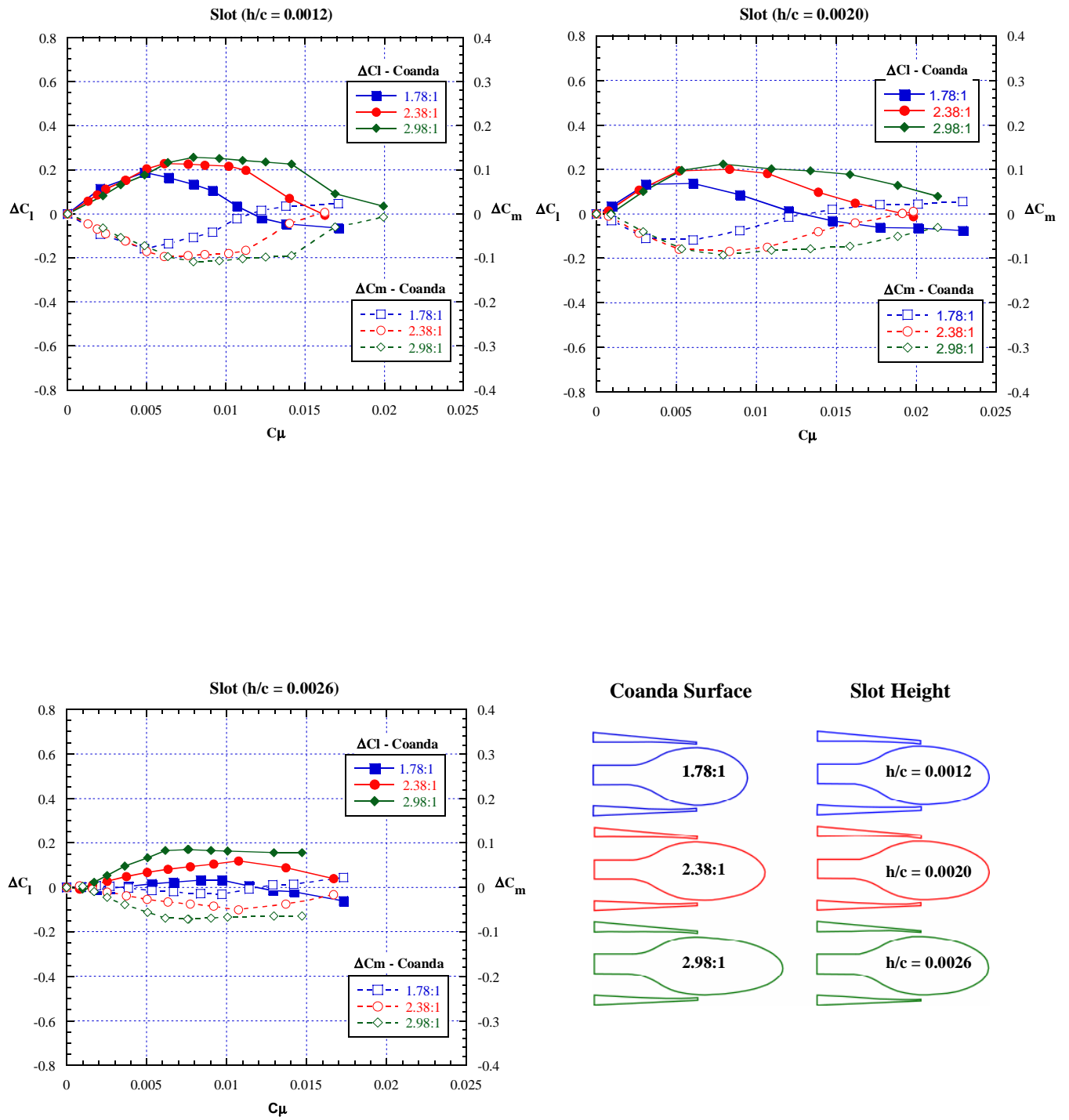


Figure 8 - Coanda surface effect, upper slot blowing, Mach = 0.8, $\alpha = +3^\circ$.

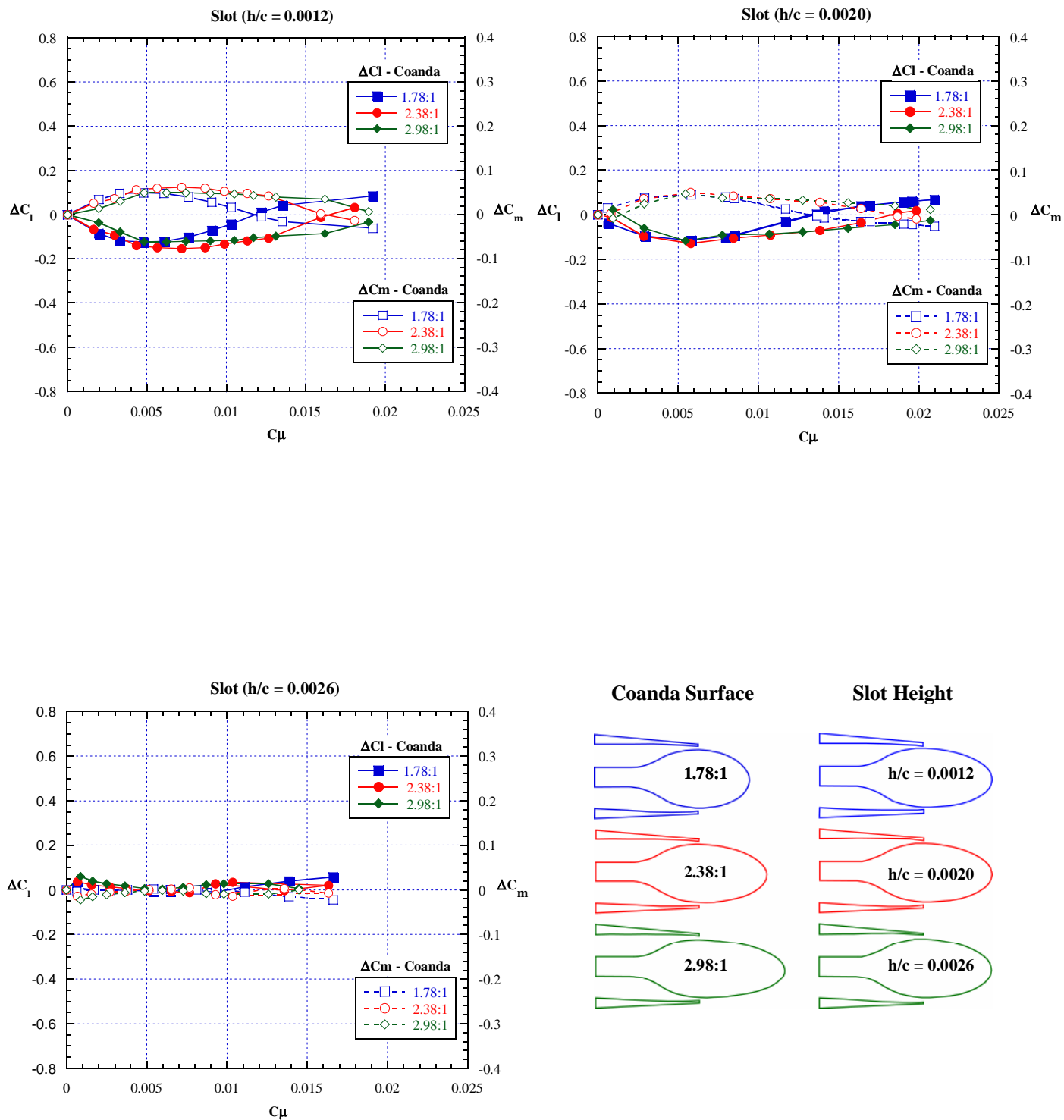


Figure 9 - Coanda surface effect, lower slot blowing, Mach = 0.8, $\alpha = +3^\circ$.

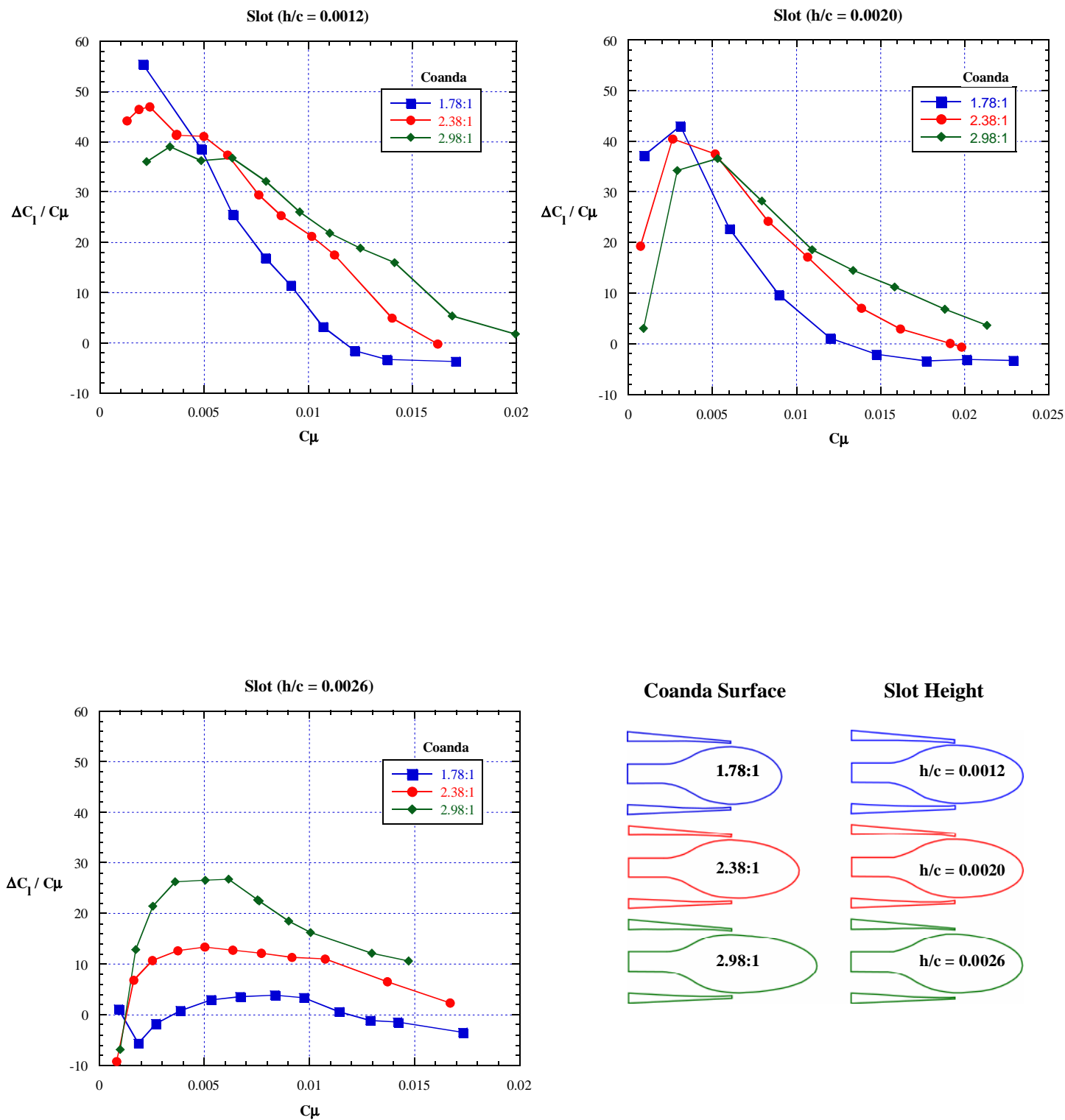


Figure 10 - Lift augmentation, Coanda surface effect, upper slot blowing, Mach = 0.8, $\alpha = +3^\circ$.

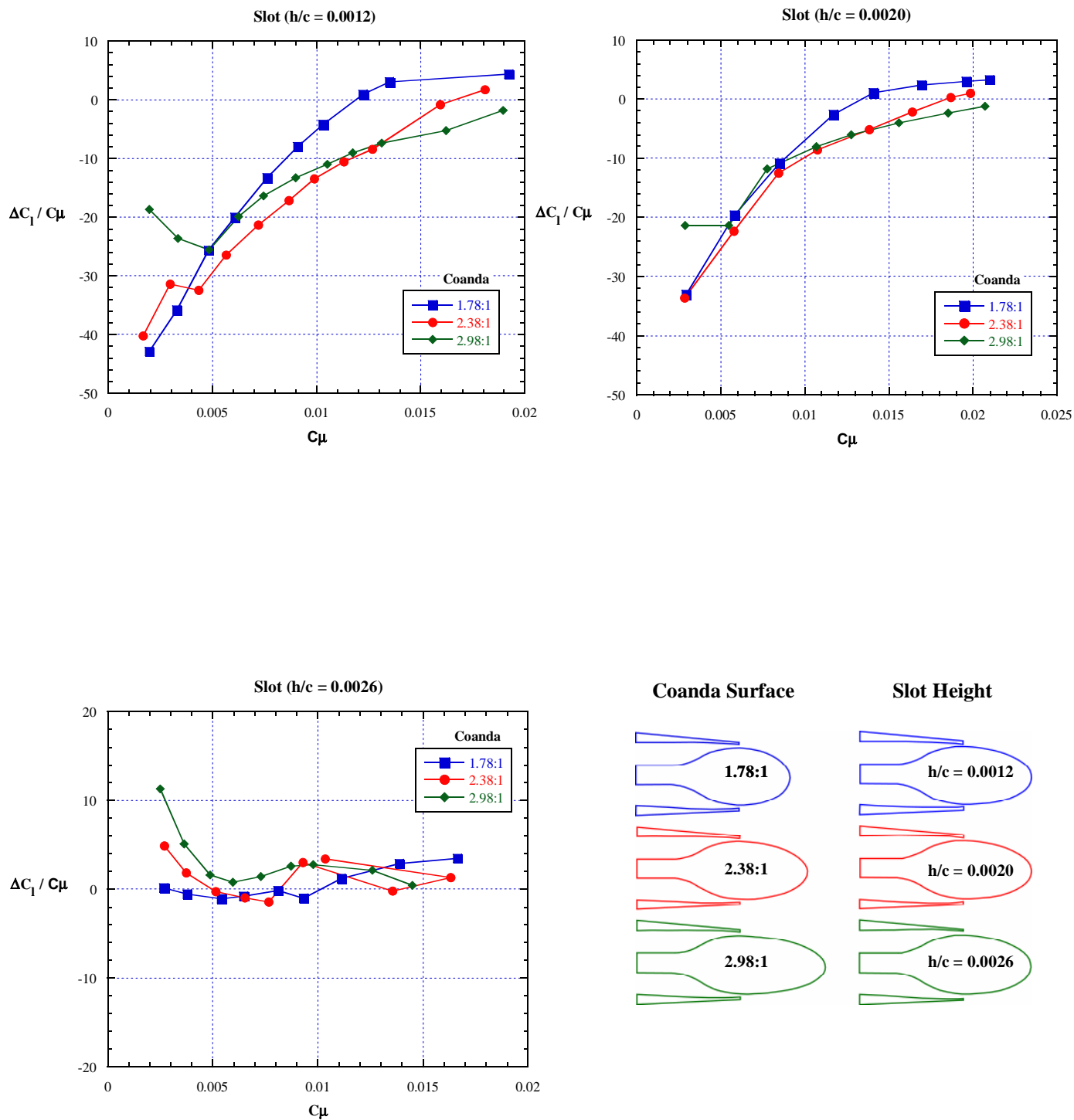


Figure 11 - Lift augmentation, Coanda surface effect, lower slot blowing, Mach = 0.8, $\alpha = +3^\circ$.

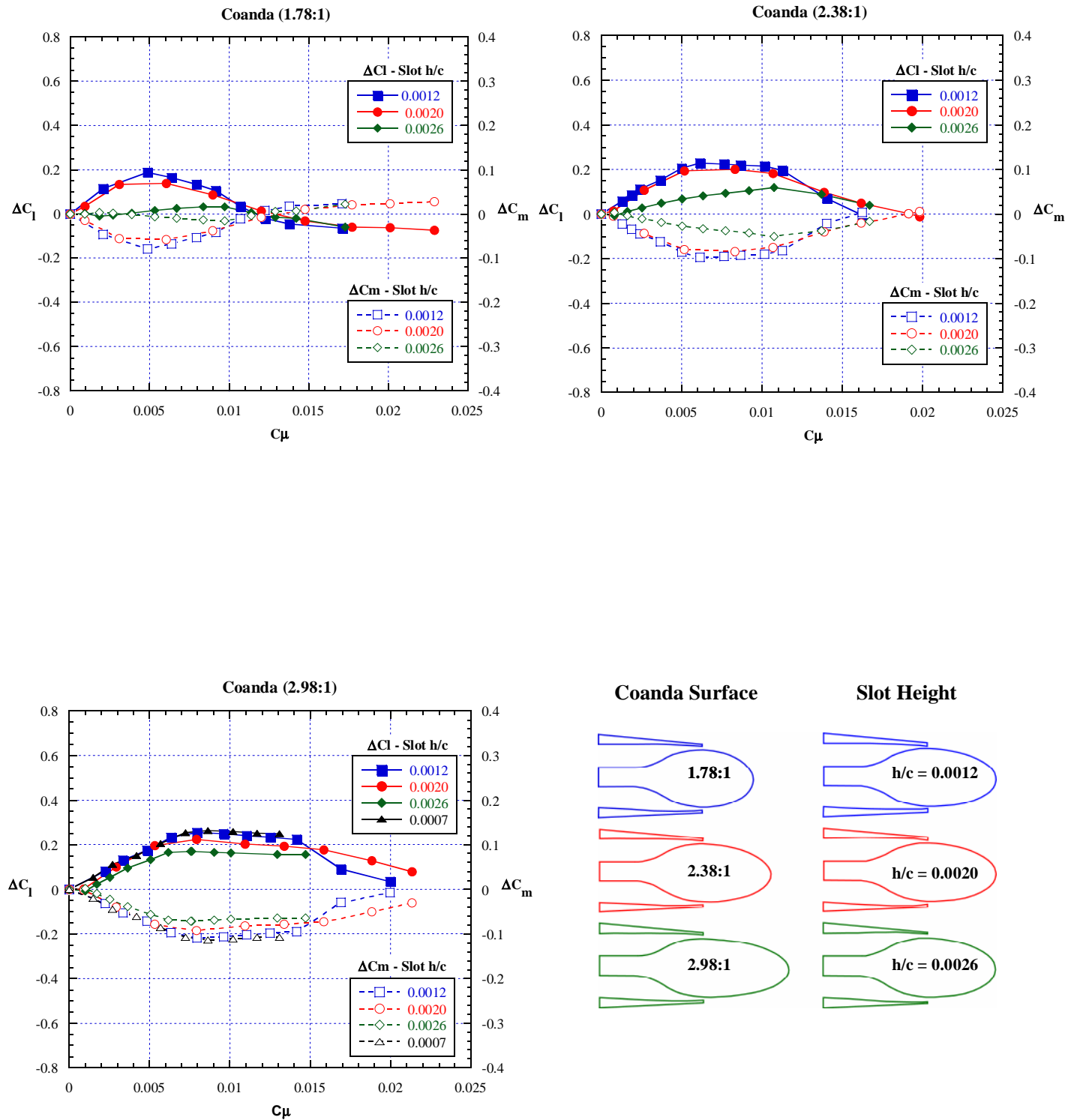


Figure 12 - Slot height effect, upper slot blowing, Mach = 0.8, $\alpha = +3^\circ$.

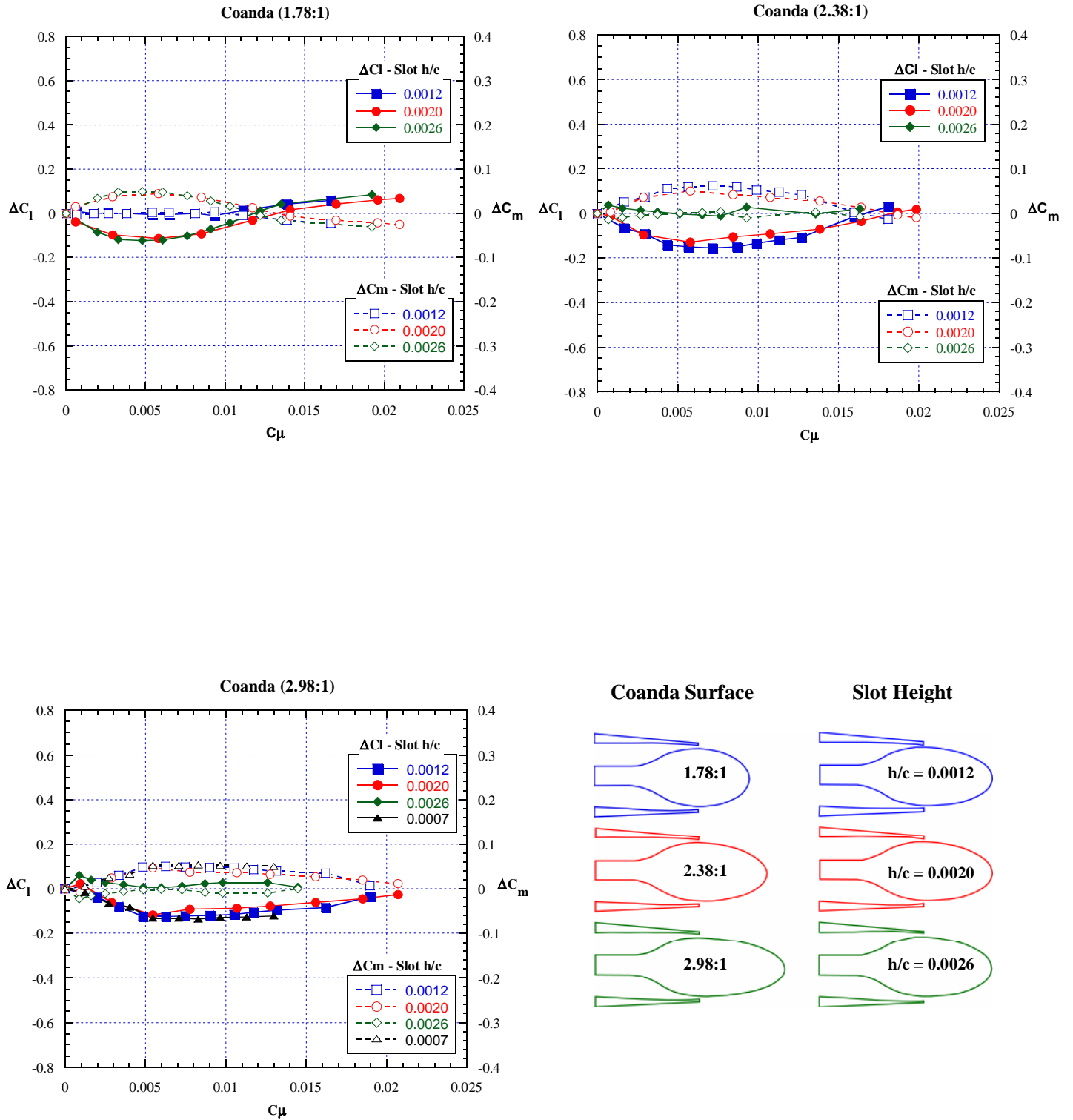


Figure 13 - Slot height effect, lower slot blowing, Mach = 0.8, $\alpha = +3^\circ$.

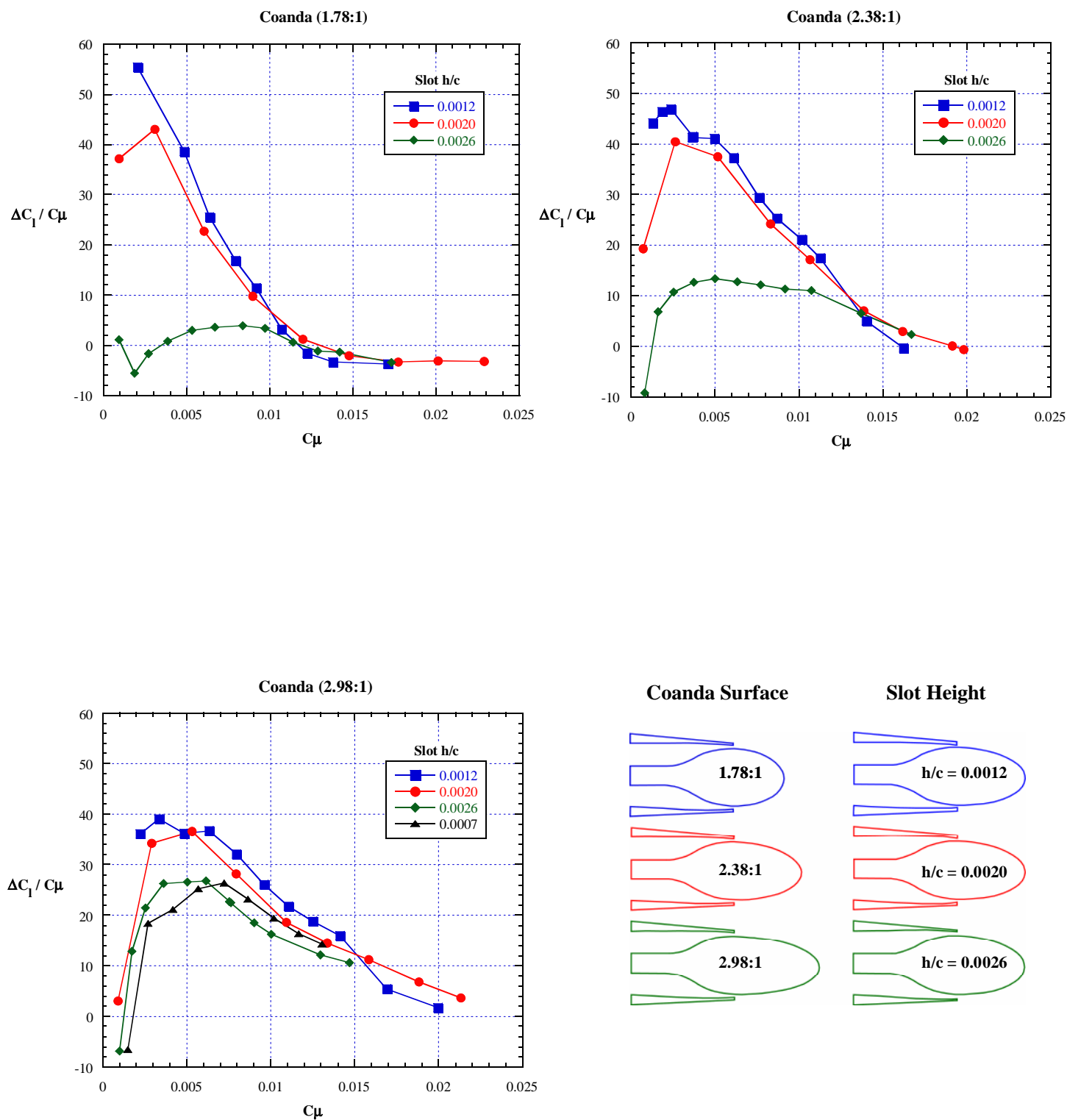


Figure 14 - Lift augmentation, slot height effect, upper slot blowing, Mach = 0.8, $\alpha = +3^\circ$.

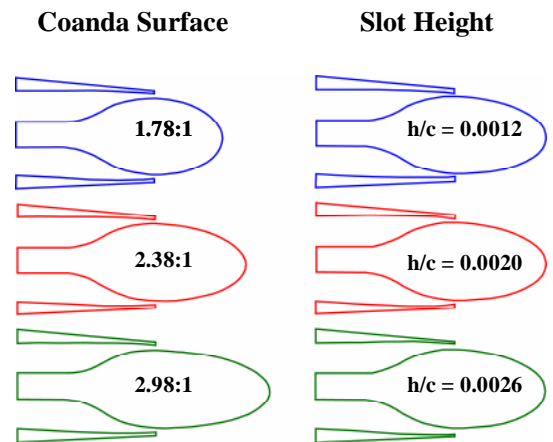
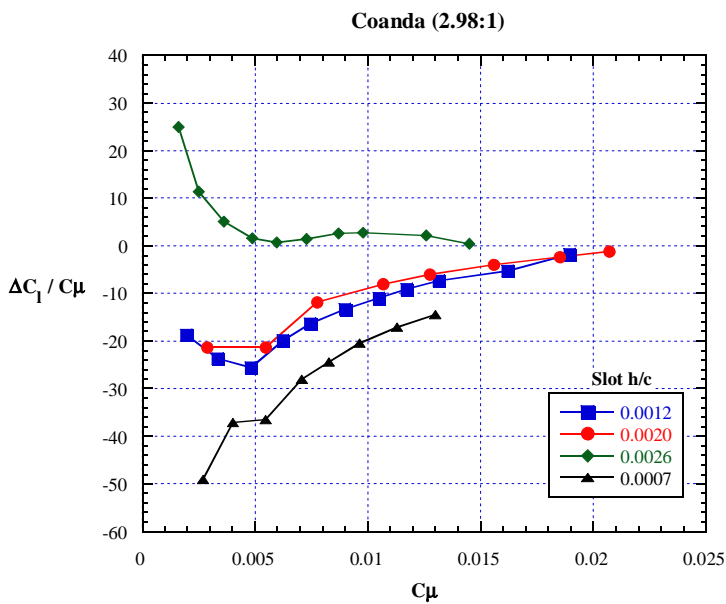
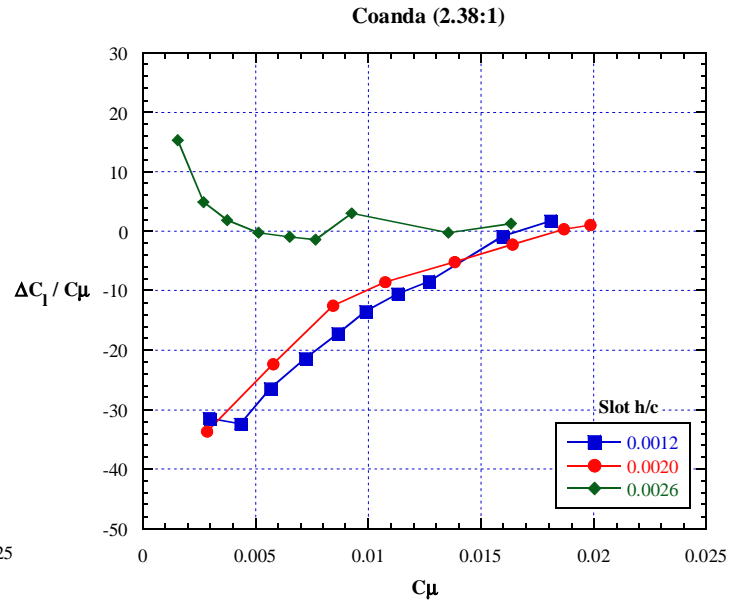
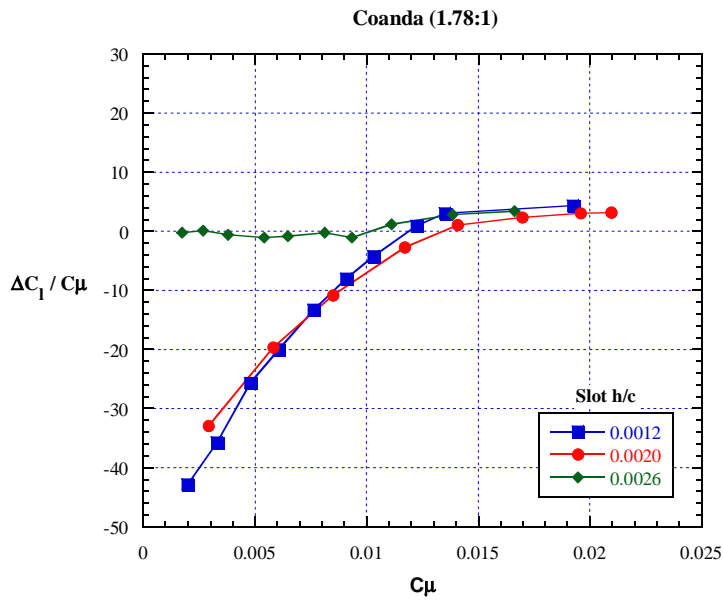


Figure 15 - Lift augmentation, slot height effect, lower slot blowing, Mach = 0.8, $\alpha = +3^\circ$.

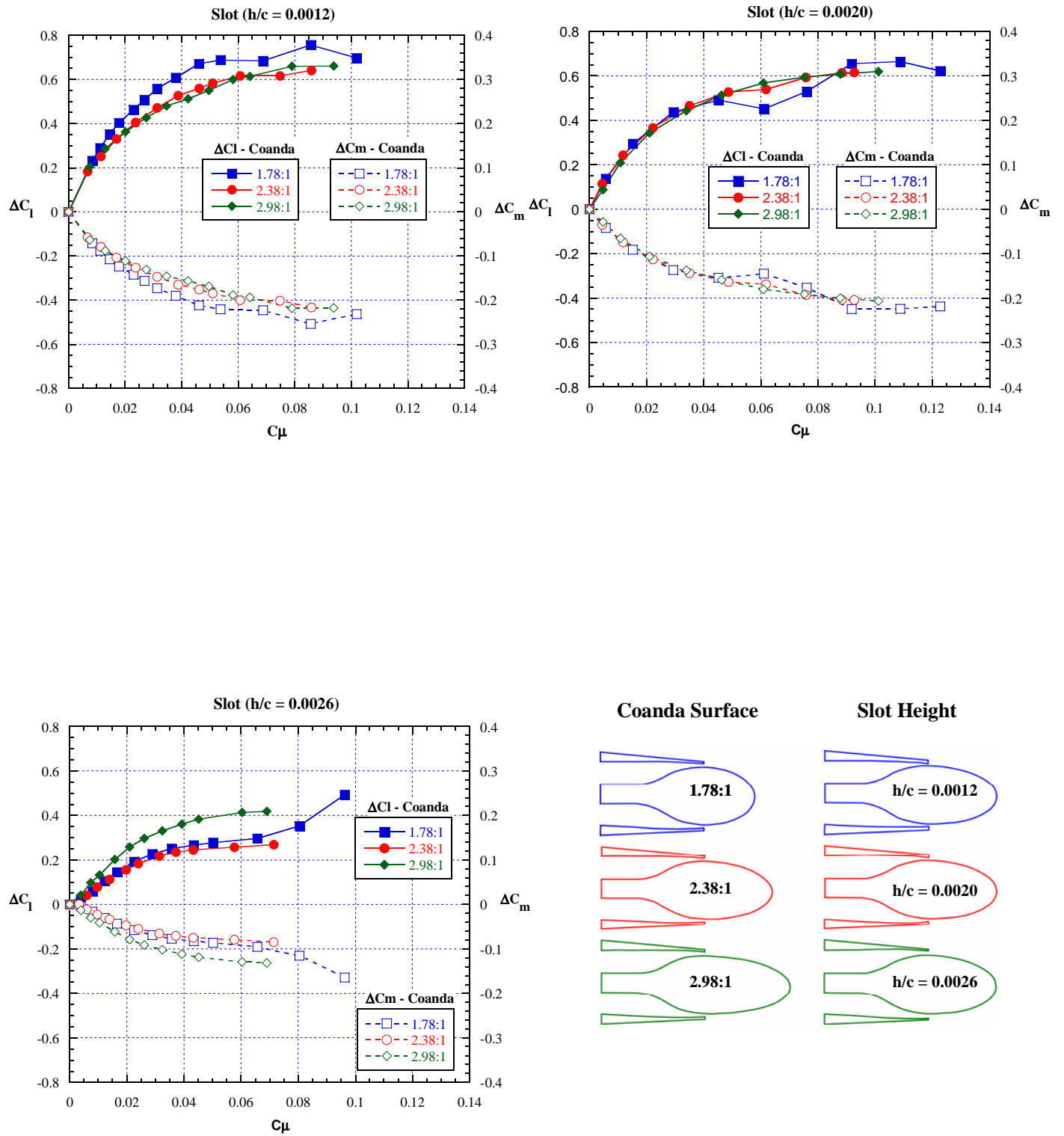


Figure 16 - Coanda surface effect, upper slot blowing, Mach = 0.3, $\alpha = +6^\circ$.

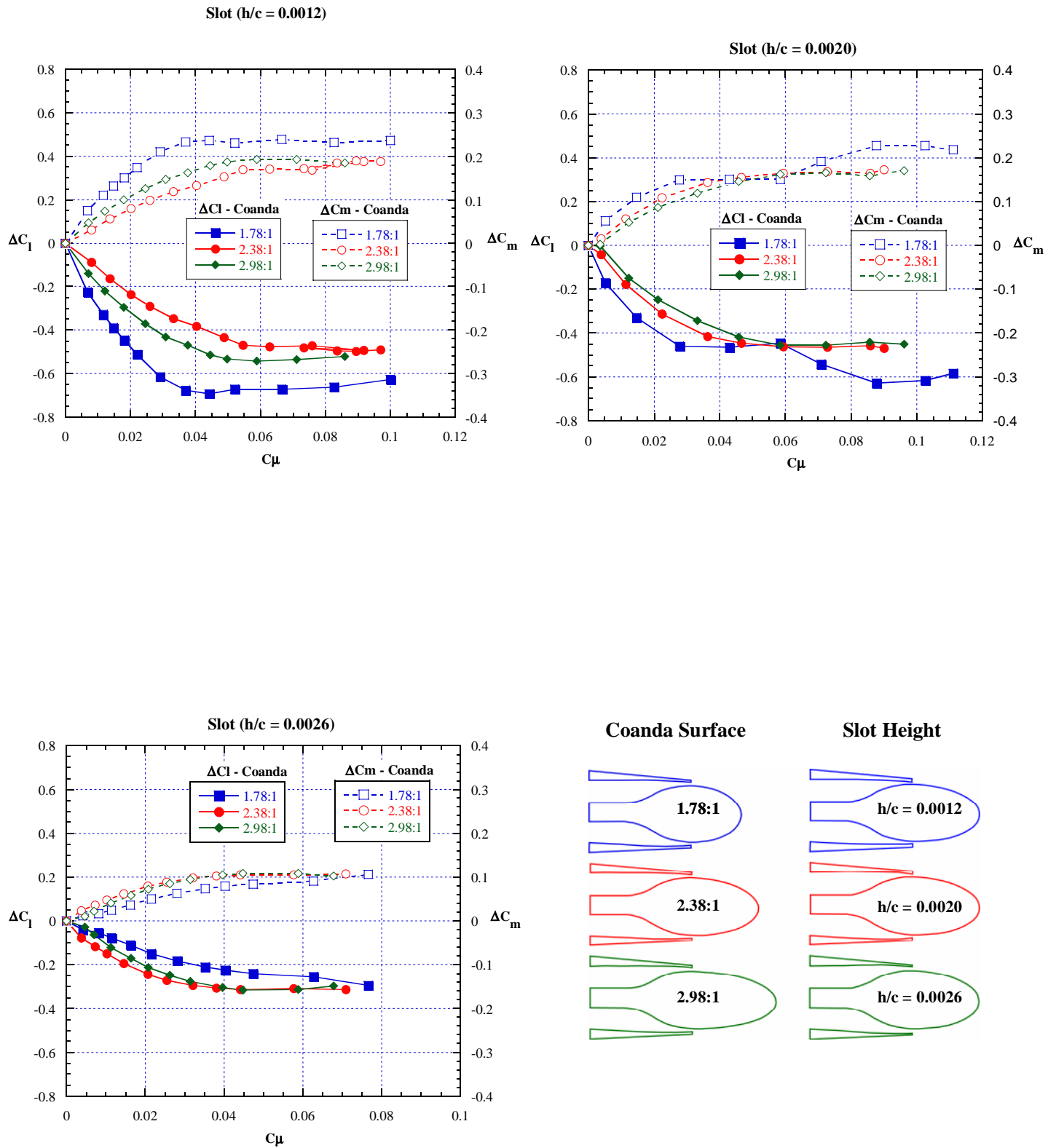


Figure 17 - Coanda surface effect, lower slot blowing, Mach = 0.3, $\alpha = +6^\circ$.

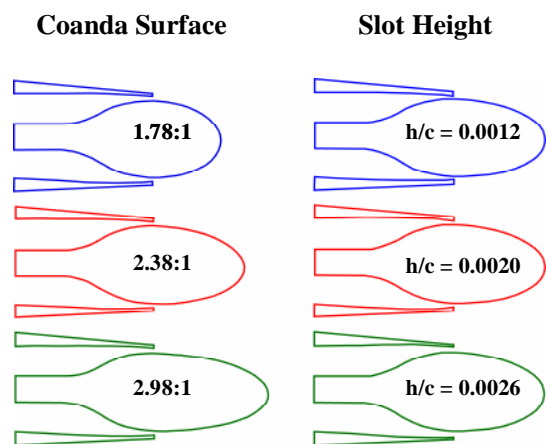
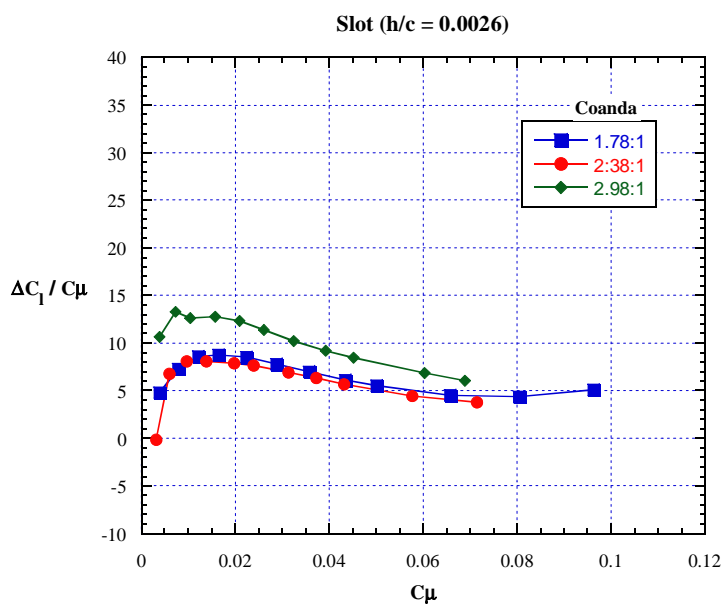
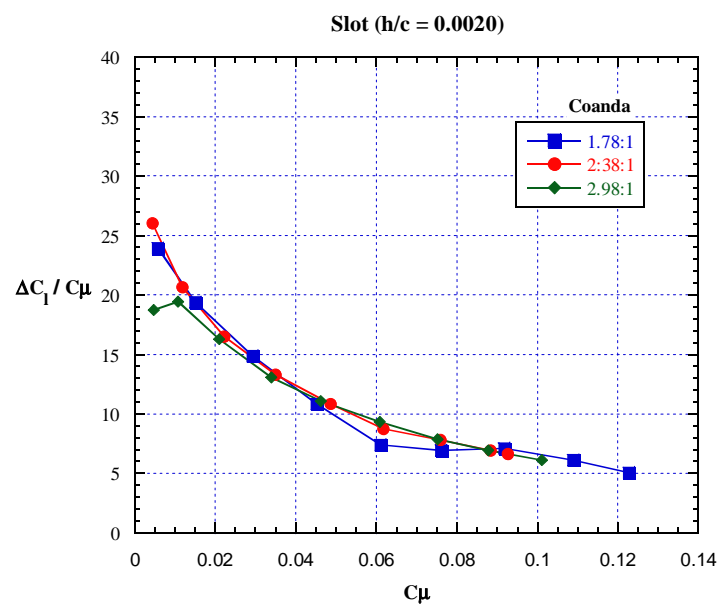
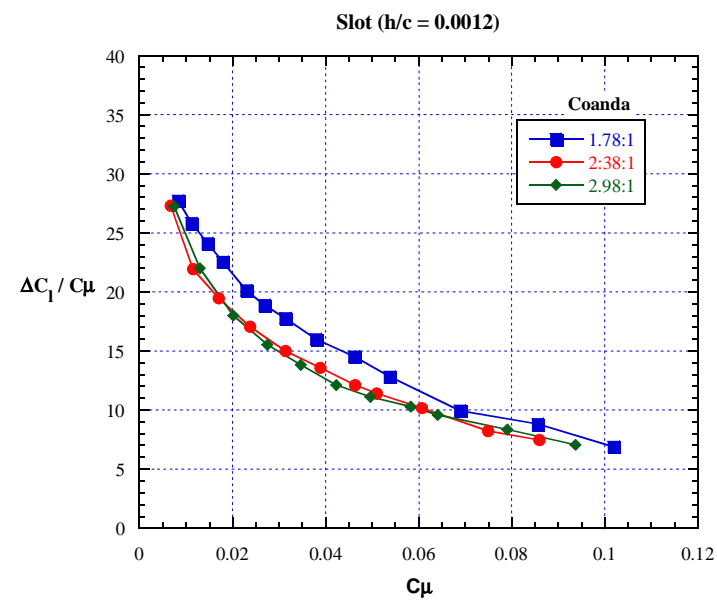


Figure 18 - Lift Augmentation, Coanda surface effect, upper slot blowing, Mach = 0.3, $\alpha = +6^\circ$.

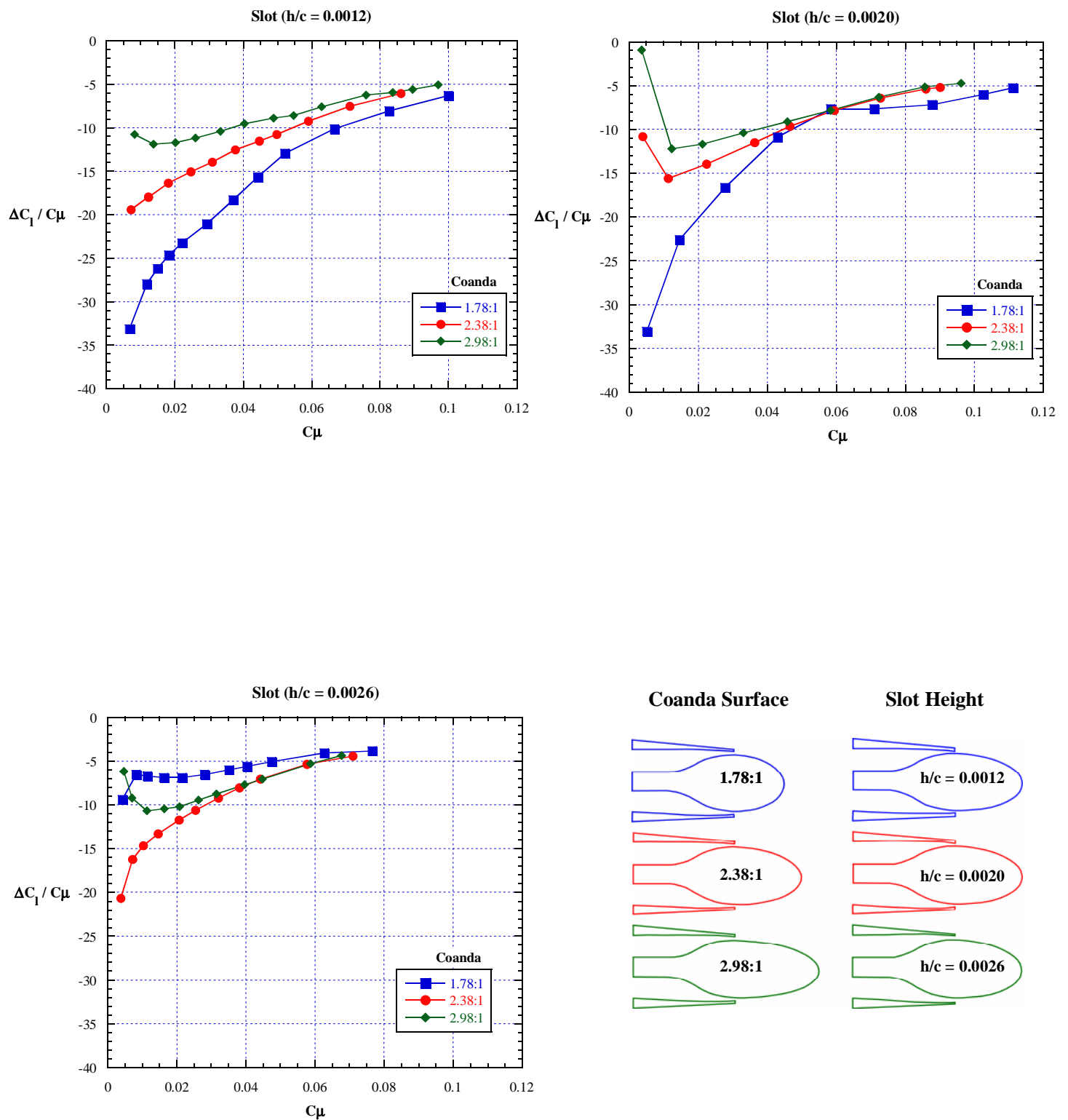


Figure 19 - Lift Augmentation, Coanda surface effect, lower slot blowing, Mach = 0.3, $\alpha = +6^\circ$.

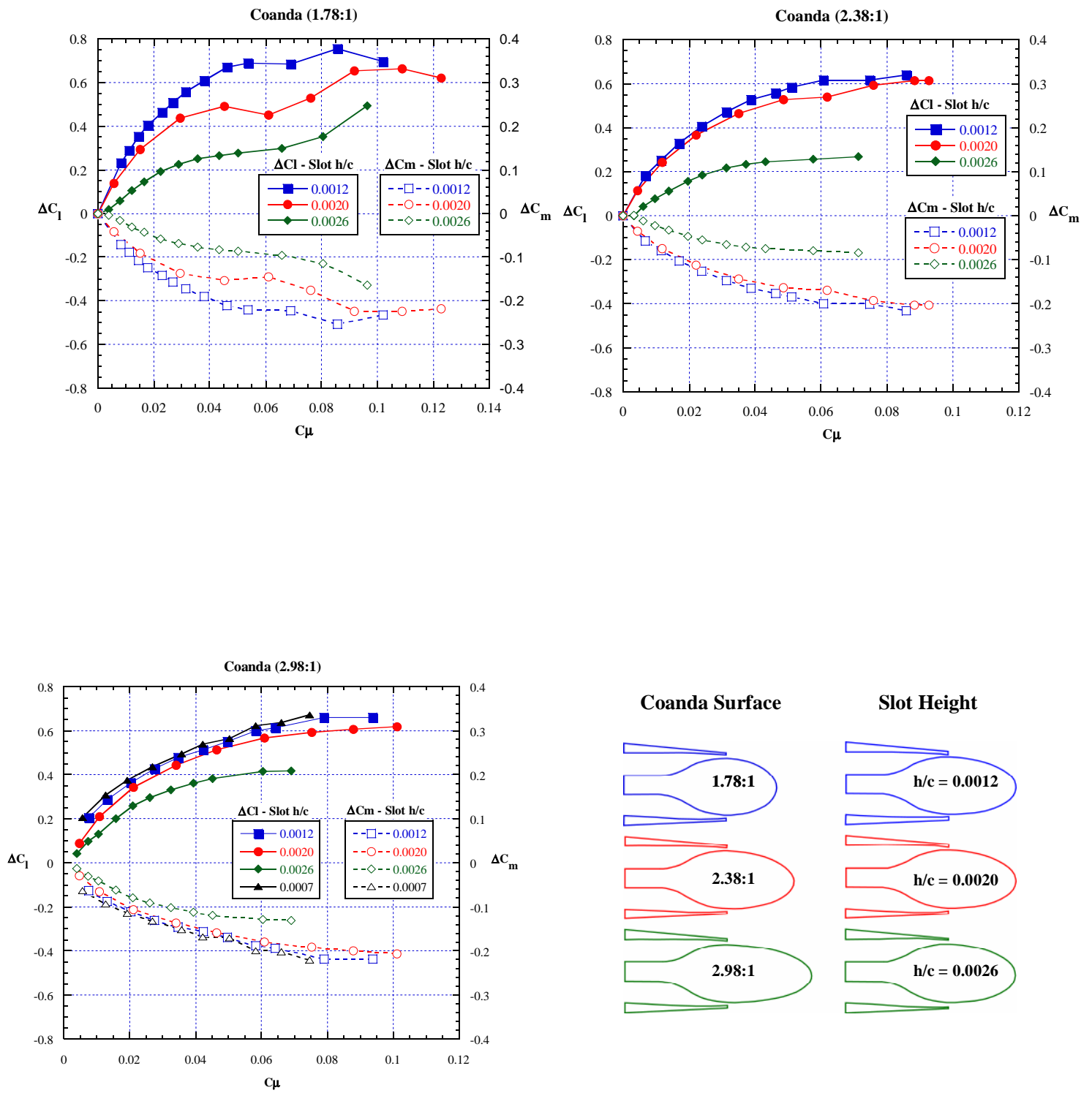


Figure 20 - Slot height effect, upper slot blowing, Mach = 0.3, $\alpha = +6^\circ$.

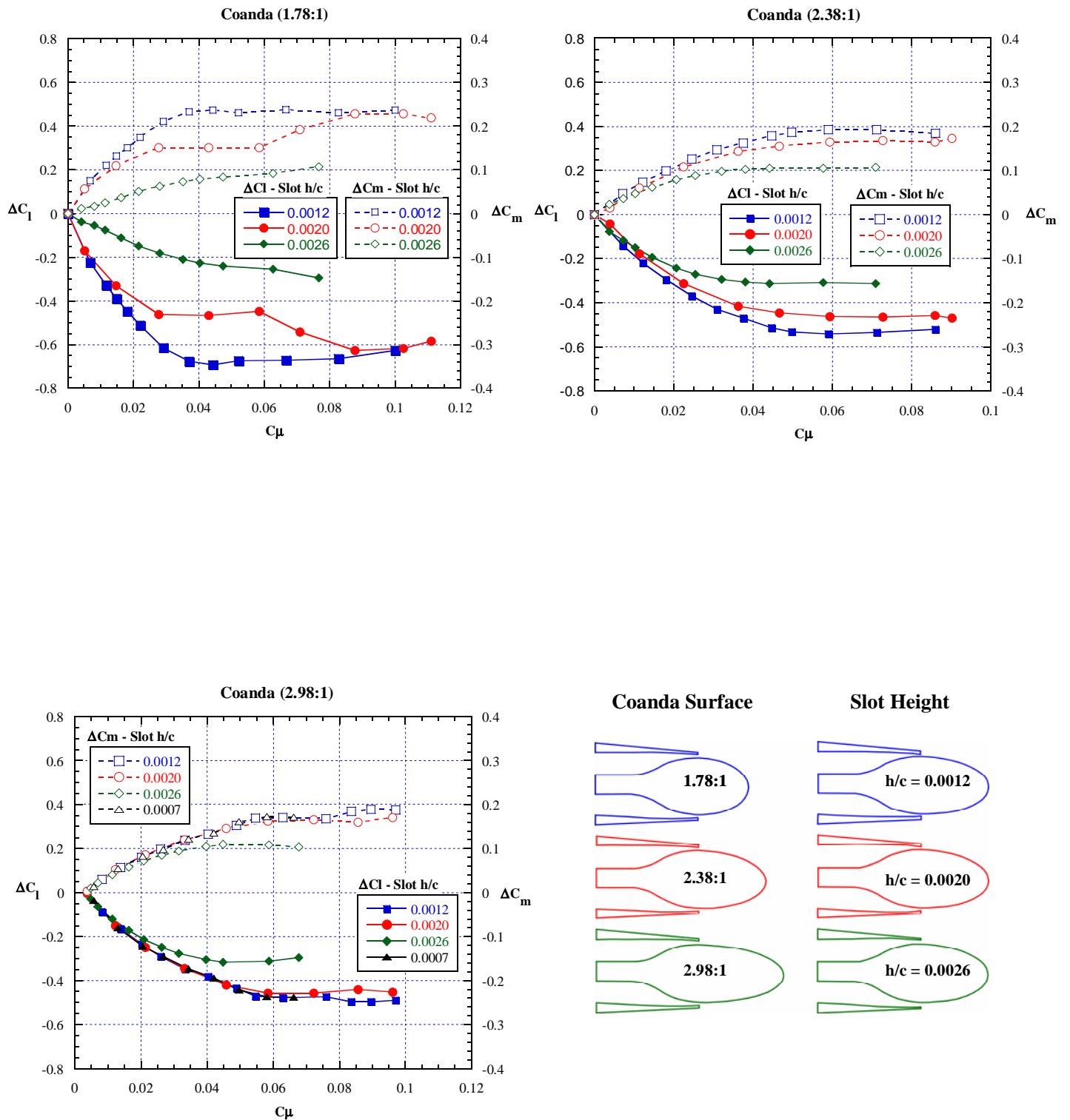


Figure 21 - Slot height effect, lower slot blowing, Mach = 0.3, $\alpha = +6^\circ$.

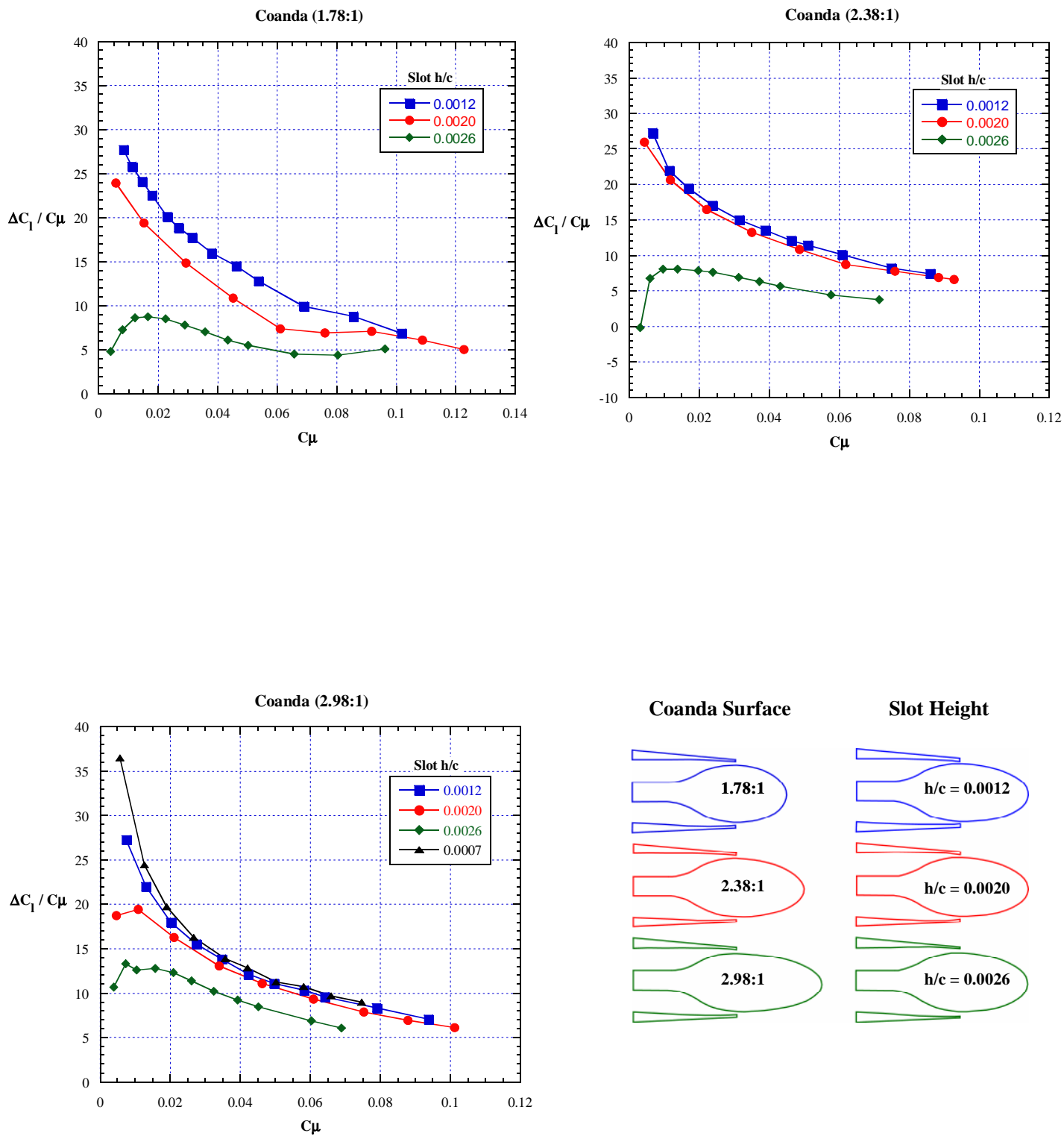


Figure 22 - Lift Augmentation, slot height effect, upper slot blowing, Mach = 0.3, $\alpha = +6^\circ$.

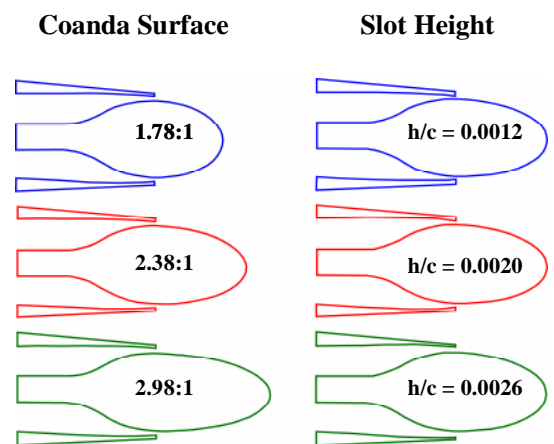
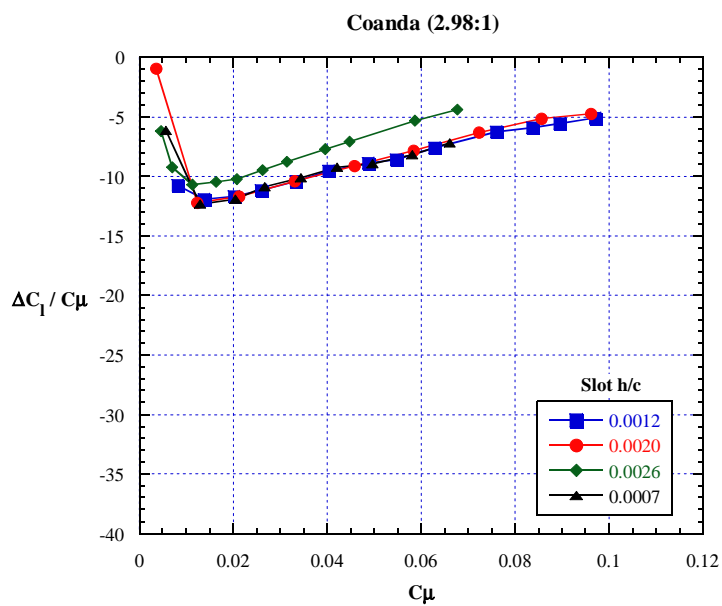
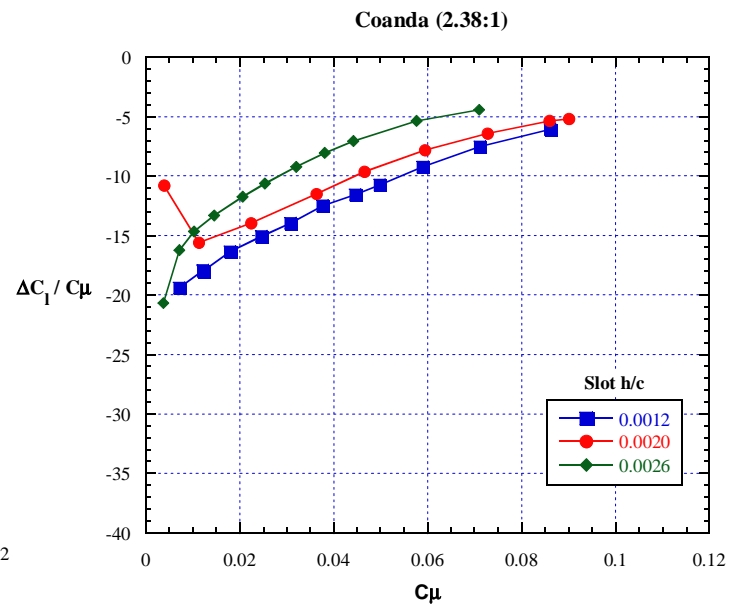
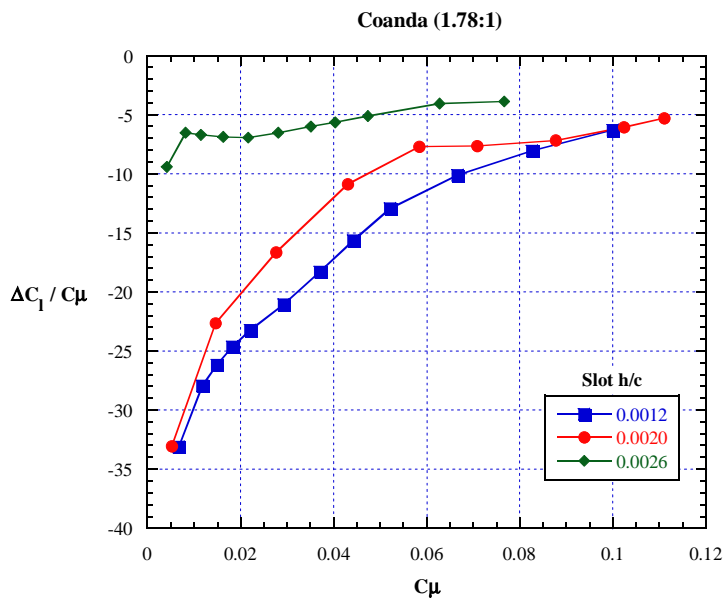


Figure 23 - Lift Augmentation, slot height effect, lower slot blowing, Mach = 0.3, $\alpha = +6^\circ$.

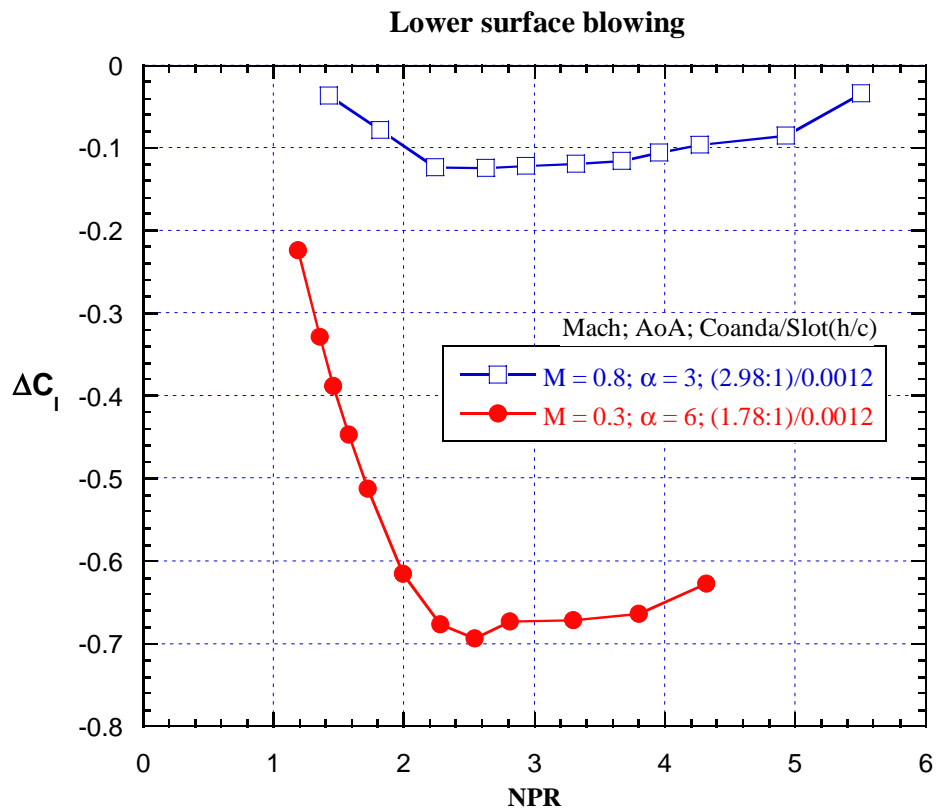
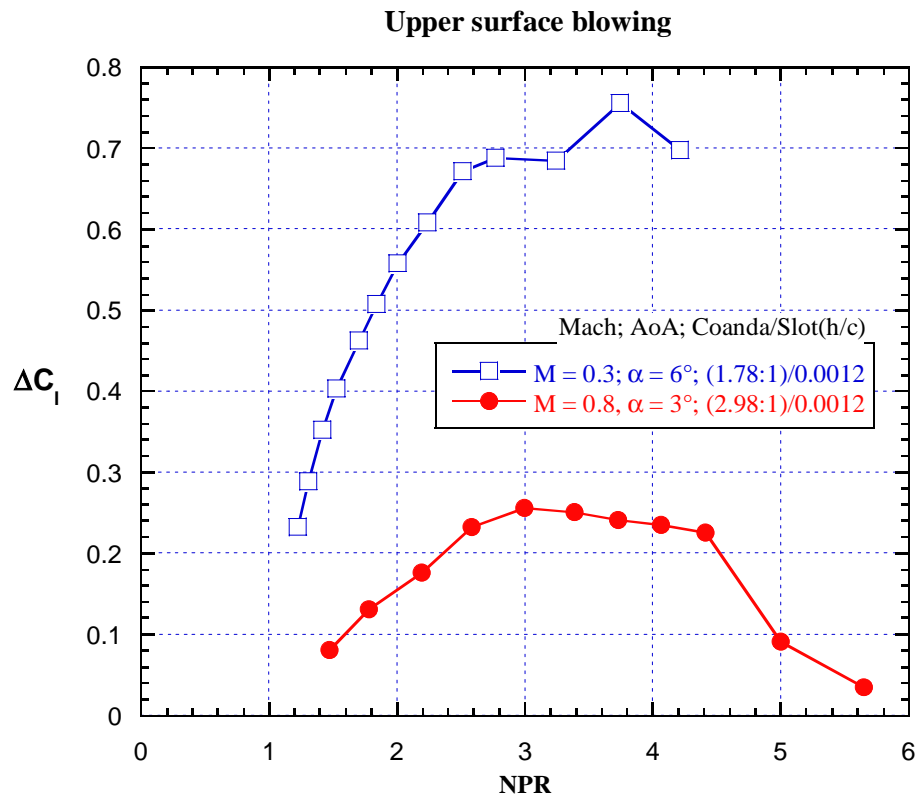
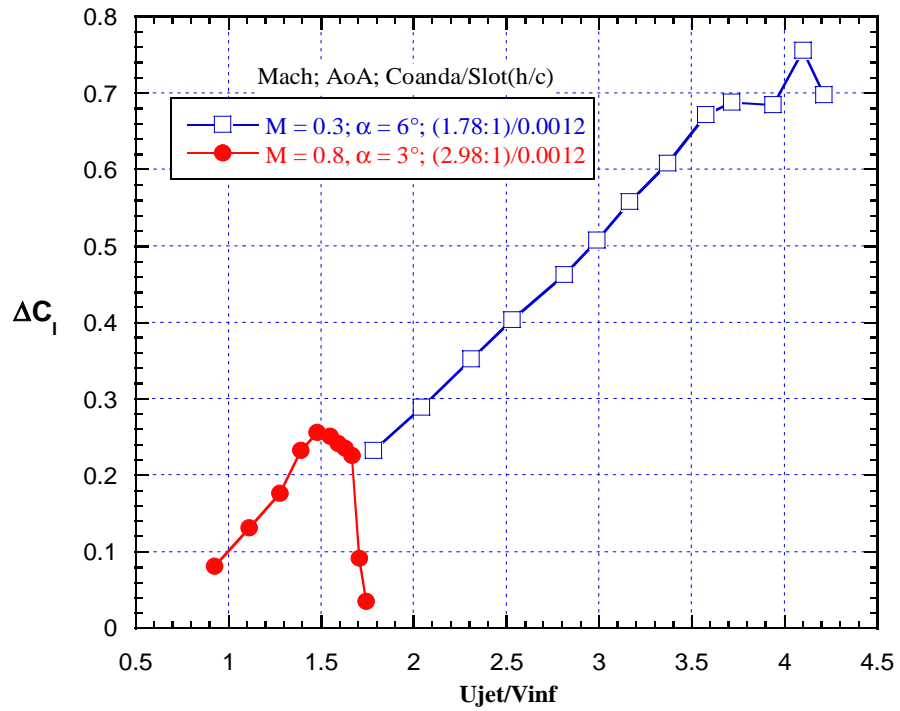


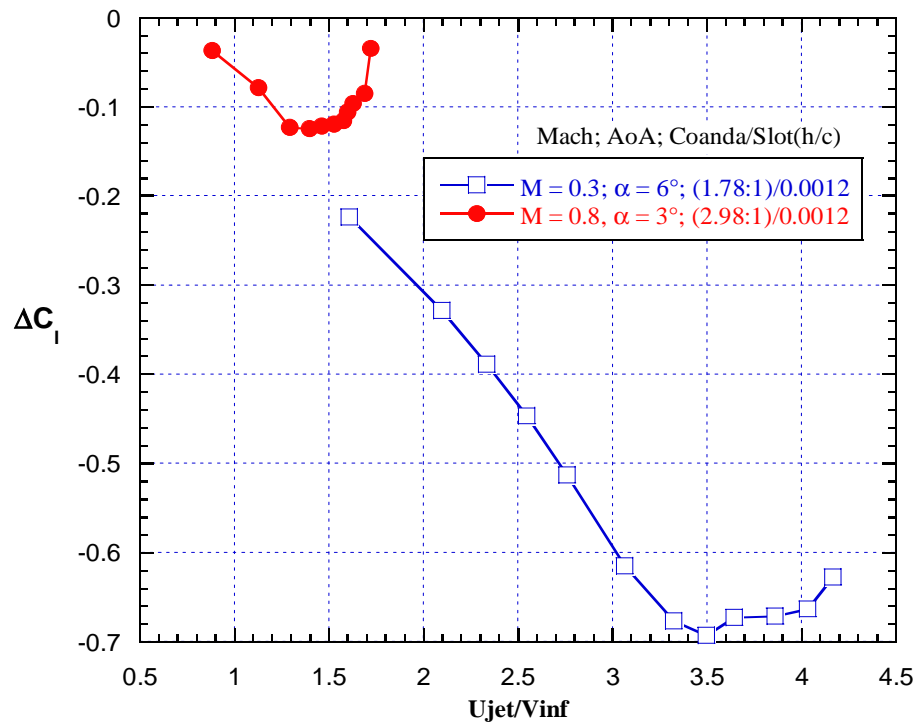
Figure 24 - Nozzle pressure ratio versus ΔC_l , upper and lower slot blowing.

Upper surface blowing



(a)

Lower surface blowing



(b)

Figure 25 - Velocity ratio versus ΔC_l , upper and lower slot blowing.

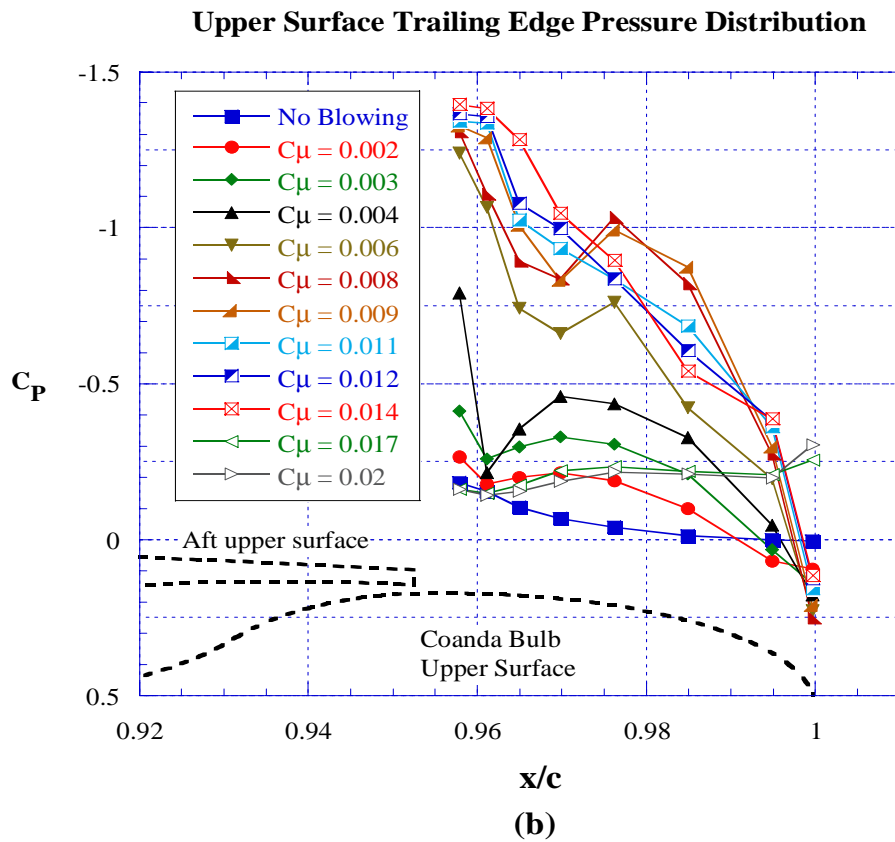
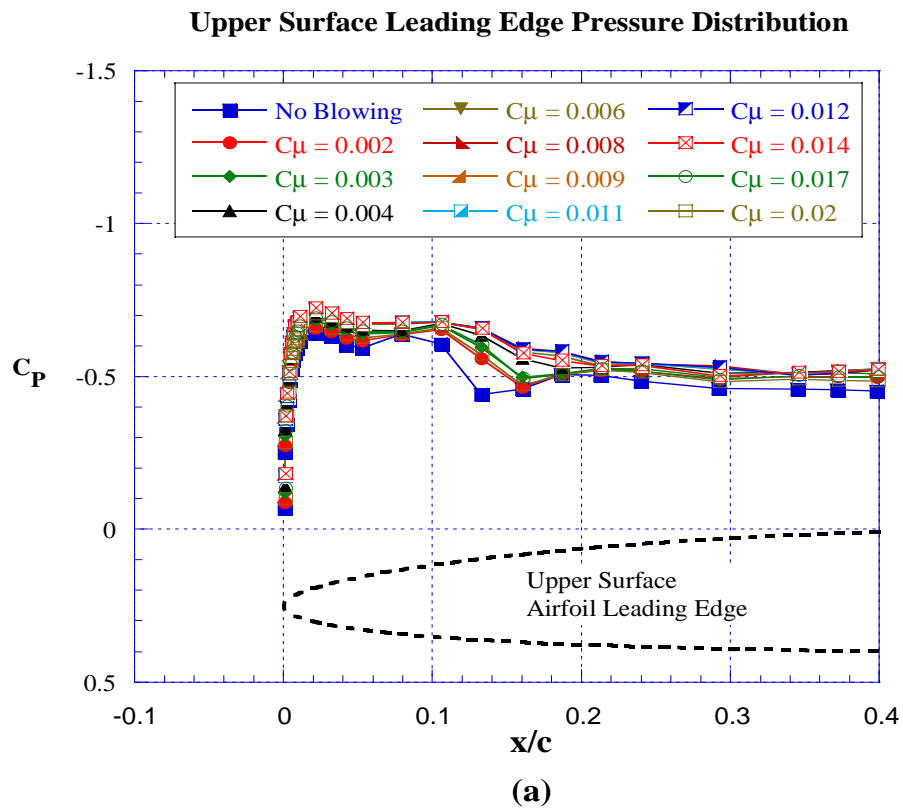


Figure 26 - Pressure distribution, C_μ effect, upper slot blowing;
Coanda (2.98:1), slot ($h/c = 0.0012$), Mach = 0.8, $\alpha = +3^\circ$.

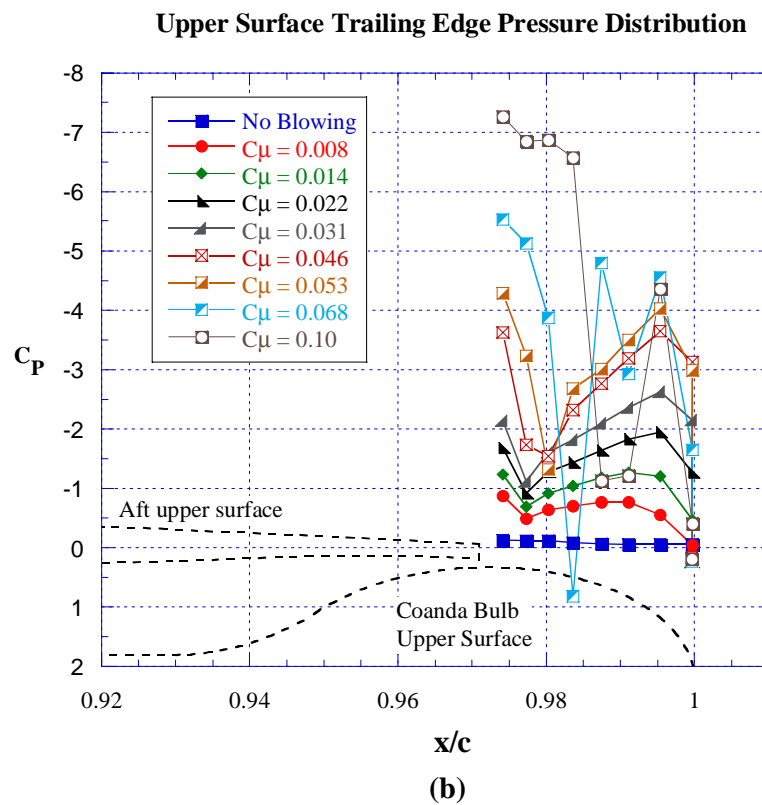
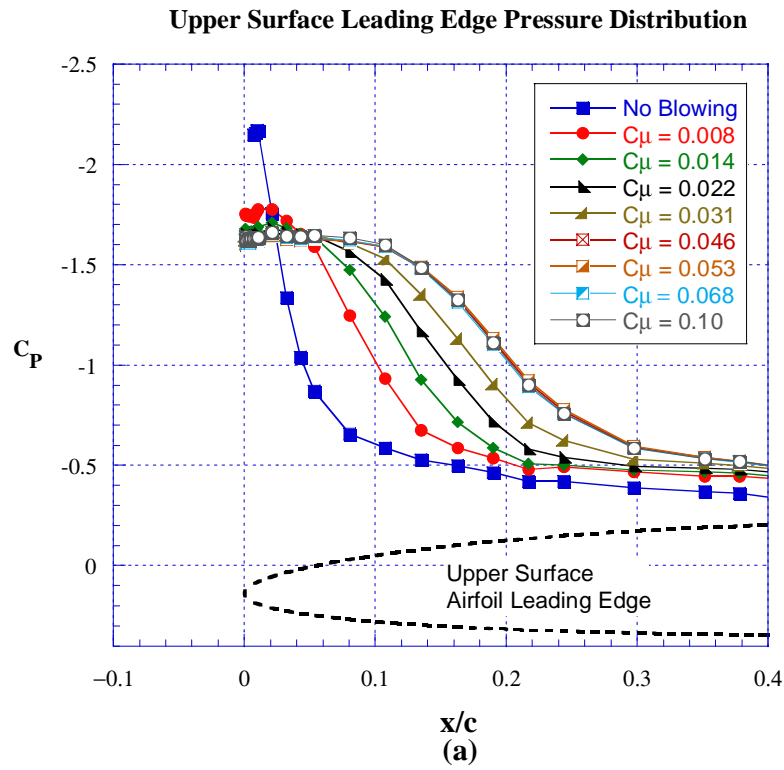


Figure 27 - Pressure distribution, C_μ effect, upper slot blowing;
Coanda (1.78:1), slot ($h/c = 0.0012$), Mach = 0.3, $\alpha = +6^\circ$.

Experimental Investigation of a Morphing Nacelle Ducted Fan

Shayne A. Kondor

Georgia Tech Research Institute
Smyrna, GA

shayne.kondor@grti.gatech.edu

Mark Moore

NASA Langley Research Center
Hampton, VA

mark.d.moore@nasa.gov

Abstract

The application of Circulation Control to the nacelle of a shrouded fan is proposed as a means to enhance off-design performance of the shrouded fan. Typically, a fixed geometry shroud is efficient at a single operating condition. Modifying circulation about the fixed geometry is proposed as a means to virtually *morph* the shroud without moving surfaces. This approach will enhance off-design-point performance with minimal complexity, weight, and cost. Termed the *Morphing Nacelle*, this concept provides an attractive propulsion option for Vertical Take-off and Landing (VTOL) aircraft, such conceptual Personal Air Vehicle (PAV) configurations proposed by NASA. An experimental proof of concept investigation of the *Morphing Nacelle* is detailed in this paper.

A powered model shrouded fan model was constructed with Circulation Control (CC) devices integrated in the inlet and exit of the nacelle. Both CC devices consisted of an annular jet slot directing a jet sheet tangent to a curved surface, generally described as a Coanda surface. The model shroud was tailored for axial flight, with a diffusing inlet, but was operated off-design condition as a static lifting fan. Thrust stand experiments were conducted to determine if the CC devices could effectively improve off-design performance of the shrouded fan. Additional tests were conducted to explore the effectiveness of the CC devices as a means to reduce peak static pressure on the ground below a lifting fan.

Experimental results showed that off-design static thrust performance of the model was improved when the CC devices were employed under certain conditions. The exhaust CC device alone, while effective in diffusing the fan exhaust and improving weight flow into shroud inlet, tended to diminish performance of the fan with increased CC jet momentum. The inlet CC device was effective at reattaching a normally stalled inlet flow condition, proving an effective means of enhancing performance. A more dramatic improvement in static thrust was obtained when the inlet and exit CC devices were operated in unison, but only over a limited range of CC jet momentums. Operating the nacelle inlet and exit CC devices together proved very effective in reducing peak ground plane static pressure, while maintaining static thrust. The Morphing Nacelle concept proved effective at enhancing off-design performance of the model; however, additional investigation is necessary to generalize the results

Background

Fan and Shroud Interactions

The shrouded (or ducted) fan presents a solution for efficient powered lift and forward flight propulsion of Vertical Take-Off and Landing (VTOL) aircraft configurations. The geometry of the shroud has a significant effect on the efficiency of the fan (or propeller) due to the mutual interaction of the shroud and fan. Shroud geometry affects the velocity and pressure at the propeller plane, while maintaining a finite loading out at the tips of the fan blades¹. With proper design consideration, performance and efficiency of the shrouded fan will exceed the performance of a similar open propeller configuration operating in the same freestream condition. However, the geometry of a shroud designed for maximum static thrust will differ significantly from a shroud designed the peak efficiency in axial translation. The sense of circulation (Γ) about an optimal shroud design reverses as the operating condition changes from static thrust generation to high-speed axial flight.

Ideally, the shroud of a static (lifting) fan features a generous bell-mouth inlet converging toward the exit nozzle (see Figure 1). Flow entering the inlet is accelerated into the fan by the sense circulation about the shroud (depicted by the yellow arrows), resulting in an overall increase in thrust (compared to an open propeller operating under the same conditions)¹, and a significant lifting pressure difference on the shroud. Accelerating shroud designs generally possess a negative camber line and thicker crosssections. While these designs are efficient at producing static thrust, they suffer significant drag penalties in axial flight; thus, are ineffective for axial flight.

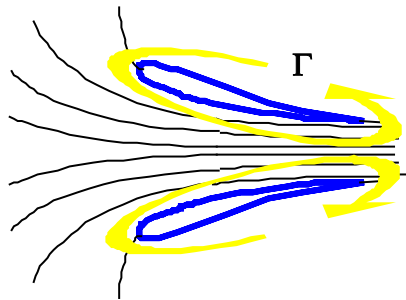


Figure 1.
Accelerating Shroud Circulation

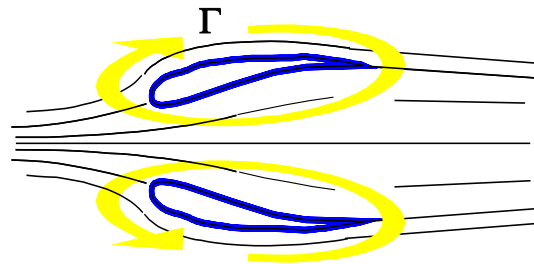


Figure 2.
Decelerating Shroud Circulation

Decelerating, or diffusing, shroud designs are generally employed for axial flight applications (see Figure 2). Decelerating shroud designs generally feature a positive camber line and a thin crosssection. In this case, circulation (Γ) on the shroud acts to decelerate the flow entering the inlet to below freestream speed. A net thrust is developed on the shroud as a result of the static pressure rise in the inlet, while the benefits of finite blade loading are realized at the propeller.

Proper shroud design for the intended operating condition will yield a net increase in performance over an open propeller of similar size.

The Morphing Nacelle Concept

The shroud geometries presented in Figures 1 & 2 are, of course, idealized cases where the camberline of the shroud is nearly a streamline in the flow. Neither design would work well in a real application that deviates from the ideal design conditions. However, a case can be made that actively modifying the circulation around the shroud may be a means to enhance effectiveness in off design operation. This can, of course, be achieved by complicated variable geometry inlets and nozzles, or alternately by applying means of circulation control to effectively *morph* a fixed geometry shroud.

The concept of modifying shroud circulation as a means to enhance propulsive performance was proposed by Morel & Lissaman² and investigated more recently by Heiges & Kondor³. The first approach sought to augment weight flow through the shrouded fan by injection of high momentum flow near the aft stagnation point of the shroud, effectively moving the upstream stagnation point, thus, affecting the entire flow field. Morel & Lissaman presented several theoretical models, treating the effect as a virtual diffuser at the fan exit; the shroud was treated as uncambered, vanishingly thin surface, with a pneumatic jet injected at an angle away from the exhaust at the shroud exit, similar to a jet flap. This jet was intended to entrain and turn the flow exhausting from the shroud, thus was termed a jet flap diffuser. The shroud and jet flap diffuser were modeled as a potential flow problem. This analysis predicted a net increase in static thrust and weight flow through the shroud, at a fixed power setting shared between the fan and the jet flap diffuser, and a propulsive efficiency gain due to an expanded wake stream tube. More recently, Heiges & Kondor developed a powered model to experimentally investigate the modification of circulation about a three dimensional shrouded fan as a means of generating control forces and moments. In the latter case, a tangent wall jet was directed over a curved surface at the shroud exit to form a Coanda surface, as shown in Figure 3. This approach was adapted from proven means of circulation control on wings⁴, and wrapped around the exit of an axisymmetric fan shroud. Tuft visualizations showed the approach to be effective in turning the efflux from the model, as well as generating significant sideforce when applied over a limited sector of the shroud exit.

Investigators in the NASA Personal Air Vehicle (PAV) program proposed the application of circulation control to a fixed geometry shroud as a means to optimize performance across a variety of flight conditions, without the weight penalty of variable geometry inlets and nozzles. This fan shroud concept was dubbed the *Circulation Control Morphing Nacelle*. In support of the PAV investigation, Georgia Tech Research Institute (GTRI) and M-Dot Aerospace developed a powered model shrouded fan with a *Circulation Control Morphing Nacelle*. Reconfigurable CC jet devices were integrated into the fan shroud inlet and nozzle exit, allowing for a variety of Morphing Nacelle approaches to be

investigated. The model was installed in the Model Test Facility thrust cell at Georgia Tech Research Institute in October 2002, and has been used in investigations of the morphing nacelle concept up to the present.

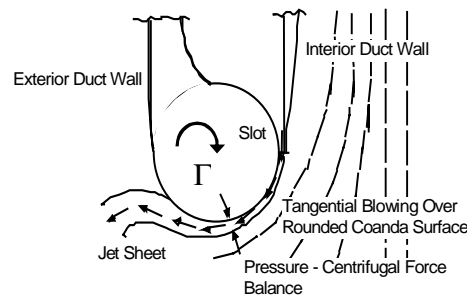


Figure 3. Section View Circulation Control Device Integrated at the Exit of an Axisymmetric Duct (adapted from Englar⁴).

Circulation Control Aerodynamics

The aerodynamic concept now known as Circulation Control (Figure 3 & Reference 4) is a means to directly enhance aerodynamic/hydrodynamic forces generated on a body of fixed geometry. The concept employs the injection of momentum into the flow field over a body in a manner that affects the entire flow field. As explained by Englar⁴ for a lifting body:

[typically] a tangential jet sheet exits over the curved trailing edge of the surface [often replacing a flap or control surface], and this curvature can turn through a full 180° or more. The jet remains attached to that curved surface because of a balance between the sub-ambient pressure in the jet sheet and the centrifugal force around the curvature. Initially, at very low blowing values, the jet entrains the boundary layer to prevent aft flow separation, and is thus a very effective boundary layer control (BLC). Eventually, as the jet continues to turn, a rise in the static pressure plus viscous shear stress and centrifugal force combine to separate the jet sheet, and a new stagnation point and streamline are formed on the lower surface. The large flow entrainment rate of the jet and the large deflection of the stagnation streamline produce a pneumatic camber, and thus pneumatic control of the airfoil's circulation and lift. Although it is a very effective BLC, the interest in this device comes from its ability to further augment the circulation and lift, and thus the name Circulation Control (CC).

Historically, the use of a jet over a segmented curved surface to entrain flow is attributed to Henri Coanda, and is often referred to as the *Coanda Effect*⁴. The curved, or turning surface, is similarly referred to as a *Coanda surface*.

The cost of affecting a change in circulation is generally related in terms of a ratio of the CC jet momentum to the momentum of the flow being affected. Mass flow (\dot{m}_{jet}) and jet speed (V_{jet}) are captured in a non-dimensional

Momentum Coefficient:
$$C_{\mu} = \frac{\dot{m}_{jet} V_{jet}}{QS} \quad (\text{eq. 1}),$$

where Q is the freestream dynamic pressure and S a reference area. It is obvious that this standard expression for C_{μ} is not suitable for a static application with zero freestream dynamic pressure. Therefore, a new static C_{μ} term was defined for static, propulsive applications such as the CC Morphing Nacelle⁵. The new nondimensional term is based on fan angular speed (N) and diameter (D) in the typical manner used to nondimensionalize propeller thrust as a Thrust

Coefficient C_{ts} ⁶:
$$C_{ts} = \frac{Thrust}{\rho_{\infty} N^2 D^4} \quad (\text{eq. 2}).$$

This definition of C_{ts} captures ambient conditions and the key fan design variables affecting the power required to impart a momentum change to the flow. Using the same denominator terms as eq. 2, a *static momentum coefficient*, $C_{\mu s}$,

is defined, similar to eq. 1 :
$$C_{\mu s} = \frac{\dot{m}_{jet} V_{jet}}{\rho_{\infty} N^2 D^4} \quad (\text{eq. 3}).$$

The ratio of $C_{\mu s}/C_t$ provides a metric of the relative power requirement for the CC jet compared to the fan.

Experimental Investigation

Experimental investigations of the CC Morphing Nacelle were conducted using a powered model fan with tangent jet devices integrated into the inlet and exhaust of the nacelle. The objective of the experimental investigation was to determine the effectiveness of Circulation Control as a means of enhancing off-design operation of a shrouded fan with fixed nacelle geometry. A shrouded fan designed for high speed axial flight (similar to the configuration in Figure 2) was tested in static operation as a free jet and in proximity of a ground plane (in order to simulate lifting fan operation). Combinations of CC jet parameters were tested to modify circulation at inlet and exhaust of the nacelle, in the sense depicted in Figure 1. Simultaneous measurements of aggregate thrust, nacelle weight flow (\dot{m}_g), and ground plane pressure profile were made at a variety of CC jet strengths - while operating a fixed fan speed.

Figure 4 depicts the powered CC Morphing Nacelle model in crosssection. The powered fan core is depicted, along with the integral CC jet devices. The curved arrows at the nacelle inlet and exit depict jet sheet direction, and sense of added circulation.

The powered model was based on a Tech Development Inc., Model 457 pneumatic tip drive fan. The fan core consisted of a single stage turbine with 16

fixed pitch blades, on a shaft supported by fixed pitch stators. High pressure air was exhausted over a segregated outer ring of turbine blades to power the fan core; drive air exhausted through the power turbine mixed with the fan core flow before exiting the nacelle. Pressure ratios up to 1.20 were feasible, operating the fan up to 35,000 RPM.

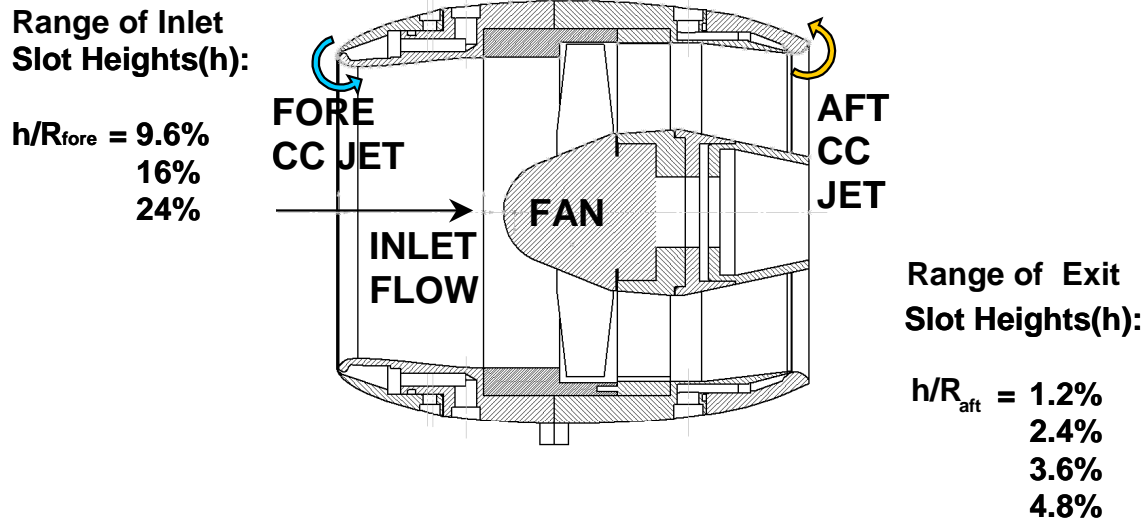


Figure 4. Section View of the Morphing Circulation Control Model

The nacelle design featured a decelerating inlet and parallel exhaust nozzle, providing a nacelle section camber similar to the decelerating shroud design depicted in Figure 2. A tangent jet slot was integrated at the leading edge of the nacelle section, intended to accelerate a jet around the maximum curvature of the inlet (the inlet wall acting as the Coanda surface). The inner and outer surfaces of the nacelle inlet were configured as concentric sections. The outer surface section could be positioned axially (along the fan centerline) to set the CC jet slot height; jet slot height (h) to inlet radius (R_{fore}) ratios could be varied from 9.6% to 24%. Similarly, a tangent jet slot was placed at the nacelle exit to generate a *virtual* diffuser effect. The jet sheet was directed over a quarter-round ring concentric to the nacelle exit. The curved surface formed by the ring was intended to act as a Coanda surface, promoting diffusion of the fan exhaust by low pressure generated over the surface. Interchangeable diffuser rings allowed for variations in CC jet slot height (h/R_{ait}) from 1.2%-4.8%, as indicated in Figure 4. The exit Coanda surface radius was double the inlet radius, accounting the difference in nondimensional slot heights.

Variations in CC jet slot height were tested in the steps listed in Figure 4. Likewise, jet momentum coefficient $C_{\mu s}$ was varied from zero up to values where fan performance was significantly diminished. The test matrix consisted of the permutations of jet slot configurations, tested over a range of $C_{\mu s}$ values for the inlet and exit jets, alone and in combination.

The powered fan model fan model (shown in the photo, Figure 5) was installed in the GTRI Model Test Facility Thrust Cell (as shown in Figure 6). The model was centered in the live, instrumented section of the thrust cell, providing

real time thrust measurement by electric load cells. Pneumatic supply lines were fed into the live balance frame (yellow frame in the photo, Figure 6) from a trapeze in order to minimize tear effects on thrust readings. Piloted pressure regulators mounted to the live balance controlled CC jet weight flow. Critical flow nozzles were placed downstream of the regulators to meter weight flow through the CC jet slots, also serving prevent communication between the fore and aft jet slots through the supply lines.

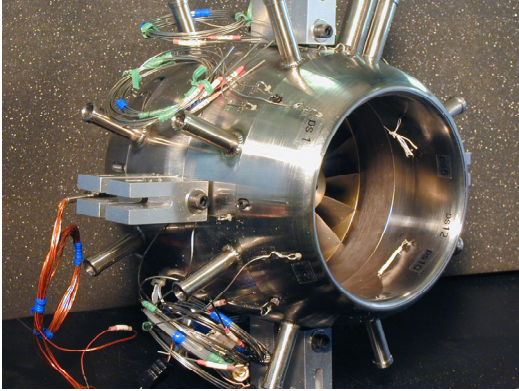


Figure 5. Powered Fan Model



Figure 6. Thrust Cell Installation

Regulating air weight flow to the outer ring of the turbine controlled fan speed; drive air pressure was regulated by feedback control to maintain constant speed.

Angular speed sensors on the fan shaft and total pressure probes downstream of the stators determined fan operating conditions. Pressure ratio (PR) was determined as the ratio of the total pressure behind the fan to ambient total pressure. Total pressure behind the fan was determined by averaging the samples from a five probe total pressure rake located immediately downstream of the stator vanes.

Jet speed at each CC jet slot (V_j) was estimated from measurements of slot plenum stagnation conditions and discharge static pressure. The jet was assumed to function as an ideal isentropic converging nozzle discharging into the nacelle flow, following the relation:

$$V_j = \sqrt{2RT_d \left(\frac{\gamma}{\gamma-1} \right) \left[1 - \frac{P_\infty}{P_d} \right]^{\left(\frac{\gamma-1}{\gamma} \right)}} \quad (\text{eq. 4})$$

Where R is the gas constant, and γ the ratio of specific heats for air; P_d and T_d are the stagnation pressure and temperature in the jet slot supply plenum. According to Englar⁷, it is accepted practice in the application of Circulation Control to assume that the flow is discharging from the nozzle to freestream static pressure P_∞ . However, in static operation, the freestream assumption does not properly capture the discharge conditions into the nacelle flow, at either the

inlet or exit jet slot. Thus, static pressures were sampled in the internal nacelle flow to determine discharge conditions at the inlet (fore) jet slot and just upstream of the exit (aft) jet slot.

Experimental Results

Baseline Ducted Fan Performance

Baseline performance of the shrouded fan model was established by operating the fan as a free jet, out of ground effect (OGE), without CC slot weight flow. This mode of operation established the baseline performance across the operational range of fan pressure ratios (PR). Thrust was measured as fan drive air momentum (thus input power) was varied. When thrust data was nondimensionalized to a *Static Thrust Coefficient* C_{ts} (ref. eq. 2), the fan and nacelle combination was found to have a consistent baseline $C_{ts} = 0.068$ over an operating range of $1.05 < PR < 1.15$ (ref. Figure 7). The relationship of fan speed to pressure ratio was essentially linear over the same range of PR , and was directly related to drive air momentum (input power).

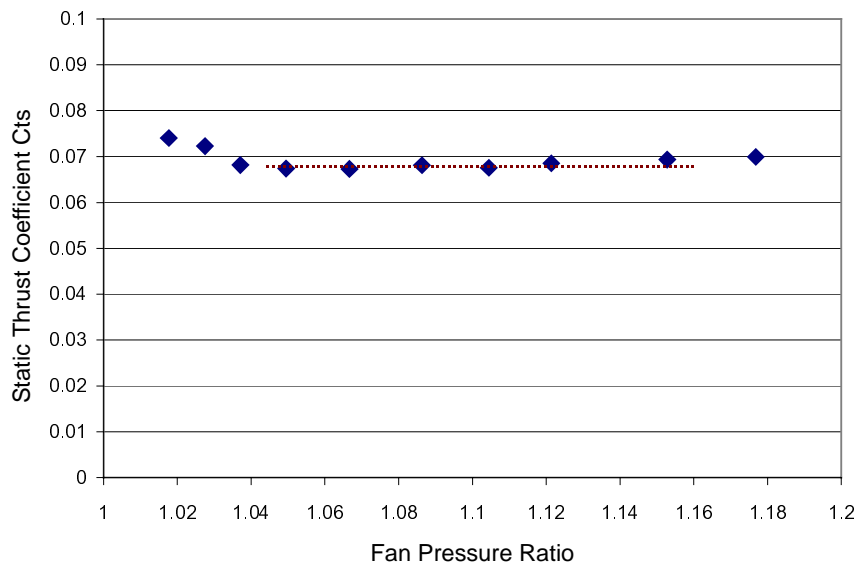


Figure 7. Static Thrust Performance of Baseline Fan-Nacelle Installation

Performance of the CC Morphing Nacelle – Free Jet

Nacelle Exit Circulation Control

The *Morphing Nacelle* was first tested in a free jet condition, the ground plane was removed from the thrust cell to provide an unobstructed path for the

fan's exhaust wake. An operating condition of $PR=1.10$ was selected as the starting point for sweeps of fore and aft CC jet momentum (values of $C_{\mu s}$).

Static operation tests were first conducted with only the exhaust CC jet active, sweeping jet strength over a range of $0 \leq C_{\mu s \text{ aft}} \leq 0.008$. Four jet slot heights were employed for this set of tests, as illustrated in Figure 4, while the turning surface radius and angle remained constant. The effect of applying CC at the fan exit proved to have a detrimental effect on overall static thrust performance, as shown in Figure 8. Modest gains in C_{ts} were obtained at values of $C_{\mu s \text{ aft}} < 0.002$, and only with the smaller jet gap heights h/R_{aft} of 1.2% and 2.4%. With increased CC jet momentum, $C_{\mu s \text{ aft}} > 0.002$, C_{ts} was generally diminished; little influence of jet slot height was noted. The weight flow into the nacelle inlet is shown in Figure 9. Weight flow was noted to rise with increasing $C_{\mu s \text{ aft}}$ up to $C_{\mu s \text{ aft}} = 0.004$, beyond which weight flow remained essentially constant. The increased weight flow indicated an increase in circulation in the sense depicted in Figure 1. An improvement in fan thrust would be expected with the increased weight flow into the nacelle inlet; however, it is thought that suction generated on the exit Coanda surface acted to reduce the overall thrust. A slight deficit in inlet weight flow is noted where the larger jet slot heights (3.6% & 4.8%) are employed. This weight flow deficit indicates that the thicker, slower jet sheets are not as effective at changing nacelle circulation as the faster thinner jet sheets.

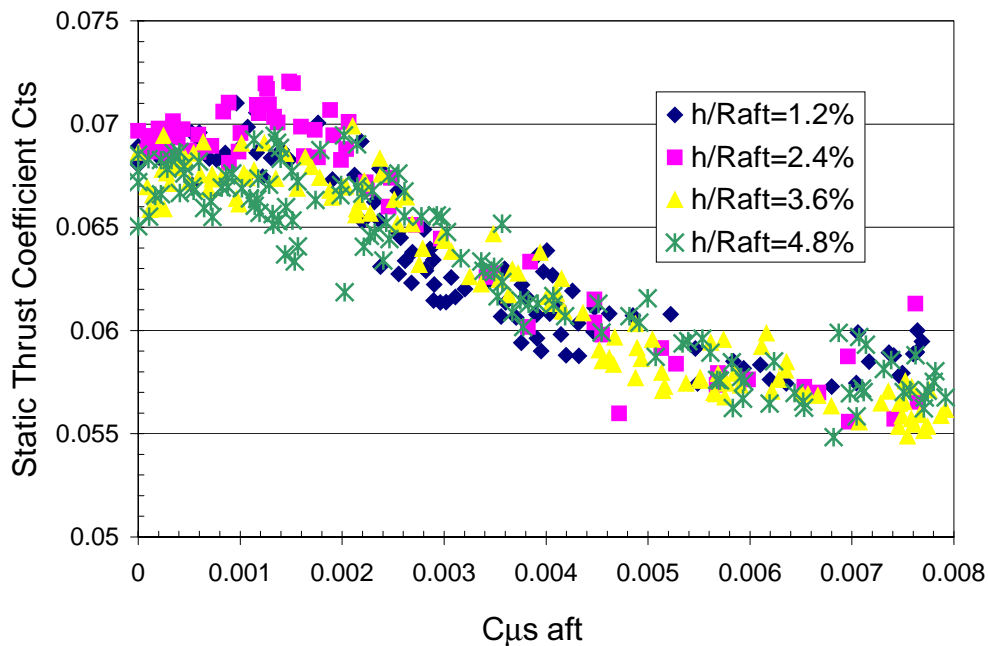


Figure 8. Static Thrust Performance with Exhaust CC Jet Active
Fan Speed 25 KRPM

Due to a lack of pressure instrumentation on the exit Coanda surface, the degree to which suction on the Coanda surface reduces the overall thrust could not be determined.

The measured fan pressure ratio remained essentially constant with variation of $C_{\mu s \text{ aft}}$, indicating that flow through the fan and stators was not detrimentally affected by the exit CC jet. Moreover, the fan speed, and fan input power setting, remained nearly constant over the range of $C_{\mu s \text{ aft}}$. Slight variations in fan speed and pressure ratio, from test point to test point, were accounted for by the nondimensional presentation of thrust as C_{ts} .

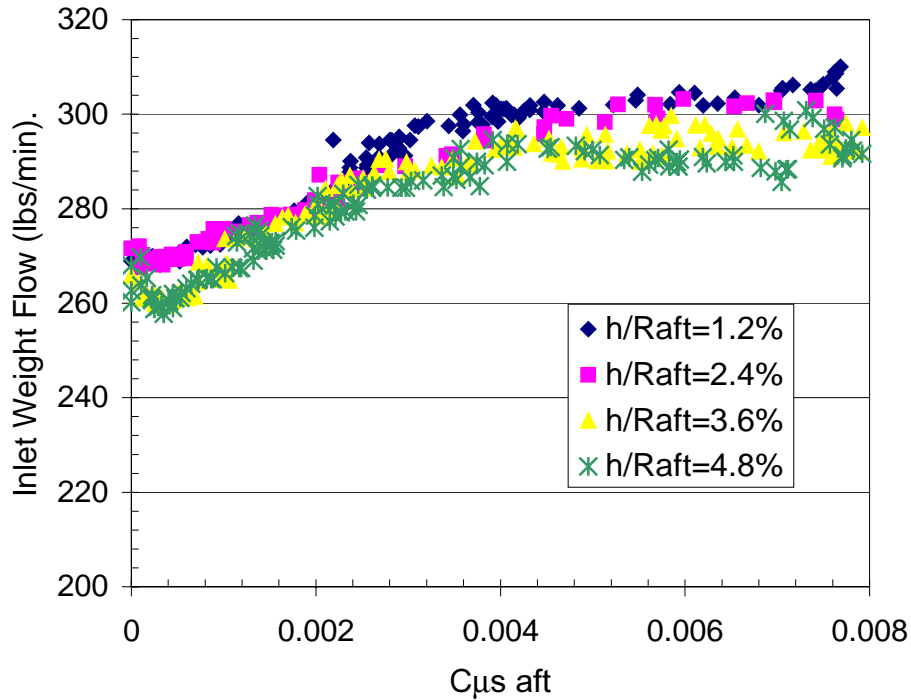


Figure 9. Nacelle Inlet Weight Flow with Exhaust CC Jet Active
Fan Speed 25 KRPM

The effect of the exit CC device on the fan efflux was explored with tuft grid visualization. The photographs in Figure 10 a, b, & c show the jet efflux from the nacelle exit at three values of $C_{\mu s \text{ aft}}$ (a false color image is presented to enhance contrast of the flow and tuft grid against the background). Tufts were placed in streamwise intervals of 1/2 of the nacelle exit diameter. The first case is the baseline jet with no CC active, showing a wake with a clear potential core, and little spreading is evident out to 3 diameters. The second and third cases reveal the effect of increasing the value of $C_{\mu s \text{ aft}}$. The application of the exit CC jet promotes a rapid spreading of the wake, and increased mixing. At very high jet strength, shown in Figure 10c, the potential core is lost by 1 dia. from the nacelle exit. This effect on the fan efflux indicates that a strong suction is generated on the Coanda surface.

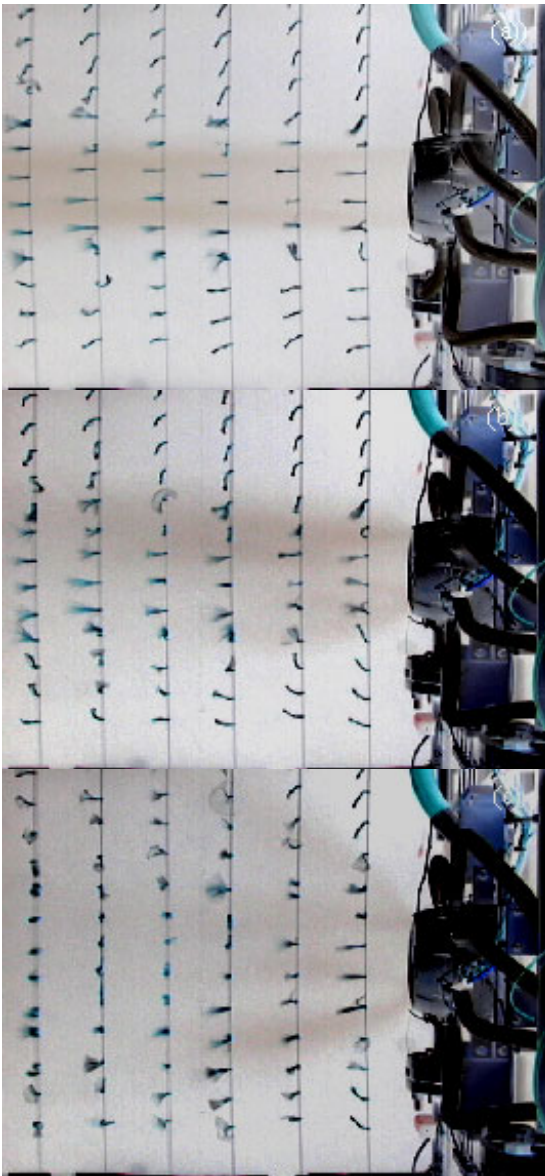


Figure 10 (a).

Fan Exhaust Flow Visualization with
 $C_{\mu s \text{ aft}} = 0$

Figure 10 (b).

Fan Exhaust Flow Visualization with
 $C_{\mu s \text{ aft}} = 0.007$

Figure 10 (a).

Fan Exhaust Flow Visualization with
 $C_{\mu s \text{ aft}} > 0.007$

Nacelle Inlet Circulation Control

The next series of test points investigated the effect of applying CC at the nacelle inlet. Three inlet CC jet slot heights were tested, as detailed in figure 4. Indicated fan pressure ratio (PR) was found to vary as $C_{\mu s \text{ fore}}$ varied, indicating a change in fan operating condition with $C_{\mu s \text{ fore}}$. Holding constant fan PR would have required constant changes in fan power input and speed. However, the fan speed remained essentially constant at a constant power setting, despite increasing jet strength; thus, it was elected to hold fan speed constant during sweeps of $C_{\mu s \text{ fore}}$.

The variation of C_{ts} with $C_{\mu s \text{ fore}}$ is presented in Figure 11. A strong coupling was noted between the jet slot height and peak improvement in static thrust (C_{ts}); the smallest jet slot opening generally produced the maximum increase in static thrust for a given value of $C_{\mu s \text{ fore}}$. A peak gain of nearly 30% in

C_{ts} , over the baseline values, was obtained with the smallest slot height ($h/R_{fore} = 9.6\%$) at $C_{\mu s fore} = 0.004$. At this slot height C_{ts} abruptly dropped once $C_{\mu s fore}$ increased beyond 0.006, indicating an abrupt change in inlet flow conditions, possibly a forced separation of inlet flow.

For any value of $C_{\mu s fore}$ jet speed over the Coanda surface is greater using a smaller slot. The faster jet will generate a lower pressure over the Coanda surface, but may not be remain attached around the sharp curvature of the nacelle's inlet. Slower, thicker jet sheets associated with the larger jet gaps will generate less suction on the leading edge, explaining the reduced performance noted with the larger jet slots. However these jets can remain attached at higher $C_{\mu s fore}$, alleviating the abrupt drop in performance note with the smallest jet slot.

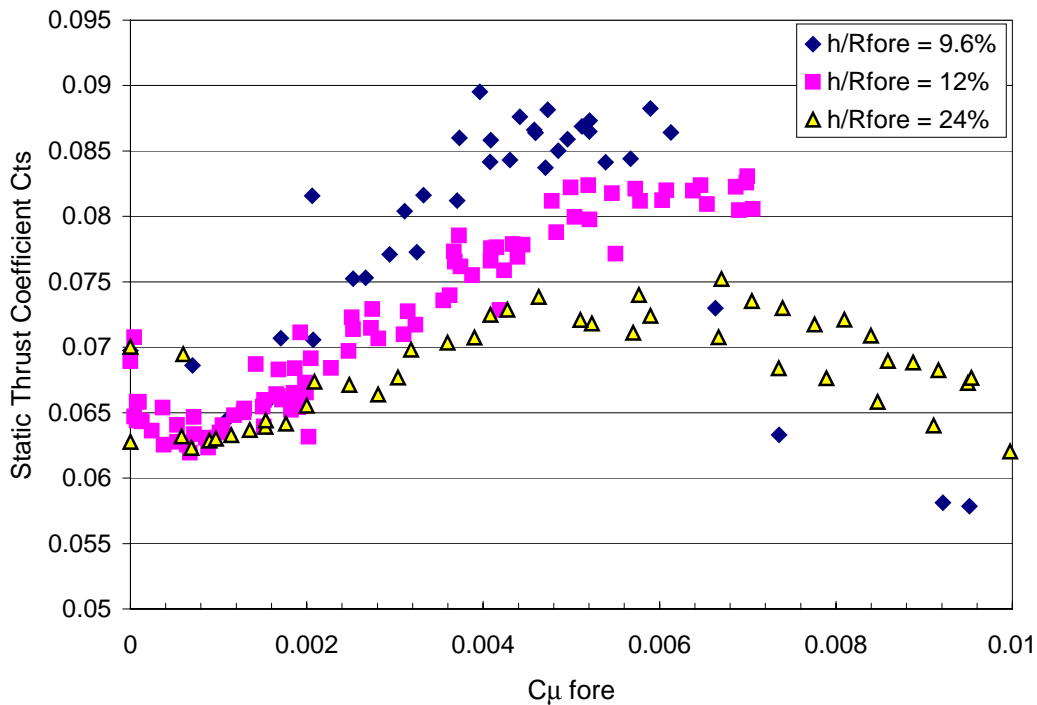


Figure 11. Static Thrust Performance with Inlet CC Jet Active

Improvements in C_{ts} for $C_{\mu s fore} > 0.002$ may be attributed to two sources: attachment of separated flow in the inlet, and suction generated in about the inlet lip (Coanda) surface by the acceleration of the jet around the inlet radius. An initial dip in C_{ts} is noted in the range of $0 < C_{\mu s fore} < 0.002$, for all slot heights. In this range inlet flow is separated, as shown by the tuft and oil flow visualizations in Figure 12 a. As $C_{\mu s fore}$ is increased the inlet flow attaches and C_{ts} subsequently rises, as does the inlet weight flow (ref. Figure 14). The attached inlet condition, with the inlet CC jet active, is shown in Figure 12 b.



Figure 12 (a). Inlet Flow $C_{\mu, \text{fore}} = 0$



Figure 12 (b). Inlet Flow $C_{\mu, \text{fore}} = 0.004$

Pressure instrumentation around the nacelle inlet was insufficient to verify the degree to which increased suction in the inlet contributed to the static thrust gains.

Combinations of Inlet and Exhaust Circulation Control

Simultaneous operation of the inlet and exit CC jets was the final free jet case tested. For these test runs, $C_{\mu, \text{aft}}$ was held constant while $C_{\mu, \text{fore}}$ was swept, and the full range of slot heights were tested. It was elected to hold fan speed constant while combinations of $C_{\mu, \text{fore}}$ & $C_{\mu, \text{aft}}$ were tested. Figure 13 presents the static thrust performance for a single slot height configuration.

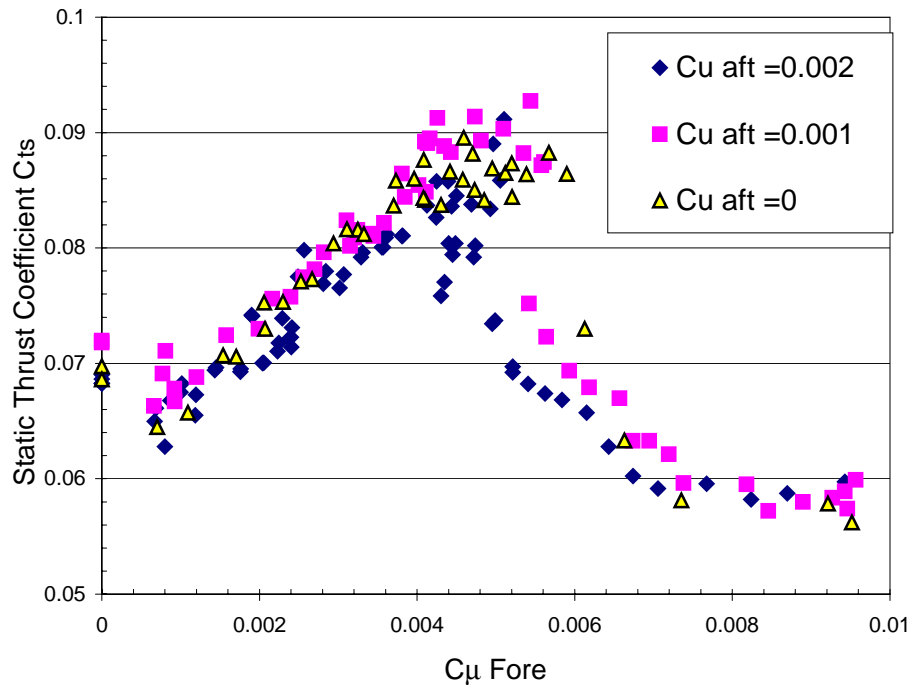


Figure 13. Static Thrust Performance with Combined Inlet and Exit CC
Fan Speed 25 KRPM, $h/R_{\text{fore}} = 9.6\%$, $h/R_{\text{aft}} = 2.4\%$

Comparing combined inlet and exit CC to the case of inlet CC only, a net gain in static thrust is noted with the application of the exit CC jet at small values ($C_{\mu \text{ aft}} = 0.001$). However, the performance is lost as $C_{\mu \text{ aft}}$ is increased (to $C_{\mu \text{ aft}} = 0.002$). In addition, the loss of thrust is greater when $C_{\mu \text{ fore}}$ is increased beyond to the value where inlet flow is forced to separate (the discontinuity occurring around $C_{\mu \text{ fore}} = 0.0055$). The characteristic response of the static thrust to increased $C_{\mu \text{ fore}}$ follows the same general trend whether $C_{\mu \text{ aft}}$ is active or inactive, indicating that the effect on inlet attachment is weakly coupled to the exit CC jet.

Increased static thrust performance at the lower value of $C_{\mu \text{ aft}}$ can be partially attributed to the increased weight flow generated by activation of the exit jet. Figure 14 illustrates an upward offset in weight flow when both CC devices are active (inlet CC jet weight flow was subtracted from the data). However, the increase in weight flow is still limited by flow condition in the inlet, abruptly dropping beyond the value of $C_{\mu \text{ fore}}$ where inlet flow is forced to separate.

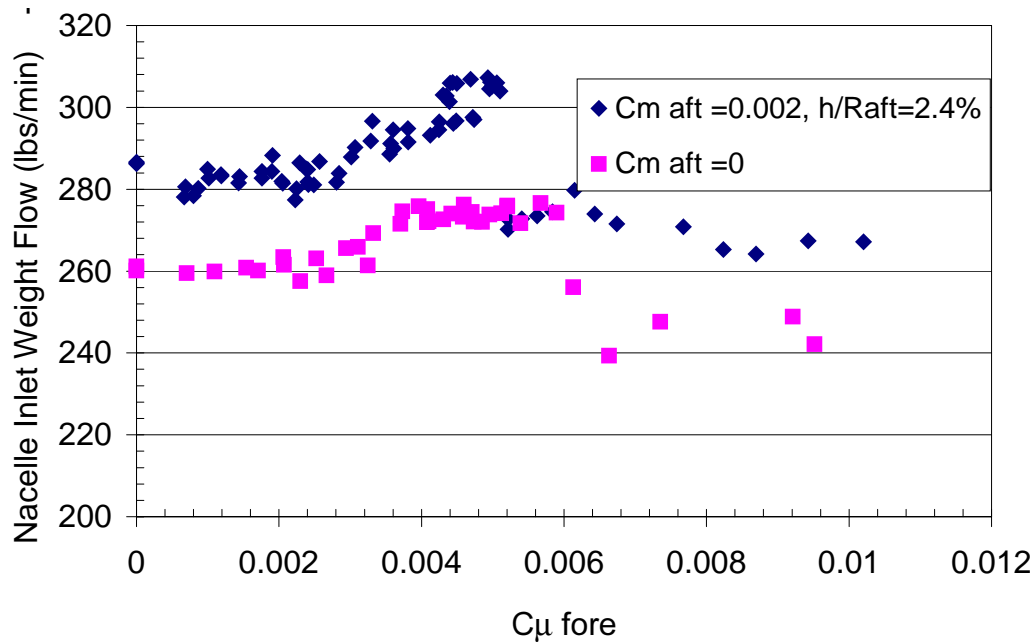


Figure 14. Nacelle Inlet Weight Flow with Inlet CC Active

Performance of the CC Morphing Nacelle – Hovering In Ground Effect

An instrumented ground plane was placed at set distances from the behind the fan exit in order to simulate hover in ground effect. The fan centerline was oriented normal to the ground plane, and in line with the central pressure tap. Ground plane static pressure taps were monitored to determine pressure at radial distances from the fan centerline.

Figure 15 presents a typical ground plane radial pressure profile, comparing cases of equivalent total thrust, with and without CC jets active.

Combinations of CC jet momentums were applied to achieve an equivalent thrust to the baseline case. As $C_{\mu s \text{ fore}}$ and $C_{\mu s \text{ aft}}$ were simultaneously increased, the peak pressure of the impinging wake was steadily reduced. Pressures inboard of 2.2 exit radii generally decreased, while outboard pressure increased (note these are radial stations and do not reflect equal ground plane areas), showing that fan momentum was retained as the wake spread over the ground.

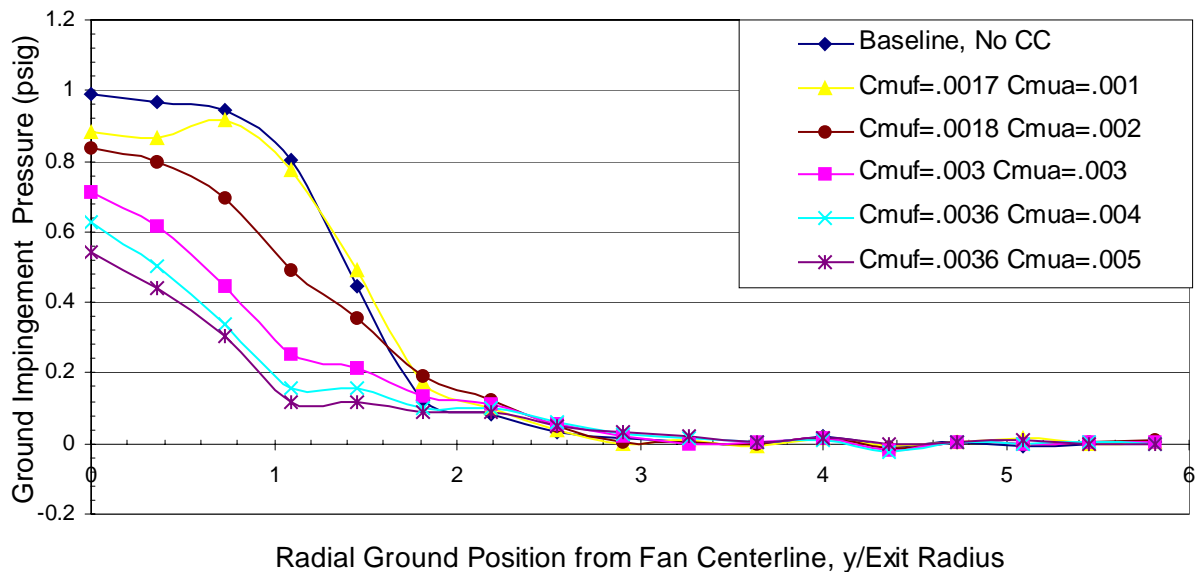


Figure 15. Ground Plane Static Pressure at 3 Exit Diameters Below the Fan
Fan Speed 25 KRPM, $h/R_{\text{fore}}=24\%$, $h/R_{\text{aft}}=4.8\%$, Thrust=44lbs ($C_t \sim 0.068$)

From the CC jet momentums listed in the legend of Figure 15, it is evident that increasing $C_{\mu s \text{ aft}}$ reduces the peak ground plane static pressure below the fan. This effect can be attributed to fan wake spreading and mixing generated by the exit CC jet (Ref. Figures 10 b & c). As $C_{\mu s \text{ aft}}$ was increased $C_{\mu s \text{ fore}}$ was likewise increased in order to maintain equivalent thrust to the baseline case. In this case suction on inlet surface may have balanced suction on the exhaust nozzle Coanda surface. It should be noted that the case presented in Figure 15 not an optimal case, it is based on maintaining constant thrust by CC jet changing CC jet parameters alone; equivalent thrust could be generated with optimal combinations of CC jet momentum at lower overall power settings.

Conclusions

Experimental results show that pneumatic jets directed over curved surfaces at the inlet and exit of the model shrouded fan nacelle improved static thrust under certain conditions. Increased weight flow through the nacelle inlet indicated that circulation about the shroud was increased by sufficient CC jet(s) momentum. The most notable improvement in static thrust coefficient was obtained when CC jet momentum was added at the nacelle inlet. CC jet

momentum applied at the exit proved far less effective in increasing static thrust, but did prove effective in reducing peak pressure impinging on the ground in simulated hover. A combination of inlet and exit CC momentum proved to be the most effective means to improve off-design performance of the shrouded fan.

Oil flow visualization showed the inlet CC jet to act as a separation control device. The diffusing inlet design, optimal for axial flight, suffered from inlet stall in static operation. The CC jet was effective in establishing flow attachment in the inlet, once sufficient momentum was injected into the flow. Improvement in static thrust performance was attributed to the improved inlet flow condition and suction generated on the nacelle's leading edge by the CC jet; however, inlet weight flow was only modestly improved indicating a small increase in circulation. The maximum performance gain was obtained with the smallest ratio of inlet jet slot height to turning radius tested: $h/R_{fore} = 9.6\%$; however, effectiveness was limited by the ability of the inlet flow to remain attached as CC jet momentum increased.

The nacelle exit CC device proved less effective in increasing static thrust, although more effective in increasing shroud circulation. Tuft flow visualization showed the exhaust flow stream tube was expanded by the exit CC device (as predicted by Lissaman for the *Jet Flap Diffuser*). An effective increase in shroud circulation was evident by the increased weight flow through the nacelle inlet. However, the only modest gains in net static thrust were obtained at very low jet momentum ($C_{\mu s \text{ aft}}$), and static thrust was diminished as the jet momentum increased. The rise in inlet weight flow and drop in static thrust, seemingly contradictory observations, could be explained by considering the pressure drop generated on the Coanda surface at the nacelle's exit. Suction over the quarter round surface provides a significant component of force opposite of the static thrust vector. This is suspected as the cause of the loss in static thrust; however, instrumentation was not available to prove this hypothesis.

Maximum static performance gains were realized when the inlet and exit CC devices were operated together. Modest values of exit CC jet momentum ($C_{\mu s \text{ aft}}$) further enhanced static thrust and nacelle inlet weight flow; however, the gains were limited inlet flow separation at high $C_{\mu s \text{ fore}}$.

The combination of inlet and exit CC devices proved effective as a means to reduce ground plane static pressure under the fan. In comparison to the baseline operation of the shrouded fan in hover, nearly a 50% reduction in peak ground plane static pressure was observed when the CC jets were operated. This reduction in peak ground plane pressure was obtained without loss in static thrust, showing the morphing nacelle concept to be a viable means to reduce ground erosion by VTOL aircraft operation.

Recommendations

Further investigation of the application of circulation control on a shrouded fan nacelle, or *Morphing Nacelle*, is warranted. The results obtained in this study are insufficient to generalize the results for application to other shrouded fan configurations. The following additional studies are recommended:

- Continued investigation in static operation with pressure taps arrayed about the nacelle, particularly within the nacelle inlet and the over nacelle exhaust nozzle Coanda surface.
- Parametric study of exit Coanda surface turning angles to determine if static thrust can be enhanced by eliminating suction generated forces opposing the thrust vector.
- Development of a computational model, based on these experimental results, allowing for parametric studies of fan and shroud design variables.
- Investigation of unsteady CC jets as a means to reduce jet momentum requirements.

Acknowledgements

The experimental study detailed in this paper was supported by NASA Langley Research Center under contracts NAG-1-02093 and NAG-1-03055.

The authors wish to acknowledge the following individuals and organizations:

- Malik Little of GTRI , for many hours at the console completing the test matrix.
- Warren Lee of GTRI, for developing and supporting the data acquisition software.
- Bob Englar of GTRI, for insight in to the implementation of circulation control on the model.
- Frank Holman, Bryan Seegers, Hugh Spilsbury, and Scott Ashley, of M-Dot Aerospace; for the detail design and manufacture of the model.
- Sandy Shapery, of Shapery Gyronautics, for providing partial financial support for the fabrication of the model and lease of the TDI Fan core.

References

1. McCormick, B., *Aerodynamics of V/STOL Flight*, Academic Press 1967.
2. Morel, J., Lissaman P., *The Jet Flap Diffuser: A New Thrust Augmenting Device*; AIAA Paper 69-777, July 1969.
3. Kondor S., Heiges, M., *Active Flow Control for Control of Ducted Rotor Systems*, AIAA Paper 2001-0117, Jan. 2001.
4. Englar, R. J., *Circulation Control Pneumatic Aerodynamics: Blown Force and Moment Augmentation and Modification; Past, Present & Future*, AIAA Paper 2000-2541.
5. Kondor, et al., *Experimental Investigation of Circulation Control on a Shrouded Fan*, AIAA Paper 2003-3409
6. Perkins & Hage, *Airplane Performance, Stability, and Control*, Wiley, 1949

Experimental Investigation of Morphing Nacelle Ducted Fan

Shayne A. Kondor
Georgia Tech Research Institute
Smyrna, GA

Mark Moore
NASA Langley Research Center
Hampton, VA

Aerospace, Transportation & Advanced
Systems Laboratory

ATAS.ppt-1

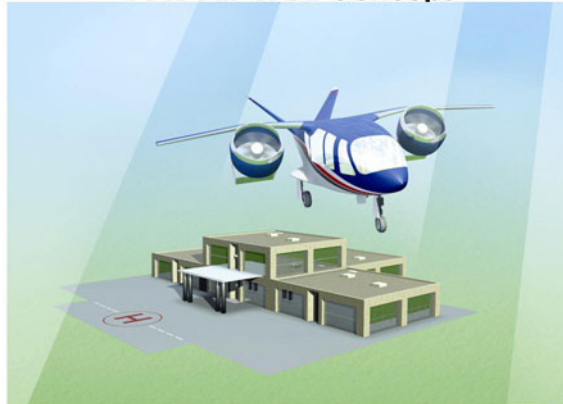
Investigation Objectives

- Investigate the “Morphing Nacelle” concept proposed for the PAV.
This nacelle will employ active pneumatic flow control, as opposed to moving surfaces to optimize off design point operation.
- Determine what, if any, propulsive performance enhancement can be gained by modifying the circulation about a fan shroud.
- Determine if ground pressure signature can be modified by a “virtual diffuser” effect expected when applying control to the nozzle.

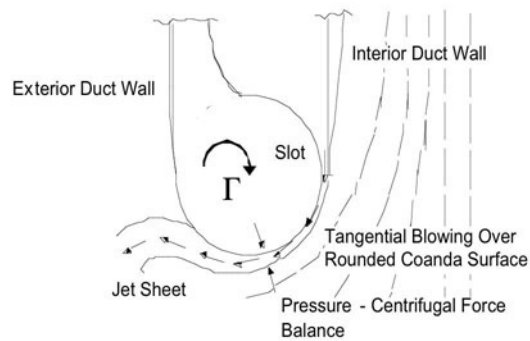
Aerospace, Transportation & Advanced
Systems Laboratory

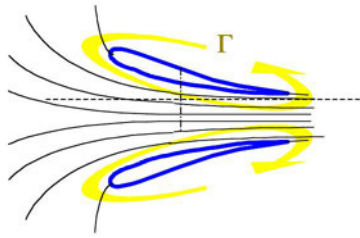
ATAS.ppt-2

PAV Air TAXI Concept



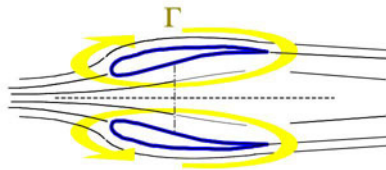
Circulation Control (CC) as Applied to Duct Exit Nozzle



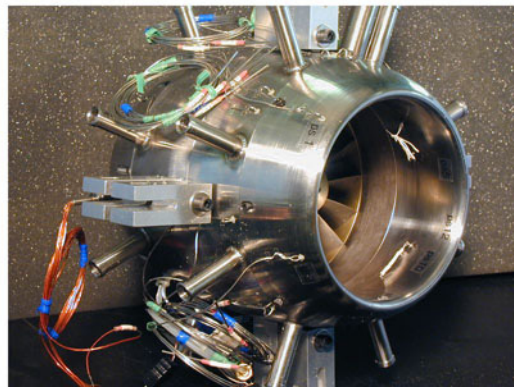


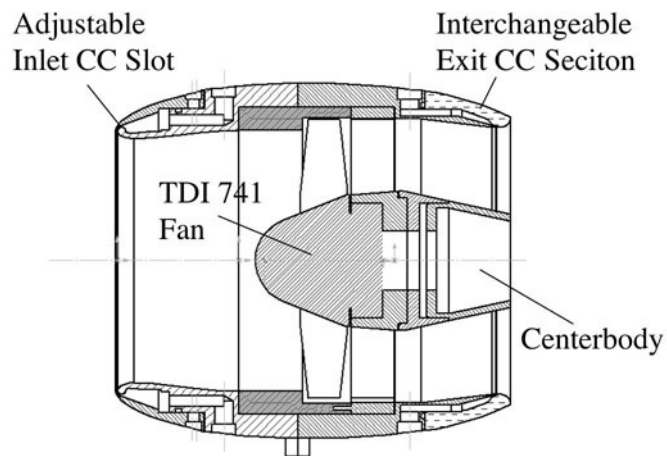
Circulation (Γ)
On a Typical Lifting Fan
(Accelerating Shroud)

Circulation (Γ)
On a Typical Translating Fan
(Decelerating Shroud)

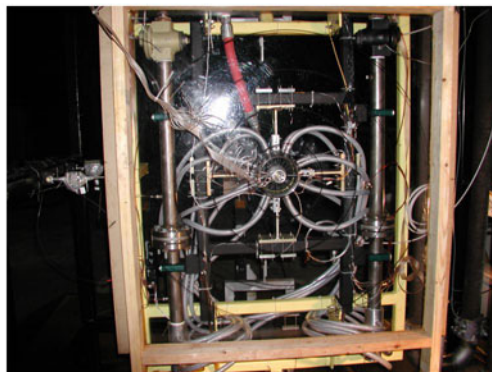


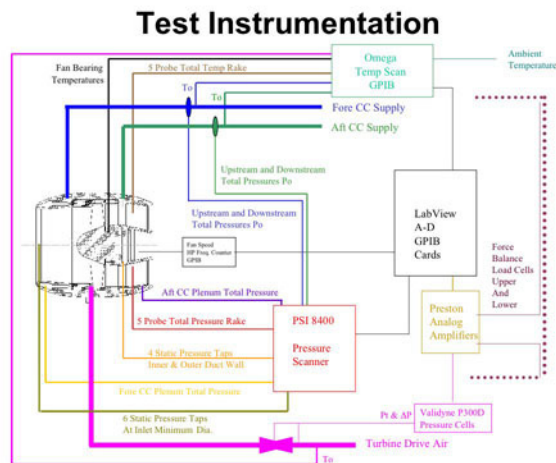
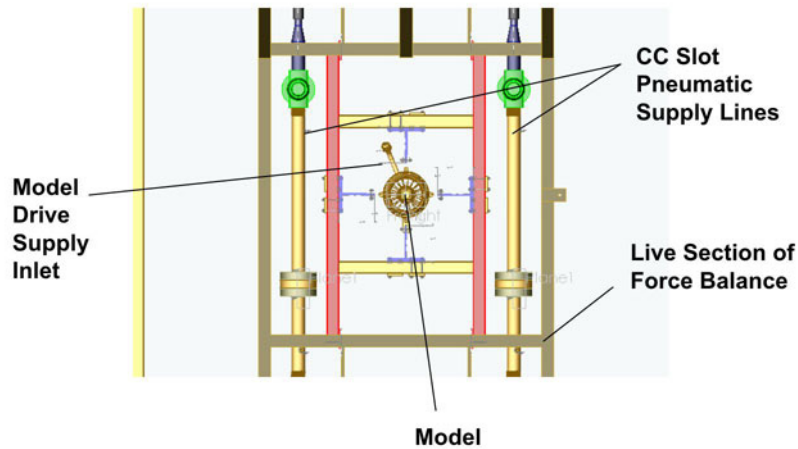
CC Shrouded Fan Model Constructed by M-DOT Aerospace





Model Installation in Thrust Cell





Data Reduction

$$C_T = \frac{\text{Thrust}}{\rho_{\infty} N^2 D^4}$$

N = Fan Rotational Speed
D = Fan Diameter
 ρ = "Freestream" (ambient) density

$$C_{\mu_s} = \frac{\dot{m}_{jet} V_{jet}}{\rho_{\infty} N^2 D^4}$$

Assuming an Isentropic Flow
Expanding to "Freestream Static"
(i.e. ambient barometric pressure):

C_{μ} Momentum Coefficient of
The CC jet, Normally Relates
Fraction Of Freestream Momentum
Employed in the Jet

$$V_j = \sqrt{2RT_d \left(\frac{\gamma}{\gamma-1} \right) \left[1 - \frac{P_{\infty}}{P_d} \right]^{\frac{\gamma-1}{\gamma}}}$$

Data Reduction - Pressures

$$PR = \frac{P_{T_{FAN}}}{P_{\infty}}$$

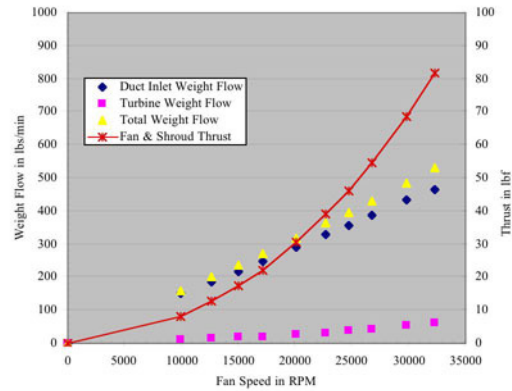
$P_{T_{FAN}}$ Sampled in the
Middle of Flow Behind the
Fan Stators

With no freestream dynamic pressure.....

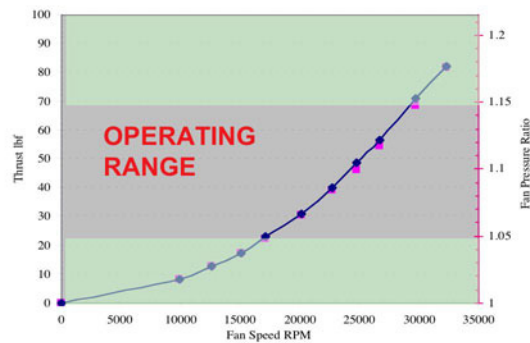
$$C'_p = \frac{P_s - P_{\infty}}{P_{T_{FAN}}}$$

Relates Fraction of Fan Total
Pressure at Ground

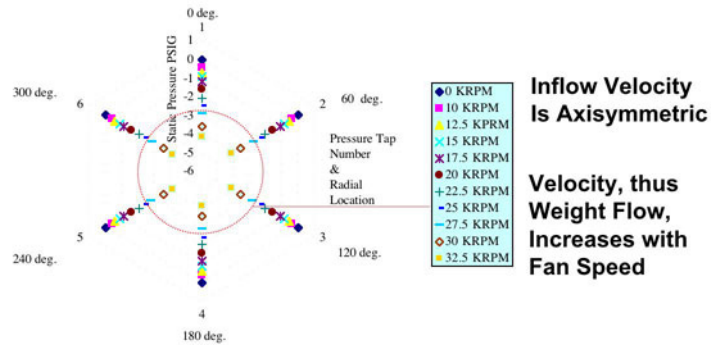
Baseline Shrouded Fan Performance



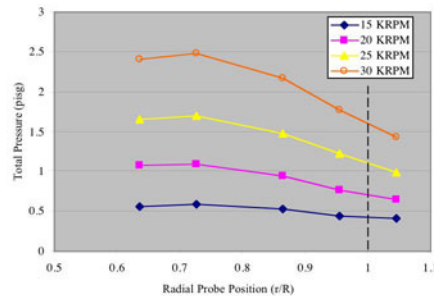
Baseline Fan Thrust Operating Out of Ground Effect



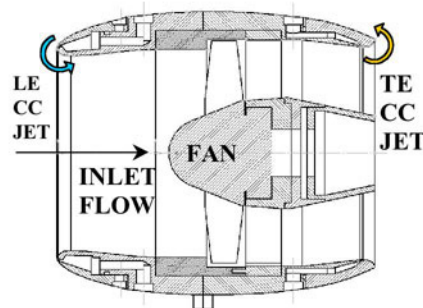
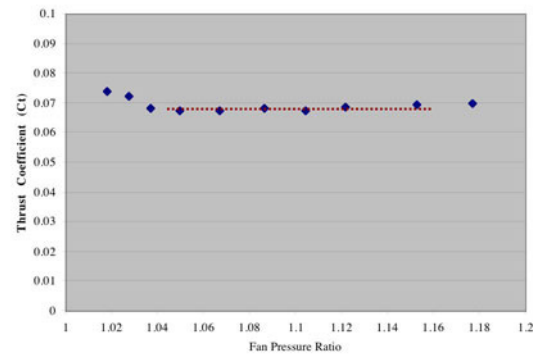
Baseline Inlet Throat Pressure Profile (Circumferential)



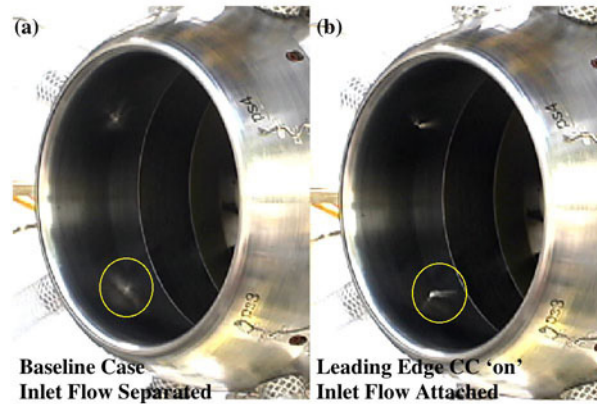
Baseline Total Pressure Profile Behind Fan (in Nozzle)



Baseline Non-Dimensional Performance

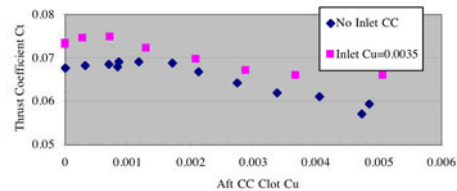


Inlet Stall in Static Operation

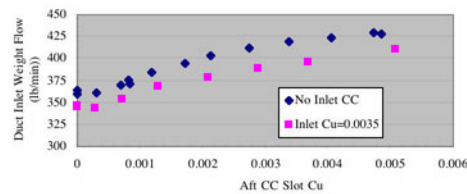


Fan Performance (OGE) with Circulation Control Applied

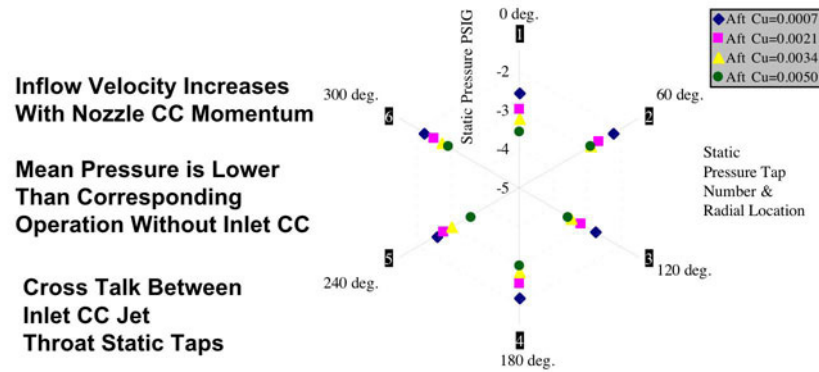
Static Thrust
Performance
Varying Nozzle
CC Jet Momentum



Corresponding
Weight Flow

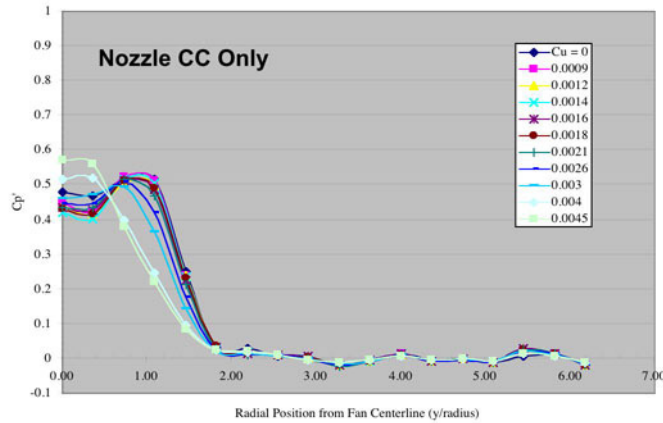


Inlet Static Pressure at Throat Inlet $C_{\mu} = 0.0035$, Nozzle C_m Sweep

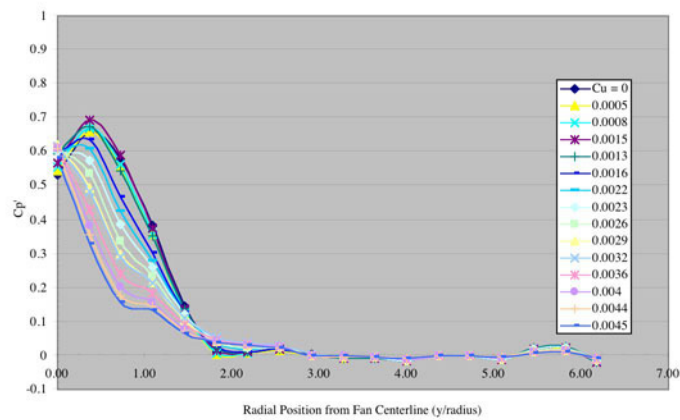


QuickTime Movie

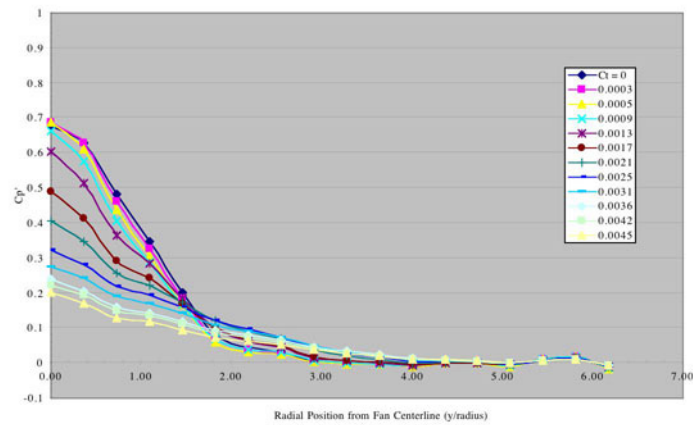
Ground Plane Pressure Signature @ H=1.5 Dia.



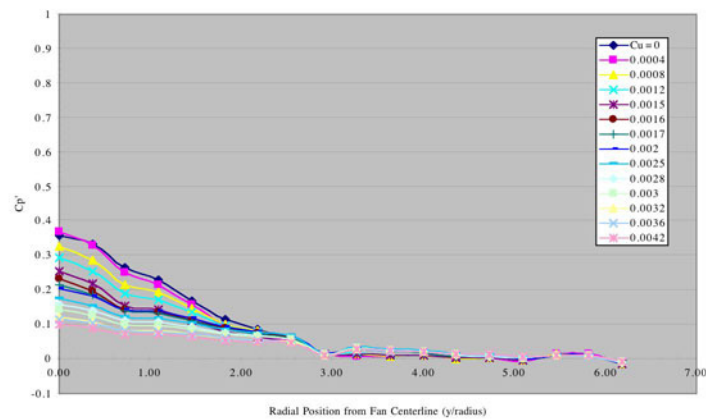
Ground Plane Pressure Signature @ H=3.0 Dia.



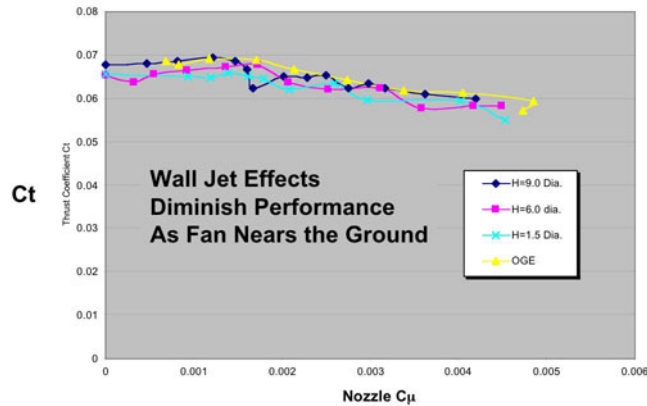
Ground Plane Pressure Signature @ H=6.0 Dia.



Ground Plane Pressure Signature @ H=9.0 Dia.



Comparison of OGE and IGE Performance



Conclusions (1)

- Inlet CC jet blowing can alleviate the stalled inlet condition present in the diffusing duct inlet – which has a positive influence on performance alone.
- Together, the action of CC jets at the duct inlet and nozzle exit can enhance the static thrust of the shrouded fan model at small values of C_{μ_s} ; however, the benefit is lost as C_{μ_s} increases.
- A limited performance enhancement is realized using the nozzle CC device; the observed thrust loss requires additional investigation.

Conclusions (2)

- Some effectiveness if demonstrated in reducing ground plane pressure; however, the interaction between the shroud and ground needs more study.
- The combined operation of inlet and nozzle CC devices must be revisited with improved instrumentation.

Recommendations (1)

- Parametric study of jet slot height effects.
- Parametric study of Coanda (turning surface) shape, especially turning angle.
- In Ground Effect (IGE) operation with a skew angle to the ground plane.
- Revised study of inlet CC jet effects, including a new method to measure inlet weight flow.

Recommendations (2)

- A CFD simulation, calibrated with the model results, for parametric analysis of shroud and CC design variables.
- Detailed flow diagnostics aimed at uncovering the flow physics underlying the CC jet interaction with the fan's flow field.

Acknowledgements

The experimental study described in this paper was supported by NASA Langley Research Center under contract number NAG-1-02093.

The authors wish to acknowledge the following individuals and organizations:

Frank Holman, Bryan Seegers, Hugh Spilsbury, and Scott Ashley of M-DOT Aerospace, for the design, manufacture and construction of the model.

Sandy Shapery, of Shapery Gyronautics, for providing partial financial support for the fabrication of the model and lease of the fan core.

A Novel Airfoil Circulation Augment Flow Control Method Using Co-Flow Jet

Ge-Cheng Zha* and Craig Paxton†
Dept. of Mechanical and Aerospace Engineering
University of Miami
Coral Gables, Florida 33124
zha@apollo.eng.miami.edu
cpaxton@mindspring.com

Abstract

A novel subsonic airfoil circulation augment technique using co-flow jet (CFJ) to achieve superior aerodynamic performance for subsonic aircraft is proved numerically by CFD simulation. The advantages of co-flow jet airfoil include high lift at high angle of attack, ultra high C_l/C_d at cruise point, and low penalty to the overall cycle efficiency of the airframe-propulsion system.

Unlike the conventional circulation control (CC) airfoil which is only suitable for landing and taking off, the CFJ airfoil can be used for the whole flying mission. No blunt leading and trailing edge is required so that the pressure drag is small. No moving parts are needed and make it easy to be implemented and weight less. The jet to enhance the circulation will be recirculated. Compared with the CC airfoil, the recirculating CFJ airfoil will significantly save fuel consumption because: 1) the power required to energize the jet is less; 2) no penalty to the jet engine thrust and efficiency due to the disposed jet mass flow since the jet mass flow is recirculated.

For the NACA2415 airfoil studied, at low AOA with moderate momentum jet coefficient, the coflow jet airfoil will not only significantly enhance the lift, but also dramatically reduce the drag, or even generate the negative drag (thrust). The mechanism is that the coflow jet can control the pressure drag by filling the wake, and could generate negative pressure drag greater than the friction drag. This may allow the aircraft to cruise with very high aerodynamic efficiency. At high AOA, both the lift and the drag are significantly higher than the airfoil with no flow control, which may enhance the performance of taking off and landing within short distance.

1 Introduction

To achieve high performance aircraft design, revolutionary technology advancement should be pursued to dramatically reduce the weight of aircraft and fuel consumption, significantly increase aircraft mission payload and maneuverability. Both the military and commercial aircraft will benefit from the same technology. As an effort toward these goals, this paper suggests a novel flow control technique to achieve high aerodynamic performance, i.e., high lift at high AOA, high C_l/C_d at cruise point, and low penalty to the overall cycle efficiency of the airframe-propulsion system.

* Associate Professor

† Graduate Student

Flow control is playing a more and more important role to improve aircraft aerodynamic performance[1][2]. To enhance lift and suppress separation, various flow control techniques have been used including rotating cylinder at leading and trailing edge[3][4][2], circulation control using tangential blowing at leading edge and trailing edge[5][6] [7][8][9][10], multi-element airfoils[11][12], pulsed jet separation control[13][14][15], etc. The different flow control methods have their different features. For example, the rotating cylinder and circulation control are generally most effective when the leading edge or trailing edge are thick. The multi-element airfoil can generate very high lift, but generally comes with large drag penalty.

In the summer of 2002, the joint research team from University of Miami(UM) and AFRL studied a new flow control concept for aircraft engine compressor blades: using co-flow wall jet on the suction surface to enhance the compressor cascade diffusion[16, 17]. Based on the CFD simulation, a very large diffusion factor, 0.965, is achieved. The diffusion factor reaches the limit of the geometry and is far greater than the current upper limit of 0.65. This paper applies the new flow control technique of the coflow jet cascade to high lift airfoil since both experience severe adverse pressure gradient at high loading.

Unlike the conventional circulation control airfoils, for which the jets are mostly implemented at leading and trailing edge, the co-flow jet (CFJ) airfoil is implemented on the majority area of the suction surface of the airfoil. The co-flow jet airfoil is to open a long slot on the airfoil suction surface from near leading edge to near trailing edge(see fig.1). A high energy jet is then injected near the leading edge tangentially and the same amount of mass flow is sucked away near the trailing edge. The turbulent shear layer between the main flow and the jet causes a strong turbulence diffusion and mixing, which enhance the lateral transport of energy and allow the main flow to overcome the severe adverse pressure gradient and stay attached at high angle of attack(AOA). At a certain AOA, the airfoil always achieve a significantly higher lift due to the augmented circulation. The operating range of AOA, hence the stall margin, is also significantly increased. The coflow jet airfoil does not rely on the Coanda effect at the leading or trailing edge, and hence the thick leading or trailing edge are not required. The technique can apply to any type of airfoils including the modern high speed thin airfoil, and can be combined with other flow control techniques.

When a flow control technique for airfoil is developed, we have to consider the overall airframe-propulsion system to make sure that the benefit outweighs the penalty. For the proposed coflow jet airfoil, since the jet blows and sucks the same amount of the mass flow, the jet hence can be recirculated to reduce the energy expenditure of the overall airframe-propulsion system compared to the blowing only method such as the circulation control. The jet blowing flow is usually from the engine. For the blowing only method, the high energy jet is dumped out and that is a penalty to the engine efficiency since the engine needs to energize the flow from the low energy free stream. The jet has higher energy state than the free stream flow even near the trailing edge. Hence less work needs to be done to energize the flow for blowing and the overall cycle efficiency can be higher. In addition to recirculating the jet flow, another energy saving of this flow control method is that it is desirable to blow the jet near leading edge where the pressure is low and to suck the jet near the trailing edge where the pressure is high.

Different from the conventional circulation control (CC) airfoil which may be most suitable for taking off and landing, the CFJ airfoil can be used for the whole flying mission from taking off, cruise, maneuver, to landing. No moving parts are needed and make it easy to be implemented and weight less. The CFJ airfoil does not require large leading edge(LE) or trailing edge(TE) and hence has small form drag as the regular modern airfoil.

A CC airfoil relies on local favorable pressure gradient on a curved surface to make the flow attached, the Coanda effect. Such favorable pressure gradient exists at the airfoil leading edge due to the suction and at the end of the trailing edge due to the low base pressure when the trailing edge is blunt. To make the CC airfoil effective, the blunt TE is hence needed, which is also the reason to create large drag at small AoA such as at cruise. At large AoA, because the mainflow can not resist the large adverse pressure gradient, the local TE favorable pressure gradient can not be achieved and hence the Coanda effect is difficult to maintain. If only TE blowing is used, the CC airfoil will usually stall at smaller AoA than the non-CC airfoil with sharp TE[18]. The CFJ airfoil significantly increase the AoA range and hence increase the safety margin of the aircraft. Above limitations of the CC airfoil may be part of the reasons that the CC airfoil has not been used for realistic aircraft so far.

For the CFJ airfoil, when the AOA is not large such as at cruising point, the pressure gradient may not be very severe. When the co-flow jet is used to enhance the lift, the mainflow around the airfoil is energized and the wake is filled to have a shallow defect shape or even protruding shape. This will reduce the drag or generate thrust (negative drag) for the airfoil. Obviously, there may be an optimum jet control to be most energy efficient. For example, it may be the optimum to achieve zero drag instead of the negative drag (thrust) because the airfoil may not be an efficient propulsion system. The filled wake will generate low noise level since there is no wake mixing. The noise level could be lower than the CC airfoil which has little wake filling effect. The enhanced lift can reduce the wing span for easy storage and reduced wet area and skin friction. The enhanced lift can also significantly shorten the taking off and landing distance. Basically, we can effectively trade the thrust to lift through CFJ at short landing and taking off without using vectored device. The special mechanism of the CFJ airfoil makes it workable for the full flying envelop.

In summary, the new flow control method proposed in this paper appears to have the following advantages: 1) It is effective to enhance lift and suppress separation. It can achieve extremely high C_l/C_d (infinity when $C_d = 0$) at low AOA(cruise), and very high lift and drag at high AOA(taking off and landing).; 2) It significantly increases the AOA operating range and stall margin; 3) It is energy efficient for the overall airframe-propulsion system; 4) It can be applied to any airfoil, thick or thin.

Above advantages of the CFJ airfoil may derive the following superior aircraft performance: 1) The CFJ airfoil works for the whole flying mission instead of only taking off and landing; 2) Economic fuel consumption; 3) Short distance taking off and landing; 4) No moving parts are needed and the implementation is not difficult; 5) Small wing span for easy storage, light weight and reduced skin friction; 6) Low noise since no high lift flap system is used; 7) The CFJ airfoil can be used for low and high speed aircraft.

The wind tunnel tests are currently in progress under the support of NASA Langley Research Center.

2 Results and Discussion

Fig.1 shows the baseline airfoil, NACA2415, and the airfoil with co-flow jet slot. The chord length is 0.3m. The coflow jet airfoil is modified from the baseline airfoil by translating the suction surface vertically lower by 1.67% of the chord. The slot surface shape is exactly the same as the original baseline airfoil suction surface. The slot inlet and exit are located at 6.72% and 88.72% of the chord from the leading edge. The slot inlet and exit faces are normal to the slot surface to ensure

that the jet will be tangential to the main flow. The slot inlet and exit area are 1.56% and 1.63% of the chord.

The Fluent CFD software is used as the tool to simulate the airfoil flows in this study. The mean flow governing equations are the 2D compressible Navier-Stokes equations. The $k - \epsilon$ turbulence model with wall function is used to save CPU time. The solutions of two typical cases are compared with the solutions using $k - \epsilon$ model integrating to the wall. The results have little difference. The full turbulent boundary layer assumption is used since the CFD solver does not have a transition model. The O-mesh is used as shown in the zoomed region around the airfoil in Fig.2. The baseline mesh has the size of 240×100 in the direction around the airfoil and in the radial direction respectively. In the coflow jet slot, the mesh size is 80×12 in the streamwise and spanwise direction respectively. A rectangular farfield boundary is used with the downstream boundary extended to 30 chord length, upstream, lower and upper boundary to 20 chord length. The y^+ is from 15-30 on the airfoil surface. The freestream Mach number is 0.3 and the Reynolds number is 1.9×10^6 . For all the computation, the jet inlet holds a constant total pressure equal to $1.315 P_{t_{freestream}}$. The jet exit static pressure is iterated to match the jet inlet mass flow rate.

2.1 CFJ Airfoil Performance

Fig.3 is the lift coefficient vs angle of attack (AOA) for the baseline airfoil and the coflow jet airfoil. For the baseline airfoil, the lift coefficient predicted by CFD agrees excellently with the experiment results at $Re = 3 \times 10^6$ [19] before stall. CFD predicts a little delayed stall and higher lift coefficient in the stall region. Fig.3 indicates that the lift of the coflow jet airfoil is increased significantly. The zero lift AOA for the baseline airfoil is -2° , and is -6° for the coflow jet airfoil. The stall AOA is increased by 2° . Hence the operating range of AOA is increased totally by 38%. The peak lift value is increased by 80%, which is the minimum lift increase. When the AOA is decreased, the lift increase is greater. For example, at AOA = 2° , the lift increase is 250%.

For the co-flow airfoil, a few selected points are recalculated using refined mesh with the size of 480×200 around the airfoil and 160×30 in the slot. The refined mesh lift coefficients are shown in Fig.3 and agrees excellently with the baseline mesh, which indicates that the numerical solutions are converged based on the mesh size.

Fig. 4 shows the streamlines at AOA = 20° . The baseline airfoil has a massive separation, while the coflow jet airfoil flow is nicely attached. The attached flow is mainly due to the turbulent mixing [16], which transfers energy from the jet to the main flow so that the main flow can overcome the severe pressure gradient to stay attached.

Fig. 5 is the isentropic Mach number distribution on the surface of the airfoil at AOA = 20° . It shows that the coflow jet airfoil creates a very strong suction effect near the leading edge and the flow is accelerated from the freestream Mach number 0.3 to the peak Mach number 1.7. The peak Mach number of the baseline airfoil is about 0.9. However, the baseline airfoil can not sustain the severe pressure gradient and the massive separation yield small loading on the aft portion of the airfoil. The coflow jet airfoil has much higher acceleration and diffusion on the suction surface and stronger deceleration on the pressure surface, which result in higher lift and circulation. Fig. 5 also shows that the leading edge stagnation point of the coflow jet airfoil is located more downstream than that of the baseline airfoil due to the higher circulation. The first spikes near the leading edge is due to the coflow jet injection which accelerates the flow on suction surface due to the mixing. The shape of the spike is not necessarily accurate and may be created by the numerical boundary

condition treatment. The second spike near the trailing edge is due to the low pressure suction at the jet exit.

Fig.6 is the Mach number contours in the leading edge region at AoA=20° for the baseline and the CFJ airfoil. It shows that the CFJ airfoil has a local supersonic region. The high energy jet mixes with the mainflow through a low momentum wake.

In this study, while the AOA varies, the coflow jet inlet total pressure is held constant to simulate a passive flow control. At different AOA, the main flow will have different static pressure at the location of the jet inlet, which determines the mass flow rate of the jet and the jet injection velocity. Hence the jet momentum coefficient varies with AOA. The jet momentum coefficient based on the conventional definition is:

$$C_\mu = \frac{\dot{m}_j V_j}{0.5 \rho_\infty U_\infty^2 S} \quad (1)$$

Fig. 7 shows the variation of C_μ vs AoA. When AoA varies from -8° to 22° , C_μ increases from 0.15 to 0.25.

Fig.8 is the drag polar for the baseline airfoil and the coflow jet airfoil. When AOA is high, both the lift and drag of the coflow jet airfoil is significantly higher than the baseline airfoil. Compare the peak lift points for both airfoils, the drag of the coflow jet airfoil is 160% higher than that of the baseline airfoil. However, when $\text{AOA} < 4^\circ$, the lift of the coflow jet airfoil is significantly higher and the drag is significantly lower than that of the baseline airfoil. When $\text{AOA} < 0^\circ$, the lift coefficient is still very large ($C_l = 0.862$ at $\text{AOA} = 0^\circ$, see fig.3), but the drag becomes negative (thrust). At $\text{AOA} = 0^\circ$, the $C_l/C_d = 2224$.

The drag of an airfoil is contributed from two sources, friction drag and pressure drag (form drag). The friction drag will always be in the opposite direction of the flight, that is, always positive. The negative drag hence must be from the pressure drag. This can be seen from fig.9, which shows the friction drag, pressure drag and total drag for the coflow airfoil respectively. Fig.9 indicates that the friction drag is fairly constant and decreases slightly near stall. However, the pressure drag varies largely. The pressure drag is the dominant contribution to the total drag near stall. When AOA is decreased, the pressure drag also decreases monotonically. When $\text{AOA} < 4^\circ$, the pressure drag becomes negative and the total drag is reduced to negative when $\text{AOA} < 0^\circ$.

Fig.10 is the drag distribution of the baseline airfoil. Similar to the coflow airfoil, the friction drag is also fairly constant compared with the pressure drag. The pressure drag decreases when the AOA is decreased from the stall region. However, the pressure drag increases when the decreasing AOA passes the zero lift point and does not become negative.

The negative drag can also be explained from the the control volume point of view. The high velocity jet will transfer the kinetic energy to the main flow due to the turbulent mixing. When the AOA is not large, the diffusion is not severe. The main flow on the suction surface has the large streamwise velocity past the trailing edge so that the streamwise velocity in the wake region is greater than the freestream velocity. This can be seen in fig.11, which shows the wake shape of the two airfoils at one chord length downstream of the trailing edge. The wake of the baseline airfoil has the usual defect shape while the wake of the coflow airfoil has the protruding shape. Fig. 12 is the Mach number contours at the trailing edge region at $\text{AoA} = 0^\circ$. It shows that the high energy jet of the CFJ airfoil fill the wake and a thrust is created.

Based on the control volume analysis, the drag is determined by

$$D = \int \int \rho U (U_\infty - U) dA \quad (2)$$

Where U is the wake velocity.

When U is greater than U_∞ , the drag is negative and becomes thrust. When the AOA is very large, the jet energy is mostly used to diffuse the flow to make the flow attached. For the current study with the constant jet inlet total pressure of $1.35Pt_{freestream}$ at $AoA=20^\circ$, the coflow jet does not provide enough energy to the main flow and the wake is very large. The pressure drag is hence overwhelming, which is desirable for short distance landing.

2.2 Energy Expenditure

The power required to energize jet is determined by the total pressure ratio between the jet exit and jet inlet. For CC airfoil which has blowing only, the jet inlet is the free stream. For the recirculating CFJ airfoil, the jet inlet is the suction exit.

To compare the power required for the blowing only CC airfoil and the recirculating CFJ airfoil, we assume that the jet mass flow rate is the same. Then the power ratio between the power required by the recirculating CFJ airfoil and the CC airfoil is:

$$\begin{aligned} P_R &= \frac{P_{CFJ}}{P_{CC}} \\ &= \frac{\eta_{CC}}{\eta_{CFJ}} \frac{((P_{02}/P_{01})^{\frac{\gamma-1}{\gamma}} - 1)_{CFJ}}{((P_{02}/P_{01})^{\frac{\gamma-1}{\gamma}} - 1)_{CC}} \end{aligned} \quad (3)$$

Where η is the efficiency of the pumping system, P_{02} and P_{01} are the total pressure at the jet inlet and exit.

Fig. 13 is the total pressure ratio against momentum coefficient for blowing only and recirculating CFJ airfoil. The solid line is the total pressure ratio of 1.315 if blowing only is used. In this study, the injection total pressure is held constant. The variation of the momentum coefficient is due to the change of AOA. The dash line is the total pressure ratio if the jet is recirculated. Since the jet still has high momentum near the suction slot and the total pressure is still fairly high, it makes the total pressure ratio of the recirculating jet varying from 1.02 to 1.11, which is significantly lower than the blowing only total pressure ratio. Please note that this comparison does not include the extra flow loss in the ducts of the injection and suction.

Fig. 14 shows the ratio of the power required for recirculating the jet and the power for blowing only. If assume the pumping systems of the blowing only and recirculating jet have the same efficiency, the solid line in Fig. 14 is the power ratio with the maximum value about 0.35 at stall. If we make a very conservative assumption that the recirculating jet pump efficiency is only half of that of the blowing only system, the power ratio shown as the dash line in Fig. 14 is still significantly lower than 1.0 and varies from 0.15 to 0.75. This means that the recirculating jet will bring a significant energy expenditure saving compared with the CC airfoil.

The other penalty that the conventional CC airfoil brings to the propulsion system is the disposed jet mass flow, which will hurt the engine thrust and efficiency.

Assume a jet engine is used to power the aircraft, the engine is tested on the ground and the nozzle expand the flow to ambient pressure. The thrust of a jet engine is then determined by the momentum difference between the inlet and nozzle. On the ground the engine flying speed is zero and hence the thrust is expressed as:

$$F = m_{nozzle} V_{nozzle} \quad (4)$$

Eq.(4) means that the thrust decrease will be directly proportional to the mass flow dumped out if a blowing only CC airfoil is used. For a recirculating CFJ airfoil, this serious penalty is avoided.

The total efficiency of jet engine is:

$$\eta = \frac{V_{\infty} m_{nozzle} (V_{nozzle} - \frac{m_{nozzle}}{m_{inlet}} V_{\infty})}{Q} \quad (5)$$

where the Q is the heat released form the combustion. If assume Q is the same, $\frac{m_{nozzle}}{m_{inlet}} \approx 1$, then η is proportional to m_{nozzle} . This means that the disposed jet flow will directly reduce the propulsion system efficiency.

In summary, compared with the CC airfoil, the recirculating CFJ airfoil will have 3 advantages to save energy expenditure: 1) the power required to energize the jet is less; 2) no penalty to the engine thrust due to the disposed jet mass flow; 3) no penalty to the engine efficiency due to the disposed jet mass flow;

Above advantages of the recirculating CFJ airfoil will be reflected as a significant benefit of fuel consumption saving. If the propulsion system for the aircraft is not a jet engine, above advantages will be equivalently transferred to other power system.

3 Work in Progress

The wind tunnel tests to prove this concept experimentally are in progress under the support of NASA Langley Research Center.

4 Conclusions

A novel subsonic airfoil flow control technique using co-flow jet to achieve superior aerodynamic performance for subsonic aircraft is proved numerically by CFD simulation.

The co-flow jet airfoil is to open a long slot on the airfoil suction surface from near leading edge to near trailing edge. A high energy jet is then injected near the leading edge tangentially and the same amount of mass flow is sucked away near the trailing edge. The jet hence can be recirculated to reduce the energy expenditure of the overall airframe-propulsion system than blowing only. The turbulent shear layer between the main flow and the jet causes a strong turbulence diffusion and mixing, which enhance the lateral transport of energy and allow the main flow to overcome the severe adverse pressure gradient and stay attached at high angel of attack(AOA). The coflow jet airfoil achieves significantly higher lift due to the augmented circulation. The airfoil does not rely on the Coanda effect at the leading or trailing edge. Hence the technique can apply to modern high speed thin airfoil, and can be combined with other flow control techniques.

The new flow control method suggested in this paper appears to have the following advantages: 1) It is an effective method to enhance lift and suppress separation. It can achieve extremely high C_l/C_d at low AOA(cruise), and very high lift and drag at high AOA(taking off and landing).; 2) It significantly increases the AOA operating range and stall margin; 3) It is energy efficient for the overall airframe-propulsion system; 4) It has little geometric limitation and generally can be applied to any airfoil, thick or thin.

Compared with the CC airfoil the recirculating CFJ airfoil will significantly save fuel consumption because: 1) the power required to energize the jet is less; 2) no penalty to the jet engine thrust and efficiency since the jet mass flow is not disposed.

Above advantages of the CFJ airfoil may derive the following superior aircraft performance: 1) The CFJ airfoil works for the whole flying mission instead of only taking off and landing; 2) Economic fuel consumption; 3) Short distance taking off and landing; 4) No moving parts are needed and the implementation is not difficult; 5) Small wing span for easy storage, light weight and reduced skin friction; 6) Low noise since no high lift flap system is used; 7) The CFJ airfoil can be used for low and high speed aircraft.

For the NACA2415 airfoil studied, at low AOA with moderate momentum jet coefficient, the coflow jet airfoil will not only significantly enhance the lift, but also dramatically reduce the drag, or even generate the negative drag (thrust). The mechanism is that the coflow jet can control the pressure drag by filling the wake, and could generate negative pressure drag greater than the friction drag. This may allow the aircraft to cruise with very high aerodynamic efficiency. At high AOA, both the lift and the drag are significantly higher than the airfoil with no flow control, which may enhance the performance of taking off or landing within short distance.

5 Acknowledgment

The authors would like to thank NASA LaRC for supporting the wind tunnel tests as Phase I research of NRA-03-LaRC-02.

References

- [1] M. Gad-el Hak, "Flow Control: The Future ," *Journal of Aircraft*, vol. 38, pp. 402–418, 2001.
- [2] M. Gad-el Hak, *Flow Control, Passive, Active, and Reactive Flow Management*. Cambridge University Press, 2000.
- [3] V. Modi, M. Fernando, and T. Yokomizo, "Drag Reduction of Bluff Bodies Through Moving Surface Boundary Layer Control." AIAA Paper No. 90-0298, 1990.
- [4] D. Cichy, J. Harris, and J. MacKay, "Flight Tests of a Rotating Cylinder Flap on a North American Rockwell YOY-10A Aircraft." NASA CR-2135, 1972.
- [5] L. C. Bradley, "An Experimental Investigation of A Sting-Mounted Finite Circulation Control Wing." M.S. Thesis, Air Force Institute of Technology, 1995.
- [6] N. Wood, L. Robert, and Z. Celik, "Control of Asymmetric Vortical Flows over Delta Wings at High Angle of Attack," *Journal of Aircraft*, vol. 27, pp. 429–435, 1990.

- [7] N. Wood and L. Robert, "Control of Vortical Lift on Delta Wings by Tangential Leading-Edge Blowing," *Journal of Aircraft*, vol. 25, pp. 236–243, 1988.
- [8] N. Wood and J. Nielsen, "Circulation Control Airfoils-Past, Present, Future." AIAA Paper 85-0204, 1985.
- [9] R. J. Englar, L. A. Trobaugh, and R. Hemmersly, "STOL Potential of the Circulation Control Wing for High-Performance Aircraft," *Journal of Aircraft*, vol. 14, pp. 175–181, 1978.
- [10] R. J. Englar, "Circulation Control for High Lift and Drag Generation on STOL Aircraft," *Journal of Aircraft*, vol. 12, pp. 457–463, 1975.
- [11] A. Smith, "High-Lift Aerodynamics," *Journal of Aircraft*, vol. 12, pp. 501–530, 1975.
- [12] J. Lin, S. Robinson, R. McGhee, and W. Valarezo, "Separation Control on High Reynolds Number Multi-Element Airfoils." AIAA Paper 92-2636, 1992.
- [13] K. McManus and J. Magill, "Airfoil Performance Enhancement Using Pulsed Jet Separation Control." AIAA Paper 97-1971, 1997.
- [14] K. McManus and J. Magill, "Separation Control in Incompressible and Compressible Flows Using Pulsed Jets." AIAA Paper 96-1948, 1996.
- [15] H. Johari and K. McManus, "Visulation of Pulsed Vortex Generator Jets for Active Control of Boundary Layer Separation." AIAA Paper 97-2021, 1997.
- [16] G.-C. Zha, (team members: David Car, and W. Copenhaver), "Super Diffusion Cascades Using Co-Flow Jet Flow Control." National Research Council Summer Faculty Final Report, Aug. 23, 2002.
- [17] D. Car, N. J. Kuprowicz, J. Estevadeordal, G.-C. Zha, and W. Copenhaver, "Stator Diffusion Enhancement Using A Re-circulating Co-flowing steady Jet." ASME GT-2004-53086, ASME TURBO EXPO 2004, June 14-17, 2004.
- [18] Y. Liu, L. N. Sankar, R. J. Englar, K. K. Ahuja, and R. Gaeta, "Computational Evaluation of the Steady and Pulsed Jet Effects on the Performance of a Circulation Control Wing Section." AIAA Paper 2004-0056, 42nd AIAA Aerospace Sciences Meeting and Exhibit, Reno, Nevada 5 - 8 Jan 2004.
- [19] J. Anderson, J.D., *Introduction to Flight, 4th edition*. McGraw-Hill Higher Education, 2000.

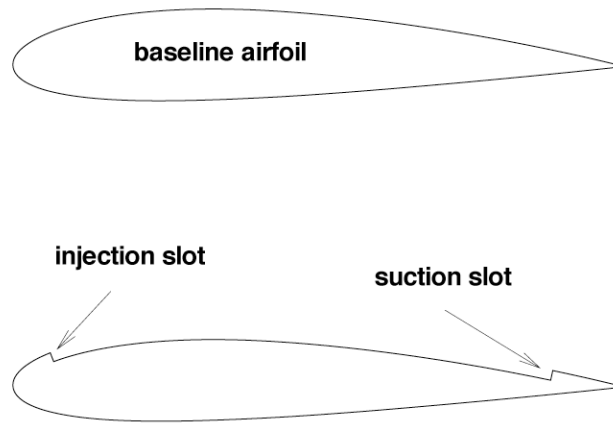


Figure 1: Baseline airfoil NACA2415 and the airfoil with co-flow jet slot.

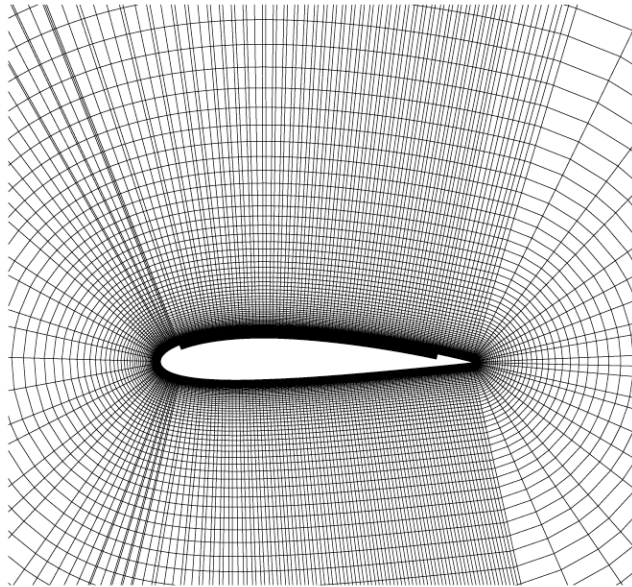


Figure 2: Zoomed mesh around the airfoil with co-flow slot.

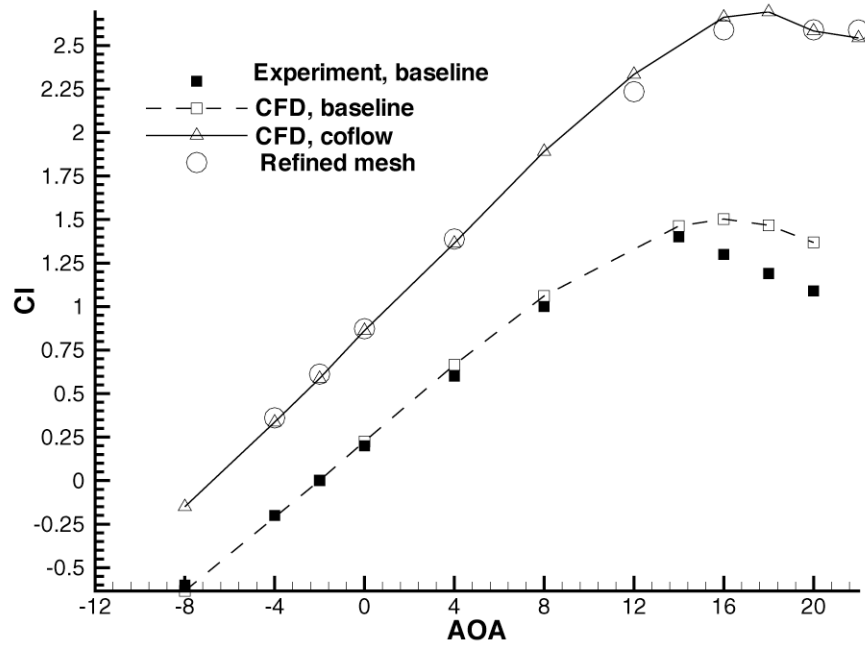


Figure 3: Lift coefficient vs angle of attack.

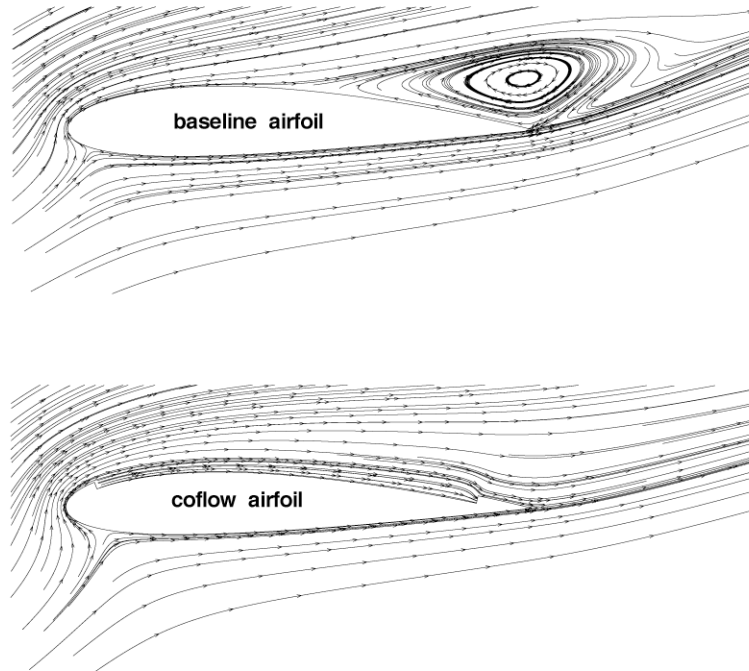


Figure 4: Streamlines at angle of attack of 20 degree.

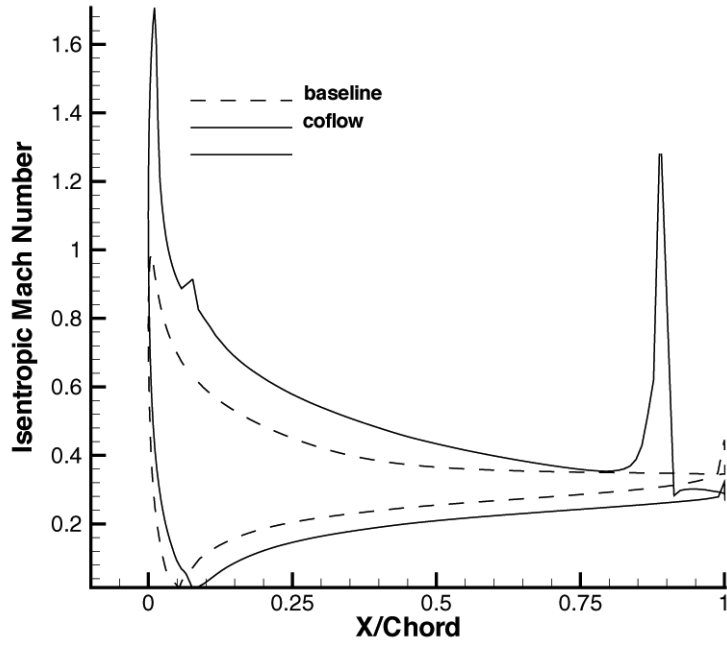


Figure 5: Surface isentropic Mach number distribution at angle of attack of 20 degree.

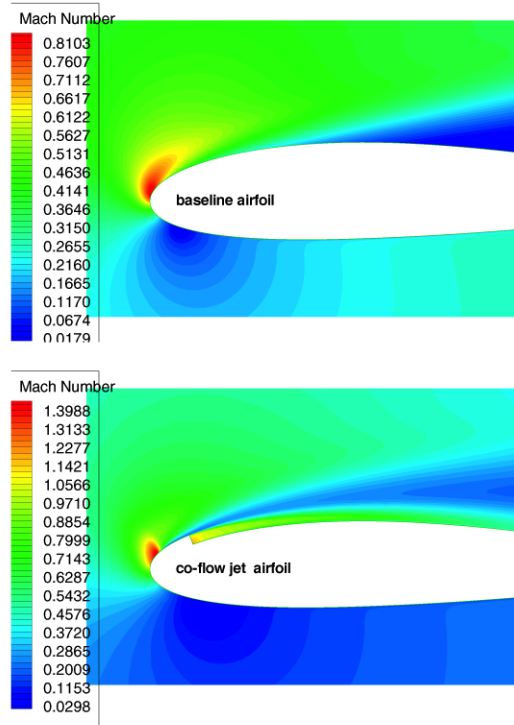


Figure 6: Mach number contours at $AoA = 20^\circ$ for the baseline and coflow jet airfoil.

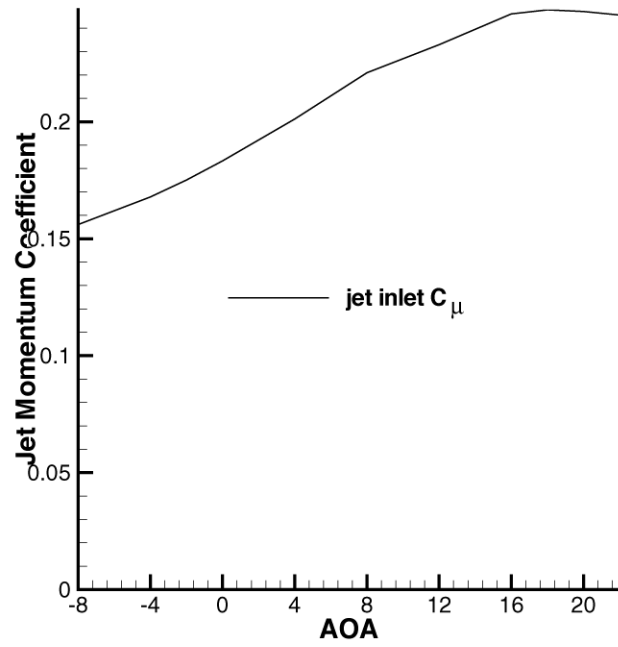


Figure 7: Jet momentum coefficient and equivalent momentum coefficient.

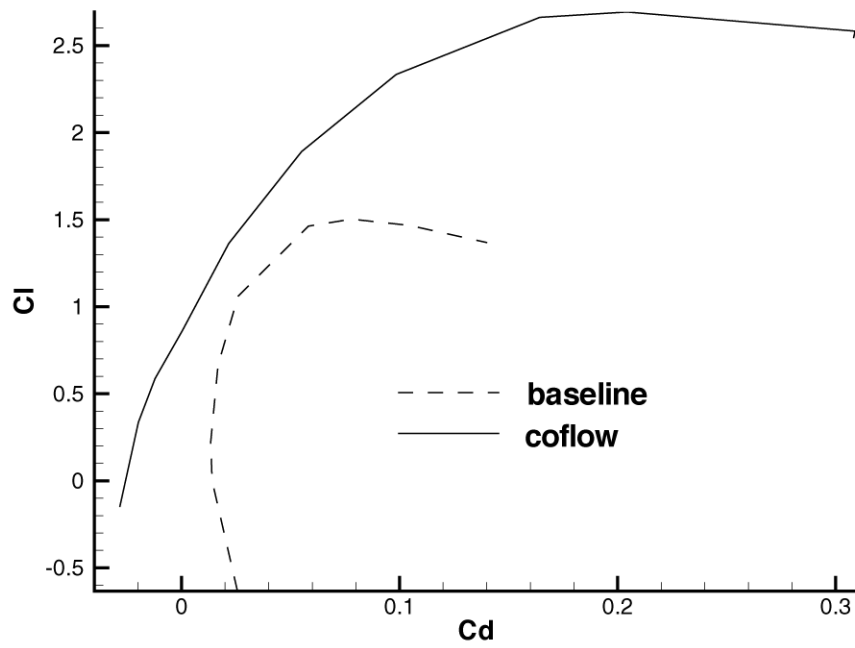


Figure 8: Drag polar for the baseline and coflow jet airfoil.

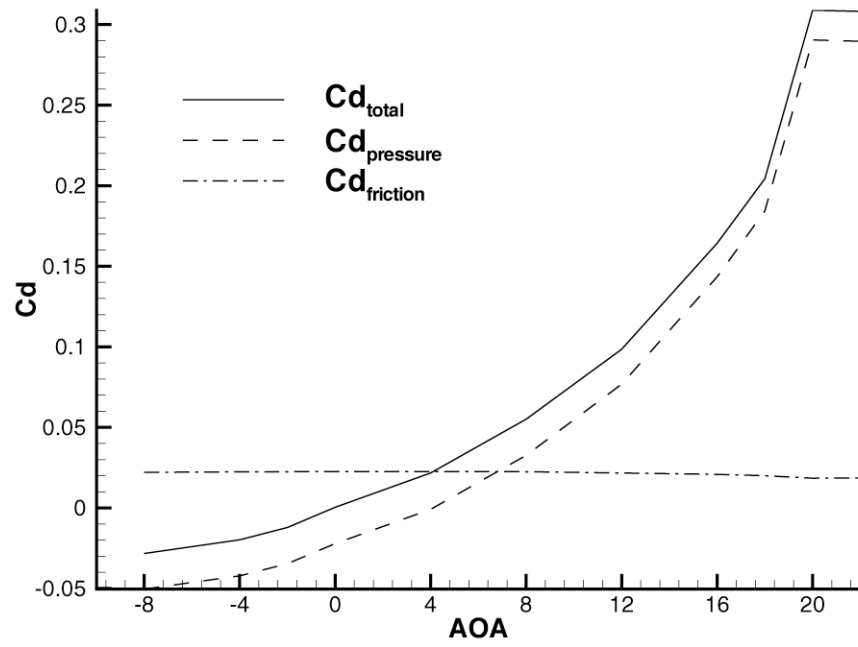


Figure 9: Calculated drag coefficients vs angle of attack for coflow jet airfoil.

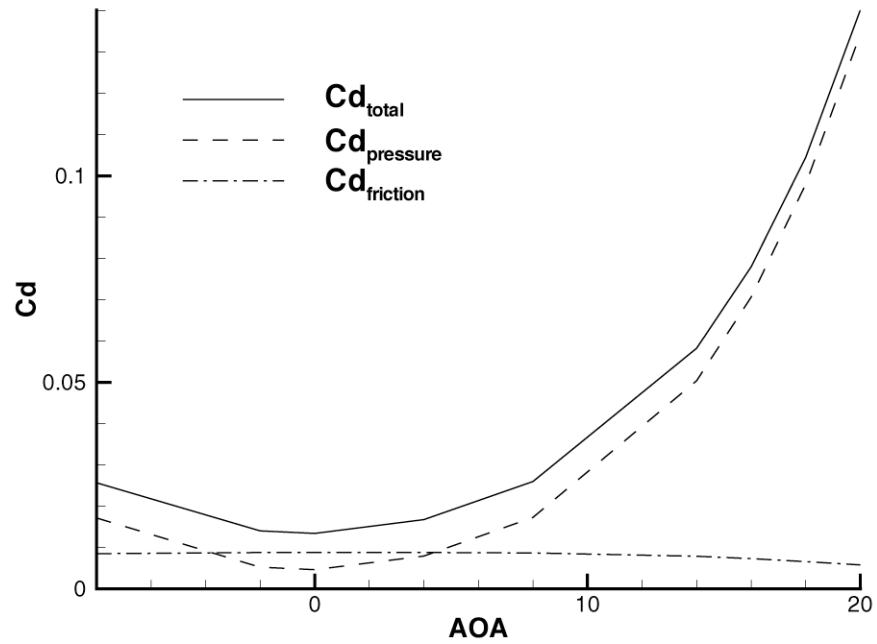


Figure 10: Calculated drag coefficients vs angle of attack for baseline airfoil.

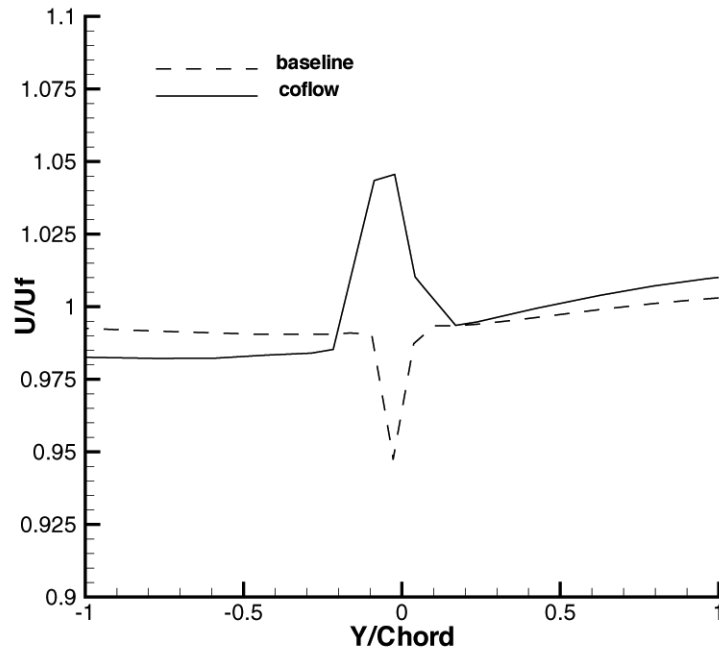


Figure 11: Wake shape for the baseline and coflow jet airfoil.

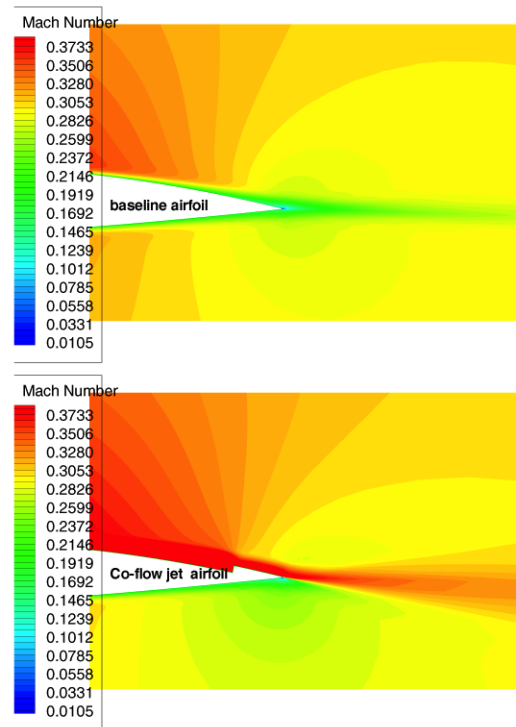


Figure 12: Wake Mach number contours at $AoA=0.0^\circ$ for the baseline and coflow jet airfoil.

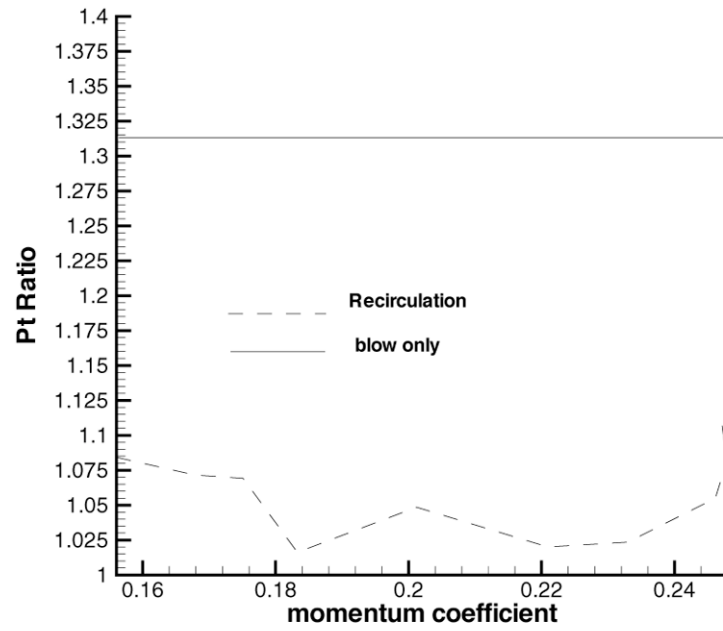


Figure 13: Total pressure ratio vs momentum coefficient for recirculating jet and blowing only.

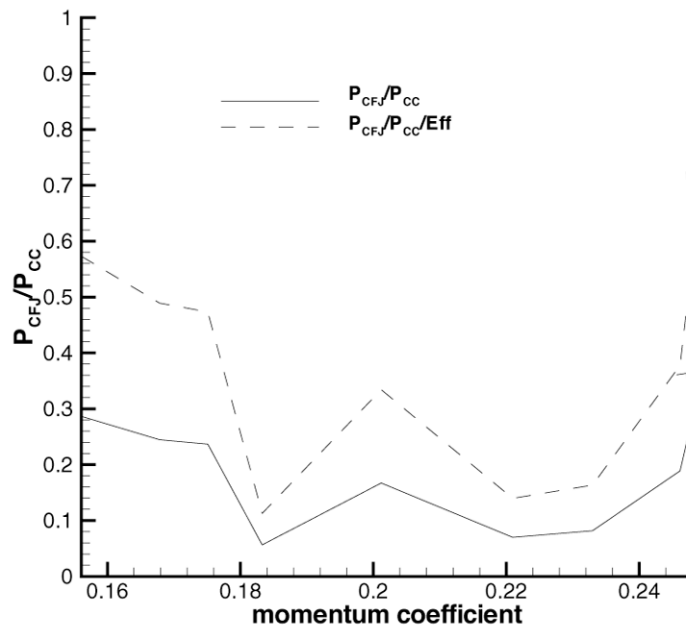


Figure 14: The ratio of the power required for jet injection for recirculating jet and blowing only.

A Novel Airfoil Circulation Augment Flow Control Method Using Co-Flow Jet

Ge-Cheng Zha and Craig D. Paxton

Dept. of Mechanical & Aerospace Engineering

University of Miami

Coral Gables, Florida 33124

E-mail: zha@apollo.eng.miami.edu

Objective:

- Develop a new circulation control method:
 - 1) Augment lift (L , L/D)
 - 2) Increase aircraft maneuverability (AoA range)
 - 3) Be energy efficient (overall airframe-propulsion system)

Review:

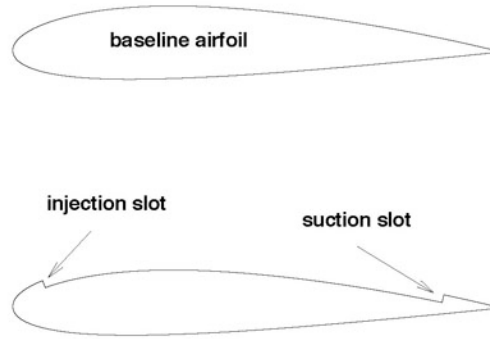
- Conventional circulation control increase lift significantly and reduce noise
- Most effective for large LE and TE radius
- Large drag at cruise and for high speed aircraft
- Hinged flap have thin TE, the complexity of the mechanical control system increased.
- Mass flow blowing penalize propulsion system efficiency
- Maneuverability reduced due to reduced AoA range
- More suitable for taking off and landing, may not used for cruise

New Circulation Control Method

- Use co-flow jet on airfoil suction surface
- Blow near LE, sucking same amount flow near TE, enhanced Coanda effect
- Turbulence mixing transfer energy from jet to mainflow
- Energized flow augment circulation
- Re-circulate jet reduce energy expenditure
- Do not need large LE or TE radius
- Can apply to low or high speed aircraft

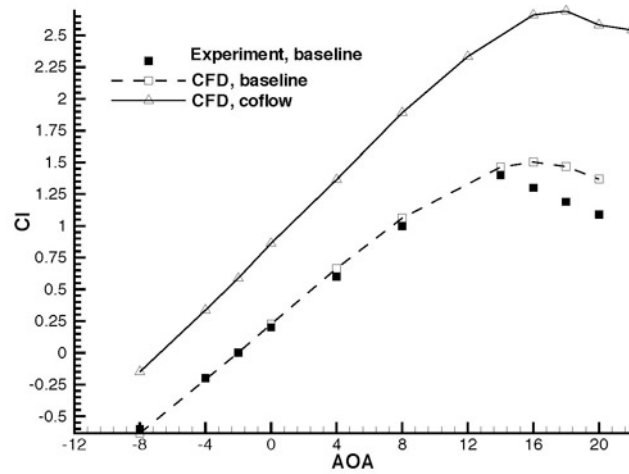
Co-Flow Jet Airfoil

NACA 2415: slot inlet at 6.72%C, outlet at 88.72%C, suction surface lowered by 1.67%C, inlet area = 1.56%C, outlet area = 1.63%C.

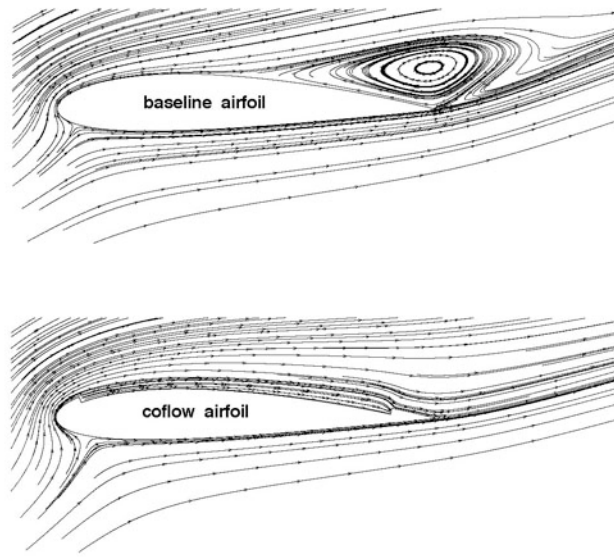


CFD Simulation

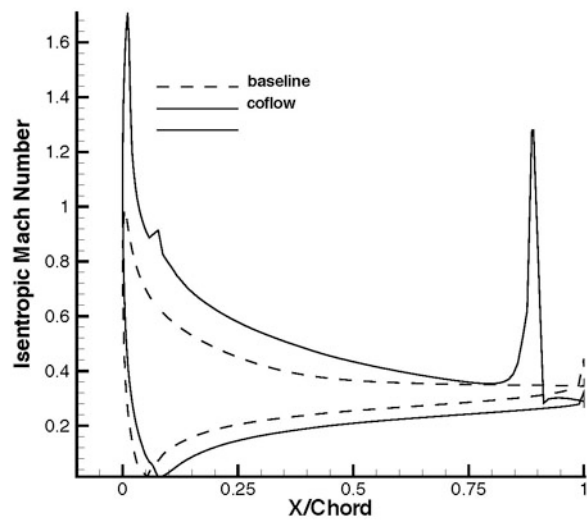
$$Re = 1.9 \cdot 10^6, M_\infty = 0.3, Pt_{jetinlet} = 1.315Pt_\infty$$



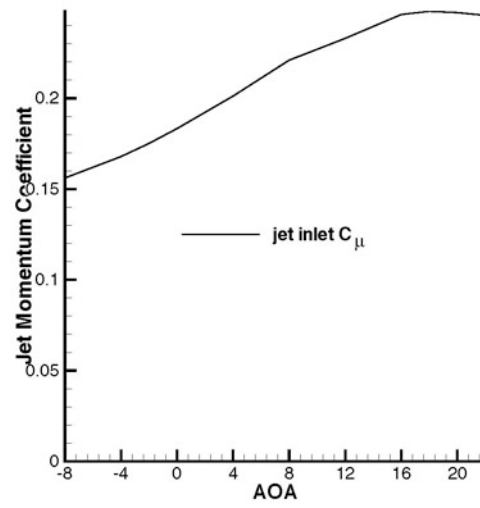
Streamlines at $AoA = 20^\circ$



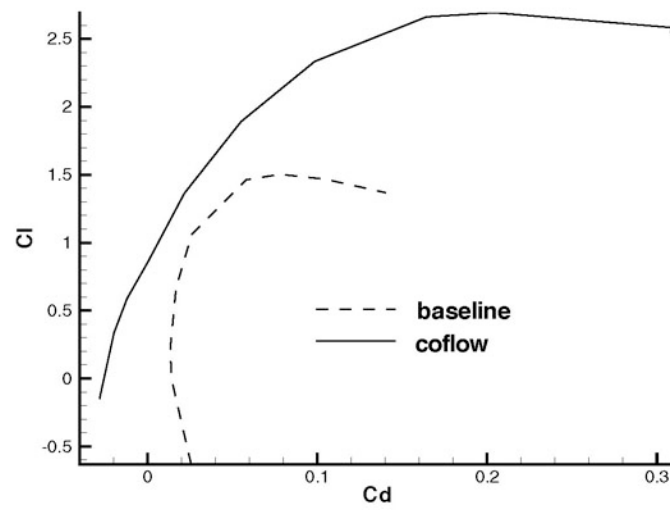
Surface Isentropic Mach Number at $AoA=20^\circ$



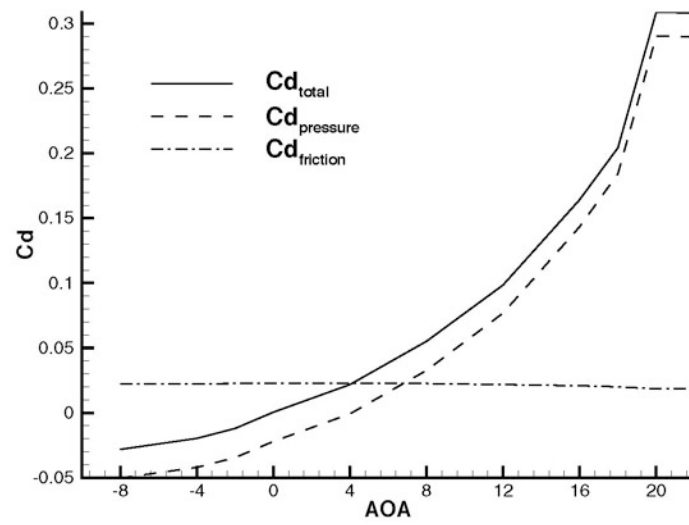
Momentum Coefficient vs AOA



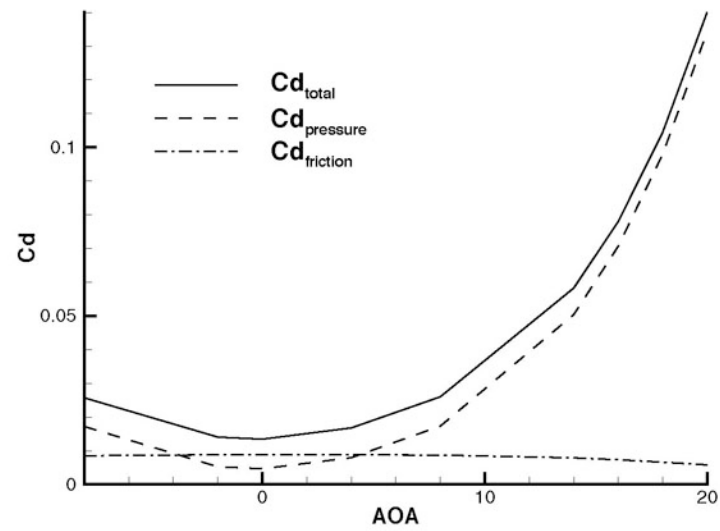
Drag Polar



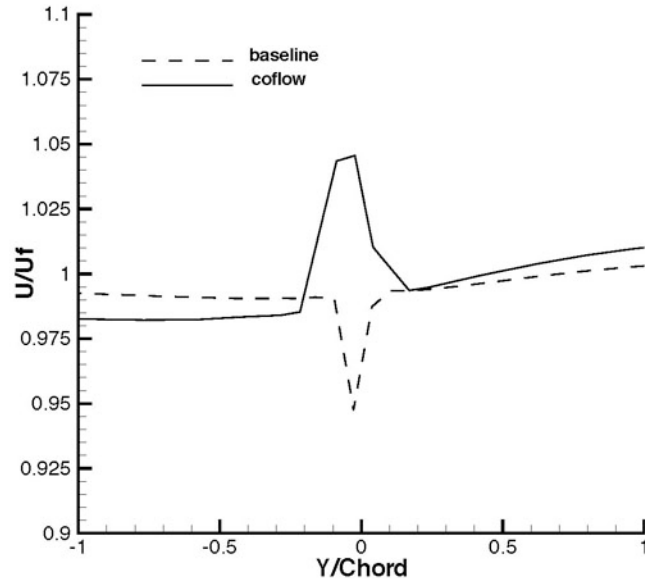
Drag vs AOA for Co-Flow Jet Airfoil



Drag vs AOA for Baseline Airfoil



Wake Profile at AOA=0°



Work required to energize jet

$$W_{isentropic} = Cp(T_{02} - T_{01})$$

$$= CpT_{01}((P_{02}/P_{01})^{\frac{\gamma-1}{\gamma}} - 1) \quad (1)$$

$$W = W_{isentropic}/\eta \quad (2)$$

If the flow control system has the same efficiency for blowing only and recirculation, the work ratio

$$W_R = \frac{W_{rec}}{W_{blow}}$$

$$= \frac{((P_{02}/P_{01})^{\frac{\gamma-1}{\gamma}} - 1)_{recirculation}}{((P_{02}/P_{01})^{\frac{\gamma-1}{\gamma}} - 1)_{blowonly}} \quad (3)$$

Assume a very conservative case:

$$\eta_{recirculation} = 0.5\eta_{blow} \quad (4)$$

$$W_R = 2 \frac{((P_{02}/P_{01})^{\frac{\gamma-1}{\gamma}} - 1)_{recirculation}}{((P_{02}/P_{01})^{\frac{\gamma-1}{\gamma}} - 1)_{blowonly}} \quad (5)$$

The P_t ratio of recirculation is smaller and hence the work required to energize the jet is less than the blowing only.

Penalty to Propulsion due to disposed jet flow

Assume test an engine on the ground and the nozzle expand to ambient,

The thrust is:

$$F = m_{nozzle} V_{nozzle} \quad (6)$$

The disposed jet flow will directly decrease thrust.

Total Efficiency of propulsion system:

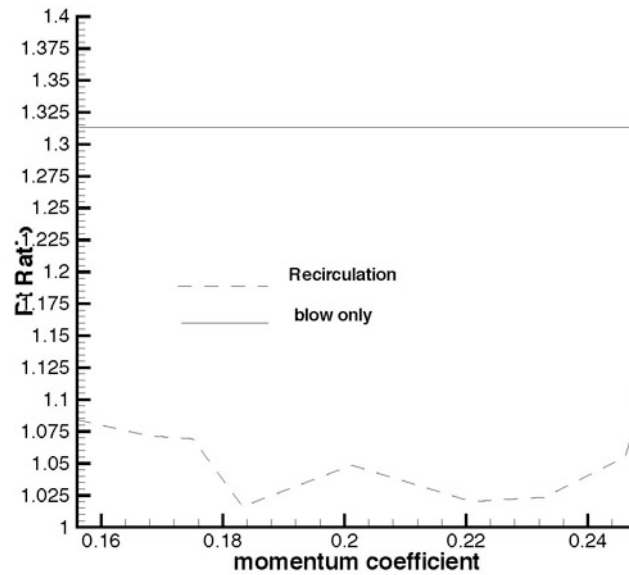
$$\eta = \frac{C_{\infty} m_{nozzle} (C_{nozzle} - \frac{m_{nozzle}}{m_{inlet}} C_{\infty})}{Q} \quad (7)$$

If assume Q is the same, $\frac{m_{nozzle}}{m_{inlet}} \approx 1$, then η is proportional to m_{nozzle} .

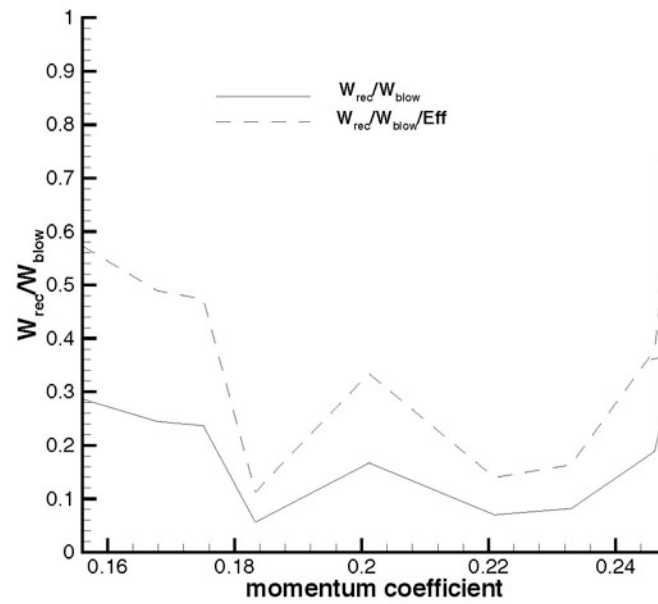
The disposed jet flow will directly reduce the propulsion system efficiency.

The recirculating co-flow jet avoid this penalty.

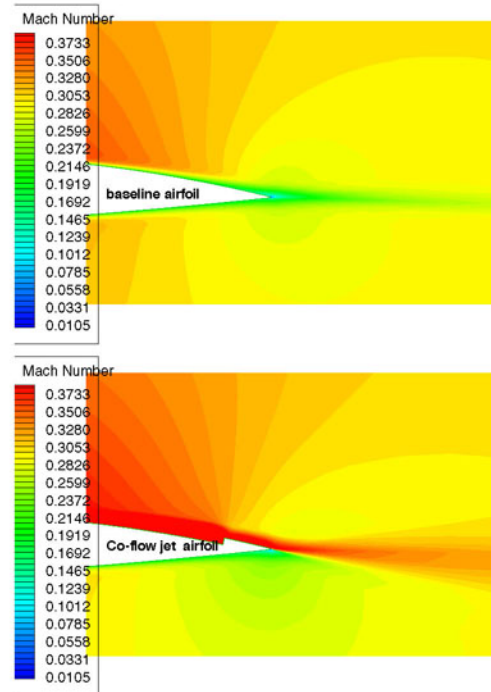
Total Pressure Ratio vs Momentum Coefficient



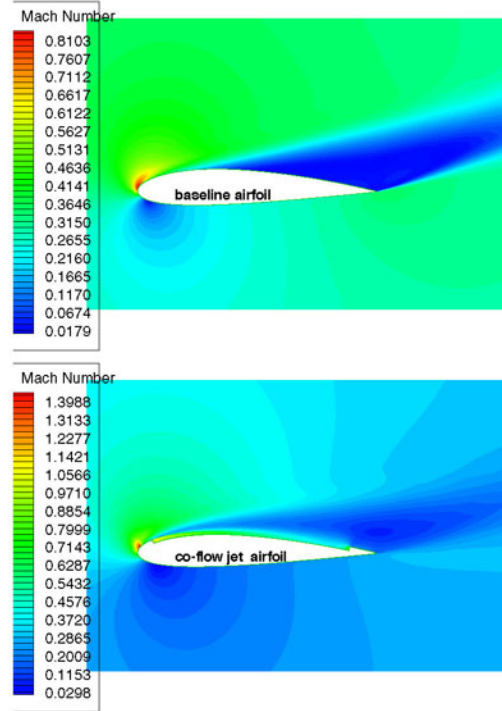
$$Work_{recirculate}/Work_{blow}$$



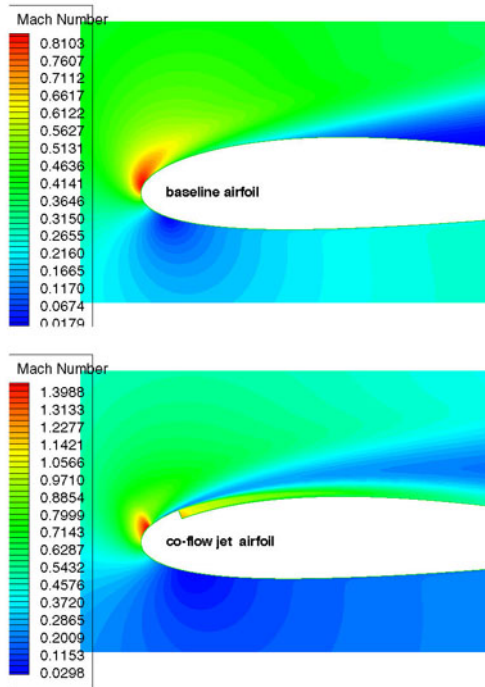
Mach Contours at TE AOA=0°



Mach Contours AOA=20°



Mach Contours at LE AOA=20°



Conclusions:

- CFD simulation shows that the lift may be significantly increased by co-flow jet.
- Stall margin may be greatly enlarged and may increase aircraft maneuverability.
- At cruise, co-flow jet may fill the wake due to surplus momentum and hence reduce drag, or create thrust, the high C_l and low C_d may yield very high aerodynamic efficiency C_l/C_d .
- At high AoA, high lift and high drag may help for short landing and taking off.
- It does not require large LE and TE and hence may be applied to any airfoil (low or high speed).
- Compared with the blowing only flow control, the recirculating co-flow jet may be much more energy efficient.
- Experiment is in progress thanks to NASA LaRC support.
- New concept and more studies needed.

NOISE REDUCTION THROUGH CIRCULATION CONTROL

Scott E. Munro^{*}, K.K. Ahuja[†], Robert J. Englar[‡]

Georgia Institute of Technology

GTRI/ATASL

Atlanta, GA 30332-0844

Abstract

Circulation control technology uses tangential blowing around a rounded trailing edge or a leading edge to change the force and moment characteristics of an aerodynamic body. This technology has been applied to circular cylinders, wings, helicopter rotors, and even to automobiles for improved aerodynamic performance. Only limited research has been conducted on the acoustic of this technology. Since wing flaps contribute to the environmental noise of an aircraft, an alternate blown high lift system without complex mechanical flaps could prove beneficial in reducing the noise of an approaching aircraft. Thus, in this study, a direct comparison of the acoustic characteristics of high lift systems employing a circulation control wing configuration and a conventional wing flapped configuration has been made. These results indicate that acoustically, a circulation control wing high lift system could be considerably more acceptable than a wing with conventional mechanical flaps.

Copyright © 2001 by K. K. Ahuja and Scott Munro. Presented as at AIAA-2001-0666, at the 39th AIAA Aerospace Sciences Meeting & Exhibit, 8-1 January 2001.

^{*} Graduate Student, School of Aerospace Engineering, Student member, now at Naval Air Warfare Center, Weapons Division China Lake, CA 93555-6100.

[†] Regents Researcher and Professor, GTRI and School of Aerospace Engineering, (Corresponding Author)

[‡] Principal Research Engineer, Georgia Tech Research Institute ATAS Lab, AIAA Associate Fellow.

Nomenclature

a - Speed of sound

c - Chord

c_l - Airfoil lift coefficient

CCW - Circulation control wing

$$C_\mu - \frac{\dot{m}V_j}{qS}$$

h - Slot height

\dot{m} - Mass flow

p - Pressure

q - $\frac{1}{2} \rho V^2$ (dynamic pressure)

R - Radial distance from jet exit to measurement location

r - Radius of CCW surface

Re - Reynolds number

SPL - Sound Pressure Level

T - Temperature

V - Velocity

α - Angle of attack

Θ - Polar angle (with respect to the flow axis)

ρ - Density

Subscripts

s - Associated with slot

T - Associated with tunnel freestream

j - Associated with jet

o - Ambient condition

Introduction

One of the major environmental dilemmas facing today's aircraft industry is noise pollution from aircraft, especially around the airport. There is a large emphasis on minimizing community noise due to operation of aircraft at and around the airport. Thus, airlines, aircraft manufacturers, NASA and the FAA have made reducing aircraft noise a priority. NASA has proposed a goal of lowering total aircraft noise emissions by 20 EPNdB by year 2020.

In order to meet this goal, NASA and other organizations have been encouraging innovative research to help reduce aircraft noise. Since a major contributor to aircraft noise on approach is airframe noise (or perhaps even on takeoff if the engine noise is eliminated), reducing this noise would be helpful in reaching the industry goals. The major airframe noise contributors are the landing gear, the slats, and the flaps. Much work has been done in these areas in the last five years in an effort to reduce their noise emissions. Of course, the best solution would be to have an aircraft without these protrusions into the flow field. Obviously an aircraft without landing gear would have serious drawbacks, but there are alternate high-lift systems that could replace conventional wing flaps and slats which have shown great promise in maintaining and even surpassing the lifting benefits of conventional flaps.

Circulation control wings (CCW) have been researched and developed extensively, primarily for the purpose of increasing performance and reducing or replacing the conventional

flap system of an aircraft.¹ Over the years the CCW systems have gone through many configuration designs for many different applications, including versions for rotorcraft, fighter aircraft, and short haul transports.¹ However, there has been limited research conducted investigating the possible acoustic benefits provided by such a system, other than occasional references to smaller noise footprints due to shorter take-off and landing distances. The only known work on acoustics of CCW is that of Salikuddin, Brown and Ahuja² where they evaluated the noise field of an upper surface blown wing with circulation control. That study, however, did not provide an indication of the acoustic benefits of a circulation control wing versus a conventional wing for the same lift.

Since CCW systems have already been shown as an adequate replacement for conventional flap systems in the aerodynamic realm,¹ they are immediately a candidate for reducing airframe noise since they eliminate much of the structure of the conventional flap system that protrudes into the flow. However, there are many issues that need to be resolved before the claims of lower noise are validated. Since the CCW system has never been evaluated on an acoustics basis, it must be optimized for this, while maintaining, at a minimum, the lift characteristics of a conventional system. The acoustic impact of several parameters must be investigated, such as the blowing slot height, slot velocity, and CCW geometric configuration (i.e., flap type and deflection angle). In order to correctly define the best combination, new areas of research will have to be investigated, including jet noise of extremely high aspect ratio nozzles, and the effects of jet turning on its noise propagation. These many issues are the motivation of the present study. The current work involves both experimental and computational efforts. Only experimental results are presented in this paper. Computational results are presented in Part II of this article and in Reference [3].

Background

The circulation control wing (CCW) concept has been researched since the 1960s. The CCW uses a rounded trailing edge (figure 1).¹ Air is blown tangentially along the upper surface from a plenum supply inside the wing through a slot just upstream of the rounded trailing edge. Blowing moves the upper surface separation point around the trailing edge, thus changing the trailing edge stagnation point location, and hence the circulation for the entire wing. The higher-speed air moving along the surface also causes a suction peak in this region and contributes to increased lift.

The slot flow remains attached to the surface due to the so-called Coanda effect.⁴ At low blowing velocities, the tangential blowing behaves similar to a boundary layer control device by adding energy to the slow moving flow near the surface. At higher blowing rates, the lift is increased by the change in circulation described above. A CCW can be designed without any mechanical moving elements if desired. This is achieved using a rounded trailing edge, where the amount of lift is controlled by the pressure valve to the supply plenum. This eliminates the need for flaps with hinges, tracks, screw drives and hydraulics.

The increment in lift generated is controlled by the non-dimensional parameter C_{μ} , defined using slot and freestream properties.

$$C_{\mu} = \frac{\dot{m}V_s}{q_{\infty}S} \quad \text{or} \quad C_{\mu} = \frac{\dot{m}V_s}{q_{\infty}c}$$

With a wing, the non-dimensionalizing area is the wing surface, S . For an airfoil, typically C_{μ} is given in C_{μ}/ft since the chord is the only available reference length. In general, a given C_{μ} will provide a given increment in the lift coefficient over the entire range of angles of attack below stall. The exception to this is when the slot jet velocities or slot heights are large enough to cause

the jet to separate prematurely. Thus, C_{μ} is used extensively in the literature when discussing circulation control.

The large circular trailing edges used in many of the early experiments evolved into a dual-radius hinged flap, mainly because the non-sharp trailing edge greatly increased drag.^{1,6, 7, 8} The hinged flap was a compromise of several desired features. The flap had a curved upper surface, like the cylindrical trailing edge, but a flat lower surface. This overcame the problem of high drag in cruise associated with the non-sharp trailing edge of the early designs. Overall, the hinged flap dual-radius design still maintained most of the circulation-control lift advantages but greatly reduced the drag problem associated with the circular trailing edge system.

The flap itself has several mechanical advantages compared to conventional Fowler flap systems. The flap is about $\frac{1}{4}$ to $\frac{1}{3}$ the size of a conventional flap. This means lower flap weight, and thus fewer structural components are required to hold it in place.⁸ The flap is also a simple hinged flap, rather than a complex Fowler type flap that requires complex gearing, tracks, and through gaps, which most likely contribute to airframe noise on their own. The reduced size and simplicity of the CCW system even with a small flap clearly offers some advantage over a conventional system.

There are many potential uses for circulation control. However, the two applications that have received the most research attention have been circulation control rotors (CCR) and CCW applied to an aircraft for short take-off and landing (STOL) capability. The reader is referred to references [1] and [5] where further details and citations on CCW research can be found. Some research pertinent to the present work is briefly mentioned below.

The Navy sponsored a full-scale flight test program on an A-6/CCW in the late 1970s. The design, tests and results are documented in references [9, 10 and 11]. Research has also

been done to investigate applying the circulation control system to a Boeing 737 type of aircraft. A summary of the effort is documented in reference [6]. The only known acoustic work on CCW configurations was performed by Salikuddin, Brown and Ahuja.² There are other potential uses for circulation control, including automotive applications^{1,12} and helicopters^{1,13} where noise reduction may also be appropriate. The acoustic benefits shown in this paper should be applicable to other areas also.

Facilities and Instrumentation

The anechoic flight simulation facility (AFSF) was used in the experiments. It is located at Georgia Tech Research Institute (GTRI) located at its Cobb County Research Facility in Smyrna, GA. The AFSF operates in an open jet wind tunnel configuration. It is an anechoic facility that allows acoustic measurements to be made in the presence of a freestream (see figure 2). The tunnel inlet has a square inlet which converges down to a 28-inch round duct. The duct terminates in an anechoic room as an open jet. Protruding out from the downstream wall is the collector, which is 4 ft. wide by 5 ft. high. The collector duct extends outside the building and ends at a centrifugal fan powered by a diesel engine. The facility is open circuit, drawing air from outdoors. The details of the facility can be found in references [14 and 15].

In the current experiments, the wings are mounted via mounting brackets to the open jet. This locates the wing across the jet opening immediately downstream of the end of the duct. Figure 3 shows one of the conventional wings mounted at the exit of the open jet. The ambient pressure in the chamber, the plenum pressure for the slot, pressures in the air supply line venturi

mass flow meter, and pressure in the inlet (for freestream velocity) were monitored on individual pressure transducers and manually recorded for each test point.

Acoustic measurements were made with B & K, 4135, 1/4" microphones. One microphone was mounted on a traverse system that translated the microphone from angles of 30° to 90° (where 0° is the freestream direction). This system was arranged to make all measurements in the fly-over plane. The microphone was connected to a multi-channel digital frequency analyzer, which is run by software on a PC.

Figure 4 shows a schematic of the blowing system for the CCW. It consists of high-pressure 3/4 inch tubing, a mass flow venturi, pressure gauges, and a muffler. On the upstream end, the tubing is connected to an existing high-pressure line with a control valve upstream. The flow passes through a mass flow venturi, and then goes through more tubing to an in-house built muffler which absorbs the upstream valve noise. Downstream of the muffler, the air passes through more tubing to inlets for the CCW plenum.

Test Models

The test model wing used in reference [6] was used as the test model for this study. This CCW model, shown in figure 5, has a supercritical baseline airfoil shape, but has many different detachable CCW trailing edge configurations. These included different sized flaps and cylindrical trailing edges. Based on past aerodynamic studies, the best overall aerodynamic characteristics were obtained with the small CCW flap configurations. The small deflectable flap allowed for low drag during cruise, but by blowing over the curved upper surface with the flap deflected, significant flow turning could still be achieved when desired. The highest lift

configuration was found to be with the flap deflected 90° . This was used as the starting configuration for the current acoustic tests.

The conventional wing had the same general shape as the CCW over most of the chord. However, its trailing edge was altered with a cut-out for a stowed flap. A single-slotted Fowler flap was attached. Two different flaps were tested. The flap was deflected 30° or 40° from the chord line to simulate a landing configuration. Both flaps spanned the entire wing, but one flap had a cut-out in at the mid-span point. Figure 6 shows the airfoil profile of the model and a drawing depicting the flap cut-out. Figure 3 is a photo of the model installed in the AFSF. The cut-out is to simulate the cut-outs on a real aircraft. Cut-outs are often present for structural reasons or to prevent engine exhaust from impinging on a lowered flap.

Technical Approach

The current work focused on optimizing a CCW system for low noise impact while maintaining aerodynamic performance sufficient for direct comparison to a conventional flapped wing configuration. The first step was to determine if and how a CCW configuration can have lower noise than a conventional system. This step involved side-by-side comparison of representative configurations under the same conditions, i.e., the same freestream flow and lift conditions. Since there are several variations of CCW systems that have been researched, a basic study of different CCW configurations was done. Since the test models were used in other aerodynamic experiments, this also allowed the use of this data when making the acoustic comparisons.

The optimized blowing configuration was compared with a conventional wing system. Basic noise spectra of the CCW and conventional wing configurations were acquired at several mean flow velocities and angle of attack. Specific cases where the different configurations had the same lift coefficient were then compared directly. Lift data from previous studies were used for this comparison.

Results and Discussion

Acoustic Optimization of Existing CCW State-of-the-Art Configurations

Since the CCW concept has been around for nearly 40 years, there have been many advances, changes, and modifications to the basic concept to improve its overall performance. To attempt to acoustically test all the different configurations would be unreasonable, since many of the changes were made to improve the system. There is little reason to acoustically test a system that is technologically surpassed by a better version. Thus, the goal of the current study is to investigate two or three of the best performing CCW configurations.

Based on previous aerodynamic work, the CCW with its flap deflected 90° was chosen as the beginning point for the study (a possible high-lift configuration for landing approach). This had the best overall high-lift aerodynamic performance of several configurations tested in previous studies. The flap was eventually adjusted to 30° deflection to prevent flap-edge vortex shedding noise that was present in the 90° case.

Six slot heights were chosen for the optimization study ranging from 0.003" to 0.020". These dimensions were chosen because they were typical slot heights used in earlier aerodynamic studies.⁶ A wide range of slot Mach numbers was evaluated, ranging from 0.3 to

1.2. The acoustically optimized CCW test configuration was compared with a conventional flap configuration. The conventional model had the same generic airfoil shape as the CCW, except near the trailing edge to accommodate the conventional flap. The flap chord was about 30% of the wing chord and deflected 40° to simulate a landing configuration. Data were acquired for each test configuration at freestream speeds of 100, 150, 200, and 250 ft/s (nominal) and at geometric angles of attack of 0° , 7° , and 14° .

The majority of the data presented in this section was acquired at a geometric angle of attack of 0° and at the highest freestream velocity of about 240 ft/s unless otherwise noted. Figure 7 shows acoustic spectra for several slot velocities with no freestream flow for the CCW with the 90° flap configuration. It shows a similar trend to the basic jet velocity scaling property developed for round jets. For the measured velocities, V^8 scaling of jet noise theory¹⁶ predicts about a 19 dB increase between the two most extreme cases, which is similar to that measured (about 16 dB) above 2 kHz. Some noise due to scrubbing of the slot jet over the flap surface is likely to be present as well.

It appears that the majority of the noise is associated with the jet noise from the slot and not due to internal model and facility noise associated with the blowing system above 2 kHz. However, below 2 kHz the scaling is not followed in the data. This is most likely due to internal noise that is generated from the flow into the wing on its way to the slot. This contaminates the signal making the noise higher for the lower slot velocities, but not affecting the higher velocities where the jet mixing noise is expected to be dominant. Thus, the difference between the data is less than predicted by the theory. This is supported by figure 8.

Figure 8 shows the spectra out to a frequency of 60 kHz. These figures show two slot heights, and hence two slot areas, at the same slot velocity. However, inside the wing the areas

in the flow path remain the same. Since the mass flow into the wing must be the same as the mass flow out, the doubling of the exit area roughly causes a doubling of the mass flow at the exit, and hence a doubling of the mass flow inside the wing. However, since all the areas inside the wing are constant, the velocity must double inside the wing in order to double the mass flow. Thus, if noise is dominated by the internal noise it should follow a sixth power law of the internal velocity, as this noise is expected to be dipole like in nature. If so, the data should reflect an 18 dB increase. However if the noise is dominated by externally produced jet mixing noise, then it will change only to the extent that the exit area has changed. Based upon the available experience/theory on round jets¹⁶ this will provide for the jet mixing noise intensity proportional to slot exit area. This translates into a 3 dB increase in noise after shifting the spectrum for $h = 0.006$ " to the left over the spectrum for $h = 0.012$ " by a factor of one octave to allow for the shift in the noise frequencies proportional to a characteristic length. This number is somewhat smaller than the observed difference in the SPL's of the two spectra in figure 8. All of these arguments assume that we can apply the lessons learned from round jets to very high aspect-ratio jets. Yet, since the noise increase is of the order of 3 dB, it can be said that internal noise is not significant in this case. The fact that the observed difference in spectral SPL's is more than the expected 3 dB could also be associated with the scrubbing noise of the CCW slot jet moving over the rounded edge. If so, it is genuinely produced outside and is not contaminated by any internal noise. Obviously, some clarification of the data is needed. To fully understand the jet noise characteristics of extremely high aspect-ratio jets without the internal noise concerns discussed here, we have fabricated a high aspect ratio nozzle (HARN). We reserve our full judgment until additional studies have been carried out on the HARN, which is being tested by the authors in an acoustically clean facility

We believe that, the data may be contaminated by noise generated internal to the wing below about 2 kHz. A muffler was built and installed in the supply line downstream of all valves to eliminate as much upstream noise as possible. However, due to the small thickness of the wing, inlets into the wing plenum are smaller than desired. This results in a relatively high velocity flow entering into the plenum with no space to absorb the noise generated.

It is believed that these noise sources may be causing a majority of the noise below 2 kHz where the noise is not following the typical V^8 jet noise scaling. For the time being, this will be noted and data below 2 kHz will be disregarded as either somewhat corrupted by internal noise or not understood until HARN data becomes available.

Figure 9 shows the noise spectra for several slot jet velocities at a constant freestream velocity and constant slot height of 0.003". There are several things to note. First, with no blowing there is a large-amplitude well-defined tone. It is also important to note that in general the very low frequency noise ($f \sim < 4$ kHz) is much greater compared to the data in figure 7. Some of this is from the tunnel noise itself (below about 500 Hz) but most of it is flow noise associated with the freestream flow around the wing. The tone is believed to be due to the shedding of vortices off the bluff trailing edge of the deflected flap. Notice that blowing, even at low slot jet velocities, significantly reduces the magnitude of the tone. However in this case it is not completely eliminated, in fact it dominates the spectra at all blowing velocities.

The tone mentioned above was unexpected. This presented a problem since the tone dominated the spectrum at all blowing conditions, thus any acoustic benefit derived from using the CCW over a conventional wing would be lost if the flap were deflected to 90° . Because of this, it was decided that reducing the flap deflection might produce a less dominant tone, but still provide enough lift with the right amount of blowing to equal that of a conventional wing.

Figure 10 shows two curves with the flap set to 30° . In this case notice that the tone is completely eliminated with a small amount of blowing. The computational study also produced the same result, and is presented in reference [3]. Not only is this advantageous for the current study, but this result could be used in other applications where similar shedding produces a distinct tone.

Data for test conditions similar to those for the 90° deflection are shown in figure 11. Again, with no blowing the tone is present. However, with small amounts of blowing the tone is completely eliminated. Since this configuration showed more promise, the remaining parameters were optimized using the 30° flap configuration. Both slot height and slot jet velocity were examined.

The effect of slot height was investigated next. Figure 12 shows data with similar freestream conditions but different slot heights. It is important to note that this figure compares different CCW configurations with the same lift. For the same C_μ at different h , the slot velocity will be different since C_μ is dependent on mass flow from the slot. Since the goal is to compare the same lift, it is best to look at the data where C_μ is constant since the same C_μ will give the same lift in most cases. There is some variation of lift with h for high C_μ , but in the C_μ range of interest here, h does not have an independent affect on the results. Thus, the data in figures 12 shows that there is a lower noise from the larger slot heights for a given lifting condition. This makes sense since C_μ is proportional to mass flow through the slot. By increasing the slot height but maintaining the same mass flow (and hence same C_μ) the jet velocity of the slot is lower. At this point it appeared that the most appropriate conditions for comparing a CCW system to a conventional system had been found. Maximize the slot height so that jet velocity is minimized.

Unfortunately it was found that above a slot height of about 0.012" the noise began to increase (for constant C_μ). Since this was contrary to the logical trend associated with what should be happening, some attention was given as to why this was happening. If one looks more closely at C_μ it contains a mass flow term. Initial results indicated that reducing the slot velocity reduced the noise. In the equation this means that V_s would decrease. If one defines the mass flow term based on the mass flow "in" rather than "out" the problem becomes evident.

$$C_\mu = \frac{\dot{m}_s V_s}{qC} = \frac{\dot{m}_{in} V_s}{qC} = \frac{(\rho_{in} A_{in} V_{in}) V_s}{qC}$$

Density will vary with the pressure in the plenum, ($\rho = P/RT$), but it varies proportionally to slot velocity (as V_s decreases, P decreases, and hence ρ decreases). Area is constant in the plenum regardless of slot height. Thus, in order to offset the decrease in V_s and ρ , V_{in} must increase. When this occurs, the internal noise associated with internal velocities will also increase. Figure 13 shows OASPL plotted versus h for constant C_μ . If it is assumed that the highest slot velocity is dominated by external jet noise, the decrease in noise due to falling V_s can also be plotted. In the figure the highest V_s occurs at the smallest h . The drop in OASPL should follow the V^8 scaling law. However, in this case keep in mind that the slot velocity drops due to an increase in slot area. Thus the final estimated curve shows dropping OASPL due to slot velocity, but at a lower rate than V^8 because of an increase in slot area.

Notice that the experimental data follows V^8 scaling for some time but eventually increases away from the estimated drop off. It is believed that this increase is due to the increasing dominance of internal noise as the slot velocity is reduced while the internal velocity is increased.

Although this finding was unfortunate it was not terribly detrimental to the study as long as one keeps in mind that proper design of the internal system will decrease the CCW noise further (in essence it should continue to drop along the estimated slot velocity curve in figure 13 as the slot velocity is decreased). Thus, any benefit found will be enhanced with careful design of the internal system.

Determining an “equal lift” condition

The next step was figuring out how to compare the two lift augmentation systems. Aerodynamic data from previous studies was used for this (specifically that in reference [6]). Aerodynamic data was available for both conventional wing configurations and the CCW in the form of lift curves (c_l vs α curves). This was convenient since for a CCW, a given C_μ will generally provide a Δc_l over the entire angle of attack range (not including the extreme high jet velocities and large slots where the jet separates from the surface). Thus, once the lift for the unblown CCW was found, this could be compared to the c_l for the conventional airfoil and the needed Δc_l was be calculated by subtracting the two values. This Δc_l was then used to determine the C_μ needed to match lift provided by the conventional wing flap system. Essentially each C_μ is analogous to a flap setting which shifts the baseline lift curve by a given amount. For the particular CCW configuration (CCW with flap at 30°), a C_μ of about 0.04 produced about the same amount of lift as the conventional wings used in the experiments.

CCW versus Conventional Wings

Two conventional wing configurations were tested. One configuration with a 30° flap spanning the entire span of the wing, and one with a flap deflected 40° spanning the entire wing

except for a cut-out region in center span (figure 6 for a drawing figure 3 for a photo of it installed in the AFSF). These wings are the same basic airfoil shape as the CCW. The wings were tested at the same flow conditions as the CCW.

Initially, the conventional wing with the 30° flap was tested. Figure 14 shows a comparison between the conventional wing with the 30° flap and the CCW configuration with lowest noise for the equivalent lift case. Since the $h \sim 0.012''$ data was the minimum CCW noise condition, it is presented in the figure. In the range between 1 kHz and 10 kHz, the CCW has noise levels similar to those of the conventional system. Unfortunately, this was not the desired result, although it does provide assurance that using the CCW system does not increase the noise to the environment in its minimum noise configuration.

However, many aircraft have a cut-out in flaps across the span. This difference contributes a fair share of noise to a conventional wing system since flap edge noise has been identified as a major contributor to airframe noise. Thus, this wing was missing a noise source that would most likely be greatly reduced in a CCW system. Since the CCW flap is much smaller, there is no need for a gap in the flap to avoid engine exhaust. Its small size would also in many cases reduce the need for gaps due to structural concerns. Thus the CCW system with a full span flap is not unreasonable.

Acoustic tests were performed on the new configuration similar to the previous tests. Figure 15 shows the comparison of the wing with the cut-out flap with the CCW. As expected, the cut-out in the flap increased the noise on the conventional system significantly and shows a significant advantage to using a CCW system in the region below 10 kHz and some advantage up to 40 kHz. Beyond 40 kHz the two systems have similar noise levels. The data in this figure and following figures have different frequency ranges to emphasize the areas in the frequency

spectrum where there are differences between the two systems. Similar results can be seen at other freestream velocities and angles of attack, however, the magnitude of the difference varies some depending on the conditions.

Up to this point, only data from a microphone at $\Theta = 90^\circ$ has been shown. This is only part of the noise picture, the changes in directivity of the noise between the two systems must be compared as well. Data were acquired at 30° , 60° , and 90° . It should be noted that there are some differences depending on the angle. Note that the 60° and 90° positions do not actually have a line-of-sight path to the slot exit which is located on the top surface of the wing. It is also worth noting that the jet from the slot leaves the trailing edge of the wing at about $\Theta = 56^\circ$. Even with freestream velocity, the jet stays relatively close to that angle for some time beyond the trailing edge of the wing.

Figure 16 compares the data for the two wing systems at $\Theta = 30^\circ$ and $\Theta = 60^\circ$. At 30° the CCW system produces no real advantage over a conventional system. However there is still some noise reduction in favor of the CCW system at 60° , similar to the 90° data shown earlier. These results indicate that a CCW system certainly has potential for reducing airframe noise. The results also show some trends of high-aspect-ratio jets, however there is still much left to study and resolve before all the aspects of the circulation control wing noise issues are solved and helpful to the design of a practical low noise CCW system.

In order to resolve some of the questions brought up by the CCW and to eliminate the possibility of internal noise contamination, a high aspect-ratio nozzle has been designed and fabricated. This nozzle is presently being tested by the authors in an anechoic facility and the intent is to produce a database of quality high aspect-ratio jet noise data that can be used to verify the speculations about internal noise in the experiments presented here. In addition this data will

be used to augment the present results by demonstrating the even greater benefits possible for a CCW high lift configuration in reducing airframe noise.

Conclusions

Due to the great interest in reducing aircraft noise, an innovative concept for eliminating a conventional flap system has been tested for its possible acoustic advantages. Previous studies have shown that the circulation control wing is an aerodynamically viable alternate for conventional mechanical flaps. This study shows that there is also a substantial advantage in the acoustic realm. The results presented showed a lower noise spectrum for a CCW system compared to a conventional system for the same lifting condition. It should be noted that even if the CCW produces noise comparable to that of a conventional wing it is an advantage. This is because a CCW is expected to be much lighter than a conventional wing.

It was also noted that the internal noise of the CCW blowing system of the model inhibited finding the full possible advantage a CCW system can offer. It is believed that careful design of a CCW blowing system, including internal details, could further improve the results shown here.

Tests are also ongoing on a very high aspect ratio nozzle to verify the characteristics and scaling of high aspect ratio rectangular nozzles similar to what is found in a CCW blowing slot. These results will provide a greater understanding of this type of jet.

Acknowledgments

This work was sponsored by NASA Grant -NAG1 - 2146 through NASA Langley, under its Breakthrough Innovative Technology Program. The authors are grateful to Dr. L. Sankar of the AE school for many helpful discussions. Thanks are also due to Mr. C. Jameson for designing the HARN nozzle and to Dr. Rick Gaeta for his assistance in the experiments and many useful discussions.

References

1. Englar, Robert J., "Circulation Control Pneumatic Aerodynamics: Blown Force and Moment Augmentation and Modification; Past, Present & Future." AIAA Paper 2000-2541, Fluids Conference, Denver, CO, June, 2000.
2. Salikuddin, M. Brown, W.H., and Ahuja, K.K. "Noise from a Circulation Control Wing with Upper Surface Blowing," Journal of Aircraft, Vol. 24 No. 1, January, 1987.
3. Liu, Yi, Sankar, Lakshmi N., Englar, Robert J., Ahuja, Krishan K. "Numerical Simulations of the Steady and Unsteady Aerodynamic Characteristics of a Circulation Control Wing." AIAA paper 2001-0704. January, 2001.
4. Dunham, J. "A theory of circulation Control by Slot-Blowing Applied to a Circular Cylinder," Journal of Fluid Mechanics, Vol. 33 Part 3, pp 495-514, 1968
5. Englar, Robert J., Applegate, Constance A. "Circulation control - A Bibliography of DTNSRDC Research and Selected Outside References: January 1969 through December

- 1983,” David W. Taylor Naval Ship Research and Development Center, DTNSRDC-84/052, 1984
6. Englar, Robert J., Smith, Marilyn J, Kelley, Sean M. and Rover, Richard C., III. “Development of Circulation Control Technology for Application to Advanced Subsonic Transport Aircraft,” AIAA Paper 93-0644, presented at AIAA Aerospace Sciences Meeting, January, 1993.
 7. Englar, R.J. and Huson, G.G. “Development of Advanced Circulation Control Wing High Lift Airfoils,” AIAA paper 83-1847, presented at AIAA Applied Aerodynamics Conference, July, 1983.
 8. Englar, Robert J. “Low-Speed Aerodynamic Characteristics of a Small, Fixed Trailing-Edge Circulation Control Wing Configuration Fitted to a Supercritical Airfoil,” David W. Taylor Naval Ship Research and Development Center, DTNSRDC/ASED-81/08, March 1981.
 9. Nichols, J.H. Jr, Englar, R.J., Harris, M. J., Huson, G.G. “Experimental Development of an Advanced Circulation Control Wing System for Navy STOL Aircraft,” AIAA paper 81-0151, presented at AIAA Aerospace Sciences Meeting, January, 1981..
 10. Pugliese, A. J., and Englar, R. J. “Flight Testing the Circulation Control Wing,” AIAA paper 79-1791, presented at AIAA Aircraft Systems and Technology Meeting, New York, August, 1979.
 11. Nichols, J.H., Jr. et al. “Development of High Lift Devices for Application to Advanced Navy Aircraft,” Report DTNSRDC-80/058, AD A084-226, April, 1980.
 12. Lane, Paul Jr. “Ground Controls,” Racecar Engineering, Vol. 9 No. 8, pp 20-23, October 1999.

13. Reader, Kenneth R. "Hover Evaluation of the Circulation Control High Speed Rotor," David W. Taylor Naval Ship Research and Development Center, Report 77-0034, June 1977
14. Ahuja, K.K., Tanna, H.K., and Tester, B.J. "An experimental Study of Transmission, Reflection and Scattering of Sound in A Free Jet Flight Simulation Facility and Comparison with Theory," Journal of Sound and Vibration, 75 (1), pp 51-85, 1981
15. Ahuja, K. K., Tester, B. J., and Tanna, H. K., "The Free Jet as a Simulator of forward Velocity Effects on Jet Noise." NASA Contractor Report # 3056, 1978.
16. Ahuja, K.K., and Bushell, K.W. "An Experimental Study of Subsonic Jet Noise and Comparison with Theory," Journal of Sound and Vibration, 30 (3), pp 317-341. 1973..
17. Tam, C.K.W. and Zaman, K.B.M.Q., "Supsonic Jet Noise from Non-Axisymmetric and Tabbed Nozzles." AIAA Paper 99-0077, 1999.
18. Tam, Christopher K.W., Auriault, Laurent, "Jet Mixing Noise from Fine Scale Turbulence." AIAA Paper 98-2354, 1998.
19. Tam, C.K.W., Golebiowski, M. and Seiner, J.M., "On the Two components of turbulent Mixing Noise from Supersonic Jets." AIAA Paper 96-1716, 1996.
20. Tam, Christopher K.W., "Influence of Nozzle Geometry on the Noise of High Speed Jets." AIAA paper 98-2255, 1998.
21. Ahuja, K.K. "Correlation and Prediction of Jet Noise," Journal of Sound and Vibration, 29 (2), pp 155-168, 1973.

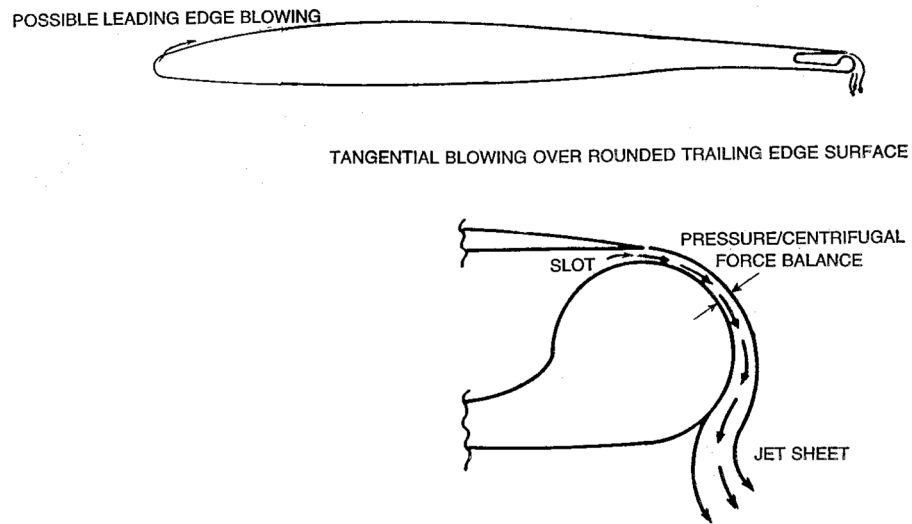


Figure 1: Schematic circulation control wing concept.

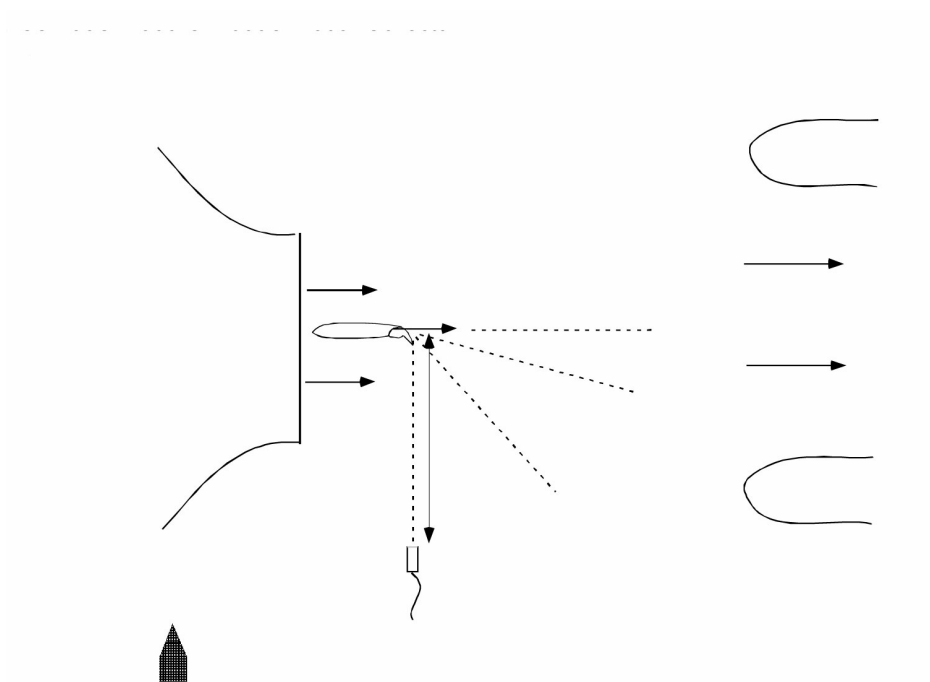


Figure 2: Schematic of Anechoic Flight Simulation Facility (AFSF).

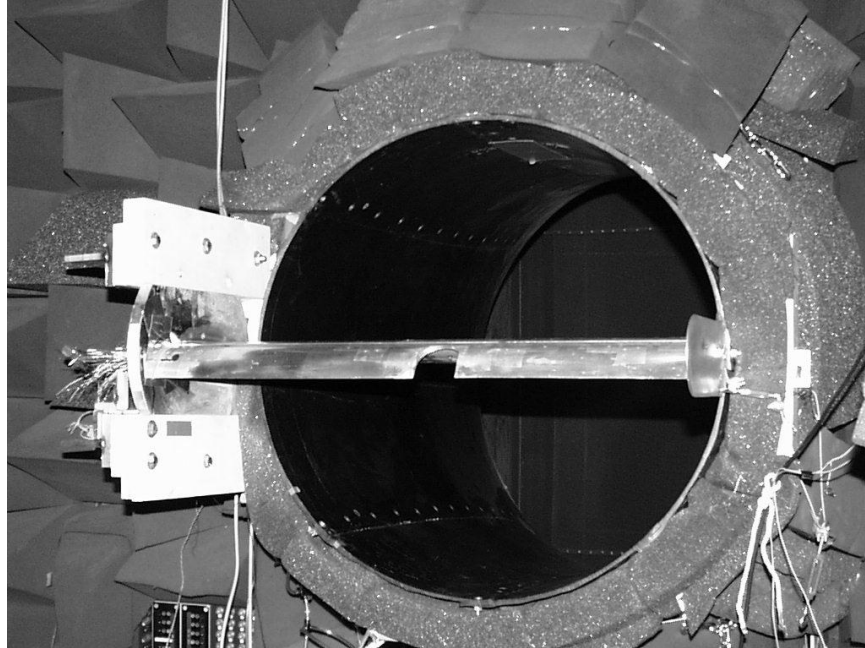


Figure 3: Photo of a conventional wing mounted in AFSF.

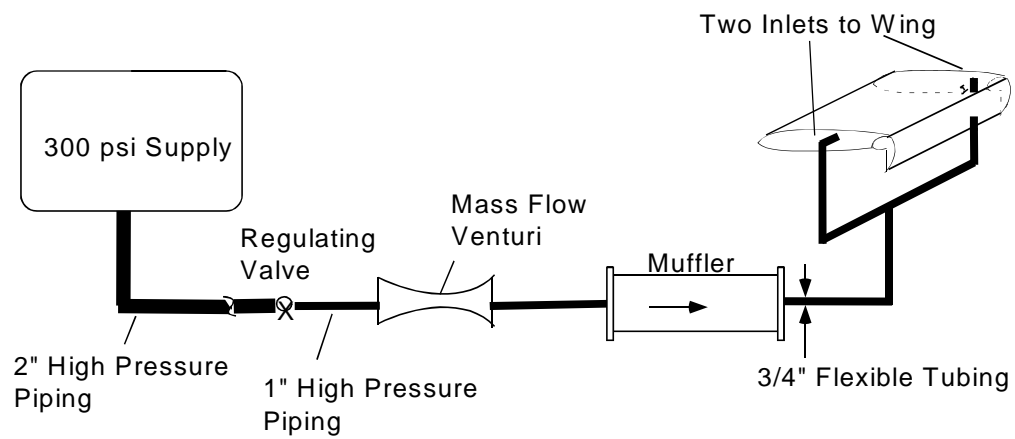


Figure 4: CCW blowing system configuration.

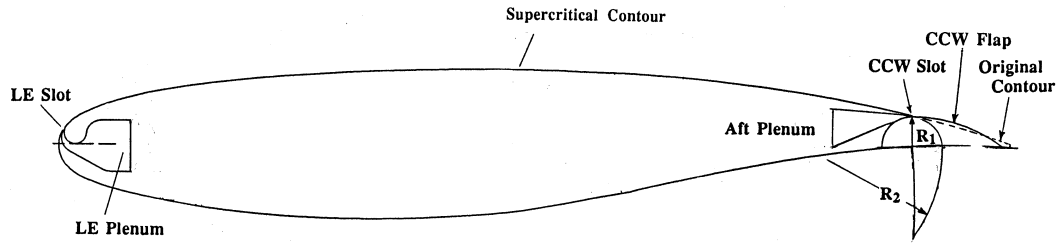
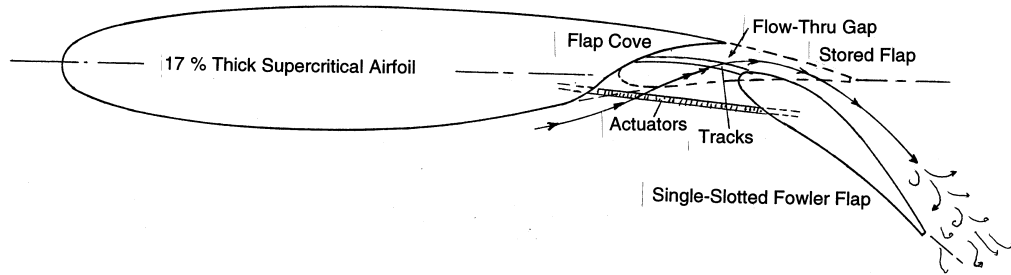
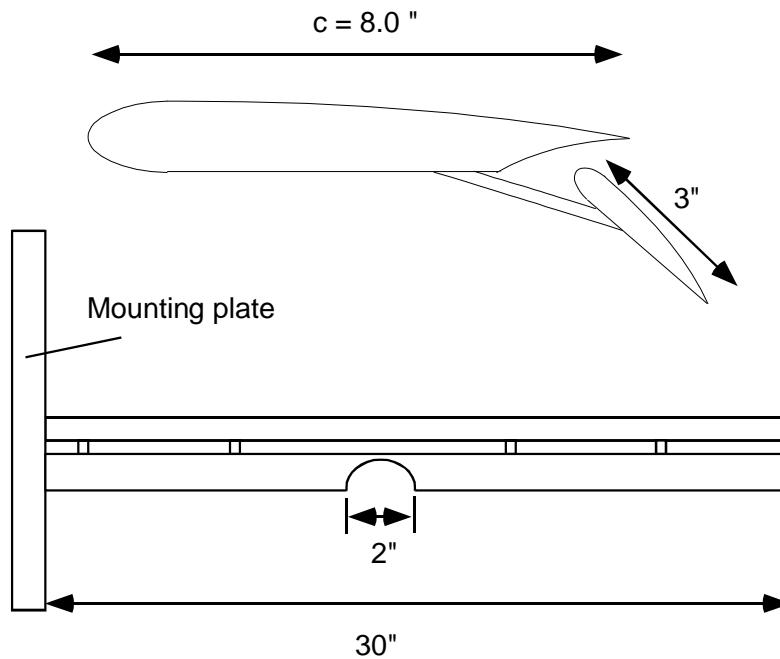


Figure 5: Schematic of CCW flap-wing configuration, generic supercritical airfoil shape..



(a)



(b)

Figure 6: (a) Schematic of conventional flap-wing configuration, generic supercritical airfoil shape (b) Drawing of conventional wing with flap with cut-out.

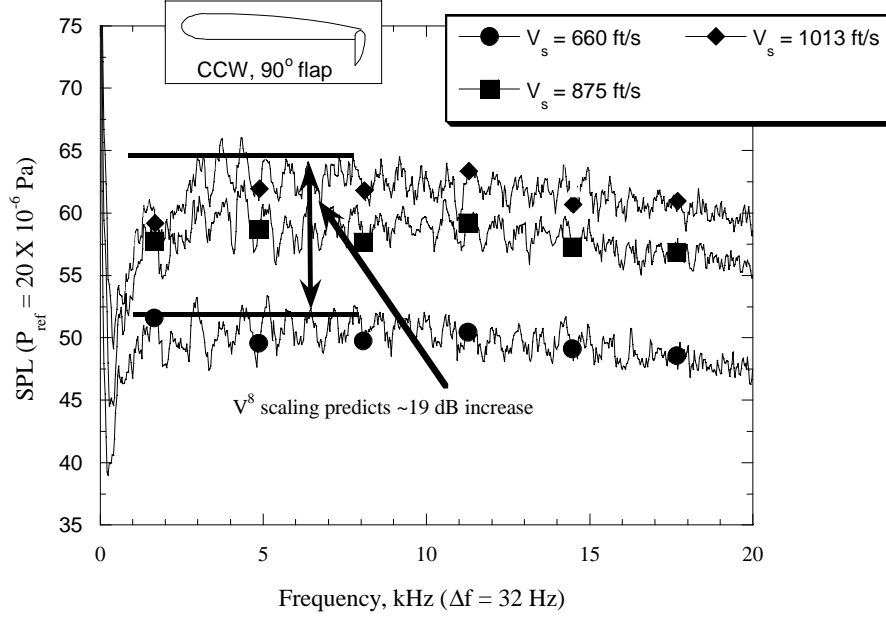


Figure 7: CCW blowing system noise spectra with no freestream flow.
 $V_T = 0$ ft/s, $h = 0.006$ "

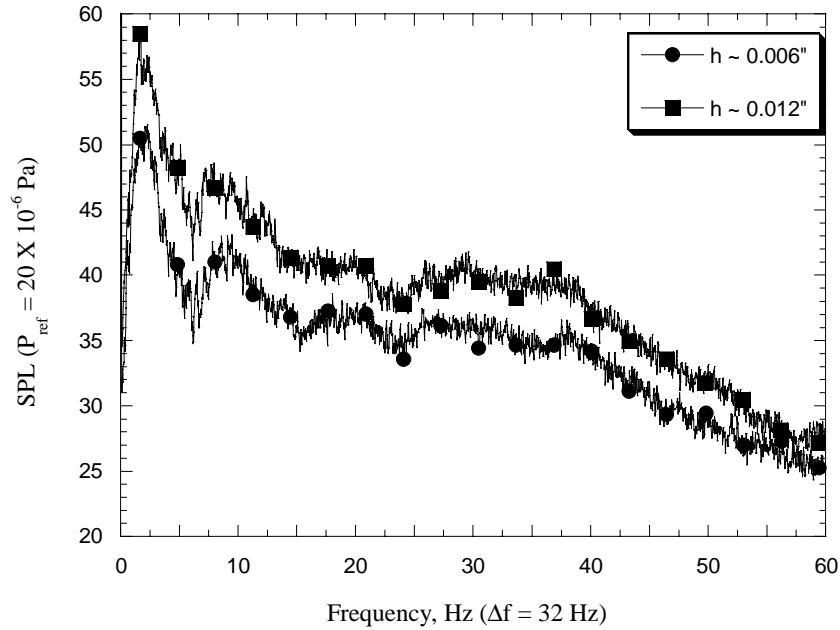
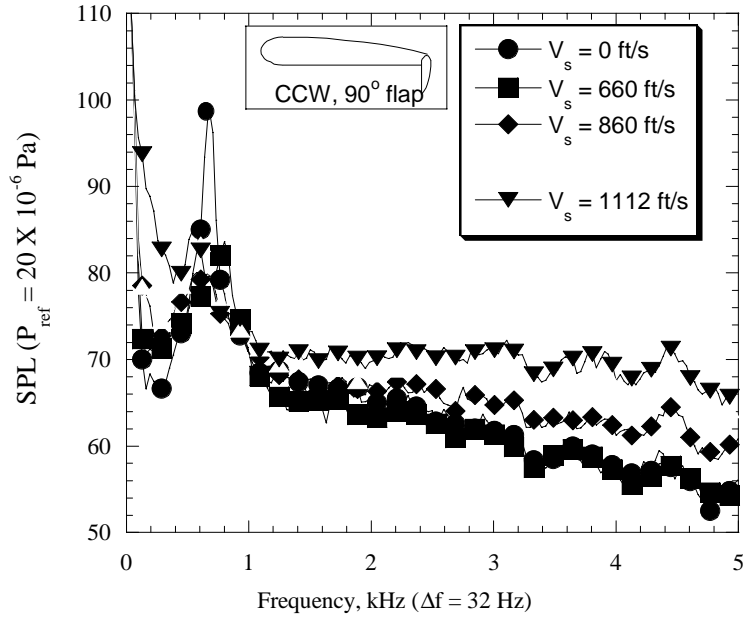
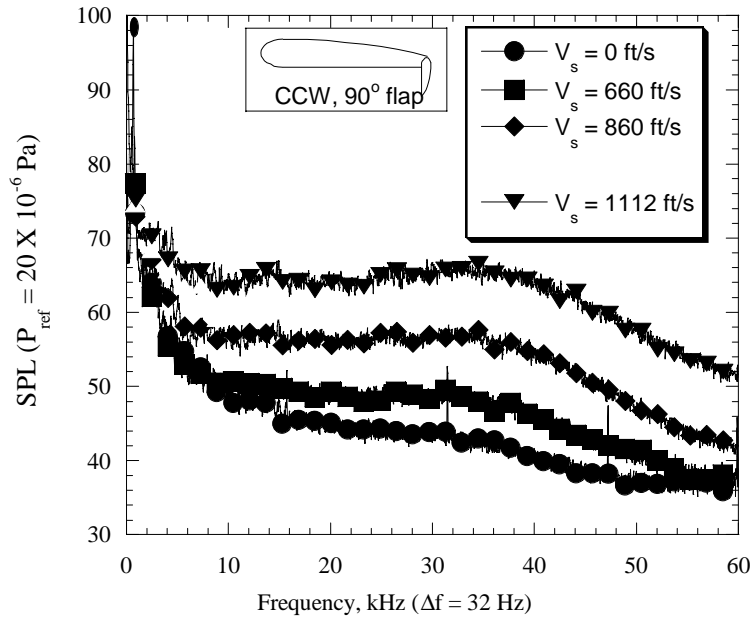


Figure 8: SPL of CCW with different h and the same V_s .
 $\Theta = 90^\circ$, $V_s = 660$ ft/s, $V_T = 0$ ft/s.



(a)



(b)

Figure 9: CCW with 90° flap and freestream velocity, $\Theta = 90^\circ$, $V_T = 220$ ft/s, (a) $f = 0 - 60$ kHz, (b) $f = 0 - 5$ kHz.

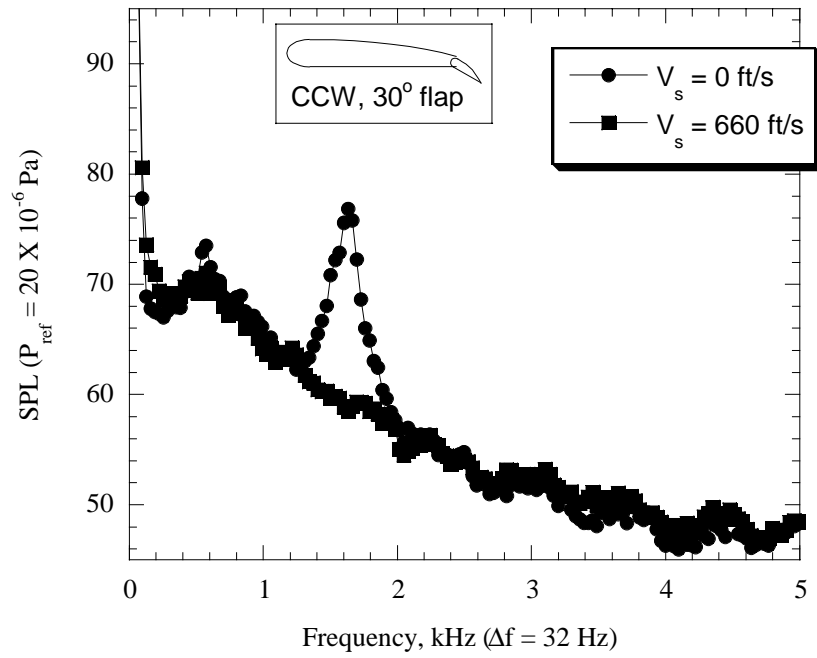


Figure 10: CCW with 30° flap and freestream velocity,
 $\Theta = 90^\circ$, $V_T = 220 \text{ ft/s}$, $f = 0 - 5 \text{ kHz}$.

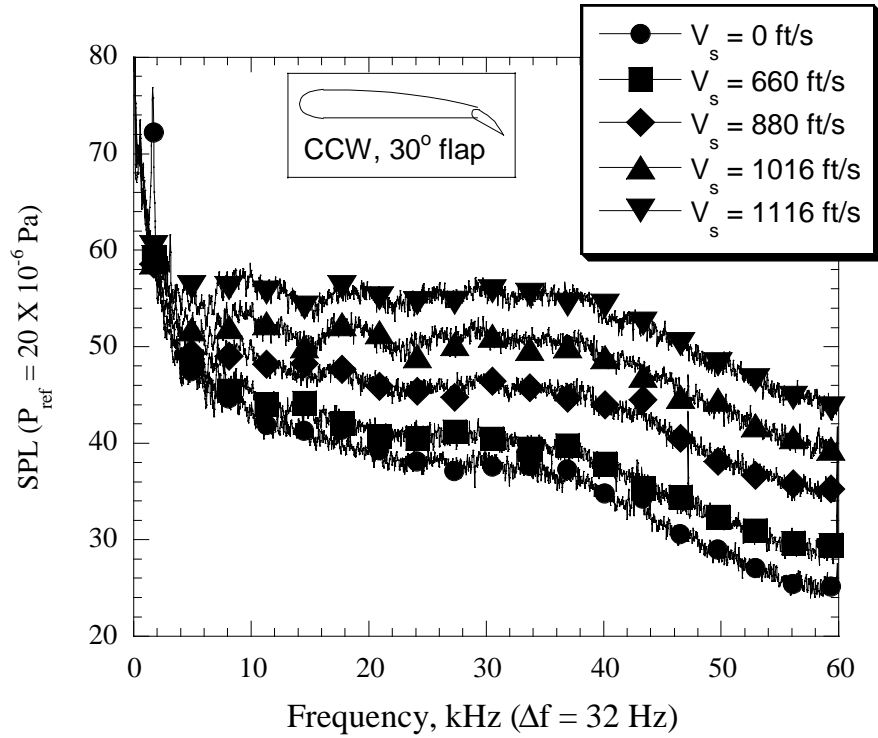


Figure 11: CCW with 30° flap and freestream velocity,
 $\Theta = 90^\circ$, $V_T = 220 \text{ ft/s}$, $f = 0 - 60 \text{ kHz}$.

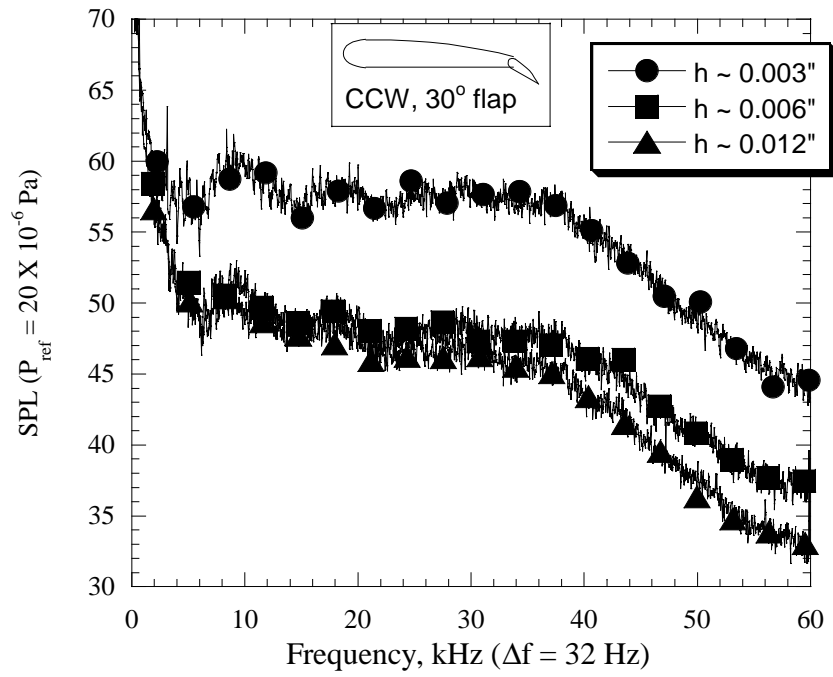


Figure 12: CCW with 30° flap at 3 different h , $C_{\mu} = 0.04$, $\Theta = 90^\circ$, $V_T = 220$ ft/s, $f = 0 - 60$ kHz.

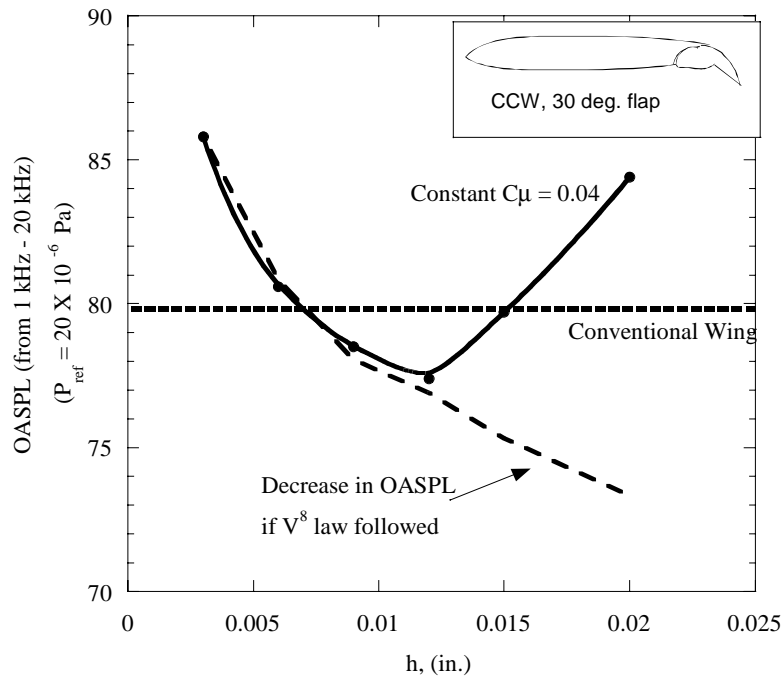


Figure 13: OASPL for various $C_{\mu} = \text{constant}$

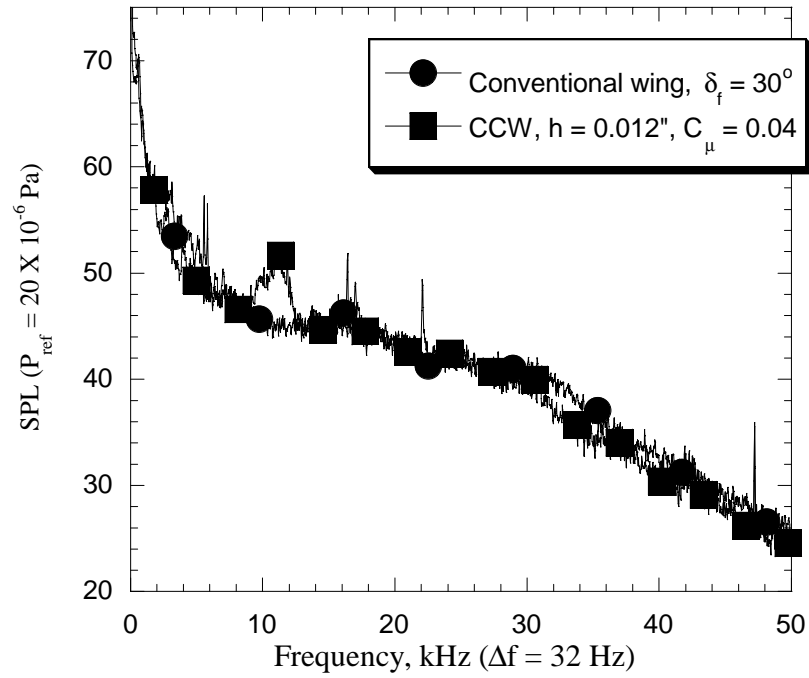


Figure 14: CCW and conventional wing 2-d flap at similar lift condition.
 $\Theta = 90^\circ$, $V_T = 220$ ft/s

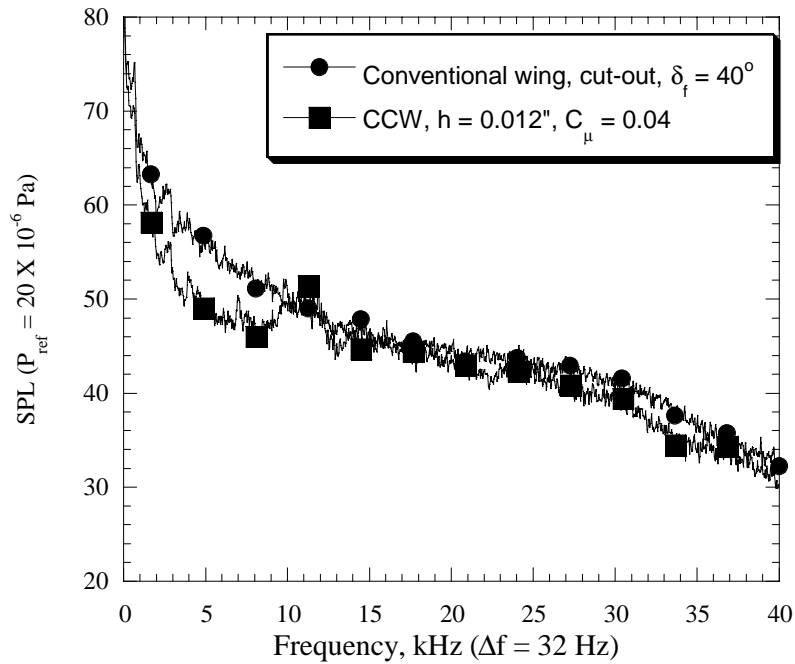
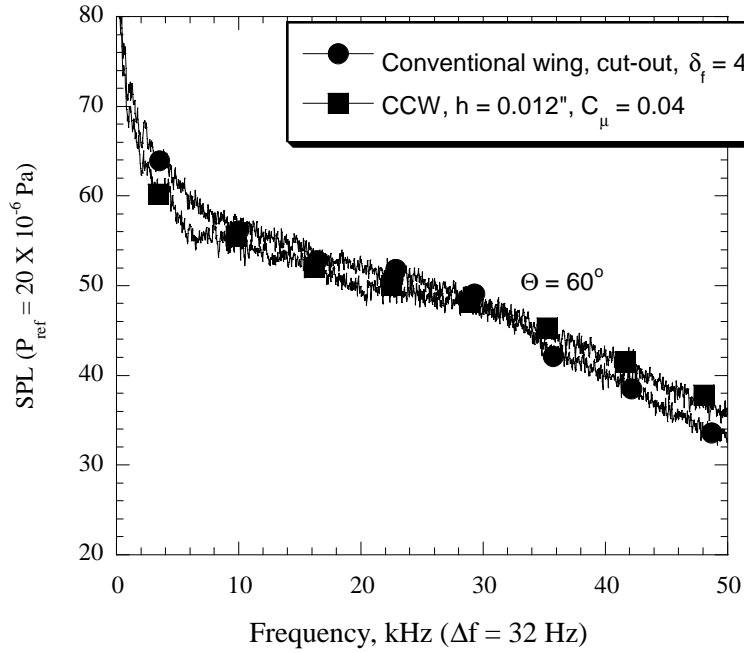
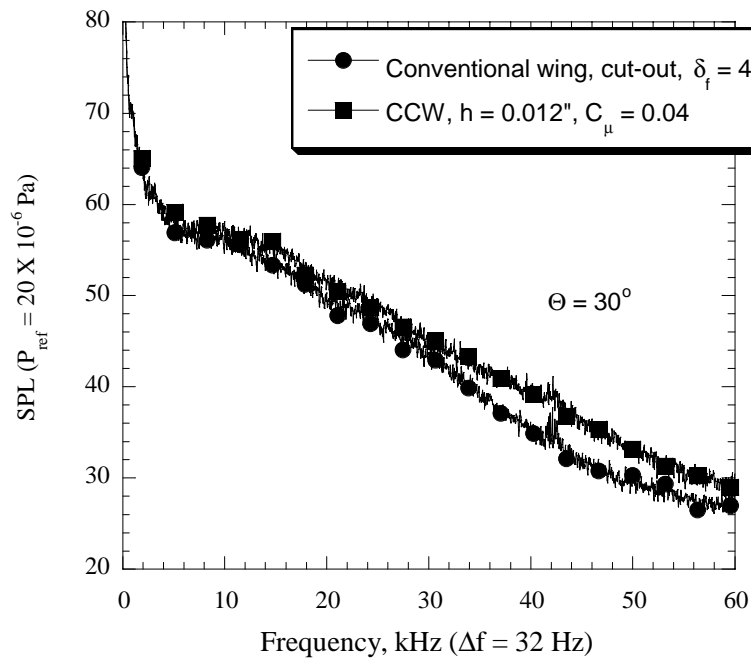


Figure 15: CCW and conventional wing with cut-out at similar lift condition.
 $\Theta = 90^\circ$, $V_T = 220$ ft/s



(a)



(b)

Figure 16: CCW and conventional wing with cut-out at similar lift condition.
 $V_T = 220 \text{ ft/s}$, (a) $\Theta = 30^\circ$, (b) $\Theta = 60^\circ$.

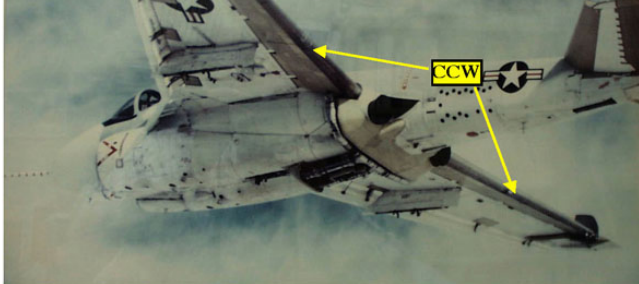
Aeroacoustic Characteristics of Circulation Control Flows

Krish K. Ahuja
Georgia Institute of Technology
GTRI/ATASL
Atlanta, GA 303 dB42
Krish.ahuja@gtri.gatech.edu
770 528 7054

*NASA/ONR Circulation Control Workshop
Hampton, VA
March 16-17, 04*

Why Aeroacoustics of Circulation Control Flows?

A-6 Circulation Control Wing STOL Demonstrator
(Englar and Navy Colleagues)



**140% Increase in Usable
 C_L**

**75 % Increase in Lifiable
Take-Off Payload**

**60 - 65 % Reduction in
Take Off and Landing
Ground Roll**

**30 - 40% Reduction in
Take Off and Approach
Speeds**

- But What Happened to the Noise Levels?
- Increased Noise Could be a show Stopper
- Decreased Noise Could be Beneficial
- Did the Noise Affect the Aircraft Performance?

Outline of the Talk

- Available Literature on Acoustics of Circulation Control Flows (Coanda Flows)
- Acoustics/Aeroacoustics 101
- CC Applications Where the Total Noise Increases
- CC Applications Where the Total Noise Decreases
- Potential of Exploiting High-Frequency Noise of CC Devices to Our Advantage
- Virtual Noise Reduction Via CC Technology
- Flow/Acoustic Interactions in Curved Shear Layers of Coanda Jets
- Concluding Remarks

Available Literature on Acoustics of Circulation Control Flows (Coanda Flows)

CC Noise Publications

Peter W. Carpenter and Colleagues, University of Warwick, Coventry, UK

- P.W. CARPENTER & P.N. Green **1983**, Noise sources in external Coanda-type gas flares. *AIAA Paper No. 83-0758*, 8 pages.
- P.W. CARPENTER & P.N. Green **1984**, Noise sources in external Coanda-type flares. *Proc. Inst. of Acoustics* **6**, Pt 1, 195-201.
- P.W. CARPENTER, Noise emission from Coanda-type waste-gas flares. *Inst. of Phys. Meeting on Unsteady Combustion and Combustion/Acoustic Interaction, Univ. of Hull, Oct. 1991*.
- P.W. CARPENTER, D.W. Bridson & P.N. Green **1986**, Features of discrete tones generated by jet flows over Coanda surfaces. *AIAA Paper No. 86-1865*, 10 pages.
- P.W. CARPENTER & P.N. Green **1997**, The aeroacoustics and aerodynamics of high-speed Coanda devices: Part 1. Conventional arrangement of exit nozzle and surface. *J. Sound & Vibration* **208**, 777-801.
- P.W. CARPENTER & C. Smith **1997**, The aeroacoustics and aerodynamics of high-speed Coanda devices: Part 2. Effects of modifications for flow control and noise reduction. *J. Sound & Vibration* **208**, 803 dB-822.
- P.W. CARPENTER **1997**, The aeroacoustics and aerodynamics of high-speed Coanda devices. *Proc. 7th Asian Congr. of Fluid Mechanics*, IIT Madras, India, 8-12 December, pp. 199-202.

CC Noise Publications

Salikuddin, Brown and Ahuja
Lockheed Georgia

- Salikuddin, M., Brown, W. H., and Ahuja, K. K., "Noise From circulation Control Wing with Upper Surface Blowing; Vol. I - Detailed Results, Final Report on Lockheed Project 84R465, Lockheed Georgia Report No. LG84ER0129, October 1984.
- Salikuddin, M., Brown, W. H., and Ahuja, K. K., "Noise From circulation Control Wing with Upper Surface Blowing; Vol. II - Summary, Final Report on Lockheed Project 84R465, Lockheed Georgia Report No. LG84ER0130, October 1984.
- Salikuddin, M., Brown, W. H., and Ahuja, K. K., "Noise from a Circulation Control Wing with Upper Surface Blowing," AIAA 85-3083, AIAA Aircraft Design Systems and Operations Meeting, Colorado Springs, CO, October 1985.
- Salikuddin, M., Brown, W. H., and Ahuja, K. K., "Noise from a Circulation Control Wing with Upper Surface Blowing," *Journal of Aircraft*, Vol. 24, No. 1, pp 55-64, 1987.
- Ahuja, K. K., "Controlling Plume Deflection by Acoustic Excitation - An Experimental Demonstration," AIAA 90-4006, 13th AIAA Aeroacoustics Conference, Tallahassee, FL, October 1990.

CC Noise Publications

M. S. Howe

- "NOISE GENERATED BY A COANDA WALL JET CIRCULATION CONTROL DEVICE," *Journal of Sound and Vibration*, 2002, 249(4), pp 679 -700.

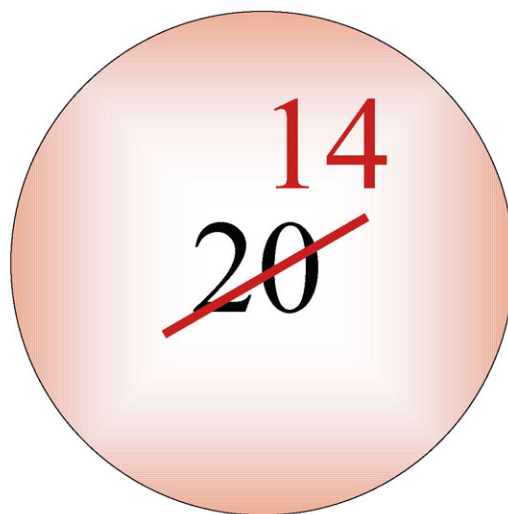
Georgia Tech Publications on CC Noise

- Liu, Y., Sankar, L., Englar R. J., and Ahuja, K. K., "Simulation of the Steady and Unsteady Aerodynamic Characteristics of a Circulation Control Wing," AIAA-2001-0704, 39th AIAA Aerospace Sciences Meeting & Exhibit, 8-1 January **2001**.
- Munro, S., Ahuja, K. K., and "Noise Reduction Through Circulation Control Technology," AIAA-2001-0666, 39th AIAA Aerospace Sciences Meeting & Exhibit, 8-1 January **2001**.
- Munro, S. and Ahuja, K. K., **2003**, 9th AIAA/CEAS Aeroacoustics Conference and Exhibit, Hilton Head, South Carolina, USA, 12 - 14 May 2003.
 - "Aeroacoustics of a High Aspect-Ratio Jet," AIAA-2003-3323
 - "Fluid Dynamics of a High Aspect- Ratio Jet," AIAA-2003-3129
 - "Development of a Prediction Scheme for Noise of High-Aspect Ratio Jets," AIAA 2003-3255

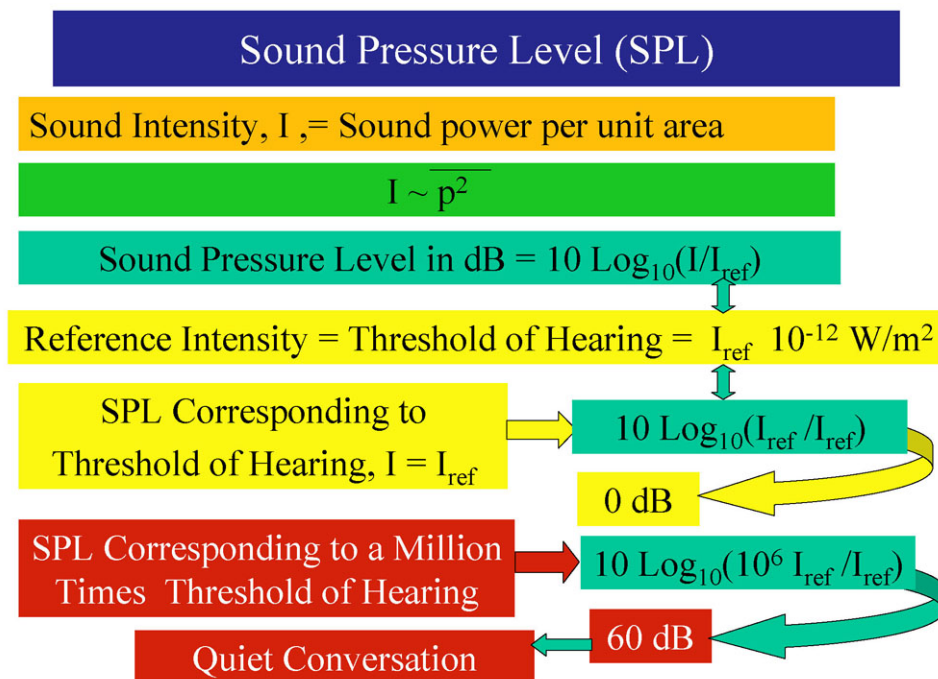
PhD Dissertations on CC Noise

- Munro, Scott Edward, "Jet Noise of High Aspect-Ratio Rectangular Nozzles with Application to Pneumatic High-Lift Devices." Georgia Institute of Technology, PhD thesis, January, **2002**.
(Advisor: Ahuja)
- Liu, Yi, "Numerical Simulations of the Aerodynamic Characteristics of Circulation Control Wing Sections." Georgia Institute of Technology, PhD thesis, January, **2003**.
(Advisor: Sankar)

Total Number of Publications on CC Flow Noise



Acoustics/Aeroacoustics 101



Sound Pressure Level (SPL)

The Ratio of Pressure Amplitudes Between a Quiet Conversation, 60 dB, and a Rock Concert, 120 dB, Is 1000.

Atmospheric Pressure Is 3500 Times Greater Than The Pressure Amplitude of a 120 dB Signal

At 120 dB, One Starts Feeling Discomfort And Experiences a Ringing in the Ears

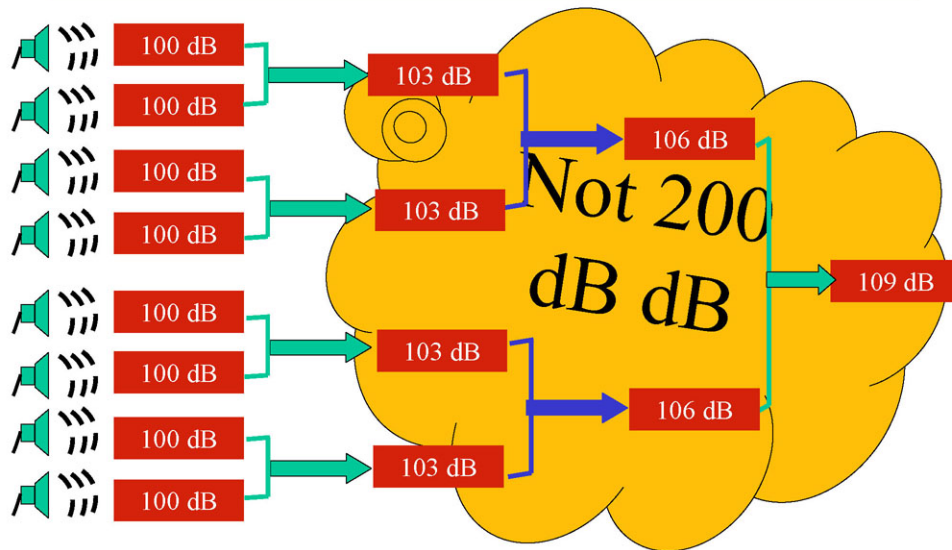
Although 120 dB Is Very Loud to Humans, It Is So Small That a Typical CFD Simulation Very Easily Loses the Sound Waves Among the Large Hydrodynamic Fluctuations

The Noise Energy of All the Worlds Population Shouting at Its Peak Voice Will Barely Be Enough to Fry an Egg!

How Much Sound?

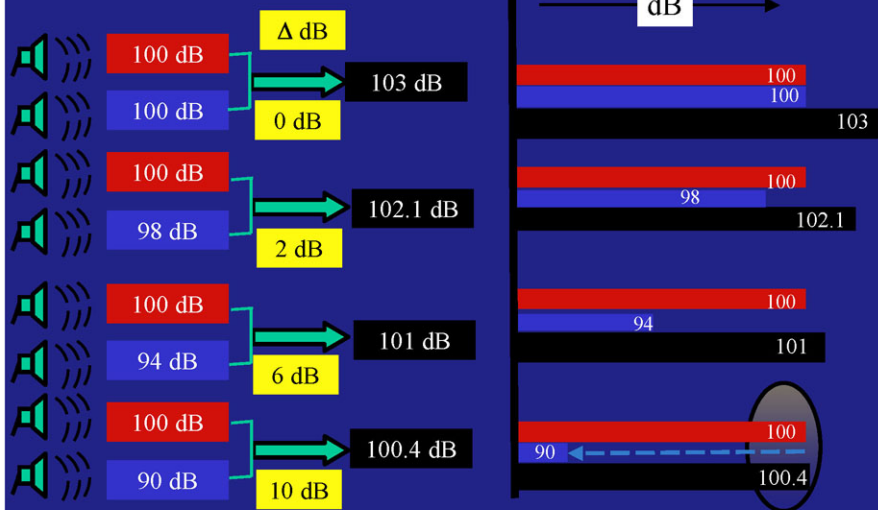
	Sound Pressure Level (dB)	Sound Pressure (pa)	Sound Intensity (watts/m ²)
30m from jet aircraft	140	200	100
Threshold of pain	130		10
	120	20	1
Chainsaw	110		0.1
Disco	100	2	0.01
	90		0.001
Curbside of busy road	80	0.2	0.0001
	70		0.00001
Conversational speech	60	0.02	0.000001
	50		0.0000001
	40	0.002	0.00000001
Quiet bedroom at night	30		0.000000001
TV studio Background	20	0.0002	0.00000000
	10		0.00000000001
Threshold of hearing	0	0.00002	0.000000000001

dB Addition



One Who Makes More Noise is the Boss!!

Lower Level has no effect if it is about 12 dB less than the higher level



Doubling the Jet Velocity increases Jet Noise
by 24 dB

$$I \sim (V/a_0)^8 \rightarrow \text{SPL} \sim 80 \text{ Log}_{10}(V/a_0)$$

$$I_1 \sim (V_1/a_0)^8$$

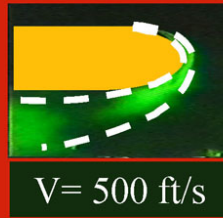
$$I_2 \sim (V_2/a_0)^8$$

$$I_2/I_1 = (V_2/V_1)^8$$

$$\text{SPL}_2 - \text{SPL}_1 = 10 \text{Log}_{10}(I_2/I_1) = 80 \text{ Log}_{10}(V_2/V_1)$$

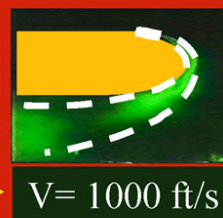
$$\text{Let } V_2 = 2V_1$$

$$\text{SPL}_2 - \text{SPL}_1 = 80 \text{ Log}_{10}(2V_1/V_1) = 80 \text{ Log}_{10}(2) = 24 \text{ dB}$$



V = 500 ft/s

Expect a
24 dB
Increase



V = 1000 ft/s

Doubling the Characteristic Length Scale
Increases Jet Noise by 6 dB

$$I \sim (L)^2 \rightarrow \text{SPL} \sim 20 \text{ Log}_{10}(L)$$

$$I_1 \sim (L_1)^2$$

$$I_2 \sim (L_2)^2$$

$$I_2/I_1 = (L_2/L_1)^2$$

$$10 \text{Log}_{10}(I_2/I_1) = 20 \text{ Log}_{10}(L_2/L_1)$$

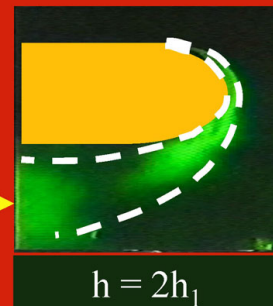
$$\text{Let } L_2 = 2L_1$$

$$\text{SPL}_2 - \text{SPL}_1 = 20 \text{ Log}_{10}(2) = 6 \text{ dB}$$



h = h₁

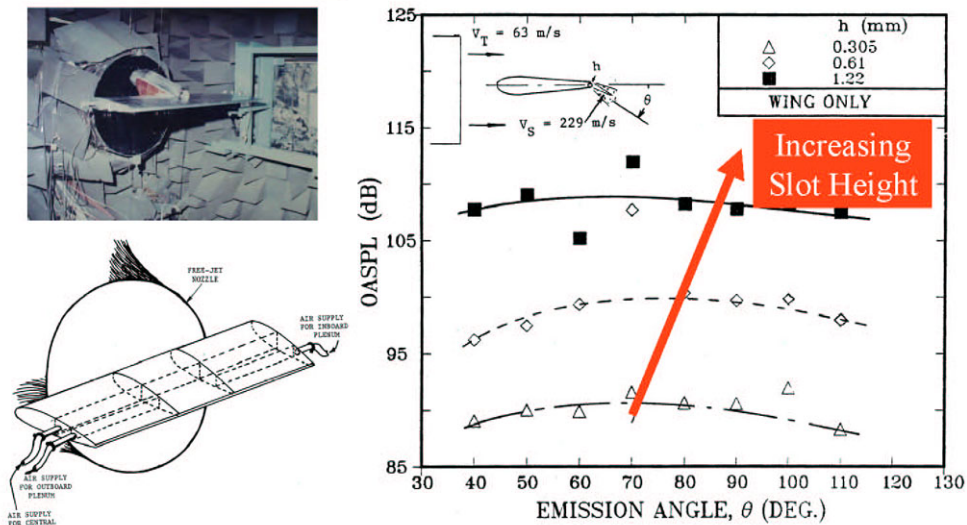
Expect a 6
dB Increase



h = 2h₁

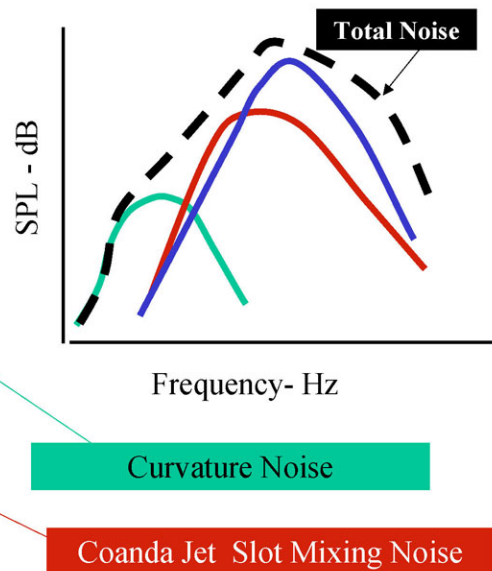
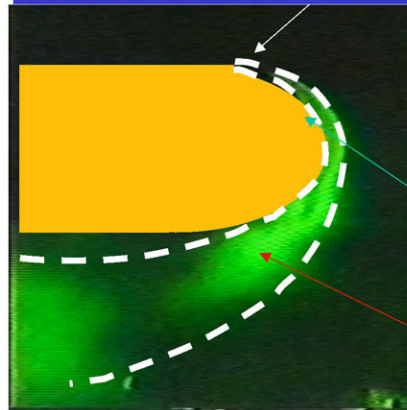
The Circulation Control Wing Noise for Three Slot Heights

(From Salikuddin, and Ahuja, *Journal of Aircraft*, Vol. 24, No. 1, pp 55-64, 1987)



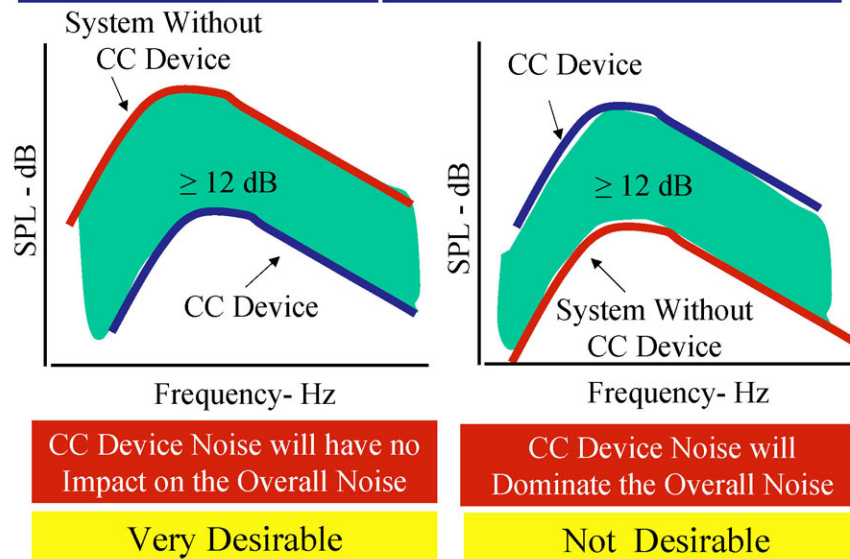
Noise Sources in a Coanda Slot Jet As Defined by Howe

Scattering of Turbulence
Near Field Pressures
Generated by the Exterior
and Interior Boundary
Layer at the Slot Lip

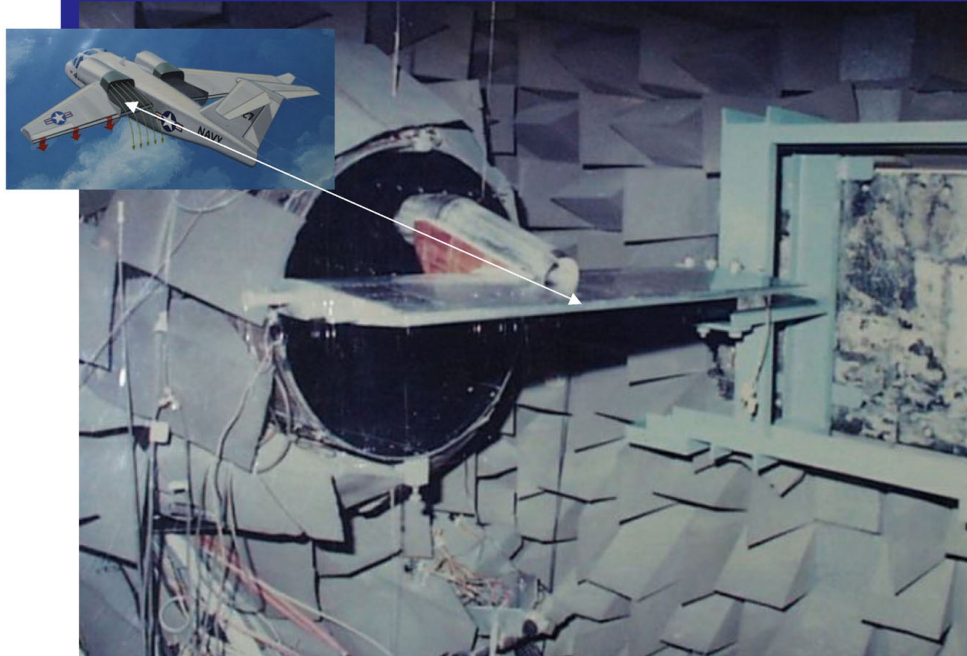


CC Applications Where Total Noise Increases

“One Who Makes Noise Is the Boss”
- Implications



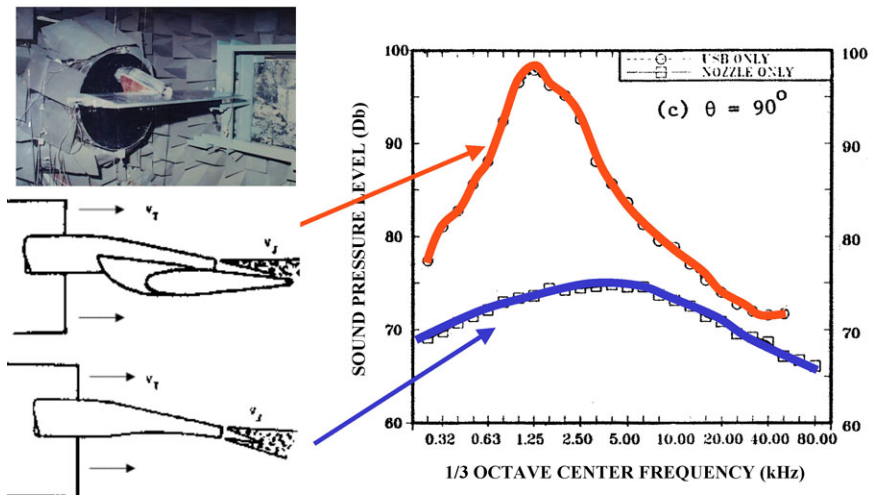
CCW with USB



Increase in Sound Pressure Levels on Mounting the Nozzle Over the Wing

$V_J = 176$ m/s, and $V_T = 0$ m/s,

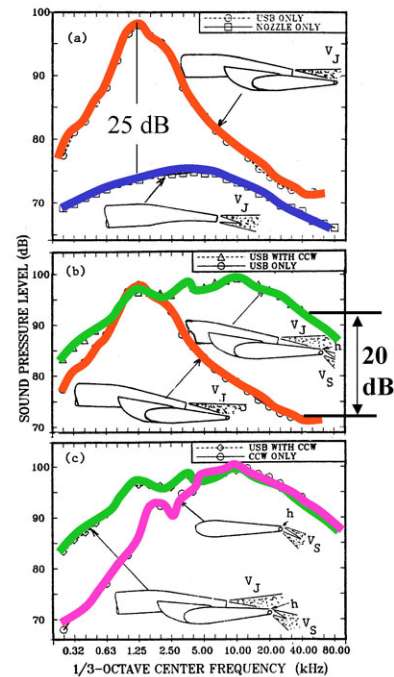
(From Salikuddin, and Ahuja, *Journal of Aircraft*, Vol. 24, No. 1, pp 55-64, 1987)



CCW Noise Dominates at High Frequencies in the USB Configuration

$V_T = 0.0 \text{ m/s}$,
 $V_J = 176 \text{ m/s}$,
 $V_S = 229 \text{ m/s}$,
 $h = 1.22 \text{ mm}$,
 and $\theta = 90^\circ$

(From Salikuddin, and Ahuja, *Journal of Aircraft*, Vol. 24, No. 1, pp 55-64, 1987)



Increased Noise in USB with CC

- The introduction of circulation control can involve large increases in the noise generated by turbulence interacting with the airfoil.
- Thus, upper surface blowing greatly increases turbofan jet noise (by 25 dB or more), caused by the “diffraction” of jet shear layer pressures by the wing trailing edge;
- *Additional* increases of as much as 20 dB are observed at high frequencies when CC is applied to deflect the jet for thrust vectoring,
- Presumably produced by the interaction of turbulence in the (near sonic) Coanda jet with the jet slot

CC Applications Where Total Noise Decreases

Comparison of Existing High-Lift Systems: Mechanical vs Pneumatic



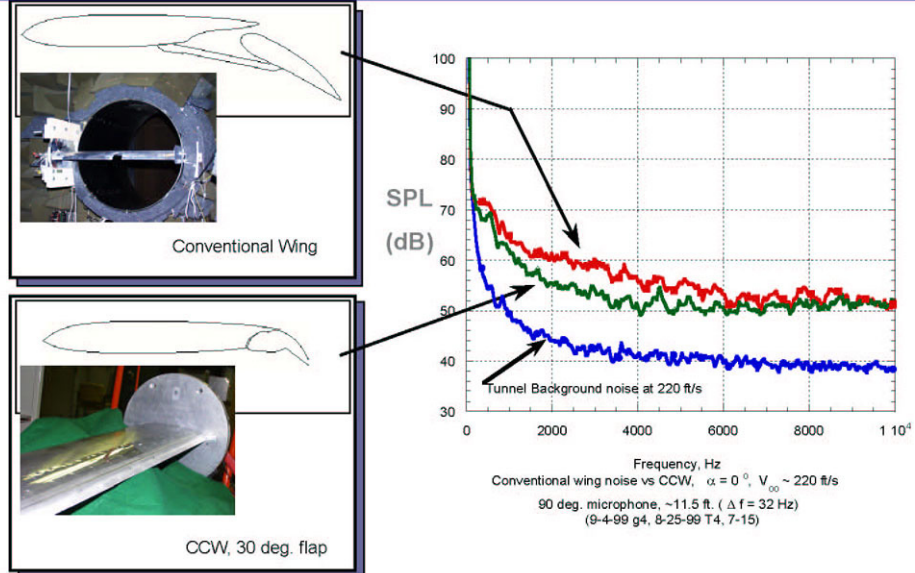
Mechanical Multi-Slotted Flaps:
Heavy, Complex, Draggy
Maximum CL = 3-5, Noisy?



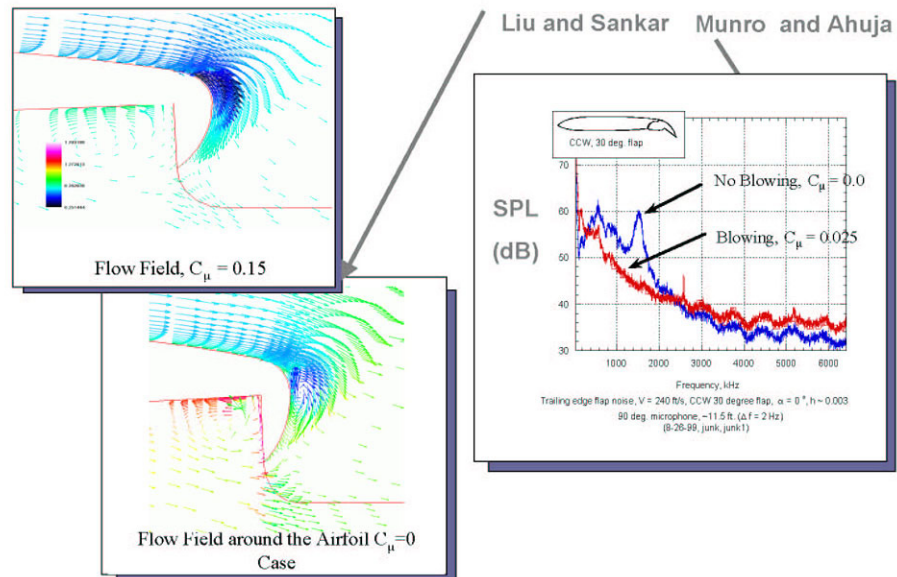
Pneumatic CCW:
Light, Simple, Variable CD
Maximum CL= 4 -7
Reduced Ground Rolls

Reduced Noise
Footprint?

Noise Reductions at Constant Lift (Conventional Wing vs. CCW Wing)

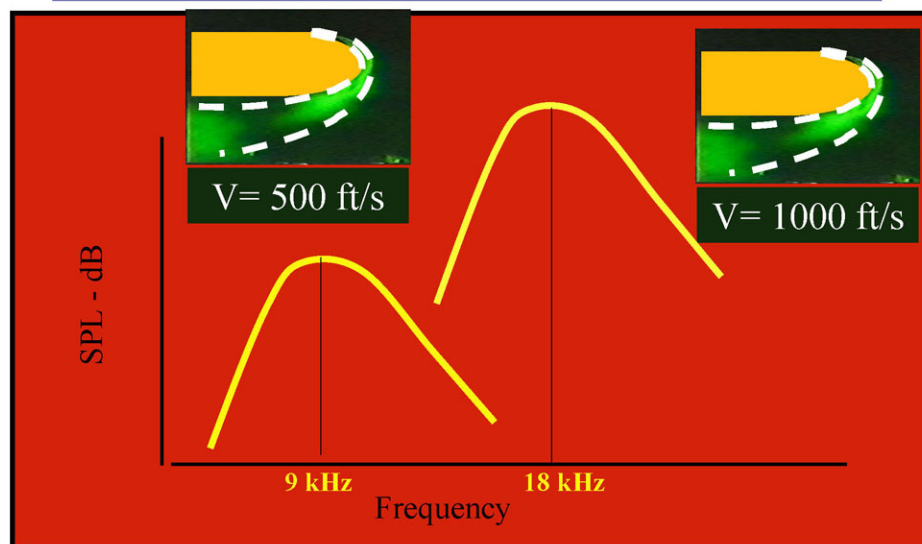


Suppression of Vortex Shedding Noise by Blowing

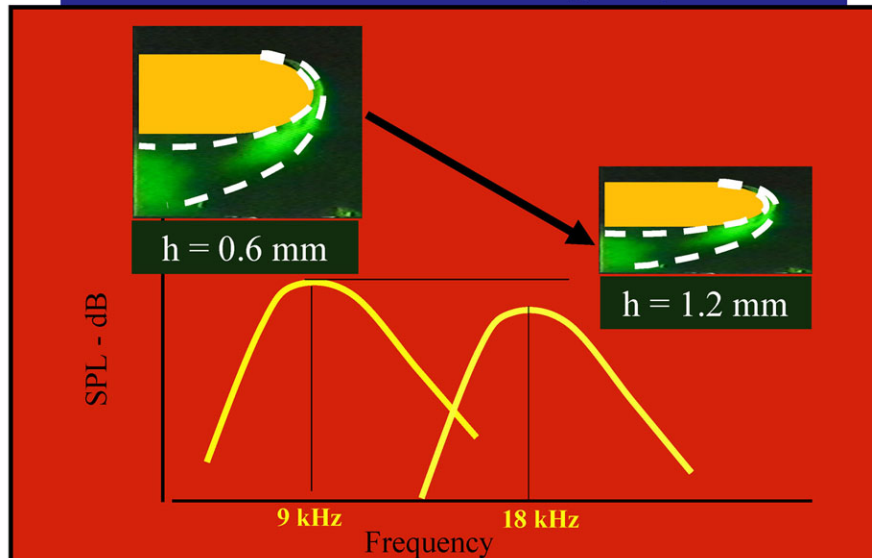


Potential of Exploiting High Frequency Noise of CC Devices to Our Advantage

Doubling the Jet Velocity Should Double the
Peak Frequency



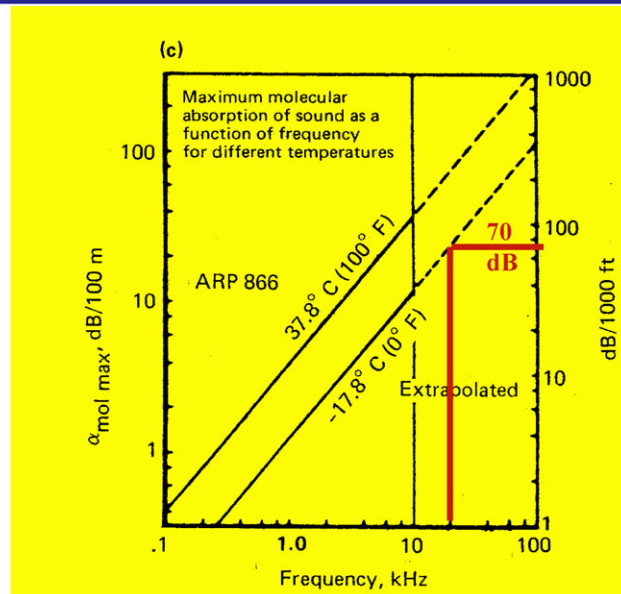
Decreasing the Slot Height by a Half Should
Double the Peak Frequency



It Maybe OK even if the
Total Noise Increases
Provided
the Slot Dimension and
Velocity is Selected
Carefully Based Upon
Aeroacoustics Understanding

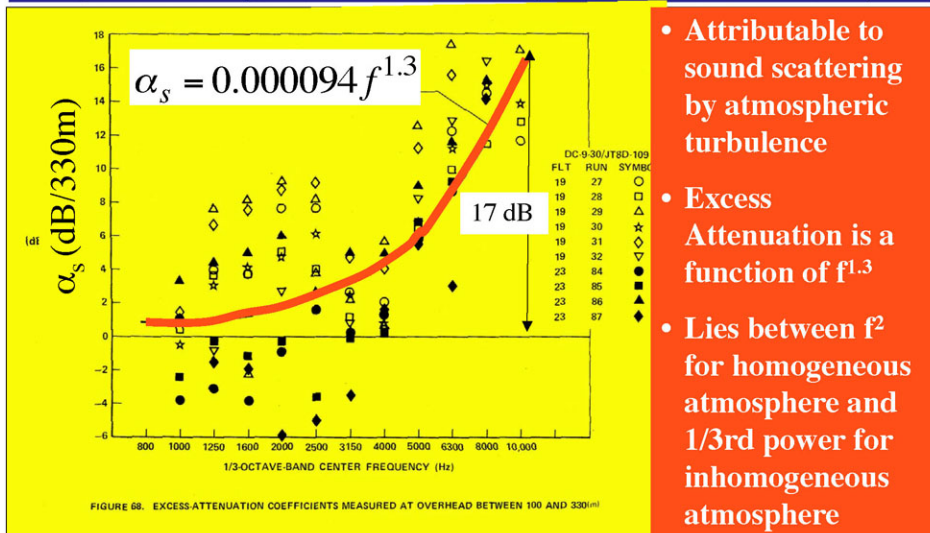
Atmospheric Absorption As a Function of Temperature

(Chun, Berman and Cowan, Boeing Final Report for Contract NAS3-18539 to NASA Glenn, 1976)

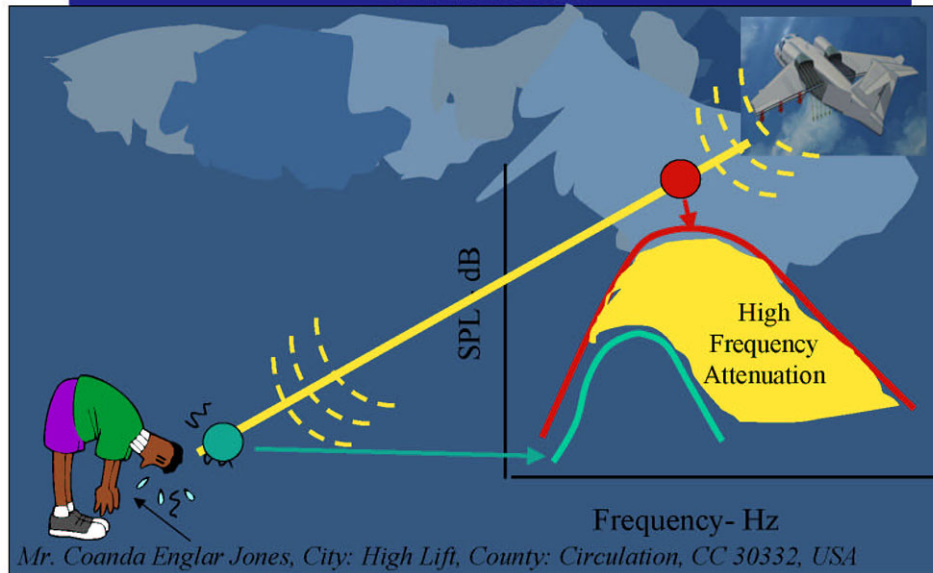


Excess Attenuation Measured at Overhead between 100 and 330 Meters

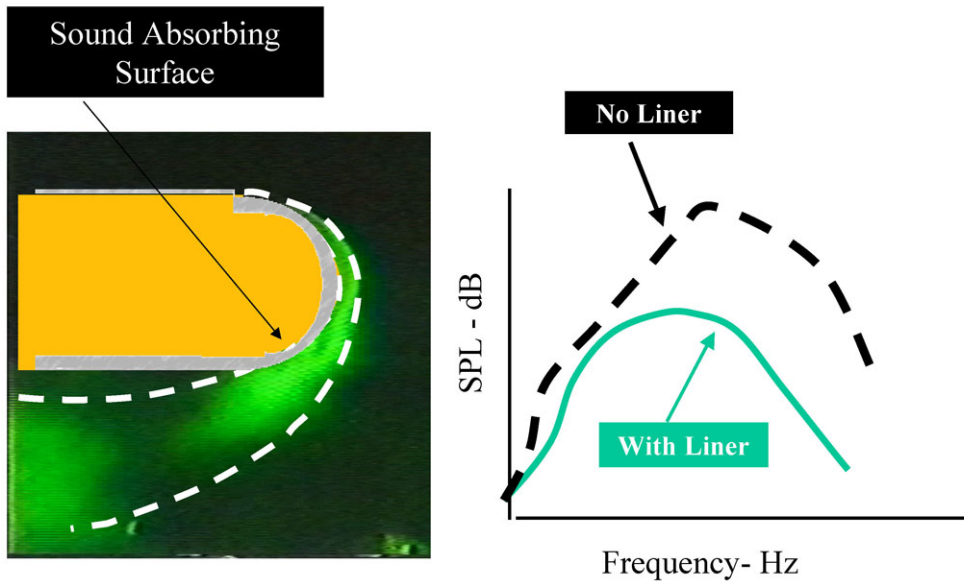
(From: Blankenship, Low, Watkins and Merriman (NASA CR 134954, MDC-J7708, 1977))



Atmospheric Attenuation of High Frequency CCW Noise

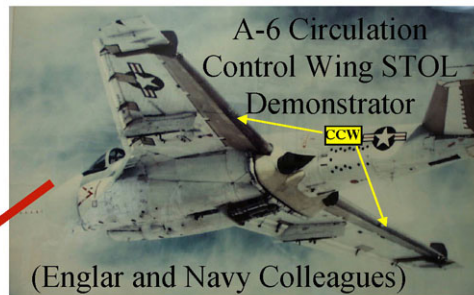


Absorbing High Frequency Noise Via a Lined Coanda Surface



Virtual Noise Reduction Via CC Technology

Virtual Noise Reduction Via CCW



140% Increase in Usable C_L

Reduced Jet Engine and Interior Noise

30 - 40% Reduction in Take
Off and Approach Speeds

Implies Reduced Airframe Noise

60 - 65 % Reduction in Take
Off and Landing Ground Roll

Implies Reduced Noise Foot Print

75 % Increase in Lifiable Take-
Off Payload

Implies Less Number of Operations and
Hence Less Day-Night Noise Levels

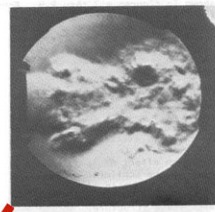
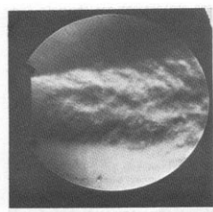
Significantly Less Aircraft
Weight

Implies Reduced Sonic Boom Signature
for Supersonic Aircraft

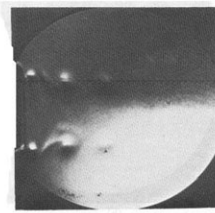
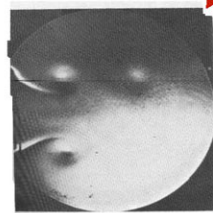
Flow/Acoustic Interactions in Curved Shear Layers of Coanda Jets

Instability Waves in Acoustically Excited Jets

Unexcited
- Single Shot



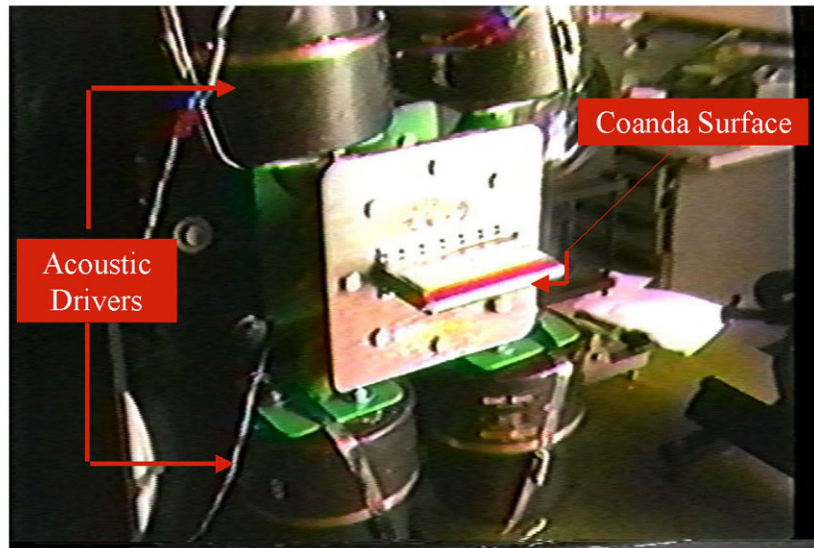
Excited
- Single Shot



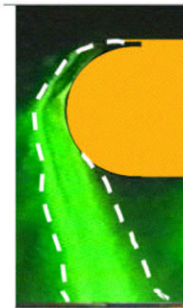
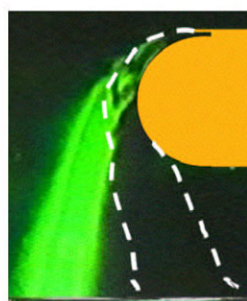
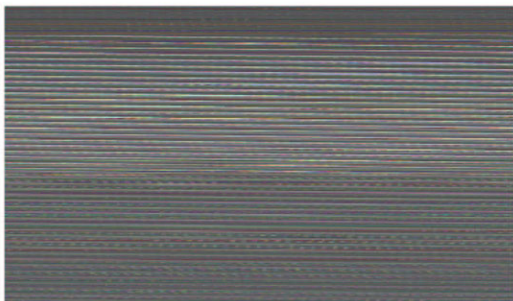
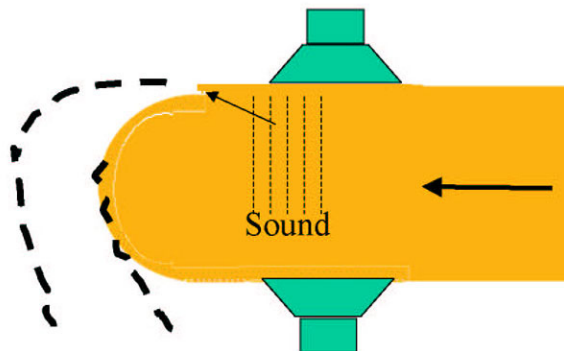
Photographically averaged

Phase-Locked Averaged Shots at two Excitation Frequencies

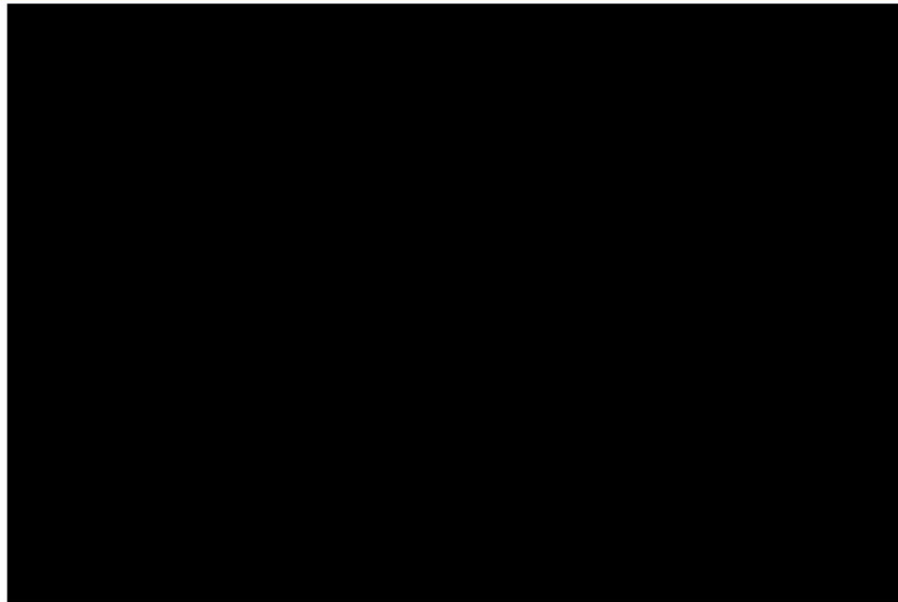
Flow/Acoustic Interactions in Coanda Flows



Flow/Acoustic
Interactions in
Coanda Flows
 $f = 1862 \text{ Hz}$



Phase-Locked Schlieren Flow Visualization



Concluding Remarks

- Aeroacoustic Studies to Date are Limited and Additional Work Should be Carried Out
- Need a Detailed Parametric Study
- Carry Out a Systems Study to Understand the Impact of CCW on Noise Footprint
- Study Role of CCW on Sonic Boom Minimization
- Understand and Monopolize on the Role of Virtual Noise Reduction Via CCW
- Understand the Role of Flow/Acoustic Interactions
- Explore Use for Non-Aerospace Applications

questions?

REPORT DOCUMENTATION PAGE					Form Approved OMB No. 0704-0188	
<p>The public reporting burden for this collection of information is estimated to average 1 hour per response, including the time for reviewing instructions, searching existing data sources, gathering and maintaining the data needed, and completing and reviewing the collection of information. Send comments regarding this burden estimate or any other aspect of this collection of information, including suggestions for reducing this burden, to Department of Defense, Washington Headquarters Services, Directorate for Information Operations and Reports (0704-0188), 1215 Jefferson Davis Highway, Suite 1204, Arlington, VA 22202-4302. Respondents should be aware that notwithstanding any other provision of law, no person shall be subject to any penalty for failing to comply with a collection of information if it does not display a currently valid OMB control number.</p> <p>PLEASE DO NOT RETURN YOUR FORM TO THE ABOVE ADDRESS.</p>						
1. REPORT DATE (DD-MM-YYYY)		2. REPORT TYPE			3. DATES COVERED (From - To)	
01- 06 - 2005		Conference Publication				
4. TITLE AND SUBTITLE Proceedings of the 2004 NASA/ONR Circulation Control Workshop				5a. CONTRACT NUMBER		
				5b. GRANT NUMBER		
				5c. PROGRAM ELEMENT NUMBER		
6. AUTHOR(S) Jones, Gregory S.; and Joslin, Ronald D. (Editors)				5d. PROJECT NUMBER		
				5e. TASK NUMBER		
				5f. WORK UNIT NUMBER 23-762-55-ME		
7. PERFORMING ORGANIZATION NAME(S) AND ADDRESS(ES) NASA Langley Research Center Hampton, VA 23681-2199				8. PERFORMING ORGANIZATION REPORT NUMBER L-18395A		
9. SPONSORING/MONITORING AGENCY NAME(S) AND ADDRESS(ES) National Aeronautics and Space Administration Washington, DC 20546-0001				10. SPONSOR/MONITOR'S ACRONYM(S) NASA		
				11. SPONSOR/MONITOR'S REPORT NUMBER(S) NASA/CP-2005-213509/PT1		
12. DISTRIBUTION/AVAILABILITY STATEMENT Unclassified - Unlimited Subject Category 02 Availability: NASA CASI (301) 621-0390						
13. SUPPLEMENTARY NOTES An electronic version can be found at http://ntrs.nasa.gov						
14. ABSTRACT As technological advances influence the efficiency and effectiveness of aerodynamic and hydrodynamic applications, designs and operations, this workshop was intended to address the technologies, systems, challenges and successes specific to Coanda driven circulation control in aerodynamics and hydrodynamics. A major goal of this workshop was to determine the 2004 state-of-the-art in circulation control and understand the roadblocks to its application. The workshop addressed applications, CFD, and experiments related to circulation control, emphasizing fundamental physics, systems analysis, and applied research. The workshop consisted of 34 single session oral presentations and written papers that focused on Naval hydrodynamic vehicles (e.g. submarines), Fixed Wing Aviation, V/STOL platforms, propulsion systems (including wind turbine systems), ground vehicles (automotive and trucks) and miscellaneous applications (e.g., poultry exhaust systems and vacuum systems). Several advanced CFD codes were benchmarked using a two-dimensional NCCR circulation control airfoil. The CFD efforts highlighted inconsistencies in turbulence modeling, separation and performance predictions.						
15. SUBJECT TERMS Circulation control; Coanda; High lift; Powered lift; Super-circulation; V/STOL; ESTOL; Advanced pneumatic flow control; Active flow control; CFD benchmarking						
16. SECURITY CLASSIFICATION OF:			17. LIMITATION OF ABSTRACT	18. NUMBER OF PAGES	19a. NAME OF RESPONSIBLE PERSON	
a. REPORT	b. ABSTRACT	c. THIS PAGE			STI Help Desk (email: help@sti.nasa.gov)	
U	U	U	UU	565	19b. TELEPHONE NUMBER (Include area code) (301) 621-0390	